frontiers | Research Topics

Polymeric microarchitectures for tissue regeneration and drug screening

Edited by
Ranjith Kumar Kankala, Y. Shrike Zhang, Lifeng Kang and Luigi Ambrosio

Published in
Frontiers in Bioengineering and Biotechnology

ISSN 1664-8714
ISBN 978-2-83251-697-3
DOI 10.3389/978-2-83251-697-3

About Frontiers

Frontiers is more than just an open access publisher of scholarly articles: it is a pioneering approach to the world of academia, radically improving the way scholarly research is managed. The grand vision of Frontiers is a world where all people have an equal opportunity to seek, share and generate knowledge. Frontiers provides immediate and permanent online open access to all its publications, but this alone is not enough to realize our grand goals.

Frontiers journal series

The Frontiers journal series is a multi-tier and interdisciplinary set of open-access, online journals, promising a paradigm shift from the current review, selection and dissemination processes in academic publishing. All Frontiers journals are driven by researchers for researchers; therefore, they constitute a service to the scholarly community. At the same time, the *Frontiers journal series* operates on a revolutionary invention, the tiered publishing system, initially addressing specific communities of scholars, and gradually climbing up to broader public understanding, thus serving the interests of the lay society, too.

Dedication to quality

Each Frontiers article is a landmark of the highest quality, thanks to genuinely collaborative interactions between authors and review editors, who include some of the world's best academicians. Research must be certified by peers before entering a stream of knowledge that may eventually reach the public - and shape society; therefore, Frontiers only applies the most rigorous and unbiased reviews. Frontiers revolutionizes research publishing by freely delivering the most outstanding research, evaluated with no bias from both the academic and social point of view. By applying the most advanced information technologies, Frontiers is catapulting scholarly publishing into a new generation.

What are Frontiers Research Topics?

Frontiers Research Topics are very popular trademarks of the *Frontiers journals series*: they are collections of at least ten articles, all centered on a particular subject. With their unique mix of varied contributions from Original Research to Review Articles, Frontiers Research Topics unify the most influential researchers, the latest key findings and historical advances in a hot research area.

Find out more on how to host your own Frontiers Research Topic or contribute to one as an author by contacting the Frontiers editorial office: frontiersin.org/about/contact

Polymeric microarchitectures for tissue regeneration and drug screening

Topic editors

Ranjith Kumar Kankala — Huaqiao University, China

Y. Shrike Zhang — Harvard Medical School, United States

Lifeng Kang — The University of Sydney, Australia

Luigi Ambrosio — Institute of Polymers, Composite and Biomaterials, Department of Chemical Sciences and Materials Technologies, National Research Council (CNR), Italy

Citation

Kankala, R. K., Zhang, Y. S., Kang, L., Ambrosio, L., eds. (2023). *Polymeric microarchitectures for tissue regeneration and drug screening*. Lausanne: Frontiers Media SA. doi: 10.3389/978-2-83251-697-3

Table of contents

frontiers | Frontiers in Bioengineering and Biotechnology

TYPE Editorial
PUBLISHED 02 February 2023
DOI 10.3389/fbioe.2023.1144991

OPEN ACCESS

EDITED AND REVIEWED BY
Hasan Uludag,
University of Alberta, Canada

*CORRESPONDENCE
Ranjith Kumar Kankala,
ranjithkankala@hqu.edu.cn

SPECIALTY SECTION
This article was submitted to Biomaterials, a section of the journal Frontiers in Bioengineering and Biotechnology

RECEIVED 15 January 2023
ACCEPTED 23 January 2023
PUBLISHED 02 February 2023

CITATION
Kankala RK, Zhang YS, Kang L and Ambrosio L (2023), Editorial: Polymeric microarchitectures for tissue regeneration and drug screening.
Front. Bioeng. Biotechnol. 11:1144991.
doi: 10.3389/fbioe.2023.1144991

Editorial: Polymeric microarchitectures for tissue regeneration and drug screening

Ranjith Kumar Kankala[1]*, Yu Shrike Zhang[2], Lifeng Kang[3] and Luigi Ambrosio[4]

[1]College of Chemical Engineering, Huaqiao University, Xiamen, Fujian, China, [2]Harvard Medical School, Boston, MA, United States, [3]Faculty of Medicine and Health, The University of Sydney, Darlington, NSW, Australia, [4]National Research Council (CNR), Roma, Lazio, Italy

KEYWORDS

microfluidics, biofabrication, tissue engineering, minimally invasive, cell delivery, drug development

Editorial on the Research Topic
Polymeric microarchitectures for tissue regeneration and drug screening

Tissue engineering aims to restore malfunctioned tissues by fabricating three-dimensional (3D) biomimetic tissue substitutes that emulate their native counterparts. This field has garnered enormous interest from researchers due to increased organ replacement therapies and the shortage of donors (Langer and Vacanti, 1993). Several advancements have resulted in the generation of highly organized 3D scaffolds to improve the control over the microenvironment for tissue growth, such as biocompatible fibrous scaffolds, photo-cross-linkable hydrogels, and 3D biodegradable porous scaffolds (Martin et al., 2004; Asakawa et al., 2010). Numerous efforts in fabricating artificial tissue constructs have been dedicated to repairing tissue damage and highlighting the significance of vascularization and innervation on tissue maturation (Leijten et al., 2016). Over the past few decades, diverse preclinical screening methods have been explored to demonstrate the pharmacological and toxicological characteristics of various therapeutic drugs. The traditional cell monolayer-based 2D approach often suffers from limitations in recapitulating the highly complex, natural extracellular matrix (ECM)-like microenvironment. Although the 3D scaffold-free cell aggregates emerged as an alternative to 2D monolayers, they fail to recapitulate critical attributes of the natural tumor microenvironment and poor survival rates of cells.

The implantation of bulk scaffolds for tissue repair often utilizes complex surgical procedures, which may generate severe inflammatory reactions resulting in the harsh microenvironment, where the survival of cells remains low (Ferrari et al., 1998; Kankala et al., 2018; Kankala et al., 2019). In this context, several biodegradable polymeric microspheres with highly open and interconnected pores have been reported, as these carriers enable exceptional cell encapsulation efficacy in their entire volume and facilitate their minimally invasive delivery. Notably, these cell-laden microspheres could further aggregate and form microtissues for tissue engineering applications. Utilizing the 3D polymeric microarchitectures harbored with cells offer enormous advantages in terms of effective cell-harboring and carrying capacities, enabling the supply of oxygen and nutrients for cell proliferation (Van Wezel, 1967; Khademhosseini et al., 2006; Jiang et al., 2016). These injectable modularized units of cell-loaded microspheres, cell lamellae, and cell-laden microgels, obtained using various biofabrication strategies, offer easy packing, minimally invasive, and improved cell retention capacity than the direct injection of cells alone (Khademhosseini et al., 2006).

Compared to traditional 2D monolayer and 3D cellular spheroids for drug screening, these cellularized polymeric microarchitectures reflect a more accurate tumor microenvironment in cellular interactions and ECM remolding toward drug evaluation and cancer research. In recent times, these innovative polymeric architectures have been explicitly applied to investigate the pharmacological and toxicological characteristics of drugs (Brancato et al., 2017; Pradhan et al., 2017).

This proposed thematic Research Topic entitled "Polymeric Microarchitectures for Tissue Regeneration and Drug Screening" is intended to explore the advancements in various innovative synthetic strategies and plausible mechanistic elucidations towards the development of polymeric microarchitectures for tissue engineering and drug screening applications. In this context, this thematic Research Topic collects articles exploring the opportunities and challenges relevant to scale-up and the clinical translation of these innovative scaffolding systems with considerations of biosafety and degradability. Moreover, this Research Topic is intended to present mechanistic views and understanding of interactions within the biological interfaces to accelerate the efficacy of polymeric microsystems through precise cell delivery and screening of therapeutics at different levels.

Prof. Niu and colleagues demonstrate the fabrication of 3D microscaffolds using the silk fibroin (SF) and chitosan (CS), as well as 1-ethyl-3-(3-dimethylaminopropyl)-carbodiimide (EDC) and sodium tripolyphosphate (TPP) as cross-linking agents (Niu et al., 2022). These EDC cross-linked microscaffolds display more uniform pores with great interconnection than the TPP cross-linked scaffolds and exhibit a water absorption ratio (percent weight change of material due to absorbed water) of around 1,000%, as well as a swelling ratio of about 72%. These spatial structures and physical properties can provide excellent adhesion sites and sufficient nutrients for cell growth. Moreover, both the cancer cell lines (LoVo and MDA-MB-231 cells) cultured on the EDC cross-linked scaffold exhibit good adhesion and spreading. The authors propose that the SF/CS microscaffolds can provide a promising *in vitro* platform for the efficacy prediction and sensitivity screening of various anticancer drugs.

The review article from Prof. Fenelon and colleagues aims to present different applications of pullulan and dextran-based biomaterials for bone tissue engineering (Ahmed Omar et al., 2022). Following the PRISMA guidelines, this article analyzes the published articles from various databases, including Pubmed, Scopus, and Web of Science. This article systematically highlights the strategies for bone regeneration capacity and fabrication processes, the addition of biological elements, and their limitations for bone tissue engineering.

Prof. Chiono and coworkers present the generation of electroconductive hydrogels ECHs based on photo-crosslinked blends of polyethylene glycol diacrylate (PEGDA) and gelatin at different PEGDA:gelatin ratios (1:1, 1.5:1, and 2:1 wt./wt.), and containing poly (3,4-ethylenedioxythiophene):poly (styrene sulfonate) (PEDOT:PSS) (0.0, 0.1, 0.3, and 0.5% w/v) (Testore et al., 2022). The authors demonstrate that using the biocomponent gelatin as a photoinitiator enables its successful incorporation into the hydrogel network. Moreover, adding PEDOTs with reduced photo-crosslinking time increases their surface features and electronic properties, enabling their potential as electrocondutable photo-curable PEGDA-gelatin/PEDOT:PSS hydrogels for cardiac tissue engineering.

Prof. Chen and colleagues demonstrate the approach of generating novel liver organoids *via* micropatterning technique, enabling the reproducible and high throughput formation of fetal liver organoids (Xu et al., 2022). These architectures with uniform morphology and deterministic size recapitulate several critical features, including fetal liver-specific gene and protein expression, glycogen storage, lipid accumulation, and protein secretion.

Prof. Tai and coworkers present the synthesis of a new chiral cross-linker for controlling the matrix morphology of peptide conformational imprints (PCIs) on magnetic particles (PCIMPs) to stabilize their recognition capability (Kanubaddi et al., 2022). These PCIMPs with helical cavities complement the PAP structure to adsorb specifically at the targeted position of papain, showing the best binding parameters to the PAP with Kd = 0.087 μM and Bmax = 4.56 μM.

Prof. Jiang and colleagues demonstrate the encapsulation of bone marrow mesenchymal stem cells (BMSCs) in alginate-chitosan-alginate microcapsules (Yuan et al., 2022). The authors systematically characterize various parameters, suggesting that the designed scaffold displays high porosity and injectability with good collapsibility and compressive strength. Owing to better new bone formation, these microcapsules combined with calcium phosphate bone cement show excellent application prospects as bone engineering materials.

The review article from Prof. X. Wang and colleagues presents the application of SF-based scaffolds for bone regeneration due to excellent biocompatibility, mechanical properties, controllable biodegradability, and structural tunability (Wu et al., 2022). The authors summarize the generation and modification of SF scaffolds and their interactions with tissues and cells toward osteogenesis.

Prof. Tunesi and coworkers propose a highly controllable method to optimize the printability of cross-linked pectin gels with $CaCO_3$ (Merli et al., 2022). Specifically, the authors achieve control over the pH as a parameter to generate multiple (pH-dependent) crosslinking kinetics without varying hydrogel composition. Further, the 3D-bioprinted pectin scaffolds show successful results for neural cell culture.

Prof. H. Wang and colleagues exploit the autologous crystallization ability of poly (ε-caprolactone) (PCL) scaffolds to generate nanoneedle arrays (Ren et al., 2022). The surface of nanoneedles coated with polydopamine shows excellent adhesion, spreading, and proliferation abilities of bone marrow mesenchymal stem cells (BMMSCs). The authors demonstrate the positive correlation between the strength of cell-cell interactions, further revealing their scope for designing tissue engineering scaffolds.

Prof. Della Porta and her group demonstrate the fabrication of fibrin scaffolds to populate two different kinds of cells, i.e., BMMSCs and skeletal myoblasts (Scala et al., 2022). Further, the addition of Peripheral blood mononuclear cells (PBMCs) fraction from blood filtration improves the influence of myogenesis. The presence of PBMCs enables the significant downregulation of pro-inflammatory cytokine gene expression. This biomimetic environment provides an excellent tool for investigating the cellular crosstalk and the influence of PBMC in myogenesis.

In the review by Prof. Kankala and colleagues, various kinds of injectable microscale modularized units by biofabrication approaches as ideal delivery vehicles for cells, and various growth factors are described (Duan et al., 2023). The authors emphasize the progress of various microcarriers that potentially pushed the borders of tissue regeneration, highlighting their design, ability to deliver cells, and substantial tissue growth *in situ* and *in vivo* from different viewpoints of materials chemistry and biology. Finally, the perspectives highlighting current challenges and expanding opportunities of these innovative carriers are summarized.

This thematic Research Topic presented several articles exploring the advancements in various innovative synthetic strategies and plausible mechanistic elucidations toward developing polymeric microarchitectures for tissue engineering and drug screening applications. As anticipated, this thematic Research Topic has collected articles presenting various innovative scaffolding systems with considerations of biosafety and degradability along with aspects of current challenges and expanding opportunities of these innovative polymeric carriers for cell delivery applications.

Author contributions

All authors listed have made a substantial, direct, and intellectual contribution to the work and approved it for publication.

Conflict of interest

LA was employed by National Research Council (CNR).

The remaining authors declare that the research was conducted in the absence of any commercial or financial relationships that could be construed as a potential conflict of interest.

Publisher's note

All claims expressed in this article are solely those of the authors and do not necessarily represent those of their affiliated organizations, or those of the publisher, the editors and the reviewers. Any product that may be evaluated in this article, or claim that may be made by its manufacturer, is not guaranteed or endorsed by the publisher.

References

Asakawa, N., Shimizu, T., Tsuda, Y., Sekiya, S., Sasagawa, T., Yamato, M., et al. (2010). Pre-vascularization of *in vitro* three-dimensional tissues created by cell sheet engineering. *Biomaterials* 31, 3903–3909. doi:10.1016/j.biomaterials.2010.01.105

Brancato, V., Comunanza, V., Imparato, G., Corà, D., Urciuolo, F., Noghero, A., et al. (2017). Bioengineered tumoral microtissues recapitulate desmoplastic reaction of pancreatic cancer. *Acta Biomater.* 49, 152–166. doi:10.1016/j.actbio.2016.11.072

Ferrari, G., Cusella-De, A. G., Coletta, M., Paolucci, E., Stornaiuolo, A., Cossu, G., et al. (1998). Muscle regeneration by bone marrow-derived myogenic progenitors. *Science* 279, 1528–1530. doi:10.1126/science.279.5356.1528

Jiang, W., Li, M., Chen, Z., and Leong, K. W. (2016). Cell-laden microfluidic microgels for tissue regeneration. *Lab a Chip* 16, 4482–4506. doi:10.1039/c6lc01193d

Kankala, R. K., Zhao, J., Liu, C.-G., Song, X.-J., Yang, D.-Y., Zhu, K., et al. (2019). Highly porous microcarriers for minimally invasive *in situ* skeletal muscle cell delivery. *Small* 15, 1901397. doi:10.1002/smll.201901397

Kankala, R. K., Zhu, K., Sun, X.-N., Liu, C.-G., Wang, S.-B., and Chen, A.-Z. (2018). Cardiac tissue engineering on the nanoscale. *ACS Biomaterials Sci. Eng.* 4, 800–818. doi:10.1021/acsbiomaterials.7b00913

Khademhosseini, A., Langer, R., Borenstein, J., and Vacanti, J. P. (2006). Microscale technologies for tissue engineering and biology. *Proc. Natl. Acad. Sci. U. S. A.* 103, 2480–2487. doi:10.1073/pnas.0507681102

Langer, R., and Vacanti, J. P. (1993). Tissue engineering. *Science* 260, 920–926. doi:10.1126/science.8493529

Leijten, J., Rouwkema, J., Zhang, Y. S., Nasajpour, A., Dokmeci, M. R., and Khademhosseini, A. (2016). Advancing tissue engineering: A tale of nano-micro-and macroscale integration. *Small* 12, 2130–2145. doi:10.1002/smll.201501798

Martin, I., Wendt, D., and Heberer, M. (2004). The role of bioreactors in tissue engineering. *Trends Biotechnol.* 22, 80–86. doi:10.1016/j.tibtech.2003.12.001

Pradhan, S., Clary, J. M., Seliktar, D., and Lipke, E. A. (2017). A three-dimensional spheroidal cancer model based on PEG-fibrinogen hydrogel microspheres. *Biomaterials* 115, 141–154. doi:10.1016/j.biomaterials.2016.10.052

Testore, D., Zoso, A., Kortaberria, G., Sangermano, M., and Chiono, V. (2022). Electroconductive photo-curable PEGDA-gelatin/PEDOT:PSS hydrogels for prospective cardiac tissue engineering application. *Front. Bioeng. Biotechnol.* 10, 897575. doi:10.3389/fbioe.2022.897575

Van Wezel, A. L. (1967). Growth of cell-strains and primary cells on micro-carriers in homogeneous culture. *Nature* 216, 64–65. doi:10.1038/216064a0

frontiers in Bioengineering and Biotechnology

ORIGINAL RESEARCH
published: 08 March 2022
doi: 10.3389/fbioe.2022.800830

Three-Dimensional Silk Fibroin/Chitosan Based Microscaffold for Anticancer Drug Screening

Hui Niu[1,2], Jiarui Xiao[2], Xiaoli Lou[1,2], Lingling Guo[2], Yongsheng Zhang[1], Runhuai Yang[3], Hao Yang[4], Shouli Wang[2] and Fuzhou Niu[5]**

[1]Department of Pathology, Second Affiliated Hospital of Soochow University, Suzhou, China, [2]School of Biology and Basic Medical Sciences, Soochow University, Suzhou, China, [3]School of Life Science, Anhui Medical University, Hefei, China, [4]Robotics and Microsystems Center, College of Mechanical and Electrical Engineering, Soochow University, Suzhou, China, [5]School of Mechanical Engineering, Suzhou University of Science and Technology, Suzhou, China

OPEN ACCESS

Edited by:
Masoud Mozafari,
University of Toronto, Canada

Reviewed by:
Feng Zhang,
Soochow University, China
Bianca Galateanu,
University of Bucharest, Romania
Payam Zarrintaj,
University of Montana, United States

***Correspondence:**
Shouli Wang
wangsoly112@hotmail.com
Fuzhou Niu
fzniu@usts.edu.cn

Specialty section:
This article was submitted to Biomaterials, a section of the journal Frontiers in Bioengineering and Biotechnology

Received: *24 October 2021*
Accepted: *16 February 2022*
Published: *08 March 2022*

Citation:
Niu H, Xiao J, Lou X, Guo L, Zhang Y, Yang R, Yang H, Wang S and Niu F (2022) Three-Dimensional Silk Fibroin/Chitosan Based Microscaffold for Anticancer Drug Screening. Front. Bioeng. Biotechnol. 10:800830. doi: 10.3389/fbioe.2022.800830

Traditional monolayer cell cultures often fail to accurately predict the anticancer activity of drug candidates, as they do not recapitulate the natural microenvironment. Recently, three-dimensional (3D) culture systems have been increasingly applied to cancer research and drug screening. Materials with good biocompatibility are crucial to create a 3D tumor microenvironment involved in such systems. In this study, natural silk fibroin (SF) and chitosan (CS) were selected as the raw materials to fabricate 3D microscaffolds; Besides, sodium tripolyphosphate (TPP), and 1-ethyl-3-(3-dimethylaminopropyl)-carbodiimide (EDC) were used as cross-linking agents. The physicochemical properties of obtained scaffolds were characterized with kinds of testing methods, including emission scanning electron microscopy, x-ray photoelectron spectroscopy, fourier transform infrared spectroscopy, water absorption, and swelling ratio analysis. Cancer cell lines (LoVo and MDA-MB-231) were then seeded on scaffolds for biocompatibility examination and drug sensitivity tests. SEM results showed that EDC cross-linked scaffolds had smaller and more uniform pores with great interconnection than the TPP cross-linked scaffolds, and the EDC cross-linked scaffold exhibited a water absorption ratio around 1000% and a swelling ratio of about 72%. These spatial structures and physical properties could provide more adhesion sites and sufficient nutrients for cell growth. Moreover, both LoVo and MDA-MB-231 cells cultured on the EDC cross-linked scaffold exhibited good adhesion and spreading. CCK8 results showed that increased chemotherapeutic drug sensitivity was observed in 3D culture compared with 2D culture, particularly in the condition of low drug dose (<1 μM). The proposed SF/CS microscaffold can provide a promising *in vitro* platform for the efficacy prediction and sensitivity screening of anticancer drugs.

Keywords: microenvironment, biomaterials, drug screening, silk fibroin/chitosan scaffold, *in vitro* tumor research model

INTRODUCTION

Most anticancer drugs that show promise in preclinical studies exhibit less or no benefit in later clinical trials, and only less than 5% of new anticancer drugs were approved (Sant and Johnston, 2017). One major cause of such a high failure rate is that conventional preclinical models can't accurately predict the efficacy and toxicity of drug candidates (Dhandapani and Goldman, 2017). Anticancer drug screening can be achieved using *in vivo* and *in vitro* methods. The application of *in vivo* models, such as patient-derived xenografts (PDX), is limited by their complexity, high cost, and associated ethical issues (Murayama and Gotoh, 2019; Invrea et al., 2020). The majority of *in vitro* assays are based on traditional two-dimensional (2D) cultures of cancer cell lines, where cells are grown on a flat surface and/or form a monolayer. However, the 2D monolayer can't effectively mimic the natural tumor microenvironment (Fontoura et al., 2020). Recently, various 3D culture models have been studied to recapitulate the tumor microenvironment (Agarwal et al., 2017; Gomez-Roman et al., 2017; Rijal and Li, 2017; Lee et al., 2018). At present, three-dimensional models include vivo-like models, microarray technology; tumor-on-a-chip platforms, pre-fabricated engineered scaffolds, scaffolds-free, liquid-overlay culture, gyratory rotation, and spinner flask spheroid cultures, and so on (Benton et al., 2014; Negrei et al., 2016; Franchi-Mendes et al., 2021; Liu et al., 2021). It has been found that cancer cells grown in 3D culture systems display different morphological and physiological properties from those in 2D culture. Overall, 3D cancer models are better to represent *in vivo* tissue and predict drug response than 2D culture systems (Kapałczyńska et al., 2018; Lim and Park, 2018).

3D scaffolding is one of the most common 3D culture techniques that has been increasingly used in tissue engineering, cancer research, and drug delivery (Shakibaei et al., 2015; Roseti et al., 2017; Wani and Veerabhadrappa, 2018; Limongi et al., 2020; Yang et al., 2020). The selection of biomaterials plays a critical role in determining the properties of obtained scaffolds and the quality of subsequent cell culture and data interpretation. Silk fibroin (SF) is a natural fibrous protein characterized by high oxygen and water permeability, good biocompatibility, and robust mechanical strength (Huang et al., 2018). SF-based nanoparticles were investigated to be used as carriers in a novel drug-delivery system, which showed a good encapsulation efficiency and release profile (Hudita et al., 2021; Radu et al., 2021). SF-based scaffolds prepared by different methods often have different biological characteristics. For instance, the porous scaffolds prepared by the salt leaching method usually have poor connectivity and cannot control the shape of the pores (Vishwanath et al., 2016). The gas foaming method avoids the use of chemical solvents and reduces the fabrication time. However, the disadvantage is that scaffolds prepared by this method usually have relatively small closed pores (Zeng et al., 2015). What's exciting is that the freeze-drying method has good application value. In freeze-drying, the porous structure of scaffolds relies on the formation of ice crystals, which is largely dependent on the parameters of prepared solutions. Previous studies of SF-based scaffolds used different concentrations of SF solution ranging from 2 to 10% (Mukhopadhyay et al., 2017; Wang et al., 2020). More importantly, Li et al. reported that when SF/CS ratio was 1: 1, the porosity and the water uptake ratio of obtained scaffolds significantly decreased as the SF/CS concentration increased from 2 to 12% (Li et al., 2017b). Thus, although the standardized protocol of SF solution preparation has been described (Huang et al., 2018), there is no consensus on the method of scaffold construction. Moreover, using only SF material to fabricate scaffolds may lead to insufficient stability in water and poor cell adhesion (Fan et al., 2020; Luetchford et al., 2020). Improved properties of SF-based scaffolds can be achieved by blending with other polymers, such as Chitosan (CS). However, the technical parameters for SF/CS microscaffold fabrication process need to be better stated; And, the effects of cross-linking agents affiliated with the scaffolds should be estimated. Besides, the application of using SF/CS microscaffolds for drug sensitivity screening was few reported.

In this study, we prepared SF/CS composite scaffolds with two kinds of cross-linking agents, sodium tripolyphosphate (TPP) and1-ethyl-3-(3-dimethylaminopropyl)-carbodiimide (EDC). The properties of scaffolds were characterized using scanning electron microscopy (SEM), attenuated total reflectance fourier transform infrared spectroscopy (ATR-FTIR), X-ray diffraction analysis (XRD), water absorption analysis, and swelling ratio analysis. LoVo cells were seeded on the scaffolds to observe cell growth and adhesion, and cell proliferation was examined with MTT assay. Finally, Lovo cells and MDA-MB-231 were used to test the chemotherapeutic drug sensitivity in three culture environments: traditional 2D culture, 3D SF/CS scaffold, and 3D SF/CS scaffold containing extract of tumor tissue. Results showed that 3D SF/CS scaffold cross-linked by EDC provides a suitable environment for cancer cell growth and has potential applications in cancer research.

MATERIALS AND METHODS

Cells and Reagents

LoVo human colon cancer and MDA-MB-231 human breast cancer cell lines were obtained from American Type Culture Collection (United States of America). 5-fluorouracil (5-FU), methotrexate (MTX), paclitaxel (PTX), oxaliplatin (OXA), irinotecan (CPT-11), and capecitabine were purchased from Sinopharm Chemical Reagent (China). CS was purchased from AK Biotech Co., Ltd. (China). Dulbecco's modified Eagle's medium (DMEM), fetal bovine serum (FBS), and phosphate-buffered saline (PBS) were from Gibco (USA). TPP was obtained from Invitrogen (USA). EDC, N-hydroxysuccinimide (NHS), lithium bromide, 1% penicillin-streptomycin, 3-(4,5-dimethylthiazol-2-yl)-2,5-diphenyltetrazoliumbromide (MTT), and dimethyl

sulfoxide (DMSO) were purchased from Sigma-Aldrich (USA). Glacial acetic acid was obtained from Sinopharm Chemical Reagent (China). Cell counting kit-8 (CCK-8) reagent was from Beyotime Biotechnology (China).

Preparation of SF Solution

The preparation of the SF solution followed the procedures described previously (Huang et al., 2018). *Bombyx mori* cocoons (Maoda Textile, China) were cut into small pieces and boiled in 0.5% sodium carbonate solutions for 3 h. The shells were washed twice with double distilled water and placed in a 60°C oven until the weight did not change. Dried shells were then dissolved in 9.3M lithium bromide solution and underwent dialysis to obtain an aqueous SF solution. The final concentration of SF solution was approximately 3% w/v.

Preparation of Chitosan Solution

At room temperature, 3 g chitosan (Aokang Biotechnology, China) was dissolved in 100 ml of glacial acetic acid solution with a concentration of 0.1 mol/L (pH = 4.6). The mixed solution was stirred thoroughly until it became clear to obtain 3% (w/v) chitosan solution.

Fabrication Process of SF/CS Composite Microscaffolds

The SF and CS solutions were first mixed in 1:1 proportion and then cross-linked by the addition of 50 mmol/L EDC and 18 mmol/L NHS or 1 mg/ml TPP solution. The mixture was processed with a gradient freezing technique followed by drying in a vacuum freeze dryer for 36–48 h to obtain EDC cross-linked and TPP-linked SF/CS scaffolds. To improve water stability, the dry prepared scaffolds were then immersed in anhydrous methanol and 10% sodium hydroxide solutions (1:1 proportion) (Tong et al., 2015; Zeng et al., 2015; Ruan et al., 2017), washed three times with deionized water, and dried in the freeze dryer for 36–48 h. SF and CS solutions were processed in the same manner to obtain pure SF and CS scaffolds.

Scanning Electron Microscopy

The microstructures of the scaffolds were detected through SEM with a JEOL JSM6460LV microscope (S-4700; Hitachi, USA). The samples were coated with sputtered gold, and their outer and inner sections were prepared by breaking scaffolds in liquid nitrogen.

Attenuated Total Reflectance Fourier Transform Infrared Spectroscopy

Measurement of the scaffolds structure ware carried out with infrared spectroscopy with an ATR-FTIR spectrophotometer (NICOLET 560, USA). The resolution was 4 cm^{-1} after the accumulation of 256 scans for each spectrum. The scanning range was 2,000–400 cm^{-1}.

X-Ray Diffraction Analysis

The microstructures of the crystalline and amorphous materials in scaffolds were studied with XRD with a fully automated X-ray diffractometer (Bruker, Germany). The experimental parameters were as follows: copper target, LynxExe array detector, 40 kV, 40 mA, scanning step length of 0.04°, and scanning speed of 35.4 s/step.

Analysis of Water Absorption and Swelling Ratio

Scaffolds of certain weights were soaked in double-distilled water for 24 h. After the water was removed from the surface, the weights of the wet scaffolds were recorded as M1. The scaffolds were then dried at 60°C until the weight did not change, and the weight was recorded as M2.

$$\text{The rate of waterabsorption} = \frac{M_2 - M_1}{M_2} \times 100\% \quad (1)$$

Certain volumes of scaffolds were used and measured as V1. The scaffolds were then soaked in double-distilled water for 24 h. After the water was removed from the surface, the volume was measured as V2.

$$\text{The swelling ratio} = \frac{V_2 - V_1}{V_1} \times 100\% \quad (2)$$

Cell Culture

For 2D culture, Lovo cells were maintained in DMEM containing 10% FBS and 1% penicillin-streptomycin. All cells were cultured at 37°C in a humidified atmosphere containing 5% CO2. For 3D culture, 3D scaffold samples were cut into circular discs for 96-well plates (Corning, USA) and sterilized under ultraviolet light. The circular matrices were immersed in 75% alcohol three times before they were used. Cells were suspended at the proper density on scaffolds and then rinsed extensively three times with sterile PBS and kept in DMEM medium for 1 h. Cells were then maintained in DMEM and incubated at 37°C, as with 2D culture.

Preparation of Fresh Tumor Tissue Extract

All procedures using mice were reviewed and approved by the Ethic Committee of Soochow University, implemented according to institutional animal ethics guidelines for the Care and Use of Research Animals established by Soochow University, and reported in adherence to the ARRIVE guidelines (Percie du Sert et al., 2020). Cancer cell (Lovo cells and MDA-MB-231cells) suspensions (1×10^6 cells/mouse) were subcutaneously injected into ten BALB/c nude mice (5–6 weeks old, 18 ± 2 g on average). Subcutaneous tumor tissue was obtained when the tumor size was around 10 mm × 10 mm, and then placed in a tissue homogenizer with liquid nitrogen for rapid grinding. The tissue was then homogenized in sterile PBS solution and centrifuged for 25 min (4°C, 15,000 rpm). The supernatant was collected and filtered with a 0.22 μm filter to remove bacteria. The filtered extract was then stored in a cryopreservation tube at -80°C. The total protein

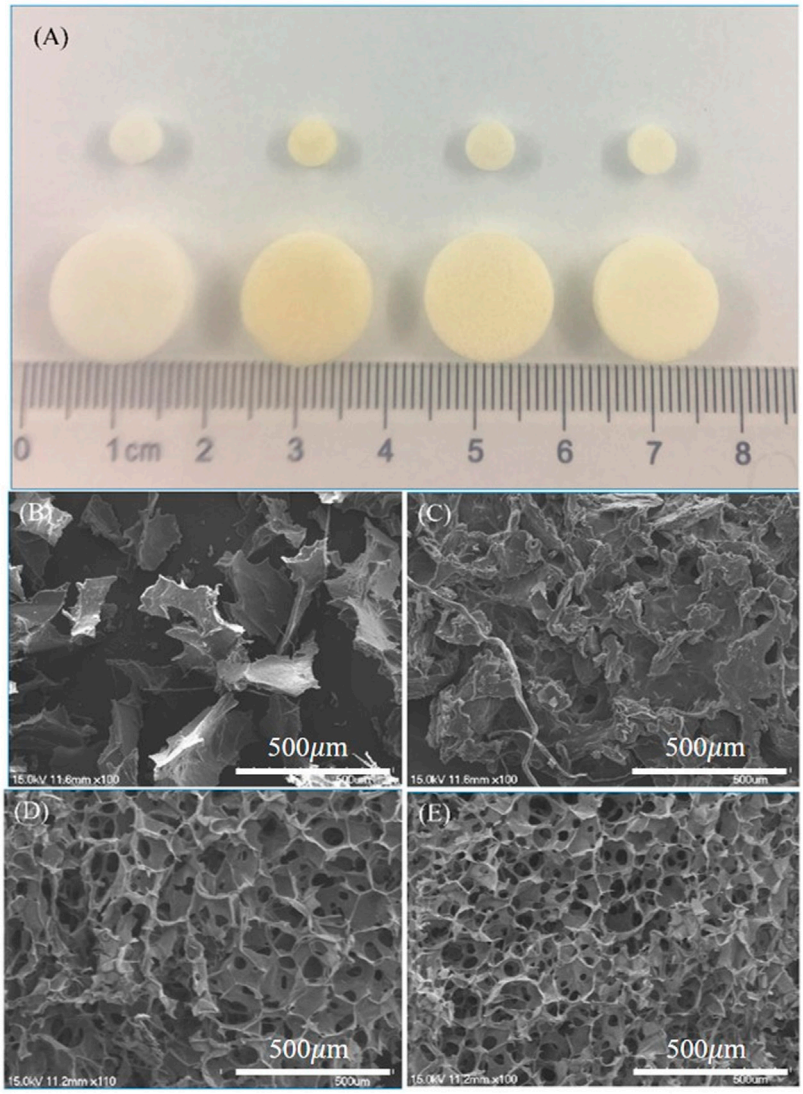

FIGURE 1 | Macroscopic and microscopic views of different 3D scaffolds. **(A)** The gross morphology of 3D scaffolds. SEM micrographs of scaffolds made of **(B)** pure SF, **(C)** pure CS, **(D)** SF/CS cross-linked by TPP, and **(E)** SF/CS cross-linked by EDC.

concentration of the tumor tissue extract was calculated with a UV/Vis spectrophotometer.

MTT Assay

A total of 5,000 cells/well (100 μl, 5×10^4cells/ml) were placed in 96-well plates in DMEM containing 10% FBS for 24 h. The cells were then incubated with 20 µl MTT (5 mg/ml) solution for 4 h. The MTT solution was removed, and the cells were incubated with 150 µL DMSO. A microplate reader (Thermo Scientific, USA) was used to measure the optical density at 560 nm.

Culture Model and Drugs Treatments

Cells were cultured in 2D plates and 3D plates as follows (determined on the basis of preliminary experiments): LoVo, 5,000 cells/well (2D) and 10,000 cells/well (3D); MDA-MB-231, 5,000 cells/well (2D) and 10,000 cells/well (3D). The drugs were added to the 2D plates after 24 h and to the 3D plates after 5 days. These drugs are 5-fluorouracil (5-FU), methotrexate (MTX), paclitaxel (PTX), oxaliplatin (OXA), irinotecan (CPT-11), and capecitabine with different concentration gradients (0.01, 0.1, 1, 10, and 100 μM), which are purchased from Sinopharm Chemical Reagent (China). The sensitivity of cells to chemotherapeutic drugs was measured by CCK8 after 48 h of drugs treatment. Experimental control wells contained only cancer cells without drugs; experimental wells contained both cells and drugs; and blank control wells contained no cells or drugs.

CCK-8 Assay

Cell viability was accessed by CCK-8 assay after 48 h of drug treatment. Cells were incubated in 20 µL CCK-8 solution at 37°C for 2 h. A microplate reader (Thermo Fisher Scientific, USA) was

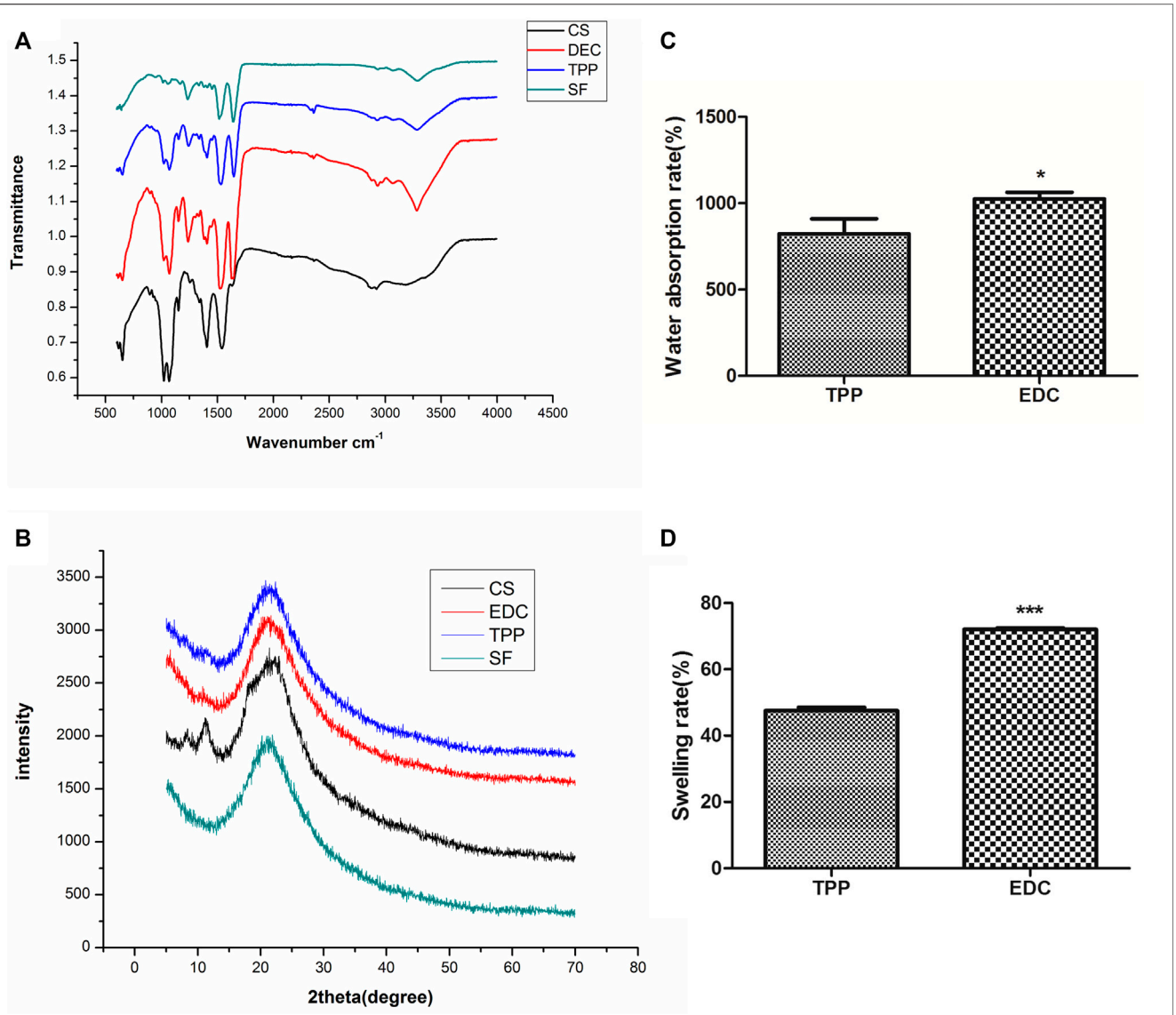

FIGURE 2 | Physicochemical properties of different 3D scaffolds. **(A)** ATR-FTIR. **(B)** XRD spectra. **(C)** Water absorption rate. **(D)** Swelling ratio.

used to measure the optical density (OD) at 450 nm. CCK-8 assays were replicated three times for each formulation and culture period. The inhibition ratio (IR) of chemotherapeutic drugs.

$$IR = \frac{OD_{experimental\ control} - OD_{experimental}}{OD_{experimental\ control} - OD_{blank\ control}} \times 100\% \quad (3)$$

Statistical Analysis

All experiments were performed in triplicate and at least three times. Data were expressed as mean ± standard deviation. The student's two-tailed *t*-test was performed with GraphPad Prism v.6 software (GraphPad Software, Inc., San Diego, CA) to compare the differences between treated groups and the corresponding control groups. A p-value <0.05 was considered statistically significant.

RESULTS

Effects of Different Cross-Linking Agents on 3D Scaffold Morphology

Each group of scaffolds was prepared with 24-well and 96-well plates. From left to right, the scaffolds were pure SF scaffold, pure CS scaffold, TPP cross-linked SF/CS scaffold and EDC cross-linked SF/CS scaffold (**Figure 1A**). The pure SF scaffold was white and brittle. The pure CS scaffold was yellow and soft. TPP and EDC cross-linked SF/CS scaffolds were yellowish-white with rough surfaces and a sponge-like texture.

To observe the internal structures of the scaffolds, we examined each group with SEM (**Figures 1B–E**). The pure SF scaffold had an unstable, coiled, and flaky structure. The pure CS scaffold formed irregular spaces with poor interconnection, which were unfavorable to the transport of nutrients. Both

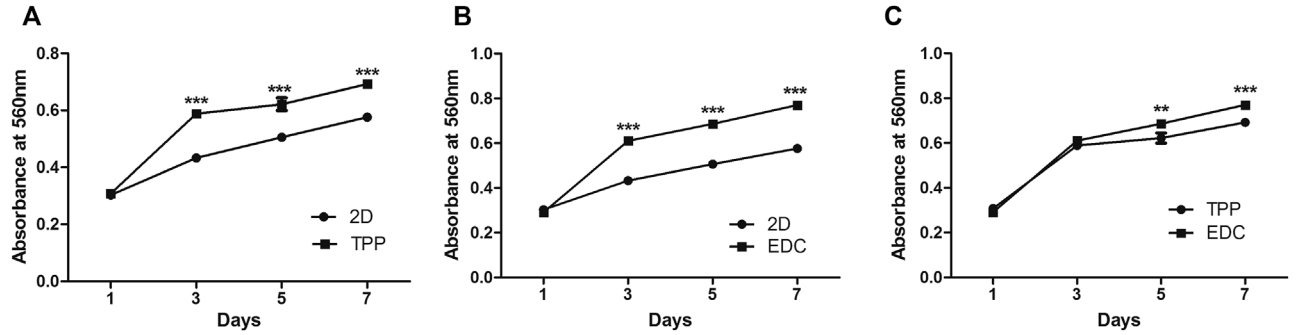

FIGURE 3 | Comparison of LoVo cell proliferation by MTT assay between two of the three conditions: namely a 2D environment, TPP cross-linked SF/CS scaffold, and EDC cross-linked SF/CS scaffold: **(A)** 2D vs TPP. **(B)** 2D vs EDC. **(C)** TPP vs EDC. $^{**}p < 0.01$, $^{***}p < 0.001$.

TPP and EDC cross-linked SF/CS scaffolds formed regular, small pore structures. Compared with TPP scaffolds, EDC cross-linked scaffolds had smaller and more uniform pores with great interconnection.

Physicochemical Properties of SF/CS Scaffolds With Different Cross-Linking Agents

ATR-FTIR

The functional group composition in the four groups of scaffolds is shown in the ATR-FTIR spectra (**Figure 2A**). The characteristic peaks at 1,625 cm^{-1}, 1,529 cm^{-1}, and 1,236 cm^{-1} represented the amide I, II, and III of SF, respectively. Pure CS alone had a characteristic absorption peak at 1,035–1,154 cm^{-1}, and its NH2 characteristic peak appeared at 1,558 cm^{-1} because its β-(1,4) glycosidic bond was interconnected. Its amide I band at 1,623 cm^{-1} was weak, because the CS used in the experiment had a 90% deacetylation. The amide I band of pure SF was between 1,650 and 1,660 cm^{-1} (1,654 cm^{-1}), thus indicating that SF has an α helix or an irregular crimped structure. The spectra of SF/CS scaffolds cross-linked by EDC or TPP showed amide I bands between 1,625 and 1,634 cm^{-1}, representing a more stable β-folded structure than that of pure SF and pure CS.

XRD

The analysis of basic composition in the four groups of scaffolds is shown in the XRD spectra (**Figure 2B**). The pure CS scaffold had the main peak at $2\theta = 20.1^{\circ}$ that corresponded to the low crystallization of CS. The 2θ peak of the pure SF scaffold was broad and appeared at 20.9°, which was characteristic of amorphous SF (α-helix or random coil structure). The peaks of EDC and TPP cross-linked SF/CS scaffolds appeared at 21.7° and 21.4° respectively, indicating that the process of cross-linking increased the crystallinity of individual materials.

Analysis of Water Absorption Rate and Swelling Ratio

In this study, only cross-linked SF/CS scaffolds were tested because the pure SF group and pure CS group were unstable and soluble in water. The results are shown in **Figures 2C,D** the EDC group had a rate of water absorption of 1000% or greater, whereas that of the TPP group was only approximately 800%. The swelling ratio of the EDC group was 72% and that of the TPP group was only approximately 47%.

Cell Proliferation in SF/CS Scaffolds Constructed by Different Cross-Linking Agents

MTT

The proliferation of cancer cells in 2D and 3D (TPP and EDC groups) environments were examined with MTT assays after 1, 3, 5, and 7 days of culture (**Figure 3**). On the first day, cancer cells mainly began early adhesion after being seeded on the scaffold material. On the third day, cells began to undergo rapid proliferation. On the fifth day, cells continued to proliferate, and the difference between the control group and the experimental group was statistically significant ($p < 0.001$), thus indicating that the cells grew better in 3D culture (**Figures 3A,B**). The difference in the proliferation rate between the two 3D groups was also significant ($p < 0.001$) (**Figure 3C**). The cells in the EDC group displayed superior proliferation ability to that of the TPP group.

SEM

The morphology of cancer cells in the TPP group and the EDC group were observed under SEM (**Figure 4**). In the TPP group, cancer cells were first scattered on the surfaces of the scaffolds (**Figure 4A**). After 3 days, small amounts of granular substances appeared around the cells (**Figure 4B**). After 5 days, large numbers of cells formed lump-like structures in the scaffold pores. The cell proliferation was active, and the amount of granular material around the cells increased (**Figure 4C**). The appearance of granular substances may be due to the degradation of dead cells, extracellular matrix, and scaffold material. The degradation of scaffold pore structures made the pore wall thinner or even caused it to disappear (**Figure 4D**). Compared with the TPP group, the EDC group exhibited better cell compatibility. The cells adhered to the scaffold and formed antenna-like structures conducive to cell division and proliferation (**Figures 4E,F**). After 5 days, the cells grew well, and the agglomerate grew towards the surroundings. The growth

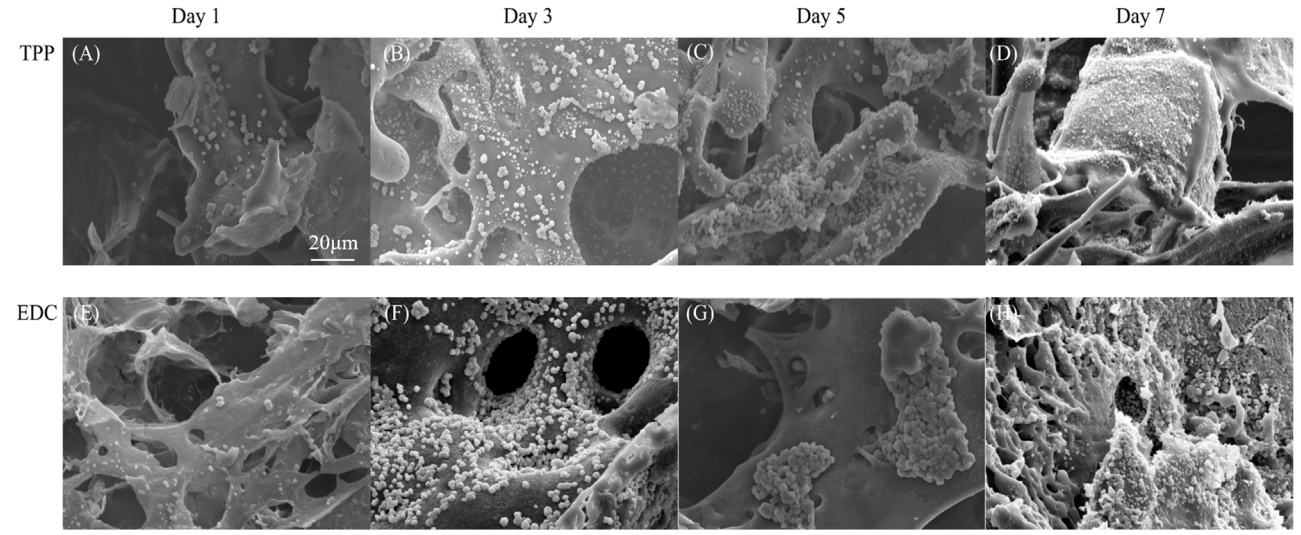

FIGURE 4 | SEM micrographs of LoVo cells cultivated on **(A-D)** TPP cross-linked scaffolds and **(E-H)** EDC cross-linked scaffolds after 1 day, 3 days, 5 days, and 7 days.

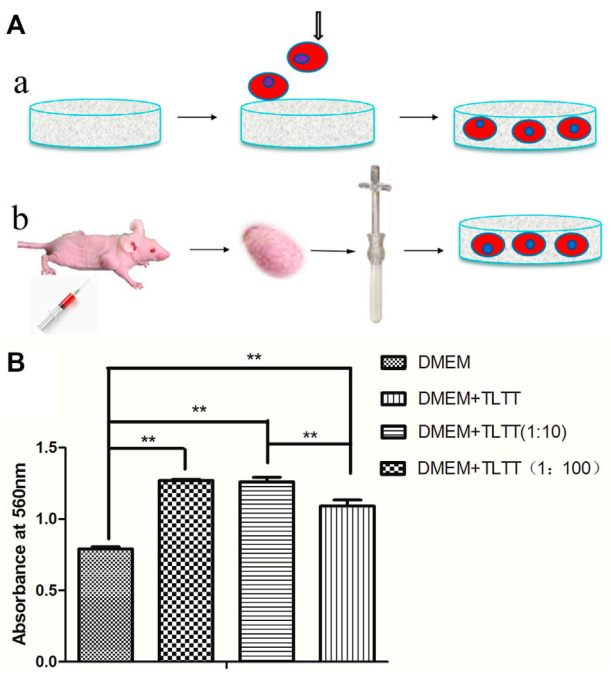

FIGURE 5 | (A) Schematic diagram of 3D tumor microenvironment by growing cancer cells on porous scaffolds **(A)** and adding tumor tissue extract to the culture system **(B)**. **(B)** Effects of tumor tissue extract with different proportions on cancer cell proliferation. $^{**}p < 0.01$, (DMEM: Dulbecco's Modified Eagle Medium containing 2% fetal bovine serum; TLTT: Stock solution of tumor tissue extract, TLTT (1:10): 10-fold diluted tumor tissue extract; TLTT (1:100): 100-fold diluted tumor tissue extract).

pattern was close to the infiltration pattern of cancer cells *in vivo* (**Figures 4G,H**). Interestingly, pore structures with different sizes formed on the surface of the cell lump, which may facilitate the transport of nutrients and metabolic substrates. The formation of pore structures in the scaffold was comparable to the process of tumor vascularization *in vivo*.

Effects of Tumor Tissue Extract on Cell Proliferation in EDC Cross-Linked SF/CS Scaffold

To simulate the tumor microenvironment *in vitro*, we added tumor tissue extract to 3D cell culture to provide the cytokines and signal transduction molecules needed for cell growth (**Figures 5A,B**). The effects of different proportions of tumor tissue extract on cell proliferation were detected with MTT assays (**Figure 5B**). The difference was statistically significant ($p < 0.05$) with 10-fold and 100-fold diluted tumor tissue fluid extract. Tumor tissue extract was beneficial to the proliferation of cancer cells under certain conditions.

In Vitro Evaluation of Chemosensitivity

Based on the test results of physicochemical properties and cell compatibility, we used EDC cross-linked SF/CS scaffold for the initial testing of chemotherapeutic drug sensitivity. Five different concentrations of chemotherapeutic drugs (namely 0.01, 0.1, 1, 10, and 100 μM) were added to the traditional 2D culture (2D group), a simple SF/CS scaffold (3D group), and an SF/CS scaffold with fresh tumor tissue extract (3D + TLTT group). The sensitivity of cells to chemotherapeutic drugs was measured by CCK8 after 48 h of drugs treatment. The results were interpreted as resistant (IR<30%), moderately sensitive (30% ≤ IR ≤ 50%), or sensitive (IR>50%).

Figure 6 illustrates the chemosensitivity of both LoVo cells and MDA-MB-231 cells in 2D, 3D, and 3D + TLTT culture environments. It can be found that the chemosensitivity in 2D and 3D culture significantly differed and higher sensitivity was

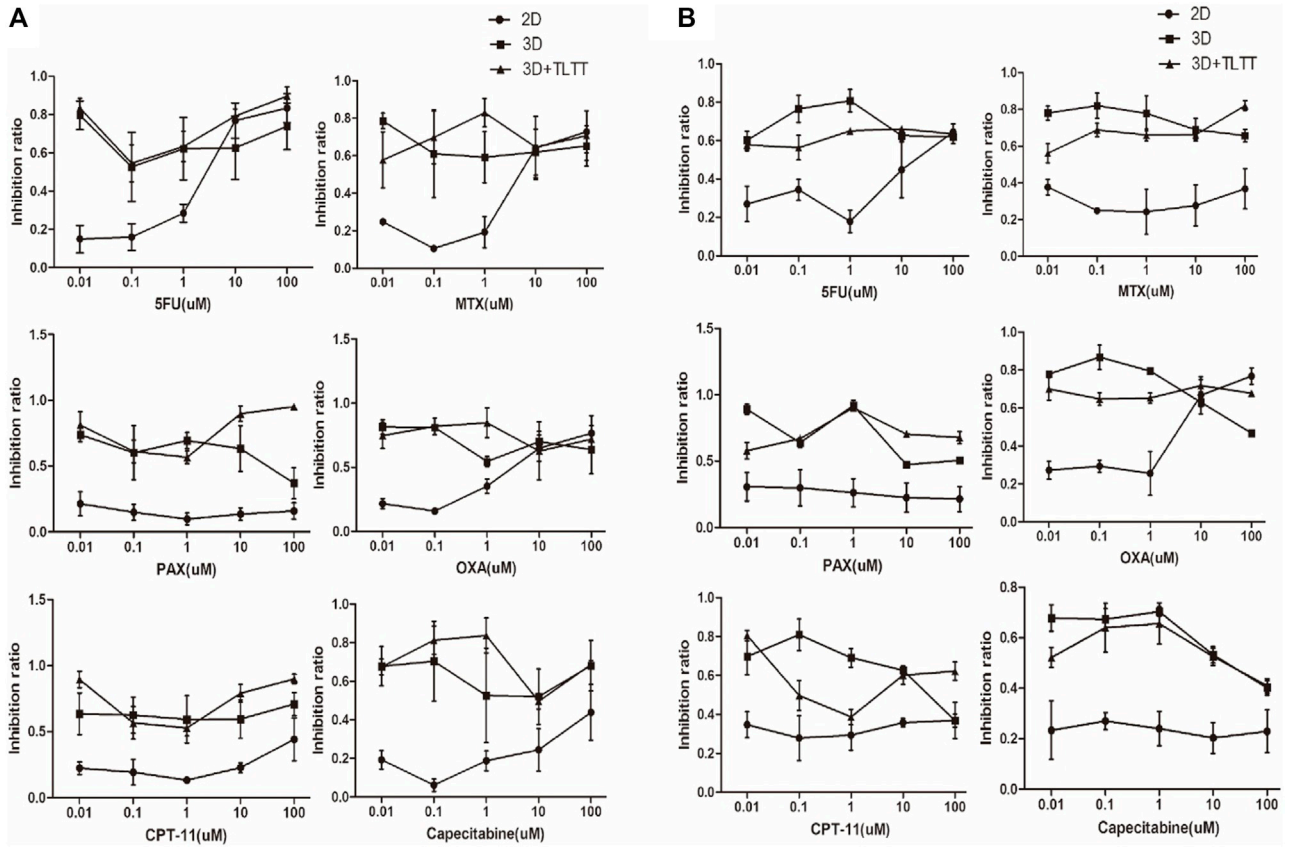

FIGURE 6 | The chemosensitivity of **(A)** LoVo cells and **(B)** MDA-MB-231 cells in 2D, 3D, and 3D + TLTT culture environments.

observed in the 3D environment when the drug concentrations were low. No significant differences were seen between the two types of 3D environment (3D and 3D + TLTT), thus indicating that the addition of tumor tissue fluid extract did not significantly affect the sensitivity to chemotherapeutic drugs. The IR data of **Figure 6** are provided in **Supplementary Tables S1, S2** respectively.

DISCUSSION

With the development of 3D culture technology, people have a new understanding and development of tumor model. The construction and application of 3D tumor model will become an inevitable trend. To date, studies showed SF is of good biocompatibility, slow degradation rate, low immunogenicity (Gholipourmalekabadi et al., 2020; Guan et al., 2020; Chen et al., 2021). And, SF-based scaffolds have been applied in diverse studies of *in vitro* tumor models (Talukdar et al., 2011; Mishra et al., 2019). SF/CS scaffolds could provide not only the space for cell tissue to form a three-dimensional (3D) structure, but also the mechanical integrity and hydration space for the diffusion of nutrients and metabolites in cells (Guan et al., 2013; Li et al., 2017b).

In the study, we established a 3D SF/CS composite scaffold that could be potentially used for the pre-screening of chemotherapeutic drugs. As high porosity and water uptake ratio are desirable for cell growth and material exchange, we selected the relatively low total concentration for scaffold fabrication in our study. The pure SF scaffold is brittle and unstable in water. The physical properties of SF scaffolds can be improved by mixing with other synthetic or natural polymers (Gobin et al., 2005; Lv and Feng, 2006). Blending SF with CS is an interaction of hydrogen bonding, causing the formation of a stable β-sheet conformation in SF (Tian et al., 2017). Usually, different cross-linking agents are used in different culture models. Cross-linking agents can be added to further stabilize the structure. At present, the crosslinking agents used in the research include EDC/NHS, TPP, glutaraldehyde (GA) and so on (Teimouri et al., 2015; Ruan et al., 2017; Auwal et al., 2018). GA crosslink can improve considerably the molecular stability and antidegradation of the chitosan (CS) solution. However, GA has certain cytotoxicity and is generally used for tissue fixation. Therefore, it is not the preferred material for our cell culture scaffolds. EDC/NHS is an alternative crosslinking agent for GA. it can not only improve the mechanical properties of scaffolds, but also rarely have cytotoxic reactions, and has good biocompatibility (Lehmann et al., 2017). In the process of preparing stratified collagen/CH-PCL scaffolds, TPP can more effectively crosslink with the amino group of chitosan (Zhu et al., 2014). Inspired by those previous works, we prepared SF/CS

scaffolds with two different crosslinking agents (EDC or TPP), and compared their morphological and physicochemical properties.

In order to explore whether different biological crosslinking agents have different effects on SF/CS 3D scaffolds. Firstly, we observed the external morphology and internal structure of the 3D scaffolds by ordinary light microscope and SEM. The experimental results show that the unstable crimp structure and lamellar structure of silk fibroin can form porous SF/CS 3D scaffolds with chitosan solution under the action of biological crosslinking agent. The two biological crosslinking agents play different roles in the formation of voids in SF/CS 3D scaffolds, and the voids formed by EDC crosslinked SF/CS 3D scaffolds are more uniform and better connected than TPP crosslinked SF/CS 3D scaffolds. In addition, ART-FTIR and XRD showed that no new chemical bond was formed in the composite process, but a simple physical bond. Moreover, the degree of crystallization peak of cross-linked scaffolds is not lower than that of pure chitosan scaffolds, which may be because the cross-linking agent increases the degree of crystallization of mixed scaffolds. Besides, compared with TPP group, EDC crosslinked SF/CS 3D scaffolds has moderate water absorption (1000%) and swelling (72%), which may provide sufficient nutrients for the growth process of cells. Most importantly, cell proliferation experiments (MTT and SEM) confirmed that EDC scaffolds were more conducive to cell growth. Through comparison and physicochemical properties, we conclude that EDC crosslinked SF/CS scaffolds could be used to obtain a good biocompatibility and structures to establish an *in vitro* tumor model, which was consistent with the results of Li et al. (Li et al., 2017a) and Zeng et al. (Zeng et al., 2015).

3D culture models have been found to profoundly affect cell growth and drug responses compared with traditional 2D culture. Our results showed that similar to the phenotypes displayed in other *in vitro* 3D tumor model, cancer cells seeded in SF/CS scaffolds grew in clusters and exhibited good adhesion (Liu et al., 2021). MTT assay showed the proliferation rate of cancer cells grown in SF/CS scaffolds was significantly higher than in 2D cell culture. Our present study tested the *in vitro* sensitivity of six chemotherapeutic drugs (5-FU, MTX, PTX, OXA, CPT-11, and capecitabine) on the LoVo and MDA-MB-231 cells. Compared with traditional 2D culture, the chemotherapeutic drug sensitivity was greater in 3D scaffolds, especially when the drug dose was low. This result is consistent with the previously reported drug sensitization effect of 3D cell culture (Shin et al., 2019). However, some studies have reported that tumor cells in 3D culture have higher drug resistance compared with traditional 2D culture (Fontoura et al., 2020). Hongisto et al. suggested that general conclusions cannot be drawn based on the observation of a single drug (Hongisto et al., 2013). Currently, we only tested the loVo and MDA-MB-231 cells, while further improvements and tests still need to be done.

3D tumor model not only provides 3D space for tumor cells to grow, but also reproduces the real growth of tumor cells in the body. Simulation of the tumor microenvironment requires both a 3D spatial structure and molecular components that facilitate cell growth *in vivo* (Rijal and Li, 2018). Here we not only analyzed the growth patterns of cancer cells in the prepared 3D scaffolds, but also investigated the effects of different proportions of tumor tissue extract on cell proliferation. Our results demonstrated that tumor tissue extract diluted by 10 or 100 times could promote cancer cell growth. However, 3D scaffolds with tumor tissue fluid extract did not significantly affect the sensitivity of chemotherapeutic drugs, thus indicating that cell proliferation of tumor cells may not correlate with the sensitivity of chemotherapeutic drugs. This may be the result of a variety of factors, and the specific mechanism still needs to be further studied.

CONCLUSION

In conclusion, we demonstrated that a 3D SF/CS microscaffold cross-linked by EDC provides a suitable environment for cancer cell growth and has potential applications in cancer research. *In vitro* chemotherapeutic drug screening showed greater sensitivity of the 3D scaffold than the traditional 2D environment, when drugs were present in low doses. The EDC cross-linked 3D SF/CS scaffold may provide a promising new platform for *in vitro* evaluation and development of anticancer drugs.

DATA AVAILABILITY STATEMENT

The original contributions presented in the study are included in the article/**Supplementary Material**, further inquiries can be directed to the corresponding authors.

AUTHOR CONTRIBUTIONS

The authors confirm that all contributors to this research are listed. Conceptualization, HN, FN, RY, and HY; methodology, LG, RY, and SW; software, validation, formal analysis, investigation, and resources, HN, FN, JX, and XL, YZ; data curation, HN; writing and visualization, HN and FN; supervision, LG and SW; project administration, HN and FN; funding acquisition, HN, HY, and FN. All authors have read and agreed to the published version of the manuscript.

FUNDING

This work was support in part by the National Natural Science Foundation of China under Grant 61903269 and 62073230, in part by the Natural Science Foundation of Jiangsu Province under Grant BK20190941, in part by the China Postdoctoral Science Foundation under Grant 2020M681517, in part by the Jiangsu Postdoctoral Science Foundation under Grant 2020Z063, and in part by Doctoral Innovation and Entrepreneurship Program of Jiangsu Province.

SUPPLEMENTARY MATERIAL

The Supplementary Material for this article can be found online at: https://www.frontiersin.org/articles/10.3389/fbioe.2022.800830/full#supplementary-material

REFERENCES

Agarwal, P., Wang, H., Sun, M., Xu, J., Zhao, S., Liu, Z., et al. (2017). Microfluidics Enabled Bottom-Up Engineering of 3D Vascularized Tumor for Drug Discovery. *ACS Nano* 11 (7), 6691–6702. doi:10.1021/acsnano.7b00824

Auwal, S. M., Zarei, M., Tan, C. P., Basri, M., and Saari, N. (2018). Enhanced Physicochemical Stability and Efficacy of Angiotensin I-Converting Enzyme (ACE) - Inhibitory Biopeptides by Chitosan Nanoparticles Optimized Using Box-Behnken Design. *Sci. Rep.* 8 (1), 10411. doi:10.1038/s41598-018-28659-5

Benton, G., Arnaoutova, I., George, J., Kleinman, H. K., and Koblinski, J. (2014). Matrigel: from Discovery and ECM Mimicry to Assays and Models for Cancer Research. *Adv. Drug Deliv. Rev.* 79-80, 3–18. doi:10.1016/j.addr.2014.06.005

Chen, Z., Zhang, Q., Li, H., Wei, Q., Zhao, X., and Chen, F. (2021). Elastin-like Polypeptide Modified Silk Fibroin Porous Scaffold Promotes Osteochondral Repair. *Bioactive Mater.* 6 (3), 589–601. doi:10.1016/j.bioactmat.2020.09.003

Dhandapani, M., and Goldman, A. (2017). Preclinical Cancer Models and Biomarkers for Drug Development: New Technologies and Emerging Tools. *J. Mol. Biomark. Diagn.* 8 (5), 356. doi:10.4172/2155-9929.1000356

Fan, Z., Xiao, L., Lu, G., Ding, Z., and Lu, Q. (2020). Water-insoluble Amorphous Silk Fibroin Scaffolds from Aqueous Solutions. *J. Biomed. Mater. Res.* 108 (3), 798–808. doi:10.1002/jbm.b.34434

Fontoura, J. C., Viezzer, C., Dos Santos, F. G., Ligabue, R. A., Weinlich, R., Puga, R. D., et al. (2020). Comparison of 2D and 3D Cell Culture Models for Cell Growth, Gene Expression and Drug Resistance. *Mater. Sci. Eng. C* 107, 110264. doi:10.1016/j.msec.2019.110264

Franchi-Mendes, T., Eduardo, R., Domenici, G., and Brito, C. (2021). 3D Cancer Models: Depicting Cellular Crosstalk within the Tumour Microenvironment. *Cancers* 13 (18), 4610. doi:10.3390/cancers13184610

Gholipourmalekabadi, M., Sapru, S., Samadikuchaksaraei, A., Reis, R. L., Kaplan, D. L., and Kundu, S. C. (2020). Silk Fibroin for Skin Injury Repair: Where Do Things Stand? *Adv. Drug Deliv. Rev.* 153, 28–53. doi:10.1016/j.addr.2019.09.003

Gobin, A. S., Froude, V. E., and Mathur, A. B. (2005). Structural and Mechanical Characteristics of Silk Fibroin and Chitosan Blend Scaffolds for Tissue Regeneration. *J. Biomed. Mater. Res.* 74A (3), 465–473. doi:10.1002/jbm.a.30382

Gomez-Roman, N., Stevenson, K., Gilmour, L., Hamilton, G., and Chalmers, A. J. (2017). A Novel 3D Human Glioblastoma Cell Culture System for Modeling Drug and Radiation Responses. *Neuro. Oncol.* 19 (2), 229–241. doi:10.1093/neuonc/nox036.091

Guan, L., Tian, P., Ge, H., Tang, X., Zhang, H., Du, L., et al. (2013). Chitosan-functionalized Silk Fibroin 3D Scaffold for Keratocyte Culture. *J. Mol. Hist.* 44 (5), 609–618. doi:10.1007/s10735-013-9508-5

Guan, Y., You, H., Cai, J., Zhang, Q., Yan, S., and You, R. (2020). Physically Crosslinked Silk Fibroin/hyaluronic Acid Scaffolds. *Carbohydr. Polym.* 239, 116232. doi:10.1016/j.carbpol.2020.116232

Hongisto, V., Jernström, S., Fey, V., Mpindi, J.-P., Kleivi Sahlberg, K., Kallioniemi, O., et al. (2013). High-Throughput 3D Screening Reveals Differences in Drug Sensitivities between Culture Models of JIMT1 Breast Cancer Cells. *PLoS ONE* 8 (10), e77232. doi:10.1371/journal.pone.0077232

Huang, W., Ling, S., Li, C., Omenetto, F. G., and Kaplan, D. L. (2018). Silkworm Silk-Based Materials and Devices Generated Using Bio-Nanotechnology. *Chem. Soc. Rev.* 47 (17), 6486–6504. doi:10.1039/c8cs00187a

Hudita, A., Radu, I., Galateanu, B., Ginghina, O., Herman, H., Balta, C., et al. (2021). Bioinspired Silk Fibroin Nano-Delivery Systems Protect against 5-FU Induced Gastrointestinal Mucositis in a Mouse Model and Display Antitumor Effects on HT-29 Colorectal Cancer Cells *In Vitro*. *Nanotoxicology* 15 (7), 973–994. doi:10.1080/17435390.2021.1943032

Invrea, F., Rovito, R., Torchiaro, E., Petti, C., Isella, C., and Medico, E. (2020). Patient-derived Xenografts (PDXs) as Model Systems for Human Cancer. *Curr. Opin. Biotechnol.* 63, 151–156. doi:10.1016/j.copbio.2020.01.003

Kapałczyńska, M., Kolenda, T., Przybyła, W., Zajączkowska, M., Teresiak, A., Filas, V., et al. (2018). 2D and 3D Cell Cultures–A Comparison of Different Types of Cancer Cell Cultures. *Arch. Med. Sci.* 14 (4), 910. doi:10.5114/aoms.2016.63743

Lee, J., Shin, D., and Roh, J.-L. (2018). Development of an *In Vitro* Cell-Sheet Cancer Model for Chemotherapeutic Screening. *Theranostics* 8 (14), 3964–3973. doi:10.7150/thno.26439

Lehmann, N., Christ, T., Daugs, A., Bloch, O., and Holinski, S. (2017). EDC Cross-Linking of Decellularized Tissue: A Promising Approach? *Tissue Eng. Part. A.* 23 (13-14), 675–682. doi:10.1089/ten.TEA.2016.0416

Li, D.-W., He, F.-L., He, J., Deng, X., Liu, Y.-L., Liu, Y.-Y., et al. (2017a). From 2D to 3D: The Morphology, Proliferation and Differentiation of MC3T3-E1 on Silk Fibroin/chitosan Matrices. *Carbohydr. Polym.* 178, 69–77. doi:10.1016/j.carbpol.2017.09.035

Li, D.-W., Lei, X., He, F.-L., He, J., Liu, Y.-L., Ye, Y.-J., et al. (2017b). Silk Fibroin/chitosan Scaffold with Tunable Properties and Low Inflammatory Response Assists the Differentiation of Bone Marrow Mesenchymal Stem Cells. *Int. J. Biol. Macromolecules* 105, 584–597. doi:10.1016/j.ijbiomac.2017.07.080

Lim, W., and Park, S. (2018). A Microfluidic Spheroid Culture Device with a Concentration Gradient Generator for High-Throughput Screening of Drug Efficacy. *Molecules* 23 (12), 3355. doi:10.3390/molecules23123355

Limongi, T., Susa, F., Allione, M., and Di Fabrizio, E. (2020). Drug Delivery Applications of Three-Dimensional Printed (3DP) Mesoporous Scaffolds. *Pharmaceutics* 12 (9), 851. doi:10.3390/pharmaceutics12090851

Liu, X., Fang, J., Huang, S., Wu, X., Xie, X., Wang, J., et al. (2021). Tumor-on-a-chip: from Bioinspired Design to Biomedical Application. *Microsyst. Nanoeng.* 7 (1), 1–23. doi:10.1038/s41378-021-00277-8

Luetchford, K. A., Chaudhuri, J. B., and De Bank, P. A. C. (2020). Silk Fibroin/gelatin Microcarriers as Scaffolds for Bone Tissue Engineering. *Mater. Sci. Eng. C* 106, 110116. doi:10.1016/j.msec.2019.110116

Lv, Q., and Feng, Q. (2006). Preparation of 3-D Regenerated Fibroin Scaffolds with Freeze Drying Method and Freeze Drying/foaming Technique. *J. Mater. Sci. Mater. Med.* 17 (12), 1349–1356. doi:10.1007/s10856-006-0610-z

Mishra, A., Mukhopadhyay, S. K., and Dey, S. (2019). Evaluation of Cyclosaplin Efficacy Using a Silk Based 3D Tumor Model. *Biomolecules* 9 (4), 123. doi:10.3390/biom9040123

Mukhopadhyay, S. K., Naskar, D., Bhattacharjee, P., Mishra, A., Kundu, S. C., Dey, S., et al. (2017). Silk Fibroin-Thelebolan Matrix: A Promising Chemopreventive Scaffold for Soft Tissue Cancer. *Colloids Surf. B: Biointerfaces* 155, 379–389. doi:10.1016/j.colsurfb.2017.04.011

Murayama, T., and Gotoh, N. (2019). Patient-Derived Xenograft Models of Breast Cancer and Their Application. *Cells* 8 (6), 621. doi:10.3390/cells8060621

Negrei, C., Hudita, A., Ginghina, O., Galateanu, B., Voicu, S. N., Stan, M., et al. (2016). Colon Cancer Cells Gene Expression Signature as Response to 5-Fluorouracil, Oxaliplatin, and Folinic Acid Treatment. *Front. Pharmacol.* 7, 172. doi:10.3389/fphar.2016.00172

Percie du Sert, N., Hurst, V., Ahluwalia, A., Alam, S., Avey, M. T., Baker, M., et al. (2020). The ARRIVE Guidelines 2.0: Updated Guidelines For Reporting Animal Research. *J. Cereb. Blood Flow. Metab.* 40 (9), 1769–1777. doi:10.1177/0271678X20943823

Radu, I. C., Hudita, A., Zaharia, C., Negrei, C., Dragomiroiu, G., Popa, D. E., et al. (2021). Silk Fibroin Nanoparticles Reveal Efficient Delivery of 5-Fu in a Ht-29 Colorectal Adenocarcinoma Model *In Vitro*. *Farmacia* 69, 113–122. doi:10.31925/farmacia.2021.1.15

Rijal, G., and Li, W. J. (2017). A Versatile 3D Tissue Matrix Scaffold System for Tumor Modeling and Drug Screening. *Sci. Adv.* 3 (9), e1700764. doi:10.1126/sciadv.1700764

Rijal, G., and Li, W. (2018). Native-mimicking *In Vitro* Microenvironment: an Elusive and Seductive Future for Tumor Modeling and Tissue Engineering. *J. Biol. Eng.* 12, 20. doi:10.1186/s13036-018-0114-7

Roseti, L., Parisi, V., Petretta, M., Cavallo, C., Desando, G., Bartolotti, I., et al. (2017). Scaffolds for Bone Tissue Engineering: State of the Art and New Perspectives. *Mater. Sci. Eng. C* 78, 1246–1262. doi:10.1016/j.msec.2017.05.017

Ruan, S.-q., Yan, L., Deng, J., Huang, W.-l., and Jiang, D.-m. (2017). Preparation of a Biphase Composite Scaffold and its Application in Tissue Engineering for Femoral Osteochondral Defects in Rabbits. *Int. Orthopaedics (Sicot)* 41 (9), 1899–1908. doi:10.1007/s00264-017-3522-2

Sant, S., and Johnston, P. A. (2017). The Production of 3D Tumor Spheroids for Cancer Drug Discovery. *Drug Discov. Today Tech.* 23, 27–36. doi:10.1016/j.ddtec.2017.03.002

Shakibaei, M., Kraehe, P., Popper, B., Shayan, P., Goel, A., and Buhrmann, C. (2015). Curcumin Potentiates Antitumor Activity of 5-fluorouracil in a 3D Alginate Tumor Microenvironment of Colorectal Cancer. *BMC Cancer* 15 (1), 1–15. doi:10.1186/s12885-015-1291-0

Shin, T. H., Kim, M., Sung, C. O., Jang, S. J., and Jeong, G. S. (2019). A One-Stop Microfluidic-Based Lung Cancer Organoid Culture Platform for

Testing Drug Sensitivity. *Lab. Chip* 19 (17), 2854–2865. doi:10.1039/c9lc00496c

Talukdar, S., Mandal, M., Hutmacher, D. W., Russell, P. J., Soekmadji, C., and Kundu, S. C. (2011). Engineered Silk Fibroin Protein 3D Matrices for *In Vitro* Tumor Model. *Biomaterials* 32 (8), 2149–2159. doi:10.1016/j.biomaterials.2010.11.052

Teimouri, A., Ebrahimi, R., Emadi, R., Beni, B. H., and Chermahini, A. N. (2015). Nano-composite of Silk Fibroin-chitosan/Nano ZrO2 for Tissue Engineering Applications: Fabrication and Morphology. *Int. J. Biol. Macromolecules* 76, 292–302. doi:10.1016/j.ijbiomac.2015.02.023

Tian, D., Li, T., Zhang, R., Wu, Q., Chen, T., Sun, P., et al. (2017). Conformations and Intermolecular Interactions in Cellulose/Silk Fibroin Blend Films: A Solid-State NMR Perspective. *J. Phys. Chem. B* 121 (25), 6108–6116. doi:10.1021/acs.jpcb.7b02838

Tong, S., Xu, D.-P., Liu, Z.-M., and Wang, X.-K. (2015). Construction and *In Vitro* Characterization of Three-Dimensional Silk Fibroinchitosan Scaffolds. *Dent. Mater. J.* 34 (4), 475–484. doi:10.4012/dmj.2014-251

Vishwanath, V., Pramanik, K., and Biswas, A. (2016). Optimization and Evaluation of Silk Fibroin-Chitosan Freeze-Dried Porous Scaffolds for Cartilage Tissue Engineering Application. *J. Biomater. Sci. Polym. Edition* 27 (7), 657–674. doi:10.1080/09205063.2016.1148303

Wang, F., Pang, Y., Chen, G., Wang, W., and Chen, Z. (2020). Enhanced Physical and Biological Properties of Chitosan Scaffold by Silk Proteins Cross-Linking. *Carbohydr. Polym.* 229, 115529. doi:10.1016/j.carbpol.2019.115529

Wani, S. U. D., and Veerabhadrappa, G. H. (2018). Silk Fibroin Based Drug Delivery Applications: Promises and Challenges. *Cdt* 19 (10), 1177–1190. doi:10.2174/1389450119666171227205525

Yang, C., Blum, N. T., Lin, J., Qu, J., and Huang, P. (2020). Biomaterial Scaffold-Based Local Drug Delivery Systems for Cancer Immunotherapy. *Sci. Bull.* 65 (17), 1489–1504. doi:10.1016/j.scib.2020.04.012

Zeng, S., Liu, L., Shi, Y., Qiu, J., Fang, W., Rong, M., et al. (2015). Characterization of Silk Fibroin/chitosan 3D Porous Scaffold and *In Vitro* Cytology. *PLoS One* 10 (6), e0128658. doi:10.1371/journal.pone.0128658

Zhu, Y., Wan, Y., Zhang, J., Yin, D., and Cheng, W. (2014). Manufacture of Layered Collagen/chitosan-Polycaprolactone Scaffolds with Biomimetic Microarchitecture. *Colloids Surf. B: Biointerfaces* 113, 352–360. doi:10.1016/j.colsurfb.2013.09.028

Conflict of Interest: The authors declare that the research was conducted in the absence of any commercial or financial relationships that could be construed as a potential conflict of interest.

The reviewer FZ declared a shared affiliation, with no collaboration, with several of the authors HN, JX, XL, LG, YZ, HY, and SW to the handling editor at the time of the review.

Publisher's Note: All claims expressed in this article are solely those of the authors and do not necessarily represent those of their affiliated organizations, or those of the publisher, the editors and the reviewers. Any product that may be evaluated in this article, or claim that may be made by its manufacturer, is not guaranteed or endorsed by the publisher.

frontiers | Frontiers in Bioengineering and Biotechnology

ORIGINAL RESEARCH
published: 24 June 2022
doi: 10.3389/fbioe.2022.897575

Electroconductive Photo-Curable PEGDA-Gelatin/PEDOT:PSS Hydrogels for Prospective Cardiac Tissue Engineering Application

Daniele Testore[1], *Alice Zoso*[1], *Galder Kortaberria*[2], *Marco Sangermano*[3†] and *Valeria Chiono*[1*†]

[1]Department of Mechanical and Aerospace Engineering, Politecnico di Torino, Turin, Italy, [2]Department of Chemical and Environmental Engineering, University of the Basque Country (UPV/EHU), Donostia, Spain, [3]Department of Applied Science and Technology, Politecnico di Torino, Turin, Italy

Electroconductive hydrogels (ECHs) have attracted interest for tissue engineering applications due to their ability to promote the regeneration of electroactive tissues. Hence, ECHs with tunable electrical and mechanical properties, bioactivity, biocompatibility and biodegradability are demanded. In this work, ECHs based on photo-crosslinked blends of polyethylene glycol diacrylate (PEGDA) and gelatin with different PEGDA:gelatin ratios (1:1, 1.5:1 and 2:1 wt./wt.), and containing poly (3,4-ethylenedioxythiophene):poly (styrene sulfonate) (PEDOT:PSS) (0.0, 0.1, 0,3 and 0.5% w/v%) were prepared. Main novelty was the use of gelatin as bioactive component and co-initiator in the photo-crosslinking process, leading to its successful incorporation in the hydrogel network. Physical properties could be modulated by the initial PEGDA:gelatin weight ratio. Pristine hydrogels with increasing PEGDA:gelatin ratio showed: (i) an increasing compressive elastic modulus from 5 to 28 kPa; (ii) a decreasing weight loss from 62% to 43% after 2 weeks incubation in phosphate buffered saline at 37°C; (iii) reduced crosslinking time; (iv) higher crosslinking density and (v) lower water absorption. The addition of PEDOT:PSS in the hydrogels reduced photo-crosslinking time (from 60 to 10 s) increasing their surface and bulk electrical properties. Finally, *in vitro* tests with human cardiac fibroblasts showed that hydrogels were cytocompatible and samples with 1.5:1 initial PEGDA: gelatin ratio promoted the highest cell adhesion at 24 h. Results from this work suggested the potential of electroconductive photo-curable PEGDA-gelatin/PEDOT:PSS hydrogels for prospective cardiac tissue engineering applications.

Keywords: hydrogels, conductivity, photo-crosslinking, PEGDA, gelatin, PEDOT:PSS, cardiac, tissue engineering

OPEN ACCESS

Edited by:
Paola Petrini,
Politecnico di Milano, Italy

Reviewed by:
Yi-Chen Ethan Li,
Feng Chia University, Taiwan
Lorenzo Sardelli,
Politecnico di Milano, Italy

***Correspondence:**
Valeria Chiono
valeria.chiono@polito.it

†*These authors share last authorship*

Specialty section:
This article was submitted to Biomaterials, a section of the journal Frontiers in Bioengineering and Biotechnology

Received: *16 March 2022*
Accepted: *07 June 2022*
Published: *24 June 2022*

Citation:
Testore D, Zoso A, Kortaberria G, Sangermano M and Chiono V (2022) Electroconductive Photo-Curable PEGDA-Gelatin/PEDOT:PSS Hydrogels for Prospective Cardiac Tissue Engineering Application. Front. Bioeng. Biotechnol. 10:897575. doi: 10.3389/fbioe.2022.897575

1 INTRODUCTION

Hydrogels are hydrophilic cross-linked polymeric networks capable of confining and retaining a significant amount of water inside their structure (Hoffman, 2012; Noè et al., 2020). Due to their biomimetic microarchitecture and highly tunable physico-chemical properties they have been increasingly studied in tissue engineering (TE) to mimic soft human tissues, promoting cell attachment, growth and differentiation (Hoffman, 2012; Cavallo et al., 2017; Rogers et al., 2020). Considering that the function of electroactive tissues in the body, such as cardiac, neural and muscle tissue, depends on intra-cellular or extra-cellular electrochemical signaling between cells, TE

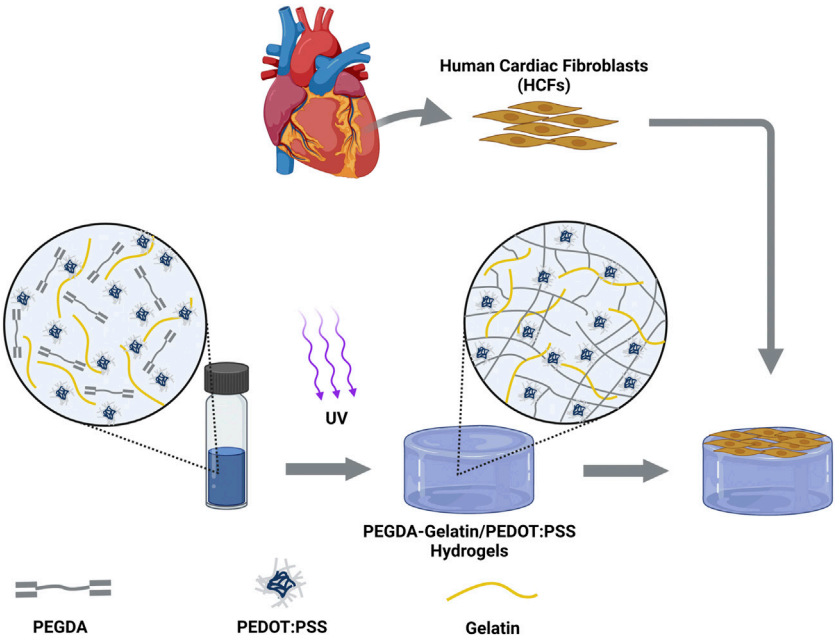

GRAPHICAL ABSTRACT |

scaffolds interacting with those tissues should be designed with electroconductive properties (Mehrali et al., 2017; Rogers et al., 2020). However, most hydrogels are typically constituted by non-conductive materials, therefore showing poor electrical properties (Wu et al., 2016).

Electroconductive hydrogels (ECHs) are a class of smart biomaterials that merge the electrical properties of intrinsically conductive components with highly hydrophilic and biocompatible hydrogel networks (Guiseppi-Elie, 2010). ECHs are currently studied for several biomedical applications, including biosensors (Ren et al., 2019; Lee et al., 2020), drug release (Qu et al., 2018; Chen et al., 2021) and tissue engineering (Roshanbinfar et al., 2018; Heo et al., 2019). Several types of conductive dopants have been combined with hydrogels networks to tune their electrical properties while showing biomimetic characteristics respect to the target tissue (Min et al., 2018). Particularly, metal nanoparticles and carbon-based nanomaterials have been widely employed to develop ECHs for tissue engineering application, obtaining highly conductive scaffolds able to improve electrical cell-to-cell communication and therefore to promote the formation of electroactive engineered tissues. However, these conductive materials are typically nonbiodegradable, they could induce oxidative stresses and long-term cytotoxicity thus hindering their clinical application (Allen et al., 2010; Sani et al., 2021).

Conductive polymers (CPs), has been considered as a valid alternative to metals or carbon-based materials in the biomedical field, thanks to their biocompatibility and different possible applications (Balint et al., 2014). Different CPs, such as polypyrrole and polyaniline (Xu et al., 2016) have been used to prepare ECHs for tissue engineering. Poly (3,4-ethylenedioxythiophene):poly (styrene-sulfonate) (PEDOT:PSS), based on a polythiophene derivative, presents high electrical conductivity (3×10^5–5×10^5 mS/cm), high chemical stability and biocompatibility (Balint et al., 2014; Min et al., 2018). The presence of PSS as a doping agent makes the whole polymeric complex easily dispersible and stable in aqueous solution at physiological conditions (Thaning et al., 2010). Previous short-term *in vivo* studies reported the biocompatibility and biodegradation of polyethylene glycol (PEG)-PEDOT:PSS particles intravenously injected in mice (Cheng et al., 2012). Thanks to its characteristics, PEDOT:PSS has been used for the design of different conductive hydrogels for electroactive tissue engineering. ECHs based on collagen, alginate and PEDOT:PSS were designed to promote the maturation and synchronous beating of neonatal rat cardiomyocytes (Roshanbinfar et al., 2018). In further studies, photo-cured gelatin methacryloyl (GelMA)-PEDOT:PSS hydrogels were initially found to support the viability and spreading of 3D encapsulated myoblasts and subsequently served as a bioink for 3D bioprinting of conductive cell-laden constructs (Spencer et al., 2018; Spencer et al., 2019). Other bioprinted conductive hydrogels for TE applications were developed combining PEDOT:PSS with methylcellulose and kappa-carrageenan (Rastin et al., 2020), or with photocurable polyethylene glycol diacrylate (PEGDA) enabling the differentiation of neural stem cells (Heo et al., 2019). Despite the wide application for tissue engineering, ECHs with tunable electrical and mechanical properties, showing also bioactivity, biocompatibility and biodegradability, are still missing.

Photo-curable hydrogels have gained significant interest in recent years, thanks to their fast gelation kinetics and the precise spatiotemporal control of their properties. In the biomedical field, several photo-crosslinkable hydrogels with tunable mechanical and chemical properties have been reported (Choi et al., 2019). Recently, an innovative photo-curable hybrid natural-synthetic hydrogel for biomedical

TABLE 1 | Compositions of the final solutions exploited for the preparation of the different PEGDA-gelatin/PEDOT:PSS hydrogels, which corresponding codes are reported in the first column.

Code for Crosslinked hydrogels	PEGDA:GELATIN (wt./wt.)	PEDOT:PSS (w/v%)
P1G1	1	0
P1G1P0.1	1	0.1
P1G1P0.3	1	0.3
P1G1P0.5	1	0.5
P1.5G1	1.5	0
P1.5G1P0.1	1.5	0.1
P1.5G1P0.3	1.5	0.3
P2G1	2	0
P2G1P0.1	2	0.1
P2G1P0.3	2	0.3

applications has been proposed by Sangermano and co-workers (Cosola et al., 2019; Zanon et al., 2021). Instead of traditional aliphatic or aromatic amines, unmodified gelatin was used as the co-initiator in a Norrish type II photo-initiating system involving PEGDA as the crosslinker and camphorquinone as the photoinitiator. Thanks to the polymerization mechanism, gelatin segments were chemically crosslinked within PEGDA network, providing arginine-glycine-aspartic acid (RGD) active cell-binding sites. Despite the good biocompatibility results reported by the mentioned works, some concerns about the cytotoxicity of camphorquinone are reported in literature (Hoshikawa et al., 2006). Furthermore, both PEGDA and gelatin are non-conductive materials and therefore unsuitable for regeneration of electroactive tissues, such as cardiac muscle.

The aim of this work was the development of electrically conductive hydrogels with tunable electrical, mechanical and bioactive properties, for tissue engineering application. The photo-curable PEGDA-gelatin photo-initiating system was used with Riboflavin (RF) as a biocompatible type II photoinitiator, replacing camphorquinone. Different PEGDA:gelatin weight ratios were tested to tune mechanical properties of hydrogels. Various concentrations of PEDOT:PSS were finely dispersed within PEGDA-gelatin precursor solutions to impart electrical conductivity to the final system. Photorheological, physico-chemical, mechanical, electrical and *in vitro* degradation properties of hydrogels were evaluated. Finally, as a proof of concept for cardiac tissue engineering application, *in vitro* biocompatibility and adhesion tests with human cardiac fibroblasts (HCF) were performed on hydrogels.

2 MATERIALS AND METHODS

2.1 Materials

Poly (ethylene glycol) diacrylate (PEGDA, Mn = 700 g/mol), Gelatin from cold water fish skin, Riboflavin 5′-phosphate sodium salt hydrate (RF) and Phosphate buffered saline (PBS, pH 7.4) were purchased from Sigma-Aldrich (Milano, Italy) and used as received without further purification. Clevios PH 1000, water based emulsion (1.0–1.3 w/v%) of poly (3,4-ethylenedioxythiophene) polystyrene sulfonate (PEDOT:PSS) was purchased from Ossila (Sheffield, United Kingdom). Deionized water (DIH_2O) was obtained by means of a reverse osmosis purification equipment.

2.2 Methods

2.2.1 Precursor Formulations and Hydrogels Preparation

Different amounts of PEGDA and gelatin powder, as described in **Table 1**, were dissolved in DIH_2O and gently stirred at room temperature until homogeneous mixtures were obtained. Three different PEGDA:gelatin (w/w) ratios were tested with fixed gelatin concentration at 8% (w/v%). The pH of the commercial PEDOT:PSS aqueous dispersion was neutralized with NaOH 1 M solution, as previously suggested (Roshanbinfar et al., 2018) and the concentration of the neutralized dispersion was systematically verified by drying and weighing. Then, as described elsewhere (Spencer et al., 2018; Rastin et al., 2020), sonication in an ice bath for 30 min was applied to the neutralized PEDOT:PSS dispersion to break large aggregates. PEDOT:PSS was slowly added by small volume increments to the PEGDA and gelatin mixture under strong stirring, to reach the desired concentrations, and the resulting solutions were stirred until they became completely homogenous. RF, previously dissolved in DIH_2O to obtain a 4.2 mM stock solution, was added to the hydrogel precursor solutions to reach the final compositions. The final concentration of RF in the solution, was fixed at 0.2 mM for all tested formulations. Finally, the precursor formulations, both pristine (without PEDOT:PSS) and doped (with PEDOT:PSS) were sonicated at 25°C for 30 min to further promote homogeneous dispersion of PEDOT:PSS (Spencer et al., 2018).

For 1.5 and 2 PEGDA:gelatin (w/w) ratios, the formulations containing 0.5% w/v of PEDOT:PSS were not prepared due to gelatin precipitation caused by their reduced water content.

Photo-cured PEGDA-gelatin and PEGDA-gelatin/PEDOT:PSS hydrogels were obtained pouring the precursor solutions within homemade silicone molds and exposing them to UV light (Hamamatsu LC8 lamp) for 300 s. The energy dose (70 mW/cm^2, unless otherwise specified) was periodically checked by means of a EIT POWERPUCK II radiometer (EIT LLC, Leesburg, United States). Unless otherwise stated, hydrogel samples were prepared with rectangular shape (12 mm × 5 mm) and proper thickness (1 mm) for obtaining a complete depth of curing for all the formulations.

2.2.2 Photorheology

Real-time photorheology was performed to investigate photopolymerization kinetics of the UV-cured hydrogels. All rheological experiments were performed on an Anton PAAR Modular Compact Rheometer (Physica MCR 302, Graz, Austria) in parallel-plate mode (25 mm diameter, 0.2 mm of gap) at 37 °C, to avoid any temperature-related physical gelation of gelatin. Preliminary amplitude sweep measurements were carried out at constant shear frequency of 1 Hz to evaluate the linear

viscoelastic region of the solutions. Subsequently, photorheological measurements were performed at the same shear frequency and 1% strain amplitude, providing the light with an Hamamatsu LC8 lamp equipped with an optical fiber precisely positioned under the bottom quartz plate. The irradiating light (60 mW/cm^2 of intensity, periodically checked by radiometer) was turned on after 60 s to allow the stabilization of the system before the onset of the photopolymerization. The evolution of the storage modulus (G′) during the time was recorded to evaluate the polymerization kinetics. Sol-gel phase transition was further evaluated by recording the cross-over points (i.e. time point where G"/G' = tan δ = 1).

2.2.3 Fourier Transform Infrared Spectroscopy

The surface chemistry of samples was analyzed by attenuated total reflectance-infrared spectroscopy (ATR-FTIR). Crosslinked samples were dried overnight, then immersed in DIH_2O at 37 °C for 24 h in order to release the unreacted fraction and finally dried again. Spectra were recorded on a Thermo Scientific Nicolet iS50 FTIR Spectrometer (Milano, Italy) equipped with a diamond crystal ATR accessory. For each sample, ATR spectra were collected in the 4,000–450 cm^{-1} wavenumber range with a resolution of 4 cm^{-1}. The analysis was carried out on three different areas for both the top and bottom sample side. Spectra of gelatin and PEGDA were also taken as reference.

2.2.4 Gelatin Release

Release of uncrosslinked gelatin from cured hydrogels was evaluated by a colorimetric test. Briefly, each dried hydrogels sample was weighed and then immersed in 5 ml of DIH_2O at 37 °C up to 24 h. At predetermined time points (1, 2, 4, 8 and 24 h), the solution was collected for gelatin release evaluation and fresh DIH_2O was added to the samples. Gelatin concentration was determined by the BCA protein assay (Smith et al., 1985), by a calibration curve obtained from solutions at known gelatin concentrations. The absorbance of each solution at 562 nm was measured by an UV-Vis spectrophotometer (Varioskan™ LUX, Thermo Scientific, United States). The released gelatin fraction was calculated as follows:

$$Gelatin\ Release\ (\%) = \frac{[Gelatin]_{supernatant}}{[Gelatin]_{total}} * 100$$

2.2.5 Water Uptake

The water uptake of hydrogels was evaluated by a gravimetric method. Briefly, after their preparation, hydrogels were completely dried overnight at room temperature and, then, weighed (W_{dry}). Completion of the drying process of hydrogels was gravimetrically assessed by zero change in dry weight of samples after overnight, 24 and 48 h storage. Subsequently, dried hydrogels were immersed in 5 ml of PBS solution per hydrogel at 37 °C for 24 h. At each time step (1, 2, 4, 8 and 24 h) samples were collected and weighed again (W_{wet}) after carefully removing the excess of water. The percentage water uptake was calculated according to the following equation:

$$Water\ Uptake\ (\%) = \frac{W_{wet} - W_{dry}}{W_{dry}} * 100$$

2.2.6 Scanning Electron Microscopy

The internal microstructure of photo-cured hydrogels was analyzed by scanning electron microscopy (SEM). After crosslinking, the hydrogels were immersed overnight in PBS at 37 °C in order to reach their equilibrium water content. Samples were then washed three times for 5 min in DIH_2O, frozen at −20 °C and, then, freeze-dried for 48 h (CoolSafe 4-15L freeze-dryer, Labogene, Scandinavia). Freeze-dried samples were rapidly soaked in liquid nitrogen, then fractured and sputter coated with platinum (Q150T Plus turbomolecular pumped coater, Quorum, United Kingdom). SEM images of fracture sections were taken by a Jeol JCM-6000 Plus benchtop SEM (Peabody, United States) operating at 5 kV. Image analysis software (ImageJ, National Institutes of Health, Bethesda, MD, United States) was used to evaluate the dimension of pores in cross-sectional images of samples.

2.2.7 Compression Test

Mechanical characterization of hydrogels was carried out by compression tests using MTS QTestTM/10 Elite controller (MTS Systems Corporation, Edan Prairie, Minnesota, United States) and TestWorks® 4 software (Edan Prairie, Minnesota, United States). Hydrogel samples were prepared in cylindrical molds (11 mm Ø), curing for 300 s at 150 mW/cm^2 in order to obtain samples with 2.5 mm thickness. The cylinders were compressed at a constant cross-head displacement rate of 0.5 mm/min until 70% strain. The Young's Modulus (E) of each sample was calculated as the slope of the initial linear portion, from 0% to 10% strain, of the stress-strain curve.

2.2.8 Electrical Measurements

Electrical properties of hydrogels were evaluated by means of sheet resistance and dielectric spectroscopy measurements. The sheet resistance (R_s) was evaluated using a conventional four-point probe method (Ossila, Sheffield, United Kingdom). Photopolymerized hydrogel surfaces were cleaned from any uncured residual and completely dried overnight at room temperature. Then, the final thickness (t) of dried films was measured with a caliber, before carrying out the measurement. Conductivity (σ) of samples was calculated according to the following equation:

$$\sigma = \frac{1}{R_s * t}$$

Dielectric spectroscopy measurements were carried out in a Novocontrol Alpha high resolution analyzer (Novocontrol Technologies GmbH & Co. KG, Montabaur, Germany) over a frequency range between 0,1 Hz and 1 MHz at room temperature. The instrument was interfaced to a computer and equipped with a Novocontrol Novocool cryogenic system (Novocontrol Technologies GmbH & Co. KG, Montabaur, Germany) for temperature control. Photopolymerized hydrogels were dried overnight at room temperature to obtain circular sheets. Samples were placed between the gold platted electrodes (10 mm diameter) in a sandwich configuration.

2.2.9 Weight Loss

Weight loss of hydrogels due to their *in vitro* dissolution/degradation was investigated by gravimetric measurement of their dry weight after incubation in PBS for different times. In detail, after cleaning sample surface from any uncrosslinked residue, prepared hydrogels were completely dried and weighed (W_i). Then the samples were incubated in 5 ml of PBS for each sample at 37 °C up to 14 days, refreshing the buffer solution every 3 days. At defined time intervals (1, 3, 7 and 14 days), samples were collected, accurately washed three times in DIH_2O for 5 min to remove residual PBS salts, dried and weighed again (W_f). The percentage of weight loss was calculated according to the following equation:

$$Weight\ Loss\ \% = \frac{W_f - W_i}{W_i} * 100$$

2.2.10 Hydrogel Cytocompatibility

Extracts derived from hydrogels with different compositions were tested for their cell cytocompatibility. *In vitro* cell tests were conducted using human cardiac fibroblasts (HCFs, PromoCell, Germany) seeded in a tissue culture 96-well at a cell density of 10,000 cells/well in complete fibroblast growth medium 3 (FGM-3, PromoCell) and maintained in a humified incubator at 37 °C, 5% CO_2.

For each sample, 100 µl of hydrogel solution was prepared by dissolving the different components in FGM-3 and polymerized in circular moulds (11 mm Ø) as previously described. Hydrogels were then rinsed with 4 ml of medium for 1 h, weighed and incubated in a 24-well with 1 ml of FGM-3 per 100 mg of hydrogel at 37 °C for 24 h. Extracts were then collected, filtered through a 0.22 µm syringe filter (polyethersulfone membrane, Carlo Erba, Italy) under a sterile hood and added to HCFs cultures.

After 24 h, extracts were removed, and cell viability was assessed by incubation with CellTiter-Blue® Cell Viability Assay (Promega, United States) for 4 h. Finally, fluorescence intensity was measured with a plate reader at ex/em = 530/590 nm. Results were reported as the average fluorescence intensity value normalized to the control (cells cultured in medium without hydrogel extracts).

2.2.11 Live/Dead Imaging

To investigate cell adhesion on hydrogels, direct contact tests with HCFs were performed and results were analysed by Live/Dead assay. Live/Dead assay quickly differentiates live from dead cells by simultaneously staining the culture with two compounds: green-fluorescent Calcein-AM, which detects intracellular esterase activity of living cells, and red-fluorescent ethidium homodimer-1 (EthD-1), which stains dead cell nuclei.

After preparation, hydrogels were sterilized by 10 min incubation with Ethanol 70% v/v, followed by 30 min UV-C irradiation in a sterile hood and a final rinsing with FGM-3 to remove ethanol residues.

Hydrogels were then cultured with HCFs seeded at a cell density of 25,000 cells/hydrogel. After 24 h cells were rinsed with PBS (ThermoFisher, United States) and tested with the Live/Dead assay (ThermoFisher, United States). Briefly, calcein-AM and EthD-1 were diluted in PBS according to manufacturer instructions. The solution was then added to cells and incubated for 30 min at room temperature in the dark. After incubation, Live/Dead solution was discarded and substituted with FGM-3. Samples were visualized using a fluorescence microscope system Nikon Ti2-E (Nikon Instruments, Japan).

2.2.12 Actin/Nuclei Staining

Cells seeded on hydrogels as described in Par 2.2.11, were fixed in paraformaldehyde 4% w/v% in PBS (PFA, Alfa Aesar) for 30 min, after 24 h and 5 days culture time. Fixed cells were permeabilized with Triton X-100 (Sigma-Aldrich) 0.5% v/v% in PBS for 10 min and blocked with bovine serum albumin (BSA, Sigma-Aldrich) 2% w/v% in PBS for 30 min. Cells were then stained with Phalloidin Green 488 (BioLegend) in BSA 2% w/v% and nuclei were counterstained with DAPI (Sigma-Aldrich). Samples were visualized using a fluorescence microscope system Nikon Ti2-E (Nikon Instruments, Japan).

2.2.13 Data Analysis

At least three parallel samples or three different repetitions for each tested formulation were analyzed in each experiment. *In vitro* cell tests were performed using technical and biological triplicates.

Data are reported as mean ± standard deviation (SD). Statistical differences between experimental groups were determined using one-way ANOVA followed by the Tukey's post hoc test for multiple comparisons. Origin (Pro), Version 2018 (OriginLab Corporation, Northampton, MA, United States) was used for all analyses and plots.

3 RESULTS AND DISCUSSION

3.1 Investigation of Photopolymerization Process

The photoactivated cross-linking process of PEGDA-gelatin hydrogels, with/without PEDOT:PSS, was investigated through photo-rheology. The photo-gelation process was monitored by recording the variations in the storage modulus (G') as a function of time.

Initial studies were carried out on the pristine formulations. As shown in **Figure 1A**, after an initial induction time with unchanged G' (i.e., the irradiation time required to induce cross-linking), G' increased as a function of irradiation time, finally reaching a plateau value, suggesting successful photopolymerization for all tested formulations. Therefore, the role of gelatin as a co-initiator in the radical photo-initiating system involving RF as type II photosensitizer was confirmed, in agreement with previous studies (Cosola et al., 2019; Zanon et al., 2021).

As expected, the reactivity of the system as well as its final viscoelastic properties could be finely modulated by varying the ratio between PEGDA and gelatin. Indeed, with increasing PEGDA:gelatin ratio, induction times and cross-over time points decreased. In more detail, induction times of 59, 45 and 43 s and cross-over times of 119, 104 and 102 s were measured for P1G1, P1.5G1 and P2G1 hydrogels, respectively (**Supplementary Table S1**). While initial slopes of the G′-time curves progressively

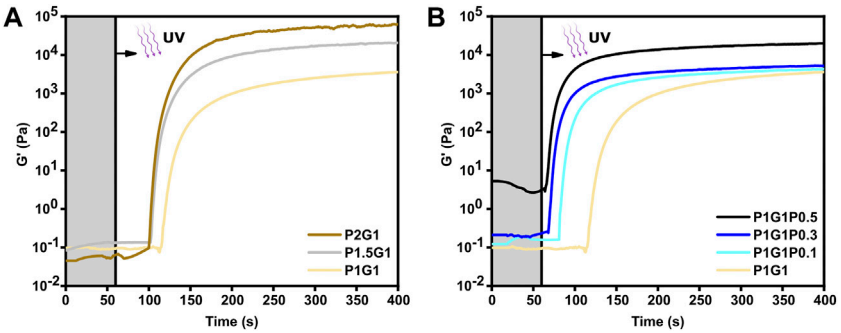

FIGURE 1 | Photopolymerization kinetics of **(A)** pristine hydrogels at different PEGDA:gelatin ratios and **(B)** P1G1 hydrogels with different PEDOT:PSS contents. UV irradiation started after 60 s (grey region).

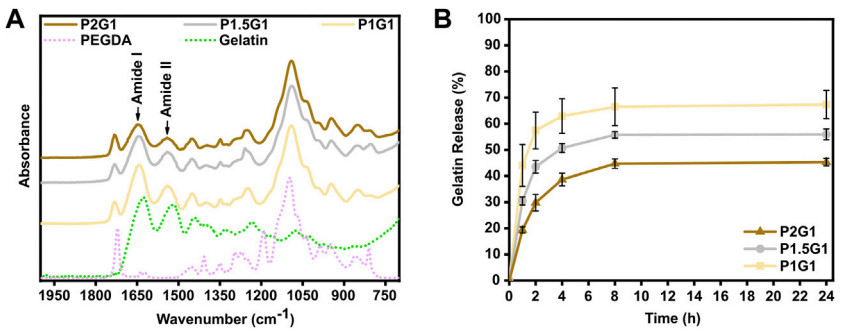

FIGURE 2 | Evaluation of chemical cross-linking of gelatin within hydrogels. **(A)** Attenuated total reflectance-infrared spectroscopy (ATR-FTIR) spectra of pristine hydrogel samples, gelatin powder and non-crosslinked PEGDA in the 2000–700 cm^{-1} wavenumber range. **(B)** Cumulative gelatin release (wt%) from pristine hydrogels at 1, 2, 4, 8 and 24 h in DIH_2O at 37 °C. Percentages are referred to the total amount of gelatin within the samples.

became steeper, suggesting an increase in the polymerization rates (**Figure 1A**). Such effects on gelation kinetics were probably due to the progressively higher concentrations of PEGDA in the precursor formulations. Accordingly, higher PEGDA:gelatin ratios resulted in higher final values of G' (**Figure 1A**), associated to an increased cross-linking density and decreased overall water content.

Previous reports on photo-crosslinkable hydrogels containing PEDOT:PSS dispersion did not investigate the influence of PEDOT:PSS concentration on the photo-crosslinking kinetics (Spencer et al., 2018; Heo et al., 2019; Spencer et al., 2019; Lin et al., 2021). In this work, photo-rheological tests were exploited to compare photo-crosslinking kinetics of pristine and doped hydrogels. Interestingly, the low PEDOT:PSS concentrations used in this work remarkedly increased photo-crosslinking kinetics. Indeed, average induction times reduced from 59 s for P1G1 samples to only 8 s for P1G1P0.5 samples (**Figure 1B**). Interestingly, P1G1P0.1 and P1G1P0.3 hydrogels reached similar plateau values of G' compared to pristine P1G1 hydrogel. The boost effect of PEDOT:PSS on polymerization process could be related to the free-radical formation on PSS chains under UV exposure (Wang et al., 2020). In this case, the presence of PSS probably enhanced the free-radical photogeneration pathway of the RF/gelatin photo-initiating system. Photo-rheological data for pristine and doped P1.5G1 and P2G1 samples evidenced similar trends (**Supplementary Figure S1A,B**).

The P1G1P0.5 formulation showed a photo-gelation kinetic comparable to that of the other doped formulations, but with a higher starting G' (**Figure 1B**). This difference was probably a consequence of the more pronounced molecular interactions between the anionic sulfonic groups of PEDOT:PSS and the cationic amino acids, such as arginine or lysine, present on the gelatin backbone (Spencer et al., 2018; Lee et al., 2020).

3.2 Gelatin Cross-Linking Within Hydrogel Network

Previous literature reported that, after taking part in the photo-induced generation of radicals, gelatin remains covalently bonded to the hydrogel network (Cosola et al., 2019; Zanon et al., 2021). In this work, initially the chemical cross-linking of gelatin was qualitatively evaluated by means of infrared spectroscopy. Afterwards, the amount of released gelatin (and, as a difference, the amount gelatin incorporated in the network)

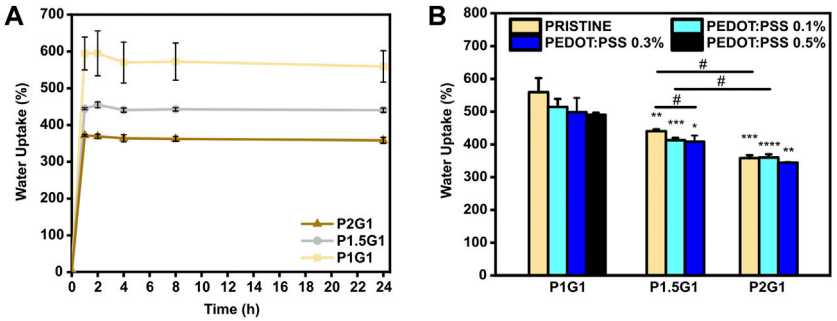

FIGURE 3 | Water uptake of hydrogels: **(A)** Behavior of water uptake percentage vs. time for pristine hydrogels incubated for 1, 2, 4, 8 and 24 h in PBS at 37°C. **(B)** Equilibrium water uptake percentage of hydrogels at 24 h $^{*}p < 0.05$, $^{**}p < 0.01$, $^{***}p < 0.001$ and $^{****}p < 0.0001$ represent significative differences in respect to P1G1 samples. $^{\#}p < 0.05$ represent significative differences for all other comparisons.

was quantified through a colorimetric test. For both analyses, the three different PEGDA-gelatin pristine formulations were compared.

ATR-FTIR characterization was performed on dried hydrogel previously washed for 24 h in DIH_2O to release its unreacted soluble fraction. Such washing step was performed at 37 °C to avoid the risk of physical aggregation of gelatin molecules (thermogelation) at lower temperature, ensuring the detection of chemically bond gelatin only. ATR-FTIR spectra of tested samples (P1G1, P1.5G1 and P2G1) showed the presence of the typical absorption bands of gelatin and PEGDA (**Figure 2A**). Particularly, the two peaks at 1,644 and 1,540 cm^{-1} were attributed to the characteristic amide I (C=O stretching mode) and amide II (N-H bending mode) bands of gelatin, respectively. These results suggested the covalent bonding of gelatin within the hydrogel network as previously reported (Cosola et al., 2019; Zanon et al., 2021). Furthermore, all tested formulations showed the presence of the typical absorption peak of carbonyl groups of PEGDA at 1724 cm^{-1} (C=O stretching mode).

Gelatin release from the pristine PEGDA-gelatin hydrogels incubated in DIH_2O at 37 °C was then evaluated by BCA assay. For all tested samples, gelatin release started immediately after incubation and increased with time, reaching a plateau at 8–24 h. The total released amount of gelatin decreased with increasing PEGDA:gelatin ratio in the formulations, suggesting that at higher PEGDA amount, more gelatin could remain entrapped in the hydrogel network. After 24 h, P1G1, P1.5G1 and P2G1 released 67 ± 5%, 56 ± 2% and the 45 ± 1% of total gelatin amount, respectively (**Supplementary Figure S2B**). The statistically significative decreasing amount of released gelatin with increasing PEGDA:gelatin ratio in hydrogels could be due to the increasing reactivity and cross-linking degree of hydrogels, as also suggested by photorheology. Acellular scaffolds for tissue engineering applications are aimed at the initiation of the host tissue regeneration process, exploiting native cell populations *in situ* (Salih, 2009). Therefore, bioactive materials with cell-adhesion active ligands need to be integrated within the scaffolds. PEGDA is biocompatible but biologically inert (Jabbari et al., 2015). On the other hand, arginine-glycine-aspartic acid (RGD) peptide, present along gelatin chains, promotes cell adhesion and spreading via integrin binding (Spencer et al., 2018). After 24 h incubation, PEGDA-gelatin hydrogels retained more than 40% of the initial gelatin content, which may support the process of cell adhesion and proliferation. Importantly, once the cells have adhered, they start to remodel the adhesion substrate, by promoting matrix degradation through the synthesis of degradative enzymes, followed by matrix enrichment/replacement with new extracellular matrix (ECM) molecules.

Furthermore, possible influence of PEDOT:PSS on gelatin incorporation was evaluated. Gelatin release profiles from P1G1P0.5 hydrogels (i.e. the samples with highest PEDOT:PSS content) were analyzed and compared to pristine samples. In doped hydrogels gelatin release kinetics slightly decreased in the first hours (**Supplementary Figure S2A**), whereas after 24 h (**Supplementary Figure S2B**) P1G1P0.5 released 61 ± 4% of gelatin with no statistically significant differences respect to P1G1 samples.

3.3 Hydrogel Water Uptake and Microstructure

Water uptake percentage of PEGDA-gelatin and PEGDA-gelatin/PEDOT:PSS hydrogels was monitored as a function of time by incubating previously dried samples in PBS (pH 7.4, 37 °C). As shown in **Figure 3A**, pristine hydrogels rapidly reached their maximum water uptake percentage after 2 h incubation, due to their high hydrophilicity. Then, water uptake percentage did not significantly change up to 24 h. Interestingly, hydrogels with progressively higher PEGDA: gelatin ratio showed progressively lower water uptake percentages at 24 h (**Figure 3B**), with values of 559 ± 43%, 440 ± 6% and 358 ± 8% for P1G1, P1.5G1 and P2G1 samples, respectively. Such trend depends on the higher concentration and crosslinking degree of hydrogels with increasing PEGDA: gelatin ratio, and is in agreement with results from photorheology and gelatin release tests.

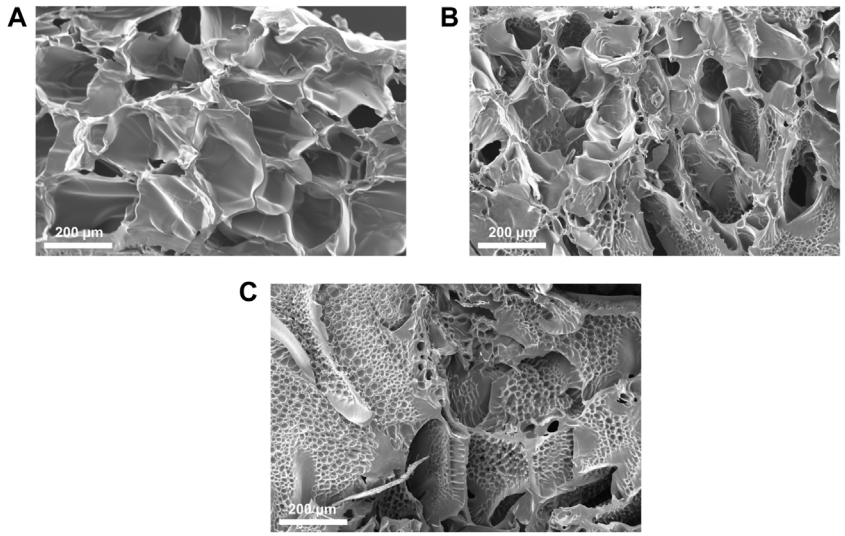

FIGURE 4 | Cross-sectional SEM images of lyophilized **(A)** P1G1, **(B)** P1.5G1 and **(C)** P2G1 pristine hydrogels (scale bars = 200 µm).

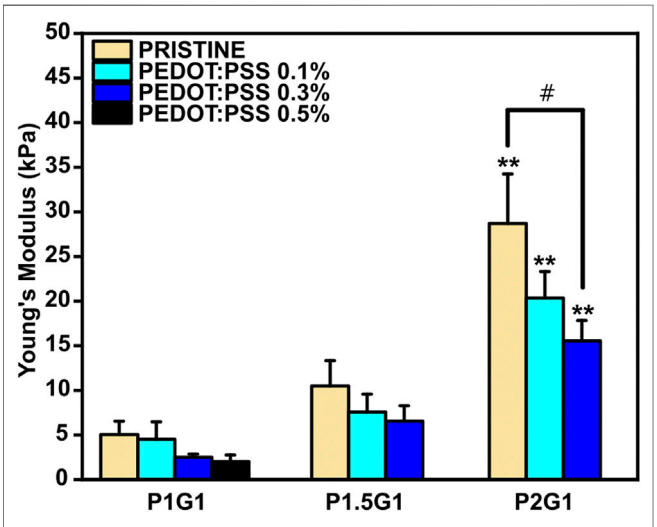

FIGURE 5 | Compressive Young's Modulus of pristine and doped hydrogels with varying PEGDA:gelatin ratios and PEDOT:PSS contents. $^{**}p < 0.01$ represent significative differences in respect to P1G1 and P1.5G1 samples. $^{\#}p < 0.05$ represent significative differences for all other comparisons.

The incorporation of increasing PEDOT:PSS amounts in hydrogels the same PEGDA:gelatin ratio did not significantly influence their water uptake (**Supplementary Figure S3A,B,C**) (**Figure 3B**). Hence, hydrogels with constant PEDOT:PSS amount continued to display a decreasing trend of the water uptake percentage with increasing PEGDA:gelatin ratio.

Water uptake ability of hydrogels influences cell behavior by affecting different hydrogel properties, such as: (i) hydrogel mesh size, which in turn affects hydrogel permeability (gas and nutrient diffusion) (Lin et al., 2011); (ii) hydrogel stiffness (Bhana et al., 2010), and (iii) electrical properties of conductive hydrogels (Navaei et al., 2019).

In this work, hydrogels showed quick water absorption and, at the same time, slight variations in PEGDA:gelatin ratios significantly changed hydrogels cross-linking degree and, therefore, their water uptake ability. Differently from previous studies which reported an influence of PEDOT:PSS content on hydrogel water uptake ability, water uptake properties of PEGDA-gelatin hydrogels were not affected by the presence of PEDOT:PSS. This result could be the result of a thorough preparation of the hydrogels, by fine dispersion of PEDOT:PSS in the precursor solution, followed by photopolymerization, as described in the Par. 3.1.

Cross-sectional SEM images of freeze-dried PEGDA-gelatin hydrogels (**Figure 4**) showed that PEGDA:gelatin ratio and hydrogel concentration influenced the microarchitecture of freeze-dried samples. All samples exhibited porous microstructures with interconnected pores and smooth pore walls that would be beneficial for cell migration and proliferation in tissue engineering applications (Parchehbaf-Kashani et al., 2020). P1G1 samples (**Figure 4A**) showed pores with average size comprised between 30 and 290 µm. P1.5G1 samples (**Figure 4B**) showed pores in the same size range, together with smaller pores (5–30 µm), which density further increased in P2G1 samples (**Figure 4C**). Such change in morphology was due to a progressively higher PEGDA content and decreased water content.

Moreover, while other freeze-dried photo-curable hydrogels for tissue engineering applications, based on GelMA or PEGDA have shown unimodal pore distribution (Lin et al., 2011; Spencer et al., 2018), the heterogeneous morphology herein obtained could be beneficial for the stimulation of different cell populations constituting the target tissue (Han et al., 2021). As an example, one previous report suggested that the presence of smaller

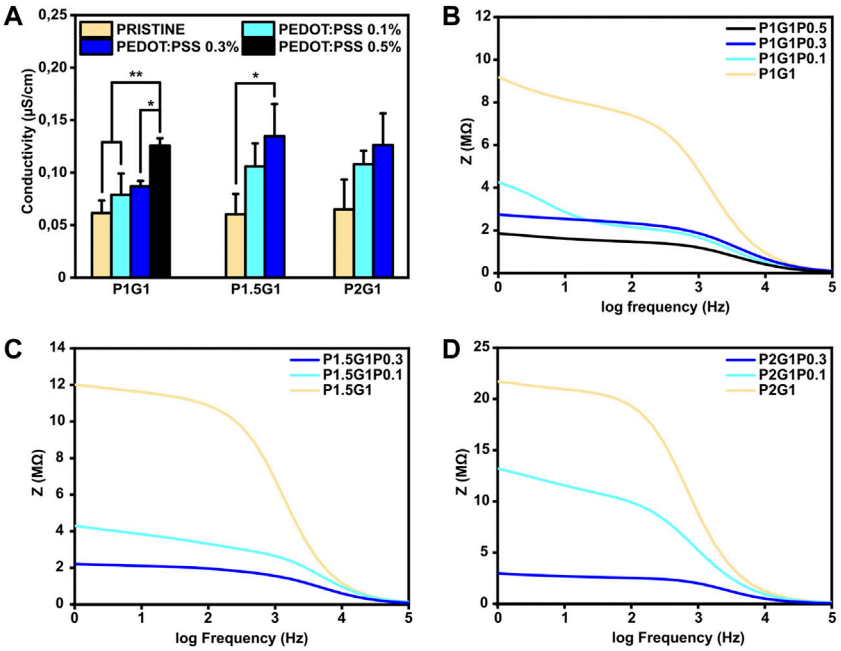

FIGURE 6 | Electrical characterization of PEGDA-gelatin/PEDOT:PSS hydrogels in a dry state. **(A)** Conductivity of all the samples with different PEGDA:gelatin ratio and PEDOT:PSS content measured with a four-point probe. **(B)**, **(C)**, **(D)** Dielectric spectroscopy of P1G1, P1.5G1 and P2G1 samples respectively. $^{*}p < 0.05$, $^{**}p < 0.01$.

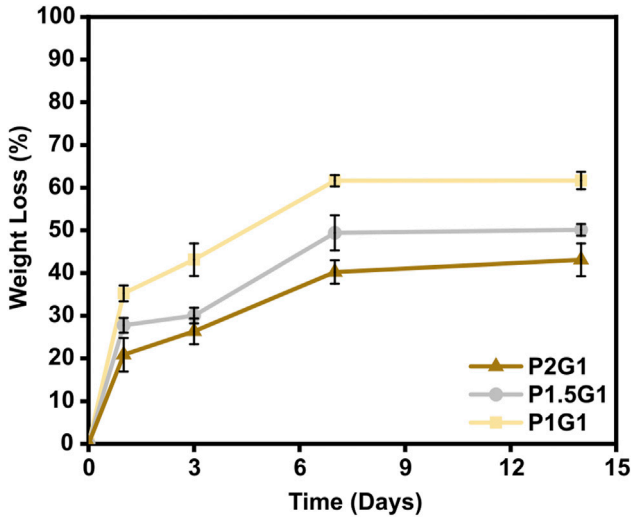

FIGURE 7 | *In vitro* weight loss curves of pristine hydrogels after 1, 3, 7 and 14 days of incubation in PBS at 37°C.

interconnected pores can favor angiogenesis with negligible fibrosis during cardiac regeneration (Finosh and Jayabalan, 2015).

Additionally, SEM images of pore wall fracture surface of freeze-dried PEGDA-gelatin hydrogels did not show a biphasic morphology, suggesting intermolecular interaction and crosslinking between the two hydrogel components.

As illustrated in **Supplementary Figure S4**, the addition of PEDOT:PSS did not affect the microstructures of hydrogels as a result of the fine dispersion of the conductive filler in the precursor solution.

3.4 Mechanical Characterization

It is well established that the three-dimensional hydrophilic microenvironment of hydrogels resembles the natural extracellular matrix (Maharjan et al., 2019). However, hydrogels are also required to display tissue-like mechanical properties for improved integration into the target tissue after implantation (Donnelly et al., 2017; Noshadi et al., 2017). In this work, compressive elastic modulus of PEGDA-gelatin hydrogels was measured from compression stress-strain tests (**Supplementary Figure S5**). The influence of different PEGDA:gelatin ratios on the final stiffness of photocured hydrogels was studied. As can be observed in **Figure 5**, elastic modulus of PEGDA-gelatin pristine hydrogels increased from 5.0 ± 1.5 kPa for P1G1, to 10.5 ± 2.8 kPa for P1.5G1 and 28.7 ± 5.5 kPa for P2G1 samples, in agreement with G' plateau value in photorheological analysis, associated with the different crosslinking degree and water content. According to previous works involving photo-curable PEGDA hydrogels (Mazzoccoli et al., 2009; Noshadi et al., 2017; Wang et al., 2018; Choi et al., 2019), in this work the initial composition of the formulation (i.e., PEGDA:gelatin ratio) allowed a fine control of hydrogel mechanical properties, together with bioactive cues integration, provided by gelatin cross-linking. Notably, the obtained values of stiffness matched the range of natural soft tissues and organs (≈0.1–1,000 kPa), particularly the one of healthy cardiac tissue (≈10–30 kPa) (Bhana et al., 2010; Liu et al., 2015). Recent reports highlighted the role of controlled physical cues in biomaterials-

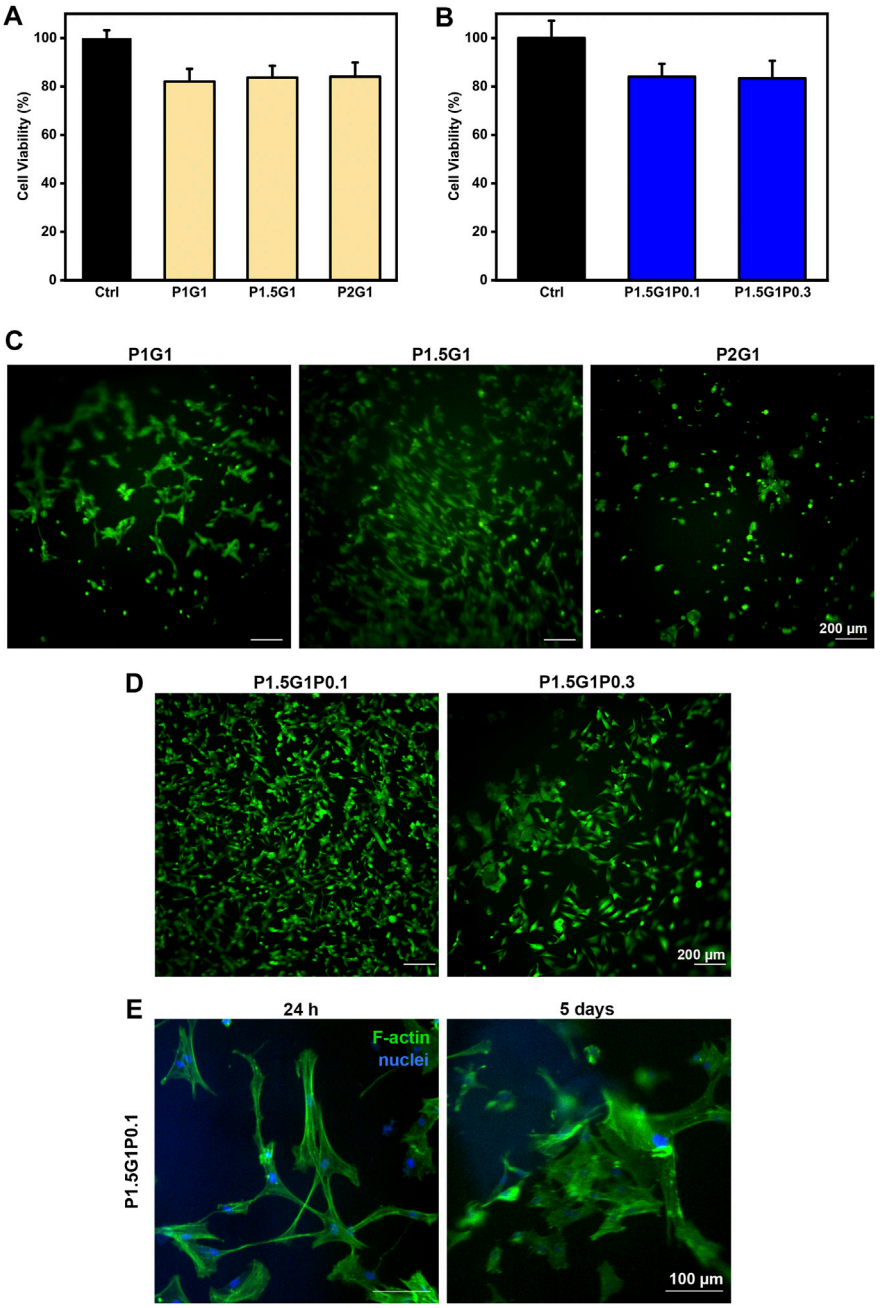

FIGURE 8 | *In vitro* cell characterization of hydrogels. **(A)**, **(B)** indirect cytocompatibility tests of human cardiac fibroblasts, evaluated at 24 h on hydrogel extracts, respectively from **(A)** pristine and **(B)** doped samples. Controls are represented by cells cultured in a medium not containing extracts. **(C)**, **(D)** Viability of HCFs in direct contact with **(C)** pristine and **(D)** doped samples, respectively, after 24 h culture time, evaluated through Live/Dead imaging (scale bars = 200 µm). **(E)** DAPI/F-actin staining of HCFs at 24 h and 5 days for morphological evaluation (scale bars = 100 µm).

mediated regenerative approaches aimed at post-infarct myocardial regeneration (Paoletti et al., 2018; Paoletti and Chiono, 2021). Hence, the tunable mechanical properties of the herein developed hydrogels make them highly interesting for further investigations in cardiac regenerative approaches.

The presence of PEDOT:PSS caused a slightly reduction in the final Young's modulus of hydrogels with the same PEGDA:gelatin ratio, with no significant differences except for P2G1 and P2G1P0.3 samples. In agreement with previous reports (Sangermano et al., 2008; Gonzalez et al., 2017; Cortés et al., 2021), the presence of UV light absorbing fillers such as PEDOT:PSS may lead to UV shielding effect reducing photopolymerization kinetics of thick samples at increasing depth from the exposed surface. Therefore, the cross-linking degree of thick cylindrical hydrogels containing PEDOT:PSS was lower on the bottom portion of the samples, affecting the final mechanical properties. Hence, obtaining a

complete depth of curing of samples, influence of PEDOT:PSS on final mechanical properties is not expected.

3.5 Electrical Characterization

The possibility to tune the electroconductive properties of PEGDA-gelatin/PEDOT:PSS hydrogels by PEDOT:PSS content was thoroughly studied. Indeed, for electroactive tissues regeneration, engineered culture substrates should mediate electrical signaling between cells (Rogers et al., 2020).

The effect of PEDOT:PSS addition on both surface and bulk conductivity of hydrogels was evaluated on dried samples.

Firstly, surface conductivities of PEGDA-gelatin/PEDOT:PSS samples were measured by standard four-point probe (**Figure 6A**). For hydrogels with constant PEGDA:gelatin ratio, conductivity increased as a function of PEDOT:PSS content. Specifically, conductivities raised from 0.06 ± 0.01 μS/cm for the pristine samples to 0.12 ± 0.01 μS/cm for P1G1P0.5 samples and to 0.13 ± 0.03 μS/cm for both P1.5G1P0.3 and P2G1P0.3 samples. Similar range of values were obtained in a previous work reporting the influence of conductive polymer addition on hydrogel conductivities in dry conditions (Guo et al., 2019). Since both gelatin and PEGDA are non-conductive materials, these preliminary results demonstrated a clear contribution of electronic transport introduced by PEDOT:PSS dispersion within the network.

In order to confirm these preliminary results and investigate the bulk electrical properties, dielectric spectroscopy, which applies an alternating current at different frequencies through the entire sample thickness, was performed. Moreover, since physiological currents typically occur in a bidirectional way, this kind of characterization is interesting to test biomaterials for electroactive TE applications (Breukers et al., 2010). As shown in **Figures 6B–D**, all tested hydrogels exhibited higher impedance at lower frequencies (resistive effect) and lower impedance at higher frequencies (capacitive effect). At 1 Hz, which is the characteristic heartbeat frequency of an adult human in resting conditions, hydrogels containing PEDOT:PSS possessed lower impedance than pristine hydrogels. As an example, for P1G1 samples (**Figure 6B**), impedance decreased from 9.1 MΩ for pristine formulation to 1.8 MΩ for P1G1P0.5 formulation. At the same time, P1.5G1 and P2G1 samples (**Figures 6C,D**) showed same trends of impedance variation. All together these results demonstrated the ability of PEDOT:PSS to enhance electroconductive properties of photocurable PEGDA-gelatin hydrogels, suggesting their potential involvement in cardiac tissue engineering.

3.6 Hydrogels *in Vitro* Weight Loss

As an important property of hydrogels for TE applications, their *in vitro* weight loss in PBS at 37 °C was evaluated. A controlled rate of weight loss is fundamental to ensure proper integration of the construct with the host tissue before complete degradation (Shie et al., 2020). PEGDA-gelatin hydrogels showed to be stable in PBS for 14 days (**Figure 7**). After 1 day of incubation, an initial weight loss of 35.2 ± 1.9%, 27.8 ± 1.7% and 20.8 ± 3.9% was measured for P1G1, P1.5G1 and P2G1 hydrogels, respectively, caused by the release of unreacted components. Interestingly, weight loss decreased with increasing PEGDA:gelatin ratio, due to the higher crosslinking degree. At longer times, samples showed a controlled weight loss profile probably due to hydrolytic degradation of gelatin and ester bonds in PEGDA component (Stillman et al., 2020). After 2 weeks, weight loss was 61.7 ± 2.0%, 50.0 ± 1.4% and 43.1 ± 3.8% for P1G1, P1.5G1 and P2G1 hydrogels, respectively.

The influence of PEDOT:PSS on the weight loss profile of hydrogels, as displayed in **Supplementary Figure S6A–C**, was mostly negligible.

Photo-induced chemical crosslinking process has previously shown to be an effective strategy to improve stability of hydrogels based on natural polymers, which are typically subjected to rapid degradation (Heo et al., 2016). Notably, as a photo-cross-linkable gelatin derivative, GelMA has been widely studied for hydrogel fabrication but its high biodegradation rate has been reported as a drawback (Wang et al., 2018). PEGDA-gelatin hydrogels developed in this work could overcome this limitation thanks to their tunable degradation rate depending on PEGDA:gelation ratio. However, since gelatin is derived from collagen, enzymatic degradation mediated by proteinases could potentially increase biodegradation rate of PEGDA-gelatin hydrogels in the presence of cells.

3.7 *In Vitro* Biological Characterization of Hydrogels

In order to evaluate the applicability of developed PEGDA-gelatin/PEDOT:PSS hydrogels as cardiac tissue engineering scaffolds, their *in vitro* cytocompatibility and capability to stimulate cell adhesion was evaluated using HCFs.

The three pristine hydrogel formulations were initially tested. Indirect cytocompatibility tests were conducted following the guidelines of the International Organization for Standardization (ISO 10993–5), incubating cells in medium containing hydrogel extracts (i.e. medium previously in contact with the different PEGDA-gelatin hydrogels). As illustrated in **Figure 8A**, HCFs cultured with extracts from each pristine formulation showed viability values higher than 80%, compared to the control (i.e. cells cultured in medium not in contact with hydrogels), suggesting non-cytotoxicity according to ISO 10993–5.

Then, HCFs adhesion and viability on pristine hydrogels was demonstrated by Live/Dead staining after 24 h (**Figure 8C**). Due to its anti-adhesive effect, an increasing content of PEGDA is expected to decrease cell attachment, which on the other hand can be promoted by gelatin (Jabbari et al., 2015). Indeed, cells incubated with P2G1 hydrogels were poorly adherent and showed a round morphology. Interestingly, higher adhesion and spreading of HCFs were observed on P1.5G1 hydrogels than on P1G1. This behavior could be due to the higher gelatin release of P1G1 samples, reducing their bioactivity. Therefore, P1.5G1 hydrogel composition was selected for further characterizations, aimed at the study of conductive PEDOT:PSS influence on HCFs behavior by indirect and direct biocompatibility assays. As shown in **Figure 8B**, HCFs cultured in the presence of extracts from P1.5G1P0.1 and P1.5G1P0.3 hydrogels showed similar cytocompatibility percentage, respect to HCFs cultured in the presence of extracts from pristine P1.5G1 hydrogel. Live and Dead images of HCFs in direct contact with hydrogels, reported in **Figure 8D**, showed a similar behavior for

P1.5G1P0.1 and P1.5G1 hydrogels, while apparently a reduced amount of viable HCFs was present on P1.5G1P0.3 hydrogels. The presence of a higher PEDOT:PSS amount probably decreased the accessibility of RGD peptide sequences for cell adhesion, slightly reducing the cell-adhesive properties of P1.5G1P0.3 hydrogels. Additionally, P1.5G1P0.1 hydrogels also demonstrated to sustain and maintain cell adhesion and a proper morphology after 24 h post-seeding and up to 5 days of culture, as confirmed by actin/nuclei staining in **Figure 8E**.

4 CONCLUSION

In this study, PEDOT:PSS was successfully incorporated within photo-curable PEGDA-gelatin networks to obtain electroconductive hydrogels. As important novelty, gelatin was exploited both as bioactive component and co-initiator in the photo-crosslinking process, leading to its successful incorporation in the hydrogel network. For the first time PEGDA-gelatin radical photo-initiating system was optimized for tissue engineering application. By increasing PEGDA:gelatin ratio from 1:1 to 2:1, the photo-crosslinking rate of hydrogels increased and a higher cross-linking density was obtained. Previous studies on ECHs with PEDOT:PSS incorporation did not investigate the influence of the conductive polymer addition on the formation of hydrogel network. In this work, photorheological tests proved that PEDOT:PSS did not hinder the photopolymerization process, but contrarily enhanced the photo-crosslinking kinetics.

The resulting PEGDA-gelatin hydrogels could be finely tuned in their mechanical, water uptake and weight loss properties by simply changing PEGDA:gelatin ratio in the starting formulation. Indeed, by increasing the initial content of PEGDA, stiffer hydrogels with a more dense microarchitecture, a reduced water uptake ability and lower weight loss at physiological conditions were obtained. The elastic compressive modulus of hydrogels was in the range of stiffness values of the native cardiac tissue (≈10–30 kPa). The addition of increasing concentrations of PEDOT:PSS within PEGDA-gelatin samples successfully enhanced their surface and bulk electrical conductivity without remarkedly affecting the physico-chemical properties of hydrogels. Hydrogels were biocompatible and successful incorporation of gelatin within the hydrogels, promoted adhesion of human cardiac fibroblasts. Particularly, P1.5G1 samples proved to have the best balance in terms of gelatin retention, water uptake, weight loss, mechanical and biological properties, promoting HCF adhesion and spreading. PEDOT:PSS containing hydrogels were also biocompatible and, particularly, P1.5G1P0.1 formulation showed superior HCF adhesion ability. In the future, P1.5G1P0.1 hydrogels could be used to promote the maturation and cell-cell interactions of contractile cells (e.g., cardiomyocytes) for cardiac tissue engineering applications.

DATA AVAILABILITY STATEMENT

The raw data supporting the conclusion of this article will be made available by the authors, without undue reservation.

AUTHOR CONTRIBUTIONS

DT performed the experiments, except for dielectric spectroscopy and biological characterization, analyzed all the data, and contributed substantially to the writing of the manuscript. AZ performed the biological assays and contributed to the elaboration and interpretation of biological results. GK performed dielectric spectroscopy measurements. MS and VC planned the experiments, supervised the work, contributed to interpretation of data, manuscript writing and revision. VC acquired funding.

FUNDING

This work was supported by BIORECAR project. The project has received funding from the European Research Council (ERC) under the European Union's Horizon 2020 Research and Innovation Programe (Grant Agreement No. 772168).

ACKNOWLEDGMENTS

The authors acknowledge support from the European Research Council (ERC) under the European Union's Horizon 2020 Research and Innovation Programe (Grant Agreement No. 772168), through BIORECAR ERC Consolidator project (www.biorecar.polito.it).

SUPPLEMENTARY MATERIAL

The Supplementary Material for this article can be found online at: https://www.frontiersin.org/articles/10.3389/fbioe.2022.897575/full#supplementary-material.

REFERENCES

Allen, M. J., Tung, V. C., and Kaner, R. B. (2010). Honeycomb Carbon: A Review of Graphene. *Chem. Rev.* 110, 132–145. doi:10.1021/cr900070d

Balint, R., Cassidy, N. J., and Cartmell, S. H. (2014). Conductive Polymers: Towards a Smart Biomaterial for Tissue Engineering. *Acta Biomater.* 10, 2341–2353. doi:10.1016/j.actbio.2014.02.015

Bhana, B., Iyer, R. K., Chen, W. L., Zhao, R., Sider, K. L., Likhitpanichkul, M., et al. (2010). Influence of Substrate Stiffness on the Phenotype of Heart Cells. *Biotechnol. Bioeng.* 105, 1148–1160. doi:10.1002/bit.22647

Breukers, R. D., Gilmore, K. J., Kita, M., Wagner, K. K., Higgins, M. J., Moulton, S. E., et al. (2010). Creating Conductive Structures for Cell Growth: Growth and Alignment of Myogenic Cell Types on Polythiophenes. *J. Biomed. Mat. Res.* 95A, 256–268. doi:10.1002/jbm.a.32822

Cavallo, A., Madaghiele, M., Masullo, U., Lionetto, M. G., and Sannino, A. (2017). Photo-Crosslinked Poly(Ethylene Glycol) Diacrylate (PEGDA) Hydrogels from Low Molecular Weight Prepolymer: Swelling and Permeation Studies. *J. Appl. Polym. Sci.* 134, 44380. doi:10.1002/APP.44380

Chen, J., Han, X., Deng, J., Zhang, J., Li, L., Ni, J., et al. (2021). An Injectable Hydrogel Based on Phenylboronic Acid Hyperbranched Macromer Encapsulating Gold Nanorods and Astragaloside IV Nanodrug for

Myocardial Infarction. *Chem. Eng. J.* 413, 127423. doi:10.1016/j.cej.2020.127423

Cheng, L., Yang, K., Chen, Q., and Liu, Z. (2012). Organic Stealth Nanoparticles for Highly Effective *In Vivo* Near-Infrared Photothermal Therapy of Cancer. *ACS Nano* 6, 5605–5613. doi:10.1021/nn301539m

Choi, J. R., Yong, K. W., Choi, J. Y., and Cowie, A. C. (2019). Recent Advances in Photo-Crosslinkable Hydrogels for Biomedical Applications. *Biotechniques* 66, 40–53. doi:10.2144/btn-2018-0083

Cortés, A., Cosola, A., Sangermano, M., Campo, M., González Prolongo, S., Pirri, C. F., et al. (2021). DLP 4D-Printing of Remotely, Modularly, and Selectively Controllable Shape Memory Polymer Nanocomposites Embedding Carbon Nanotubes. *Adv. Funct. Mat.* 31, 2106774. doi:10.1002/adfm.202106774

Cosola, A., Chiappone, A., Martinengo, C., Grützmacher, H., and Sangermano, M. (2019). Gelatin Type A from Porcine Skin Used as Co-Initiator in a Radical Photo-Initiating System. *Polym. (Basel)* 11 (11), 1901. doi:10.3390/polym11111901

Donnelly, P. E., Chen, T., Finch, A., Brial, C., Maher, S. A., and Torzilli, P. A. (2017). Photocrosslinked Tyramine-Substituted Hyaluronate Hydrogels with Tunable Mechanical Properties Improve Immediate Tissue-Hydrogel Interfacial Strength in Articular Cartilage. *J. Biomater. Sci. Polym. Ed.* 28, 582–600. doi:10.1080/09205063.2017.1289035

Finosh, G. T., and Jayabalan, M. (2015). Hybrid Amphiphilic Bimodal Hydrogels Having Mechanical and Biological Recognition Characteristics for Cardiac Tissue Engineering. *RSC Adv.* 5, 38183–38201. doi:10.1039/C5RA04448K

Gonzalez, G., Chiappone, A., Roppolo, I., Fantino, E., Bertana, V., Perrucci, F., et al. (2017). Development of 3D Printable Formulations Containing CNT with Enhanced Electrical Properties. *Polymer* 109, 246–253. doi:10.1016/j.polymer.2016.12.051

Guiseppi-Elie, A. (2010). Electroconductive Hydrogels: Synthesis, Characterization and Biomedical Applications. *Biomaterials* 31, 2701–2716. doi:10.1016/J.BIOMATERIALS.2009.12.052

Guo, B., Qu, J., Zhao, X., and Zhang, M. (2019). Degradable Conductive Self-Healing Hydrogels Based on Dextran-Graft-Tetraaniline and N-Carboxyethyl Chitosan as Injectable Carriers for Myoblast Cell Therapy and Muscle Regeneration. *Acta Biomater.* 84, 180–193. doi:10.1016/j.actbio.2018.12.008

Han, Y., Lian, M., Wu, Q., Qiao, Z., Sun, B., and Dai, K. (2021). Effect of Pore Size on Cell Behavior Using Melt Electrowritten Scaffolds. *Front. Bioeng. Biotechnol.* 9, 629270. doi:10.3389/fbioe.2021.629270

Heo, D. N., Lee, S.-J., Timsina, R., Qiu, X., Castro, N. J., and Zhang, L. G. (2019). Development of 3D Printable Conductive Hydrogel with Crystallized PEDOT:PSS for Neural Tissue Engineering. *Mat. Sci. Eng. C* 99, 582–590. doi:10.1016/j.msec.2019.02.008

Heo, J., Koh, R. H., Shim, W., Kim, H. D., Yim, H.-G., and Hwang, N. S. (2016). Riboflavin-Induced Photo-Crosslinking of Collagen Hydrogel and its Application in Meniscus Tissue Engineering. *Drug Deliv. Transl. Res.* 6, 148–158. doi:10.1007/s13346-015-0224-4

Hoffman, A. S. (2012). Hydrogels for Biomedical Applications. *Adv. Drug Deliv. Rev.* 64, 18–23. doi:10.1016/J.ADDR.2012.09.010

Hoshikawa, A., Nakayama, Y., Matsuda, T., Oda, H., Nakamura, K., and Mabuchi, K. (2006). Encapsulation of Chondrocytes in Photopolymerizable Styrenated Gelatin for Cartilage Tissue Engineering. *Tissue Eng.* 12 (8), 2333–2341. doi:10.1089/ten.2006.12.2333

Jabbari, E., Sarvestani, S. K., Daneshian, L., and Moeinzadeh, S. (2015). Optimum 3D Matrix Stiffness for Maintenance of Cancer Stem Cells is Dependent on Tissue Origin of Cancer Cells. *PLoS One* 10, e0132377. doi:10.1371/JOURNAL.PONE.0132377

Lee, Y., Yim, S.-G., Lee, G. W., Kim, S., Kim, H. S., Hwang, D. Y., et al. (2020). Self-Adherent Biodegradable Gelatin-Based Hydrogel Electrodes for Electrocardiography Monitoring. *Sensors* 20, 5737. doi:10.3390/s20205737

Lin, S., Sangaj, N., Razafiarison, T., Zhang, C., and Varghese, S. (2011). Influence of Physical Properties of Biomaterials on Cellular Behavior. *Pharm. Res.* 28, 1422–1430. doi:10.1007/s11095-011-0378-9

Lin, Y.-X., Li, S.-H., and Huang, W.-C. (2021). Fabrication of Soft Tissue Scaffold-Mimicked Microelectrode Arrays Using Enzyme-Mediated Transfer Printing. *Micromachines* 12, 1057. doi:10.3390/mi12091057

Liu, J., Zheng, H., Poh, P., Machens, H.-G., and Schilling, A. (2015). Hydrogels for Engineering of Perfusable Vascular Networks. *Int. J. Mol. Sci.* 16, 15997–16016. doi:10.3390/ijms160715997

Maharjan, B., Kumar, D., Awasthi, G. P., Bhattarai, D. P., Kim, J. Y., Park, C. H., et al. (2019). Synthesis and Characterization of Gold/Silica Hybrid Nanoparticles Incorporated Gelatin Methacrylate Conductive Hydrogels for H9C2 Cardiac Cell Compatibility Study. *Compos. Part B Eng.* 177, 107415. doi:10.1016/j.compositesb.2019.107415

Mazzoccoli, J. P., Feke, D. L., Baskaran, H., and Pintauro, P. N. (2009). Mechanical and Cell Viability Properties of Crosslinked Low- and High-Molecular Weight Poly(Ethylene Glycol) Diacrylate Blends. *J. Biomed. Mat. Res.* 93 (2), 558–566. doi:10.1002/jbm.a.32563

Mehrali, M., Thakur, A., Pennisi, C. P., Talebian, S., Arpanaei, A., Nikkhah, M., et al. (2017). Nanoreinforced Hydrogels for Tissue Engineering: Biomaterials that are Compatible with Load-Bearing and Electroactive Tissues. *Adv. Mat.* 29, 1603612. doi:10.1002/ADMA.201603612

Min, J., Patel, M., and Koh, W.-G. (2018). Incorporation of Conductive Materials into Hydrogels for Tissue Engineering Applications. *Polymers* 10, 1078. doi:10.3390/polym10101078

Navaei, A., Rahmani Eliato, K., Ros, R., Migrino, R. Q., Willis, B. C., and Nikkhah, M. (2019). The Influence of Electrically Conductive and Non-Conductive Nanocomposite Scaffolds on the Maturation and Excitability of Engineered Cardiac Tissues. *Biomater. Sci.* 7, 585–595. doi:10.1039/c8bm01050a

Noè, C., Tonda-Turo, C., Chiappone, A., Sangermano, M., and Hakkarainen, M. (2020). Light Processable Starch Hydrogels. *Polymers* 12, 1359. doi:10.3390/POLYM12061359

Noshadi, I., Walker, B. W., Portillo-Lara, R., Shirzaei Sani, E., Gomes, N., Aziziyan, M. R., et al. (2017). Engineering Biodegradable and Biocompatible Bio-Ionic Liquid Conjugated Hydrogels with Tunable Conductivity and Mechanical Properties. *Sci. Rep.* 7, 1–18. doi:10.1038/s41598-017-04280-w

Paoletti, C., and Chiono, V. (2021). Bioengineering Methods in MicroRNA-Mediated Direct Reprogramming of Fibroblasts Into Cardiomyocytes. *Front. Cardiovasc. Med.* 8, 750438. doi:10.3389/fcvm.2021.750438

Paoletti, C., Divieto, C., and Chiono, V. (2018). Impact of Biomaterials on Differentiation and Reprogramming Approaches for the Generation of Functional Cardiomyocytes. *Cells* 7, 114. doi:10.3390/cells7090114

Parchehbaf-Kashani, M., Sepantafar, M., Talkhabi, M., Sayahpour, F. A., Baharvand, H., Pahlavan, S., et al. (2020). Design and Characterization of an Electroconductive Scaffold for Cardiomyocytes Based Biomedical Assays. *Mat. Sci. Eng. C* 109, 110603. doi:10.1016/j.msec.2019.110603

Qu, J., Zhao, X., Ma, P. X., and Guo, B. (2018). Injectable Antibacterial Conductive Hydrogels with Dual Response to an Electric Field and pH for Localized "Smart" Drug Release. *Acta Biomater.* 72, 55–69. doi:10.1016/J.ACTBIO.2018.03.018

Rastin, H., Zhang, B., Bi, J., Hassan, K., Tung, T. T., and Losic, D. (2020). 3D Printing of Cell-Laden Electroconductive Bioinks for Tissue Engineering Applications. *J. Mat. Chem. B* 8, 5862–5876. doi:10.1039/D0TB00627K

Ren, K., Cheng, Y., Huang, C., Chen, R., Wang, Z., and Wei, J. (2019). Self-Healing Conductive Hydrogels Based on Alginate, Gelatin and Polypyrrole Serve as a Repairable Circuit and a Mechanical Sensor. *J. Mat. Chem. B* 7, 5704–5712. doi:10.1039/c9tb01214a

Rogers, Z. J., Zeevi, M. P., Koppes, R., and Bencherif, S. A. (2020). Electroconductive Hydrogels for Tissue Engineering: Current Status and Future Perspectives. *Bioelectricity* 2, 279–292. doi:10.1089/bioe.2020.0025

Roshanbinfar, K., Vogt, L., Greber, B., Diecke, S., Boccaccini, A. R., Scheibel, T., et al. (2018). Electroconductive Biohybrid Hydrogel for Enhanced Maturation and Beating Properties of Engineered Cardiac Tissues. *Adv. Funct. Mat.* 28, 1803951. doi:10.1002/adfm.201803951

Salih, V. (2009). "Biodegradable Scaffolds for Tissue Engineering," in *Cellular Response to Biomaterials* (Elsevier), 185–211. doi:10.1533/9781845695477.2.185

Sangermano, M., Pegel, S., Pötschke, P., and Voit, B. (2008). Antistatic Epoxy Coatings with Carbon Nanotubes Obtained by Cationic Photopolymerization. *Macromol. Rapid Commun.* 29, 396–400. doi:10.1002/marc.200700720

Sani, A., Cao, C., and Cui, D. (2021). Toxicity of Gold Nanoparticles (AuNPs): A Review. *Biochem. Biophys. Rep.* 26, 100991. doi:10.1016/j.bbrep.2021.100991

Shie, M.-Y., Lee, J.-J., Ho, C.-C., Yen, S.-Y., Ng, H. Y., and Chen, Y.-W. (2020). Effects of Gelatin Methacrylate Bio-Ink Concentration on Mechano-Physical Properties and Human Dermal Fibroblast Behavior. *Polymers* 12, 1930. doi:10.3390/polym12091930

Smith, P. K., Krohn, R. I., Hermanson, G. T., Mallia, A. K., Gartner, F. H., Provenzano, M. D., et al. (1985). Measurement of Protein Using Bicinchoninic Acid. *Anal. Biochem.* 150, 76–85. doi:10.1016/0003-2697(85)90442-7

Spencer, A. R., Primbetova, A., Koppes, A. N., Koppes, R. A., Fenniri, H., and Annabi, N. (2018). Electroconductive Gelatin Methacryloyl-PEDOT:PSS Composite Hydrogels: Design, Synthesis, and Properties. *ACS Biomater. Sci. Eng.* 4, 1558–1567. doi:10.1021/acsbiomaterials.8b00135

Spencer, A. R., Shirzaei Sani, E., Soucy, J. R., Corbet, C. C., Primbetova, A., Koppes, R. A., et al. (2019). Bioprinting of a Cell-Laden Conductive Hydrogel Composite. *ACS Appl. Mat. Interfaces* 11, 30518–30533. doi:10.1021/acsami.9b07353

Stillman, Z., Jarai, B. M., Raman, N., Patel, P., and Fromen, C. A. (2020). Degradation Profiles of Poly(Ethylene Glycol)diacrylate (PEGDA)-based Hydrogel Nanoparticles. *Polym. Chem.* 11, 568–580. doi:10.1039/C9PY01206K

Thaning, E. M., Asplund, M. L. M., Nyberg, T. A., Inganäs, O. W., and von Holst, H. (2010). Stability of Poly(3,4-Ethylene Dioxythiophene) Materials Intended for Implants. *J. Biomed. Mat. Res.* 93B, 407–415. doi:10.1002/jbm.b.31597

Wang, X., Li, M., Feng, G., and Ge, M. (2020). On the Mechanism of Conductivity Enhancement in PEDOT:PSS/PVA Blend Fiber Induced by UV-Light Irradiation. *Appl. Phys. A* 126, 1–7. doi:10.1007/s00339-019-3271-8

Wang, Y., Ma, M., Wang, J., Zhang, W., Lu, W., Gao, Y., et al. (2018). Development of a Photo-Crosslinking, Biodegradable GelMA/PEGDA Hydrogel for Guided Bone Regeneration Materials. *Materials* 11, 1345. doi:10.3390/ma11081345

Wu, Y., Chen, Y. X., Yan, J., Quinn, D., Dong, P., Sawyer, S. W., et al. (2016). Fabrication of Conductive Gelatin Methacrylate-Polyaniline Hydrogels. *Acta Biomater.* 33, 122–130. doi:10.1016/J.ACTBIO.2016.01.036

Xu, B., Bai, T., Sinclair, A., Wang, W., Wu, Q., Gao, F., et al. (2016). Directed Neural Stem Cell Differentiation on Polyaniline-Coated High Strength Hydrogels. *Mater. Today Chem.* 1-2, 15–22. doi:10.1016/j.mtchem.2016.10.002

Zanon, M., Baruffaldi, D., Sangermano, M., Pirri, C. F., Frascella, F., and Chiappone, A. (2021). Visible Light-Induced Crosslinking of Unmodified Gelatin with PEGDA for DLP-3D Printable Hydrogels. *Eur. Polym. J.* 160, 110813. doi:10.1016/j.eurpolymj.2021.110813

Conflict of Interest: The authors declare that the research was conducted in the absence of any commercial or financial relationships that could be construed as a potential conflict of interest.

Publisher's Note: All claims expressed in this article are solely those of the authors and do not necessarily represent those of their affiliated organizations, or those of the publisher, the editors and the reviewers. Any product that may be evaluated in this article, or claim that may be made by its manufacturer, is not guaranteed or endorsed by the publisher.

frontiers | Frontiers in Bioengineering and Biotechnology

SYSTEMATIC REVIEW
published: 30 June 2022
doi: 10.3389/fbioe.2022.889481

Recent Advances of Pullulan and/or Dextran-Based Materials for Bone Tissue Engineering Strategies in Preclinical Studies: A Systematic Review

Naïma Ahmed Omar[1], *Joëlle Amédée*[1], *Didier Letourneur*[2,3], *Jean-Christophe Fricain*[1,4] *and Mathilde Fenelon*[1,4]*

[1]Université de Bordeaux, INSERM U1026, BIOTIS, Bordeaux, France, [2]SILTISS, Saint-Viance, France, [3]Université Paris Cité, Université Sorbonne Paris Nord, INSERM U1148, LVTS, X Bichat Hospital, Université de Paris, Paris, France, [4]Service de Chirurgie Orale, CHU Bordeaux, Bordeaux, France

Bone tissue engineering (BTE) strategies are increasingly investigated to overcome the limitations of currently used bone substitutes and to improve the bone regeneration process. Among the natural polymers used for tissue engineering, dextran and pullulan appear as natural hydrophilic polysaccharides that became promising biomaterials for BTE. This systematic review aimed to present the different published applications of pullulan and dextran-based biomaterials for BTE. An electronic search in Pubmed, Scopus, and Web of Science databases was conducted. Selection of articles was performed following PRISMA guidelines. This systematic review led to the inclusion of 28 articles on the use of pullulan and/or dextran-based biomaterials to promote bone regeneration in preclinical models. Sixteen studies focused on dextran-based materials for bone regeneration, six on pullulan substitutes and six on the combination of pullulan and dextran. Several strategies have been developed to provide bone regeneration capacity, mainly through their fabrication processes (functionalization methods, cross-linking process), or the addition of bioactive elements. We have summarized here the strategies employed to use the polysaccharide scaffolds (fabrication process, composition, application usages, route of administration), and we highlighted their relevance and limitations for BTE applications.

Keywords: pullulan, dextran, bone tissue engineering, natural polymers, polysaccharides, bone regeneration

OPEN ACCESS

Edited by:
Adil Denizli,
Hacettepe University, Turkey

Reviewed by:
Jennifer Patterson,
Instituto IMDEA Materiales, Spain
Vikas Rana,
Punjabi University, India

***Correspondence:**
Mathilde Fenelon
mathilde.fenelon@u-bordeaux.fr

Specialty section:
This article was submitted to Biomaterials, a section of the journal Frontiers in Bioengineering and Biotechnology

Received: *04 March 2022*
Accepted: *23 May 2022*
Published: *30 June 2022*

Citation:
Ahmed Omar N, Amédée J, Letourneur D, Fricain J-C and Fenelon M (2022) Recent Advances of Pullulan and/or Dextran-Based Materials for Bone Tissue Engineering Strategies in Preclinical Studies: A Systematic Review. Front. Bioeng. Biotechnol. 10:889481. doi: 10.3389/fbioe.2022.889481

1 INTRODUCTION

Improving bone regeneration after traumatic injuries, pathologies, or tumors resection has been and still remains a surgical challenge since decades. To date, autologous bone grafting (Dimitriou et al., 2011; Lanza et al., 2014) is the gold standard technique for bone reconstruction, as it is induced by a non-immunogenic way, the properties required for bone regeneration [i.e., osteoinduction, osteoconduction, and osteogenesis (Dimitriou et al., 2011; Lanza et al., 2014)]. However, this method has some important drawbacks due to its limited availability and inherent complications from the surgical procedures (donor site injury and morbidity) (Dimitriou et al., 2011).

Bone tissue engineering (BTE) strategies have thus emerged to develop alternatives to conventional autologous bone graft reconstruction. BTE approach is usually based on a combination of scaffolds with cells and/or bioactive molecules to provide the conditions required for bone formation. Design of scaffolds that mimic the mechanical and structural features of bone extracellular matrix (Filippi et al., 2020) that is highlighted. Biomaterials for bone scaffolding applications are critical to enable cell viability and proliferation, osteodifferentiation, angiogenesis, host integration, and when needed load bearing (Roseti et al., 2017; Kashirina et al., 2019). Calcium phosphate cements (CPC) such as hydroxyapatite (HA) or β-tricalcium phosphate (β-TCP) are thus the most commonly used scaffolds for BTE applications (Ana et al., 2018; Liang et al., 2021).

Recently, a number of natural polymers, such as chitosan, collagen, gelatin, hyaluronic acid, or alginate has gained an increasing interest (Tang et al., 2021). They often show biocompatibility, biodegradability, and share similar structures to the natural extracellular matrix (Filippi et al., 2020). An interesting property of polymeric scaffolds is their ability to be easily designed according to the desired three-dimensional structure, such as hydrogels, macroporous scaffolds, microspheres, or micro-molded matrices (Mallick and Cox, 2013; Wu et al., 2021). Polysaccharides are one type of natural polymers that are composed of molecules linked through a glycosidic linkage (Hussain et al., 2017). Among them, dextran and pullulan are both exopolysaccharides, which are secreted into the surrounding environment of microorganisms by cell wall-anchored enzymes (Hussain et al., 2017). They have already been used for medical research since they are biocompatible, biodegradable, and present no immunogenic reaction (Prajapati et al., 2013; Banerjee and Bandopadhyay, 2016). For example, dextran was used as plasma expander (Banerjee and Bandopadhyay, 2016), drug carrier to target organs [e.g., colon (Hovgaard and Brøndsted, 1995; Simonsen et al., 1995), skin (Sun et al., 2011)] or as a molecular imaging tracer for magnetic resonance imaging (Tassa et al., 2011; Banerjee and Bandopadhyay, 2016) (e.g., dextran-coated iron oxide nanoparticles). Pullulan-based materials have been used as an excipient in pharmaceutical tablets (Prajapati et al., 2013). Some researchers also focused on its potential as a plasma-blood substitute (Prajapati et al., 2013) like dextran derivatives, as a drug delivery system (Fundueanu et al., 2003) or as a fluorescent probe for medical imaging (Morimoto et al., 2005b).

The use of these two polysaccharides for BTE has thus been investigated to design biological scaffolds for bone regeneration. In the last decades, several studies focused on the production of pullulan and/or dextran-based scaffolds combined with CPC or growth factors, and investigated their potential for BTE. However, there is no report summarizing the development of pullulan and/or dextran-based bone materials, functionalization methods and their applications to promote bone regeneration. This review aims to identify the different strategies of pullulan and/or dextran-based substitutes for bone tissue engineering applications in preclinical studies since no clinical application were reported in the online search.

2 MATERIALS AND METHODS

This systematic review was performed according to the Preferred Reporting Items for Systematic Reviews and Meta-Analyses (PRISMA) guidelines (Moher et al., 2015). A protocol was specified and registered on the database International Prospective Register of Systematic Reviews (PROSPERO) (registration number CRD42021220920) and is available from: https://www.crd.york.ac.uk/prospero/display_record.php?ID=CRD42021220920.

2.1 Focused Question

This systematic review was performed to address the following focused question: "What are the best strategies of using pullulan and/or dextran in bone regeneration in preclinical models?"

2.2 Search Strategy

An electronic search of the MedLine (PubMed), Embase (Scopus), and Web of science databases was carried out. Medical subject headlings (MeSH) terms were combined with keywords and Boolean operators to search databases. All searches were performed from October 2020 to February 2022 by focusing on studies written in English or French and published between January 2000 and February 2022. The searching query used for the research was: ("pullulan" OR "dextran") AND ["bone (MeSH)" OR "bone regeneration (MeSH)"]. Additional articles were also searched by manually screening the list of references of all publications selected by the search.

2.3 Eligibility Criteria

Preclinical controlled trials using pullulan and/or dextran substitutes to induce bone regeneration were considered. All animal studies (all type, all sexes) were eligible if they assessed new bone formation in a bone defect or subcutaneously. *In vitro* studies, clinical trials and reviews were excluded.

2.4 Screening Methods and Data Extraction

Two independent reviewers (NA and MF) screened the titles and abstracts. For eligible studies that matched with the inclusion criteria, full texts were then assessed. Any disagreement between the reviewers over the eligibility of particular studies was resolved through discussion with a third reviewer (J-CF).

In order to extract relevant data from included studies, structurable tables were made with the following data: authors, animal models, type of defect or implantation site, conditions tested (with the number of defects created or scaffolds implanted), composition of the scaffolds, cross-linking reagents, adjuvants (e.g., growths factors, cell lines, mineralized molecules), material design, observation period, and experimental analysis with results. For any missing data, authors were contacted by e-mail to complete tables.

2.5 Quality Assessment and Analysis of the Data

Methodological quality of individual studies was assessed using the collaborative Evidence-Based Complementary and

TABLE 1 | Characterization of scaffold used in the included studies.

Author (Year)	Polysaccharide composition	Biocomposite scaffold (additional polymers and ceramics)	Functionalization of dextran, pullulan or pullulan/dextran scaffolds	Cross-linking process (cross-linker used)	Material aspect	Bioactive components
Lafont et al. (2004)	Dextran	—	Carboxymethyl, benzylamide and sulfate	—	Aqueous solution (loaded into collagen sponges)	—
Maire et al. (2005a)	Dextran	—	Carboxylate, benzylamide and sulfate (three different D.S. expressed in %: 0, 2, and 18)	Chemical cross-linking (STMP)	Hydrogel	BMP-2
Chen et al. (2005)	Dextran	Gelatin	—	Chemical cross-linking	Microspheres	BMP-2
Chen et al. (2006)	Dextran	Gelatin	Glycidyl methacrylate (three different D.S. referring to the number of methacrylated groups per 100 glucopyranose residues: 4.7, 6.3, and 7.8)	Chemical cross-linking (Polyethylene glycol)	Microspheres	IGF-1
Chen et al. (2007)	Dextran	Gelatin	Glycidyl methacrylate	Chemical cross-linking	Hydrogel	—
	Dextran	Polyethylene glycol	Glycidyl methacrylate	Chemical cross-linking	Microspheres	BMP-2
Degat et al. (2007)	Dextran	—	Carboxymethyl, benzylamide	—	Aqueous solution (loaded into collagen sponges)	BMP-2
Abbah et al. (2012)	Dextran/Alginate	—	Diethylaminoethyl	Physical cross-linking ($CaCl_2$)	Microspheres (loaded into polymeric sponges)	BMP-2
Bölgen et al. (2013)	Dextran	Hydroxyethyl methacrylate Lactate	—	Chemical cross-linking (Methylenebisacrylamide)	Cryogel (disc-shaped)	MSCs
Togami et al. (2014)	Dextran	Polyvinyl formal	—	—	Sponges	—
Ritz et al. (2018)	Dextran	—	Carboxymethyl and epoxy benzophenone	Chemical cross-linking (UV radiation)	Hydrogel (disc-shaped)	BMP-7 SDF-1 HUVEC hOB
Chen et al. (2019)	Dextran	—	Sulfate	—	Aqueous solution (loaded into gelatin sponges)	BMP-2
Ding et al. (2019)	Dextran/Chitosan	Strontium-doped HA	Formylbenzoic	Chemical cross-linking	Hydrogel (injected, *in situ* forming)	—
Fang et al. (2019)	Dextran	Polyacrylamide HA	Urethane methacrylate	Physical cross-linking (SDS/SMA micelles)	Hydrogel (disc-shaped)	—
Shoji et al. (2020)	Dextran	—	Tyramine	Chemical cross-linking (H_2O_2, HRP)	Hydrogel (injected, *in situ* forming)	bFGF
Yu et al. (2020)	Dextran	—	—	—	Aqueous solution (loaded into gelatin sponges)	BMP-2
Wang et al. (2021)	Dextran	PLGA HA	Aldehyde and catechol	Chemical cross-linking (Schiff reaction)	Hydrogel (injected, *in situ forming*)	Bisphosphonate
Hayashi et al. (2009)	Pullulan	—	Cholesteryl and acryloyl	Chemical cross-linking (thiol-bearing polyethylene glycol)	Hydrogel (hemisphere-shaped)	BMP-2
Miyahara et al. (2011)	Pullulan	—	Cholesteryl and acryloyl	Chemical cross-linking (thiol-bearing polyethylene glycol)	Hydrogel (membrane)	—
Fujioka-Kobayashi et al. (2012)	Pullulan	—	Cholesteryl and acryloyl	Chemical cross-linking (thiol-bearing polyethylene glycol)	Hydrogel (disc-shaped)	BMP-2 and/or FGF18
Takahata et al. (2015)	Pullulan	β-TCP	Phosphate	—	NS	—
Charoenlarp et al. (2018)	Pullulan	—	Cholesteryl and acryloyl	Chemical cross-linking (thiol-bearing polyethylene glycol and/or RGD peptides)	Hydrogel (disc-shaped)	BMP-2 and FGF18
Popescu et al. (2019)	Pullulan/Alginate	Bioglass containing X%CuO (X = 0.5 or 1.5)	—	—	NS	—

(Continued on following page)

TABLE 1 | (*Continued*) Characterization of scaffold used in the included studies.

Author (Year)	Polysaccharide composition	Biocomposite scaffold (additional polymers and ceramics)	Functionalization of dextran, pullulan or pullulan/dextran scaffolds	Cross-linking process (cross-linker used)	Material aspect	Bioactive components
Fricain et al. (2013)	Pullulan/Dextran	HA	—	Chemical cross-linking (STMP)	Hydrogel (sponges)	—
Schlaubitz et al. (2014)	Pullulan/Dextran	HA	—	Chemical cross-linking (STMP)	Microspheres	—
Frasca et al. (2017)	Pullulan/Dextran	—	—	Chemical cross-linking (STMP)	Hydrogel (sponges)	MSCs
Ribot et al. (2017)	Pullulan/Dextran	HA and/or fucoidan	—	Chemical cross-linking (STMP)	Microspheres	—
Fricain et al. (2018)	Pullulan/Dextran	HA	—	Chemical cross-linking (STMP)	Microspheres	—
Maurel et al. (2021)	Pullulan/Dextran	HA	—	Chemical cross-linking (STMP)	Microspheres	—

bFGF, basic fibroblast growth factor; BMP, bone morphogenetic protein; β-TCP, beta-tricalcium phosphate; CuO, copper oxide; D.S., degree of substitution; FGF, fibroblast growth factor; HA, hydroxyapatite; HEMA, hydroxyethyl methacrylate; H_2O_2, hydrogen peroxide; hOB, human osteoblast; HRP, horseradish peroxidase; HUVEC, human umbilical vein endothelial cells; IGF, insulin-like growth factor; MSCs, mesenchymal stromal cells; NS, not specified; PEG, polyethylene glycol; PLGA, poly-(L-glutamic acid); RGD, arginine-glycine-aspartate; SDF-1, stromal-derived growth factor; SDS, sodium dodecyl sulfate; SMA, stearyl methacrylate; STMP, sodium trimetaphosphate; (—), not applicable.

Alternative Medicine approach to meta-analysis and review of animal data in experimental infarction (CAMARADES) 10-item quality checklist (Macleod et al., 2004) and SYRCLE's risk of bias tool (Hooijmans et al., 2014). These tools enabled to build a modified checklist by using eight items for relevance: 1) Peer reviewed publication; 2) Control of the temperature in the animal facilities; 3) Random allocation to treatment or control; 4) Blinded assessment of outcomes; 5) Animal model description; 6) Sample size calculation; 7) Compliance with animal welfare regulation; 8) Statement of potential conflict of interest. Data analysis was then performed in a descriptive way since the information obtained did not enable meta-analyses.

3 RESULTS

3.1 Search Outcomes

Database screening yielded to 713 publications after duplicates removal. Among these publications, 35 articles were selected for potential inclusion after title and abstract reading. Full texts of these 35 articles were reviewed. Seven of the 35 studies were excluded for not meeting the inclusion criteria. No additional study was added for selection after manually screening the list of references of selected publications. Finally, 28 studies were included for this systematic review: 16 used dextran-derived biomaterials (Lafont et al., 2004; Maire et al., 2005a; Chen et al., 2005; Chen et al., 2006; Chen et al., 2007; Degat et al., 2009; Abbah et al., 2012; Bölgen et al., 2014; Ritz et al., 2018; Chen et al., 2019; Ding et al., 2019; Fang et al., 2019) for bone regeneration, six used pullulan-derived biomaterials (Hayashi et al., 2009; Fujioka-Kobayashi et al., 2012; Miyahara et al., 2012; Takahata et al., 2015; Charoenlarp et al., 2018; Popescu et al., 2020) and six used a combination of these two polysaccharides (Fricain et al., 2013; Fricain et al., 2018; Schlaubitz et al., 2014; Frasca et al., 2017; Ribot et al., 2017) (**Table 1**). A flowchart of the selection and inclusion process, based on PRISMA recommendations is presented in **Figure 1**. Risk of bias ranged from low to high and detailed results of methodological quality are presented in **Figures 2**, **3**. Sample size calculation and blinded assessment of outcomes showed the highest risk of bias.

3.2 Experimental Models

Most studies (25 out of 28 studies) were carried out on small animals (e.g., mice, rats, rabbits), and only few studies investigated bone formation in larger animal models (e.g., pigs, sheeps, goats, and dogs). Experimental procedures were performed ectopically (17%), or orthotopically (83%) (**Figure 4**). Ectopic bone formation was investigated in six studies using subcutaneous implantation in the back of animals or by muscular implantation (e.g., leg muscles) (**Table 2**) (Maire et al., 2005a; Degat et al., 2009; Hayashi et al., 2009; Fricain et al., 2013; Chen et al., 2019; Yu et al., 2020). Orthotopic implantations were mainly performed on maxillofacial defects and long bone defects (**Tables 3**, **4**, **5**) (Lafont et al., 2004; Chen et al., 2005; Chen et al., 2006; Chen et al., 2007; Hayashi et al., 2009; Abbah et al., 2012; Fujioka-Kobayashi et al., 2012; Miyahara et al., 2012; Fricain et al., 2013; Bölgen et al., 2014; Schlaubitz et al., 2014; Takahata et al., 2015; Togami et al., 2015; Frasca et al., 2017; Ribot et al., 2017; Charoenlarp et al., 2018; Fricain et al., 2018; Ritz et al., 2018; Ding et al., 2019; Fang et al., 2019; Popescu et al., 2020; Shoji et al., 2020; Maurel et al., 2021; Wang et al., 2021). Nine studies investigated calvarial defects, six studies focused on mandibular or maxillary defects (e.g., periodontal, sinus bone augmentation), whereas 10 studies were performed on femoral defects (e.g., condyle, epiphysis, metaphysis), one study on ulnar defect and one study on tibial defect. Two studies assessed vertebral bone defects regeneration. Bone formation was investigated radiographically mainly using micro-computed tomography (micro-CT) and/or by histological analysis.

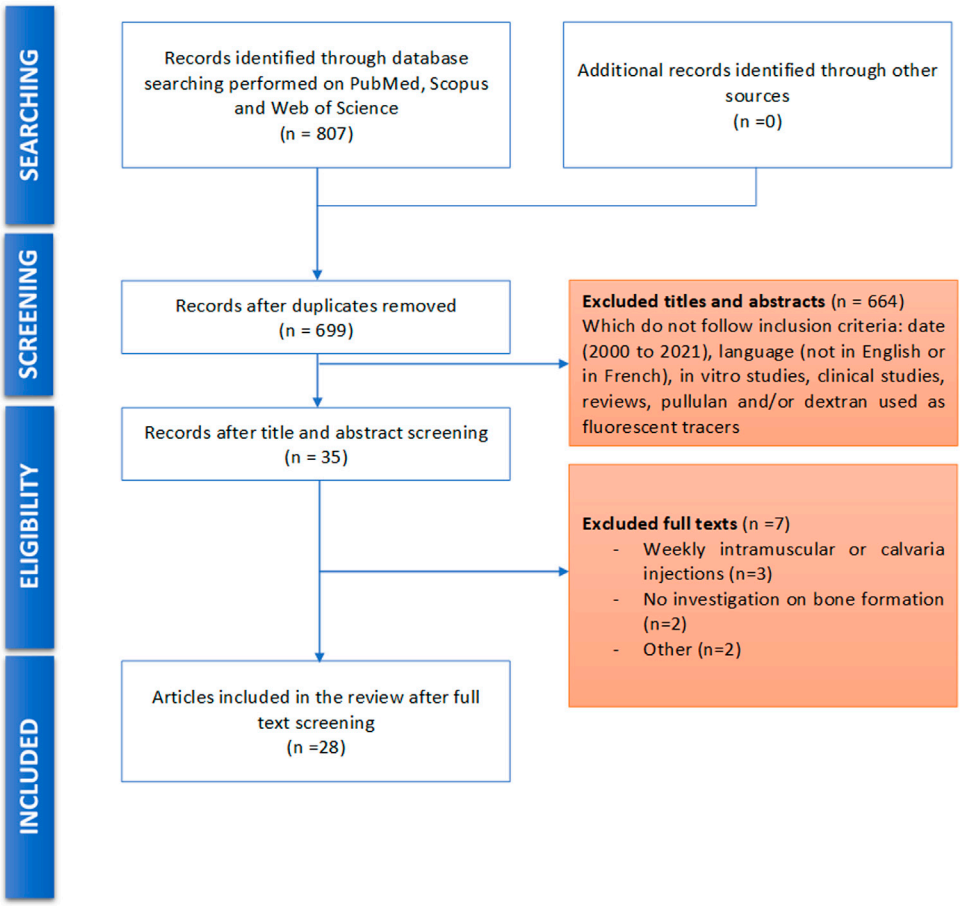

FIGURE 1 | Flow diagram of the screened publications.

3.3 Polysaccharide-Based Materials

Among the 28 studies included, 24 used either dextran or pullulan as the main component for biomaterial design (Lafont et al., 2004; Chen et al., 2005; Maire et al., 2005a; Chen et al., 2006; Chen et al., 2007; Degat et al., 2009; Hayashi et al., 2009; Abbah et al., 2012; Fujioka-Kobayashi et al., 2012; Miyahara et al., 2012; Bölgen et al., 2014; Takahata et al., 2015; Charoenlarp et al., 2018; Ritz et al., 2018; Chen et al., 2019; Ding et al., 2019; Fang et al., 2019; Popescu et al., 2020) and six used a combination of these two polysaccharides (Fricain et al., 2013; Schlaubitz et al., 2014; Frasca et al., 2017; Ribot et al., 2017; Fricain et al., 2018) (**Table 1**). In most cases, when pullulan or dextran was used alone, chemical functionalization of the polysaccharide was performed to improve the cross-linking process and/or to promote their binding capacity to growth factors. For dextran derivatives, acrylate groups (Chen et al., 2006; Chen et al., 2007) (e.g., glycidyl methacrylate, urethane methacrylate), amine or amide derivatives (Lafont et al., 2004; Maire et al., 2005a; Degat et al., 2009; Abbah et al., 2012; Shoji et al., 2020) (e.g., benzylamide, diethylaminoethyl, tyramine), carboxyl (Lafont et al., 2004; Degat et al., 2009; Ritz et al., 2018) (e.g., carboxylate, carboxymethyl, formylbenzoic), aldehyde (Wang et al., 2021), catechol (Wang et al., 2021) (i.e., dopamine), or sulfated groups (Chen et al., 2019) were added to the dextran backbone in 11 studies. Concerning pullulan derivatives, acrylate groups (Hayashi et al., 2009; Fujioka-Kobayashi et al., 2012; Miyahara et al., 2012; Charoenlarp et al., 2018) (e.g., acryloyl, cholesteryl) or phosphate groups (Takahata et al., 2015) were added for functionalization in five studies. No chemical modification was reported for compositions using both polysaccharides (Fricain et al., 2013; Schlaubitz et al., 2014; Frasca et al., 2017; Ribot et al., 2017; Fricain et al., 2018; Maurel et al., 2021).

Physical cross-linking and chemical cross-linking were used for hydrogels (Kumari and Badwaik, 2019). Physically cross-linked of dextran-derived biomaterials were identified in two studies by using ionic cross-linking [e.g., calcium chloride (Abbah et al., 2012)] or by micellar reaction [e.g., sodium dodecyl sulfate/stearyl methacrylate (Fang et al., 2019) (SDS/SMA) micelles]. Chemical cross-linking was the most commonly used procedure. For chemically cross-linked dextran and/or pullulan-derived biomaterials, a wide range of reagents and reactions were employed, such as methylenebisacrylamide (Bölgen et al., 2014) (MBAm), polyethylene glycol (Chen et al., 2006) (PEG), thiol group-modified polyethylene glycol (Hayashi et al., 2009; Fujioka-Kobayashi et al., 2012; Miyahara et al., 2012; Charoenlarp et al., 2018) (PEGSH), PEGSH with "arginine-glycine-aspartate"

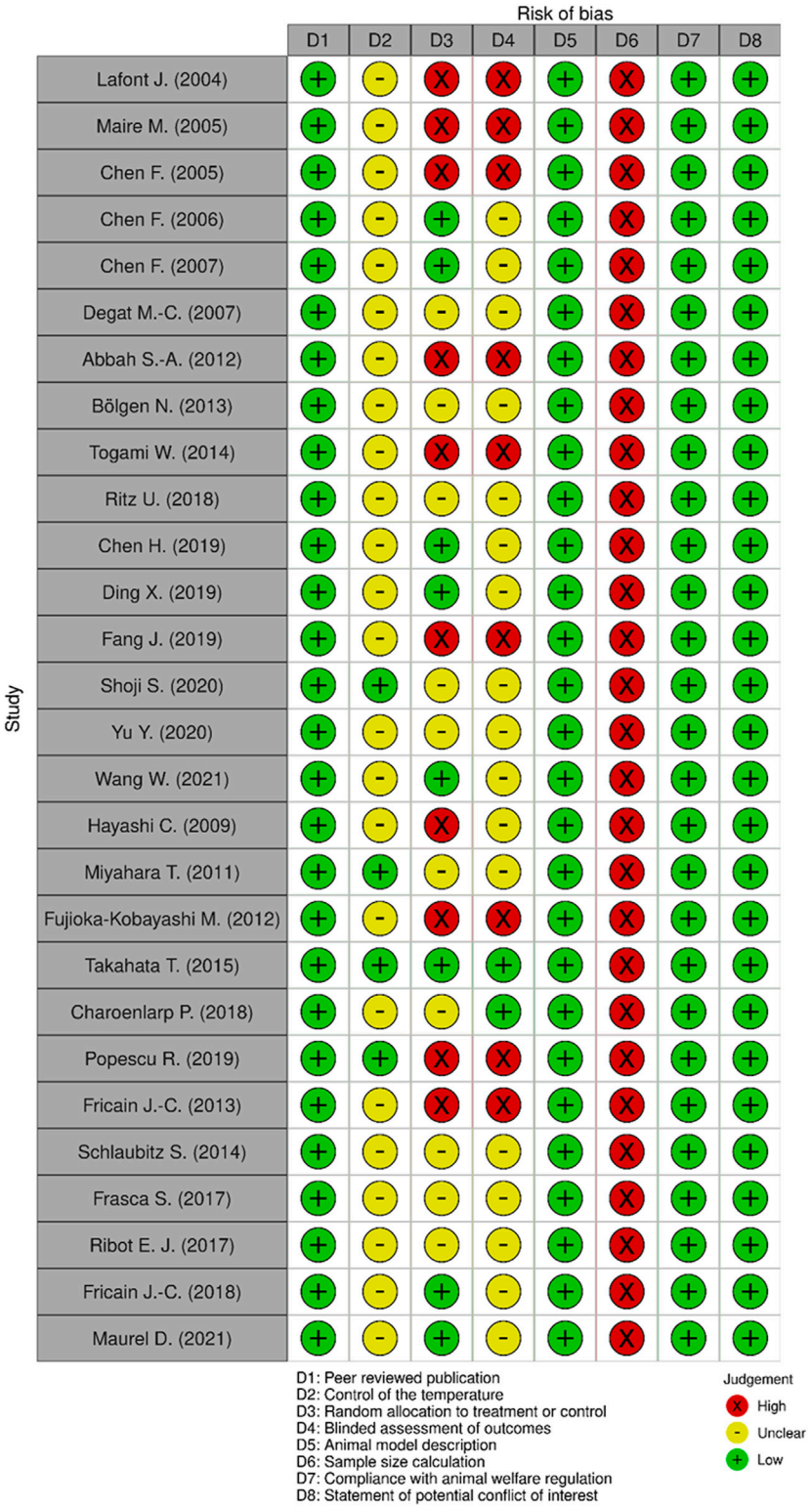

FIGURE 2 | Quality assessment of each included study using a modified CAMARADES checklist.

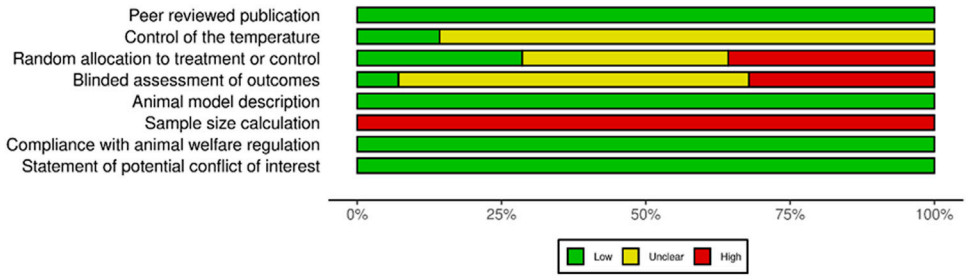

FIGURE 3 | Summary of risk of bias assessment for the included studies using a modified CAMARADES checklist.

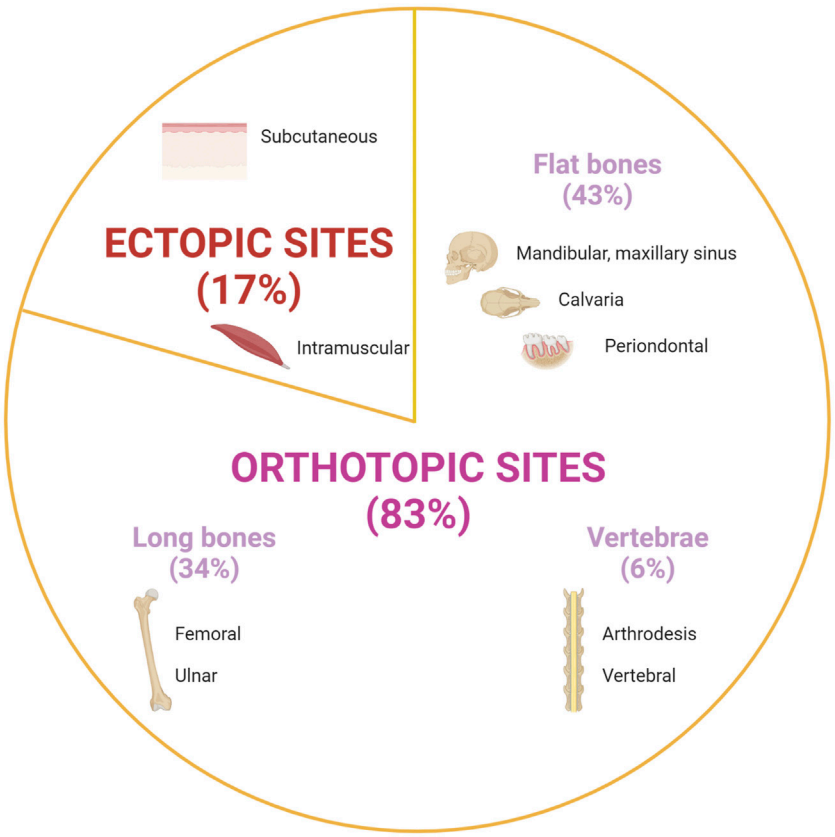

FIGURE 4 | Implantation sites of pullulan and/or dextran-based scaffolds to assess their potential for bone regeneration. Created with BioRender.com.

(RGD) peptides (Charoenlarp et al., 2018), sodium trimetaphosphate (Maire et al., 2005a; Fricain et al., 2013; Schlaubitz et al., 2014; Frasca et al., 2017; Ribot et al., 2017; Fricain et al., 2018; Maurel et al., 2021) (STMP), through Schiff reaction (imine bonding) (Wang et al., 2021), through enzymatic reaction (Shoji et al., 2020) (e.g., hydrogen peroxide, horseradish peroxidase) or by activating a photocross-linking group using UV light (Ritz et al., 2018).

We have identified three main routes of administration of these biomaterials in implantation sites. They could be implanted as an injectable hydrogel or microspheres/microbeads (e.g., dextran and/or pullulan-derived biomaterials), as an aqueous solution adsorbed on a collagen or a polyvinyl alcohol sponge [e.g., dextran-derived biomaterials (Lafont et al., 2004; Degat et al., 2009; Togami et al., 2015; Chen et al., 2019; Yu et al., 2020)] or as a membrane for guided bone regeneration [e.g., pullulan-derived biomaterial (Miyahara et al., 2012)].

To induce or enhance bone formation, various elements were directly added in these scaffolds to generate composite scaffolds (**Figure 5**). Bioceramics, such as hydroxyapatite (HA) (Fricain et al., 2013; Schlaubitz et al., 2014; Ribot et al., 2017; Fricain et al.,

TABLE 2 | Preclinical studies using Dextran and/or Pullulan scaffold in ectopic sites.

Author (Year)	Animal model (sex; species); n, number of animals used	Implantation site, dimension of the implanted material	Conditions (N, number of total implanted materials per condition)	Observation time [in day (D), week (W) or month (M)]	Experimental analysis	Results
Maire et al. (2005b)	Rat (male, Sprague Dawley), *n* = 21	Muscle implantation (back)	1: BMP (N = 20) 2: Dextran (DS 0%) + BMP (N = 14)	7 W	2D X-ray (qualitative analysis)	Dextran (DS 18%) + BMP showed large radiopaque areas compared to other groups (no statistical significance due to heterogeneity within the same group)
		Collagen sponge Diameter: 7 mm Height: 7 mm	3: Dextran (DS 2%) + BMP (N = 14) 4: Dextran (DS 18%) + BMP (N = 14)		Stevenel blue and Van Gieson Picrofuschin staining (Bone formation); Von Kossa staining (qualitative analysis)	For Dextran (DS 18%) + BMP group, bone formation occurred through endochondral ossification or by intramembranous ossification
Degat et al. (2007)	Rat (male, Sprague Dawley), *n* = 24	Subcutaneous (back)	1: BMP-2 (N = 6) 2: Dextran (1 µg) + BMP-2 (N = 6)	4 W	Calcium mass (µg/implant)	Dextran (10 µg) + BMP-2 ** > BMP-2
		Collagen sponge Diameter: 3 mm Height: 2 mm	3: Dextran (10 µg) + BMP-2 (N = 6) 4: Dextran (100 µg) + BMP-2 (N = 6)			BMP-2 * > Dextran (100 µg) + BMP-2
Chen et al. (2019)	Mouse (male, C57BL/6), *n* = 3	Muscle implantation (leg) Gelatin sponge size Length: 0.5 cm Width: 0.5 cm Height: 0.3 cm	1: BMP-2 (N=NS) 2: Chitosan + BMP-2 (N=NS) 3: Dextran + BMP-2 (N=NS) 4: PSS + BMP-2 (N=NS)	2 W	Wet and ash weights of ectopic bone (g)	No significant difference observed between Dextran + BMP-2 and BMP-2 alone groups
				4 W	Masson's Trichrome staining (qualitative analysis)	Dextran + BMP-2 less bone formation compared to other groups
Yu et al. (2020)	Mouse (male, C56BL/6), *n* = 40	Muscle implantation (leg) Gelatin sponge size: NS	1: BMP-2 (10 µg) (N = 16) 2: BMP-2 (15 µg) (N = 16) 3: Heparin + BMP-2 (N = 16) 4: Chitosan + BMP-2 (N = 16) 5: Dextran + BMP-2 (N = 16)	2 W	Micro-CT (BVF in %)	No significant difference between groups
				4 W	Masson's Trichrome staining; TRAP+ staining (qualitative analysis)	At 4W: for Dextran + BMP-2 group, traces of trabecular bone and bone resorption occurred
Hayashi et al. (2009)	Mouse (male, ICR), *n* = NS	Muscle implantation (leg) Diameter: 2.5 mm Height: NS	1: Pullulan (N = 3–4) 2: Pullulan + BMP-2 (2 µg) (N = 3–4)	3 W	Micro-CT (BV in mm^3)	No significant difference between Pullulan and Pullulan + BMP-2 group
Fricain et al. (2013)	Mouse (NS, Balb/c), *n* = NS	Subcutaneous (back) Diameter: 4 mm Height: 4 mm	1: Pullulan/ Dextran (N = 6) 2: Pullulan/ Dextran + HA (N = 6)	15 D 30 D 60 D	Micro-CT (MC in mg; MD in mg/cm^3) Enzyme Immunoassay for BMP-2 (pg/mg protein)	Pullulan/Dextran + HA ** > Pullulan/ Dextran Pullulan/Dextran + HA * > Pullulan/ Dextran
	Goat (NS) *n* = 7	Muscle implantation (back) Diameter: 10 mm Depth: 10 mm	1: Pullulan/ Dextran (N = 12) 2: Pullulan/ Dextran + HA (N = 12)	1 M 6 M	Micro-CT (qualitative analysis) Von Kossa staining; Masson's Trichrome staining (qualitative analysis)	Osteoid tissue formation for Pullulan/ Dextran + HA group Osteoid tissue formation for Pullulan/ Dextran + HA group

*BMP, bone morphogenetic protein; BV, bone volume; BVF, bone volume fraction; D.S., degree of substitution; HA, hydroxyapatite; MC, mineral content; MD, mineral density; NS, not specified; PSS, poly (sodium-p-styrenesulfonate); * p < 0.05; ** p < 0.01.*

TABLE 3 | Preclinical studies using Dextran scaffolds for bone regeneration in orthotopic sites.

Author (Year)	Animal model (sex; species); n, number of animals used	Type of defect (defect size)	Conditions (N, number of defects created in total per condition)	Observation time [in day (D), week (W) or month (M)]	Experimental analysis	Results
Lafont et al. (2004)	Rat (male, Wistar), *n* = 98	Calvaria Ø: 5 mm	1: PBS (N = 49) 2: Dextran (N = 49)	1 D 2 D 3 D 4 D 5 D 6 D 7 D	2D x-ray analysis (Bone Repair in %) Toluidine blue staining (ALP staining, qualitative analysis)	At 7D: Dextran *** > PBS For Dextran group: at 5D, bone formation began at the edges of the defect and bone nodules appeared at 6D
Chen et al. (2005)	Dog (female, Beagle), *n* = 12	Periodontal class III furcation (2nd, 3rd and 4th premolars) H: 5 mm	1: CPC covered by Simple Membrane (N = 33) 2: CPC + BMP-2 covered by Simple Membrane (N = 32) 3: Dextran/Gelatin + BMP-2 in CPC covered by Functionalized Membrane (N = 34)	8 W	HE staining (New bone area in %)	Dextran/Gelatin + BMP-2 ** > CPC
Chen et al. (2006)	Dog (male, Beagle), *n* = 12	Periodontal class III furcation (2nd and 3rd molars) H: 5 mm	1: Empty (N = 16) 2: Dextran (D.S. = 6.3)/ Gelatin (N = 16) 3: IGF-1 (N = 16) 4: Dextran (D.S. = 4.7)/ Gelatin + IGF-1 (N = 16) 5: Dextran (D.S. = 6.3)/ Gelatin + IGF-1 (N = 16) 6: Dextran (D.S. = 7.8)/ Gelatin + IGF-1 (N = 16)	4 W 8 W	2D X-Ray (qualitative analysis) HE staining; Modified Mallory's Trichrome staining (Morphometric analysis of new bone in %)	For Dextran/Gelatin containing IGF groups, new bone formation was observable Dextran (D.S. = 4.7)/Gelatin + IGF-1 * > Dextran (D.S. = 7.8)/ Gelatin + IGF-1
Chen et al. (2007)	Dog (male, Mongrel), *n* = 6	Periodontal class III furcation (2nd and 3rd premolars) H: 5 mm	1: Dextran/Gelatin (N = 16) 2: Dextran/Gelatin + microsphere BMP (N = 16) 3: Dextran/Gelatin + aqueous BMP (N = 16)	8 W	Modified Mallory's Trichrome staining (Height of new bone regenerated in mm; % of regenerated new bone)	Dextran/Gelatin + microsphere BMP ** > Dextran/Gelatin + aqueous BMP * > Dextran/ Gelatin
Abbah et al. (2012)	Rat (male, Sprague Dawley), *n* = 38	Arthrodesis (iliac bone L3, L4 fusion) Bioresorbable mPCL-TCP scaffold L: 4 mm W: 4 mm H: 4 mm	1: Empty (N = 6) 2: Alginate + BMP-2 (N = 8) 3: PLO + BMP-2 (N = 8) 4: PLA + BMP-2 (N = 8) 5: DEAE-Dextran + BMP-2 (N = 8)	6 W	Micro-CT (BVF in %) Masson's Trichrome staining (qualitative analysis)	PLA + BMP-2 ** > DEAD-Dextran + BMP-2 DEAD-Dextran: new bone tissue was thin and sparse
Bölgen et al. (2013)	Rat (NS, Sprague Dawley), *n* = 57	Calvaria Ø: 8 mm	1: HEMA/Lactate/Dextran (N = 29) 2: HEMA/Lactate/Dextran + MSCs (N = 28)	30 D 90 D 180 D	HE staining; Masson's Trichrome staining (New bone/Total cavity ratio)	At 180D: HEMA/Lactate/ Dextran > HEMA/Lactate/ Dextran + MSCs *

(Continued on following page)

2018; Ding et al., 2019; Fang et al., 2019; Maurel et al., 2021; Wang et al., 2021), β-tricalcium phosphate (Takahata et al., 2015) (β-TCP) or bioactive glass (Popescu et al., 2020) were thus added to the scaffolds in nine studies, whereas another natural or synthetic polymer was combined to the scaffold in nine studies (Chen et al., 2005; Chen et al., 2006; Chen et al., 2007; Abbah et al., 2012; Togami et al., 2015; Ding et al., 2019; Fang et al., 2019; Popescu et al., 2020; Wang et al., 2021).

TABLE 3 | (*Continued*) Preclinical studies using Dextran scaffolds for bone regeneration in orthotopic sites.

Author (Year)	Animal model (sex; species); n, number of animals used	Type of defect (defect size)	Conditions (N, number of defects created in total per condition)	Observation time [in day (D), week (W) or month (M)]	Experimental analysis	Results
Togami et al. (2014)	Rabbit (male, Japanese) *n* = 9	Femoral (epiphysis)	1: PVF/Dextran without water holding capability (N = 9)	2 W	Micro-CT (BV/TV in %; BMD in mg/cm^3)	At 4W and 6W: PVF/Dextran water holding capability ** > PVF/Dextran without water holding capability
		Ø: 4 mm	2: PVF/Dextran with water holding capability (N = 9)	4 W	HE staining (Ratio of bone formation per area in %)	PVF/Dextran water holding capability > PVF/Dextran without water holding capability ***
		H: 10 mm		6 W		Newly trabecular bone with lamellar structures for PVF/Dextran water holding capability
Ritz et al. (2018)	Mouse (NS, Athymic nude), *n* = 40	Calvaria Ø: 2.7 mm	1: Empty (N = 2) 2: Dextran (N = 16) 3: Dextran + HUVEC (N = 16) 4: Dextran + HUVEC/hOB (N = 14) 5: Dextran + SDF-1 (N = 16) 6: Dextran + BMP-7 (N = 16)	8 W	Micro-CT (BV/TV in Voxel)	Dextran + HUVEC * > Empty Dextran + SDF-1 * > Empty
					HE staining (qualitative analysis)	For Dextran + HUVEC or SDF-1 groups: fibrous membrane structure complemented by a thin bony structure covering the whole defect
Ding et al. (2019)	Rat (NS, Sprague Dawley), *n* = 24	Calvaria	1: Chitosan/Dextran (N = 6) 2: Chitosan/Dextran + HA (N = 6)	4 W	Micro-CT (BV/TV in %)	Chitosan/Dextran + Sr100HA* > Chitosan/Dextran + HA * > Chitosan/Dextran
		Ø: 5 mm	3: Chitosan/Dextran + Sr50HA (N = 6) 4: Chitosan/Dextran + Sr100HA (N = 6)	8 W	HE staining (New bone area fraction in %); Masson's Trichrome staining (Regenerated collagen in %)	Chitosan/Dextran + Sr100HA * > Chitosan/Dextran
Fang et al. (2019)	Rabbit (female, New Zealand), *n* = 18	Femoral (condyle)	1: Dextran/Polyacrylamide (N = 18)	0 D	Micro-CT (BMC in mg; BV in mm^3)	At 30D: HA-Dextran/Polyacrylamide ** > Dextran/Polyacrylamide
		Ø: 3 mm H: 5 mm	2: Dextran/Polyacrylamide + HA (N = 18)	30 D 90 D	HE staining; Masson's Trichrome staining (qualitative analysis)	At 30D: HA-Dextran/Polyacrylamide groups sowed osteoid tissue formation which was not observed without HA
Shoji et al. (2020)	Mouse (NS, C57BL/6J), *n* = NS	Femur fracture L: 10 mm W: 4 mm	1: Empty (N=NS) 2: Dextran + PBS (N = 8) 3: Dextran + bFGF (N = 8)	4 W	Micro-CT (BV in mm^3; BMC in mg)	Dextran + bFGF * > Empty
					HE staining (qualitative analysis)	Large calluses and newly formed bone at fracture site for Dextran + bFGF group
Wang et al. (2021)	Rats (female, Sprague Dawley) *n* = 18	Calvaria Ø: 4 mm	1: Empty (N = 9) 2: Dextran/PLGA + HA + BP (N = 9)	4 W 8 W	Micro-CT (BVF in %; BMD in g/cc; trabecular number in mm^{-1})	Dextran/PLGA + HA + BP * > Empty
				12 W	HE staining; Toluidine blue staining (qualitative analysis)	At 8W: for Dextran/PLGA + HA + BP group, large area of woven bone and thin lamellar structure

*BMC, bone mineral content; BMD, bone mineral density; BMP, bone morphogenic protein; BP, bisphosphonate; BV, bone volume; BV/TV, bone volume over total volume; β-TCP, beta-tricalcium phosphate; BVF, bone volume fraction; CPC, calcium phosphate ceramic; DEAE, diethylaminoethyl; D.S., degree of substitution; H, height; HA, hydroxyapatite; HE, hematoxylin and eosin; HEMA, hydroxyethyl methacrylate; hOB, human osteoblast; HUVEC, human umbilical vein endothelial cells; L, length; MC, mineral content; MD, mineral density; Micro-CT, micro-computed tomography; mPCL-TCP, medical grade poly (ε-caprolactone)—β-tricalcium phosphate; MSCs, mesenchymal stromal cells; n/s not significant; NaCl, sodium chloride; PBS, phosphate buffer saline; PLA, poly-L-arginine; PLO, poly-L-ornithine; PVF, polyvinyl formol; Sr, strontium; W, width * p < 0.05; ** p < 0.01; *** p < 0.001; ø, diameter.*

TABLE 4 | Preclinical studies using Pullulan scaffolds for bone regeneration in orthotopic sites.

Author (Year)	Animal model (sex; species); n, number of animals used	Type of defect (defect size)	Conditions (N, number of defects created in total per condition)	Observation time [in day (D), week (W) or month (M)]	Experimental analysis	Results
Hayashi et al. (2009)	Mouse (male, ICR), *n* = NS	Calvaria implantation (without defect) Ø: 4.6 mm H: NS	1: Pullulan (N=NS) 2: Pullulan + BMP-2 (0.1 μg) (N=NS) 3: Pullulan + BMP-2 (1 μg) (N=NS) 4: Pullulan + BMP-2 (1.5 μg) (N=NS) 4: Pullulan + BMP-2 (2 μg) (N=NS)	14 D	Micro-CT (BV in mm^3)	No significant difference between groups
					HE staining; Von Kossa staining (qualitative analysis)	Pullulan + BMP-2 stimulation of osteoblast activity to form new bone
	Mouse (male, ICR), *n* = NS	Calvaria Ø: 4.6 mm H: NS	1: Empty (N=NS) 2: Pullulan (N=NS) 3: Pullulan + BMP-2 (1 μg) (N=NS) 4: Pullulan + BMP-2 (2 μg) (N=NS)	4 W	Micro-CT (qualitative analysis)	Pullulan alone failed to repair bone defect Pullulan + BMP-2 (2 μg) full repair of bone defect
					HE staining (qualitative analysis)	New bone formation at the edges of the defect for Pullulan + BMP-2 groups
Miyahara et al. (2011)	Rat (NS, Wistar), *n* = 36	Calvaria Ø: 5 mm H: NS	1: Empty (N = 24) 2: Collagen membrane (N = 24) 3: Pullulan membrane (N = 24)	2 W 4 W 8 W	Micro-CT (BV in mm^3) HE staining (qualitative analysis)	At 4W: Pullulan membrane * > Collagen membrane Collagen membrane: immature bone synthesized on both sides of the membrane Pullulan membrane: Mature bone synthesized; regeneration occurred under the membrane
Fujioka-Kobayashi et al. (2012)	Mouse (NS, C57BL/6N), *n* = 43	Calvaria Ø: 3 mm H: 5 mm	1: Pullulan + PBS (N = 11) 2: Pullulan + FGF18 (N = 10) 3: Pullulan + BMP-2 (N = 11) 4: Pullulan + FGF18 + BMP-2 (N = 11)	0 W 1 W 2 W 3 W 6 W 8 W	Micro-CT (Bone healing in %) Alizarin Red and Calcein staining (qualitative analysis)	At 8W: Pullulan + FGF18 + BMP-2 * > Pullulan + BMP-2 Newly bone synthesis in the defect in Pullulan + BMP-2 and Pullulan + FGF18 + BMP-2 groups
	Mouse (NS, Osx1-GFP::Cre/B26B), *n* = 6	Calvaria Ø: 3 mm H: NS	1: Pullulan-Rh + PBS (N = 3) 2: Pullulan-Rh + FGF18 + BMP-2 (N = 3)	2 W	X-gal staining	Osterix 1 gene activated for the formation of new bone in Pullulan-Rh + FGF18 + BMP-2 group
Takahata et al. (2015)	Rabbit (female, New Zealand), *n* = 6	Ulnar (diaphysis) L: 10 mm	1: α-TCP (N=NS) 2: Pullulan + β-TCP (N=NS)	4W 8W	HE staining; Safranin O staining (qualitative analysis)	Mature bone formation for Pullulan + β-TCP group Fragmented bone ingrowth for α-TCP group
	Mouse (female, C57BL/6J), *n* = 13	Femoral (Intramedular injection) Size: NA	1: Empty (N = 4) 2: Pullulan (N = 4) 3: Pullulan + β-TCP (N = 4)	4W	Micro-CT (BMD in mg/cm^3)	Pullulan + β-TCP * > Empty
			1: Empty (N = 3) 2: Pullulan (N = 3) 3: Pullulan + β-TCP (N = 3)	2 W 5 W 8 W	HE staining (qualitative analysis)	At 5W: bone formation began for Pullulan + β-TCP group
	Pig (female, NS), *n* = 4	Vertebral body Size: 1 cm^2	1: Empty (N=NS) 2: α-TCP (N=NS)	8 W	Micro-CT (CT number in Hounsfield Unit)	Pullulan + β-TCP ** > Empty

(Continued on following page)

TABLE 4 | (*Continued*) Preclinical studies using Pullulan scaffolds for bone regeneration in orthotopic sites.

Author (Year)	Animal model (sex; species); n, number of animals used	Type of defect (defect size)	Conditions (N, number of defects created in total per condition)	Observation time [in day (D), week (W) or month (M)]	Experimental analysis	Results
			3: Pullulan + β-TCP (N=NS)			
			1: α-TCP (N=NS)	4 W	HE staining (qualitative analysis)	At 4W: bone defect recovered by bone healing for Pullulan + β-TCP group whereas α-TCP group demonstrated fragmented bone ingrowth
			2: Pullulan + β-TCP (N=NS)	8 W		
Charoenlarp et al. (2018)	Mouse (male, C57BL/6N), *n* = 6–10 per condition	Calvaria Ø: 3 mm H: NS	1: Pullulan (air) + PBS (N=NS)	0 W	Micro-CT (% of healing)	At 8W: Pullulan (cross-linked RGD) + BMP-2 + FGF18 * > Pullulan (freeze-dried) + BMP-2 + FGF18
			2: Pullulan (freeze-dried) + PBS (N=NS)	1 W		
			3: Pullulan (cross-linked RGD) + PBS (N=NS)	2 W		
			4: Pullulan (air) + BMP-2 + FGF18 (N=NS)	3 W		
			5: Pullulan (freeze-dried) + BMP-2 + FGF18 (N=NS)	4 W		
			6: Pullulan (cross-linked RGD) + BMP-2 + FGF18 (N=NS)	6 W		
				8 W	Modified Tetrachrome staining (qualitative analysis)	Whether Pullulan was cross-linked with RGD peptides or freeze-dried and combined with BMP-2 and FGF18, it showed trabecular bone formation with calcified bone fragmented
	Mouse (male, ICR), *n* = 3–4 per condition	Calvaria Ø: 3 mm H: NS	1: Pullulan (cross-linked RGD) + PBS (N=NS)	1 W	Modified Tetrachrome staining (qualitative analysis)	Presence of osteoblasts in Pullulan (cross-linked RGD) + BMP-2 + FGF18 and bone regeneration begun under the nanogel
			2: Pullulan (cross-linked RGD) + BMP-2 + FGF18 (N=NS)			
Popescu et al. (2019)	Rat (male, Wistar), *n* = 30	Femoral (diaphysis, unicortical) W: 2 mm	1: Alginate/ Pullulan (N=NS)	0 D	MRI (Bone defect width in μm)	All groups showed a decrease in bone defect size but it was faster for Alginate/Pullulan/1.5CuBG group (No statistical comparison done)
			2: Alginate/Pullulan + β-TCP/HA (N=NS)	5 D		
			3: Alginate/Pullulan/ 0.5CuBG (N=NS)	28 D		
			4: Alginate/Pullulan/ 1.5CuBG (N=NS)	0 D	HE staining (qualitative analysis)	Alginate/Pullulan/0.5 or 1.5CuBG showed osteoid tissue formation with parallel organized fibers
			5: Alginate/Pullulan/ BG (N=NS)	35 D		

*BG, bioglass; BMD, bone mineral density; BMP, bone morphogenic protein; BV, bone volume; β-TCP, beta-tricalcium phosphate; H, height; HA, hydroxyapatite; HE, hematoxylin and eosin; L, length; Micro-CT, micro-computed tomography; NA, not applicable; NaCl sodium chloride; NS, not specified; PBS, phosphate buffer saline; Rh rhodamine; W, width; X-gal 5-bromo-4-chloro-3-indolyl-b-D-galactopyranoside; * p < 0.05; ** p < 0.01; *** p < 0.001; ø, diameter.*

Another reported strategy to enhance bone formation was the incorporation of bioactive molecules to these biomaterials to create a delivery system. Growth factors were employed in 13 studies, namely, bone morphogenetic proteins (Chen et al., 2005; Maire et al., 2005a; Chen et al., 2007; Degat et al., 2009; Hayashi et al., 2009; Abbah et al., 2012; Fujioka-Kobayashi et al., 2012; Charoenlarp et al., 2018; Chen et al., 2019; Yu et al., 2020) (e.g., BMP-2 and BMP-7), basic fibroblast growth factor (Shoji et al., 2020) (bFGF), fibroblast growth factor (Fujioka-Kobayashi et al., 2012; Charoenlarp et al., 2018) (FGF18), insulin-like growth factor (Chen et al., 2006) (IGF-1) and stromal-derived growth factor (Ritz et al., 2018) (SDF-1). One study reported the

TABLE 5 | Preclinical studies using Dextran and Pullulan scaffolds for bone regeneration in orthotopic sites.

Author (Year)	Animal model (sex; species); n, number of animals used	Type of defect (defect size)	Conditions (N, number of defects created in total per condition)	Observation time [in day (D), week (W) or month (M)]	Experimental analysis	Results
Fricain et al. (2013)	Rat (NS, Wistar), *n* = NS	Femoral (condyle) Ø: 5 mm H: 6 mm	1: Empty (N = 6) 2: Pullulan/Dextran (N = 18) 3: Pullulan/Dextran + HA (N = 18)	15 D 30 D 90 D	Micro-CT (MC in mg; MD in mg/cm^3) Von Kossa staining; Masson's Trichrome staining (qualitative analysis)	Pullulan/Dextran + HA * > Pullulan/Dextran * > Empty Tissue mineralization was more important for Pullulan/Dextran + HA than Pullulan/Dextran
	Goat (NS), *n* = 7	Mandibular Ø: 10 mm H: 8 mm	1: Empty (N = 2) 2: Pullulan/Dextran + HA (N = 10)	1 M 6 M	Micro-CT (qualitative analysis) Von Kossa staining; Masson's Trichrome staining (qualitative analysis)	Osteoid tissue formation observed for Pullulan/Dextran + HA group New osteoid tissue formation for Pullulan/Dextran + HA group and mineralized tissue
		Tibial (epiphysis) L: 40 mm W: 12 mm	1: Empty (N = 2) 2: Pullulan/Dextran + HA (N = 10)	1 M 6 M	Micro-CT (qualitative analysis) Von Kossa staining; Masson's Trichrome staining (qualitative analysis)	Mineralized tissue within the defect for Pullulan/Dextran + HA group Induction of mineralized tissue with organized lamellar bone by Pullulan/Dextran + HA group
Schlaubitz et al. (2014)	Rat (female, Wistar RjHan), *n* = 18	Femoral (condyle) Size: 38 mm^3	1: Empty (N = 18) 2: Pullulan/Dextran + HA (N = 18)	15 D 30 D 70 D	Micro-CT (BMC in mg; BMD in mg/cc) Von Kossa staining (osteoid within the region of interest in %)	Pullulan/Dextran + HA ** > Empty Pullulan/Dextran + HA ** > Empty
Frasca et al. (2017)	Rat (male, Lewis), *n* = 90	Femoral metaphysis Ø: 3 mm H: 5 mm	1; Empty (N = 30) 2: MSCs (N = 30) 3: Pullulan/Dextran (N = 30) 4: Pullulan/Dextran + MSCs (N = 30) 5: HA/β-TCP (N = 30) 6: HA/β-TCP + MSCs (N = 30)	7 D 30 D 90 D	Micro-CT (BV/TV in %) Von Kossa staining; Masson's Trichrome staining (qualitative analysis)	At 30D: Pullulan/Dextran + MSCs* > MSCs For Pullulan/Dextran with or without MSCs groups, formation of trabecular and cortical bones
Ribot et al. (2017)	Rat (female, Wistar RjHan), *n* = 33	Femoral condyle Ø: 3,5 mm H: 4 mm	1: Pullulan/Dextran + Fucoidan (N = 15) 2: Pullulan/Dextran + HA (N = 12) 3: Pullulan/Dextran + Fucoidan + HA (N = 18) 1: Pullulan/Dextran + Fucoidan (N = 24) 2: Pullulan/Dextran + HA (N = 24) 3: Pullulan/Dextran + Fucoidan + HA (N = 30)	1 W 3 W 5 W	MRI (Volume of hyper intense signal in mm^3) Micro-CT (BV/TV in %) Masson's Trichrome staining (% of mature bone per defect)	At 3W: Pullulan/Dextran + Fucoidan > Pullulan/Dextran + Fucoidan + HA * > Pullulan/Dextran + HA * At 5W: Pullulan/Dextran + HA** > Pullulan/Dextran + Fucoidan + HA** > Pullulan/Dextran + Fucoidan At 3W: Pullulan/Dextran + HA * > Pullulan/Dextran + Fucoidan + HA * > Pullulan/Dextran + Fucoidan
Fricain et al. (2018)	Sheep (NS), *n* = 12	Maxillary sinus (i.e. sinus lift procedure)	1: Bio-Oss® (N = 12) 2: Pullulan/Dextran + HA (N = 12)	0 M 3 M 6 M	Micro-CT (MV/TV ratio) Masson's Trichrome staining (Bone tissue in mm^2)	Pullulan/Dextran + HA ≈ Bio-Oss® (n/s) Pullulan/Dextran + HA ≈ Bio-Oss® *

(Continued on following page)

TABLE 5 | (*Continued*) Preclinical studies using Dextran and Pullulan scaffolds for bone regeneration in orthotopic sites.

Author (Year)	Animal model (sex; species); n, number of animals used	Type of defect (defect size)	Conditions (N, number of defects created in total per condition)	Observation time [in day (D), week (W) or month (M)]	Experimental analysis	Results
Maurel et al. (2021)	Rat (female, NS), *n* = 6	Femoral condyle	1: Pullulan/Dextran + HA resuspended in NaCl 0.9% (N = 6)	30 D	Micro-CT (BV/TV ratio)	No significant difference between the two groups
		Ø: 4 mm H: 6 mm	2: Pullulan/Dextran + HA resuspended in autologous blood (N = 6)	60 D	Masson's Trichrome staining (new bone surface in %)	Osteoid tissue formation with trabecular-like structures for both conditions
	Sheep (NS), *n* = 3	Maxillary sinus (i.e. sinus lift procedure)	1: Pullulan/Dextran + HA resuspended in NaCl 0.9% (N = 3)	3 M	Cone Beam Computer Tomography (MV/TV ratio)	No significant difference between the two groups
			2: Pullulan/Dextran + HA resuspended in autologous blood (N = 3)		Masson's Trichrome staining (new bone surface in %)	Osteoid tissue formation for both conditions

*BMC, bone mineral content; BMD, bone mineral density; BV/TV, bone volume over total volume; β-TCP, beta-tricalcium phosphate; H, height; HA, hydroxyapatite; L, length; MC, mineral content; MD, mineral density; Micro-CT, micro-computed tomography; MRI, magnetic resonance imaging; MSCs, mesenchymal stromal cells; MV/TV, mineral volume over total volume; NS, not specified; NaCl, sodium chloride; * p < 0.05; ** p < 0.01; ø, diameter.*

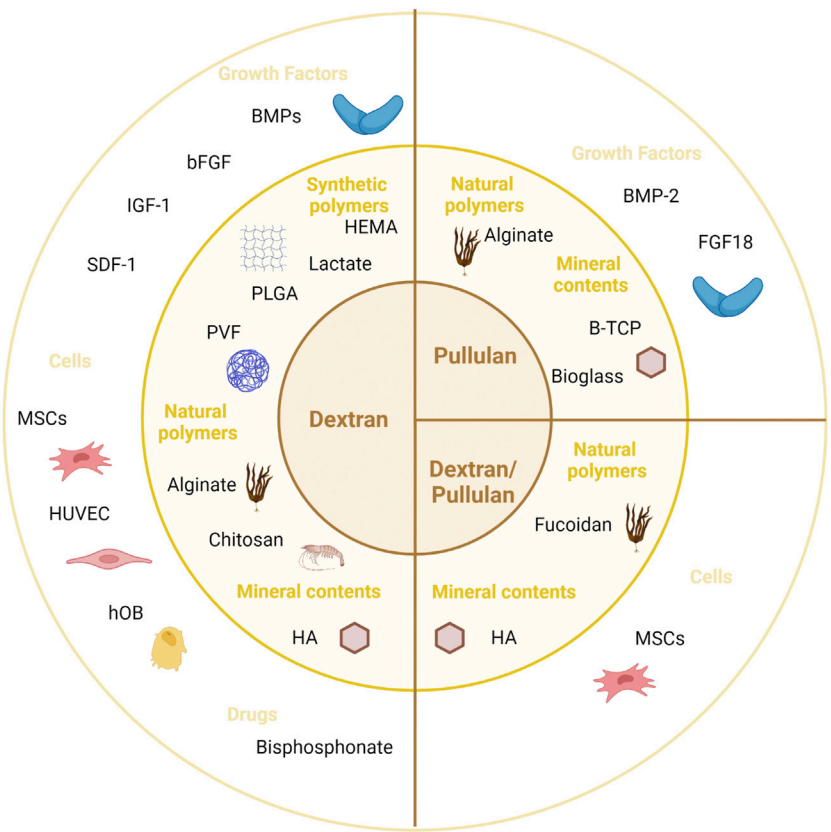

FIGURE 5 | Dextran and/or pullulan-based scaffolds for bone tissue engineering applications. Created with BioRender.com. bFGF, basic fibroblast growth factor; BMP, bone morphogenetic protein; B-TCP, beta-tricalcium phosphate; FGF, fibroblast growth factor; HA, hydroxyapatite; HEMA, hydroxyethyl methacrylate; hOB, human osteoblast; HRP, horseradish peroxidase; HUVEC, human umbilical vein endothelial cells; IGF, insulin-like growth factor; MSCs, mesenchymal stromal cells; PLGA, poly-(L-glutamic acid); PVF, polyvinyl formal; SDF, stromal-derived growth factor.

incorporation into the scaffold of bisphosphonate, which exhibits strong affinity with hydroxyapatite (Wang et al., 2021).

Incorporation of cells into the polysaccharide scaffolds was the last identified procedure to promote bone regeneration (three studies). Three types of cells have been incorporated to scaffolds to promote bone regeneration: rat mesenchymal stromal cells (Bölgen et al., 2014; Frasca et al., 2017) (MSCs), human umbilical vein endothelial cells (Ritz et al., 2018) (HUVEC), or human osteoblasts (Ritz et al., 2018).

For all these different strategies, the performance for regenerating bone tissue is examined in the following sections.

3.4 Evaluation of Performance of Polysaccharide-Based Materials for Bone Formation

3.4.1 Dextran-Based Materials for Bone Regeneration

Twelve studies investigated orthotopic bone formation by using dextran-based biomaterials and four studies investigated ectopic bone formation in rodents (**Tables 2**, **3**).

3.4.1.1 Dextran-Based Materials as a Bone Graft Substitute

To determine bone regeneration ability of dextran-derived biomaterials, several studies combined this polysaccharide with natural or synthetic polymers. For example, polyvinyl formal (PVF) sponges have been coated with dextran to enhance the poor osteogenic ability of this synthetic polymer due to its fibrous construction (Togami et al., 2015). Investigation of the water holding capability of the scaffold revealed that dextran-coated PVF sponge with high water capability significantly improved bone formation in a rat femoral defect.

Three studies assessed the osteogenic capability improvement of dextran-based hydrogels loaded with mineral particles. Dextran-based hydrogel combined with a synthetic polymer (polyacrylamide) loaded or not with hydroxyapatite (HA) particles was implanted into a rabbit femoral defect (Fang et al., 2019). Bone regeneration was significantly improved in the presence of HA. In another case, dextran was mixed to chitosan with strontium-doped mineral particles to further improve bone regeneration (Ding et al., 2019). Nanohydroxyapatite particles doped with increasing molar ratios of strontium (0%, 50%, and 100%) were incorporated into the polymeric mixture and implanted in a rat calvarial defect model. The adjunction of nanohydroxyapatite doped with 100% strontium significantly enhanced bone regeneration, whereas the dextran-based hydrogel without strontium-nanohydroxyapatite showed the lowest regeneration rate.

Finally, an injectable hydrogel composed of dextran and poly (L-glutamic acid) inspired from mussel adhesion to design an adhesive, self-healing biomaterial with osteogenic properties through HA and bisphosphonate incorporation inside the scaffold was designed by Wang et al. (2021). Scaffolds were implanted in a rat calvarial defect and showed a significant enhancement of bone regeneration compared with control.

3.4.1.2 Dextran-Based Material to Create Heparan Sulfate Mimetic Molecules (i.e., Regenerating Agent, RGTA®)

Regenerating Agents (RGTA®) are polysaccharides designed to replace altered heparan sulfate in injured tissues (Barritault et al., 2017). They are derived from dextran that is chemically modified by sulfate and carboxyl groups. One of these RGTA®, derived from dextran, was investigated for bone regeneration in a rat calvarial defect model (Lafont et al., 2004). Where dextran backbone was functionalized with methylcarboxyl, benzylamide, and sulfate groups. Two conditions were applied on a collagen sponge either with a solution of dextran derivatives like RGTA® or with PBS. Bone healing occurred earlier with the dextran derivative at 7 days after implantation.

3.4.1.3 Dextran-Based Material as a Potential Cell Carrier System

Scaffold designed for BTE loaded with cells can act as a carrier system if cells loaded on the scaffold stay inside to recruit endogenous cells, or can act as a cell delivery system if cells migrate to the surrounding tissue (Lalande et al., 2011). Two studies reported the use of dextran-derived biomaterials as a carrier for cell delivery (Bölgen et al., 2014; Ritz et al., 2018). A dextran-based cryogel was implanted in a rat calvarial defect loaded with or without stem cells (rat MSCs) (Bölgen et al., 2014). Bone regeneration significantly increased over time in both conditions. However, no significant difference was evidenced between the "scaffold-stem cells" group and the cell-free scaffold group whatever the time point (30 and 90 days). These results were consistent with another study focusing on a dextran-based material loaded with HUVECs and osteoblasts. (Ritz et al., 2018). Dextran-based hydrogels were either loaded with a monoculture of HUVECs or a co-culture of human osteoblasts with HUVECs. Results at 8 weeks showed that hydrogels loaded with HUVECs significantly enhanced bone formation compared with the defect left empty. However, this study showed no significant difference between the "scaffold-cells" group and the cell-free scaffold group, thereby demonstrating that a use of dextran-based hydrogels as a cell carrier system to deliver rat MSCs or HUVECs fail to enhance dextran osteogenic properties.

3.4.1.4 Dextran-Based Material as a Growth Factor Carrier

Dextran-derived biomaterials were also reported as growth factor carriers to promote bone regeneration. As previously mentioned, dextran polysaccharide chains have been chemically modified by amine, amide, carboxyl or acrylic groups to promote growth factor delivery system. Those modifications were performed either to 1) cross-link the polymeric scaffold to enable the encapsulation of growth factors or 2) to directly interact with them.

Four studies investigated the osteoinductive potential of dextran-based materials as a delivery growth factor system in ectopic bone formation models (Maire et al., 2005a; Degat et al., 2009; Chen et al., 2019; Yu et al., 2020) (**Table 2**).

Maire et al. (2005a) used modified dextran with different degrees of substitution of hydroxyl groups (i.e., number of modified groups adding per 100 glucose units) and combined extracted bovine BMP-2 (0.5 and 5 μg) to analyze ectopic bone

formation and calcification. Modification of the dextran backbone enabled cross-linking of the scaffold. It appeared that depending on the functionalization rate of dextran (e.g., degree of substitution of 0%, 2% or 18% w/w), BMP-2 was gradually delivered to the surrounding environment to promote bone formation and calcification. The highest growth factor retention was observed using the highest functionalized dextran content (D.S. = 18%). Small concentration of BMP (0.5 µg) failed to induce bone formation regardless of the functionalization rate.

In another study, the number of carboxymethyl and benzylamide groups (i.e., for cross-linking purpose) on dextran backbone was modified to investigate subcutaneously BMP-2 delivery (Degat et al., 2009). A dose-dependent trend was observed: 1 or 10 µg of modified dextran were sufficient to induce ectopic bone formation whereas a higher concentration of this dextran derivative (100 µg) inhibited such formation.

The impact of sulfated groups on different polymers (e.g., chitosan, dextran) and its ability to release rhBMP-2 (10 µg) was determined in a mouse muscle implantation model (Chen et al., 2019). Dextran substitutes improved binding with cytokine (e.g., rhBMP-2) through electrostatic interactions but generated few bones ectopically compared with chitosan. It was hypothesized that the modified dextran having less sulfated groups than the modified sulfated chitosan, it failed to properly deliver rhBMP-2 and induce bone formation.

The last study in ectopic model by Yu et al. (2020). confirmed these findings by loading unmodified dextran with rhBMP-2. It appeared that dextran scaffold generated few trabecular structures after 8 weeks.

Five studies reported the use of dextran-based materials as a delivery growth factor in orthotopic bone models. Dextran-based microbeads modified with an amino group, diethylaminoethyl (DEAE) was investigated in a rat arthrodesis model (Abbah et al., 2012). Dextran-based scaffold failed to successfully deliver BMP-2 (5 µg) and to induce bone formation as shown by micro-CT analysis. In comparison, another amino group (i.e., tyramine) was used to modify dextran backbone in a mice fracture model (Shoji et al., 2020). This association has improved the delivery of b-FGF and accelerate bone formation. Large calluses and new bone areas were observed at the fracture site.

Another team assessed the potential of dextran/gelatin scaffolds to act as a delivery growth factors system [e.g., BMP-2 (Chen et al., 2005; Chen et al., 2007) or IGF-1 (Chen et al., 2006)] in a periodontal defect model on dogs. Chemical properties of dextran/gelatin scaffold were investigated by functionalized dextran (Chen et al., 2006), and growth factors entrapment inside the scaffold (Chen et al., 2005; Chen et al., 2007). Here, the functionalization of dextran backbone only played a role on the reticulation process of the biomaterial. In their first study (Chen et al., 2005), dextran/gelatin microspheres were combined with BMP-2 and mixed in CPC to fill periodontal defect. In addition, a chitosan membrane loaded with these microspheres was added to cover the defect. Compared with the control group (i.e., CPC covered by chitosan membrane), dextran/gelatin microspheres covered with the chitosan membrane presented new bone formation 8 weeks after surgery.

Another approach concerns the dextran functionalization with glycidyl methacrylate at different degrees of substitution (e.g., 4.7, 6.3, and 7.8) combined with IGF-1 (Chen et al., 2006). Dextran with the smallest rate of substitution (D.S. = 4.7) showed positive results to properly deliver IGF-1 and then regenerate bone.

Chen et al. (2007) investigated whether BMP-2 had to be adsorbed or loaded through microsphere encapsulation in the dextran/gelatin scaffold. BMP-2 activity seemed to be better preserved when loaded in dextran/gelatin microspheres in the scaffold compared when it was adsorbed at the surface of the material.

Finally, dextran scaffold was successfully loaded with stromal-derived growth factor (SDF-1) in a mice calvarial defect. Bone regeneration was significantly improved compared with the empty defect (Ritz et al., 2018), but without significant difference with the growth factor-free scaffold.

3.4.2 Bone Formation With Pullulan Substitutes

Six studies investigated orthotopic bone formation by using pullulan-based biomaterials and one study assessed ectopic bone formation in rodents (**Tables 2**, **4**).

3.4.2.1 Pullulan-Based Materials as a Bone Graft Substitute

Numerous studies described the performance of composite materials with pullulan. Combination of pullulan to alginate and bioactive glasses with various percentage of copper oxide to regenerate bone was investigated in a rat femoral defect and was compared with a commercial β-TCP/HA substitute embedded in an alginate-pullulan composite scaffold (Popescu et al., 2020). A progressive healing of bone was observed whatever the tested scaffold composition. Interestingly, a regeneration process was also observed when the alginate–pullulan composite materials were implanted in such orthotopic site without an osteoconductive component (i.e., β-TCP/HA and bioglass), thereby suggesting the potential of these materials for BTE applications. However, there was no empty group as a control in this study.

Phosphorylated-pullulan mixed with β-TCP had been tested in three different models, a rabbit ulnar defect, a pig vertebral defect, and a mouse femoral injection (Takahata et al., 2015). It showed similar bone regeneration compared to a clinical bone substitute made of α-TCP (Biopex-R®) in a rabbit ulnar bone defect model. Additionally, implantation of the composite scaffold induced new bone formation at 4 and 8 weeks, whereas Biopex-R® remained isolated from the surrounding bone at 8 weeks.

3.4.2.2 Pullulan-Based Material as a Potential Growth Factor Carrier

Three studies mentioned the substitution of pullulan main chains by cholesteryl and acryloyl groups to proceed cross-linking between pullulan macromolecules and then to establish a growth factor delivery system (Hayashi et al., 2009; Fujioka-Kobayashi et al., 2012; Charoenlarp et al., 2018). Modified pullulan successfully delivered BMP-2 (2 µg) and induced bone formation ectopically in a mice model (Hayashi et al., 2009). The

potential of this scaffold to deliver BMP-2 and promote bone regeneration by varying BMP-2 concentration was then determined in an orthotopic mouse calvarial model. Implantation of pullulan-based hydrogel containing 2 µg of BMP-2 showed the best results which was evidenced by the complete healing of the critical defect. One study described the effect of a co-administration of FGF18 and BMP-2 implanted in a bone defect using a pullulan-based hydrogel (Fujioka-Kobayashi et al., 2012). The amount of newly formed bone was higher when both growth factors were delivered, suggesting that this system improved the efficiency of BMP2-dependent bone healing in a mouse calvarial defect model.

Charoenlarp et al. (2018) also used pullulan-based materials to act as a delivery system for multiple growth factors (i.e., BMP-2 and FGF18). They assessed their growth factor release pattern and observed an initial burst followed by a gradual sustained release more than 1 week. They also observed that functionalization with RGD peptides during synthesis of gels enhanced bone healing as growth factors interact with the repeated units.

3.4.2.3 Pullulan-Based Membrane for Guided Bone Regeneration

A nanogel membrane made with cholesteryl and acryloyl-binding pullulan was evaluated for guiding bone regeneration (Miyahara et al., 2012). This nanogel membrane was compared with a commercially available collagen membrane (Koken Tissue Guide®) in a rat calvarial defect and they both stimulated bone regeneration compared with the control, in which no membrane was applied. Earlier bone regeneration was significantly enhanced with the pullulan-based nanogel membrane and newly formed bone was more mature 2 weeks after surgery.

3.4.3 Pullulan/Dextran-Based Materials for Bone Regeneration

Six studies investigated orthotopic bone formation by using pullulan/dextran-based biomaterials in which one study also assessed ectopic bone formation in rodents and goats (**Tables 2**, **5**).

3.4.3.1 Pullulan/Dextran-Based Substitute Used as a Bone Graft Substitute

One team focused on a composite scaffold combining a pullulan/dextran-based material with HA particles to promote osteogenesis (Fricain et al., 2013; Schlaubitz et al., 2014; Ribot et al., 2017; Fricain et al., 2018; Maurel et al., 2021). Firstly, this biomaterial was supplemented or not with hydroxyapatite in heterotopic and orthotopic sites on mice and goat to investigate the osteoinductive and osteoconductive properties (Fricain et al., 2013). Subcutaneous and intra-muscular implantations on small and large mammals revealed that this pullulan/dextran scaffold combined with HA enabled osteoid tissue formation. Besides, the composite scaffold induced a highly mineralized tissue in three different bony sites (e.g., femur, mandible, and tibia), as well as osteoid tissue and bone tissue regeneration in direct contact to the matrix. The same composite scaffold was then designed as cross-linked microbeads to be implanted in a rat femoral defect (Schlaubitz et al., 2014). Bone regeneration was significantly enhanced compared with the empty group. Interestingly, one study compared in a maxillary bone defect in sheep this pullulan/dextran-based scaffold with HA to a widely used clinical xenograft (BioOss®) (Fricain et al., 2018). Similar results were obtained for both materials. These composite microbeads were also either reconstituted in saline buffer or autologous blood to investigate the role of this vehicle for bone regeneration (Maurel et al., 2021). They displayed important mineralization process without significant difference, thereby suggesting that reconstitution of microbeads with autologous blood is not required. A study focused on the interest of Magnetic Resonance Imaging (MRI) for longitudinal evaluation of three different biomaterials based on pullulan/dextran and containing either fucoidan and/or HA for bone regeneration in a rat femoral bone defect (Ribot et al., 2017). The high sensitivity of MRI showed that the material without HA was the least efficient for bone regeneration, which was confirmed by micro-CT images and histology. After 5 weeks, pullulan/dextran-based scaffold containing either HA alone or Fucoidan plus HA showed similar results.

3.4.3.2 Pullulan/Dextran-Based Material as a Potential Stem Cell Vehicle

Pullulan/dextran polysaccharide-based scaffold supplemented with MSCs was compared with a commercially available CPC bone substitute (Calciresorb C35®) (Frasca et al., 2017) for their ability to promote bone regeneration once loaded with cells. They were implanted alone or combined with syngenic MSCs from rat bone marrow. After 1 month, MSCs combined with these biomaterials significantly enhanced bone healing compared with their respective group without MSCs. After 3 months, bone regeneration was significantly enhanced for each condition without difference between cellularized and non-cellularized biomaterials. Results also showed that pullulan/dextran substitutes had a better resorption rate than CPC particles.

4 DISCUSSION

The purpose of this work was to review the design of pullulan and/or dextran-derived biomaterials used for bone regeneration. Polysaccharide scaffolds were systematically analyzed. These scaffolds were mostly used as a bone substitute (13 studies) or as a growth factor delivery system (13 studies). Three studies investigated the ability of these polysaccharide-based scaffolds to act as cell carriers for BTE applications and only one study suggested the use of a pullulan-based nanogel as a membrane for guided bone regeneration (Miyahara et al., 2012). The present systematic review showed that most of the pullulan-based and dextran-based materials underwent functionalization methods for BTE applications. Chemical functionalization is the most widely used approach to improve reticulation process and/or to promote their binding capacity to growth factors, thus enhancing their potential to act as growth factors carrier. The

introduction of charged groups also seemed to provide binding sites for host cells to adhere to the material (Filippi et al., 2020). Addition of acrylate groups (e.g., acryloyl, cholesteryl) was the most reported process to functionalize pullulan-based hydrogel (Hayashi et al., 2009; Fujioka-Kobayashi et al., 2012; Miyahara et al., 2012; Charoenlarp et al., 2018). Hydrogels of cholesterol-bearing pullulan are already considered as unique materials for various drug delivery applications (Morimoto et al., 2005a; Kato et al., 2007). Combination of cholesteryl group-associated hydrophobic domains and hydrophilic polysaccharide chains provides an amphiphilic hydrogel that shows effective drug-trapping sites in itself (Akiyoshi et al., 1998).

A wide range of functionalization methods were used for dextran-based materials, making it impossible to select a specific one for these polysaccharide-based materials. Interestingly, no chemical modification of pullulan/dextran-based matrix was also reported (Fricain et al., 2013; Schlaubitz et al., 2014; Frasca et al., 2017; Ribot et al., 2017; Fricain et al., 2018; Maurel et al., 2021).

This review also highlights the significant use of cross-linking reagents for these polysaccharide-based biomaterials synthesis. Cross-linkers have attracted much attention to enhance the biological functionality and mechanical properties of biopolymers (Oryan et al., 2018; Krishnakumar et al., 2019). Cross-linking strategies vary depending on the chemical nature of the biomaterials. This review emphasized that chemical cross-linkers were extensively used in the included studies. This is consistent with previous studies that establish that chemical cross-linking is the most commonly employed strategy to develop bone substitutes (Krishnakumar et al., 2019). For instance, successful chemical cross-linking of pullulan/dextran-based materials was carried out using the cross-linking agent STMP (Fricain et al., 2013; Schlaubitz et al., 2014; Frasca et al., 2017; Ribot et al., 2017; Fricain et al., 2018; Maurel et al., 2021). STMP is a nontoxic cross-linker, already used in the food industry (to cross-link starch) or for pharmaceutical applications (for hydrogels synthesis) (Gliko-Kabir et al., 2000; Lack et al., 2007). The present review outlined that pullulan/dextran-based materials were cross-linked with STMP. However, it should be mentioned that all the works carried out on pullulan/dextran-based materials comes from the same group. Pullulan-based materials were successfully cross-linked with thiol-bearing in four studies (Hayashi et al., 2009; Fujioka-Kobayashi et al., 2012; Miyahara et al., 2012; Charoenlarp et al., 2018), whereas no cross-linking reagents were used in two studies. Finally, cross-linking strategies were less employed to functionally modify dextran-based materials (only half of the included studies). Furthermore, each study focused on a different cross-linking process, making it difficult to draw conclusions.

Biomaterial design also plays a key role in promoting bone healing. In the present review, we outlined that these polysaccharide-derived biomaterials are mainly used as hydrogels or microbeads. A growing interest for polymer hydrogels in BTE is arising (Tang et al., 2021) as they exhibit several promising properties in a context of bone repair: they are ready-to-use material that can be molded to any shape, size, or form, thereby fitting easily in the bone defect (Li et al., 2021). Six studies designed disc-shaped hydrogels to adjust calvarial bone defects (Hayashi et al., 2009; Fujioka-Kobayashi et al., 2012; Bölgen et al., 2014; Charoenlarp et al., 2018; Ritz et al., 2018; Fang et al., 2019). Otherwise, *in situ* forming hydrogels were directly injected into the defect area, molding the defect site (Ding et al., 2019; Shoji et al., 2020), thereby ensuring a tight interface with the surrounding bone (El-Sherbiny and Yacoub, 2013; Maisani et al., 2018). Microbeads can be also easily adapted to a complex bone defect. Injectable hydrogels or microbeads allow minimal invasion of surrounding tissues during delivery (Ding et al., 2019).

Hydrogels also are good candidates to incorporate cells or growth factors and act as a delivery system. Pullulan and/or dextran-based materials display unique properties in the field of bone regeneration compared with commonly used bone substitutes. They exhibit resorption ability (Miyahara et al., 2012; Bölgen et al., 2014; Frasca et al., 2017), thereby ensuring the gradual replacement with newly formed bone compared with HA/TCP ceramics that exhibit extensive *in situ* resorption latencies (Keller et al., 2012). Another interesting property of these polymers is their radiotransparency (Hayashi et al., 2009; Frasca et al., 2017; Fricain et al., 2018) meaning that it allows to follow radiologically the new bone formation.

Several studies investigated the osteogenic properties of these polysaccharides-derived biomaterials through the adjunction of mineral contents. Most of these studies show a significant improvement of bone regeneration by incorporation of mineral contents. HA supplementation was used in eight of these 10 studies. This stimulates bone tissue formation and gives osteoconductive properties to the biomaterial. In addition, dextran and/or pullulan have been reinforced with mineral materials to overcome their weak physical properties (Fricain et al., 2013; Schlaubitz et al., 2014; Takahata et al., 2015; Ribot et al., 2017; Fricain et al., 2018; Ding et al., 2019; Fang et al., 2019; Popescu et al., 2020; Maurel et al., 2021; Wang et al., 2021) and then improve their mechanical strength.

Another reported strategy to enhance bone regeneration of dextran and/or pullulan-based materials was the encapsulation of growth factors. Growth factors are widely used in BTE to provide more regulating cues to target cell proliferation and differentiation and effective bone repair (Tang et al., 2021). A total of 13 studies reported the ability of pullulan-based materials and dextran-based materials to deliver growth factors. Most of them (i.e., 11 studies) focused on BMP-2 which play critical roles in bone regeneration process (Rao et al., 2018; Tang et al., 2021). A sustained release of this growth factor appeared to be difficult as heterotopic bone formation is usually observed due to its overexpression. Customization of biomaterials could be an alternative to regulate BMP-2 delivery. For example, chemical modification of polysaccharides was performed to enhance growth factors bearing within the scaffold to act as a drug delivery system. The addition of carboxylate, benzylamide, and sulfated groups to dextran-based scaffold enabled to mimic heparin-like compounds (Lafont et al., 2004; Maire et al., 2005a; Degat et al., 2009), which is one of the ECM

components that has high affinity with growth factors. Functionalized dextran thus exhibits binding capacity to heparin-binding growth factors, such as transforming growth factor-b1 (TGF-b1) (Maire et al., 2005b). As TGF-b1 and BMP-2 belong to the same superfamily and share one third of structural homology, functionalized dextran has the ability to bind to BMP-2 through its heparin-binding site (Maire et al., 2005a). This could be an alternative to the currently used collagen sponges that are approved by FDA to deliver BMP-2 (Maire et al., 2005a). Interestingly, heterotopic bone formation of BMP-2 loaded with heparin microparticles was investigated at high and low concentrations (0.12 and 0.01 mg/kg body weight) in a rat femoral defect (Hettiaratchi et al., 2020; Vantucci et al., 2021). BMP-2 delivery alone led to heterotopic bone formation whatever the concentration used. But when it was combined to heparin microparticles at a high dosage (30 µg per graft), a sustained release was observed and seemed to regulate bone formation.

Interestingly, no study reported the use of a pullulan/dextran-based material to deliver growth factor. This could be explained by the ability of these matrices to retain local growth factors (Fricain et al., 2013). The combination of these two polysaccharides might be an ideal candidate to provide a growth factor-free biomaterial for BTE applications.

Finally, three studies investigated dextran or pullulan/dextran-based hydrogels capability to incorporate progenitor cells to promote bone healing (Bölgen et al., 2014; Frasca et al., 2017; Ritz et al., 2018). Two approaches can be evidenced in such scaffolds. In one hand, cells entrapped into the scaffold can migrate at the defect site to initiate the ossification process. On the other hand, they can stay inside the scaffold to recruit local factors. In these three studies, only one mentioned the use of pullulan/dextran biomaterial as a cell delivery system (Frasca et al., 2017). The two others did not specify the role of their biomaterial on the delivery of cells. Concerning the angiogenesis process of these biomaterials in bone defects, it was observed in all studies. However, no significant difference in bone regeneration amount was observed between the seeded scaffold and the cell-free scaffold in two studies, thereby suggesting that using dextran-based material as a potential cell carrier system does not increase its osteogenic potential. This could be related to a low ability of these polysaccharide-based hydrogels to support cell adhesion and proliferation. To overcome this drawback, Frasca et al. (2017) proposed a sequential multiple MSC administration strategy to cover the entirety of the repair process kinetic.

Only three studies (Takahata et al., 2015; Frasca et al., 2017; Fricain et al., 2018) compared the pullulan and pullulan/dextran-based materials to commercialized and commonly used bone substitutes. These commercial devices were either xenograft (e.g., Bio-Oss®, extract from the mineral part of bovine bone) or alloplastic bone substitutes (e.g., Calciresorb C35®, composed of HA and TCP and Biopex-R®, composed of a-TCP). Pullulan and pullulan/dextran-based materials seemed to be at least as efficient as these conventional and commercially available bone substitutes. Besides, alloplastic bone substitutes showed poor host integration and failed to completely resorb *in vivo,* thereby preventing their replacement by newly formed bone. However, further studies comparing these polysaccharides to commercially used bone substitutes should be conducted to draw formal conclusions.

Finally, there are limitations related to the present systematic review that must be mentioned. One limitation of this study is the heterogeneity in animal models and the wide types of bone defects performed in the included studies, thereby making it difficult to compare studies. Calvarial and femoral defects were the most commonly used model to assess bone regeneration in these studies. Femoral defect may be more appropriate to consider load-bearing capacity of polysaccharide scaffolds when necessary (Taguchi and Lopez, 2021). Another identified drawback of this systematic review is the low number of studies investigating the mechanical properties of the materials (Abbah et al., 2012; Takahata et al., 2015; Ding et al., 2019; Fang et al., 2019). Among four studies, only one study evaluated the compressive strength directly on the bone with the investigating constructs (Abbah et al., 2012). It would be interesting to further evaluate the mechanical properties of these constructs and their evolution in time that should match the natural bone properties (Yunus Basha et al., 2015) to favor host bone integration (Giannoudis et al., 2007). Another interesting parameter to consider when evaluating a biomaterial for bone regeneration is the defect size, as non-critical size defect may heal spontaneously. Originally, critical-sized defect can be defined as the smallest size tissue defect that will not completely heal over the natural lifetime of an animal (Schmitz and Hollinger, 1986; Spicer et al., 2012). In practice, a defect is considered as critical-sized defect if it does not fully heal during the experimental time observation (Gosain et al., 2000; McGovern et al., 2018). Among the 28 included studies, all experiments using calvarial defects could be considered as critical-sized defect [e.g., more than 2 mm in mouse; more than 5 mm in rats (Taguchi and Lopez, 2021)]. For other bone models (e.g., tibia, ulnar, vertebrae), knowledge on the size considered as critical defect in those models could not be found in the literature. It would thus be interesting to compare these polysaccharides using the same animal model. The lack of empty defect condition as control in 13 studies (Lafont et al., 2004; Chen et al., 2005; Chen et al., 2007; Fujioka-Kobayashi et al., 2012; Bölgen et al., 2014; Togami et al., 2015; Ribot et al., 2017; Charoenlarp et al., 2018; Fricain et al., 2018; Ding et al., 2019; Fang et al., 2019; Popescu et al., 2020; Maurel et al., 2021), prevented readers to conclude on the relevance of the model used and the tested scaffolds. Further studies including an empty defect condition in the animal experimental design would be necessary to increase the relevance of results. We also observed that none of the included studies performed the required sample size calculation for each condition before conducting the experiments. It would be useful to report these data in future studies to better understand the study design. In addition, only two studies conducted a blinded assessment of outcomes. Blind assessment of the collected data reduces the risk of bias when interpreting the data. If

possible, this methodological parameter should be implemented in future preclinical studies to strengthen the level of evidence.

5 CONCLUSION

The present study emphasized that pullulan and/or dextran-based materials display unique properties for BTE applications. Moreover, this review is expected to provide clear information on the chemical functionalization of the pullulan-based and dextran-based materials and the cross-linking strategies for BTE applications. Interestingly, these polysaccharides are used as injectable hydrogels or microbeads that easily fit the bone defect. Incorporation of mineral contents such as hydroxyapatite to the pullulan and/or dextran-based biomaterials significantly enhance bone regeneration. We also outlined that the association of pullulan and dextran is a solution to obtain a biomaterial, deprived of growth factors or living cells to promote bone formation. Studies comparing these biomaterials with commercialized and clinically used products are too limited and further studies are required to draw more conclusions.

AUTHOR CONTRIBUTIONS

MF and J-CF contributed to conception and design of the study. Online screening of the included studied and extraction of the data were performed by two independent reviewers (MF and NA). NA wrote the first draft of the manuscript helped by MF. All authors contributed to manuscript revision, read, and approved the submitted version.

FUNDING

The authors declare that this study received funding from SILTISS. The funder had the following involvement in the study: Partial funding of PhD of NAO, manuscript revision, reading, and approval of the submitted version.

ACKNOWLEDGMENTS

The authors would like to thank the ANR (Agence Nationale de la Recherche) for financial support. The authors also acknowledge Siltiss.

REFERENCES

Abbah, S.-A., Liu, J., Lam, R. W. M., Goh, J. C. H., and Wong, H.-K. (2012). *In Vivo* bioactivity of rhBMP-2 Delivered with Novel Polyelectrolyte Complexation Shells Assembled on an Alginate Microbead Core Template. *J. Control. Release* 162, 364–372. doi:10.1016/j.jconrel.2012.07.027

Akiyoshi, K., Kobayashi, S., Shichibe, S., Mix, D., Baudys, M., Wan Kim, S., et al. (1998). Self-assembled Hydrogel Nanoparticle of Cholesterol-Bearing Pullulan as a Carrier of Protein Drugs: Complexation and Stabilization of Insulin. *J. Control. Release* 54, 313–320. doi:10.1016/s0168-3659(98)00017-0

Ana, I. D., Satria, G. A. P., Dewi, A. H., and Ardhani, R. (2018). Bioceramics for Clinical Application in Regenerative Dentistry. *Adv. Exp. Med. Biol.* 1077, 309–316. doi:10.1007/978-981-13-0947-2_16

Banerjee, A., and Bandopadhyay, R. (2016). Use of Dextran Nanoparticle: A Paradigm Shift in Bacterial Exopolysaccharide Based Biomedical Applications. *Int. J. Biol. Macromol.* 87, 295–301. doi:10.1016/j.ijbiomac.2016.02.059

Barritault, D., Gilbert-Sirieix, M., Rice, K. L., Siñeriz, F., Papy-Garcia, D., Baudouin, C., et al. (2017). RGTA or ReGeneraTing Agents Mimic Heparan Sulfate in Regenerative Medicine: from Concept to Curing Patients. *Glycoconj. J.* 34, 325–338. doi:10.1007/s10719-016-9744-5

Bölgen, N., Korkusuz, P., Vargel, İ., Kılıç, E., Güzel, E., Çavuşoğlu, T., et al. (2014). Stem Cell Suspension Injected HEMA-Lactate-Dextran Cryogels for Regeneration of Critical Sized Bone Defects. *Artif. Cells, Nanomedicine, Biotechnol.* 42, 70–77. doi:10.3109/21691401.2013.775578

Charoenlarp, P., Rajendran, A. K., Fujihara, R., Kojima, T., Nakahama, K.-i., Sasaki, Y., et al. (2018). The Improvement of Calvarial Bone Healing by Durable Nanogel-Crosslinked Materials. *J. Biomaterials Sci. Polym. Ed.* 29, 1876–1894. doi:10.1080/09205063.2018.1517403

Chen, F.-m., Zhao, Y.-m., Wu, H., Deng, Z.-h., Wang, Q.-t., Zhou, W., et al. (2006). Enhancement of Periodontal Tissue Regeneration by Locally Controlled Delivery of Insulin-like Growth Factor-I from Dextran-Co-Gelatin Microspheres. *J. Control. Release* 114, 209–222. doi:10.1016/j.jconrel.2006.05.014

Chen, F.-M., Zhao, Y.-M., Zhang, R., Jin, T., Sun, H.-H., Wu, Z.-F., et al. (2007). Periodontal Regeneration Using Novel Glycidyl Methacrylated Dextran (Dex-GMA)/gelatin Scaffolds Containing Microspheres Loaded with Bone Morphogenetic Proteins. *J. Control. Release* 121, 81–90. doi:10.1016/j.jconrel.2007.05.023

Chen, F., Wu, Z., Wang, Q., Wu, H., Zhang, Y., Nie, X., et al. (2005). Preparation and Biological Characteristics of Recombinant Human Bone Morphogenetic Protein-2-Loaded Dextran-Co-Gelatin Hydrogel Microspheres, *In Vitro* and *In Vivo* Studies. *Pharmacology* 75, 133–144. doi:10.1159/000088212

Chen, H., Yu, Y., Wang, C., Wang, J., and Liu, C. (2019). The Regulatory Role of Sulfated Polysaccharides in Facilitating rhBMP-2-Induced Osteogenesis. *Biomater. Sci.* 7, 4375–4387. doi:10.1039/c9bm00529c

Degat, M.-C., Dubreucq, G., Meunier, A., Dahri-Correia, L., Sedel, L., Petite, H., et al. (2009). Enhancement of the Biological Activity of BMP-2 by Synthetic Dextran Derivatives. *J. Biomed. Mat. Res.* 88A, 174–183. doi:10.1002/jbm.a.31884

Dimitriou, R., Jones, E., McGonagle, D., and Giannoudis, P. V. (2011). Bone Regeneration: Current Concepts and Future Directions. *BMC Med.* 9, 66. doi:10.1186/1741-7015-9-66

Ding, X., Li, X., Li, C., Qi, M., Zhang, Z., Sun, X., et al. (2019). Chitosan/Dextran Hydrogel Constructs Containing Strontium-Doped Hydroxyapatite with Enhanced Osteogenic Potential in Rat Cranium. *ACS Biomater. Sci. Eng.* 5, 4574–4586. doi:10.1021/acsbiomaterials.9b00584

El-Sherbiny, I. M., and Yacoub, M. H. (2013). Hydrogel Scaffolds for Tissue Engineering: Progress and Challenges. *Glob. Cardiol. Sci. Pract.* 2013, 38–342. doi:10.5339/gcsp.2013.38

Fang, J., Li, P., Lu, X., Fang, L., Lü, X., and Ren, F. (2019). A Strong, Tough, and Osteoconductive Hydroxyapatite Mineralized Polyacrylamide/dextran Hydrogel for Bone Tissue Regeneration. *Acta Biomater.* 88, 503–513. doi:10.1016/j.actbio.2019.02.019

Filippi, M., Born, G., Chaaban, M., and Scherberich, A. (2020). Natural Polymeric Scaffolds in Bone Regeneration. *Front. Bioeng. Biotechnol.* 8, 474. doi:10.3389/fbioe.2020.00474

Frasca, S., Norol, F., Le Visage, C., Collombet, J.-M., Letourneur, D., Holy, X., et al. (2017). Calcium-phosphate Ceramics and Polysaccharide-Based Hydrogel Scaffolds Combined with Mesenchymal Stem Cell Differently Support Bone Repair in Rats. *J. Mater Sci. Mater Med.* 28, 35. doi:10.1007/s10856-016-5839-6

Fricain, J. C., Aid, R., Lanouar, S., Maurel, D. B., Le Nihouannen, D., Delmond, S., et al. (2018). In-vitro and Iin-Vvivo Design and Validation of an Injectable Polysaccharide-Hydroxyapatite Composite Material for Sinus Floor Augmentation. *Dent. Mater.* 34, 1024–1035. doi:10.1016/j.dental.2018.03.021

Fricain, J. C., Schlaubitz, S., Le Visage, C., Arnault, I., Derkaoui, S. M., Siadous, R., et al. (2013). A Nano-Hydroxyapatite - Pullulan/dextran Polysaccharide Composite Macroporous Material for Bone Tissue Engineering. *Biomaterials* 34, 2947–2959. doi:10.1016/j.biomaterials.2013.01.049

Fujioka-Kobayashi, M., Ota, M. S., Shimoda, A., Nakahama, K.-i., Akiyoshi, K., Miyamoto, Y., et al. (2012). Cholesteryl Group- and Acryloyl Group-Bearing Pullulan Nanogel to Deliver BMP2 and FGF18 for Bone Tissue Engineering. *Biomaterials* 33, 7613–7620. doi:10.1016/j.biomaterials.2012.06.075

Fundueanu, G., Constantin, M., Mihai, D., Bortolotti, F., Cortesi, R., Ascenzi, P., et al. (2003). Pullulan-cyclodextrin Microspheres. *J. Chromatogr. B* 791, 407–419. doi:10.1016/s1570-0232(03)00258-7

Giannoudis, P. V., Einhorn, T. A., and Marsh, D. (2007). Fracture Healing: the Diamond Concept. *Injury* 38 (Suppl. 4), S3–S6. doi:10.1016/s0020-1383(08)70003-2

Gliko-Kabir, I., Yagen, B., Penhasi, A., and Rubinstein, A. (2000). Phosphated Crosslinked Guar for Colon-specific Drug Delivery. *J. Control. Release* 63, 121–127. doi:10.1016/S0168-3659(99)00179-0

Gosain, A. K., Song, L., Yu, P., Mehrara, B. J., Maeda, C. Y., Gold, L. I., et al. (2000). Osteogenesis in Cranial Defects: Reassessment of the Concept of Critical Size and the Expression of TGF-β Isoforms. *Plastic Reconstr. Surg.* 106, 360–371. doi:10.1097/00006534-200008000-00018

Hayashi, C., Hasegawa, U., Saita, Y., Hemmi, H., Hayata, T., Nakashima, K., et al. (2009). Osteoblastic Bone Formation Is Induced by Using Nanogel-Crosslinking Hydrogel as Novel Scaffold for Bone Growth Factor. *J. Cell. Physiol.* 220, 1–7. doi:10.1002/jcp.21760

Hettiaratchi, M. H., Krishnan, L., Rouse, T., Chou, C., McDevitt, T. C., and Guldberg, R. E. (2020). Heparin-mediated Delivery of Bone Morphogenetic Protein-2 Improves Spatial Localization of Bone Regeneration. *Sci. Adv.* 6, eaay1240. doi:10.1126/sciadv.aay1240

Hooijmans, C. R., Rovers, M. M., de Vries, R. B., Leenaars, M., Ritskes-Hoitinga, M., and Langendam, M. W. (2014). SYRCLE's Risk of Bias Tool for Animal Studies. *BMC Med. Res. Methodol.* 14, 43. doi:10.1186/1471-2288-14-43

Hovgaard, L., and Brøndsted, H. (1995). Dextran Hydrogels for Colon-specific Drug Delivery. *J. Control. Release* 36, 159–166. doi:10.1016/0168-3659(95)00049-E

Hussain, A., Zia, K. M., Tabasum, S., Noreen, A., Ali, M., Iqbal, R., et al. (2017). Blends and Composites of Exopolysaccharides; Properties and Applications: A Review. *Int. J. Biol. Macromol.* 94, 10–27. doi:10.1016/j.ijbiomac.2016.09.104

Kashirina, A., Yao, Y., Liu, Y., and Leng, J. (2019). Biopolymers as Bone Substitutes: a Review. *Biomater. Sci.* 7, 3961–3983. doi:10.1039/c9bm00664h

Kato, N., Hasegawa, U., Morimoto, N., Saita, Y., Nakashima, K., Ezura, Y., et al. (2007). Nanogel-based Delivery System Enhances PGE2 Effects on Bone Formation. *J. Cell. Biochem.* 101, 1063–1070. doi:10.1002/jcb.21160

Keller, J., Brink, S., Busse, B., Schilling, A. F., Schinke, T., Amling, M., et al. (2012). Divergent Resorbability and Effects on Osteoclast Formation of Commonly Used Bone Substitutes in a Human In Vitro-assay. *PloS One* 7, e46757. doi:10.1371/journal.pone.0046757

Krishnakumar, G. S., Sampath, S., Muthusamy, S., and John, M. A. (2019). Importance of Crosslinking Strategies in Designing Smart Biomaterials for Bone Tissue Engineering: A Systematic Review. *Mater. Sci. Eng. C* 96, 941–954. doi:10.1016/j.msec.2018.11.081

Kumari, L., and Badwaik, H. R. (2019). "Polysaccharide-based Nanogels for Drug and Gene Delivery," in *Polysaccharide Carriers for Drug Delivery*. Editors S. Maiti and S. Jana (Sawston, United Kingdom: Woodhead Publishing), 497–557. doi:10.1016/B978-0-08-102553-6.00018-0

Lack, S., Dulong, V., Picton, L., Cerf, D. L., and Condamine, E. (2007). High-resolution Nuclear Magnetic Resonance Spectroscopy Studies of Polysaccharides Crosslinked by Sodium Trimetaphosphate: a Proposal for the Reaction Mechanism. *Carbohydr. Res.* 342, 943–953. doi:10.1016/j.carres.2007.01.011

Lafont, J., Blanquaert, F., Colombier, M. L., Barritault, D., Carueelle, J.-P., and Saffar, J.-L. (2004). Kinetic Study of Early Regenerative Effects of RGTA11, a Heparan Sulfate Mimetic, in Rat Craniotomy Defects. *Calcif. Tissue Int.* 75, 517–525. doi:10.1007/s00223-004-0012-5

Lalande, C., Miraux, S., Miraux, S., Derkaoui, S., Mornet, S., Bareille, R., et al. (2011). Magnetic Resonance Imaging Tracking of Human Adipose Derived Stromal Cells within Three-Dimensional Scaffolds for Bone Tissue Engineering. *eCM* 21, 341–354. doi:10.22203/ecm.v021a25

Li, X., Yang, Z., Fang, L., Ma, C., Zhao, Y., Liu, H., et al. (2021). Hydrogel Composites with Different Dimensional Nanoparticles for Bone Regeneration. *Macromol. Rapid Commun.* 42, 2100362. doi:10.1002/marc.202100362

Liang, W., Wu, X., Dong, Y., Shao, R., Chen, X., Zhou, P., et al. (2021). *In Vivo* behavior of Bioactive Glass-Based Composites in Animal Models for Bone Regeneration. *Biomater. Sci.* 9, 1924–1944. doi:10.1039/d0bm01663b

Macleod, M. R., O'Collins, T., Howells, D. W., and Donnan, G. A. (2004). Pooling of Animal Experimental Data Reveals Influence of Study Design and Publication Bias. *Stroke* 35, 1203–1208. doi:10.1161/01.STR.0000125719.25853.20

Maire, M., Chaubet, F., Mary, P., Blanchat, C., Meunier, A., and Logeartavramoglou, D. (2005a). Bovine BMP Osteoinductive Potential Enhanced by Functionalized Dextran-Derived Hydrogels. *Biomaterials* 26, 5085–5092. doi:10.1016/j.biomaterials.2005.01.020

Maire, M., Logeart-Avramoglou, D., Degat, M.-C., and Chaubet, F. (2005b). Retention of Transforming Growth Factor β1 Using Functionalized Dextran-Based Hydrogels. *Biomaterials* 26, 1771–1780. doi:10.1016/j.biomaterials.2004.06.003

Maisani, M., Sindhu, K. R., Fenelon, M., Siadous, R., Rey, S., Mantovani, D., et al. (2018). Prolonged Delivery of BMP-2 by a Non-polymer Hydrogel for Bone Defect Regeneration. *Drug Deliv. Transl. Res.* 8, 178–190. doi:10.1007/s13346-017-0451-y

Mallick, K. K., and Cox, S. C. (2013). Biomaterial Scaffolds for Tissue Engineering. *Front. Biosci.* 5, 341–360. doi:10.2741/e620

Maurel, D. B., Fénelon, M., Aid-Launais, R., Bidault, L., Le Nir, A., Renard, M., et al. (2021). Bone Regeneration in Both Small and Large Preclinical Bone Defect Models Using an Injectable Polymer-based Substitute Containing Hydroxyapatite and Reconstituted with Saline or Autologous Blood. *J. Biomed. Mater Res.* 109, 1840–1848. doi:10.1002/jbm.a.37176

McGovern, J. A., Griffin, M., and Hutmacher, D. W. (2018). Animal Models for Bone Tissue Engineering and Modelling Disease. *Dis. Model. Mech.* 11, dmm033084. doi:10.1242/dmm.033084

Miyahara, T., Nyan, M., Shimoda, A., Yamamoto, Y., Kuroda, S., Shiota, M., et al. (2012). Exploitation of a Novel Polysaccharide Nanogel Cross-Linking Membrane for Guided Bone Regeneration (GBR). *J. Tissue Eng. Regen. Med.* 6, 666–672. doi:10.1002/term.475

Moher, D., Shamseer, L., Shamseer, L., Clarke, M., Ghersi, D., Liberati, A., et al. (2015). Preferred Reporting Items for Systematic Review and Meta-Analysis Protocols (PRISMA-P) 2015 Statement. *Syst. Rev.* 4, 1. doi:10.1186/2046-4053-4-1

Morimoto, N., Endo, T., Iwasaki, Y., and Akiyoshi, K. (2005a). Design of Hybrid Hydrogels with Self-Assembled Nanogels as Cross-Linkers: Interaction with Proteins and Chaperone-like Activity. *Biomacromolecules* 6, 1829–1834. doi:10.1021/bm050156x

Morimoto, N., Endo, T., Ohtomi, M., Iwasaki, Y., and Akiyoshi, K. (2005b). Hybrid Nanogels with Physical and Chemical Cross-Linking Structures as Nanocarriers. *Macromol. Biosci.* 5, 710–716. doi:10.1002/mabi.200500051

Oryan, A., Kamali, A., Moshiri, A., Baharvand, H., and Daemi, H. (2018). Chemical Crosslinking of Biopolymeric Scaffolds: Current Knowledge and Future Directions of Crosslinked Engineered Bone Scaffolds. *Int. J. Biol. Macromol.* 107, 678–688. doi:10.1016/j.ijbiomac.2017.08.184

Popescu, R. A., Tăbăran, F. A., Bogdan, S., Fărcă□anu, A., Purdoiu, R., Magyari, K., et al. (2020). Bone Regeneration Response in an Experimental Long Bone Defect Orthotopically Implanted with Alginate-pullulan-glass-ceramic Composite Scaffolds. *J. Biomed. Mater Res.* 108, 1129–1140. doi:10.1002/jbm.b.34464

Prajapati, V. D., Jani, G. K., and Khanda, S. M. (2013). Pullulan: an Exopolysaccharide and its Various Applications. *Carbohydr. Polym.* 95, 540–549. doi:10.1016/j.carbpol.2013.02.082

R. Lanza, R. Langer, and J. Vacanti (Editors) (2014). *Principles of Tissue Engineering*. 4th ed. (Elsevier). doi:10.1016/C2011-0-07193-4

Rao, S. H., Harini, B., Shadamarshan, R. P. K., Balagangadharan, K., and Selvamurugan, N. (2018). Natural and Synthetic Polymers/bioceramics/bioactive Compounds-Mediated Cell Signalling in Bone Tissue Engineering. *Int. J. Biol. Macromol.* 110, 88–96. doi:10.1016/j.ijbiomac.2017.09.029

Ribot, E. J., Tournier, C., Aid-Launais, R., Koonjoo, N., Oliveira, H., Trotier, A. J., et al. (2017). 3D Anatomical and Perfusion MRI for Longitudinal Evaluation of Biomaterials for Bone Regeneration of Femoral Bone Defect in Rats. *Sci. Rep.* 7, 6100. doi:10.1038/s41598-017-06258-0

Ritz, U., Eberhardt, M., Klein, A., Frank, P., Götz, H., Hofmann, A., et al. (2018). Photocrosslinked Dextran-Based Hydrogels as Carrier System for the Cells and Cytokines Induce Bone Regeneration in Critical Size Defects in Mice. *Gels* 4, 63. doi:10.3390/gels4030063

Roseti, L., Parisi, V., Petretta, M., Cavallo, C., Desando, G., Bartolotti, I., et al. (2017). Scaffolds for Bone Tissue Engineering: State of the Art and New Perspectives. *Mater. Sci. Eng. C* 78, 1246–1262. doi:10.1016/j.msec.2017.05.017

Schlaubitz, S., Derkaoui, S. M., Marosa, L., Miraux, S., Renard, M., Catros, S., et al. (2014). Pullulan/dextran/nHA Macroporous Composite Beads for Bone Repair in a Femoral Condyle Defect in Rats. *PloS One* 9, e110251. doi:10.1371/journal.pone.0110251

Schmitz, J. P., and Hollinger, J. O. (1986). The Critical Size Defect as an Experimental Model for Craniomandibulofacial Nonunions. *Clin. Orthop. Relat. Res.* 205, 299–308. doi:10.1097/00003086-198604000-00036

Shoji, S., Uchida, K., Saito, W., Sekiguchi, H., Inoue, G., Miyagi, M., et al. (2020). Acceleration of Bone Healing by In Situ-Forming Dextran-Tyramine Conjugates Containing Basic Fibroblast Growth Factor in Mice. *Cureus* 12, e10085. doi:10.7759/cureus.10085

Simonsen, L., Hovgaard, L., Mortensen, P. B., and Brøndsted, H. (1995). Dextran Hydrogels for Colon-specific Drug Delivery. V. Degradation in Human Intestinal Incubation Models. *Eur. J. Pharm. Sci.* 3, 329–337. doi:10.1016/0928-0987(95)00023-6

Spicer, P. P., Kretlow, J. D., Young, S., Jansen, J. A., Kasper, F. K., and Mikos, A. G. (2012). Evaluation of Bone Regeneration Using the Rat Critical Size Calvarial Defect. *Nat. Protoc.* 7, 1918–1929. doi:10.1038/nprot.2012.113

Sun, G., Zhang, X., Shen, Y.-I., Sebastian, R., Dickinson, L. E., Fox-Talbot, K., et al. (2011). Dextran Hydrogel Scaffolds Enhance Angiogenic Responses and Promote Complete Skin Regeneration during Burn Wound Healing. *Proc. Natl. Acad. Sci. U.S.A.* 108, 20976–20981. doi:10.1073/pnas.1115973108

Taguchi, T., and Lopez, M. J. (2021). An Overview of De Novo Bone Generation in Animal Models. *J. Orthop. Res.* 39, 7–21. doi:10.1002/jor.24852

Takahata, T., Okihara, T., Yoshida, Y., Yoshihara, K., Shiozaki, Y., Yoshida, A., et al. (2015). Bone Engineering by Phosphorylated-Pullulan and β -TCP Composite. *Biomed. Mat.* 10, 065009. doi:10.1088/1748-6041/10/6/065009

Tang, G., Liu, Z., Liu, Y., Yu, J., Wang, X., Tan, Z., et al. (2021). Recent Trends in the Development of Bone Regenerative Biomaterials. *Front. Cell Dev. Biol.* 9, 665813. doi:10.3389/fcell.2021.665813

Tassa, C., Shaw, S. Y., and Weissleder, R. (2011). Dextran-coated Iron Oxide Nanoparticles: a Versatile Platform for Targeted Molecular Imaging, Molecular Diagnostics, and Therapy. *Acc. Chem. Res.* 44, 842–852. doi:10.1021/ar200084x

Togami, W., Sei, A., Okada, T., Taniwaki, T., Fujimoto, T., Tahata, S., et al. (2015). Effects of the Water-Holding Capability of Polyvinyl Formal Sponges on Osteogenic Ability Inin Vivoexperiments. *J. Biomed. Mat. Res.* 103, 188–194. doi:10.1002/jbm.b.33200

Vantucci, C. E., Krishan, L., Cheng, A., Prather, A., Roy, K., and Guldberg, R. E. (2021). BMP-2 Delivery Strategy Modulates Local Bone Regeneration and Systemic Immune Responses to Complex Extremity Trauma. *Biomater. Sci.* 9, 1668–1682. doi:10.1039/d0bm01728k

Wang, B., Liu, J., Niu, D., Wu, N., Yun, W., Wang, W., et al. (2021). Mussel-Inspired Bisphosphonated Injectable Nanocomposite Hydrogels with Adhesive, Self-Healing, and Osteogenic Properties for Bone Regeneration. *ACS Appl. Mat. Interfaces* 13, 32673–32689. doi:10.1021/acsami.1c06058

Wu, D. T., Munguia-Lopez, J. G., Cho, Y. W., Ma, X., Song, V., Zhu, Z., et al. (2021). Polymeric Scaffolds for Dental, Oral, and Craniofacial Regenerative Medicine. *Molecules* 26, 7043. doi:10.3390/molecules26227043

Yu, Y., Chen, R., Yuan, Y., Wang, J., and Liu, C. (2020). Affinity-selected Polysaccharide for rhBMP-2-Induced Osteogenesis via BMP Receptor Activation. *Appl. Mater. Today* 20, 100681. doi:10.1016/j.apmt.2020.100681

Yunus Basha, R., T.S., S. K., and Doble, M. (2015). Design of Biocomposite Materials for Bone Tissue Regeneration. *Mater. Sci. Eng. C* 57, 452–463. doi:10.1016/j.msec.2015.07.016

Conflict of Interest: Author DL was employed by company SILTISS.

The remaining authors declare that the research was conducted in the absence of any commercial or financial relationships that could be construed as a potential conflict of interest.

Publisher's Note: All claims expressed in this article are solely those of the authors and do not necessarily represent those of their affiliated organizations, or those of the publisher, the editors and the reviewers. Any product that may be evaluated in this article, or claim that may be made by its manufacturer, is not guaranteed or endorsed by the publisher.

frontiers | Frontiers in Bioengineering and Biotechnology

TYPE Original Research
PUBLISHED 10 August 2022
DOI 10.3389/fbioe.2022.937595

OPEN ACCESS

EDITED BY
Lifeng Kang,
The University of Sydney, Australia

REVIEWED BY
Jane Wang,
National Tsing Hua University, Taiwan
Bong Geun Chung,
Sogang University, South Korea
Sun Min Kim,
Inha University, South Korea

*CORRESPONDENCE
Pu Chen,
puchen@whu.edu.cn

†These authors have contributed equally to this work

SPECIALTY SECTION
This article was submitted to Biomaterials, a section of the journal Frontiers in Bioengineering and Biotechnology

RECEIVED 06 May 2022
ACCEPTED 05 July 2022
PUBLISHED 10 August 2022

CITATION
Xu X, Jiang S, Gu L, Li B, Xu F, Li C and Chen P (2022), High-throughput bioengineering of homogenous and functional human-induced pluripotent stem cells-derived liver organoids via micropatterning technique. *Front. Bioeng. Biotechnol.* 10:937595. doi: 10.3389/fbioe.2022.937595

High-throughput bioengineering of homogenous and functional human-induced pluripotent stem cells-derived liver organoids *via* micropatterning technique

Xiaodong Xu[1,2†], Shanqing Jiang[1†], Longjun Gu[1], Bin Li[1], Fang Xu[1], Changyong Li[1] and Pu Chen[1,2,3*]

[1]Tissue Engineering and Organ Manufacturing (TEOM) Lab, Department of Biomedical Engineering, Wuhan University TaiKang Medical School (School of Basic Medical Sciences), Wuhan, China, [2]Hubei Province Key Laboratory of Allergy and Immunology, Wuhan University TaiKang Medical School (School of Basic Medical Sciences), Wuhan, China, [3]Institute of Hepatobiliary Diseases of Wuhan University, Hubei Engineering Center of Natural Polymers-based Medical Materials, Zhongnan Hospital of Wuhan University, Wuhan, China

Human pluripotent stem cell-derived liver organoids are emerging as more human-relevant *in vitro* models for studying liver diseases and hepatotoxicity than traditional hepatocyte cultures and animal models. The generation of liver organoids is based on the Matrigel dome method. However, the organoids constructed by this method display significant heterogeneity in their morphology, size, and maturity. Additionally, the formed organoid is randomly encapsulated in the Matrigel dome, which is not convenient for *in situ* staining and imaging. Here, we demonstrate an approach to generate a novel type of liver organoids via micropatterning technique. This approach enables the reproducible and high-throughput formation of bioengineered fetal liver organoids with uniform morphology and deterministic size and location in a multiwell plate. The liver organoids constructed by this technique closely recapitulate some critical features of human liver development at the fetal stage, including fetal liver-specific gene and protein expression, glycogen storage, lipid accumulation, and protein secretion. Additionally, the organoids allow whole-mount *in-situ* staining and imaging. Overall, this new type of liver organoids is compatible with the pharmaceutical industry's widely-used preclinical drug discovery tools and will facilitate liver drug screening and hepatotoxic assessment.

KEYWORDS

liver organoids, human induced pluripotent stem cells, micropatterning technique, homogeneity, hepatotoxicity

1 Introduction

As an essential metabolic organ of the human body, the liver performs a variety of fundamental physiological functions, including detoxification, digestion, and metabolism. Liver dysfunction may arise in many hepatic diseases and can also be caused by various factors such as viruses, alcohol use, and drug-induced liver injury (DILI). Among these factors, DILI is a major cause of acute liver failure (ALF) and one of the leading indications for liver transplantation (Chalasani et al., 2015; Xu et al., 2022). It's reported that the annual incidence of DILI in the general population ranges between 13 and 24 cases per 100,000 inhabitants (Sgro et al., 2002; Bjornsson et al., 2013; Shen et al., 2019; Kamath et al., 2021). DILI is a rare potential complication in pregnant women, but it can adversely affect both the mother and the fetus. Clinical trials seldomly study drug's hepatoxic effects in pregnant women due to ethical and safety concerns unless the drug is specifically used in pregnant women (Kamath et al., 2021). It is therefore essential to establish a research model relevant to human fetal livers in order to study the drug's hepatotoxicity in fetuses.

Pluripotent stem cell (PSC) derived human liver organoids (HLOs) are emerging humanized liver models and are have been increasingly used in mechanistic studies of liver diseases and evaluation of drug's hepatotoxicity. Compared with the two-dimensional (2D) hepatic cell culture model, PSC-derived HLOs can reconstitute three-dimensional (3D) intercellular and heterocellular communications as well as cell-extracellular matrix interactions in the native liver microenvironment and thus better emulate liver physiological functions and tissue homeostasis (Ouchi et al., 2019). Moreover, unlike liver tissue-derived HLOs that are specified to the endoderm fate and only contain hepatic parenchymal cells, PSC-derived HLOs can contain both parenchymal and nonparenchymal cells of liver tissue (Goulart et al., 2019; Velazquez et al., 2021). Furthermore, PSC-derived HLOs are humanized and have the developmental trajectory and metabolic characteristics more relevant to human liver than animal models.

At present, the Matrigel dome method is a gold standard for generating PSC-derived HLOs. Specifically, PSCs or PSC-derived stem cells are encapsulated in the Matrigel dome and experience multistage differentiation and culture, and ultimately form hundreds of heterogeneous liver organoids in the Matrigel dome (Ouchi et al., 2019; Shinozawa et al., 2021). However, the initial cell encapsulation process is highly randomized. A complex cell microenvironment, especially nonuniform inter-organoid communications, leads to great heterogeneity in organoid formation within or between individual domes, manifested explicitly in morphology, size, and maturity. Moreover, randomly distributed organoids in the dome are not convenient with whole-mount *in-situ* imaging and long-term the same single organoid monitoring. These issues seriously hamper PSC-derived HLOs' wide application in liver diseases and hepatotoxicity.

In this study, we demonstrate a simple and reliable method to generate deterministic liver organoids from human-induced pluripotent stem cells (hiPSCs). We employed the hiPSC micropatterning technique to define adhesion regions of hiPSCs and therefore determine the location, arrangement, and size of individual organoids at the bottom of a standard multiwell plate. To generate hiPSC-derived HLOs on the micropatterned cell-adhesion substrate (MPCS), we initially differentiated hiPSCs into foregut stem cells (FSCs). We then seeded FSCs on the MPCS for subsequent liver differentiation. During the differentiation, morphogenesis and functional maturation of individual organoids are regulated due to the constrained physical boundary of organoid growth and deterministic inter-organoid locations. Therefore, micropatterned HLOs (mpHLOs) were homogeneous in size, morphology, and maturity. Furthermore, we characterized the mpHLOs by liver-specific biomarkers and functional assays. Finally, we used the mpHLOs as a human-relevant fetus liver model to study the fetal hepatotoxicity of drugs.

2 Materials and methods

2.1 Fabrication of micropatterned cell-adhesion substrate

We fabricated MPCS for the organoid formation and culture (Figures 1A,B). Briefly, the MPCS was fabricated in a 24-well plate by oxygen plasma treatment of a perforated-PDMS-film-covered PEG surface. The perforated PDMS film was fabricated by clamping and solidifying PDMS prepolymer on a SU-8 positive mold (Figure 1A). The SU-8 positive mold was fabricated using the standard photolithography method with a SU-8 photoresist (Ma et al., 2015). Component A and component B of PDMS prepolymer were mixed with a ratio of 10:1 and degassed via a vacuum pump. The degassed PDMS prepolymer was pipetted onto a SU-8 positive mold and then covered by a 0.2 mm thick PMMA slide. Next, the PMMA-PDMS-SU-8 complex was sandwiched by two glass slides and a bench clamp. The PDMS prepolymer in the complex was cured in an 80°C oven for 2 hours. The plate was first treated with oxygen plasma at 550 W for 1 min and then covered with PEG prepolymer solution (Figure 1B). The PEG prepolymer solution in a 50-ml tube is comprised of 0.15 g of PEG 1000, 1.8 ml of PEG 400, 14.55 ml of Isopropyl alcohol (IPA), and 0.45 ml of Milli-Q water. The prepolymer solution was vortexed for at least 3 min for homogenization. A 40 mg of Irgacure 2,959 was then dissolved into the prepolymer

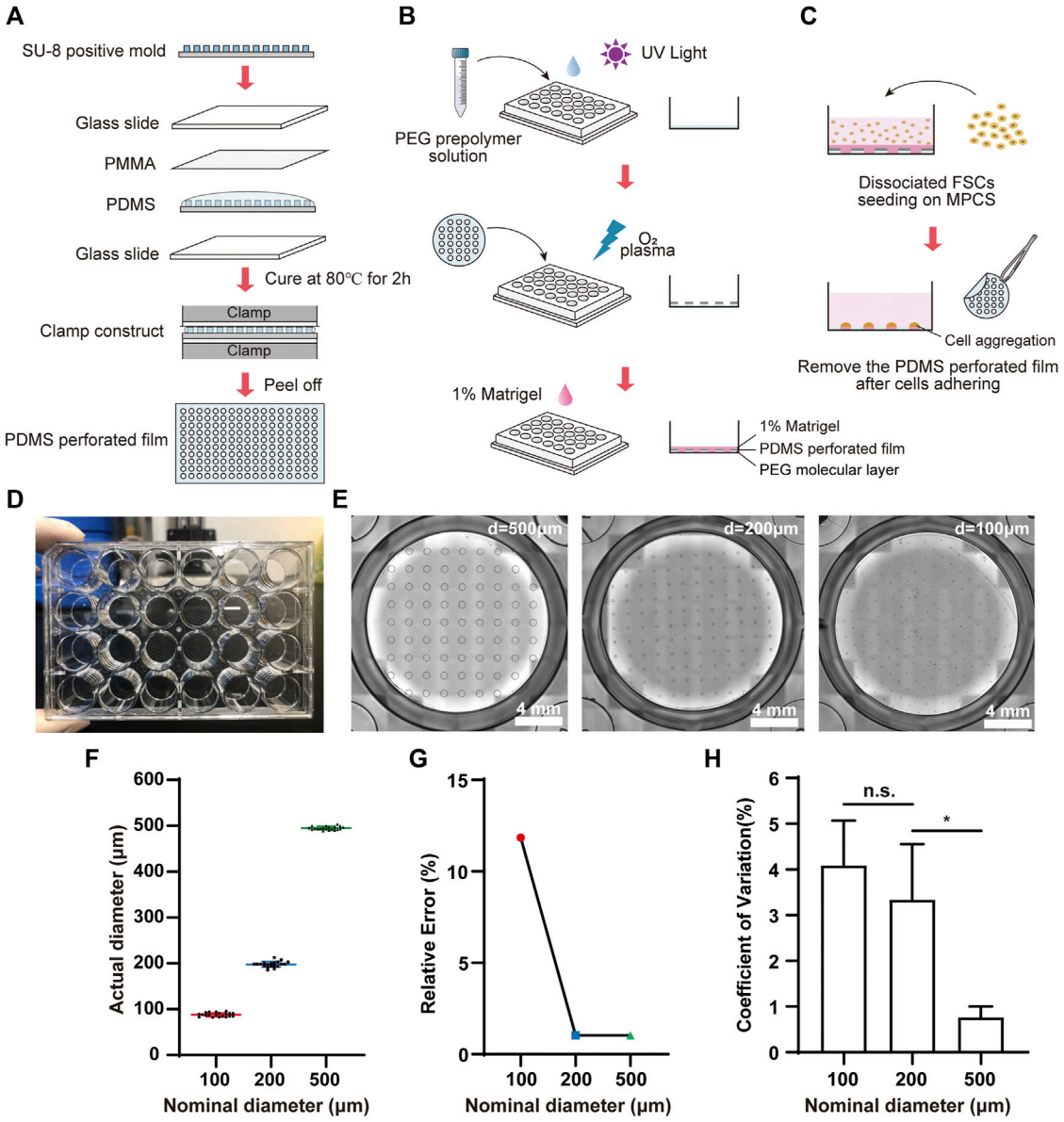

FIGURE 1
Fabrication and characterization of MPCS. Schematic diagram of **(A)** the fabrication process for perforated PDMS film, **(B)** PEG coating, and **(C)** cell seeding on the MPCS. **(D)** Photograph of MPCS. **(E)** Bright field images of MPCS with circular patterns of 500 μm, 200 μm, and 100 μm in diameter from left to right, respectively. **(F)** Scatter plot (mean ± SD, n = 20), **(G)** Relative error (n = 20), and **(H)** CVs of actual diameters of the perforated PDMS film (n = 6). Data are the mean ± SD and analyzed by One-way analysis of variance, *p < 0.05, **p < 0.01, ***p < 0.001, ****p < 0.0001.

solution. Then, the prepolymer solution was added to a 24-well plate and photo-crosslinked with ultraviolet exposure for 1 min using a photolithography machine. The plate was washed with 70% alcohol three times to remove the remaining PEG monomers (Hoang et al., 2018). The PEG-coated plate was covered by the tailored perforated PDMS film and placed at 80°C ovens for 10 min. Then the plate was treated three times with 4-min oxygen plasma at 700 W with an interval of 3 min to remove the PEG regions not covered by the PDMS film. Before cell seeding, the PEG-coated plate was sterilized by UV for 1 hour, washed with Dulbecco's phosphate-buffered saline (DPBS), and coated with 1% (v/v) Matrigel for 1 hour in an incubator. DPBS was obtained by ten-fold dilution of (10×DPBS) with Milli-Q water. All reagent information in this article is given in Supplementary Table S1.

2.2 Human-induced pluripotent stem cells maintenance culture

HiPSCs were maintained in Nuwacell™ ncTarget hPSC Medium (ncTarget), passaged via Accutase detachment, and reseeded in the Vitronectin (VTN)-coated 6-well plate containing ncTarget with 10 μM Y-27632.

2.3 Foregut induction

HiPSCs were differentiated into FSCs using a previously reported method with minor modifications (Thompson and Takebe, 2020). Briefly, hiPSCs were detached by Accutase and were seeded on VTN-coated tissue culture plates with 100,000 cells/cm^2. Differentiation was started when the cell confluence reached 85–90%. The medium was changed to RPMI 1640 medium containing 100 ng/ml Activin A and 50 ng/ml bone morphogenetic protein 4 (BMP4) on Day 1, 100 ng/ml Activin A and 0.2% Knockout serum replacement (KSR) on Day 2, and 100 ng/ml Activin A and 2% KSR on Day 3. On Day 4–6, the cells were cultured in Advanced DMEM/F12 with B27 and N2 containing 500 ng/ml fibroblast growth factor-2 (FGF2) and 3 μM CHIR99021. Cells were maintained at 37°C in 5% CO_2 with 95% air, and the culture medium was changed every day.

2.4 Micropatterning of human-induced pluripotent stem cells-derived foregut stem cells

On Day 6, FSCs were detached by Accutase for 3 min at 37°C, then suspended in Advanced DMEM/F12 with B27 and N2, containing 80 ng/ml FGF2, 3 μM CHIR99021, and 10 μM Y-27632. The FSCs were seeded on the MPCS with a seeding concentration of 3.2×10^5 cells/cm^2. At 4-h after seeding, the FSCs adhered to the substrate, and the PDMS film was then carefully removed from the substrate using a sharp tweezer, leaving the micropatterned FSC regions (Figure 1C). Then the FSCs were washed with DPBS gently. The medium was replaced by the same formula above without the addition of Y-27632. The cells were maintained at 37°C in 5% CO_2 with 95% air.

2.5 Generation of human liver organoids

On Day 6, the FSCs were seeded on the MPCS and cultured in Liver Organoid Formation Medium for 4 days. The medium was replaced every 2 days. On Day 10, the culture medium was switched to Liver Organoid Specification Medium and replaced every 2 days until Day 14. Then, the culture medium was switched to a Complete hepatocyte culture Medium and replaced every 2 days until Day 24. HLO induction and culture were maintained at 37°C in 5% CO_2 with 95% air.

2.6 RNA-seq and data analysis

On Day 24, mpHLOs were washed gently three times with DPBS. The total RNAs of mpHLOs were extracted following the Total RNA Extraction Reagent (Trizol) manually. The library and sequencing of transcriptome were prepared using Illumina HiSeq X Ten (Novogene Bioinformatics Technology Co., Ltd., Beijing, China). The mapping of 100-bp paired-end reads to genes was undertaken using HTSeq v0.6.0 software, while fragments per kilobase of transcript per million fragments mapped (FPKM) were also analyzed.

2.7 Real-time quantitative PCR

Total mRNAs were isolated from the cells and HLOs using the Trizol reagent. cDNAs were synthesized using ABScript III RT Master Mix. qPCR was performed using 2X Universal SYBR Green Fast qPCR Mix denaturation at 95°C for 1 min, annealing at 58°C for 30 s, and extension at 72°C for 30 s. All primers' information is described in Supplementary Table S1. The expression levels were normalized relative to the expression of the housekeeping gene GAPDH using the comparative Ct-method $2^{-\triangle\triangle Ct}$.

2.8 Immunochemistry and image analysis

For monolayer hiPSCs culture, the cells were fixed with 4% (w/v) paraformaldehyde for 15 min at room temperature (RT). Then the cells were blocked with 1% (w/v) bovine serum albumin (BSA) for 1 hour, incubated with primary antibodies overnight at 4°C, and washed three times with DPBS for 5 min. Then the cells were incubated with secondary antibodies for 2 hours at RT. After the reaction, the cells were washed three times with DPBS for 15 min.

For 2.5D organoid culture, the cells were fixed with 4% (w/v) paraformaldehyde overnight, permeabilized twice with 0.5% (v/v) Triton X-100 on a shaker for 20 min each time at a speed of 60 rpm, and blocked with 1% (w/v) BSA and 5% (v/v) Triton X-100 for 1 hour on a shaker at RT. Unless otherwise specified below, the rotation speed of the shaker was 60 rpm. Antibody diluent was prepared from DPBS, 1% (w/v) BSA and 0.1% (w/v) saponin. The samples were then incubated with primary antibodies for 24 h on a shaker at 4°C and washed three to four times with 0.5% (v/v) Triton X-100 for 20 min each time. Subsequently, secondary antibodies were incubated for at least 24 h on a shaker at 4°C. The samples were washed three times with 0.5% (v/v) Triton X-100 for 10–20 min each time. Finally,

cell nuclei were stained with 4,6-diamidino-2-phenylindole (DAPI), and the fluorescence images were taken using an Olympus inverted microscope. ImageJ software analyzes the average fluorescence intensity of the images.

Detailed antibody information and dilution ratio is described in Supplementary Table S1 in the supplementary information.

2.9 Periodic-acid-Schiff and nile red staining assays

On Day 24, liver organoids were fixed in 4% (w/v) paraformaldehyde at 4°C overnight. The fixed organoids were then washed with DPBS and transferred to a 15% (w/v) sucrose solution at 4°C overnight, then to a 30% (w/v) sucrose solution for dehydration. HLOs were frozen and sectioned into 10 μm-thick slices using a cryostat. These cryosections of the HLOs were stained using a Periodic-acid-Schiff (PAS) reagent kit to visualize glycogen synthesis. The cryosections were stained with a 500 nM Nile Red reagent to visualize intracellular lipid accumulation. The stained cryosections were washed twice with DPBS to remove excessive reagents. Image acquisition was conducted either with a bright-field microscope or a confocal epi-fluorescence microscope.

2.10 Elisa analysis of albumin and urea detection assays

On Days 10, 14, and 24, the culture media over the past 48 h were collected from individual wells and stored at −80°C for albumin and urea measurement. Albumin concentration in the medium was measured using the Human Albumin ELISA Kit. Urea concentration in the medium was determined using the QuantiChrom Urea Assay Kit.

2.11 Statistical analysis

All data were analyzed using GraphPad Prism version 8.0.2 for Windows. Data were presented as mean ± SD. Shapiro-Wilk test was used for normal distribution assay. For single comparisons, a Student's t-test was used. For multiple comparisons, one-way analysis of variance (ANOVA) was used with a Bonferroni post-test. Statistical significance of variables following skewed distribution was determined by Kruskal–Wallis test or Dunn's multiple comparison test. $^{****}p < 0.0001$, $^{***}p < 0.001$, $^{**}p < 0.01$, $^{*}p < 0.05$, n. s. = not significance ($p > 0.05$). The sample sizes were indicated in the Figure legends.

3 Results

3.1 Characterization of micropatterned cell-adhesion substrate

We fabricated the MPCS (Figures 1A–D) and then characterized the micropatterns using bright-field image analysis. The MPCS was fabricated with a size-varied circular micropattern (500 μm, 200 μm, and 100 μm in diameter) (Figure 1E). The image analysis indicated that the micropatterning technique enabled fabricating circular micropatterns with an actual diameter consistent with the nominal diameter (Figure 1F). Specifically, the micropatterning technique allowed less than 2% relative error for fabricating micropatterns larger than 200 μm (Figure 1G). Additionally, the fabricated micropatterns were highly repeatable, with a coefficient of variation (CV) of less than 5% in their sizes (Figure 1H).

3.2 Characterization of human-induced pluripotent stem cells-derived micropatterned HLOs

We generated mpHLOs via two-stage differentiation from hiPSCs (Figure 2A). Briefly, monolayer-cultured hiPSCs were first differentiated into FSCs using a previously reported method with minor modifications (Thompson and Takebe, 2020). On Day 6, FSCs formed, indicated by the spontaneous occurrence of stratification and cell aggregation (Figure 2B). FSCs were dissociated into single cells, then seeded on the MPCS for subsequent 18-day culture and differentiation. On Day 10, the micropatterned monolayer cells formed a dome-shaped multilayer cytoarchitecture. The cytoarchitecture became thick and opaque in the subsequent culture until Day 24 (Figures 2B,C).

The mpHLOs were compatible with the widely-used standard multiwell-plate culture system. A single well in the 24-well plate could accommodate a maximum 65 of 500 μm-sized HLOs with an inter-space of 1.5 mm (Figure 2D). Conversely, HLOs generated by the Matrigel dome method were randomly distributed in the Matrigel and showed significant heterogeneity in their size and morphology (Figure 2E). The bright-field image analysis indicated that the mpHLOs on Day 24 displayed a much lower area dispersion than the HLOs in the Matrigel dome method (Figure 2F). Specifically, the area CVs of mpHLOs are significantly lower than that of HLOs in Matrigel domes (Figure 2G).

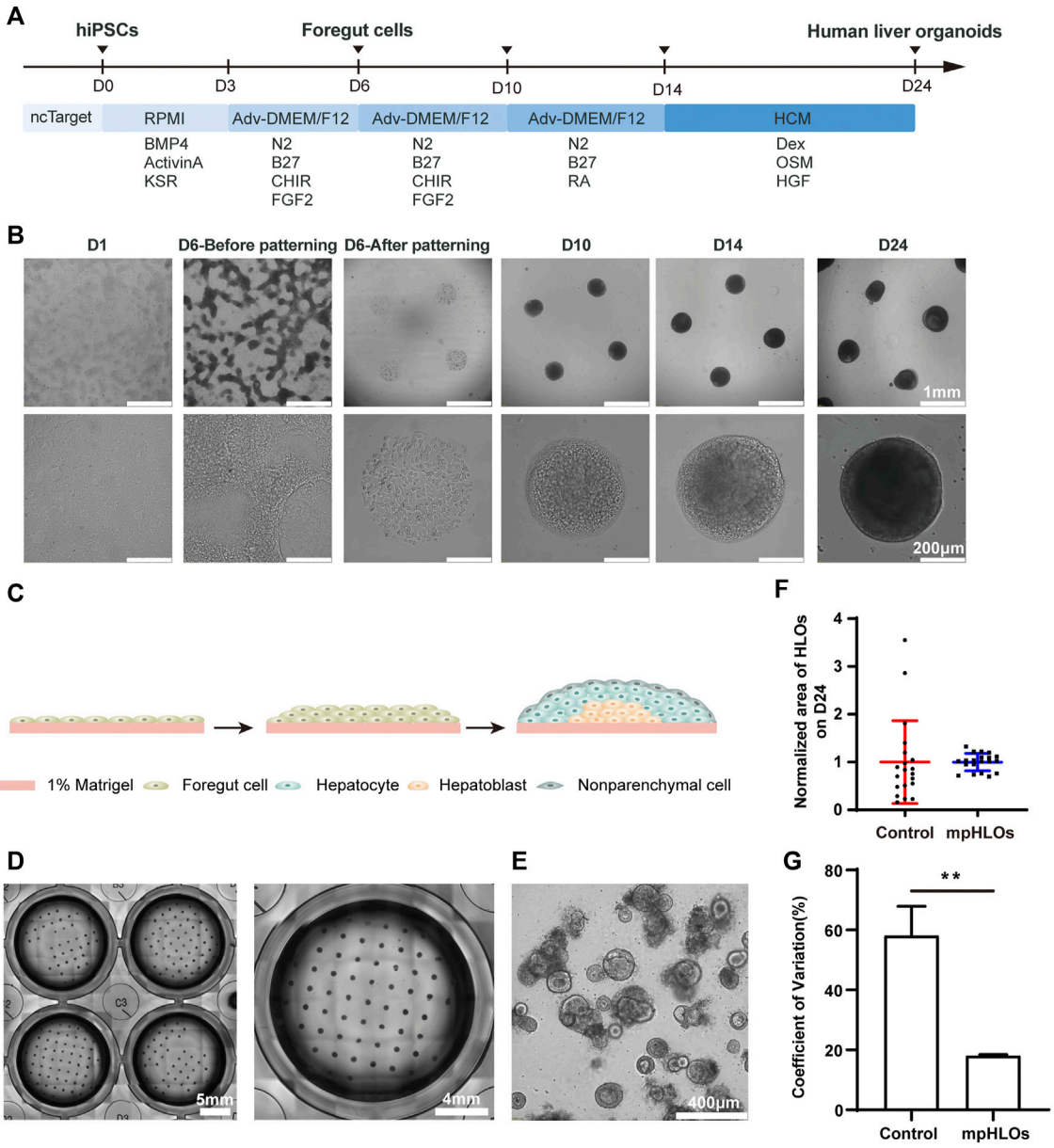

FIGURE 2
Characterization of hiPSC-derived mpHLOs. **(A)** Culture timeline diagram of mpHLOs. **(B)**Time-lapse images of generation of mpHLOs. mpHLOs are circular patterns with a diameter of 500 μm. **(C)** Schematic diagram of mpHLOs. **(D)** Bright-field images of mpHLOs in 24-well plate. **(E)** HLOs in Matrigel dome. **(F)** Normalized area of HLOs (n = 20). **(G)** CVs of HLOs (n = 6). Data are the mean ± SD and analyzed by Student's t test, *p < 0.05, **p < 0.01, ***p < 0.001, ****p < 0.0001.

3.3 Characterization of liver-specific gene and protein expressions

To further characterize the global gene expression profile of mpHLOs, we performed RNA sequencing of cells dissociated from mpHLOs on Day 24. Compared with the conventional Matrigel dome group, 29802 genes co-expressed in both the groups and 3,253 genes were uniquely expressed in the MPCS group (Figure 3A). We performed a differential gene expression (DGE) analysis of liver development and cell specification genes. The result indicated that mpHLOs showed higher expression of matured hepatocyte-specific genes and liver non-parenchymal cell-specific genes. The control group showed higher expression of biliary epithelial cell-specific genes and fetal hepatocyte-specific specific genes. Simultaneously, mpHLOs showed higher liver

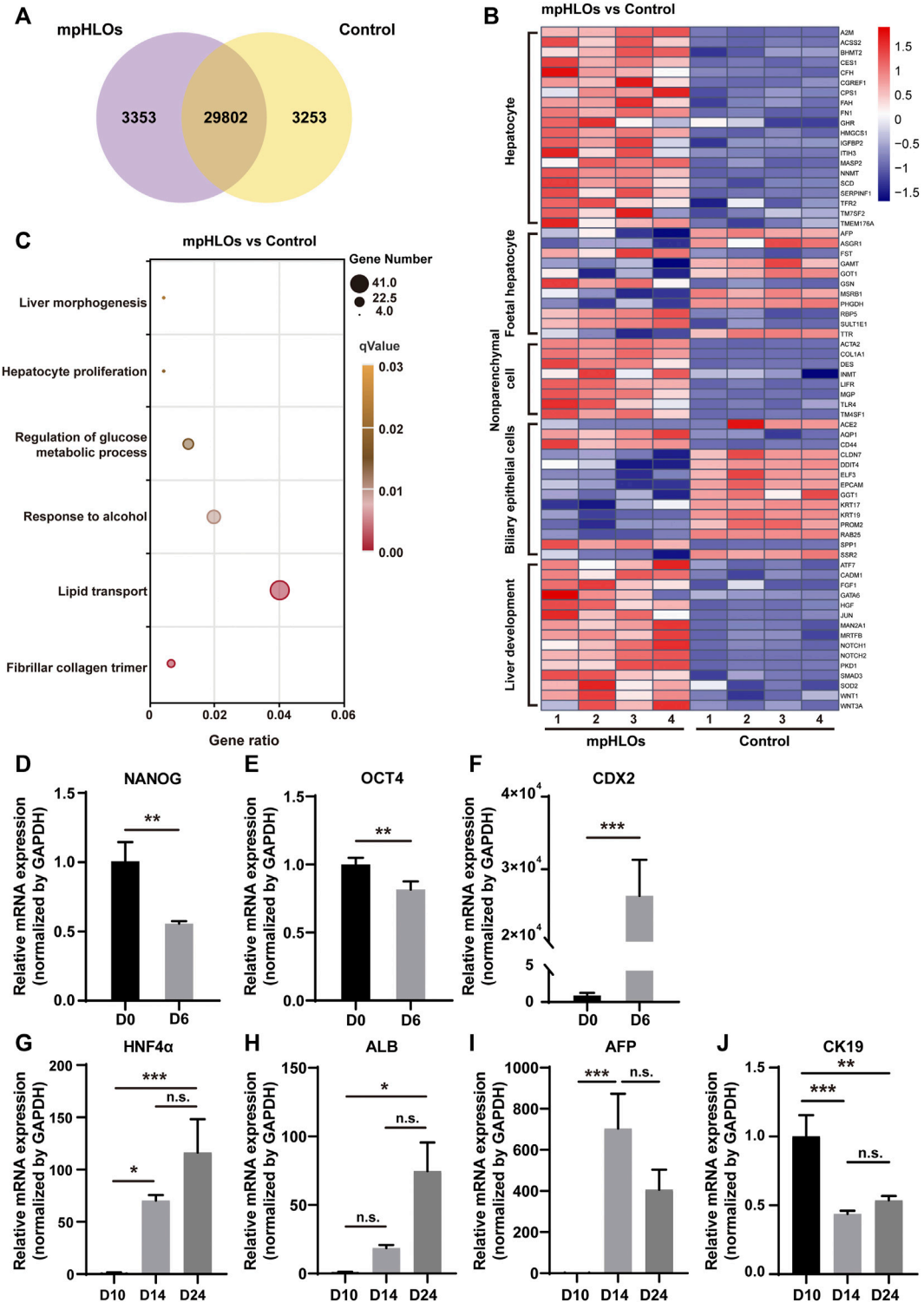

FIGURE 3
The transcriptomic analysis and relative mRNA expression of key genes in differentiation process. **(A)** Venn diagram shows the number of co-expressing and differentially expressing genes between mpHLOs and HLOs in the Matrigel dome (Control). **(B)** Heat map shows gene expression in hepatocyte, fetal hepatocyte, nonparenchymal cell, biliary epithelial cell, and liver development. **(C)** Bubble diagram indicates up-regulated genes enrichment by Gene Ontology analysis. **(D)** The pluripotency gene NANOG and **(E)** OCT4. **(F)**The posterior foregut gene CDX2. **(G)** The hepatic gene HNF4α. **(H)** The hepatic gene ALB. **(I)** The hepatic progenitor gene AFP. **(J)** The cholangiocyte gene CK19. Gene expression is shown as fold changes during two-week differentiation relative to the levels in D10 group, as determined by qPCR. Data are the mean ± SD ($n = 3$) and analyzed by Student's t test or One-way analysis of variance, *$p < 0.05$, **$p < 0.01$, ***$p < 0.001$, ****$p < 0.0001$.

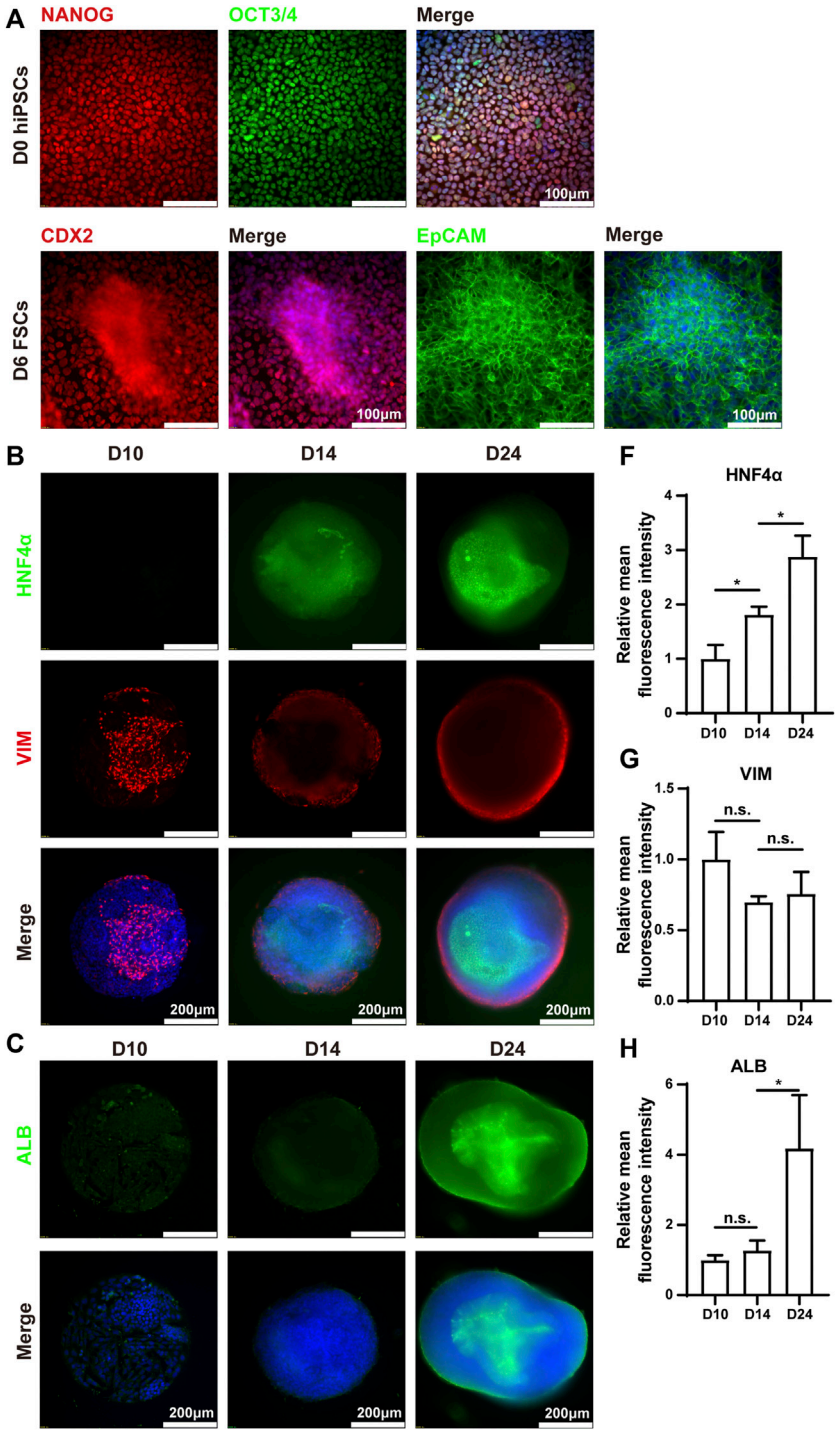

FIGURE 4
Immunohistochemistry analysis of mpHLOs. **(A)** Immunofluorescence staining of hiPSCs and FSCs for pluripotency markers NANOG and OCT4, posterior foregut marker CDX2, epithelial marker EpCAM. Immunofluorescence staining of mpHLOs for **(B)** hepatic maker HNF4α and mesenchymal marker VIM, **(C)** hepatic marker ALB, **(D)** epithelial marker EpCAM and hepatoblasts marker AFP, and **(E)** cholangiocyte marker CK19. **(F–K)** Semi-quantification analysis of immunofluorescence staining. Data are presented as the mean ± SD (n = 3) and analyzed by One-way analysis of variance, *p < 0.05, **p < 0.01, ***p < 0.001, ****p < 0.0001.

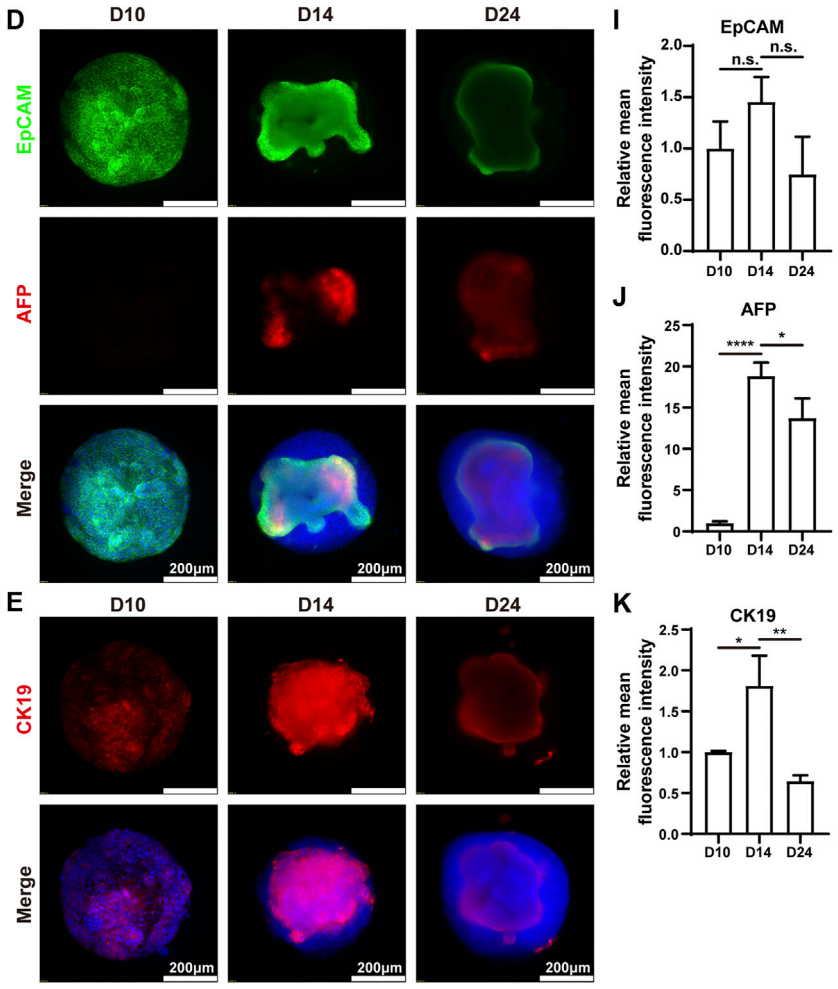

FIGURE 4

development-related gene expression than the control group (Figure 3B). Furthermore, gene ontology (GO) term enrichment analysis indicated that the biological processes enriched in this gene set were associated with liver functions such as lipid transport, response to alcohol, and regulation of glucose metabolic process (Figure 3C).

We characterized liver-specific gene and protein expressions in the mpHLOs using qPCR and immunofluorescence analysis. On Day 6, the mRNA expression levels of the pluripotency-associated stem cell markers, NANOG and OCT4, were decreased. In contrast, posterior foregut marker CDX2 significantly was increased (Figures 3D–F), revealing that hiPSCs were differentiated into FSCs. The mRNA levels of hepatic markers, albumin (ALB), and hepatocyte nuclear factor 4 alpha (HNF4α) were upregulated over 14-day differentiation since Day 10 (Figures 3G,H). Moreover, the mRNA expression of hepatoblasts marker α-fetoprotein (AFP) was increased from Day 10 to Day 14 and then decreased from Day 14 to Day 24 (Figure 3I). The above results indicated hepatic specification and maturation of the mpHLOs. In addition, the cholangiocyte marker cytokeratin 19 (CK19) was identified at distinct stages of organoid differentiation (Figure 3J), indicating the immature state of the mpHLOs.

Immunofluorescence analysis was performed to verify the above results. The results demonstrated that hiPSCs expressed pluripotent markers (NANOG and OCT3/4) on Day 0. On Day 6, the differentiated cells expressed posterior foregut marker CDX2 and epithelial marker EpCAM (Figure 4A). The protein expression levels of ALB and HNF4α were increased from Day 10 to Day 24, which was highly consistent with the corresponding mRNA expression (Figures 4B,C). Interestingly, the protein expression of vimentin (VIM), a mesenchymal marker, emerged sparsely on the surface of the HLOs on Day 10, indicating the existence of non-parenchymal cells. These VIM-positive cell populations increased over the subsequent 2 weeks and

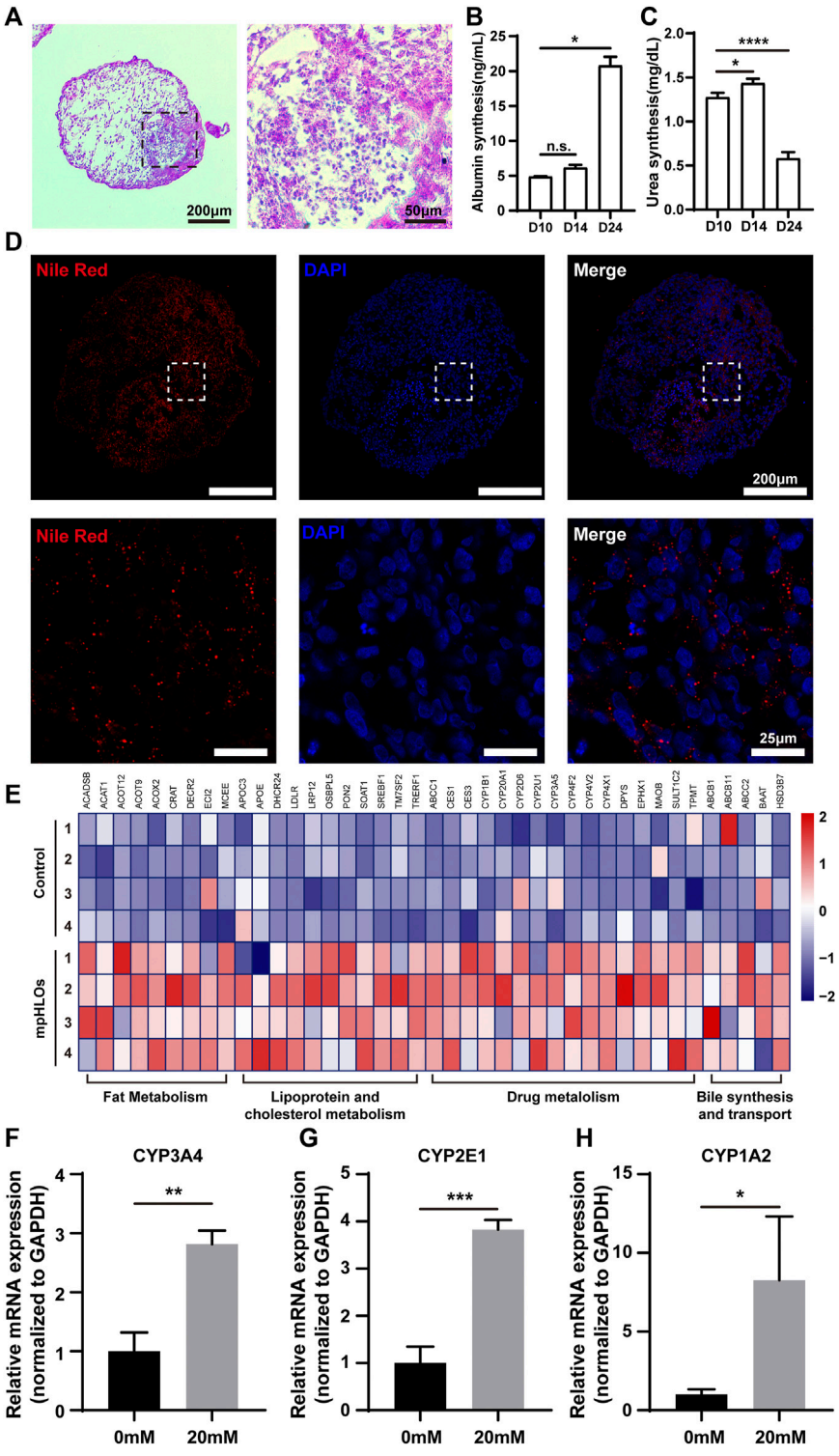

FIGURE 5
Functional characterization of mpHLOs. **(A)** Glycogen storage of mpHLOs. **(B–C)** Albumin and urea secretion during two-week differentiation. **(D)** Lipid accumulation of mpHLOs. **(E)** Heat map indicates differential gene expression analysis of liver specific function genes. **(F–H)** Relative mRNA expression of CYP450 enzymes (CYP3A4, CYP2E1, and CYP1A2) after 48 h treatment with 0 and 20 mM APAP. Data are shown as the fold changes in expression relative to the levels without treatment. Data are the mean ± SD (n = 3) and analyzed by Student's t test or One-way analysis of variance, *p < 0.05, **p < 0.01, ***p < 0.001, ****p < 0.0001.

ultimately formed an outer shell at the surface of mpHLOs (Figure 4B). Notably, all the cells expressed EpCAM on Day 10, implying their hepatic stem cell identity. Moreover, these EpCAM positive cells decreased over the differentiation and finally existed only in the core of the mpHLOs (Figure 4D). Like the EpCAM expression, CK19 was expressed in nearly all the cells in the HLOs on Day 10 and then expressed only in the core of the HLOs on Day 24. However, these CK19 positive cells experienced the first upregulation and then downregulation in the expression level during the two-week differentiation (Figure 4E). Additionally, AFP didn't express on Day 10 and then showed on Day 14 in the core of the HLOs (Figure 4D), further confirming the emergence of hepatoblasts. High magnifed images are shown in Supplementary Figure S1.

3.4 Functional characterization of micropatterned HLOs

We further examined liver-specific functions of the mpHLOs. Specifically, mpHLOs on Day 24 were stained positive by PAS and Nile Red staining assays, indicating their lipid and glycogen synthesis functions (Figures 5A,D). Furthermore, ELISA analysis indicated that albumin in the culture medium increased over the two-week differentiation. Meanwhile, urea was also detected in the supernatant (Figures 5B,C). In addition, the mpHLOs highly expressed genes encoded for proteins and enzymes that are important for essential liver functions, including bile synthesis and transport, lipoprotein and cholesterol metabolism, drug metabolism, and fat metabolism (Figure 5E).

To evaluate the metabolic capacity of mpHLOs, we used the clinical drug APAP to assess the acute toxic effects of a hepatotoxicant on the liver organoids. The liver organoids were treated for 48 h with a 20 mM concentration of APAP, and then RNA was extracted for qPCR. As shown in Figures 5F–H, all three cytochrome P450 enzymes showed higher expression levels after APAP treatment.

4 Discussion

PSC-derived HLOs are considered promising humanized organotypic models for mechanistic studies of human liver disease and evaluation of hepatoxicity. However, the heterogeneity of PSC-derived HLOs represents a great challenge that hampers the HLOs from widespread biomedical applications. Here, We address this issue by bioengineering of PSC-derived HLOs with MPCS. Specifically, seeded PSC-derived foregut stem cells can only attach to cell-adhesive microregions determined by the micropatterning technique. When the adhered foregut stem cells reach about 100% cell confluence on the microregions, continuous cell proliferation results in cell stratification and the formation of multilayer cytoarchitecture. After two-week differentiation from Day 10 to Day 24, dome-shaped HLOs are generated with a predefined boundary on the substrate. Additionally, the geometric features such as the interspace and the size of the individual HLOs are determined by the predefined MPCS. We constructed circular mpHLOs with diameters of 100, 200, and 500 μm. Compared to the 500 μm diameter mpHLOs, the 100, and 200 μm mpHLOs displayed same phenotype and protein expression pattern on Day 14 (Supplementary Figure S2), but easily detached from the MPCS during the culture medium exchange. Therefore, we chose to use the 500 μm mpHLOs for subsequent experiments. We design the HLOs with the same size and equal interspace distance from their neighboring HLOs, and the biochemical microenvironments over individual organoids are homogenized. Therefore, the maturity of individual organoids is comparable during the differentation. Moreover, the deterministic locations and controlled sizes of individual organoids facilitate *in-situ* monitoring and whole-mount imaging. The morphology analysis indicates that the area CVs of mpHLOs are significantly lower than that of HLOs in Matrigel domes. Micropatterned substrate is a commonly-used bioengineering approach for tissue culture. Previously, Bhatia's group employed MPCS to co-culture primary hepatocytes with endothelial cells and fibroblast cells. Cells were self-organized in the patterned microregions and formed a heterocellular liver model, which was applied to emulate the hepatitis viral infection of the adult human liver (March et al., 2015). Additionally, Khetani's group developed an *in vitro* liver model containing hiPSC-derived hepatic cells and murine embryonic fibroblasts on the micropatterned substrate. They explored this model for long-term drug toxicity assessment (Ware et al., 2015). Compared to these co-culture systems, We differentiated FSCs *in situ* into mpHLO spontaneously containing liver parenchymal and non-parenchymal cells without addition of non-isogenic cells. Moreover, the formation of mpHLOs displays a similar differentiation process to liver development *in vivo*.

Our liver organoids exhibit a strong hepatic fate, but they are immature in functionalities and demonstrate fetal liver features. Immunofluorescence analysis indicates that the mpHLOs are stained intensely for CK19 and EpCAM, weakly for ALB, but negatively for AFP on Day 10 (Figures 4B–E). The protein expression pattern has been previously identified as the phenotypes of hepatic stem cells (hHpSCs) (Schmelzer et al., 2006). hHpSCs are located in the canals of Hering, which is a stem niche in liver (Roskams et al., 2004; Schmelzer et al., 2007). On Day 14, most of the cells in the HLOs positively expressed albumin, AFP, and CK19, which is similar to the expression pattern of hepatoblast in the fetal liver. On Day 24, mpHLOs were stained strongly for ALB, HNF4α, weakly for EpCAM, AFP, and CK19. Hepatoblasts are the dominant cell population in fetal and neonatal livers, and they decline in numbers with age and are found as < 0.1% in normal adult human liver. Fetal livers express high level of AFP, elevated level of ALB, and low level of CK19. The protein expression pattern of mpHLOs is similar to the expression of fetal and neonatal liver (Schmelzer et al., 2006; Si-Tayeb et al., 2010; Lee et al., 2016).

Immunofluorescence staining also demonstrates that non-parenchymal cells are at the periphery of the mpHLOs while hepatoblast and immature hepatocytes are at the interior (Figure 2C). Although not fully matured, mpHLOs display liver-specific functions, including albumin secretion, urea production, glycogen synthesis, and lipid synthesis (Figures 5A–E).

To date, there are only a few models available to study the hepatotoxicity of drugs on human fetuses. Here, our mpHLOs provide an *in vitro* model of the fetal liver for relevant studies. Previous studies demonstrated that Acetaminophen (APAP), the most commonly recommended analgesia in pregnancy, can cross the placenta and cause fetal and maternal hepatocytes damage at toxic doses. Specifically, fetal hepatocytes metabolize APAP into hepatoxic metabolites that cause hepatic necrosis (Wilkes et al., 2005; Laine et al., 2009). In our study, the expression of Cytochrome P450 enzymes was significantly up-regulated after APAP treatment for 48 h (Figure 5F), suggesting that mpHLOs are sensitive to drug treatment and can therefore be used as a model for evaluating drug fetal hepatotoxicity.

We admit that our mpHLOs have some limitations. Compared to primary hepatocyte culture, the maturity of mpHLOs is insufficient. For example, the albumin secretion quantity of mpHLOs is much lower than reported in some previous articles (Wang et al., 2018). In addition, the cytoarchitecture of the mpHLOs is different from the liver-specific functional unit, namely the hepatic lobule. We will address these limitations and improve the fidelity of mpHLOs in their function and cellular structure by employing co-culture or dynamic culture strategies.

5 Conclusion

Overall, we develop a novel *in vitro* liver model by bioengineering hiPSC-derived liver organoid. The technique to generate the model is high-throughput and reproducible. The liver organoid is uniform and allows whole-mount imaging under a confocal microscope. We believe that this novel liver organoid model will enable the understanding of drug-induced fetal liver injury and provide an innovative platform for basic research in fetal liver development and diseases.

Data availability statement

All data needed to evaluate the conclusions in the paper are presented in the paper and/or Supplementary Material. More detailed data will be made available to interested investigators upon request. The RNA-seq data accompanying the research has been uploaded to sequence read archive (SRA) with the accession number PRJNA837011.

Author contributions

Conceptualization: PC; Data curation: PC and XX; Formal analysis: XX and SJ; Funding acquisition: PC; Investigation: XX, SJ, LG, BL, FX, and PC; Methodology: XX, SJ, and PC; Project administration: PC; Resources: PC; Software: XX, BL, and FX; Supervision: PC; Validation: XX, SJ, and LG; Visualization: XX and SJ; Writing original draft: XX and PC; Writing-review and editing: PC, CL, and XX.

Funding

This work was supported by the National Key Research and Development Program of China (No. 2018YFA0109000) and the Applied Foundational Research Program of Wuhan Municipal Science and Technology Bureau (No.2018010401011296).

Acknowledgments

Thanks for technical support from Innovations in stem cell and organoids project (ISCO) and Medical research center for structural biology of Wuhan University TaiKang Medical School (School of Basic Medical Sciences). Special thanks to Zhiqiang Xin, Xiang Ye From Nuwacell Biotechnologies Co., Ltd. for their technical assistance in hiPSC culture.

Conflict of interest

The authors declare that the research was conducted in the absence of any commercial or financial relationships that could be construed as a potential conflict of interest.

Publisher's note

Supplementary material

The Supplementary Material for this article can be found online at: https://www.frontiersin.org/articles/10.3389/fbioe.2022.937595/full#supplementary-material

References

Bjornsson, E. S., Bergmann, O. M., Bjornsson, H. K., Kvaran, R. B., and Olafsson, S. (2013). Incidence, presentation, and outcomes in patients with drug-induced liver injury in the general population of Iceland. *Gastroenterology* 144 (7), 1419–1425.e3. doi:10.1053/j.gastro.2013.02.006

Chalasani, N., Bonkovsky, H. L., Fontana, R., Lee, W., Stolz, A., Talwalkar, J., et al. (2015). Features and outcomes of 899 patients with drug-induced liver injury: The DILIN prospective study. *Gastroenterology* 148 (7), 1340–1352.e7. doi:10.1053/j.gastro.2015.03.006

Goulart, E., de Caires-Junior, L. C., Telles-Silva, K. A., Araujo, B. H. S., Kobayashi, G. S., Musso, C. M., et al. (2019). Adult and iPS-derived non-parenchymal cells regulate liver organoid development through differential modulation of Wnt and TGF-β. *Stem Cell Res. Ther.* 10 (1), 258. doi:10.1186/s13287-019-1367-x

Hoang, P., Wang, J., Conklin, B. R., Healy, K. E., and Ma, Z. (2018). Generation of spatial-patterned early-developing cardiac organoids using human pluripotent stem cells. *Nat. Protoc.* 13 (4), 723–737. doi:10.1038/nprot.2018.006

Kamath, P., Kamath, A., and Ullal, S. D. (2021). Liver injury associated with drug intake during pregnancy. *World J. Hepatol.* 13 (7), 747–762. doi:10.4254/wjh.v13.i7.747

Laine, J. E., Auriola, S., Pasanen, M., and Juvonen, R. O. (2009). Acetaminophen bioactivation by human cytochrome P450 enzymes and animal microsomes. *Xenobiotica* 39 (1), 11–21. doi:10.1080/00498250802512830

Lee, D. H., Park, J. O., Kim, T. S., Kim, S. K., Kim, T. H., Kim, M. C., et al. (2016). LATS-YAP/TAZ controls lineage specification by regulating TGFβ signaling and Hnf4α expression during liver development. *Nat. Commun.* 7, 11961. doi:10.1038/ncomms11961

Ma, Z., Wang, J., Loskill, P., Huebsch, N., Koo, S., Svedlund, F. L., et al. (2015). Self-organizing human cardiac microchambers mediated by geometric confinement. *Nat. Commun.* 6, 7413. doi:10.1038/ncomms8413

March, S., Ramanan, V., Trehan, K., Ng, S., Galstian, A., Gural, N., et al. (2015). Micropatterned coculture of primary human hepatocytes and supportive cells for the study of hepatotropic pathogens. *Nat. Protoc.* 10 (12), 2027–2053. doi:10.1038/nprot.2015.128

Ouchi, R., Togo, S., Kimura, M., Shinozawa, T., Koido, M., Koike, H., et al. (2019). Modeling steatohepatitis in humans with pluripotent stem cell-derived organoids. *Cell Metab.* 30 (2), 374–384.e6. doi:10.1016/j.cmet.2019.05.007

Roskams, T. A., Theise, N. D., Balabaud, C., Bhagat, G., Bhathal, P. S., Bioulac-Sage, P., et al. (2004). Nomenclature of the finer branches of the biliary tree: Canals, ductules, and ductular reactions in human livers. *Hepatology* 39 (6), 1739–1745. doi:10.1002/hep.20130

Schmelzer, E., Wauthier, E., and Reid, L. M. (2006). The phenotypes of pluripotent human hepatic progenitors. *Stem Cells* 24 (8), 1852–1858. doi:10.1634/stemcells.2006-0036

Schmelzer, E., Zhang, L., Bruce, A., Wauthier, E., Ludlow, J., Yao, H. L., et al. (2007). Human hepatic stem cells from fetal and postnatal donors. *J. Exp. Med.* 204 (8), 1973–1987. doi:10.1084/jem.20061603

Sgro, C., Clinard, F., Ouazir, K., Chanay, H., Allard, C., Guilleminet, C., et al. (2002). Incidence of drug-induced hepatic injuries: A French population-based study. *Hepatology* 36 (2), 451–455. doi:10.1053/jhep.2002.34857

Shen, T., Liu, Y., Shang, J., Xie, Q., Li, J., Yan, M., et al. (2019). Incidence and etiology of drug-induced liver injury in mainland China. *Gastroenterology* 156 (8), 2230–2241.e11. doi:10.1053/j.gastro.2019.02.002

Shinozawa, T., Kimura, M., Cai, Y., Saiki, N., Yoneyama, Y., Ouchi, R., et al. (2021). High-fidelity drug-induced liver injury screen using human pluripotent stem cell-derived organoids. *Gastroenterology* 160 (3), 831–846.e10. doi:10.1053/j.gastro.2020.10.002

Si-Tayeb, K., Lemaigre, F. P., and Duncan, S. A. (2010). Organogenesis and development of the liver. *Dev. Cell* 18 (2), 175–189. doi:10.1016/j.devcel.2010.01.011

Thompson, W. L., and Takebe, T. (2020). Generation of multi-cellular human liver organoids from pluripotent stem cells. *Methods Cell Biol.* 159, 47–68. doi:10.1016/bs.mcb.2020.03.009

Velazquez, J. J., LeGraw, R., Moghadam, F., Tan, Y., Kilbourne, J., Maggiore, J. C., et al. (2021). Gene regulatory network analysis and engineering directs development and vascularization of multilineage human liver organoids. *Cell Syst.* 12 (1), 41–55.e11. doi:10.1016/j.cels.2020.11.002

Wang, Y., Wang, H., Deng, P., Chen, W., Guo, Y., Tao, T., et al. (2018). *In situ* differentiation and generation of functional liver organoids from human iPSCs in a 3D perfusable chip system. *Lab. Chip* 18 (23), 3606–3616. doi:10.1039/c8lc00869h

Ware, B. R., Berger, D. R., and Khetani, S. R. (2015). Prediction of drug-induced liver injury in micropatterned Co-cultures containing iPSC-derived human hepatocytes. *Toxicol. Sci.* 145 (2), 252–262. doi:10.1093/toxsci/kfv048

Wilkes, J. M., Clark, L. E., and Herrera, J. L. (2005). Acetaminophen overdose in pregnancy. *South. Med. J.* 98 (11), 1118–1122. doi:10.1097/01.smj.0000184792.15407.51

Xu, J., Pan, D., Liao, W., Jia, Z., Pan, M., Weng, J., et al. (2022). Application of 3D hepatic plate-like liver model for statin-induced hepatotoxicity evaluation. *Front. Bioeng. Biotechnol.* 10, 826093. doi:10.3389/fbioe.2022.826093

frontiers | Frontiers in Bioengineering and Biotechnology

TYPE Original Research
PUBLISHED 16 August 2022
DOI 10.3389/fbioe.2022.943751

OPEN ACCESS

EDITED BY
Lifeng Kang,
The University of Sydney, Australia

REVIEWED BY
Tushar Kumeria,
University of New South Wales, Australia
Blaž Likozar,
National Institute of Chemistry, Slovenia
Kun Xue,
Institute of Materials Research and Engineering (A*STAR), Singapore

*CORRESPONDENCE
Chung-Yin Lin,
winwood7@mail.cgu.edu.tw
Dar-Fu Tai,
dftai@gms.ndhu.edu.tw

SPECIALTY SECTION
This article was submitted to Biomaterials, a section of the journal Frontiers in Bioengineering and Biotechnology

RECEIVED 14 May 2022
ACCEPTED 11 July 2022
PUBLISHED 16 August 2022

CITATION
Kanubaddi KR, Yang C-L, Huang P-Y, Lin C-Y, Tai D-F and Lee C-H (2022), Peptide conformational imprints enhanced the catalytic activity of papain for esterification.
Front. Bioeng. Biotechnol. 10:943751.
doi: 10.3389/fbioe.2022.943751

Peptide conformational imprints enhanced the catalytic activity of papain for esterification

Kiran Reddy Kanubaddi[1], Ching-Lun Yang[2], Pei-Yu Huang[2], Chung-Yin Lin[3,4]*, Dar-Fu Tai[2]* and Chia-Hung Lee[1]

[1]Department of Life Science and Institute of Biotechnology, National Dong Hwa University, Hualien, Taiwan, [2]Department of Chemistry, National Dong Hwa University, Hualien, Taiwan, [3]Medical Imaging Research Center, Institute for Radiological Research, Chang Gung University, Taoyuan, Taiwan, [4]Department of Neurology, Chang Gung Memorial Hospital, College of Medicine, Chang Gung University, Taoyuan, Taiwan

Peptide conformational imprints (PCIs) offer a promising perspective to directly generate binding sites for preserving enzymes with high catalytic activity and stability. In this study, we synthesized a new chiral cross-linker cost-effectively for controlling the matrix morphology of PCIs on magnetic particles (PCIMPs) to stabilize their recognition capability. Meanwhile, based on the flank part of the sequences on papain (PAP), three epitope peptides were selected and synthesized. Molecularly imprinted polymers (MIPs) were then fabricated in the presence of the epitope peptide using our new cross-linker on magnetic particles (MPs) to generate PCIMPs. PCIMPs were formed with helical cavities that complement the PAP structure to adsorb specifically at the targeted position of PAP. PCIMPs$^{65-79}$ were found to have the best binding parameters to the PAP with K_d = 0.087 μM and B_{max} = 4.56 μM. Upon esterification of *N*-Boc-His-OH, proton nuclear magnetic resonance (^{1}H-NMR) was used to monitor the yield of the reaction and evaluate the activity of PAP/PCIMPs. The kinetic parameters of PAP/PCIMPs$^{65-79}$ were calculated as V_{max} = 3.0 μM s^{-1}, K_m = 5 × 10^{-2} M, k_{cat} = 1.1 × 10^{-1} s^{-1}, and k_{cat}/K_m = 2.2 M^{-1} s^{-1}. In addition, PAP is bound tightly to PCIMPs to sustain its activity after four consecutive cycles.

KEYWORDS

esterification, molecularly imprinted polymers, papain, peptide conformational imprints, enzyme immobilization

Introduction

Papain (PAP) is a cysteine protease (EC 3.4.22.2) found in papaya tease. Its substrate contains arginine or lysine residue and is commonly used in the food industry. PAP acts as a highly specific and effective biocatalyst and has been reported to catalyze carbon–carbon formation in organic synthesis (Cajnko et al., 2020; Cajnko et al., 2021; Bjelić et al., 2022). It operated under mild reaction conditions and separated easily from the reaction mixture (Morcelle et al., 2006; Jeong et al., 2011; Llerena-Suster et al., 2012; Cao et al., 2015). PAP-mediated esterification has been studied previously. It decreases the environmental

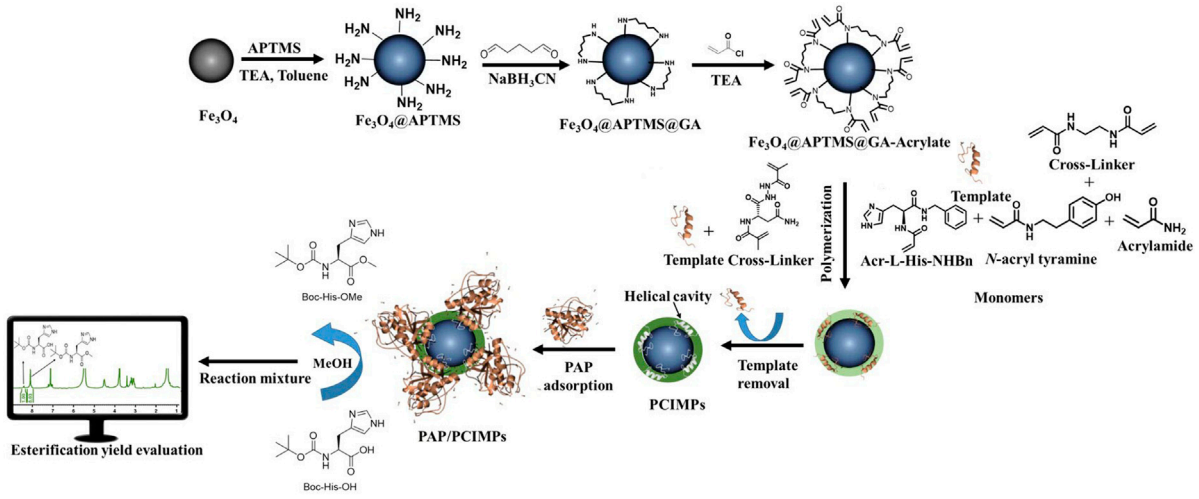

FIGURE 1
Schematic diagram of the (Top) fabrication of MPs to PCIMPs using cross-linker, monomers, and template (Bottom) application of PCIMPs using their binding mechanisms toward PAP and PAP/PCIMPs catalyzed esterification and yield evaluation under the monitor. APTMS, 3-aminopropyl trimethoxysilane; TEA, trimethylamine; GA, glutaraldehyde; MPs, magnetic particles; PAP, papain; PCIs, peptide conformational imprints; PCIMPs, peptide conformational imprint magnetic particles.

impact of chemical alterations that typically require acyl chlorides or toxic coupling agents. In fact, PAP is usually utilized for trans-esterification of alkyl or vinyl esters in a medium with low water content (Prabhakar et al., 2017; Marathe et al., 2020). Moreover, PAP was also found to possess esterase activity in a biphasic system or an aqueous solution, and *N*-Boc amino acid esters were synthesized (Cantacuzène et al., 1987; de Beer et al., 2012). PAP shows remarkable catalytic performance in esterification, transesterification, and hydrolysis (Jeong et al., 2011; Anwar et al., 2017), but some of its properties may not fit industrial requirements due to inherent limitations such as lack of reusability, instability in organic solvents at high temperatures, and denaturing at different pH ranges (Homaei et al., 2010; Sheldon, 2011; Homaei, 2015).

Over the last five decades, numerous methods have been developed to immobilize all classes of enzymes. Enzyme immobilization technology was developed to reduce drawbacks and make them reusable at a commercial level (Homaei et al., 2013; Mohamad et al., 2015; Liang et al., 2021). Immobilized enzymes as catalysts were reviewed (Basso and Serban, 2019; Kankala et al., 2019). Previously, Tai and colleagues immobilized PAP on Sephadex G-50 to convert *N*-protected amino acids to their methyl esters (Tai et al., 1989). Since then, many efforts have been dedicated to utilizing PAP as a biocatalyst for diverse catalytic applications. For example, Storer and colleagues immobilized PAP on celite (PAP/celite) to catalyze the esterification of Cbz-glycine with methanol as a substrate in 12 different solvents of widely varying polarity (Stevenson and Storer, 1991). *N*-Cbz-L-alanine was converted to its corresponding esters with 2-phenethyl alcohol by using PAP/celite (Shih et al., 1997). Although these techniques can improve enzyme stability, they might also be accountable for restrictions in local and global protein flexibility. Inevitably, protein conformation was unstable under harsh synthesis conditions (Secundo, 2013; Hoarau et al., 2017). Enzymes lose their structure orientation during immobilization processes, which plays a crucial role in reducing enzymatic activity (Basso and Serban, 2019; Nguyen et al., 2019).

The fabrication of peptide conformational imprints (PCIs) on magnetic particles (PCIMPs) is a delicate process to immobilize enzymes (Chou et al., 2020; Kanubaddi et al., 2021). A helical peptide fragment of the enzyme was used as a template to form molecularly imprinted polymers (MIPs). As helical peptide segment-mediated PCIMPs were constructed, elegant helical cavities complementary to the enzyme structure can be achieved (Chou et al., 2020; Kanubaddi et al., 2021). By taking this dynamic property into account, the selection of the template (Figure 1) was crucial to generate helical cavities using PCIs. Binding enzymes tightly at the target position is the key issue in keeping enzymes flexible as well as stable. The advantage of this method is to create accessible binding sites on the surface of MPs and enable *catalytic active sites* with less interference during catalysis. The novelty of this work is to monitor the esterification yield of Boc-His-OH directly using ^{1}H-NMR with great accuracy; demonstrate the activation effect of PCIMPs on the esterification activity of PAP; and sustain the esterification process of PAP/PCIMPs for four consecutive cycles. Finally, the immobilized enzyme is contemplated to further increase the efficiency and convenience in the catalysis of the reverse reaction of hydrolysis.

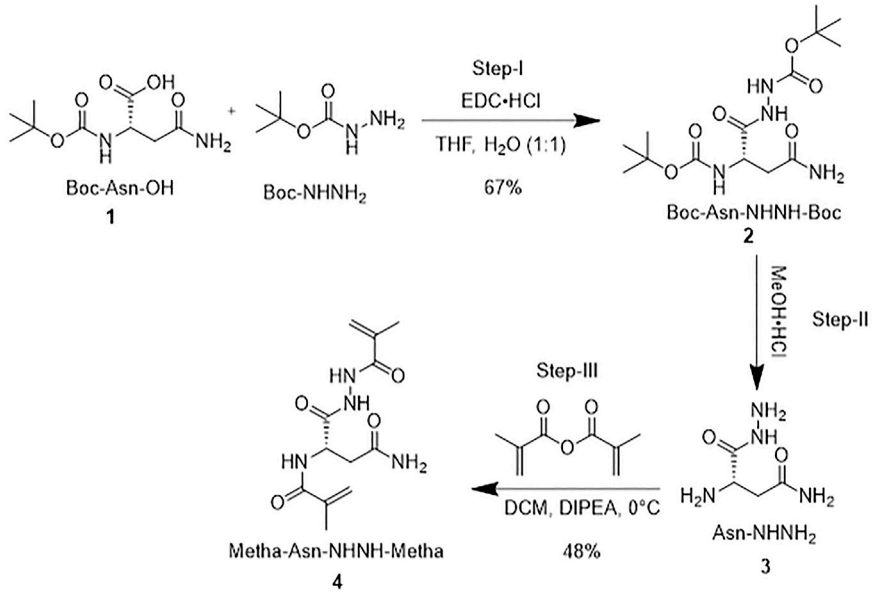

SCHEME 1
Synthesis of a cross-linker.

Our research methods can be divided into four main categories: 1) synthesis of a cross-linker and monomers from asparagine; 2) fabrication of PCIMPs using a single cross-linker; 3) adsorption of PAP to PCIMPs to obtain binding parameters; 4) operation of PAP/PCIMP-catalyzed esterification to observe enzyme kinetics.

Materials and methods

The synthesis of the monomers is described in our previous studies. Briefly, Acr-L-His-NHBn (Tai et al., 2011) was prepared using the following steps. Initially, Boc-L-His-OMe was synthesized using Boc-His-OH and methanol by adding PAP as a catalyst (Tai et al., 1989). Then, the obtained Boc-L-His-OMe was converted to Boc-L-His-NHBn using benzylamine in the presence of PAP. Next, trifluoroacetic acid was used to deprotect the Boc group to form *L*-His-NHBn (Tai, 2003); then, acrylation of *L*-His-NHBn was carried out to obtain Acr-L-His-NHBn. Finally, another monomer, *N*-acryl tyramine, was prepared by acylation with acrylic chloride of tyramine hydrochloride (Singh et al., 2013).

Synthesis of a cross-linker (Metha-Asn-NHNH-Metha)

Scheme 1 shows the synthetic route of the cross-linker. Briefly, a mixture of Boc-L-Asn-OH (1 g, 1 eq) and Boc-$NHNH_2$ (0.68 g, 1.2 eq) was dissolved in a water (H_2O)/tetrahydrofuran (THF) mixture (1:1) and stirred for a few minutes. Later, 3-(ethyliminomethyleneamino)-*N,N*-dimethylpropan-1-amine hydrochloride (EDC·HCl; 0.828 g, 1 equiv) was added portion-wise to the solution, stirred for 4 hours, and monitored by thin layer chromatography (TLC). The solution was extracted into ethyl acetate (EtOAc, 10 ml) and washed with 0.1 N hydrochloric acid (HCl), followed by H_2O and saturated brine solution. The organic layer was passed through sodium sulfate (Na_2SO_4). The solvent was removed under a rotary evaporator to obtain **2** as a white solid (1.0 g, 67%). Boc-L-Asn-NHNH-Boc **2** (1 g) was dissolved in 10 ml of methanolic HCl (4 M). The mixture was stirred for 4 h at 0°C. After that, the solvent was evaporated under the rotary evaporator at room temperature (RT) and washed three times with diethyl ether (Et_2O, 10 ml) to form a precipitate. The solid was dried under vacuum at 0°C to obtain 0.5 g of *L*-Asn-$NHNH_2$ **3**. It was then dissolved in 10 ml of dry dichloromethane (DCM) and flushed with nitrogen (N_2). Methacrylic anhydride (2 equiv.), followed by *N,N*-diisopropylethylamine (DIPEA; 5 equiv) were added dropwise and stirred overnight at 0°C under N_2. Finally, the solution was extracted into DCM. The organic layer was washed with 0.1 N HCl, followed by H_2O and saturated brine solution. The organic layer was mixed with anhydrous Na_2SO_4 to remove moisture and was purified by column chromatography. A solid was precipitated with a mixture of DCM and hexane solvents, which was further dried at 0°C and stored at −5°C. In this way, cross-linker **4** was obtained with a 48% yield (see the entire process in Supplementary Figure S2).

Synthesis of the template

The peptide segments, such as $PAP^{65–79}$ (GGYPW SALQLVAQYG), PAP^{65-78} (GGYPWSALQLVAQY), PAP^{66-79} (GYPWSALQLVAQYG), and PAP^{66-78} (GYPWSALQLVAQY) were synthesized using solid-phase chemistry of the fluorenylmethoxycarbonyl (Fmoc) method (Collins et al., 2014). The template (peptide residues) was synthesized using a CEM Discover Microwave-assisted Peptide synthesizer (Kohan Co., Taipei, Taiwan) as described previously (Collins et al., 2014; Lin et al., 2019; Kanubaddi et al., 2021). Subsequently, the purity of these peptides was monitored by HPLC equipped with an RP-18, using a mobile phase of 75:25 v/v methanol/water at RT and at a flow rate of 1 ml/min. Sharp peaks were observed at a retention time of ~19 min, known as a template (Supplementary Figure S1A); these peptides' purity was observed to be ~88%. The template samples such as $PAP^{65–79}$, $PAP^{65–78}$, and $PAP^{66–79}$ were analyzed using a Shimadzu Matrix-Assisted Laser Desorption/Ionization-Time of Flight (MALDI/TOF) mass spectrometer (MS) (Kyoto, Japan), and PAP^{66-78} (GYPWSALQLVAQY) was analyzed using Bruker Autoflex MALDI/TOF mass spectrometry (Germany) with 2,5-dihydroxybenzoic acid (DHB) as the matrix. of The sharp peaks of PAP^{66-78} were observed in the HPLC chromatogram at a retention time of ~3 min, and purity was observed to be ~95% (Supplementary Figure S1C). The reported *m/z* values of $PAP^{65–79}$, $PAP^{65–78}$, $PAP^{66–79}$, and $PAP^{66–78}$ were observed, respectively, at 1610.78 $[M + H]^+$, 1552.50, 1552.74 as shown in Supplementary Figure S1B, and 1517.951 $[M + Na]^+$ (Supplementary Figure S1D).

Preparation of PCIMPs

The synthesis of Fe_3O_4, Fe_3O_4@APTMS, Fe_3O_4@APTMS-GA, and Fe_3O_4@APTMS-GA-acrylate was carried out as described previously (Ding et al., 2006; Yang et al., 2017; Kanubaddi et al., 2021). Furthermore, for the preparation of PCIMPs using a cross-linker, 5.6 mM of the cross-linker (Metha-Asn-NHNH-Metha) and 0.014 mM of the template ($PAP^{65–79}$, PAP^{65-78}, or PAP^{66-79}) were dissolved in 12 ml of trifluoroethanol (TFE)/H_2O = 7: 3. For fabrication of PCIMPs using monomers, acrylamide (AA) (0.24 mM), *N*-Acr-L-His-NHBn (0.24 mM), *N*-acryltyramine (0.48 mM), and the cross-linker *N,N′*-ethylene bisacrylamide (0.84 mM), and 0.014 mM of the template (PAP^{66-78}) were dissolved in 6 ml of TFE/ H_2O = 7: 3. The combination was stirred for 1 h to make a pre-self-assembled mixture. Then 100 mg of Fe_3O_4@APTMS-GA-acrylate was added to the mixture and stirred for another 1 h, followed by 500 µl (10%, W/W) of ammonium persulfate (initiator) and 250 µl (5%, W/V) of tetramethylethylenediamine (TEMED), stirred at RT for 24 h in the presence of N_2. Next, the resultant mixture was washed four times with 5% acetic acid (aq), containing 0.5% tween@20 and rinsed with H_2O. Finally, the pore structures formed from different template molecules and were denoted as $PCIMPs^{65–79}$, $PCIMPs^{65–78}$, and $PCIMPs^{66–79}$ (Kanubaddi et al., 2021). The compositions of other PCIMPs are given in Supplementary Table S1;these were synthesized using the same procedure.

Physicochemical characterization of MPs and PCIMPs

The presence of PCIs fabricating on MPs was confirmed using Fourier transform infrared (FT-IR) spectroscopy (Bruker TENSOR 27, Ettlingen, Germany). The morphology of functionalized MPs and PCIMPs was observed under a Field Emission-Scanning Electron Microscope (FE-SEM, JOEL JSM-7000F/JEOL Ltd. Japan) equipped with an Oxford Instruments X-Max EDS system and operated at an acceleration voltage of 200 kV. The elemental analysis was performed by energy-dispersive X-ray spectroscopy (EDS). To demonstrate the amine groups on the surface of MPs, Ninhydrin reagent in the detection of grafted functional groups was assessed. For the Ninhydrin test (Albert Brown Ltd., Leicester, United Kingdom), the samples were placed into the Ninhydrin gel vials provided and incubated at 60°C for 30 min. The vials were then inspected and scored according to the following scale: 0, no color (negative); 1, slight purple color; and 2, dark purple color.

Determination of binding affinities of PCIMPs

To prevent the non-specific binding sites' adsorption on PCIMPs, can binding experiments were carried out for a few minutes. Briefly, 20 mg of PCIMPs was suspended in 1 ml of H_2O containing specific initial PAP concentrations (0.125, 0.25, 0.5, 1.0, and 2.0 mg/ml). After being shaken at 25°C for 5 min, the mixture was separated using a magnet. Then, 200 µl of the supernatant was taken out and measured using a Fluorescence Microplate Reader at E_{ex}/E_{em} = 290 nm/350 nm. The binding affinities of PCIMPs were evaluated using the Scatchard analysis equation (1) (Gerdon et al., 2005; Diltemiz et al., 2009; Tai et al., 2012; Kanubaddi et al., 2021),

$$[RL]/[L] = (B_{max} - [RL])/K_d \quad (1)$$

where [L] is the concentration of PAP in the solution, [RL] is the concentration of the bound PAP from the solution, B_{max} represents the maximum number of binding sites, and K_d is the ligand dissociation constant.

Immobilization of papain (PAP/PCIMPs)

Briefly, 10 mg of PAP was dissolved in 1 ml of H_2O and 20 mg of PCIMPs was added to the solution to incubate for 4 h. The resulting PAP/PCIMPs were collected and washed with

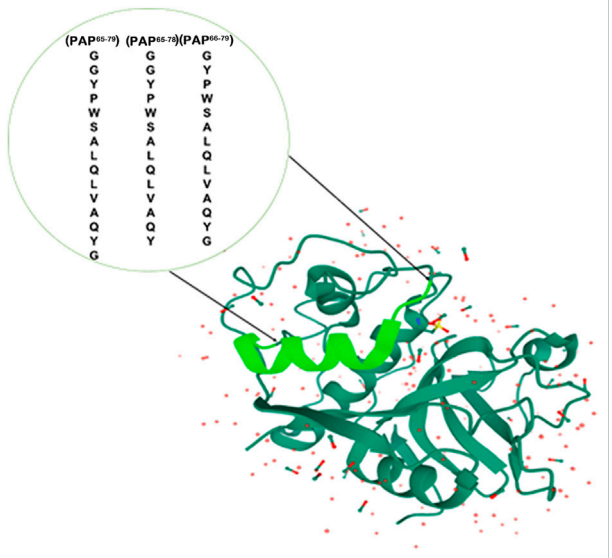

FIGURE 2
The selected sequence is in pale green. These segments consist of the series, i.e., PAP^{65-79}, PAP^{65-78}, and PAP^{66-79}. (The crystal structure of PAP was reproduced from https://www.rcsb.org/3d-view/9PAP, and PDB ID: 9PAP.)

H_2O. Finally, the PAP/PCIMPs obtained were dried at 0°C and stored in a sealed vial at 4°C until further use.

Determination of esterification activity of PAP and immobilization PAP (PAP/PCIMPs) by the ^{1}H-NMR method

The esterification activity of PAP and PAP/PCIMPs was determined using the ^{1}H-NMR method. The starting material was Boc-L-His-OH and the product was Boc-L-His-OMe, which was observed over time. The percentage of esterification rate was calculated by using the following equation (2):

$$Yield = \frac{Product\ integral\ values}{(Starting\ integral\ values + product\ integral\ values)} \times 100 \quad (2)$$

To determine the esterification activity of PAP and PAP/PCIMPs, a solution of Boc-L-His-OH (0.1 M) was prepared in dry methanol (MeOH). Then, an enzymatic reaction in organic solvents was carried out, with modifications of earlier reported methods (Zaks and Klibanov, 1985; Belyaeva et al., 2002). First, 20 mg of PAP was added to Boc-L-His-OH (0.1 M) in 2 ml of MeOH, followed by 50 µl of water. Then, the reaction was carried out at 20°C for 48 h. For immobilized enzyme, 20 mg of PAP/PCIMPs was added to a Boc-L-His-OH (0.1 M) solution and incubated for 48 h, and the product concentration was monitored for 48 h with samples taken every 8 h by ^{1}H-NMR. The same procedure was also used for the adsorption test. For de-adsorption, we used acetonitrilcan (ACN): H_2O to remove the PAP, and repeated the process four times.

Determination of kinetic constants of PAP and PAP/PCIMPs

The kinetic parameters of PAP and PAP/PCIMPs were determined using varying concentrations of Boc-L-His-OH (0.06, 0.08, and 0.1 M) in 2 ml of dry MeOH. Then, 20 mg of PAP/PCIMPs was added to each concentration and incubated. For every 8 h interval, 100 µl of the aliquot was withdrawn, dried in a vacuum, and monitored by ^{1}H-NMR. Finally, the kinetic parameters of PAP and PAP/PCIMPs were evaluated using the Michaelis–Menten kinetics plot obtained from the following equation 3:

$$v = \frac{(V_{max}[S])}{((K_m) + [S])} \quad (3)$$

where v is the velocity, V_{max} is the maximum rate of enzyme activity, [S] is the substrate's concentration, and K_m is the Michaelis half-saturation constant.

The turnover number (k_{cat}) was determined using the following equation 4:

$$k_{cat} = V_{max}/[E] \quad (4)$$

where V_{max} is the maximum rate of enzyme activity and [E] is the concentration of the enzyme (Bossi et al., 2012).

Reusability analysis

To demonstrate the reusability performance of the PCIMPs' imprinted materials, stable catalytic activity was compared with the PAP-immobilized Sephadex G-25 (Tai et al., 1989) and PAP, respectively. The $PAP/PCIMPs^{65-79}$ were also examined with the same catalytic activity at different times to determine reuse performance.

Results and Discussion

Rational selection of the template and its analysis

To obtain unique protein recognition on the surface of MPs, the helical peptide residues in the template are the critical parameters. The selection of template peptide fragments is based on the flank part of the spatial protein structure to limit their interference during catalysis. The length of the peptide segments such as 14–15-mer from the flexible structure on the surface of MPs can be helpful during the process of protein rebinding (Tai et al., 2011; Bossi et al., 2012; Kanubaddi et al., 2021). Therefore, the chosen 14–15-mer peptide

TABLE 1 List of the selected peptide segments as a template.

Sequence	Residue	Theoretical		MALDI-TOF MW (avg)
		pI[a]	MW (avg)[a]	
(PAP^{65-79}) GGYPWSALQLVAQYG	15	5.52	1609.80	1610.78
(PAP^{65-78}) GGYPWSALQLVAQY	14	5.52	1552.75	1552.50
(PAP^{66-79}) GYPWSALQLVAQYG	14	5.52	1552.75	1552.74
(PAP^{66-78}) GYPWSALQLVAQY	13	5.52	1495.70	1517.95

[a]pI and MW values were calculated from the Expasy website.

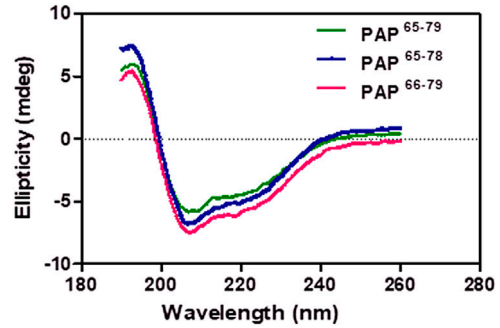

FIGURE 3
The CD spectra of PAP^{65-79}, PAP^{65-78}, and PAP^{66-79} segments.

sequences containing PAP^{65-79}, PAP^{65-78}, and PAP^{66-79} of the PAP were selected as a template. The location of the template is shown in Figure 2, and the list of the peptides is described in Table 1.

Helical conformational analysis

The helical structure of our designed peptides (PAP^{65-79}, PAP^{65-78}, and PAP^{66-79}) were examined using a J-715 spectropolarimeter (Jasco Inc., Japan). The synthesized peptides gave a well-defined secondary conformation by circular dichroism (CD) of the peptide solution (20 mM; TFE/H_2O = 7:3). As shown in Figure 3, the CD spectra exhibited positive peaks at around 193 nm and two minimum negative bands at 207 and 218 nm, indicating α-helix structures' predominance. Accordingly, the peptides were stabilized as a helical conformation in a mixed solvent (TFE/H_2O) to allow the formation of helical cavities with a PCIMPs-based method (Chou et al., 2020; Kanubaddi et al., 2021).

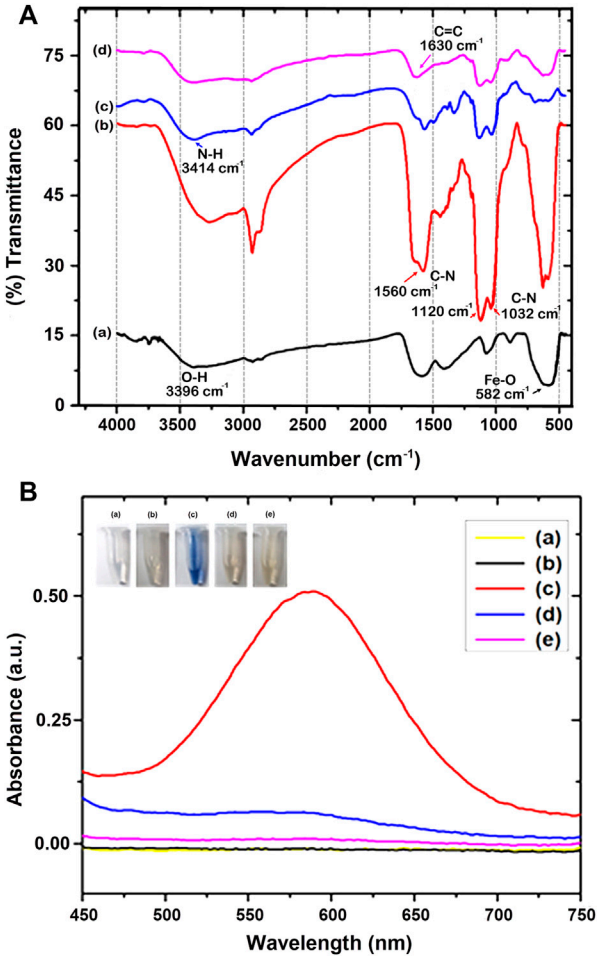

FIGURE 4
(A) FT-IR spectra of **(a)** Fe_3O_4, **(b)** Fe_3O_4@APTMS, **(c)** Fe_3O_4@APTMS-GA, and **(d)** Fe_3O_4@APTMS-GA-acrylate. **(B)** Ninhydrin assay **(a)** Ninhydrin, **(b)** Fe_3O_4, **(c)** Fe_3O_4-APTMS, **(d)** Fe_3O_4-APTMS@GA, and **(e)** Fe_3O_4-APTMS@GA-acrylate.

Preparation of a cross-linker (Metha-L-Asn-NHNH-Metha)

The synthesis of the cross-linker is straightforward, as outlined in Scheme 1. First, Boc-L-Asn-OH **1** was coupled with Boc-$NHNH_2$ via EDC to generate **2**. The Boc protecting group of **2** was then deprotected using MeOH·HCl to obtain **3**. Finally, after acylating with twofold methacryloyl chloride, cross-linker **4** was obtained. The role of the synthesized cross-linker is also kind of a functional monomer. The cross-linker can form more rigid PCIMPs for improving the binding affinity and forming stable PCIMPs. It was attributed to cooperative hydrogen bonding or electrostatic interactions with the protein molecule. Moreover, it possesses an amino group that can easily interact with the substrate to enhance the productive catalytic activity of PAP/PCIMPs.

Proposed mechanism of formation of PCIMPs and their interaction with the template and PAP

Because of self-assembly, the amino group of the cross-linkers attached to the template with ionic bonding and hydrogen bonding. Meanwhile, the monomers, cross-linkers, and Fe_3O_4@APTMSGA-acrylate were attached to each other with the hydrophobic acryloyl group. All the monomers and cross-linkers were thus attached to the template and Fe_3O_4@APTMS-GA-acrylate in a preorganized manner. Afterward, the formulation of PCIMPs took place in an organized manner. The free-radical polymerization process of a cross-linker was initiated by ammonium persulfate and TEMED. TEMED accelerates the rate of formation of free radicals from persulfate. These, in turn, catalyze polymerization. The persulfate free radical converts the methacrylate group of the cross-linker to free radicals, which react with unreacted ones to begin the polymer chain reaction. The elongating polymer chain is randomly cross-linked with Fe_3O_4@APTMS-GA-acrylate, resulting in the production of 3D polymer networks; the interaction of the polymer with the template via ionic bonding and hydrogen bonding to produce a template–PCIMPs complex. This is formed in a large excess of a crosslinking agent to form a 3D polymer network. After the polymerization process, template molecules are removed using an amphiphilic solvent. The role of the synthesized cross-linker is also of a dual-function monomer. The cross-linker can form more rigid PCIMPs to improve the binding affinity and stabilize PCIMPs. It was attributed to cooperative hydrogen bonding, ionic bonding, and electrostatic interactions with the protein molecule. Moreover, it possesses an amino group that can easily interact with the substrate to enhance the catalytic activity of PAP/PCIMPs.

Physical characterization of MPs and PCIMPs

The fabrication of MPs is shown in Figure 4A, and is characterized by Fourier transform infrared (FT-IR) spectroscopy (Bruker TENSOR 27, Ettlingen, Germany). In the beginning, the bare Fe_3O_4 sample reflected only a few functional groups prominently, such as iron oxide and hydroxide groups. The broad peak at around 582 cm^{-1} was ascribed to the Fe-O, and a peak at 3,396 $cm.^{-1}$ (Figure 4A,a). Later, APTMS immobilized on Fe_3O_4 resulted in additional peaks around 1,032 cm^{-1}, 1,120 cm^{-1}, and 1,560 $cm.^{1}$ (C-N vibration), and a maximum at 3,420 cm^{-1}, which could be ascribed to the silanol group (Si-O) and NH_2 (Kurtan and Baykal, 2014; Farjadian et al., 2016; Yang Y. et al., 2018; Gao et al., 2018; Kanubaddi et al., 2021), respectively. These characteristic peaks of APTMS molecules indicate their successful coating on Fe_3O_4 (Figure 4A,b). In addition, the C-H stretching peaks at ~ 2,900 cm^{-1} are due to the presence in the alkyl chain of $APTMS_{43-44}$. Besides, no peak was observed at 1,739 cm^{-1}, indicating that C=O at both ends of the glutaraldehyde functional groups reacted with NH_2. This was attributed to the formation of a secondary amine. The unique peak at 3,414 cm^{-1} was ascribed to the N-H group (Figure 4A,c). Further, as seen in Figure 4A,d, the peak at 1,630 $cm.^{-1}$, ascribed as the characteristic peak of C=C, suggests successfully conjugated acrylation on MPs (Secundo, 2013; Farjadian et al., 2015; Kanubaddi et al., 2021).

Furthermore, the successful modification of the amine group on the surface of Fe_3O_4 was confirmed by the Ninhydrin test (Figure 4B), using our established method (Kuo et al., 2015). We treated the modified Fe_3O_4 samples with a 1 ml Ninhydrin solution at 60°C for 30 min. After the reaction, the MPs were centrifuged. The solvent was measured in UV-Vis, and the characteristic absorption of Ruhemann's purple was shown at 580 nm., which can be labeled as primary amine-modified on the surface of Fe_3O_4. However, when treated with secondary amine-modified Fe_3O_4 nanoparticles (Fe_3O_4@APTMS-GA), ninhydrin cannot produce Ruhemann's purple color (Kuo et al., 2015). When we compared Ruhemann's purple absorbent intensities, Fe_3O_4-APTMS showed high intensity, whereas Fe_3O_4@APTMS-GA and Fe_3O_4@APTMS-GA-acrylate samples showed low intensities. This shows that GA is successfully modified on the amine-modified Fe_3O_4 nanoparticles. The reactivity of ninhydrin with various surface-functionalized Fe_3O_4 samples provides further evidence to confirm successive chemical modifications on the Fe_3O_4 surfaces.

Eventually, the surface morphology of functionalized MPs and PCIMPs was subsequently characterized by Field Emission-Scanning

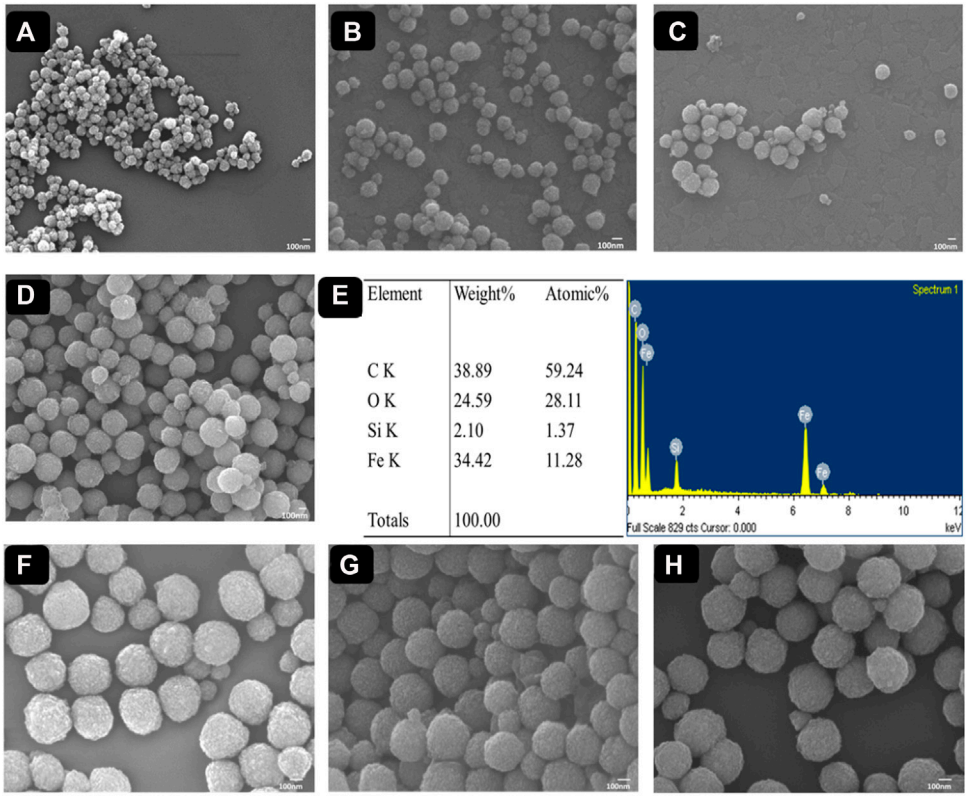

FIGURE 5
FE-SEM images of **(A)** Fe_3O_4, **(B)** Fe_3O_4@APTMS, **(C)** Fe_3O_4@APTMS-GA, and **(D)** Fe_3O_4@APTMS-GA-acrylate. The EDX spectrum image of **(E)** Fe_3O_4@APTMS-GA-acrylate. FE-SEM images of **(F)** PCIMPs$^{65-79}$, **(G)** PCIMPs$^{65-78}$, and **(H)** PCIMPs$^{66-79}$.

TABLE 2 Optimization of the formation of PCIMPs and affinity values toward PAP.

Formulation	Residue	Template (mM)	Monomers (mM)	Cross-linker (mM)	K_d (μM)	B_{max} (μM)	Yield (%)
PCIMPs$^{65-79}$	15	PAP$^{65-79}$ (~0.014)	—	5.6[a]	0.087	4.56	89
PCIMPs$^{65-78}$	14	PAP$^{65-78}$ (~0.014)	—	5.6[a]	0.17	0.52	77
PCIMPs$^{66-79}$	14	PAP$^{66-79}$ (~0.014)	—	5.6[a]	0.13	0.49	79.2
PCIMPs$^{66-78}$	13	PAP$^{66-78}$ (~0.014)	AA (0.24), Acr-L-His-NHBn (0.24), N-acryl tyramine (0.48)	0.84[b]	0.097	3.45	84.5
NIP	—	—	—	—	—-	—-	<5

Note: 100 mg of Fe_3O_4@APTMS-GA-acrylate was used in the preparation of PCIMPs. The volume of all polymerization solvents was 12 ml (TFE/H_2O = 7: 3). Monomers (AA, acrylamide, Acr-L-His-NHBn, and *N*-acryl tyramine), cross-linkers = [a]Metha-Asn-NHNH-Metha and [b]EBAA (*N*,*N*′-ethylene bisacrylamide). NIP, non-imprinted polymer. The purity of the template plays an important role in the binding affinity. For example, 13-mer peptide has a high purity of ~95% compared with the 14-mer (~88%). Therefore, 13-mer grafted PCIMPs$^{66-78}$ have higher binding affinity when compared to those of 14-mer grafted PCIMPs$^{66-79}$ and PCIMPs$^{65-78}$.

Electron Microscopy (FE-SEM) observations (JEOL JSM-7000F/ JEOL Ltd. Microscope from Tokyo, Japan). It was apparent from the FE-SEM images of Fe_3O_4 nanoparticles that their successively surface-functionalized samples were uniform, and their spherical shape can be seen in Figure 5. We determined the shape of MPs and PCIMPs based on the Feret diameter analysis measurement. The diameter of each particle was calculated on one axis of the particle. We also measured the size of the particle directly based on its FE-SEM image. The FE-SEM image shows that Fe_3O_4 is a spherical shape, with an average size of ~142 nm, as shown in Figure 5A. Moreover, APTMS coated on the surface of Fe_3O_4. An increase in particle size was observed, the average size being ~175 nm, indicating the

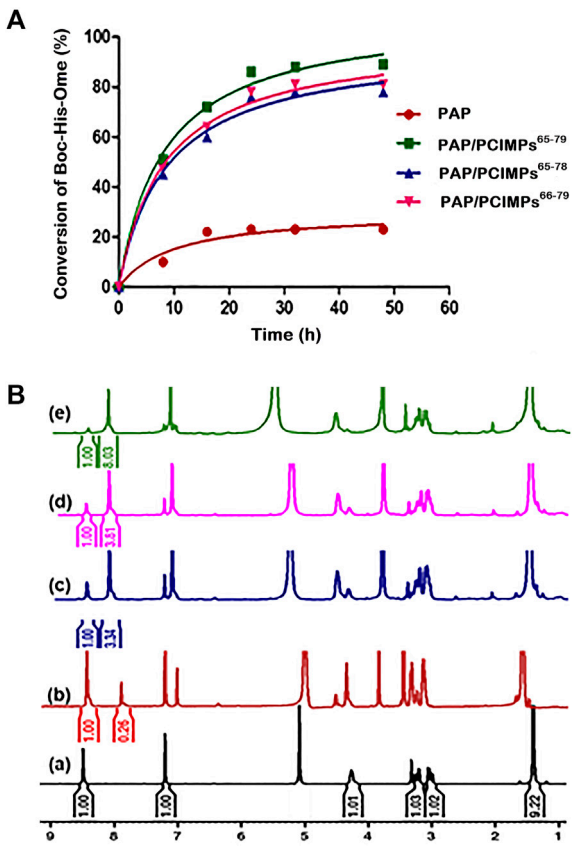

FIGURE 6
(A) Results of esterification of Boc-His-OH at 35°C at various intervals of reaction times. **(B)** ^{1}H-NMR spectra of **(a)** the starting material (Boc-His-OH), and the reaction mixture of the starting material and ester formed by **(b)** PAP, **(c)** PAP/PCIMPs$^{65-78}$, **(d)** PAP/PCIMPs$^{66-79}$, and **(e)** PAP/PCIMPs$^{65-79}$ (no of scans used = 32, solvent = CD_3OD).

successful immobilization of APTMS on Fe_3O_4, (Figure 5B). Further, immobilization of GA on modified MPs resulted in a uniform shape and size of ~228 nm (Figure 5C). Moreover, acrylate functionalization on modified MPs shows that the average size was ~260 nm (Figure 5D). The elemental analysis from the Energy-dispersive X-ray Spectroscopy (EDS) image (Figure 5E) showed that Fe_3O_4@APTMS-GA-acrylate possessed the highest content of the C element over Fe, Si, O, and N species. Successful modification of acrylate on modified MPs was also observed. Among all PCIMPs, as shown in Figures 5F–H, the 15-mer fabricated PCIMPs$^{65-79}$ were comparatively larger, around 375 nm. Other 14-mer fabricated PCIMPs$^{65-78}$ and PCIMPs$^{66-79}$ showed similar sizes (~360 nm.).

Fabrication of PCIMPs to capture PAP

To further improve the PCIMPs' fabrication, it was also necessary to create recognition sites that are complementary to protein recognition. The L-asparagine derivative (Metha-Asn-NHNH-Metha) was introduced as a cross-linker. The role of the cross-linker is to control the surface morphology of the polymer matrix and stabilize the imprinted binding sites, retaining their molecular recognition capability (Sellergren, 1999; Vasapollo et al., 2011). As shown in Supplementary Table S1, PCIMPs were fabricated with different concentrations of cross-linker and template. As the amount of the cross-linker and template increased, it helped to increase the binding affinity toward the mother protein. Meanwhile, adding a cross-linker formed more rigid PCIMPs and resulted in a more stable catalyst.

The PCIMPs-grafted 15- and 14-mer peptides were then tested for their ability to bind their mother protein, as described previously (Tai et al., 2012). As shown in Table 2, it was found that PCIMPs$^{65-79}$ had more significant binding affinities, while the other two, PCIMPs$^{65-78}$ and PCIMPs$^{66-79}$, exhibited lower affinity. It was previously reported that the higher the number of residues in the template, the better binding affinity was observed (Tai et al., 2011; Kanubaddi et al., 2021). Accordingly, for PCIMP-grafted 15-mer peptides, the best K_d value was 0.087 μM, and it had a better affinity than the PCIMP-griated 14-mer peptides. Interestingly, among PCIMP-grafted 14-mer peptides, PCIMPs$^{66-79}$ had the best K_d value (0.13 μM), whereas PCIMPs$^{65-78}$ exhibited the lowest value (0.17 μM). Moreover, our developed PCIMPs generated binding sites that complemented protein recognition and consequently produced higher affinity toward targeted protein PAP. The elegant helical cavities stamping approach was compared with the other MIPs-grafted methods, based on the binding affinities and absorption time. Our results showed a higher affinity of PAP to PCIMPs$^{65-79}$ than other observed MIPs-grafting approaches (Yang et al., 2016; Xu et al., 2018; Boitard et al., 2019).

The traditional synthetic method developed for 13-mer grafted PCIMPs$^{66-78}$ was also compared with the fabricated PCIMPs with the cross-linker to detect PAP. In this preparation method, to improve the fabrication of PCIMPs$^{66-78}$, we introduced two monomers, chiral histidine derivative (Acr-L-His-NHBn) and *N*-acryl tyramine. Interestingly, as displayed in Table 2, we observed that 13-mer-grafted PCIMPs$^{66-78}$ led to higher affinity toward the analyte (K_d = 0.097 μM) when compared to fabricated 14-mer-grafted PCIMPs using the cross-linker (Metha-Asn-NHNH-Metha), i.e., PCIMPs$^{65-78}$ (K_d = 0.17 μM) and PCIMPs$^{66-79}$ (K_d = 0.13 μM). Moreover, the traditional formulated 13-mer-grafted PCIMPs had a better affinity toward PAP than the 14-mer-grafted PCIMPs using the cross-linker (Tai et al., 2011). Furthermore, monomers such as Acr-L-His-NHBn and *N*-acryl tyramine helped to strengthen affinity for PAP and helped harden the surface of the polymer matrix on PCIMPs,$^{66-78}$ and reduced swelling while imprinting integrity (Yang et al., 2013). In addition, adding the cross-linker (EBBA) formed more rigid PCIMPs$^{66-78}$ and produced a more stable catalytic activity (Tai et al., 2011). There was also a tendency for longer peptide residues to sustain a stable

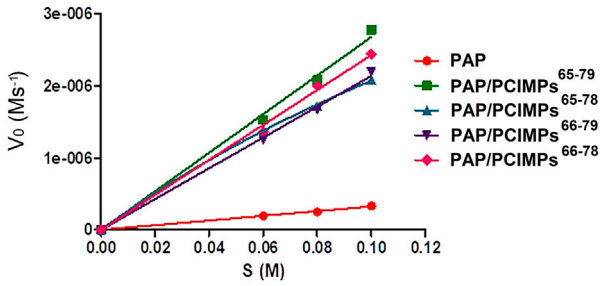

FIGURE 7
Michaelis–Menten plot of PAP and PAP/PCIMPs obtained with various concentrations of Boc-His-OH.

conformation throughout the polymerization process. For instance, 15 mer-grafted PCIMPs$^{65–79}$ fabricated with Metha-Asn-NHNH-Metha showed a higher binding affinity toward PAP compared to the 13-mer and 14-mer PCIMPs. Therefore, fabricated PCIMPs$^{65–79}$ using a cross-linker resulted in better protein binding and higher catalytic performance.

Evaluation of esterification activity of PAP and PAP/PCIMPs by using ^{1}H-NMR

The maximum conversion of our PAP/PCIMPs was achieved in 24 hours (Figure 6A). Thus, the same duration (i.e., 24 hours) was chosen for the study of PAP/PCIMPs. The performance of the fabricated PAP/PCIMPs$^{65–79}$ in catalyzing the esterification of *N*-protected amino acid was compared with the previous results. Accordingly, PAP/celite catalyzed esterification of *N*-protected amino acids in various organic solvents for 4 days. The desired product was obtained by silica gel chromatography, and purified esters were measured with ^{1}H NMR. Their highest conversion was 71%, and reusability was not measured in this study (Shih et al., 1997). In another study, PAP was immobilized separately with eight kinds of adsorbents in a buffer solution. Among them, Sephadex G-50 was found to be the best adsorbent for immobilization of PAP. Accordingly, the PAP/Sephadex G-50 catalyzed esterification of *N*-substituted amino acids in MeOH for 2 days. Although this method shows a significant yield in esterification compared with other studies, PAP/Sephadex G-50 was difficult to reuse (Tai et al., 1989). Upon a comprehensive evaluation of *N*-protected amino acid esterification, the PCIMPs approach provided significant advantages over other methods. It was evident that the helical cavities created recognition sites on the MP surface and tightly bound the enzyme. As a result, it demonstrated better catalytic activity for esterification in comparison with previously conducted studies. The best catalytic performance of PAP/PCIMPs$^{65–79}$ for the esterification of Boc-L-His-OH was 89% in 24 h.

The data suggested a trend that initially crude PAP catalyzed hydrolysis of substrates rapidly. However, due to the amount of substrate decreasing, the rate of hydrolysis gradually decreased after 8 h; the reaction reached equilibrium after 48 h. The PAP reaction was found to produce the lowest final yield (20.6%), which can be attributed to certain protein instability features in organic solvents, thereby decreasing enzyme activity (Stepankova et al., 2013). As for PAP/PCIMPs, the highest yield (89%) was attained with PAP/PCIMPs$^{65–79}$ in 24 h. The performances of PAP/PCIMPs$^{66-79}$ and PAP/PCIMPs$^{65-78}$ were lower, at 79.2% and ~77%, respectively. This shows that PCIMPs' imprinted materials are highly stable in organic solvents when compared to crude PAP, and enhance the yield of esterification for up to 48 h. In comparison, the yield catalyzed by traditional formulated PAP/PCIMPs$^{66-78}$ was 84.5% (Supplementary Figure S3), higher than those of PAP/PCIMPs$^{66-79}$ and PAP/PCIMPs$^{65-78}$, but 4% lower than that of PAP/PCIMPs$^{65–79}$.

To measure the reaction yield accurately, esterification yields were characterized using ^{1}H-NMR. The spectra were acquired at a frequency of 300 MHz on a Bruker (from Billerica, Massachusetts, United States) and Ultrashield (9.4 T) spectrometer using a 5-mm BBo probe at 296.2 K. To calculate the conversion of Boc-L-His-OH to Boc-L-His-OMe, the ratio between the integral relevant to the hydrogen group of the imidazole ring of Boc-L-His-OH and corresponding to the hydrogen group of Boc-L-His-OMe was compared to calculate the yield of the reaction based on Equation 2. As shown in Figure 6B,a, the chemical displacement at 8.5 ppm was a hydrogen group of the imidazole of the original material (Boc-L-His-OH), while the proton value was equal to 1. The imidazole of the product (Boc-L-His-OMe) was similar, at 8 ppm. The finding of a peak at 3.8 ppm was representative of α proton.

Kinetic parameters of PAP and PAP/PCIMPs

The Michaelis–Menten equation was applied to determine the enzyme kinetic parameters for PAP catalyzed reaction. In the present study, kinetic parameters of PAP and PAP/PCIMPs were determined by changing the Boc-L-His-OH concentration from 0.06 to 0.1 M. It was then calculated using the Michaelis–Menten plot, as shown in Figure 7.

As shown in Table 3, the V_{max} values were found to be 0.33 and 3.05 μM s^{-1} for PAP and PAP/PCIMPs$^{65–79}$, while the performances of PAP/PCIMPs$^{65-78}$ and PAP/PCIMPs$^{66–79}$ were at 2.08 μM s^{-1} and 2.2 μM s^{-1}, respectively. The K_m of PAP was found to be the highest at 5.5 × 10^{-2} M. The lowest K_m value was attained with PAP/PCIMPs$^{65–79}$ as 5 × 10^{-2} M, whereas the K_m value for PAP/PCIMPs$^{65-78}$ and PAP/PCIMPs$^{66–79}$ were 5.2 × 10^{-2} and 5.3 × 10^{-2} M, respectively. The K_m value in PAP/PCIMPs was lower than that in the native enzyme. Consequently, PAP/PCIMPs have a greater affinity for the substrate than the PAP (Chen et al., 1998; Meridor and Gedanken, 2013). According to our calculation, PAP/PCIMPs possess the higher V_{max} value and the

TABLE 3 Kinetic parameters obtained from the Michaelis–Menten kinetics plot.

	PAP	PAP/PCIMPs$^{65-79}$	PAP/PCIMPs$^{65-78}$	PAP/PCIMPs$^{66-79}$	PAP/PCIMPs$^{66-78}$
V_{max} (M·s^{-1})	3.3×10^{-7}	3.05×10^{-6}	2.08×10^{-6}	2.2×10^{-6}	2.4×10^{-6}
K_m (M)	5.5×10^{-2}	5×10^{-2}	5.2×10^{-2}	5.3×10^{-2}	5.3×10^{-2}
k_{cat} (s^{-1})	7.8×10^{-4}	$\mathbf{1.1 \times 10^{-1}}$	6.8×10^{-3}	7×10^{-2}	7.2×10^{-2}
k_{cat}/K_m (M^{-1}·s^{-1})	0.014	2	1.3	1.32	1.35

Note: 13-mer grafted PCIMPs$^{66-78}$ were prepared using Acr-L-His-NHBn and *N*-acryl tyramine monomers to help harden the polymer matrix's surface and form a strong affinity for the PAP compared to the 14-mer-grafted PCIMPs. Furthermore, adding a cross-linker (EBBA) developed more rigid PCIMPs$^{66-78}$ and produced a more stable catalytic activity. Therefore, PCIMPs$^{66-78}$ contain better esterification kinetic values than those of PCIMPs$^{66-79}$ and PCIMPs$^{65-78}$. PAP, papain; PCIs, peptide conformational imprints; PCIMPs, peptide conformational imprint magnetic particles; PCIMPs66-78, PCIMPs-grafted 13-mer peptide; PCIMPs65-78 and PCIMPs66-79, PCIMPs-grafted 14-mer peptides; PCIMPs65-79, PCIMPs-grafted 15-mer peptide.

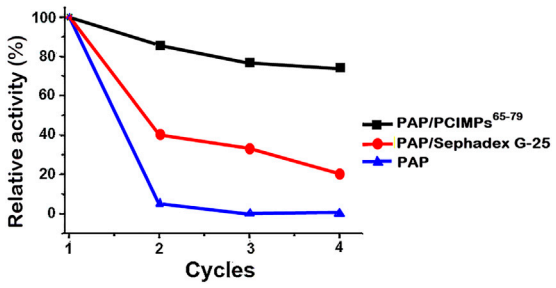

FIGURE 8
Reusability of PAP/PCIMPs$^{65-79}$, PAP/Sephadex-G-25, and PAP.

lower K_m value. Among all PAP/PCIMPs, PAP/PCIMPs$^{65-79}$ have the best kinetic parameters to effectively promote the activity of PAP after immobilization (Sun et al., 2018).

As shown in Table 3, the turnover (k_{cat}) value of PAP (7.8×10^{-4} s^{-1}) was lower than those of PAP/PCIMPs$^{65-79}$ (1.1×10^{-1} s^{-1}), PAP/PCIMPs$^{65-78}$ (6.8×10^{-2} s^{-1}), and PAP/PCIMPs$^{66-79}$ (7×10^{-2} s^{-1}), which could be attributed to the higher catalytic efficiency of immobilized PAP than the free enzyme. The higher k_{cat} value was possible due to the favorable interaction between the carrier (PCIMPs) and the enzyme (PAP), which addressed the PAP fold into the optimized conformation on the PCIMPs' surface. Among all PAP/PCIMPs, the highest k_{cat} value for PAP/PCIMPs$^{65-79}$ was 1.1×10^{-1} s^{-1} ·, and were 6.8×10^{-2}, and 7×10^{-2} s^{-1} or PAP/PCIMPs$^{65-78}$· and PAP/PCIMPs$^{66-79}$, respectively. Similarly, the catalytic efficiency (k_{cat}/K_m) value of the PAP was 0.014 M^{-1} s^{-1}, whereas it was 2 M^{-1} s^{-1} for PAP/PCIMPs$^{65-79}$;PAP/PCIMPs$^{65-78}$ and PAP/PCIMPs$^{66-79}$ had similar values (~1.3 M^{-1} s^{-1}). The values of all PAP/PCIMPs were higher than that of the free PAP. This is probably because PAP/PCIMPs can maintain enzymatic activity and preserve favorable enzyme conformations (Wong et al., 2017; Yang L. et al., 2018; Li et al., 2019).

Moreover, we examined the kinetic parameters of traditionally formulated PAP/PCIMPs$^{66-78}$ by increasing the Boc-L-His-OH concentration from 0.6, 0.8, and 0.1 M to 0.66, 0.88, and 0.11 M. As shown in Table 3, the V_{max} value of PAP/PCIMPs$^{66-78}$ was 2.4 μM s^{-1}, which was higher than those of PAP/PCIMPs$^{65-78}$ (2.08 μM s^{-1}), and PAP/PCIMPs$^{66-79}$ (2.2 μM s^{-1}) fabricated with Metha-Asn-NHNH-Metha. Thus, evidence supporting higher substrate concentrations increased considerably, while reaction rate increased significantly, changing the kinetic parameters. Thus, we can conclude that it appears worthwhile to increase substrates for PAP/PCIMPs$^{66-78}$.

Reusability

Another promising feature of PCIMPs is the rebinding of proteins and reusability. Once the PCIMPs are used for the application, the imprinted material used should be desorpted and reused. This will result in the sustainable repeated use of the material.

To demonstrate regeneration ability and reusability of imprinted materials of PCIMPs$^{65-79}$, adsorption–desorption cycles were repeated four times using the same imprinted material, as shown in Figure 8. The partially dried imprinted materials of PCIMPs containing methanol were blow-dried in a fume hood, and the damp PCIMPs-imprinted material was used for subsequent runs. The resulting product was preserved at 0°C for future use.

The amount of Boc-L-His-OMe-produced yield in the first cycle was set as 100%. The yield of Boc-L-His-OMe slightly declined after the first reuse. However, the yield remained around 80% in the last two cycles, proving that imprinted polymer particles can be regenerated and reused. Additionally, PAP/PCIMPs exhibited stable catalytic activity in the reusability studies, compared with the PAP/Sephadex G-25 and PAP. PAP/Sephadex G-25 declined to a 20% yield after the fourth cycle, and PAP did not show any significant reusability. Long-term stability and reusability of PAP/PCIMPs were high compared to the PAP/Sephadex G-25 and PAP.

Conclusion

In summary, we succeeded in synthesizing a new chiral cross-linker, Metha-Asn-NHNH-Metha, from L-asparagine. Fabrication of the helical peptides using this cross-linker to form PCIMPs was accomplished by molecular imprinting technology. Among all the helical peptides used, 15-mer PCIMPs[65–79] gained the highest binding affinity toward PAP and achieved the highest catalytic activity. Therefore, the fabrication of PCIMPs can provide an easy route to develop specific protein binding/adsorption and maintain enzyme catalytic activity.

Although trypsin flexibility interfered with the inhibitive effect on capturing the α-helix region during hydrolysis (Kanubaddi et al., 2021), PCIMPs were found to improve papain stability and robustness for esterification. This could be because the amount of water in esterification is much reduced in the reaction medium resulting in greater stability/activity of PAP/PCIMPs than PAP itself. The reuse displayed a small decrease in catalytic activity after four consecutive usages of the immobilized enzyme. Therefore, we conclude that our investigations will lead to more applications of these types of nanobiocatalysts in the future.

Data availability statement

The original contributions presented in the study are included in the article/Supplementary Material. Further inquiries can be directed to the corresponding authors.

Author contributions

KR, C-LY, and P-YH contributed to the execution of experiments, data analysis, and interpretation. KR, C-YL, D-FT, and C-HL contributed to the review and editing. C-YL, D-FT, and C-HL contributed to the study concept and design, data analysis and interpretation, securing of funding, and writing the manuscript. All authors have read and agreed to the published version of the draft of the manuscript.

Funding

This work is partially supported by the Taiwan Ministry of Science and Technology (MOST 106-2113-M-259-005 and 109-2221-E-182-008-MY3).

Conflict of interest

The authors declare that the research was conducted in the absence of any commercial or financial relationships that could be construed as a potential conflict of interest.

Publisher's note

All claims expressed in this article are solely those of the authors and do not necessarily represent those of their affiliated organizations, or those of the publisher, the editors, and the reviewers. Any product that may be evaluated in this article, or claim that may be made by its manufacturer, is not guaranteed or endorsed by the publisher.

Supplementary material

The Supplementary Material for this article can be found online at: https://www.frontiersin.org/articles/10.3389/fbioe.2022.943751/full#supplementary-material

References

Anwar, M., Rasul, M. G., and Ashwath, N. (Editors) (2017). *IEEE 7th International Conference on Power and Energy Systems (ICPES) - optimization of biodiesel production process from papaya (*Carica papaya*) seed oil.* Toronto, Canada: IEEE. pp 131-134.

Basso, A., and Serban, S. (2019). Industrial applications of immobilized enzymes—a review. *Mol. Catal.* 479, 110607. doi:10.1016/j.mcat.2019.110607

Belyaeva, E. A., Gra, D. V., and Eremeev, N. L. (2002). On the mechanism of interaction of organic solvents with the active site of alpha-chymotrypsin. *Biochemistry.* 67 (9), 1032–1036. doi:10.1023/a:1020530220774

Bjelić, A., Hočevar, B., Grilc, M., Novak, U., and Likozar, B. (2022). A review of sustainable lignocellulose biorefining applying (natural) deep eutectic solvents (DESs) for separations, catalysis and enzymatic biotransformation processes. *Rev. Chem. Eng.* 38 (3), 243–272. doi:10.1515/revce-2019-0077

Boitard, C., Lamouri, A., Ménager, C., and Griffete, N. (2019). Whole protein imprinting over magnetic nanoparticles using photopolymerization. *ACS Appl. Polym. Mat.* 1 (5), 928–932. doi:10.1021/acsapm.9b00109

Bossi, A. M., Sharma, P. S., Montana, L., Zoccatelli, G., Laub, O., Levi, R., et al. (2012). Fingerprint-imprinted polymer: Rational selection of peptide epitope templates for the determination of proteins by molecularly imprinted polymers. *Anal. Chem.* 84 (9), 4036–4041. doi:10.1021/ac203422r

Cajnko, M. M., Novak, U., Grilc, M., and Likozar, B. (2020). Enzymatic conversion reactions of 5-hydroxymethylfurfural (HMF) to bio-based 2, 5-diformylfuran (DFF) and 2, 5-furandicarboxylic acid (FDCA) with air: Mechanisms, pathways and synthesis selectivity. *Biotechnol. Biofuels* 13, 66. doi:10.1186/s13068-020-01705-z

Cajnko, M. M., Oblak, J., Grilc, M., and Likozar, B. (2021). Enzymatic bioconversion process of lignin: Mechanisms, reactions and kinetics. *Bioresour. Technol.* 340, 125655. doi:10.1016/j.biortech.2021.125655

Cantacuzène, D., Pascal, F., and Guerreiro, C. (1987). Synthesis of amino acid esters by papain. *Tetrahedron* 43 (8), 1823–1826. doi:10.1016/s0040-4020(01)81493-9

Cao, S-L., Xu, H., Li, X-H., Lou, W-Y., and Zong, M-H. (2015). Papain@Magnetic nanocrystalline cellulose nanobiocatalyst: A highly efficient biocatalyst for dipeptide biosynthesis in deep eutectic solvents. *ACS Sustain. Chem. Eng.* 3 (7), 1589–1599. doi:10.1021/acssuschemeng.5b00290

Chen, J-P., Sun, Y-M., and Chu, D-H. (1998). Immobilization of alpha-amylase to a composite temperature-sensitive membrane for starch hydrolysis. *Biotechnol. Prog.* 14 (3), 473–478. doi:10.1021/bp9800384

Chou, C-Y., Lin, C-Y., Wu, C-H., and Tai, D-F. (2020). Sensing HIV protease and its inhibitor using "helical epitope"-imprinted polymers. *Sensors (Basel)* 20 (12), 3592. doi:10.3390/s20123592

Collins, J. M., Porter, K. A., Singh, S. K., and Vanier, G. S. (2014). High-efficiency solid phase peptide synthesis (HE-SPPS). *Org. Lett.* 16 (3), 940–943. doi:10.1021/ol4036825

de Beer, R. J., Zarzycka, B., Mariman, M., Amatdjais-Groenen, H. I., Mulders, M. J., Quaedflieg, P. J., et al. (2012). Papain-specific activating esters in aqueous dipeptide synthesis. *ChemBioChem* 13 (9), 1319–1326. doi:10.1002/cbic.201200017

Diltemiz, S. E., Hür, D., Ersöz, A., Denizli, A., and Say, R. (2009). Designing of MIP based QCM sensor having thymine recognition sites based on biomimicking DNA approach. *Biosens. Bioelectron. X.* 25 (3), 599–603. doi:10.1016/j.bios.2009.01.032

Ding, S., Xing, Y., Radosz, M., and Shen, Y. (2006). Magnetic nanoparticle supported catalyst for atom transfer radical polymerization. *Macromolecules* 39 (19), 6399–6405. doi:10.1021/ma061062y

Farjadian, F., Ghasemi, S., and Mohammadi-Samani, S. (2016). Hydroxyl-modified magnetite nanoparticles as novel carrier for delivery of methotrexate. *Int. J. Pharm. X.* 504 (1-2), 110–116. doi:10.1016/j.ijpharm.2016.03.022

Farjadian, F., Hosseini, M., Ghasemi, S., and Tamami, B. (2015). Phosphinite-functionalized silica and hexagonal mesoporous silica containing palladium nanoparticles in heck coupling reaction: Synthesis, characterization, and catalytic activity. *RSC Adv.* 5 (97), 79976–79987. doi:10.1039/c5ra16131b

Gao, Z., Yi, Y., Zhao, J., Xia, Y., Jiang, M., Cao, F., et al. (2018). Co-immobilization of laccase and TEMPO onto amino-functionalized magnetic Fe3O4 nanoparticles and its application in acid fuchsin decolorization. *Bioresour. Bioprocess.* 5 (1), 27. doi:10.1186/s40643-018-0215-7

Gerdon, A. E., Wright, D. W., and Cliffel, D. E. (2005). Quartz crystal microbalance detection of glutathione-protected nanoclusters using antibody recognition. *Anal. Chem.* 77 (1), 304–310. doi:10.1021/ac048953t

Hoarau, M., Badieyan, S., and Marsh, E. N. G. (2017). Immobilized enzymes: Understanding enzyme - surface interactions at the molecular level. *Org. Biomol. Chem.* 15 (45), 9539–9551. doi:10.1039/c7ob01880k

Homaei, A. (2015). Enhanced activity and stability of papain immobilized on CNBr-activated sepharose. *Int. J. Biol. Macromol.* 75, 373–377. doi:10.1016/j.ijbiomac.2015.01.055

Homaei, A. A., Sajedi, R. H., Sariri, R., Seyfzadeh, S., and Stevanato, R. (2010). Cysteine enhances activity and stability of immobilized papain. *Amino Acids* 38 (3), 937–942. doi:10.1007/s00726-009-0302-3

Homaei, A. A., Sariri, R., Vianello, F., and Stevanato, R. (2013). Enzyme immobilization: An update. *J. Chem. Biol.* 6 (4), 185–205. doi:10.1007/s12154-013-0102-9

Jeong, J., Lee, S-Y., and Hur, W. (2011). Composition variation of papain-catalyzed esterification of a fibroin peptide mixture. *Biotechnol. Bioprocess Eng.* 16 (4), 654–660. doi:10.1007/s12257-011-0076-9

Kankala, R. K., Zhang, H., Liu, C-G., Kanubaddi, K. R., Lee, C-H., Wang, S-B., et al. (2019). Metal species–encapsulated mesoporous silica nanoparticles: Current advancements and latest breakthroughs. *Adv. Funct. Mat.* 29 (43), 1902652. doi:10.1002/adfm.201902652

Kanubaddi, K. R., Huang, P-Y., Chang, Y-L., Wu, C-H., Li, W., Kankala, R. K., et al. (2021). Deviation of trypsin activity using peptide conformational imprints. *Nanomater. (Basel)* 11 (2), 334. doi:10.3390/nano11020334

Kuo, Y-M., Kuthati, Y., Kankala, R. K., Wei, P-R., Weng, C-F., Liu, C-L., et al. (2015). Layered double hydroxide nanoparticles to enhance organ-specific targeting and the anti-proliferative effect of cisplatin. *J. Mat. Chem. B* 3 (17), 3447–3458. doi:10.1039/c4tb01989j

Kurtan, U., and Baykal, A. (2014). Fabrication and characterization of Fe3O4@APTES@PAMAM-Ag highly active and recyclable magnetic nanocatalyst: Catalytic reduction of 4-nitrophenol. *Mat. Res. Bull.* 60, 79–87. doi:10.1016/j.materresbull.2014.08.016

Li, R., Yang, J., Xiao, Y., and Long, L. (2019). *In vivo* immobilization of an organophosphorus hydrolyzing enzyme on bacterial polyhydroxyalkanoate nanogranules. *Microb. Cell Fact.* 18 (1), 166. doi:10.1186/s12934-019-1201-2

Liang, X., Liu, Y., Wen, K., Jiang, W., and Li, Q. (2021). Immobilized enzymes in inorganic hybrid nanoflowers for biocatalytic and biosensing applications. *J. Mat. Chem. B* 9 (37), 7597–7607. doi:10.1039/d1tb01476e

Lin, C-Y., Tsai, S-H., and Tai, D-F. (2019). Detection of oxytocin, atrial natriuretic peptide, and brain natriuretic peptide using novel imprinted polymers produced with amphiphilic monomers. *J. Pept. Sci.* 25 (3), e3150. doi:10.1002/psc.3150

Llerena-Suster, C. R., José, C., Collins, S. E., Briand, L. E., and Morcelle, S. R. (2012). Investigation of the structure and proteolytic activity of papain in aqueous miscible organic media. *Process Biochem.* 47 (1), 47–56. doi:10.1016/j.procbio.2011.10.003

Marathe, S. J., Shah, N. N., and Singhal, R. S. (2020). Enzymatic synthesis of fatty acid esters of trehalose: Process optimization, characterization of the esters and evaluation of their bioactivities. *Bioorg. Chem.* 94, 103460. doi:10.1016/j.bioorg.2019.103460

Meridor, D., and Gedanken, A. (2013). Preparation of enzyme nanoparticles and studying the catalytic activity of the immobilized nanoparticles on polyethylene films. *Ultrason. Sonochem.* 20 (1), 425–431. doi:10.1016/j.ultsonch.2012.06.005

Mohamad, N. R., Marzuki, N. H. C., Buang, N. A., Huyop, F., and Wahab, R. A. (2015). An overview of technologies for immobilization of enzymes and surface analysis techniques for immobilized enzymes. *Biotechnol. Biotechnol. Equip.* 29 (2), 205–220. doi:10.1080/13102818.2015.1008192

Morcelle, S. R., Barberis, S., Priolo, N., Caffini, N. O., and Clapés, P. (2006). Comparative behaviour of proteinases from the latex of Carica papaya and Funastrum clausum as catalysts for the synthesis of Z-Ala-Phe-OMe. *J. Mol. Catal. B Enzym.* 41 (3), 117–124. doi:10.1016/j.molcatb.2006.05.007

Nguyen, H. H., Lee, S. H., Lee, U. J., Fermin, C. D., and Kim, M. (2019). Immobilized enzymes in biosensor applications. *Mater. (Basel)* 12 (1), 121. doi:10.3390/ma12010121

Prabhakar, S., Vivès, T., Ferrières, V., Benvegnu, T., Legentil, L., Lemiègre, L., et al. (2017). A fully enzymatic esterification/transesterification sequence for the preparation of symmetrical and unsymmetrical trehalose diacyl conjugates. *Green Chem.* 19 (4), 987–995. doi:10.1039/c6gc02680j

Secundo, F. (2013). Conformational changes of enzymes upon immobilisation. *Chem. Soc. Rev.* 42 (15), 6250. doi:10.1039/c3cs35495d

Sellergren, B. (1999). Polymer- and template-related factors influencing the efficiency in molecularly imprinted solid-phase extractions. *TrAC Trends Anal. Chem.* 18 (3), 164–174. doi:10.1016/s0165-9936(98)00117-4

Sheldon, R. A. (2011). Characteristic features and biotechnological applications of cross-linked enzyme aggregates (CLEAs). *Appl. Microbiol. Biotechnol.* 92 (3), 467–477. doi:10.1007/s00253-011-3554-2

Shih, I-L., Chiu, L-C., Lai, C-T., Liaw, W-C., and Tai, D-F. (1997). Enzymes catalyzed esterification of N-protected amino acids with secondary alcohols. *Biotechnol. Lett.* 19 (9), 857–859. doi:10.1023/a:1018329402408

Singh, R. K., Tiwari, M. K., Singh, R., and Lee, J. K. (2013). From protein engineering to immobilization: Promising strategies for the upgrade of industrial enzymes. *Int. J. Mol. Sci.* 14 (1), 1232–1277. doi:10.3390/ijms14011232

Stepankova, V., Bidmanova, S., Koudelakova, T., Prokop, Z., Chaloupkova, R., Damborsky, J., et al. (2013). Strategies for stabilization of enzymes in organic solvents. *ACS Catal.* 3 (12), 2823–2836. doi:10.1021/cs400684x

Stevenson, D. E., and Storer, A. C. (1991). Papain in organic solvents: Determination of conditions suitable for biocatalysis and the effect on substrate specificity and inhibition. *Biotechnol. Bioeng.* 37 (6), 519–527. doi:10.1002/bit.260370605

Sun, X., Zhu, W., and Matyjaszewski, K. (2018). Protection of opening lids: Very high catalytic activity of lipase immobilized on core-shell nanoparticles. *Macromolecules* 51 (2), 289–296. doi:10.1021/acs.macromol.7b02361

Tai, D-F., Fu, S-L., Chuang, S-F., and Tsai, H. (1989). Papain catalyzed esterification in polar organic solvents. *Biotechnol. Lett.* 11 (3), 173–176. doi:10.1007/bf01026051

Tai, D-F., Ho, Y-F., Wu, C-H., Lin, T-C., Lu, K-H., Lin, K-S., et al. (2011). Artificial-epitope mapping for CK-MB assay. *Analyst* 136 (11), 2230. doi:10.1039/c0an00919a

Tai, D-F., Lin, Y-F., Lu, K-H., Chen, G-Y., and Shu, H-C. (2012). A direct immersion system for peptide enrichment. *J. Chin. Chem. Soc.* 59 (3), 338–344. doi:10.1002/jccs.201100635

Tai, D-F. (2003). Enzymatic peptide synthesis: From the substrate point of view. *Curr. Org. Chem.* 7, 515–554. doi:10.2174/1385272033486819

Vasapollo, G., Sole, R. D., Mergola, L., Lazzoi, M. R., Scardino, A., Scorrano, S., et al. (2011). Molecularly imprinted polymers: Present and future prospective. *Int. J. Mol. Sci.* 12 (9), 5908–5945. doi:10.3390/ijms12095908

Wong, D-E., Senecal, K. J., and Goddard, J. M. (2017). Immobilization of chymotrypsin on hierarchical nylon 6, 6 nanofiber improves enzyme performance. *Colloids Surfaces B Biointerfaces* 154, 270–278. doi:10.1016/j.colsurfb.2017.03.033

Xu, J., Prost, E., Haupt, K., and Sum Bui, TseB. (2018). Direct and sensitive determination of trypsin in human urine using a water-soluble signaling fluorescent molecularly imprinted polymer nanoprobe. *Sensors Actuators B Chem.* 258, 10–17. doi:10.1016/j.snb.2017.11.077

Yang, C., Yan, X., Guo, H., and Fu, G. (2016). Synthesis of surface protein-imprinted nanoparticles endowed with reversible physical cross-links. *Biosens. Bioelectron. X.* 75, 129–135. doi:10.1016/j.bios.2015.08.033

Yang, H-H., Lu, K-H., Lin, Y-F., Tsai, S-H., Chakraborty, S., Zhai, W-J., et al. (2013). Depletion of albumin and immunoglobulin G from human serum using epitope-imprinted polymers as artificial antibodies. *J. Biomed. Mat. Res. A* 101 (7), 1935–1942. doi:10.1002/jbm.a.34491

Yang, L., Tian, J., Meng, J., Zhao, R., Li, C., Ma, J., et al. (2018). Modification and characterization of Fe3O4 nanoparticles for use in adsorption of alkaloids. *Molecules* 23 (3), 562. doi:10.3390/molecules23030562

Yang, Q., Zhu, Y., Luo, B., Lan, F., Wu, Y., Gu, Z., et al. (2017). pH-Responsive magnetic nanospheres for the reversibly selective capture and release of glycoproteins. *J. Mat. Chem. B* 5 (6), 1236–1245. doi:10.1039/c6tb02662a

Yang, Y., Wang, S., Zhou, Z., Zhang, R., Shen, H., Song, J., et al. (2018). Enhanced reusability and activity: DNA directed immobilization of enzyme on polydopamine modified magnetic nanoparticles. *Biochem. Eng. J.* 137, 108–115. doi:10.1016/j.bej.2018.05.019

Zaks, A., and Klibanov, A. M. (1985). Enzyme-catalyzed processes in organic solvents. *Proc. Natl. Acad. Sci. U. S. A.* 82 (10), 3192–3196. doi:10.1073/pnas.82.10.3192

frontiers | Frontiers in Bioengineering and Biotechnology

TYPE Original Research
PUBLISHED 06 October 2022
DOI 10.3389/fbioe.2022.1005954

OPEN ACCESS

EDITED BY
Oommen Varghese,
Uppsala University, Sweden

REVIEWED BY
Venkatesan Jayachandran,
Yenepoya University, India
Wujie Zhang,
Milwaukee School of Engineering,
United States

*CORRESPONDENCE
Dan Meng,
orangeate2002@163.com
Qingsong Jiang,
qsjiang@ccmu.edu.cn

SPECIALTY SECTION
This article was submitted to Biomaterials, a section of the journal Frontiers in Bioengineering and Biotechnology

RECEIVED 28 July 2022
ACCEPTED 26 September 2022
PUBLISHED 06 October 2022

CITATION
Yuan Y, Shen L, Liu T, He L, Meng D and Jiang Q (2022), Physicochemical properties of bone marrow mesenchymal stem cells encapsulated in microcapsules combined with calcium phosphate cement and their ectopic bone formation.
Front. Bioeng. Biotechnol. 10:1005954.
doi: 10.3389/fbioe.2022.1005954

Physicochemical properties of bone marrow mesenchymal stem cells encapsulated in microcapsules combined with calcium phosphate cement and their ectopic bone formation

Yafei Yuan[1], Lipei Shen[1], Tiankun Liu[2], Lin He[1], Dan Meng[1]* and Qingsong Jiang[1]*

[1]Beijing Stomatological Hospital, School of Stomatology, Capital Medical University, Beijing, China, [2]Biomanufacturing Center, Department of Mechanical Engineering, Tsinghua University, Beijing, China

Calcium phosphate bone cement (CPC) serves as an excellent scaffold material for bone tissue engineering owing to its good biocompatibility, injectability, self-setting property and three-dimensional porous structure. However, its clinical use is limited due to the cytotoxic effect of its setting reaction on cells and difficulties in degradation into bone. In this study, bone marrow mesenchymal stem cells (BMSCs) were encapsulated in alginate chitosan alginate (ACA) microcapsules and compounded with calcium phosphate bone cement. Changes in the compressive strength, porosity, injectability and collapsibility of CPC at different volume ratios of microcapsules were evaluated. At a 40% volume ratio of microcapsules, the composite scaffold displayed high porosity and injectability with good collapsibility and compressive strength. Cell live/dead double staining, Cell Counting Kit-8 (CCK-8) assays and scanning electron microscopy were used to detect the viability, proliferation and adhesion of cells after cell microcapsules were combined with CPC. The results revealed that cells protected by microcapsules proliferated and adhered better than those that were directly combined with CPC paste, and cell microcapsules could effectively form macropores in scaffold material. The composite was subsequently implanted subcutaneously on the backs of nude mice, and ectopic osteogenesis of the scaffold was detected *via* haematoxylin-eosin (H&E), Masson's trichrome and Goldner's trichrome staining. CPC clearly displayed better new bone formation function and degradability after addition of pure microcapsules and cell microcapsules. Furthermore, the cell microcapsule treatment group showed greater osteogenesis than the pure microcapsule group. Collectively, these results indicate that BMSCs encapsulated in ACA microcapsules combined with CPC composite scaffolds have good application prospects as bone tissue engineering materials.

KEYWORDS

microcapsule, calcium phosphate cement, bone marrow mesenchymal stem cells, scaffold, tissue engineering

Introduction

Calcium phosphate cement (CPC) has significant similarities with hydroxyapatite, the main component of human bone. Soluble calcium and inorganic phosphate generated by the decomposition of calcium phosphate crystals can be effectively used by cells to form new bone (Wang et al., 2014a; Thrivikraman et al., 2017) and are widely applied as synthetic bone graft materials. The injectability and self-setting ability of CPC facilitates injection into irregular bone defect cavities using minimally invasive surgery and solidification *in situ* to fit the shape of the bone defect, which reduces the shaping time of the graft material and trauma of the operation (Alves et al., 2008; Low et al., 2010; Liu et al., 2016). However, poor degradability and osteoinductivity properties greatly limit its applications. Over the years, researchers have attempted to improve the biocompatibility, bone induction and porosity of CPC by adding bioactive factors, metal and nonmetal ions, organic compounds, drugs or stem cells (Wang et al., 2014b). However, this issue has not been resolved, so this material is not commonly used in oral treatment.

BMSCs are widely used in stem cell therapy owing to their self-renewal ability, rapid proliferation *in vitro*, rich separation sources, immune regulatory ability, and multidirectional and high osteogenic differentiation (Chu et al., 2020; Mohanty et al., 2020; Purwaningrum et al., 2021). In bone tissue engineering applications, bone marrow mesenchymal stem cells are often used to generate composite biomaterials with scaffolds to improve osteogenic properties and promote new bone formation (Liu et al., 2010; Wang et al., 2013; Chen et al., 2014; Lee et al., 2019; Arthur and Gronthos, 2020; Oryan et al., 2020). However, CPC paste exerts toxic effects during the setting reaction, which is not conducive to the growth of adhesion cells on its surface (Zhao et al., 2010). Simon et al. (2004) reported that during the process of solidification, cell survival was enhanced in cases where cells were not in direct contact with CPC.

Therefore, to solve the above problems, this study used microencapsulation (ACA)-encapsulated BMSCs and mixed them with CPC to form an injectable composite. On the one hand, encapsulating BMSCs in microcapsules can isolate cells from CPCs, prevent the toxicity of CPC paste, and improve cell viability, thereby further enhancing the osteogenic properties of composites. Due to the unique microenvironment and immune isolation, microencapsulation technology shows potential for tissue engineering and regenerative medicine (Xia et al., 2012; Wang et al., 2014c). Alginate and chitosan have been used to generate multilayered hollow microcapsules due to their good biocompatibility, low cost and similar structure to the extracellular matrix (Ribeiro et al., 2018). ACA microcapsules appear to be the perfect choice to provide cells for tissue

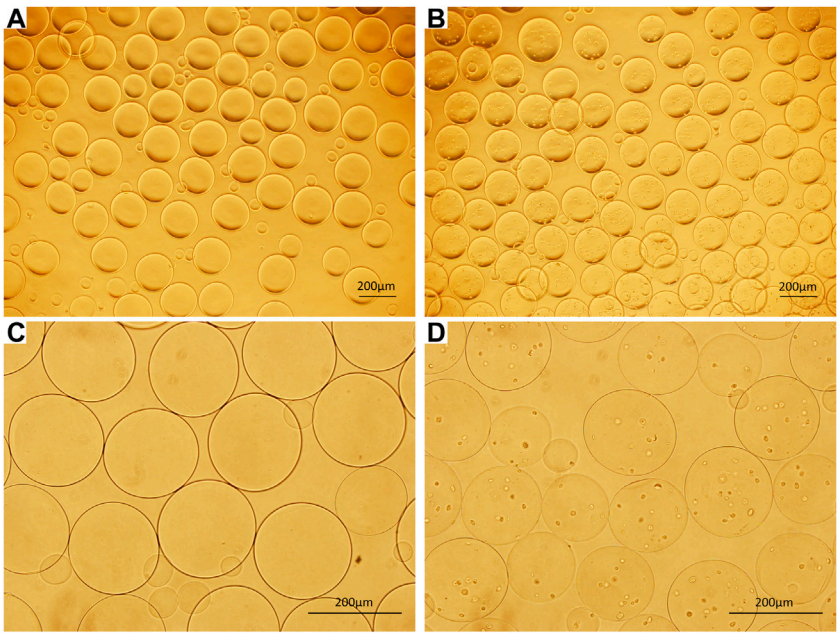

FIGURE 1
(A) ACA microcapsules (40×). **(B)** Cell microcapsules (40×). **(C)** ACA microcapsules (100×). **(D)** Cell microcapsules (100×), bar = 200 μm.

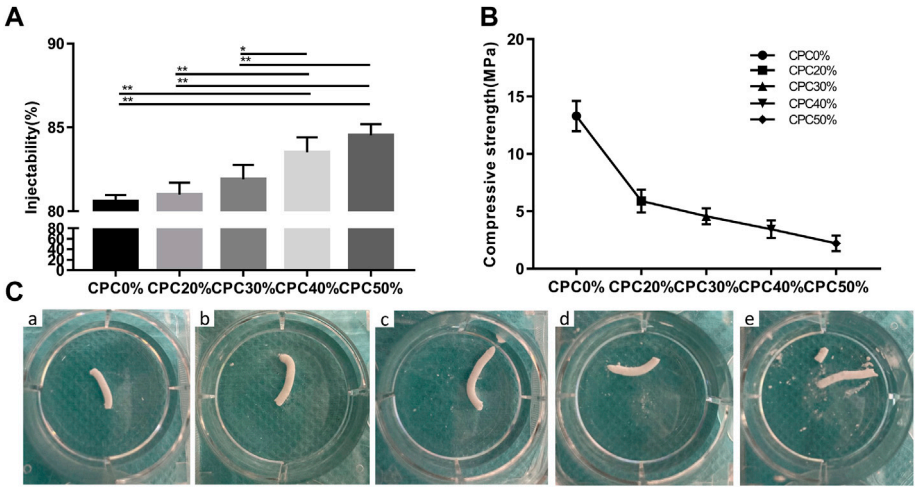

FIGURE 2
(A) Injectability of composite scaffolds with different microcapsule volume ratios. **(B)** Compressive strengths of composite scaffolds with different microcapsule volume ratios. **(C)** Images of composite scaffolds with different microcapsule volume ratios at 24 h after injection of normal saline. **(A)** CPC0%, **(B)** CPC20%, **(C)** CPC30%, **(D)** CPC40%, **(E)** CPC50%. (*: $p < 0.05$, **: $p < 0.01$).

engineering. Zhang et al. (2017) used AC microcapsules encapsulating HUVEC-CS cells to construct vascularized tissues. Long et al. (2017) comicroencapsulated BMSCs and mouse pancreatic β cells for the treatment of diabetic mice. However, there are few related studies on the application of ACA microcapsules in the oral cavity. On the other hand, the use of ACA to increase the porosity of CPC results in a three-dimensional cell-carrying scaffold with interconnected micropores and macropores and improves its osteogenic properties. Previous studies have found that in addition to the micropores (<50 μm) of CPC itself, which can increase the area of protein adsorption and cell attachment, the interconnected macropores (>100 μm) formed by microcapsules are important for bone ingrowth, blood vessel crawling, cell migration, and nutrition delivery (Grosfeld et al., 2020). Therefore, this study will utilize a simple and efficient electrospraying method for the preparation of BMSC-loaded microcapsules mixed with CPC to form an injectable composite that can be applied in the oral cavity.

Materials and methods

Preparation of alginate-chitosan-alginate-encapsulated bone marrow mesenchymal stem cells and alginate-chitosan-alginate/calcium phosphate cement composite scaffolds

Alginate-chitosan-alginate (ACA) microcapsules were prepared by an electrospraying method. Sodium alginate (1.5%; A0682, Sigma) was injected through a 10 ml syringe, which was fixed on a syringe pump (LSP02-1B, Longer Pump, China) and connected to the positive pole of a DC electric field (BGG, BME I Co., Ltd. China). With the basic parameters of a voltage of 5.0 kV, the syringe pump was started at a speed of 15 ml/h, a receiving distance of 2 cm, and a pinhole diameter of 0.21 mm. Then, 1.5% (w/v) sodium alginate solution was dropped evenly into 1.1% (w/v) calcium chloride solution (Shanghai Test, China) to obtain calcium alginate microspheres. The microspheres formed were successively reacted with 0.6% (w/v) chitosan (C8320, Solarbio, China; molecular weight: 100,000, deacetylation>90%, pH 6.3) for 15 min and 0.05% (w/v) sodium alginate solution for 5 min, washed with normal saline (NS), and liquefied with 55 mmol/L sodium citrate solution (pH 5.6, Shanghai Test) for 10 min to obtain ACA microcapsules. When 10^6/ml bone marrow mesenchymal stem cells (BMSCs) were added to 1.5% (w/v) sodium alginate and the other steps were the same, cell microcapsules were prepared.

CPC powder was composed of α-TCP [α-$Ca_3(PO_4)_2$], calcium dihydrogen phosphate monohydrate [$Ca(H_2PO_4)_2H_2O$] and calcium carbonate ($CaCO_3$) at a 10: 3.5:1.5 M ratio, and the solidifying liquid used was sodium dihydrogen phosphate (NaH_2PO_4)/sodium hydrogen phosphate (Na_2HPO_4) solution at an equal molar ratio. The powder/liquid ratio was 1 g:1 ml. ACA microcapsules were mixed with CPC at proportions of 0%, 20%, 30%, 40%, and 50% (v/v) with solidifying liquid. The final CPC samples were labelled CPC0%, CPC20%, CPC30%, CPC40% and CPC50% according to the ACA microcapsule proportion.

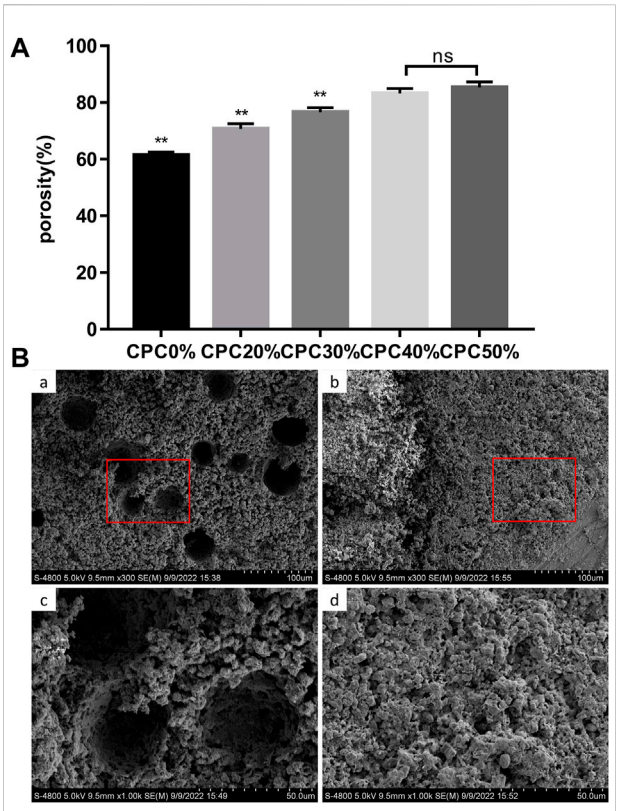

FIGURE 3
(A) Porosity of composite scaffolds with different microcapsule volume ratios measured with the Archimedes drainage method. **(B)** Pore distribution of composite scaffolds observed *via* electron microscopy: **(A)** and **(C)** CPC + ACA, **(B)** and **(D)** CPC. (*: $p < 0.05$, **: $p < 0.01$, ns: $p > 0.05$).

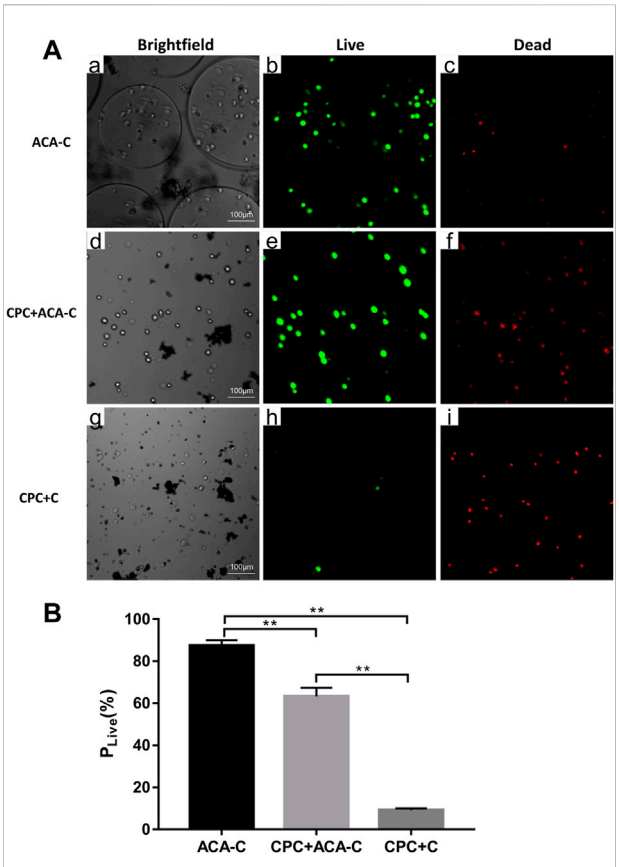

FIGURE 4
(A) Live/dead-stained ACA-C, CPC + ACA-C and CPC + C cells observed *via* laser scanning confocal microscopy. The live cells were green, and the dead cells were red, bar = 100 μm. **(B)** Percentage of live cells in the ACA-C, CPC + ACA-C and CPC + C groups (**: $p < 0.01$).

Injectability test

A 5 ml syringe containing different ratios of microcapsules mixed with CPC was placed in a universal testing machine (Autograph AG-X plus; Shimadzu, Japan) and fixed vertically, and the biomaterial passed through at a rate of 10 mm/min until the pushing force reached 100 N. The total mass of the material was recorded as M1, and the mass of the remaining material after pushing was recorded as M2. Injectability was calculated as (M1—M2)/M1*100%.

Compressive strength test

For determination of the compressive strength of the composite scaffold, CPC0%, CPC20%, CPC30%, CPC40% and CPC50% were placed in moulds with a diameter of 6 mm and height of 10 mm to generate standard specimens ($n = 4$), which were loaded in a universal testing machine to determine compression resistance at a speed of 1 mm/min.

Anti-washout testing

Each group of composite biomaterials was loaded into a 5 ml syringe, injected in NS, and incubated at 37°C and >90% humidity. Images were obtained at 0 s and 24 h to examine collapse of the biomaterials.

Evaluation of porosity

The Archimedes drainage method was employed to evaluate the porosity of all specimens. The dry weight of each sample was determined (recorded as M0). Samples were placed in a clean beaker, submerged in water and heated to the boiling point for 2 h until the water completely penetrated each sample. After termination of heating, the samples were cooled to room temperature, and weights were obtained (recorded as M1). Following removal of each sample, moisture on the surface was wiped off, and the weight was recorded (M2). Porosity

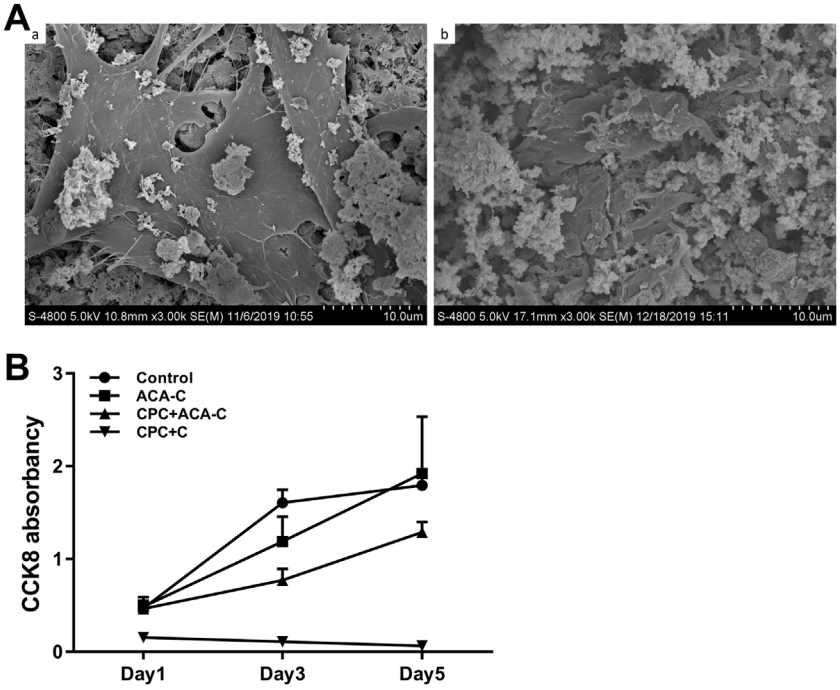

FIGURE 5
(A) Adhesion of BMSCs on the CPC surface observed *via* electron microscopy. **(A)** BMSCs seeded on CPC discs, **(B)** BMSCs encapsulated in ACA microcapsules seeded on CPC paste. **(B)** CCK-8 results of the control, ACA-C, CPC + ACA and CPC + C groups at 1, 3, and 5 days.

was calculated as (M2-M0)/M1. The pore distribution of the composite scaffold was examined using FE-SEM (Hitachi S-4800; Hitachi, Tokyo, Japan).

Cell live/dead double staining

Cells of the same density (10^6 cells/ml) were encapsulated into ACA microcapsules and composited with CPC or directly composited with CPC. At 24 h, the composite scaffolds were carefully broken, and the cells were harvested by a cell strainer. The cells in the ACA-C (ACA microcapsules purely encapsulating BMSCs), CPC + ACA-C (composite of cell microcapsules and CPC paste) and CPC + C (cells and CPC paste composite) groups were plated and live/dead stained (CA1630, Solarbio, China) at 24 h. The experimental results were observed and photographed under a laser scanning confocal microscope (ECLIPSE-Ti, Nikon, Japan). The percentage of live cells was $P_{Live} = N_{Live}/(N_{Live} + N_{Dead})$. Experimental results were statistically analysed.

Cell attachment assay

Electron microscopy was used to examine the adhesion of bone marrow mesenchymal stem cells on the CPC surface. The cells were divided into the CPC paste (BMSCs seeded on CPC paste), CPC disc (BMSCs seeded on CPC disc), and CPC + ACA-C groups (BMSCs encapsulated in ACA microcapsules seeded in CPC paste). Each group of composites was suspended in culture medium, incubated at 37°C and 5% CO2 for 24 h, and subsequently fixed in 2.5% glutaraldehyde. After dehydration, drying and gold spraying, the adhesion of cells from each group on the surface of bone cement was examined under an electron microscope.

Cell proliferation analysis

The CCK-8 assay was employed to assess the proliferation of cells. The cells were divided into the control (adherent culture of BMSCs), ACA-C (ACA microcapsules purely encapsulating BMSCs), CPC + ACA-C (composite of cell microcapsules and CPC paste), and CPC + C groups (cells and CPC paste composite). All four groups of cells were plated, and CCK-8 detection was performed on Days 1, 3, and 5 (n = 5). Experimental results were plotted and statistically analysed.

Ectopic bone formation analysis

All surgeries were performed in accordance with a protocol approved by the Animal Welfare Committee of the Beijing

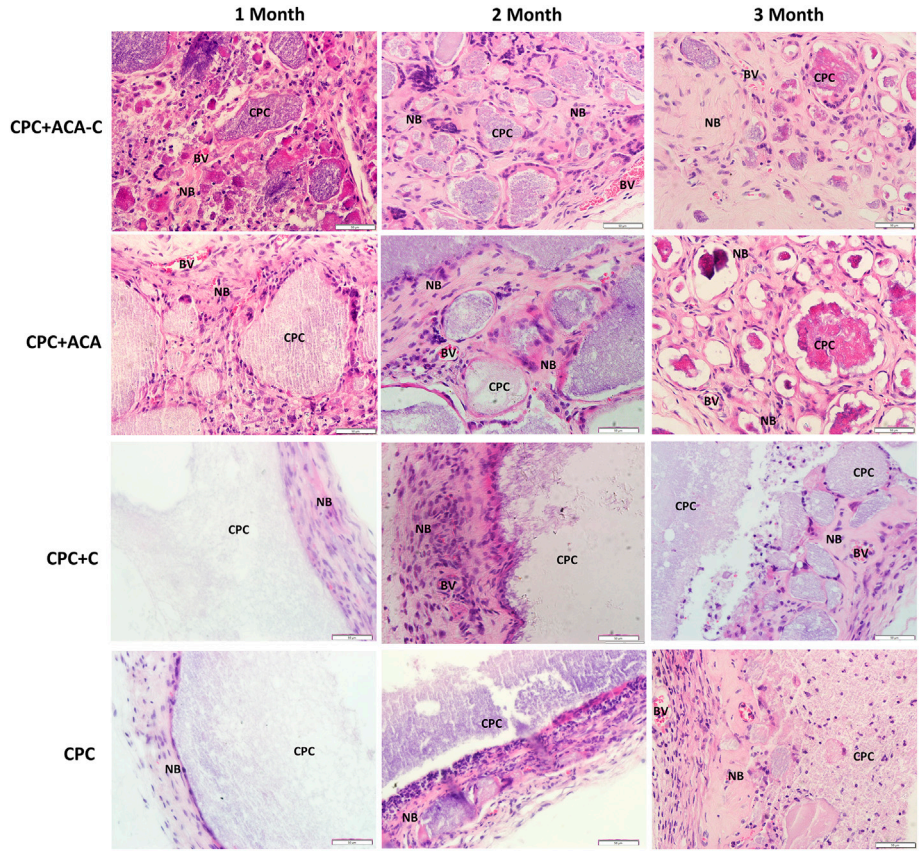

FIGURE 6
H&E-stained tissue sections of the CPC + ACA-C, CPC + ACA, CPC + C and CPC groups after 1, 2 and 3 months of implantation (NB: newly formed bone; CPC: implanted samples; BV: blood vessel; bar = 50 μm).

Stomatological Hospital, Capital Medical University. Twenty-one 6-week-old male nude mice were used as hosts. Experimental mice were divided into four groups (n = 5). Mice were anaesthetized intraperitoneally with 5% chloral hydrate (10 ml/kg body weight). CPC, CPC + C, CPC + ACA and CPC + ACA-C biomaterials were implanted subcutaneously into the backs of nude mice, and the back of each nude mouse was replanted at three sites. Experimental animals were sacrificed after 4, 8 and 12 weeks for harvesting of the specimens. The obtained specimens were fixed in 10% neutral buffered formaldehyde for 2 days, decalcified, dehydrated, embedded, sliced and subjected to H&E, Masson's trichrome and Goldner's trichrome staining. Images of stained sections were obtained under a microscope (BX61, Olympus, Japan).

Statistical analysis

All results are expressed as the mean ± standard deviation (SD). The experimental data of each group showed a normal distribution and homogeneity of variance. One-way analysis of variance (ANOVA) was performed to determine significant effects of the variables. p values < 0.05 were considered statistically significant.

Results

Alginate-chitosan-alginate microcapsules

Microcapsules with uniform sizes and diameters of approximately 200–400 μm were prepared by electrospraying (Figure 1).

Injectability of the alginate-chitosan-alginate/calcium phosphate cement scaffold

The injectability of composite scaffolds with varying microcapsule volumes is presented in Figure 2A. Injectability experiments revealed an increase in the injectability coefficient

with increasing microcapsule proportions. Notably, only the injectability coefficients of CPC40% and CPC50% were significantly different from those of CPC0%. However, the differences between the CPC40% and CPC50% groups were not significant.

Compressive strength of the alginate-chitosan-alginate/calcium phosphate cement scaffold

Figure 2B shows the compressive strength of each group of composite scaffolds. The compressive strength of bone cement decreased gradually with the increase in microcapsule volume ratio, but the strength of each group still met that of jaw cancellous bone (2–20 MPa), which can be effectively used for bone transplantation in nonload-bearing areas of the jaw.

Anti-washout ability of the alginate-chitosan-alginate/calcium phosphate cement scaffold

The images of each composite scaffold group at 24 h after injection of normal saline are depicted in Figure 2C. At a microcapsule volume of ≤ 40%, the composite scaffold continued to maintain a good shape with effective anti-washout ability at 24 h. However, at a 50% microcapsule volume ratio, the composite scaffold partially collapsed.

Porosity of the alginate-chitosan-alginate/calcium phosphate cement scaffold

The porosity values of each group of composite scaffolds measured with the Archimedes drainage method are presented in Figure 3A. The porosity clearly increased with the microcapsule volume ratio. Notably, there was a significant difference between each group except the CPC40% and CPC50% groups. In electron microscopy analysis of the cross-sections of composite biomaterials (Figure 3B), CPC displayed 23.706 ± 20.323 μm microporous structures, while the cross-section of CPC combined with microcapsules revealed macropores with diameters of 305.701 ± 103.299 μm in addition to micropores. At the bottom of the macropores, the micropores could also be seen communicating with the surrounding region.

Cell viability

The live/dead staining results are shown in Figure 4. Under a laser scanning confocal microscope, the live cells were green, and the dead cells were red. In the ACA-C group, most of the cells survived, and the percentage of live cells was 87.455% ± 2.511%. In the CPC + ACA-C group, due to the setting reaction of CPC, some cells died, and the percentage of live cells was 63.26% ± 4.15%. However, in the CPC + C group, a large number of cells died, and the percentage of live cells was 9.099% ± 0.971%. There was a statistically significant difference between each group (**: $p < 0.01$).

Cell adhesion

The adhesion of cells on the CPC surface was examined *via* electron microscopy after 24 h. Cells did not adhere to the CPC surface upon direct seeding onto CPC paste. In the CPC disc group, BMSCs could be tiled on the surface of CPC. Obvious cell pseudopodia and bulges were detected under a high-power microscope (Figure 5A). Upon encapsulation of cells in microcapsules in combination with CPC paste, cells adhered to the surface of CPC, but the morphology was more three-dimensional, and cell pseudopodia were not obvious (Figure 5(Ab)).

Cell proliferation

Data from the CCK-8 assay are presented in Figure 5B. We observed stable proliferation in the control and ACA-C groups. Cells in the CPC + ACA-C group showed proliferation in the prophase and proliferated slowly in the anaphase, while those in the CPC + C group showed large-scale cell death.

Histopathology

The H&E and Masson's trichrome staining results of subcutaneous replantation in nude mice are shown in Figures 6, 7. At 1 month, only a small amount of new bone-like tissue was observed in each group. In the CPC and CPC + C groups, cells mainly surrounded the periphery of the scaffold, with some protruding from the periphery into the scaffold. In the CPC + ACA and CPC + ACA-C groups, a large proportion of cells infiltrated and degraded the scaffold. Staining at 2 months revealed immature newly formed bone tissue deposition and segmentation around the nondegraded scaffold in the CPC + ACA and CPC + ACA-C groups. In the CPC and CPC + C groups, immature newly formed bone tissue was observed only at the periphery of the scaffold, with infiltration of some peripheral cells. Data from staining at 3 months showed an increase in new bone-like tissue in the CPC + ACA and CPC + ACA-C groups, along with degradation of the scaffold into smaller fragments. In the CPC and CPC + C groups, new bone-like tissue was produced

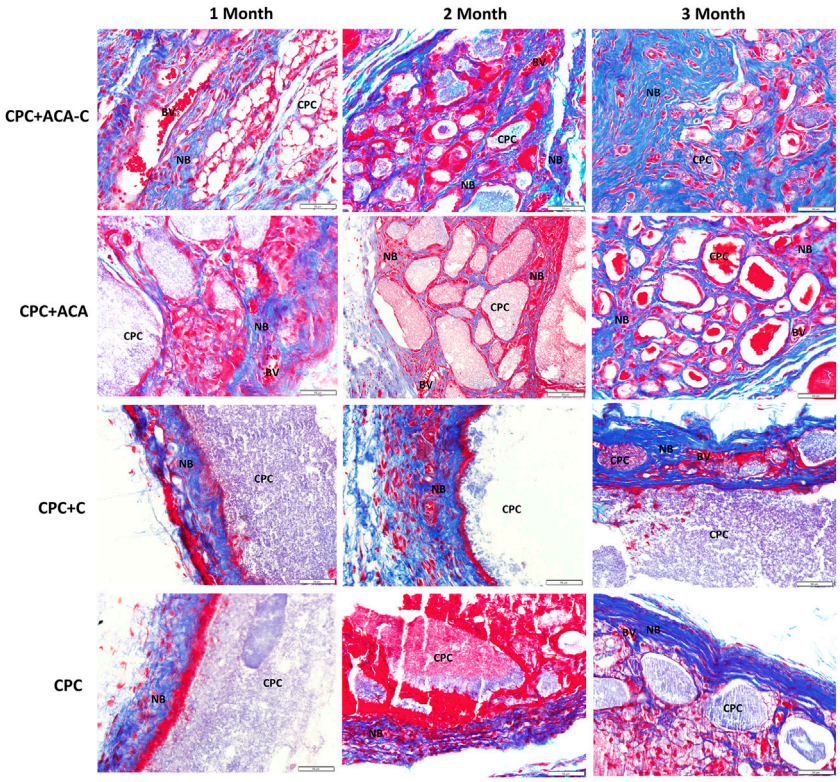

FIGURE 7
Masson's trichrome-stained tissue sections of the CPC + ACA-C, CPC + ACA, CPC + C and CPC groups after 1, 2 and 3 months of implantation (NB: newly formed bone; CPC: implanted samples; BV: blood vessel; bar = 50 μm).

in the periphery. However, the degree of cell infiltration remained limited to the periphery.

Goldner's trichrome staining results are presented in Figure 8. In the CPC + ACA and CPC + ACA-C groups, the interior of the scaffold was divided into small sections by nonmineralized osteoid mixed with mineralized bone at 2 months. At 3 months, the osteoid was basically replaced with mineralized bone, and the scaffold degraded into smaller fragments. The interface between mineralized bone and biomaterial comprised incompletely mineralized osteoids. In the CPC and CPC + C groups, a small amount of mineralized bone surrounded the nondegraded scaffold at the periphery of the material at 2 months, and nonmineralized osteoids protruding into the scaffold were observed between the mineralized bone and scaffold. At 3 months, an increased quantity of peripheral mineralized bone with protrusion into the scaffold was evident. Image-Pro Plus was applied to measure the percentage of new bone area of each group at this time point. The data showed that the mineralized areas of the CPC + ACA and CPC + ACA-C groups were significantly greater than those of the CPC and CPC + C groups. Furthermore, the mineralized area of the CPC + ACA-C group was greater than that of the CPC + ACA group.

Discussion

After combination with hydrogel microcapsules, the injectability and porosity of CPC were significantly increased. The injectability and porosity of a composite mixture with 40% microcapsule content were significantly higher than those of calcium phosphate bone cement, along with good collapse resistance. The compressive strength value was determined to be 3.44 ± 0.77 MPa, which meets the requirements of cancellous bone. With a further increase in the proportion of microcapsules, the composites showed a propensity to collapse and decreased compressive strength. Good injectability (Tariq et al., 2019) and self-setting properties facilitate access of CPC to the bone defect area in a minimally invasive manner, allowing it to solidify *in situ* to adapt to the shape of the cavity. Due to its anti-washout ability, CPC is resistant to loss of bone graft material caused by scouring of body fluid and blood before solidification. Accordingly, we conducted subsequent animal experiments using microcapsule composites with a volume ratio of 40%.

Increasing the porosity of CPC promoted degradation, cell migration, adhesion, proliferation and osteogenic differentiation, along with enhanced angiogenesis and inward bone growth.

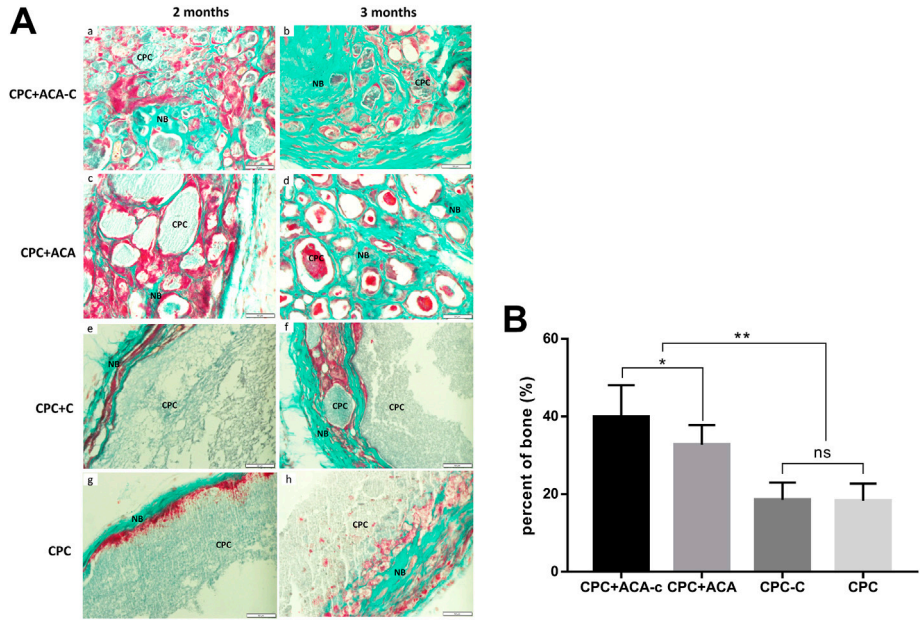

FIGURE 8
(A) Goldner's trichrome-stained tissue sections of the CPC + ACA-C, CPC + ACA, CPC + C and CPC groups after 2 and 3 months of implantation, bar = 50 μm; **(B)** Newly formed bone areas of Goldner's trichrome-stained tissue sections after 3 months (NB: newly formed bone; CPC: implanted samples; *: $p < 0.05$, **: $p < 0.01$).

Moreover, larger pore sizes led to greater cell infiltration and angiogenesis (Klijn et al., 2012; Loh and Choong, 2013). Earlier research (Loh and Choong, 2013; Qiao et al., 2013) suggested that macropores are conducive to cell crawling and vascular growth. Luo et al. (Luo et al., 2021) found that TA scaffolds with a pore size of 400–600 μM had a stronger ability to promote cell adhesion, proliferation and osteogenic differentiation *in vitro*. Several studies have also shown that three-dimensional structures comprising macropores hundreds of microns in size interconnected with pores several microns in size promote cell infiltration and vascular crawling, and the micronanostructures improve the transport of nutrients and metabolic waste and adsorption of bioactive molecules, which contributes to the degradation of scaffold materials and bone formation (Zhang et al., 2013; Guda et al., 2014; Zhou et al., 2019). In experiments, upon addition of microcapsules, the porosity of scaffold materials was significantly increased. The combination with microcapsules at a volume ratio of 40% led to an ~20% increase in total porosity. Electron microscopy analyses revealed that macropores (hundreds of microns) and pores (tens of microns) were alternately connected with each other. Cell microcapsules not only transport stem cells for scaffold formulations but also form macropores 300–400 μm in size *in situ*. Compared with CPC (with pores a few microns to tens of microns in size), microcapsules promoted the degradation and osteogenesis of biomaterials to a greater extent. A notable limitation of high porosity is a decrease in CPC compressive strength. However, in nonload-bearing areas, such as the craniomaxillofacial region, new bone formation at the expense of mechanical strength is acceptable (Muallah et al., 2021).

In addition, the crosslinking of sodium alginate and Ca^{2+} formed calcium alginate microspheres, and chitosan was used as a coating to electrostatically interact with sodium alginate to form ACA microcapsules, which improved its mechanical strength and stability (Suvarna et al., 2018; Hajifathaliha et al., 2021). Thus, ACA microcapsules can be used as an effective strategy to provide probiotics, proteins and cells to protect against acidity and large amounts of environmental proteases (Cui et al., 2018; Zhang et al., 2020). Cell microcapsules combined with CPC protected cells, reduced the toxicity of CPC solidification, and delivered seed cells to injectable CPC scaffolds. Data from CCK-8, cell live/dead staining and cell adhesion morphology experiments indicate that although cells within ACA microcapsules are protected after CPC solidification, they are still subjected to some damage, resulting in a decline in the cellular state. However, compared with nonencapsulated cells, microcapsule protection enables greater adherence of cells on the surface of CPC after solidification, which subsequently plays a role in the process of osteogenesis after bone cementing. Additionally, microcapsules can degrade into pores *in situ* and release seed cells.

Examination of ectopic osteogenesis on the backs of nude mice revealed stronger osteogenic capability of composite scaffolds with pure microcapsules and BMSC-encapsulating microcapsules. H&E and Masson's trichrome staining showed that upon addition of microcapsules, cells and blood vessels infiltrated the scaffold. This phenomenon led to fragmentation of the scaffold and degradation of

the biomaterial from the inside, prolonged at any time with a gradual decrease in the area of residual material. In the CPC and CPC + C groups, cells and blood vessels were observed only at the periphery, which gradually degraded the scaffold with regeneration of bone, and the biomaterial was degraded from the periphery to the interior. The experimental results suggest that macropores produced by the addition of microcapsules promote the infiltration of cells and blood vessels and accelerate the degradation of scaffolds into bone. Data from Goldner's trichrome staining were consistent with the H&E results. At 2 months after replantation, osteoids were observed in the CPC + ACA and CPC + ACA-C groups. The material was decomposed into blocks within the scaffold and mixed with mineralized bone. In the CPC and CPC + C groups, only narrow mineralized bone and osteoid wrapped around the scaffold were observed at the periphery, with protrusion of osteoid into the edge of the scaffold to an extent. At 3 months after replantation, the CPC + ACA and CPC + ACA-C groups formed significantly more mineralized bone than the CPC and CPC + C groups. However, compared with the CPC + ACA group, the CPC + ACA-C group showed a stronger osteogenic ability, and the area of mineralized bone was increased from 32.50% ± 6.14%–41.10% ± 8.55%, supporting the theory that BMSCs combined with CPC secrete cytokines or recruit new cells to accelerate scaffold degradation and promote new bone formation. The activities of these cell microcapsules in increasing the pore sizes of scaffolds and accelerating osteogenesis and degradation are valuable for tissue engineering applications.

In bone defects of the nonload-bearing area, CPC + ACA and CPC + ACA-C composite scaffolds could effectively adapt to the shape of the cavity and showed better degradation performance than CPC to match the rate of osteogenesis. Moreover, with the addition of seed cells, these composite biomaterials produced cytokines more rapidly for participation in ectopic osteogenesis.

Conclusion

In summary, at a 40% volume ratio of cell microcapsules to CPC, composite scaffolds have optimal physicochemical properties that meet the requirements of jaw defect scaffolds, and ACA microcapsules effectively protect cells from toxic effects of the setting reaction of CPC. Ectopic bone formation experiments further confirmed that the combination of CPC with ACA cell microcapsules improves the degradation performance and new bone formation ability, supporting the application prospects of this composite biomaterial in bone tissue engineering.

Data availability statement

The original contributions presented in the study are included in the article/supplementary material, further inquiries can be directed to the corresponding authors.

Ethics statement

The animal study was reviewed and approved by Animal Welfare Committee of the Beijing Stomatological Hospital, Capital Medical University.

Author contributions

Conceptualization, YY and DM; Methodology, YY and DM; Formal analysis, YY; Investigation, YY and LS; Resources, YY and TL; Data Curation, YY and LH; Writing—Original Draft, YY; Writing—Review and; Editing, QJ and DM; Funding acquisition, QJ and DM.

Funding

This work was supported by National Natural Science Foundation of China (Grant No. 81600901). The capital health research and development of special (Grant No. 2022-1-2141).

Conflict of interest

The authors declare that the research was conducted in the absence of any commercial or financial relationships that could be construed as a potential conflict of interest.

Publisher's note

All claims expressed in this article are solely those of the authors and do not necessarily represent those of their affiliated organizations, or those of the publisher, the editors and the reviewers. Any product that may be evaluated in this article, or claim that may be made by its manufacturer, is not guaranteed or endorsed by the publisher.

References

Alves, H. L., Dos Santos, L. A., and Bergmann, C. P. (2008). Injectability evaluation of tricalcium phosphate bone cement. *J. Mat. Sci. Mat. Med.* 19, 2241–2246. doi:10.1007/s10856-007-3329-6

Arthur, A., and Gronthos, S. (2020). Clinical application of bone marrow mesenchymal stem/stromal cells to repair skeletal tissue. *Int. J. Mol. Sci.* 21, 9759. doi:10.3390/ijms21249759

Chen, Y., Bai, B., Zhang, S., Ye, J., Zhai, H., Chen, Y., et al. (2014). Study of a novel three-dimensional scaffold to repair bone defect in rabbit. *J. Biomed. Mat. Res. A* 102, 1294–1304. doi:10.1002/jbm.a.34788

Chu, D. T., Phuong, T. N. T., Tien, N. L. B., Tran, D. K., Thanh, V. V., Quang, T. L., et al. (2020). An update on the progress of isolation, culture, storage, and clinical application of human bone marrow mesenchymal stem/stromal cells. *Int. J. Mol. Sci.* 21, 708. doi:10.3390/ijms21030708

Cui, L. H., Yan, C. G., Li, H. S., Kim, W. S., Hong, L., Kang, S. K., et al. (2018). A new method of producing a natural antibacterial peptide by encapsulated probiotics internalized with inulin nanoparticles as prebiotics. *J. Microbiol. Biotechnol.* 28, 510–519. doi:10.4014/jmb.1712.12008

Grosfeld, E. C., Smith, B. T., Santoro, M., Lodoso-Torrecilla, I., Jansen, J. A., Ulrich, D. J., et al. (2020). Fast dissolving glucose porogens for early calcium phosphate cement degradation and bone regeneration. *Biomed. Mat.* 15, 025002. doi:10.1088/1748-605x/ab5f9c

Guda, T., Walker, J. A., Singleton, B., Hernandez, J., Oh, D. S., Appleford, M. R., et al. (2014). Hydroxyapatite scaffold pore architecture effects in large bone defects *in vivo*. *J. Biomater. Appl.* 28, 1016–1027. doi:10.1177/0885328213491790

Hajifathaliha, F., Mahboubi, A., Bolourchian, N., Mohit, E., and Nematollahi, L. (2021). Multilayer alginate microcapsules for live cell microencapsulation; is there any preference for selecting cationic polymers? *Iran. J. Pharm. Res.* 20, 173–182. doi:10.22037/ijpr.2020.114096.14660

Klijn, R. J., van den Beucken, J. J., Félix Lanao, R. P., Veldhuis, G., Leeuwenburgh, S. C., Wolke, J. G., et al. (2012). Three different strategies to obtain porous calcium phosphate cements: Comparison of performance in a rat skull bone augmentation model. *Tissue Eng. Part A* 18, 1171–1182. doi:10.1089/ten.tea.2011.0444

Lee, Y. C., Chan, Y. H., Hsieh, S. C., Lew, W. Z., and Feng, S. W. (2019). Comparing the osteogenic potentials and bone regeneration capacities of bone marrow and dental pulp mesenchymal stem cells in a rabbit calvarial bone defect model. *Int. J. Mol. Sci.* 20, 5015. doi:10.3390/ijms20205015

Liu, H., Guan, Y., Wei, D., Gao, C., Yang, H., and Yang, L. (2016). Reinforcement of injectable calcium phosphate cement by gelatinized starches. *J. Biomed. Mat. Res.* 104, 615–625. doi:10.1002/jbm.b.33434

Liu, X., Li, X., Fan, Y., Zhang, G., Li, D., Dong, W., et al. (2010). Repairing goat tibia segmental bone defect using scaffold cultured with mesenchymal stem cells. *J. Biomed. Mat. Res. B Appl. Biomater.* 94, 44–52. doi:10.1002/jbm.b.31622

Loh, Q. L., and Choong, C. (2013). Three-dimensional scaffolds for tissue engineering applications: Role of porosity and pore size. *Tissue Eng. Part B Rev.* 19, 485–502. doi:10.1089/ten.teb.2012.0437

Long, R., Liu, Y., Wang, S., Ye, L., and He, P. (2017). Co-microencapsulation of BMSCs and mouse pancreatic (3 cells for improving the efficacy of type I diabetes therapy. *Int. J. Artif. Organs* 40, 169–175. doi:10.5301/ijao.5000555

Low, K. L., Tan, S. H., Zein, S. H., Roether, J. A., Mouriño, V., and Boccaccini, A. R. (2010). Calcium phosphate-based composites as injectable bone substitute materials. *J. Biomed. Mat. Res. B Appl. Biomater.* 94, 273–286. doi:10.1002/jbm.b.31619

Luo, C., Wang, C., Wu, X., Xie, X., Wang, C., Zhao, C., et al. (2021). Influence of porous tantalum scaffold pore size on osteogenesis and osteointegration: A comprehensive study based on 3D-printing technology. *Mater. Sci. Eng. C* 129, 112382. doi:10.1016/j.msec.2021.112382

Mohanty, A., Polisetti, N., and Vemuganti, G. K. (2020). Immunomodulatory properties of bone marrow mesenchymal stem cells. *J. Biosci.* 45, 98. doi:10.1007/s12038-020-00068-9

Muallah, D., Sembdner, P., Holtzhausen, S., Meissner, H., Hutsky, A., Ellmann, D., et al. (2021). Adapting the pore size of individual, 3D-printed CPC scaffolds in maxillofacial surgery. *J. Clin. Med.* 10, 2654. doi:10.3390/jcm10122654

Oryan, A., Hassanajili, S., Sahvieh, S., and Azarpira, N. (2020). Effectiveness of mesenchymal stem cell-seeded onto the 3D polylactic acid/polycaprolactone/hydroxyapatite scaffold on the radius bone defect in rat. *Life Sci.* 257, 118038. doi:10.1016/j.lfs.2020.118038

Purwaningrum, M., Jamilah, N. S., Purbantoro, S. D., Sawangmake, C., and Nantavisai, S. (2021). Comparative characteristic study from bone marrow-derived mesenchymal stem cells. *J. Vet. Sci.* 22, e74. doi:10.4142/jvs.2021.22.e74

Qiao, P., Wang, J., Xie, Q., Li, F., Dong, L., and Xu, T. (2013). Injectable calcium phosphate-alginate-chitosan microencapsulated MC3T3-E1 cell paste for bone tissue engineering *in vivo*. *Mater. Sci. Eng. C* 33, 4633–4639. doi:10.1016/j.msec.2013.07.022

Ribeiro, C., Borges, J., Costa, A. M. S., Gaspar, V. M., Bermudez, V. Z., and Mano, J. F. (2018). Preparation of well-dispersed chitosan/alginate hollow multilayered microcapsules for enhanced cellular internalization. *Mol. (Basel, Switz.* 23, 625. doi:10.3390/molecules23030625

Simon, C. G., Jr., Guthrie, W. F., and Wang, F. W. (2004). Cell seeding into calcium phosphate cement. *J. Biomed. Mat. Res.* 68, 628–639. doi:10.1002/jbm.a.20008

Suvarna, S., Dsouza, J., Ragavan, M. L., and Das, N. (2018). Potential probiotic characterization and effect of encapsulation of probiotic yeast strains on survival in simulated gastrointestinal tract condition. *Food Sci. Biotechnol.* 27, 745–753. doi:10.1007/s10068-018-0310-8

Tariq, U., Hussain, R., Tufail, K., Haider, Z., Tariq, R., and Ali, J. (2019). Injectable dicalcium phosphate bone cement prepared from biphasic calcium phosphate extracted from lamb bone. *Mater. Sci. Eng. C* 103, 109863. doi:10.1016/j.msec.2019.109863

Thrivikraman, G., Athirasala, A., Twohig, C., Boda, S. K., and Bertassoni, L. E. (2017). Biomaterials for craniofacial bone regeneration. *Dent. Clin. N. Am.* 61, 835–856. doi:10.1016/j.cden.2017.06.003

Wang, J., Qiao, P., Dong, L., Li, F., Xu, T., and Xie, Q. (2014). Microencapsulated rBMMSCs/calcium phosphate cement for bone formation *in vivo*. *Bio-medical Mater. Eng.* 24, 835–843. doi:10.3233/bme-130875

Wang, P., Zhao, L., Chen, W., Liu, X., Weir, M. D., and Xu, H. H. (2014). Stem cells and calcium phosphate cement scaffolds for bone regeneration. *J. Dent. Res.* 93, 618–625. doi:10.1177/0022034514534689

Wang, P., Zhao, L., Liu, J., Weir, M. D., Zhou, X., and Xu, H. H. (2014). Bone tissue engineering *via* nanostructured calcium phosphate biomaterials and stem cells. *Bone Res.* 2, 14017. doi:10.1038/boneres.2014.17

Wang, X., Wang, Y., Gou, W., Lu, Q., Peng, J., and Lu, S. (2013). Role of mesenchymal stem cells in bone regeneration and fracture repair: A review. *Int. Orthop.* 37, 2491–2498. doi:10.1007/s00264-013-2059-2

Xia, Y., Mei, F., Duan, Y., Gao, Y., Xiong, Z., Zhang, T., et al. (2012). Bone tissue engineering using bone marrow stromal cells and an injectable sodium alginate/gelatin scaffold. *J. Biomed. Mat. Res. A* 100, 1044–1050. doi:10.1002/jbm.a.33232

Zhang, J., Li, H. H., Chen, Y. F., Chen, L. H., Tang, H. G., Kong, F. B., et al. (2020). Microencapsulation of immunoglobulin Y: Optimization with response surface morphology and controlled release during simulated gastrointestinal digestion. *J. Zhejiang Univ. Sci. B* 21, 611–627. doi:10.1631/jzus.b2000172

Zhang, J., Zhou, H., Yang, K., Yuan, Y., and Liu, C. (2013). RhBMP-2-loaded calcium silicate/calcium phosphate cement scaffold with hierarchically porous structure for enhanced bone tissue regeneration. *Biomaterials* 34, 9381–9392. doi:10.1016/j.biomaterials.2013.08.059

Zhang, W., Choi, J. K., and He, X. (2017). Engineering microvascularized 3D tissue using alginate-chitosan microcapsules. *J. Biomater. tissue Eng.* 7, 170–173. doi:10.1166/jbt.2017.1547

Zhao, L., Weir, M. D., and Xu, H. H. (2010). Human umbilical cord stem cell encapsulation in calcium phosphate scaffolds for bone engineering. *Biomaterials* 31, 3848–3857. doi:10.1016/j.biomaterials.2010.01.093

Zhou, K., Yu, P., Shi, X., Ling, T., Zeng, W., Chen, A., et al. (2019). Hierarchically porous hydroxyapatite hybrid scaffold incorporated with reduced graphene oxide for rapid bone ingrowth and repair. *ACS Nano* 13, 9595–9606. doi:10.1021/acsnano.9b04723

frontiers | Frontiers in Bioengineering and Biotechnology

TYPE Review
PUBLISHED 25 November 2022
DOI 10.3389/fbioe.2022.1054379

OPEN ACCESS

EDITED BY
Y. Shrike Zhang,
Harvard Medical School, United States

REVIEWED BY
Xiaolin Cui,
The Chinese University of Hong Kong, Shenzhen, China
Gang Li,
Soochow University, China
Bram Soliman,
University of Otago, Christchurch, New Zealand

*CORRESPONDENCE
Cancan Zhao,
617167464@qq.com
Xudong Wang,
xudongwang70@hotmail.com

SPECIALTY SECTION
This article was submitted to Biomaterials, a section of the journal Frontiers in Bioengineering and Biotechnology

RECEIVED 26 September 2022
ACCEPTED 17 November 2022
PUBLISHED 25 November 2022

CITATION
Wu H, Lin K, Zhao C and Wang X (2022), Silk fibroin scaffolds: A promising candidate for bone regeneration. *Front. Bioeng. Biotechnol.* 10:1054379. doi: 10.3389/fbioe.2022.1054379

Silk fibroin scaffolds: A promising candidate for bone regeneration

Hao Wu[1,2,3,4], Kaili Lin[1,2,3,4], Cancan Zhao[1,2,3,4]* and Xudong Wang[1,2,3,4]*

[1]Department of Oral and Cranio-Maxillofacial Surgery, Shanghai Ninth People's Hospital, Shanghai Jiao Tong University School of Medicine, Shanghai, China, [2]College of Stomatology, Shanghai Jiao Tong University, Shanghai, China, [3]Shanghai Key Laboratory of Stomatology, National Center for Stomatology, National Clinical Research Center for Oral Diseases, Shanghai, China, [4]Research Unit of Oral and Maxillofacial Regenerative Medicine, Chinese Academy of Medical Sciences, Shanghai, China

It remains a big challenge in clinical practice to repair large-sized bone defects and many factors limit the application of autografts and allografts, The application of exogenous scaffolds is an alternate strategy for bone regeneration, among which the silk fibroin (SF) scaffold is a promising candidate. Due to the advantages of excellent biocompatibility, satisfying mechanical property, controllable biodegradability and structural adjustability, SF scaffolds exhibit great potential in bone regeneration with the help of well-designed structures, bioactive components and functional surface modification. This review will summarize the cell and tissue interaction with SF scaffolds, techniques to fabricate SF-based scaffolds and modifications of SF scaffolds to enhance osteogenesis, which will provide a deep and comprehensive insight into SF scaffolds and inspire the design and fabrication of novel SF scaffolds for superior osteogenic performance. However, there still needs more comprehensive efforts to promote better clinical translation of SF scaffolds, including more experiments in big animal models and clinical trials. Furthermore, deeper investigations are also in demand to reveal the degradation and clearing mechanisms of SF scaffolds and evaluate the influence of degradation products.

KEYWORDS

silk fibroin (SF), bone regeneration, scaffolds, biocompatibility, biodegradability, osteogenesis

1 Introduction

Caused by trauma, tumor and other pathological factors, bone defects can lead to dysfunctions and destruction of the musculoskeletal system (Burger et al., 2022). It remains challenging to achieve ideal bone regeneration in clinical practice (Lee et al., 2022; Mirkhalaf et al., 2022). Autografts and allografts are commonly applied to repair defected bones, but many factors limited their applications (Kundu et al., 2013; Guo et al., 2021). The application of exogenous scaffolds as bone substitutes seems an alternate strategy. The ideal scaffolds for bone regeneration should provide a biomimicking microenvironment to promote desirable cellular responses, which possess excellent biocompatibility, optimized mechanical properties, desirable morphology and

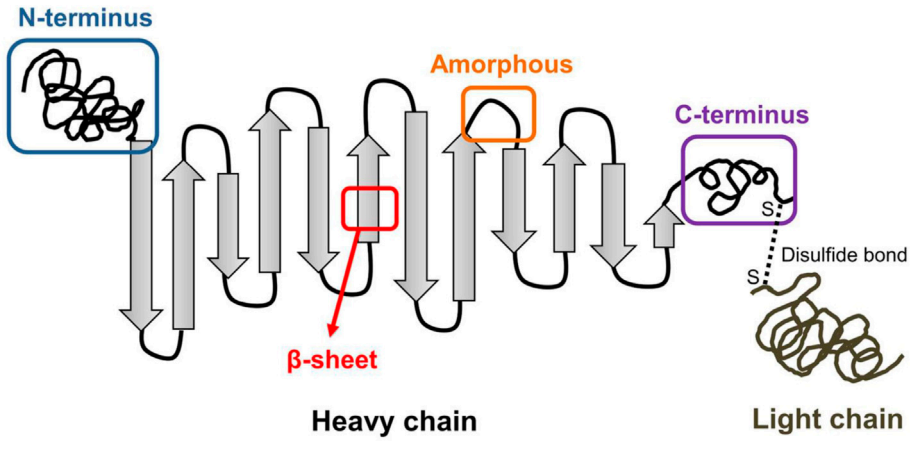

FIGURE 1
Illustration of SF structure including the heavy chain and light chain. (Wongpinyochit et al., 2018). Copyright 2018 American Chemical Society.

structure. The desired biodegradability with safe by-products and controllable diffusion is also important (Zhang and King, 2020).

Among plenty scaffolds, silk fibroin (SF) is a promising candidate with numerous researches (Wenhao et al., 2020; Shen et al., 2022). In the structure of SF, the light (L) chains, heavy (H) chains and the hydrophobically linked glycoprotein P25 are crosslinked to form an H-L complex with anti-parallel beta-sheets (β-sheets) (Figure 1) (Wongpinyochit et al., 2018; Zuluaga-Velez et al., 2021). SF scaffolds have many advantages, including excellent biocompatibility, satisfying mechanical property, controllable biodegradability and structural adjustability (Zhang et al., 2021; Zuluaga-Velez et al., 2021; Li and Sun, 2022). Compared with biodegradable synthetic polymers such as poly (lactic acid) (PLA), SF scaffolds exhibit better biocompatibility and cell adhesion performance (Wenk et al., 2011). Besides, due to the formation of *β*-sheets, SF scaffolds have better mechanical properties than collagens and chitosan (CS), with ultimate tensile strength of 300–740 MPa (Koh et al., 2015; Wang et al., 2020).

However, compared with native bone tissue, the mechanical properties of pure SF scaffolds are still insufficient (Melke et al., 2016; Soundarya et al., 2018). Further improvement is in demand to achieve better osteogenic capacity (Wu et al., 2021). Due to outstanding tunability, SF can be modified into different formats for certain applications, such as films, hydrogels and porous structures (Bakhshandeh et al., 2021). Besides, different organic and inorganic components can be mixed with pure SF to fabricate hybrid scaffolds to improve mechanical and biological performance (Wu et al., 2021). Another important modification method is surface modification, including physical modification, chemical modification and surface functionalization by bioactive components, which can make as-prepared SF scaffolds more bioactive (Hardy et al., 2018; Wang et al., 2019; Moses and Mandal, 2022).

Despite the large number of related researches, there still lack deep investigations on the long-term *in vivo* safety of SF scaffolds, which is closely related to the degradation products. The studies on degradation and cleaning mechanism of SF scaffolds are also far from satisfactory. It can be helpful to deeply understand the *in vivo* interaction of SF scaffolds with hosts' tissues to better inspire further modifications. Moreover, among numerous fabrication techniques and modification methods, it can be difficult to make a suitable choice for different applications, where a comprehensive classification and summary can be helpful.

Herein, we summarize the cell and tissue interaction with SF scaffolds, the fabrication techniques and modifications for better bone regeneration (Figure 2). We hope to give a deep insight into the SF scaffolds applied in bone regeneration and inspire research enthusiasm for better development and improvement of SF scaffolds.

2 Cell and tissue interaction with Silk fibroin scaffolds

As a highly dynamic vascularized tissue, bone tissue consists of cellular components, extracellular matrix (ECM) and minerals. Through achieving a deeper understanding of SF's interaction with cellular and non-cellular components, the design of advanced SF-based scaffolds can be better inspired.

2.1 Immune response

Silk materials have been proved biocompatible with long history of application, but some rarely-happened adverse

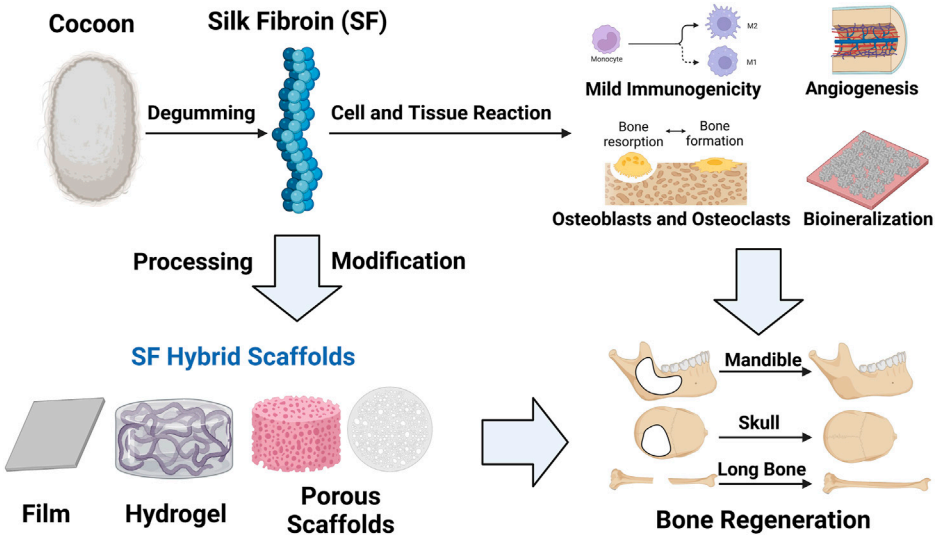

FIGURE 2
Graphical diagram for fabrication of SF scaffolds and their cell and tissue responses, which makes contributions to bone regeneration. (Created with BioRender.com).

immunological events cannot be ruled out, which may be caused by the presence of silk sericin (SS) proteins. Wang et al. (Wang et al., 2020) combined SF and SS in different mass ratios and detected the immune responses caused by different scaffolds. The results showed that the macrophages were activated by the addition of SS and secreted more proinflammation (M1)-related cytokines. The SF itself showed satisfying biocompatibility with higher antiinflammation (M2) phenotype ratio of macrophages. As for *in vivo* evaluation, Gorenkova et al. (Gorenkova et al., 2021) evaluated the immune response of self-assembled SF hydrogels *via* Balb/c mice models. The inflammatory response was comparable or even lower than the benchmark material, polyethylene glycol (PEG), which did not activate tissue regeneration and served as the baseline marker for tissue responses. Overall, these studies demonstrate that the SF scaffolds can exhibit favorable biocompatibility after degumming and sterilization.

Despite these encouraging researches, there still exist problems about long term *in vivo* safety of SF scaffolds and long-term immune responses need further investigation to achieve better understanding. The immune response to degradation products of SF scaffolds should also be considered, where the production of proinflammatory cytokine and phagocytosis may be induced by fractions of SF fibers (Gellynck et al., 2008). Lundmark et al. (Lundmark et al., 2005) found that the degradation products of SF could cause amyloidogenesis and tissue degeneration. Therefore, it is necessary to carry out long-term studies of SF scaffolds on their degradation products.

2.2 Osteogenic cellular response

Meinel et al. (2005) claimed that the plain silk scaffolds could only provide an appropriate environment for cellular proliferation, where the ingrown cells showed poor osteogenic differentiation. However, later researches demonstrated that SF could activate expression of osteogenesis-related genes, including alkaline phosphatase (ALP), Runt-related transcription factor 2 (Runx2), collagen I (COL I), osterix, osteocalcin (OCN) and CD29/CD44 (Miyamoto et al., 2013; Panda et al., 2015). Jung et al. (2013) found the SF could serve as the suppressor of the Notch pathway, which could down-regulate of osteogenesis and thus promote osteogenesis. The amide groups and high *ß*-sheet contents of SF could also induce osteogenic differentiation, where the *ß*-sheet structure could provide a stiff matrix environment for osteoblasts.

However, considering results of other *in vivo* experiments, plain SF scaffolds have insufficient ability to completely regenerate large bone defects (Mottaghitalab et al., 2015). Uebersax et al. (2013) implanted two different SF scaffolds into the long bones of sheep and found the poor bone formation in both scaffolds. Song et al. (2011) applied SF film to repair rabbit calvarial defects (φ 8 mm), and found the calvarial defects actually failed to completely recover after 8 weeks. Notably, when pre-seeded with undifferentiated stem cells before implanted, the capability of bone formation can be significantly improved with pre-differentiated cells (Park et al., 2015; Sartika et al., 2020). Considering the long-term procedure of autologous cell isolation and culture, the cell-free SF scaffold is still a better choice.

2.3 Bone resorption

During bone regeneration, it is important to take bone homeostasis into consideration, which is maintained by the balance of dynamic bone formation and resorption. Osteoblasts originate from multipotent mesenchymal stem cells (MSCs) and secrete the osteoid matrix. Osteoclasts arise from the mononuclear cell lineage and are responsible for bone matrix resorption (Borciani et al., 2020).

However, so far, only a few literatures are focused on interaction between SF scaffolds and osteoclasts. Jones et al. (Jones et al., 2009) cultured murine osteoblasts and osteoclasts on SF scaffolds. When monocytes were cultured separately, cells aggregated together and the expression of tartrate resistant acid phosphatase (TRAP) was positive, as the osteoclast marker. However, when co-cultured with osteoblasts, individual TRAP positive cells spread evenly amongst osteoblasts, forming a homogeneous layer. Furthermore, Chon et al. (Chon et al., 2012) reported that SF hydrolysate could inhibit RANKL-induced TRAP formation, osteoclast-related gene expression and signaling pathways in RAW 264.7 cells. Meanwhile, the SF hydrolysate could induce apoptosis signaling cascades of osteoclasts. On this basis, SF scaffolds seem an ideal choice for bone regeneration to repair bone defects with its capacity to inhibit activity of osteoclasts. However, more researches should be carried out in this field to further understand the effect of SF scaffolds on osteoclasts and bone remodeling.

2.4 Vascular ingrowth

The vascular ingrowth is another important factor of bone regeneration, which can improve oxygen and nutrient diffusion (Li et al., 2021). It also influences the differentiation of MSCs into osteoblasts and osteoid formation (Yan et al., 2019; Song et al., 2020). The enhanced osteogenic differentiation promotes the secretion of soluble factors, such as bone morphogenetic protein-2 (BMP-2) and beta-catenin, and in turn benefits the vascularization process (Niu et al., 2019). During the biomineralization period, it is also helpful to form functional vascular networks and thus achieve desired bone formation.

The mild inflammatory response can induce the vascular growth and the ingrowth of vessels into SF scaffolds (Thurber et al., 2015; Rameshbabu et al., 2020). Usually, SF scaffolds used for bone regeneration exhibit high porosity and thus allow the vessel ingrowth, which can be improved by pre-seeded cells before implantations. Watchararot et al. (2021) seeded human adipose-derived stem cells (hADSC) onto SF scaffolds and implanted them into chick chorioallantoic membrane with the pore diameter of 513.96 ± 4.99 μm and porosity of 77.34 ± 6.96%. A capillary network of spoke-wheel pattern was induced by the seeded scaffolds 3 weeks earlier than unseeded scaffolds, indicating an early angiogenesis. Sun et al. (Sun et al., 2016) also found the co-cultural of endothelial cells and human mesenchymal stem cells (hMSCs) could significantly improve angiogenesis of SF scaffolds which might result from vascular endothelial growth factor (VEGF) and other angiogenic factors secreted by the pre-seeded cells.

2.5 Matrix mineralization

Biomineralization of bone ECM is highly dynamic but well-regulated to obtain diverse organic-inorganic hybrid structures (Kundu et al., 2020). Native bone ECM exhibits three-dimensional (3D) structure with porous morphology and organic-inorganic components. The different physiologic conditions and ECM compositions also influence the deposition of hydroxyapatite (HAP) nanocrystals (Thrivikraman et al., 2019). The mineralized matrix can in turn induce osteogenic differentiation and the formation of mature bone tissues (Xiong et al., 2011). Therefore, an ideal bone graft should have capability to induce biomineralization, similar to natural bone ECM.

SF scaffolds have been proved able to improve the deposition of HAP nanocrystals in simulated body fluid (SBF) solution (Zaharia et al., 2012; Nourmohammadi et al., 2017; Kundu et al., 2020). The amorphous spacers can serve as nucleation sites and promote the deposition of HAP crystals, which is similar to the role of Col I in natural bone (Marelli et al., 2012; Jin et al., 2015; Vetsch et al., 2015). After pretreatment, the formation of HAP crystallization can be facilitated by the electrostatic interaction between the functional groups and calcium ions (Ca^{2+}) (Choi et al., 2012). Huang et al. (Huang et al., 2021) fabricated organized SF film and study the deposition of amorphous calcium phosphate (CaP) in phosphate buffer saline (PBS) and enzyme solution, where a mixture of tricalcium phosphate (TCP) and HAP crystals formed in PBS solution but only HAP crystals could be observed in enzyme solution. The difference possibly resulted from the degradation of SF induced by enzyme, which led to different SF contents and solution pH environment. Meanwhile, it is also interesting to find SF scaffolds from different sources have different performance in biomineralization process. Zhang et al. (Zhang et al., 2020) compared the effect of *Antheraea pernyi* SF and *Bombyx mori* SF fibers as templates of biomineralization and found the *Antheraea pernyi* SF could induce better mineralization, which resulted from more acidic amino acids of hydrophilic amorphous fractions. Sahu et al. (2015) also found nonmulberry SF scaffolds had better osteoconductivity and biomineralization performance than mulberry SF scaffolds.

TABLE 1 Summary of fabrication techniques of SF scaffolds for bone regeneration.

Scaffold type	Silk source	Fabrication techniques	Bioactive components	References
Mat	*Bombyx mori*	Electrospinning	Calcium zinc silicate	Hadisi et al. (2020)
Mat	*Bombyx mori*	Electrospinning	HAP	Valarmathi and Sumathi, (2020)
Mat	*Bombyx mori*	Electrospinning	Laponite	Atrian et al. (2019)
Mat	*Bombyx mori*	Electrospinning	Bioactive glass (BG) and HAP	Liu et al. (2019)
Sponge	*Bombyx mori*	Freeze drying	Alumina	Zafar et al. (2020)
Sponge	*Bombyx mori*	Freeze drying	HAP	Nie et al. (2019)
Sponge	*Bombyx mori*	Glycerol crosslinking and directional field freeze technology	HAP and graphene oxide (GO)	Wang et al. (2020b)
Sponge	*Bombyx mori*	EDC/NHS click-chemistry method	HAP, carboxymethyl CS, cellulose nanocrystals and strontium	Zhang et al. (2019)
Sponge	*Bombyx mori*	Glutaraldehyde crosslinking and freeze drying	CS and magnetite	Aliramaji et al. (2017)
Sponge	*Bombyx mori*	Freeze drying	Titanium dioxide (TiO_2)	Johari et al. (2017)
Sponge	*Bombyx mori*	Freeze drying	Fluoridated TiO_2	Johari et al. (2018a)
Sponge	*Bombyx mori*	Freeze drying	TiO_2	Johari et al. (2018b)
Sponge	*Bombyx mori*	HRP-crosslinking, salt leaching and freeze drying	β-TCP	Ribeiro et al. (2019)
Hydrogel	*Bombyx mori*	Sonication and crosslinking	Vancomycin and halloysite	Avani et al. (2020)
Hydrogel	*Bombyx mori*	Heating and crosslinking	DFO and HAP	Wang et al. (2021)
Hydrogel	*Bombyx mori and Antheraea assama*	HRP-crosslinking	HAP and strontium	Moses et al. (2020)
Hydrogel	*Bombyx mori*	Free radical polymerization technique	Magnetite	Tanasa et al. (2020)
Hydrogel	*Bombyx mori*	3D bioprinting	Gelatin, riboflavin, articular cartilage-derived progenitor cells (ACPCs), dental pulp derived stem cells (DPSCs), hMSCs.	Piluso et al. (2020)
Hydrogel	*Bombyx mori*	3D bioprinting	Tris (2,2′-bipyridyl) dichlororuthenium hexahydrate (Ru) and sodium persulfate (SPS), Human articular chondrocytes (HACs)	Cui et al. (2020)
Hydrogel	*Bombyx mori*	Photo-initiated crosslinking	Ru, SPS,	Bap tista et al. (2020)
Film	*Bombyx mori*	*In situ* co-precipitation	HAP	Mobika et al. (2020)
Film	*Bombyx mori*	*In situ* co-precipitation	Chlorin e6	Huang et al. (2022)
Film	Not mentioned	Plasma splashing procedure	CS, polyethylene terephthalate, HAP	Jiang et al. (2020)

3 Techniques to fabricate Silk fibroin hybrid scaffolds

The techniques to fabricate different SF-based scaffolds depend on the formats they appeared in bone regeneration, such as films, hydrogels and porous scaffolds, which have been summarized in Table 1.

3.1 Silk fibroin hybrid films

On basis of deposition techniques and drying processes, the technology to fabricate SF films has been well developed, including *in-situ* co-precipitation method (Mobika et al., 2020; Huang et al., 2022), plasma splashing procedure (Jiang et al., 2020) and matrix-assisted pulsed laser evaporation (Miroiu et al., 2010). To achieve better functionalization, during film preparation, external components can be added, like HAP, silver (Ag) and other bioactive factors, which makes SF hybrid films multifunctional and thus further enhance osteogenesis, including better mechanical properties, angiogenesis, antiinflammation, antibacterial capacity and so on. Jabbari et al. (Jabbari et al., 2019) developed a CS/SF hybrid film *via* solvent casting method, loading reduced graphene oxide (rGO). With the addition of rGO, the swelling ratio and conformability of hybrid film was accordingly increased, and the evaluation of ALP activity and alizarin red staining also demonstrated the promoted osteogenic performance.

3.2 Silk fibroin hybrid hydrogels

The cross-linking techniques are widely used to fabricate SF hydrogels, including mechanical cross-linking, chemical

crosslinking, enzymatic crosslinking and light triggered crosslinking techniques. The mechanical cross-linking technique is simple and economical *via* ultrasound pulses or temperature changes. As for chemical cross-linking, enzymatic crosslinking and light-triggered crosslinking techniques, external components should be introduced as initiators to achieve better crosslinking. For example, the horseradish peroxidase (HRP) cross-linking technique can control the sol-gel transition better and increase the content of *ß*-sheets (Moses et al., 2020; Zuluaga-Velez et al., 2021). Furthermore, immersing SF in methanol or ethanol can transform α-helix structure into *ß*-sheet structure and thus improve the mechanical properties of as-prepared SF hydrogels (Johari et al., 2018a). Piluso et al. (Piluso et al., 2020) developed a rapid riboflavin-mediated crosslinking technique to fabricate cytocompatible SF hydrogel with different riboflavin/sodium persulfate (Ru/SPS) ratio, which exhibited a viability over 80% for all cell types.

With the development of addictive manufacture, 3D printing has become an efficient on-demand manufacturing technique for SF hydrogel, which can help create individual scaffolds of both small and large scale. Furthermore, the cell-laden 3D bioprinting technique permits living cells and biomaterials to be placed in highly organized scaffolds to form complex structures for different applications, which is one of the latest trends in regenerative medicine (Buitrago et al., 2018). Sharma et al. (Sharma et al., 2019) used 3D bioprinting to fabricate a hBMSCs-laden SF/gelatin/$CaCl_2$ hybrid hydrogel with sustained release of Ca^{2+} and increased *ß*-sheet contents, which facilitated the osteogenic differentiation and mineralization of the hBMSCs through Wnt/β-catenin pathway. However, due to the formation of *ß*-sheet, the increase of stiffness and crystallinity can make SF hydrogels brittle and hard to be remodeled by cells (Partlow et al., 2014). In order to overcome the challenges for cell encapsulation, different alternative crosslinking techniques have been explored for cell-laden SF hydrogels, such as chemical crosslinking, enzymatic crosslinking and other redox-based crosslinking, among which photo-triggered crosslinking technique exhibit great potential (Raia et al., 2017; Cui et al., 2020). Cui et al. (Cui et al., 2020) developed a rapid photoredox crosslinking technique to fabricate SF hydrogel, which allowed high cell densities (15 million cells/mL) for cell encapsulation and retained high cell viability (>80%) simultaneously. The photocrosslinked SF hydrogel could reduce spontaneous transition to *ß*-sheet and possess more stable mechanical properties, demonstrating the immense potential of this crosslinking system for biofabrication and tissue regeneration.

3.3 Silk fibroin hybrid porous structures

Porous SF scaffolds include flat structures and sponge-like structures. Flat structures can be formed by fibers and exhibit porous characteristic. Almost all the reported fibers are fabricated by electrospinning, and only a few are achieved by knitting machines (Shi et al., 2013; Biagiotti et al., 2022) or spray-drying/pressing (Dong et al., 2020). Sponge-like structures are the most common reported format as porous scaffolds, showing 3D porosities (Hollister, 2005). Sponge-like structures can be achieved by directional temperature field freezing technology (Wang et al., 2020), salt leaching (Samal et al., 2015; Yan et al., 2015), sonication (Gholipourmalekabadi et al., 2015), 3D-printing (Jia et al., 2019), crosslinking (Teimouri et al., 2015; Aliramaji et al., 2017) and combination of layer-by-layer process and freeze drying (Jia et al., 2019). The pore sizes of freeze-dried sponges are below 100 μm, but they can be controlled by changing solvents, pH and temperature (Kundu et al., 2013). *Via* particle leaching, solvent casting or gas-foaming techniques, the pore structures can be better controlled (Harris et al., 1998).

4 Modifications of silk fibroin hybrid scaffolds for osteogenesis

The plain SF scaffolds exhibit limited osteogenic activity. Modifications should be carried out to enhance osteogenic activity of plain SF scaffolds. In this part, we classify different modification methods in to three kinds: composition adjustment, structure design and surface modification.

4.1 Composition adjustment of silk fibroin hybrid scaffolds

4.1.1 Silk fibroin/inorganics hybrid scaffolds

The bioactive inorganic components applied to form SF/inorganics hybrid biomaterials include CaP (Gupta et al., 2016; Shao et al., 2016; Ribeiro et al., 2018), graphene oxide (GO) (Balu et al., 2018; Wang et al., 2018), titanium dioxide (TiO_2) (Pan et al., 2014; Johari et al., 2018a), silica (SiO_2) (Mieszawska et al., 2010; Maleki et al., 2019) and bioactive glass (BG) (Bidgoli et al., 2019; Du et al., 2019).

The CaP, SiO_2, TiO_2, and BG components can be classified into ceramic biomaterials, exhibiting osteoconductivity, good compression and corrosion resistance, among which HAP has been most applied (Wu et al., 2022). HAP has similar structure and chemical composition with natural bone, which allows them to provide a biomimetic interface for facilitated osseointegration. Ko et al. (2018) integrated HAP with SF scaffolds *via* blending and alternate soaking, and the modulus was over two times of plain SF scaffolds, which also induced better osteogenic differentiation of human adipose-derived mesenchymal stem cells (hADMSCs) and bone regeneration of calvarial defects (Figure 3). SiO_2 and BG are also promising for bone regeneration, whose degradation products show osteoconductive properties

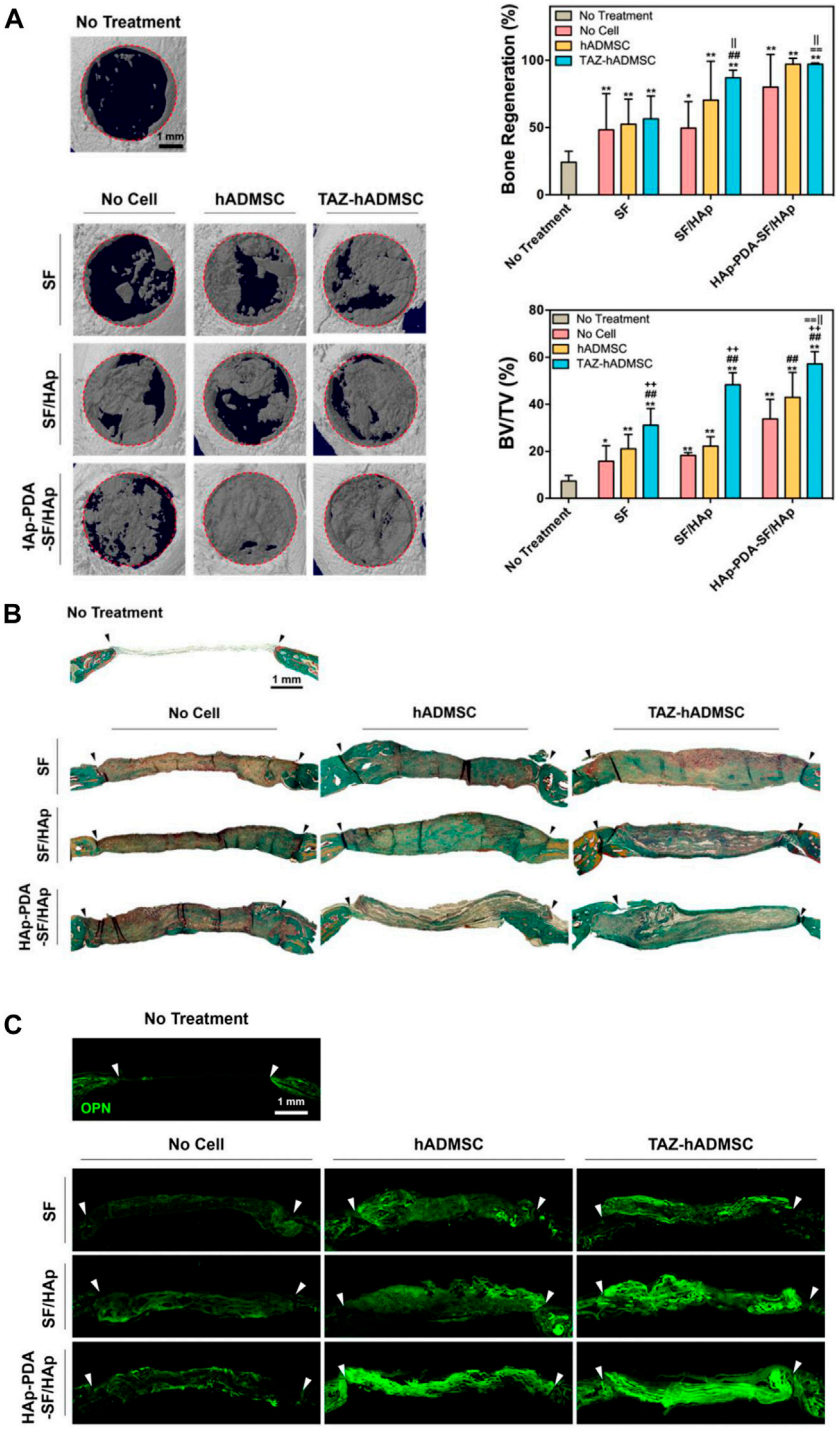

FIGURE 3
In vivo evaluation of the HAP-functionalized SF scaffolds. **(A)** 3D images of the regenerated calvarial defects treated by different scaffolds and quantitative evaluation. **(B)** Goldner's trichrome staining of regenerated calvarial defects. **(C)** Osteopontin immunofluorescence staining of regenerated calvarial defects after different treatments. (Ko et al., 2018) Copyright 2018 American Chemical Society.

(Nikolova and Chavali, 2019). Combining TiO_2 nanoparticles with SF scaffolds can facilitate scaffolds with better biocompatibility and osteoconductivity, where TiO_2 can help SF hybrid scaffolds to mechanically interlock with bone tissues and promote cell attachment and proliferation (Johari et al., 2017). TiO_2 can also enhance the mechanical properties of

hybrid biomaterials *via* facilitating the formation of *ß*-sheet structure (Pan et al., 2014).

GO is one of graphene derivatives, showing good biocompatibility and osteogenic activities, which is another important inorganic component for SF modification. The great advantage to incorporate GO into SF scaffolds is the improvement of mechanical property (Balu et al., 2018). Moreover, SF/GO hybrid scaffolds also show improved biocompatibility and antibacterial property (Wang et al., 2018). Shuai et al. (Shuai et al., 2018) developed SF/GO matrix to evaluate its effect on stem cell fate, where the modulus increased with introduction of GO and the unique topography could promote early adhesion and osteogenic differentiation of hMSCs without additional inducers.

4.1.2 Silk fibroin/organics hybrid scaffolds

The bioactive organic components applied to form SF/inorganics hybrid scaffolds include synthetic and natural polymers, such as polycaprolactone (PCL) (Bhattacharjee et al., 2016; Cengiz et al., 2019; Cengiz et al., 2020), collagen (Shi et al., 2017; Bandyopadhyay and Mandal, 2020), CS (Bissoyi et al., 2018), cellulose (Lee et al., 2013; Barud et al., 2015), alginate (ALG) (Zhang et al., 2015; Patil and Singh, 2019) and so on.

PCL is one of main synthetic polymers applied in SF hybrid scaffolds (Dong et al., 2021). The as-prepared scaffolds possess the osteoconductive effect of SF and osteogenic effect of PCL simultaneously, making it excellent for bone regeneration (Li et al., 2020). Bhattacharjee et al. (Bhattacharjee et al., 2016) fabricated SF/PCL nanofibers *via* electrospinning, where the tensile strength increased by about one fold and the osteogenic differentiation was enhanced compared with plain PCL scaffold.

Introduction of natural polymers seems a feasible approach to enhance cell attachment and osteogenesis due to their favorable biocompatibility and biofunctional components (Wang et al., 2016). SF/collagen and SF/gelatin hybrid scaffolds can exhibit excellent biocompatibility and ECM-mimicking structure, which is able to accelerate the bone formation (Bharadwaz and Jayasuriya, 2020; Wu et al., 2021). SF/CS scaffolds also have great potential in bone regeneration due to the bioactive RGD sequence (Bissoyi et al., 2018). Meanwhile, the combination of cellulose with SF can improve the biodegradability and provide more space for bone regeneration (Ni et al., 2020). Introducing ALG into SF scaffolds can be a promising approach to overcome the poor cell-adhesive property of ALG and the ALG can replace the role of gelatin with lower cost (Patil and Singh, 2019). Perteghella et al. (Perteghella et al., 2017) developed ALG/SF microcarriers with spherical geometry and average diameter of 400 μm, where MSCs adhered rapidly and preserved their potential of multi-lineage differentiation in this innovative 3D culture system.

4.2 Structural design of SF hybrid scaffolds

4.2.1 Films

The favorable performance of SF film makes it a promising strategy for bone regeneration. Li et al. (2022) combined SS and SF to fabricate hybrid films and the breaking strength and breaking elongation increased significantly, which also exhibited faster and well-regulated HAP deposition rate than plain SF films. Furthermore, topographical pattering of SF films can help to achieve better osteogenic performance *in vivo*. Sayin et al. (2017) prepared collagen/SF hybrid films with microchannel patterns, and human osteoblasts and adipose-derived stem cells (ADSCs) were seeded and aligned on the ridges and in the grooves of the patterned film, where stimulate anisotropic osteogenesis was simulated.

Notably, SF film is also an effective barrier to avoid collapse of surrounding soft tissues into the defect cavity and ensure the successful bone repair. Smeets et al. (2017) evaluated three different SF films and commercial collagen membranes. Compare to collagens, the lower resorbability of SF membranes could promote bone regeneration for a longer period. Therefore, SF films are able to meet some special demands of bone regeneration.

4.2.2 Porous scaffolds

Porous SF scaffolds have ideal structures for bone regeneration due to their great similarity to the *in vivo* microenvironment. Varkey et al. (2015) compared the impact of different SF structures on MG63 cell attachment and proliferation. The sponge structure showed the highest porosity of 67% and could maintain its structural integrity, where the secreted collagen also increased with culture time, demonstrating the increasing production of ECM. Correia et al. (2012) also fabricated SF porous scaffolds with different pore sizes to investigate their effects, where the SF scaffold with 400–600 μm pore sizes showed better HAP deposition and expression of osteogenic proteins, and further promoted bone tissue formation, demonstrating the importance of scaffold's pore structures.

However, the mechanical properties of SF porous scaffolds are not satisfying, which limits its application in load-bearing locations. To obtain better mechanical and biological outcomes, external components have been incorporated with SF porous sponges (Kundu et al., 2013). Gupta et al. (2016) fabricated a biomimetic, osteoconductive tricomposite scaffold using HAP, SF fiber from *Antheraea assama* and its SF solution. The SF-reinforced tricomposite scaffolds exhibited about 5-fold higher compressive modulus and better osteogenic capacity. Therefore, SF-based biomimic porous scaffolds with tough mechanical properties are promising in application of bone regeneration. However, it is still insufficient for load-bearing bone and further investigations should be carried out.

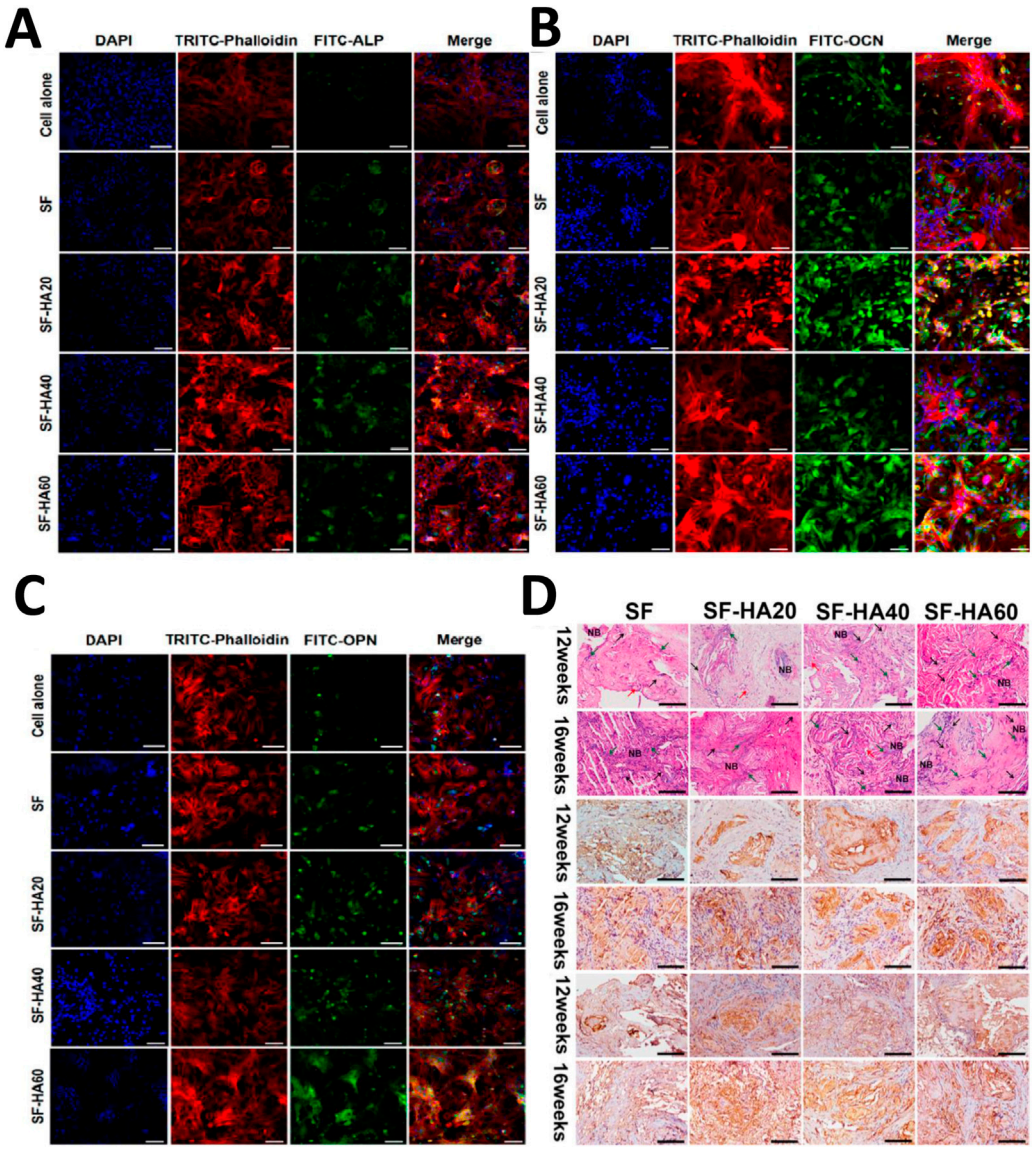

FIGURE 4
Immunofluorescence staining and histological analysis of osteogenic capacity *in vitro* and *in vivo*. **(A)** ALP expression after 7 days in different hydrogels. **(B)** OCN expression after 21 days in different hydrogels. **(C)** OPN expression after 21 days in different hydrogels. The nucleus was stained blue by DAPI and the F-actin was stained red by tetramethylrhodamine (TRITC) conjugated to phalloidin, while ALP, OCN, and OPN were stained green by antibodies conjugated with fluorescein isothiocyanate (FITC). **(D)** HE and immunohistochemistry staining of OCN and OPN in different hydrogels. (Ding et al., 2017) Copyright 2017 American Chemical Society.

4.2.3 Hydrogels

Due to the similarity to microenvironmental of natural tissues, hydrogels have remarkable advantages in bone regeneration (Liaw et al., 2018). SF hydrogels have been widely developed *via* various crosslinking techniques. Ding et al. (2017) fabricated an injectable SF-based hydrogel *via* the combination of water-dispersible SF-HAP nanoparticles and the thixotropic SF nanofiber hydrogel. This nano-scale hydrogel system with homogeneously-distributed HAP nanoparticles showed good biocompatibility and osteogenesis *in vitro*, as well as better bone formation *in vivo* (Figure 4). Ribeiro et al. (2015) combined SF and nano HAP to develop hybrid hydrogels with favorable porosity, mechanical properties and osteoconductivity, which improved cellular metabolism and ALP activity of MG63 cells. These researches have proved the efficiency of SF hybrid hydrogels to induce bone regeneration.

Furthermore, SF hydrogels are ideal drug carriers. An injectable SF-based hybrid hydrogel prepared by

Roohaniesfahani et al. (2019) exhibited the capacity to release bioactive silicon, strontium, and magnesium ions simultaneously to promote osteogenesis and angiogenesis. The seeded osteoblasts showed promoted cell proliferation, ALP activity, and enhanced osteogenic gene expression compared to plain SF hydrogel. The *in vivo* results exhibited decreased fibrous capsule formation and increased new blood vessels around the hydrogel. Besides, multiple SF hydrogels have been prepared to improve their osteogenic capacities with sustainable release of bioactive factors (Ding et al., 2019; Avani et al., 2020; Zarrin et al., 2022). Therefore, SF hydrogels exhibit significant advantages when serving as bioactive scaffolds for bone repair both as matrices and carriers.

4.3 Surface modification of SF hybrid scaffolds

4.3.1 Physical modification

Physical modifications of SF scaffolds include ultraviolet (UV) treatment, gas treatment and plasma treatment (Lau et al., 2020). UV irradiation of SF scaffolds can increase wettability and improve cell adhesion without obvious weight loss, crystallinity change and strength decrease (Li et al., 2012; Khosravi et al., 2018). As a powerful oxidizing agent, ozone (O_3) gas treatment can increase the pliability of SF scaffolds because of the oxidation of amino acid residues (Li et al., 2012). Plasma treatment of SF scaffolds by different working gases (SO_2, NH_3, and O_2) can increase the antithrombogenicity and cellular activity, making it a potential modification technique for bone regeneration (Uchida et al., 2014; Ribeiro et al., 2016). Wang et al. (2019) used a unique vacuum UV/O_3 activation method to treat SF film, which improved the biocompatibility with BMSCs and osteogenesis *in vivo*. Kondyurin et al. (2018) applied plasma immersion ion implantation (PIII) to treat SF scaffold and receive a carbon-rich structure, which enhanced its interaction with both proteins and cells and exhibited significantly higher levels of cell adhesion and proliferation.

4.3.2 Chemical modification

Considering the active groups of peptide chains, SF scaffolds have plenty of active modification sites, which allows different techniques for chemical modification, such as grafting copolymerization techniques and introduction of chemical agents (Murphy et al., 2008; Zhou et al., 2017; Zhou et al., 2018). Hardy et al. (2018) used a simple and rapid photochemical modification technique to initiate the polymerization and thus decorated the SF scaffolds with poly (acrylic acid) (PAA), poly (methacrylic acid) (PMAA), and poly (allylamine) (PAAm). The results showed that the PAA- and PMAA-functionalized SF scaffolds can be well-mineralized, indicating their potential in bone regeneration.

In term of 3D bioprinting of SF hydrogels, modification of vinyl-containing functional groups can help accelerate crosslinking process, especially methacrylate, which can make as-prepared glycidyl-methacrylate-modified SF (SF-MA) hydrogels photocurable. Barroso et al. studied the effect of the SF-MA solution pH on the properties of SF-MA hydrogels, where the SF-MA prepared at pH 5 exhibited better mechanical properties than that prepared in pH 7 and 8, and the hydrogel pH did not affect the good biocompatibility of as-prepared SF hydrogels.

4.3.3 Surface functionalization

As for SF scaffolds, it is necessary to further improve osteogenesis especially in the repair of critical-sized or weight-bearing bone defects. Bioactive components and cells loaded on SF scaffolds have received increasing attention in bone regeneration. Different cytokines, drugs and pre-cultured cells can directly regulate cell behavior and promote bone regeneration.

During cell recruitment, proliferation and osteogenesis, cytokines play an important role (Lei et al., 2021; Wu et al., 2021). Loading cytokines on SF scaffolds is a promising method to direct cell differentiation and promote bone formation, including BMP-2 (Niu et al., 2017; Song et al., 2018), stromal-derived factor-1 (SDF-1) (Shen et al., 2016), VEGF (Besheli et al., 2018; Fitzpatrick et al., 2021), DFO (Wang et al., 2017; Ding et al., 2019) and so on. Fitzpatrick et al. (2021) generated multi-functionalized 3D-printed SF/HAP scaffolds loading BMP-2. VEGF and neural growth factor (NGF) to accelerate bone regeneration. The modulus of as-prepared scaffolds significantly increased and the expression of osteogenesis-related genes (Runx2, OPN, bone sialoprotein) was up-regulated by the synergistic enhancement of three factors.

Infection and inflammation are significant challenges during bone regeneration. Drug-loading SF scaffolds seem a promising strategy to overcome these problems with application of antibacterial and anti-inflammatory drugs, such as gentamicin (Sharma et al., 2016), vancomycin (Besheli et al., 2017), Ag nanoparticles (AgNPs) (Zhou et al., 2017), dexamethasone (Moses and Mandal, 2022) and so on. Notably, combination of AgNPs and conventional antibiotics can achieve stronger antimicrobial performance and thus promote bone regeneration. Zhou et al. (Zhou et al., 2017) loaded AgNPs/gentamicin on SF scaffolds with the assistance of polydopamine, where AgNPs and gentamicin effectively inhibited adhesion and proliferation of *S. aureus*, and improved cell adhesion, proliferation and osteogenic differentiation simultaneously. (Figure 5). However, it still remains a challenge to avoid rapid drug releasing and obtain sustainable release and functionalization *in vivo*.

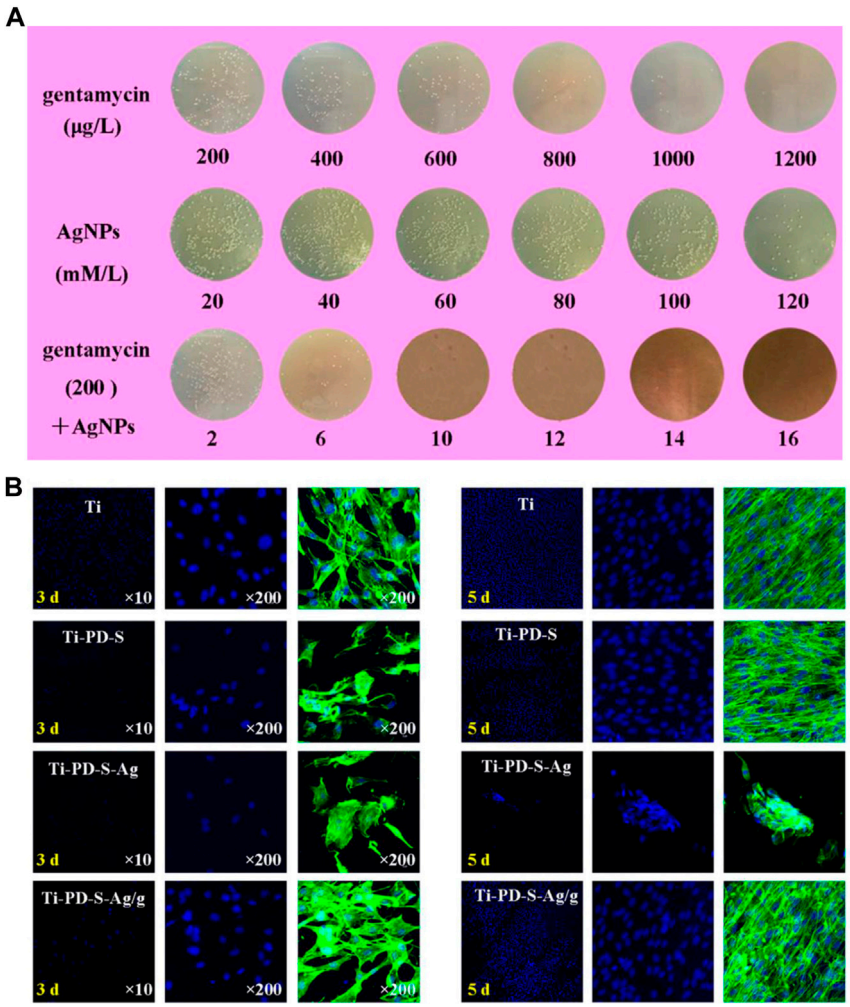

FIGURE 5
Antibacterial activities and biocompatibility of AgNPs/gentamicin-loaded SF scaffolds. **(A)** Quantitative evaluation of *S. aureus* cultured on different samples after 24 h **(B)** MC3T3 cell morphologies detected by fluorescent staining of FITC and DAPI (Zhou et al., 2017). Copyright 2017 American Chemical Society.

Besides, BMSCs and ADSCs are often seeded on SF scaffolds before implantation as bioactive components due to their differentiation potential. Plenty of researches indicated that pre-cultured BMSCs could effectively promote bone regeneration (Herrmann et al., 2015; Gao et al., 2016). Similarly, ADSCs exhibit anticipated osteogenic performance in different SF scaffolds, where ADSCs-loaded SF scaffolds can promote biomineralization and bone formation (Chen et al., 2016; Sartika et al., 2020). However, ADSCs alone are hard to achieve ideal differentiation towards osteoblasts without bioactive molecules or factors. It is essential to apply bioactive components as osteogenic inducers.

5 Conclusion and outlooks

SF scaffolds exhibit great potential in bone regeneration due to advantages of biocompatibility, biodegradability, mechanical strength and structural adjustability. With the rapid development of modern technology, a wide range of techniques has been employed to fabricate different types of SF scaffolds, such as films, porous scaffolds and hydrogels. For better functionalization and osteogenesis, SF scaffolds have been modified with plenty of components to maximize its mechanical and biological functional properties, such as angiogenesis, antibiosis, antiinflammation and cell-laden capacity. Based on recent technical advances in fabrication of SF scaffolds, researchers can better design and fabricate SF

scaffolds according to practical demands of bone regeneration. Especially, with the development of 3D bioprinting, it has been feasible to achieve accurate shape and structures according the bone defects, which can accommodate living-cell patterning to mimic native bone tissues. These encouraging advancements have open up new opportunities in the application of SF scaffolds in bone regeneration, where controllable biodegradation and good mechanical properties are critically required.

Furthermore, SF hybrid scaffolds are able to simulate the natural bone microenvironment and promote osteogenesis with the help of well-designed structures, bioactive components and functional surface modification. However, there still lack sufficient studies on evaluation of SF scaffolds in big animal models such as dogs and pigs, which is necessary before future clinical applications. Meanwhile, considering their long-term close contact with tissues and the potential cytotoxicity and immunogenicity related to degradation products, it is vital to resolve the concerns of long-term *in vivo* safety of SF scaffolds. Therefore, although various techniques have been developed, it still needs more deep investigations to achieve comprehensive understanding of SF scaffolds.

Notably, although SF scaffolds have been investigated for a long time, it still has not been approved by regulatory authorities for any clinical application in bone regeneration. The clinical translation of such a Class III medical device can be quite time and cost-consuming and the translation process from bench to bedside is still unfamiliar to most researchers. So far, no clinical trials of SF scaffolds for bone regeneration have been registered in ClinicalTrials.gov or reported. Taken together, to promote better clinical translation of SF scaffolds for bone regeneration, more efforts should be carried out.

- More comprehensive investigations are required for deeper understanding of the degradation and clearing mechanisms of different SF scaffolds.
- More high-quality researches are in demand for further investigation on the degradation products of SF scaffolds to resolve concerns on the clinical use of SF scaffolds.
- More comprehensive translational researches for SF scaffolds are needed to make further steps to realize effective clinical translation, especially experiments in big animal models and clinical trials.

Overall, SF scaffolds are promising candidates to promote osteogenesis and have great potential in the field of medical devices for bone regeneration. This review intends to reveal the interaction between SF scaffolds and hosts' cells and tissues, as well as up-to-date research status, which provides a deep and comprehensive insight into SF scaffolds for bone regeneration. It will help provide strong evidence to support the development and improvement of SF scaffolds for superior osteogenic performance.

Author contributions

HW has written the manuscript text and CZ is responsive for the revision. XW and KL have conceived the concept of this review.

Funding

This review was supported by National Natural Science Foundation of China (81871490, 82001006, 82071096), the Interdisciplinary Program of Shanghai Jiao Tong University (YG2022ZD014, YG2021ZD12), Science and Technology Commission of Shanghai Municipality (21DZ2294600, 21490711700), Program of Shanghai Academic/Technology Research Leader (20XD1433100, 19XD1434500), Double Hundred Plan (20191819), and CAMS Innovation Fund for Medical Sciences (CIFMS) (2019-I2M-5-037).

Conflict of interest

The authors declare that the research was conducted in the absence of any commercial or financial relationships that could be construed as a potential conflict of interest.

Publisher's note

All claims expressed in this article are solely those of the authors and do not necessarily represent those of their affiliated organizations, or those of the publisher, the editors and the reviewers. Any product that may be evaluated in this article, or claim that may be made by its manufacturer, is not guaranteed or endorsed by the publisher.

References

Aliramaji, S., Zamanian, A., and Mozafari, M. (2017). Super-paramagnetic responsive silk fibroin/chitosan/magnetite scaffolds with tunable pore structures for bone tissue engineering applications. *Mater. Sci. Eng. C* 70, 736–744. doi:10.1016/j.msec.2016.09.039

Atrian, M., Kharaziha, M., Emadi, R., and Alihosseini, F. (2019). Silk-Laponite® fibrous membranes for bone tissue engineering. *Appl. Clay Sci.* 174, 90–99. doi:10.1016/j.clay.2019.03.038

Avani, F., Damoogh, S., Mottaghitalab, F., Karkhaneh, A., and Farokhi, M. (2020). Vancomycin loaded halloysite nanotubes embedded in silk fibroin hydrogel applicable for bone tissue engineering. *Int. J. Polym. Mater. Polym. Biomaterials* 69, 32–43. doi:10.1080/00914037.2019.1616201

Bakhshandeh, B., Nateghi, S. S., Gazani, M. M., Dehghani, Z., and Mohammadzadeh, F. (2021). A review on advances in the applications of spider

silk in biomedical issues. *Int. J. Biol. Macromol.* 192, 258–271. doi:10.1016/j.ijbiomac.2021.09.201

Balu, R., Reeder, S., Knott, R., Mata, J., De Campo, L., Dutta, N. K., et al. (2018). Tough photocrosslinked silk fibroin/graphene oxide nanocomposite hydrogels. *Langmuir* 34 (31), 9238–9251. doi:10.1021/acs.langmuir.8b01141

Bandyopadhyay, A., and Mandal, B. B. (2020). A three-dimensional printed silk-based biomimetic tri-layered meniscus for potential patient-specific implantation. *Biofabrication* 12, 015003. doi:10.1088/1758-5090/ab40fa

Baptista, M., Joukhdar, H., Alcala-Orozco, C. R., Lau, K., Jiang, S., Cui, X., et al. (2020). Silk fibroin photo-lyogels containing microchannels as a biomaterial platform for *in situ* tissue engineering. *Biomater. Sci.* 8 (24), 7093–7105. doi:10.1039/d0bm01010c

Barud, H. G. O., Barud, H. D., Cavicchioli, M., Do Amaral, T. S., De Oliveira, O. B., Santos, D. M., et al. (2015). Preparation and characterization of a bacterial cellulose/silk fibroin sponge scaffold for tissue regeneration. *Carbohydr. Polym.* 128, 41–51. doi:10.1016/j.carbpol.2015.04.007

Besheli, N. H., Damoogh, S., Zafar, B., Mottaghitalab, F., Motasadizadeh, H., Rezaei, F., et al. (2018). Preparation of a codelivery system based on vancomycin/silk scaffold containing silk nanoparticle loaded VEGF. *ACS Biomater. Sci. Eng.* 4 (8), 2836–2846. doi:10.1021/acsbiomaterials.8b00149

Besheli, N. H., Mottaghitalab, F., Eslami, M., Gholami, M., Kundu, S. C., Kaplan, D. L., et al. (2017). Sustainable release of vancomycin from silk fibroin nanoparticles for treating severe bone infection in rat tibia osteomyelitis model. *ACS Appl. Mat. Interfaces* 9 (6), 5128–5138. doi:10.1021/acsami.6b14912

Bharadwaz, A., and Jayasuriya, A. C. (2020). Recent trends in the application of widely used natural and synthetic polymer nanocomposites in bone tissue regeneration. *Mater. Sci. Eng. C* 110, 110698. doi:10.1016/j.msec.2020.110698

Bhattacharjee, P., Kundu, B., Naskar, D., Kim, H. W., Bhattacharya, D., Maiti, T. K., et al. (2016). Potential of inherent RGD containing silk fibroin–poly (∈-caprolactone) nanofibrous matrix for bone tissue engineering. *Cell. Tissue Res.* 363 (2), 525–540. doi:10.1007/s00441-015-2232-6

Biagiotti, M., Bassani, G. A., Chiarini, A., Vincoli, V. T., Dal Pra, I., Cosentino, C., et al. (2022). Three-Layered silk fibroin tubular scaffold for the repair and regeneration of small caliber blood vessels: From design to *in vivo* pilot tests. *Front. Bioeng. Biotechnol.* 10, 356. doi:10.3389/fbioe.2019.00356

Bidgoli, M. R., Alemzadeh, I., Tamjid, E., Khafaji, M., and Vossoughi, M. (2019). Fabrication of hierarchically porous silk fibroin-bioactive glass composite scaffold via indirect 3D printing: Effect of particle size on physico-mechanical properties and *in vitro* cellular behavior. *Mater. Sci. Eng. C* 103, 109688. doi:10.1016/j.msec.2019.04.067

Bissoyi, A., Singh, A. K., Pattanayak, S. K., Bit, A., Sinha, S. K., Patel, A., et al. (2018). Understanding the molecular mechanism of improved proliferation and osteogenic potential of human mesenchymal stem cells grown on a polyelectrolyte complex derived from non-mulberry silk fibroin and chitosan. *Biomed. Mat.* 13 (1), 015011. doi:10.1088/1748-605X/aa890c

Borciani, G., Montalbano, G., Baldini, N., Cerqueni, G., Vitale-Brovarone, C., and Ciapetti, G. (2020). Co-culture systems of osteoblasts and osteoclasts: Simulating *in vitro* bone remodeling in regenerative approaches. *Acta Biomater.* 108, 22–45. doi:10.1016/j.actbio.2020.03.043

Buitrago, J. O., Patel, K. D., El-Fiqi, A., Lee, J. H., Kundu, B., Lee, H. H., et al. (2018). Silk fibroin/collagen protein hybrid cell-encapsulating hydrogels with tunable gelation and improved physical and biological properties. *Acta Biomater.* 69, 218–233. doi:10.1016/j.actbio.2017.12.026

Burger, M. G., Grosso, A., Briquez, P. S., Born, G. M. E., Lunger, A., Schrenk, F., et al. (2022). Robust coupling of angiogenesis and osteogenesis by VEGF-decorated matrices for bone regeneration. *Acta Biomater.* 149, 111–125. doi:10.1016/j.actbio.2022.07.014

Cengiz, I. F., Maia, F. R., Morais, A. D., Silva-Correia, J., Pereira, H., Canadas, R. F., et al. (2020). Entrapped in cage (EiC) scaffolds of 3D-printed polycaprolactone and porous silk fibroin for meniscus tissue engineering. *Biofabrication* 12 (2), 025028. doi:10.1088/1758-5090/ab779f

Cengiz, I. F., Pereira, H., Espregueira-Mendes, J., Kwon, I. K., Reis, R. L., and Oliveira, J. M. (2019). Suturable regenerated silk fibroin scaffold reinforced with 3D-printed polycaprolactone mesh: Biomechanical performance and subcutaneous implantation. *J. Mat. Sci. Mat. Med.* 30 (6), 63. doi:10.1007/s10856-019-6265-3

Chen, H. B., Qian, Y. Z., Xia, Y., Chen, G., Dai, Y., Li, N., et al. (2016). Enhanced osteogenesis of ADSCs by the synergistic effect of aligned fibers containing collagen I. *ACS Appl. Mat. Interfaces* 8 (43), 29289–29297. doi:10.1021/acsami.6b08791

Choi, Y., Cho, S. Y., Park, D. J., Park, H. H., Heo, S., and Jin, H. J. (2012). Silk fibroin particles as templates for mineralization of calcium-deficient hydroxyapatite. *J. Biomed. Mat. Res.* 100 (8), 2029–2034. doi:10.1002/jbm.b.32766

Chon, J. W., Kim, H., Jeon, H. N., Park, K., Lee, K. G., Yeo, J. H., et al. (2012). Silk fibroin hydrolysate inhibits osteoclastogenesis and induces apoptosis of osteoclasts derived from RAW 264.7 cells. *Int. J. Mol. Med.* 30 (5), 1203–1210. doi:10.3892/ijmm.2012.1120

Correia, C., Bhumiratana, S., Yan, L. P., Oliveira, A. L., Gimble, J. M., Rockwood, D., et al. (2012). Development of silk-based scaffolds for tissue engineering of bone from human adipose-derived stem cells. *Acta Biomater.* 8 (7), 2483–2492. doi:10.1016/j.actbio.2012.03.019

Cui, X., Soliman, B. G., Alcala-Orozco, C. R., Li, J., Vis, M. a. M., Santos, M., et al. (2020). Rapid photocrosslinking of silk hydrogels with high cell density and enhanced shape fidelity. *Adv. Healthc. Mat.* 9 (22), e2001801. doi:10.1002/adhm.202001801

Ding, Z. Z., Han, H. Y., Fan, Z. H., Lu, H. J., Sang, Y. H., Yao, Y. L., et al. (2017). Nanoscale silk-hydroxyapatite hydrogels for injectable bone biomaterials. *ACS Appl. Mat. Interfaces* 9 (20), 16913–16921. doi:10.1021/acsami.7b03932

Ding, Z. Z., Zhou, M. L., Zhou, Z. Y., Zhang, W. J., Jiang, X. Q., Lu, X. H., et al. (2019). Injectable silk nanofiber hydrogels for sustained release of small-molecule drugs and vascularization. *ACS Biomater. Sci. Eng.* 5 (8), 4077–4088. doi:10.1021/acsbiomaterials.9b00621

Dong, L. L., Li, L. H., Song, Y., Fang, Y. N., Liu, J. L., Chen, P. X., et al. (2021). MSC-derived immunomodulatory extracellular matrix functionalized electrospun fibers for mitigating foreign-body reaction and tendon adhesion. *Acta Biomater.* 133, 280–296. doi:10.1016/j.actbio.2021.04.035

Dong, Y. D., Hong, M. M., Dai, R. Z., Wu, H. Y., and Zhu, P. (2020). Engineered bioactive nanoparticles incorporated biofunctionalized ECM/silk proteins based cardiac patches combined with MSCs for the repair of myocardial infarction: *In vitro* and *in vivo* evaluations. *Sci. Total Environ.* 707, 707 135976. doi:10.1016/j.scitotenv.2019.135976

Du, X. Y., Wei, D. X., Huang, L., Zhu, M., Zhang, Y. P., and Zhu, Y. F. (2019). 3D printing of mesoporous bioactive glass/silk fibroin composite scaffolds for bone tissue engineering. *Mater. Sci. Eng. C* 103, 109731. doi:10.1016/j.msec.2019.05.016

Fitzpatrick, V., Martin-Moldes, Z., Deck, A., Torres-Sanchez, R., Valat, A., Cairns, D., et al. (2021). Functionalized 3D-printed silk-hydroxyapatite scaffolds for enhanced bone regeneration with innervation and vascularization. *Biomaterials* 276, 120995. doi:10.1016/j.biomaterials.2021.120995

Gao, M., Chen, J. J., Lin, G. W., Li, S. W., Wang, L., Qin, A. J., et al. (2016). Long-term tracking of the osteogenic differentiation of mouse BMSCs by aggregation-induced emission nanoparticles. *ACS Appl. Mat. Interfaces* 8 (28), 17878–17884. doi:10.1021/acsami.6b05471

Gellynck, K., Verdonk, P. C. M., Van Nimmen, E., Almqvist, K. F., Gheysens, T., Schoukens, G., et al. (2008). Silkworm and spider silk scaffolds for chondrocyte support. *J. Mat. Sci. Mat. Med.* 19, 3399–3409. doi:10.1007/s10856-008-3474-6

Gholipourmalekabadi, M., Mozafari, M., Gholipourmalekabadi, M., Bojnordi, M. N., Hashemi-Soteh, M. B., Salimi, M., et al. (2015). *In vitro* and *in vivo* evaluations of three-dimensional hydroxyapatite/silk fibroin nanocomposite scaffolds. *Biotechnol. Appl. Biochem.* 62 (4), 441–450. doi:10.1002/bab.1285

Gorenkova, N., Maitz, M. F., Bohme, G., Alhadrami, H. A., Jiffri, E. H., Totten, J. D., et al. (2021). The innate immune response of self-assembling silk fibroin hydrogels. *Biomater. Sci.* 9 (21), 7194–7204. doi:10.1039/d1bm00936b

Guo, L. Q., Liang, Z. H., Yang, L., Du, W. Y., Yu, T., Tang, H. Y., et al. (2021). The role of natural polymers in bone tissue engineering. *J. Control. Release* 338, 571–582. doi:10.1016/j.jconrel.2021.08.055

Gupta, P., Adhikary, M., Christakiran, M. J., Kumar, M., Bhardwaj, N., and Mandal, B. B. (2016). Biomimetic, osteoconductive non-mulberry silk fiber reinforced tricomposite scaffolds for bone tissue engineering. *ACS Appl. Mat. Interfaces* 8 (45), 30797–30810. doi:10.1021/acsami.6b11366

Hadisi, Z., Bakhsheshi-Rad, H. R., Walsh, T., Dehghan, M. M., Farzad-Mohajeri, S., Gholami, H., et al. (2020). *In vitro* and *in vivo* evaluation of silk fibroin-hardystonite-gentamicin nanofibrous scaffold for tissue engineering applications. *Polym. Test.* 91, 106698. doi:10.1016/j.polymertesting.2020.106698

Hardy, J. G., Bertin, A., Torres-Rendon, J. G., Leal-Egana, A., Humenik, M., Bauer, F., et al. (2018). Facile photochemical modification of silk protein-based biomaterials. *Macromol. Biosci.* 18 (11), e1800216. doi:10.1002/mabi.201800216

Harris, L. D., Kim, B. S., and Mooney, D. J. (1998). Open pore biodegradable matrices formed with gas foaming. *J. Biomed. Mat. Res.* 42, 396–402. doi:10.1002/(sici)1097-4636(19981205)42:3<396::aid-jbm7>3.0.co;2-e

Herrmann, M., Verrier, S., and Alini, M. (2015). Strategies to stimulate mobilization and homing of endogenous stem and progenitor cells for bone tissue repair. *Front. Bioeng. Biotechnol.* 3, 79. doi:10.3389/fbioe.2015.00079

Hollister, S. J. (2005). Porous scaffold design for tissue engineering. *Nat. Mat.* 4 (7), 518–524. doi:10.1038/nmat1421

Huang, T. T., Zhou, Z. H., Li, Q. Y., Tang, X. X., Chen, X. L., Ge, Y. F., et al. (2022). Light-triggered adhesive silk-based film for effective photodynamic antibacterial therapy and rapid hemostasis. *Front. Bioeng. Biotechnol.* 9, 820434. doi:10.3389/fbioe.2021.820434

Huang, Y., Zou, Z. Y., Ping, H., Lei, L. W., Xie, J. J., Xie, H., et al. (2021). Mineralization of calcium phosphate induced by a silk fibroin film under different biological conditions. *RSC Adv.* 11, 18590–18596. doi:10.1039/d1ra02199k

Jabbari, F., Hesaraki, S., and Houshmand, B. (2019). The physical, mechanical, and biological properties of silk fibroin/chitosan/reduced graphene oxide composite membranes for guided bone regeneration. *J. Biomaterials Sci. Polym. Ed.* 30, 1779–1802. doi:10.1080/09205063.2019.1666235 Ed.

Jia, Z. J., Zhou, W. H., Yan, J. L., Xiong, P., Guo, H., Cheng, Y., et al. (2019). Constructing multilayer silk protein/nanosilver biofunctionalized hierarchically structured 3D printed Ti6Al4 V scaffold for repair of infective bone defects. *ACS Biomater. Sci. Eng.* 5, 244–261. doi:10.1021/acsbiomaterials.8b00857

Jiang, S. B., Liu, X. D., Liu, Y., Liu, J., He, W. D., and Dong, Y. F. (2020). Synthesis of silver @hydroxyapatite nanoparticles based biocomposite and their assessment for viability of Osseointegration for rabbit knee joint anterior cruciate ligament rehabilitation. *J. Photochem. Photobiol. B Biol.* 202, 111677. doi:10.1016/j.jphotobiol.2019.111677

Jin, Y. S., Kundu, B., Cai, Y. R., Kundu, S. C., and Yao, J. M. (2015). Bio-inspired mineralization of hydroxyapatite in 3D silk fibroin hydrogel for bone tissue engineering. *Colloids Surfaces B Biointerfaces* 134, 339–345. doi:10.1016/j.colsurfb.2015.07.015

Johari, N., Hosseini, H. R. M., and Samadikuchaksaraei, A. (2018a). Novel fluoridated silk fibroin/TiO2 nanocomposite scaffolds for bone tissue engineering. *Mater. Sci. Eng. C* 82, 265–276. doi:10.1016/j.msec.2017.09.001

Johari, N., Hosseini, H. R. M., and Samadikuchaksaraei, A. (2017). Optimized composition of nanocomposite scaffolds formed from silk fibroin and nano-TiO2 for bone tissue engineering. *Mater. Sci. Eng. C* 79, 783–792. doi:10.1016/j.msec.2017.05.105

Johari, N., Hosseini, H. R. M., Taromi, N., Arasteh, S., Kazemnejad, S., and Samadikuchaksaraei, A. (2018b). Evaluation of bioactivity and biocompatibility of silk fibroin/TiO_2 nanocomposite. *J. Med. Biol. Eng.* 38, 99–105. doi:10.1007/s40846-017-0295-4

Jones, G. L., Motta, A., Marshall, M. J., El Haj, A. J., and Cartmell, S. H. (2009). Osteoblast: Osteoclast co-cultures on silk fibroin, chitosan and PLLA films. *Biomaterials* 30 (29), 5376–5384. doi:10.1016/j.biomaterials.2009.07.028

Jung, S. R., Song, N. J., Yang, D. K., Cho, Y. J., Kim, B. J., Hong, J. W., et al. (2013). Silk proteins stimulate osteoblast differentiation by suppressing the Notch signaling pathway in mesenchymal stem cells. *Nutr. Res.* 33 (2), 162–170. doi:10.1016/j.nutres.2012.11.006

Khosravi, A., Ghasemi-Mobarakeh, L., Mollahosseini, H., Ajalloueian, F., Rad, M. M., Norouzi, M. R., et al. (2018). Immobilization of silk fibroin on the surface of PCL nanofibrous scaffolds for tissue engineering applications. *J. Appl. Polym. Sci.* 135, 46684. doi:10.1002/app.46684

Ko, E., Lee, J. S., Kim, H., Yang, S. Y., Yang, D., Yang, K., et al. (2018). Electrospun silk fibroin nanofibrous scaffolds with two-stage hydroxyapatite functionalization for enhancing the osteogenic differentiation of human adipose-derived mesenchymal stem cells. *ACS Appl. Mat. Interfaces* 10, 7614–7625. doi:10.1021/acsami.7b03328

Koh, L. D., Cheng, Y., Teng, C. P., Khin, Y. W., Loh, X. J., Tee, S. Y., et al. (2015). Structures, mechanical properties and applications of silk fibroin materials. *Prog. Polym. Sci.* 46, 86–110. doi:10.1016/j.progpolymsci.2015.02.001

Kondyurin, A., Lau, K., Tang, F., Akhavan, B., Chrzanowski, W., Lord, M. S., et al. (2018). Plasma ion implantation of silk biomaterials enabling direct covalent immobilization of bioactive agents for enhanced cellular responses. *ACS Appl. Mat. Interfaces* 10 (21), 17605–17616. doi:10.1021/acsami.8b03182

Kundu, B., Brancato, V., Oliveira, J. M., Correlo, V. M., Reis, R. L., and Kundu, S. C. (2020). Silk fibroin promotes mineralization of gellan gum hydrogels. *Int. J. Biol. Macromol.* 153, 1328–1334. doi:10.1016/j.ijbiomac.2019.10.269

Kundu, B., Rajkhowa, R., Kundu, S. C., and Wang, X. G. (2013). Silk fibroin biomaterials for tissue regenerations. *Adv. Drug Deliv. Rev.* 65, 457–470. doi:10.1016/j.addr.2012.09.043

Lau, K., Akhavan, B., Lord, M. S., Bilek, M. M., and Rnjak-Kovacina, J. (2020). Dry surface treatments of silk biomaterials and their utility in biomedical applications. *ACS Biomater. Sci. Eng.* 6, 5431–5452. doi:10.1021/acsbiomaterials.0c00888

Lee, J., Huh, S. J., Seok, J. M., Lee, S., Byun, H., Jang, G. N., et al. (2022). Surface engineering of 3D-printed scaffolds with minerals and a pro-angiogenic factor for vascularized bone regeneration. *Acta Biomater.* 140, 730–744. doi:10.1016/j.actbio.2021.12.007

Lee, J. M., Kim, J. H., Lee, O. J., and Park, C. H. (2013). The fixation effect of a silk fibroin–bacterial cellulose composite plate in segmental defects of the zygomatic Arch<subtitle>An experimental study</subtitle><alt-title>Silk fibroin–bacterial cellulose composite plate</alt-title>. *JAMA Otolaryngol. Head. Neck Surg.* 139 (6), 629–635. doi:10.1001/jamaoto.2013.3044

Lei, T. Y., Zhang, T., Ju, W., Chen, X., Heng, B. C., Shen, W. L., et al. (2021). Biomimetic strategies for tendon/ligament-to-bone interface regeneration. *Bioact. Mat.* 6, 2491–2510. doi:10.1016/j.bioactmat.2021.01.022

Li, G. F., and Sun, S. (2022). Silk fibroin-based biomaterials for tissue engineering applications. *Molecules* 27 (9), 2757. doi:10.3390/molecules27092757

Li, G. H., Liu, H., Li, T. D., and Wang, J. Y. (2012). Surface modification and functionalization of silk fibroin fibers/fabric toward high performance applications. *Mater. Sci. Eng. C* 32 (4), 627–636. doi:10.1016/j.msec.2011.12.013

Li, J. L., Cao, F., Wu, B., Yang, J. H., Xu, W. W., Wang, W. D., et al. (2021). Immobilization of bioactive vascular endothelial growth factor onto Ca-deficient hydroxyapatite-coated Mg by covalent bonding using polydopamine. *J. Orthop. Transl.* 30, 82–92. doi:10.1016/j.jot.2021.06.002

Li, M., Tian, W., Zhang, Y., Song, H., Yu, Y. X., Chen, X. S., et al. (2022). Enhanced silk fibroin/sericin composite film: Preparation, mechanical properties and mineralization activity. *Polym. (Basel).* 14 (12), 2466. doi:10.3390/polym14122466

Li, Y. Y., Chen, M. X., Zhou, W. H., Gao, S., Luo, X. J., Peng, L. Q., et al. (2020). Cell-free 3D wet-electrospun PCL/silk fibroin/Sr2+ scaffold promotes successful total meniscus regeneration in a rabbit model. *Acta Biomater.* 113, 196–209. doi:10.1016/j.actbio.2020.06.017

Liaw, C. Y., Ji, S., and Guvendiren, M. (2018). Engineering 3D hydrogels for personalized *in vitro* human tissue models. *Adv. Healthc. Mat.* 7, 1701165. doi:10.1002/adhm.201701165

Liu, T., Chen, Y. R., Lai, D. Z., Zhang, L. X., Pan, X. D., Chen, J. Y., et al. (2019). Biomimetic fabrication of new bioceramics-introduced fibrous scaffolds: From physicochemical characteristics to *in vitro* biological properties. *Mater. Sci. Eng. C* 94, 547–557. doi:10.1016/j.msec.2018.09.063

Lundmark, K., Westermark, G. T., Olsen, A., and Westermark, P. (2005). Protein fibrils in nature can enhance amyloid protein A amyloidosis in mice: Cross-seeding as a disease mechanism. *Proc. Natl. Acad. Sci. U. S. A.* 102 (17), 6098–6102. doi:10.1073/pnas.0501814102

Maleki, H., Shahbazi, M. A., Montes, S., Hosseini, S. H., Eskandari, M. R., Zaunschirm, S., et al. (2019). Mechanically strong silica-silk fibroin bioaerogel: A hybrid scaffold with ordered honeycomb micromorphology and multiscale porosity for bone regeneration. *ACS Appl. Mat. Interfaces* 11 (19), 17256–17269. doi:10.1021/acsami.9b04283

Marelli, B., Ghezzi, C. E., Alessandrino, A., Barralet, J. E., Freddi, G., and Nazhat, S. N. (2012). Silk fibroin derived polypeptide-induced biomineralization of collagen. *Biomaterials* 33 (1), 102–108. doi:10.1016/j.biomaterials.2011.09.039

Meinel, L., Fajardo, R., Hofmann, S., Langer, R., Chen, J., Snyder, B., et al. (2005). Silk implants for the healing of critical size bone defects. *Bone* 37 (5), 688–698. doi:10.1016/j.bone.2005.06.010

Melke, J., Midha, S., Ghosh, S., Ito, K., and Hofmann, S. (2016). Silk fibroin as biomaterial for bone tissue engineering. *Acta Biomater.* 31, 1–16. doi:10.1016/j.actbio.2015.09.005

Mieszawska, A. J., Fourligas, N., Georgakoudi, I., Ouhib, N. M., Belton, D. J., Perry, C. C., et al. (2010). Osteoinductive silk-silica composite biomaterials for bone regeneration. *Biomaterials* 31 (34), 8902–8910. doi:10.1016/j.biomaterials.2010.07.109

Mirkhalaf, M., Men, Y., Wang, R., No, Y., and Zreiqat, H. (2022). Personalized 3D printed bone scaffolds: A review. *Acta Biomater.* In Press. doi:10.1016/j.actbio.2022.04.014

Miroiu, F. M., Socol, G., Visan, A., Stefan, N., Craciun, D., Craciun, V., et al. (2010). Composite biocompatible hydroxyapatite-silk fibroin coatings for medical implants obtained by Matrix Assisted Pulsed Laser Evaporation. *Mater. Sci. Eng. B* 169, 151–158. doi:10.1016/j.mseb.2009.10.004

Miyamoto, S., Koyanagi, R., Nakazawa, Y., Nagano, A., Abiko, Y., Inada, M., et al. (2013). *Bombyx mori* silk fibroin scaffolds for bone regeneration studied by bone differentiation experiment. *J. Biosci. Bioeng.* 115 (5), 575–578. doi:10.1016/j.jbiosc.2012.11.021

Mobika, J., Rajkumar, M., Sibi, S. P. L., and Priya, V. N. (2020). Fabrication of bioactive hydroxyapatite/silk fibroin/gelatin cross-linked nanocomposite for biomedical application. *Mat. Chem. Phys.* 250, 123187. doi:10.1016/j.matchemphys.2020.123187

Moses, J. C., and Mandal, B. B. (2022). Mesoporous silk-bioactive glass nanocomposites as drug eluting multifunctional conformal coatings for improving osseointegration and bactericidal properties of metal implants. *ACS Appl. Mat. Interfaces* 14 (13), 14961–14980. doi:10.1021/acsami.2c00093

Moses, J. C., Saha, T., and Mandal, B. B. (2020). Chondroprotective and osteogenic effects of silk-based bioinks in developing 3D bioprinted osteochondral interface. *Bioprinting* 17, e00067. doi:10.1016/j.bprint.2019.e00067

Mottaghitalab, F., Hosseinkhani, H., Shokrgozar, M. A., Mao, C. B., Yang, M. Y., and Farokhi, M. (2015). Silk as a potential candidate for bone tissue engineering. *J. Control. Release* 215, 112–128. doi:10.1016/j.jconrel.2015.07.031

Murphy, A. R., John, P. S., and Kaplan, D. L. (2008). Modification of silk fibroin using diazonium coupling chemistry and the effects on hMSC proliferation and differentiation. *Biomaterials* 29 (19), 2829–2838. doi:10.1016/j.biomaterials.2008.03.039

Ni, T. Y., Liu, M., Zhang, Y. J., Cao, Y., and Pei, R. J. (2020). 3D bioprinting of bone marrow mesenchymal stem cell-laden silk fibroin Double network scaffolds for cartilage tissue repair. *Bioconjug. Chem.* 31 (8), 1938–1947. doi:10.1021/acs.bioconjchem.0c00298

Nie, L., Zhang, H., Ren, A. S., Li, Y. Z., Fu, G., Cannon, R. D., et al. (2019). Nano-hydroxyapatite mineralized silk fibroin porous scaffold for tooth extraction site preservation. *Dent. Mat.* 35 (10), 1397–1407. doi:10.1016/j.dental.2019.07.024

Nikolova, M. P., and Chavali, M. S. (2019). Recent advances in biomaterials for 3D scaffolds: A review. *Bioact. Mat.* 4, 271–292. doi:10.1016/j.bioactmat.2019.10.005

Niu, B. J., Li, B., Gu, Y., Shen, X. F., Liu, Y., and Chen, L. (2017). *In vitro* evaluation of electrospun silk fibroin/nano-hydroxyapatite/BMP-2 scaffolds for bone regeneration. *J. Biomaterials Sci. Polym. Ed.* 28 (3), 257–270. doi:10.1080/09205063.2016.1262163

Niu, X. L., Chen, Y. M., Qi, L., Liang, G. Q., Wang, Y., Zhang, L. P., et al. (2019). Hypoxia regulates angeogenic-osteogenic coupling process via up-regulating IL-6 and IL-8 in human osteoblastic cells through hypoxia-inducible factor 1 alpha pathway. *Cytokine* 113, 117–127. doi:10.1016/j.cyto.2018.06.022

Nourmohammadi, J., Roshanfar, F., Farokhi, M., and Nazarpak, M. H. (2017). Silk fibroin/kappa-carrageenan composite scaffolds with enhanced biomimetic mineralization for bone regeneration applications. *Mater. Sci. Eng. C* 76, 951–958. doi:10.1016/j.msec.2017.03.166

Pan, H., Zhang, Y. P., Shao, H. L., Hu, X. C., Li, X. H., Tian, F., et al. (2014). Nanoconfined crystallites toughen artificial silk. *J. Mat. Chem. B* 2 (10), 1408–1414. doi:10.1039/c3tb21148g

Panda, N. N., Biswas, A., Pramanik, K., and Jonnalagadda, S. (2015). Enhanced osteogenic potential of human mesenchymal stem cells on electrospun nanofibrous scaffolds prepared from eri-tasar silk fibroin. *J. Biomed. Mat. Res.* 103, 971–982. doi:10.1002/jbm.b.33272

Park, J.-Y., Yang, C., Jung, I.-H., Lim, H.-C., Lee, J.-S., Jung, U.-W., et al. (2015). Regeneration of rabbit calvarial defects using cells-implanted nano-hydroxyapatite coated silk scaffolds. *Biomater. Res.* 19, 7. doi:10.1186/s40824-015-0027-1

Partlow, B. P., Hanna, C. W., Rnjak-Kovacina, J., Moreau, J. E., Applegate, M. B., Burke, K. A., et al. (2014). Highly tunable elastomeric silk biomaterials. *Adv. Funct. Mat.* 24 (29), 4615–4624. doi:10.1002/adfm.201400526

Patil, S., and Singh, N. (2019). Silk fibroin-alginate based beads for human mesenchymal stem cell differentiation in 3D. *Biomater. Sci.* 7 (11), 4687–4697. doi:10.1039/c9bm01000a

Perteghella, S., Martella, E., De Girolamo, L., Orfei, C. P., Pierini, M., Fumagalli, V., et al. (2017). Fabrication of innovative silk/alginate microcarriers for mesenchymal stem cell delivery and tissue regeneration. *Int. J. Mol. Sci.* 18 (9), 1829. doi:10.3390/ijms18091829

Piluso, S., Flores Gomez, D., Dokter, I., Moreira Texeira, L., Li, Y., Leijten, J., et al. (2020). Rapid and cytocompatible cell-laden silk hydrogel formation via riboflavin-mediated crosslinking. *J. Mat. Chem. B* 8 (41), 9566–9575. doi:10.1039/d0tb01731k

Raia, N. R., Partlow, B. P., Mcgill, M., Kimmerling, E. P., Ghezzi, C. E., and Kaplan, D. L. (2017). Enzymatically crosslinked silk-hyaluronic acid hydrogels. *Biomaterials* 131, 58–67. doi:10.1016/j.biomaterials.2017.03.046

Rameshbabu, A. P., Bankoti, K., Datta, S., Subramani, E., Apoorva, A., Ghosh, P., et al. (2020). Bioinspired 3D porous human placental derived extracellular matrix/silk fibroin sponges for accelerated bone regeneration. *Mater. Sci. Eng. C* 113, 110990. doi:10.1016/j.msec.2020.110990

Ribeiro, M., De Moraes, M. A., Beppu, M. M., Garcia, M. P., Fernandes, M. H., Monteiro, F. J., et al. (2015). Development of silk fibroin/nanohydroxyapatite composite hydrogels for bone tissue engineering. *Eur. Polym. J.* 67, 66–77. doi:10.1016/j.eurpolymj.2015.03.056

Ribeiro, M., Fernandes, M. H., Beppu, M. M., Monteiro, F. J., and Ferraz, M. P. (2018). Silk fibroin/nanohydroxyapatite hydrogels for promoted bioactivity and osteoblastic proliferation and differentiation of human bone marrow stromal cells. *Mater. Sci. Eng. C* 89, 336–345. doi:10.1016/j.msec.2018.04.034

Ribeiro, V. P., Almeida, L. R., Martins, A. R., Pashkuleva, I., Marques, A. P., Ribeiro, A. S., et al. (2016). Influence of different surface modification treatments on silk biotextiles for tissue engineering applications. *J. Biomed. Mat. Res.* 104 (3), 496–507. doi:10.1002/jbm.b.33400

Ribeiro, V. P., Pina, S., Costa, J. B., Cengiz, I. F., Garcia-Fernandez, L., Fernandez-Gutierrez, M. D., et al. (2019). Enzymatically cross-linked silk fibroin-based hierarchical scaffolds for osteochondral regeneration. *ACS Appl. Mat. Interfaces* 11 (4), 3781–3799. doi:10.1021/acsami.8b21259

Roohaniesfahani, I., Wang, J., No, Y. J., De Candia, C., Miao, X. C., Lu, Z. F., et al. (2019). Modulatory effect of simultaneously released magnesium, strontium, and silicon ions on injectable silk hydrogels for bone regeneration. *Mater. Sci. Eng. C* 94, 976–987. doi:10.1016/j.msec.2018.10.053

Sahu, N., Baligar, P., Midha, S., Kundu, B., Bhattacharjee, M., Mukherjee, S., et al. (2015). Nonmulberry silk fibroin scaffold shows superior osteoconductivity than mulberry silk fibroin in calvarial bone regeneration. *Adv. Healthc. Mat.* 4 (11), 1709–1721. doi:10.1002/adhm.201500283

Samal, S. K., Dash, M., Shelyakova, T., Declercq, H. A., Uhlarz, M., Banobre-Lopez, M., et al. (2015). Biomimetic magnetic silk scaffolds. *ACS Appl. Mat. Interfaces* 7, 6282–6292. doi:10.1021/acsami.5b00529

Sartika, D., Wang, C. H., Wang, D. H., Cherng, J. H., Chang, S. J., Fan, G. Y., et al. (2020). Human adipose-derived mesenchymal stem cells-incorporated silk fibroin as a potential bio-scaffold in guiding bone regeneration. *Polym. (Basel).* 12 (4), 853. doi:10.3390/polym12040853

Sayin, E., Rashid, R. H., Rodriguez-Cabello, J. C., Elsheikh, A., Baran, E. T., and Hasirci, V. (2017). Human adipose derived stem cells are superior to human osteoblasts (HOB) in bone tissue engineering on a collagen-fibroin-ELR blend. *Bioact. Mat.* 2, 71–81. doi:10.1016/j.bioactmat.2017.04.001

Shao, W. L., He, J. X., Sang, F., Ding, B., Chen, L., Cui, S. Z., et al. (2016). Coaxial electrospun aligned tussah silk fibroin nanostructured fiber scaffolds embedded with hydroxyapatite-tussah silk fibroin nanoparticles for bone tissue engineering. *Mater. Sci. Eng. C* 58, 342–351. doi:10.1016/j.msec.2015.08.046

Sharma, A., Desando, G., Petretta, M., Chawla, S., Bartolotti, I., Manferdini, C., et al. (2019). Investigating the role of sustained calcium release in silk-gelatin-based three-dimensional bioprinted constructs for enhancing the osteogenic differentiation of human bone marrow derived mesenchymal stromal cells. *ACS Biomater. Sci. Eng.* 5 (3), 1518–1533. doi:10.1021/acsbiomaterials.8b01631

Sharma, S., Bano, S., Ghosh, A. S., Mandal, M., Kim, H. W., Dey, T., et al. (2016). Silk fibroin nanoparticles support *in vitro* sustained antibiotic release and osteogenesis on titanium surface. *Nanomedicine Nanotechnol. Biol. Med.* 12 (5), 1193–1204. doi:10.1016/j.nano.2015.12.385

Shen, K., Duan, A., Cheng, J. Q., Yuan, T., Zhou, J. C., Song, H. H., et al. (2022). Exosomes derived from hypoxia preconditioned mesenchymal stem cells laden in a silk hydrogel promote cartilage regeneration via the miR-205-5p/PTEN/AKT pathway. *Acta Biomater.* 143, 173–188. doi:10.1016/j.actbio.2022.02.026

Shen, X. F., Zhang, Y. X., Gu, Y., Xu, Y., Liu, Y., Li, B., et al. (2016). Sequential and sustained release of SDF-1 and BMP-2 from silk fibroin-nanohydroxyapatite scaffold for the enhancement of bone regeneration. *Biomaterials* 106, 205–216. doi:10.1016/j.biomaterials.2016.08.023

Shi, P. J., Teh, T. K. H., Toh, S. L., and Goh, J. C. H. (2013). Variation of the effect of calcium phosphate enhancement of implanted silk fibroin ligament bone integration. *Biomaterials* 34 (24), 5947–5957. doi:10.1016/j.biomaterials.2013.04.046

Shi, W. L., Sun, M. Y., Hu, X. Q., Ren, B., Cheng, J., Li, C. X., et al. (2017). Structurally and functionally optimized silk-fibroin-gelatin scaffold using 3D printing to repair cartilage injury *in vitro* and *in vivo*. *Adv. Mat.* 29, 1701089. doi:10.1002/adma.201701089

Shuai, Y. J., Mao, C. B., and Yang, M. Y. (2018). Protein nanofibril assemblies templated by graphene oxide nanosheets accelerate early cell adhesion and induce osteogenic differentiation of human mesenchymal stem cells. *ACS Appl. Mat. Interfaces* 10 (38), 31988–31997. doi:10.1021/acsami.8b11811

Smeets, R., Knabe, C., Kolk, A., Rheinnecker, M., Grobe, A., Heiland, M., et al. (2017). Novel silk protein barrier membranes for guided bone regeneration. *J. Biomed. Mat. Res.* 105 (8), 2603–2611. doi:10.1002/jbm.b.33795

Song, J., Kim, J., Woo, H. M., Yoon, B., Park, H., Park, C., et al. (2018). Repair of rabbit radial bone defects using bone morphogenetic protein-2 combined with 3D porous silk fibroin/-tricalcium phosphate hybrid scaffolds. *J. Biomaterials Sci. Polym. Ed.* 29 (6), 716–729. doi:10.1080/09205063.2018.1438126

Song, J. Y., Kim, S. G., Lee, J. W., Chae, W. S., Kweon, H., Jo, Y. Y., et al. (2011). Accelerated healing with the use of a silk fibroin membrane for the guided bone regeneration technique. *Oral Surg. Oral Med. Oral Pathology Oral Radiology Endodontology* 112 (6), e26–e33. doi:10.1016/j.tripleo.2011.05.002

Song, Y., Wu, H., Gao, Y., Li, J. Q., Lin, K. F., Liu, B., et al. (2020). Zinc silicate/nano-hydroxyapatite/collagen scaffolds promote angiogenesis and bone regeneration via the p38 MAPK pathway in activated monocytes. *ACS Appl. Mat. Interfaces* 12 (14), 16058–16075. doi:10.1021/acsami.0c00470

Soundarya, S. P., Menon, A. H., Chandran, S. V., and Selvamurugan, N. (2018). Bone tissue engineering: Scaffold preparation using chitosan and other biomaterials with different design and fabrication techniques. *Int. J. Biol. Macromol.* 119, 1228–1239. doi:10.1016/j.ijbiomac.2018.08.056

Sun, W., Motta, A., Shi, Y., Seekamp, A., Schmidt, H., Gorb, S. N., et al. (2016). Co-culture of outgrowth endothelial cells with human mesenchymal stem cells in

silk fibroin hydrogels promotes angiogenesis. *Biomed. Mat.* 11 (3), 035009. doi:10.1088/1748-6041/11/3/035009

Tanasa, E., Zaharia, C., Hudita, A., Radu, I. C., Costache, M., and Galateanu, B. (2020). Impact of the magnetic field on 3T3-E1 preosteoblasts inside SMART silk fibroin-based scaffolds decorated with magnetic nanoparticles. *Mater. Sci. Eng. C* 110, 110714. doi:10.1016/j.msec.2020.110714

Teimouri, A., Ebrahimi, R., Emadi, R., Beni, B. H., and Chermahini, A. N. (2015). Nano-composite of silk fibroin-chitosan/Nano ZrO2 for tissue engineering applications: Fabrication and morphology. *Int. J. Biol. Macromol.* 76, 292–302. doi:10.1016/j.ijbiomac.2015.02.023

Thrivikraman, G., Athirasala, A., Gordon, R., Zhang, L. M., Bergan, R., Keene, D. R., et al. (2019). Rapid fabrication of vascularized and innervated cell-laden bone models with biomimetic intrafibrillar collagen mineralization. *Nat. Commun.* 10 (1), 3520. doi:10.1038/s41467-019-11455-8

Thurber, A. E., Omenetto, F. G., and Kaplan, D. L. (2015). *In vivo* bioresponses to silk proteins. *Biomaterials* 71, 145–157. doi:10.1016/j.biomaterials.2015.08.039

Uchida, R., Bhawal, U. K., Kiba, H., Arai, K., Tanimoto, Y., Kuboyama, N., et al. (2014). Effect of plasma-irradiated silk fibroin in bone regeneration. *J. Biosci. Bioeng.* 118 (3), 333–340. doi:10.1016/j.jbiosc.2014.02.016

Uebersax, L., Apfel, T., Nuss, K. M. R., Vogt, R., Kim, H. Y., Meinel, L., et al. (2013). Biocompatibility and osteoconduction of macroporous silk fibroin implants in cortical defects in sheep. *Eur. J. Pharm. Biopharm.* 85 (1), 107–118. doi:10.1016/j.ejpb.2013.05.008

Valarmathi, N., and Sumathi, S. (2020). Biomimetic hydroxyapatite/silkfibre/methylcellulose composites for bone tissue engineering applications. *New J. Chem.* 44, 4647–4663. doi:10.1039/C9NJ05592D

Varkey, A., Venugopal, E., Sugumaran, P., Janarthanan, G., Pillai, M. M., Rajendran, S., et al. (2015). Impact of silk fibroin-based scaffold structures on human osteoblast MG63 cell attachment and proliferation. *Int. J. Nanomedicine* 10 (1), 43–51. doi:10.2147/IJN.S82209

Vetsch, J. R., Paulsen, S. J., Muller, R., and Hofmann, S. (2015). Effect of fetal bovine serum on mineralization in silk fibroin scaffolds. *Acta Biomater.* 13, 277–285. doi:10.1016/j.actbio.2014.11.025

Wang, C. X., Fang, H., Qi, X. Y., Hang, C. J., Sun, Y. R., Peng, Z. B., et al. (2019). Silk fibroin film-coated MgZnCa alloy with enhanced *in vitro* and *in vivo* performance prepared using surface activation. *Acta Biomater.* 91, 99–111. doi:10.1016/j.actbio.2019.04.048

Wang, F. P., Pang, Y. N., Chen, G. B., Wang, W. W., and Chen, Z. M. (2020a). Enhanced physical and biological properties of chitosan scaffold by silk proteins cross-linking. *Carbohydr. Polym.* 229, 115529. doi:10.1016/j.carbpol.2019.115529

Wang, J. L., Wang, L. N., Zhou, Z. Y., Lai, H. J., Xu, P., Liao, L., et al. (2016). Biodegradable polymer membranes applied in guided bone/tissue regeneration: A review. *Polym. (Basel).* 8 (4), 115. doi:10.3390/polym8040115

Wang, K. K., Cheng, W. N., Ding, Z. Z., Xu, G., Zheng, X., Li, M. R., et al. (2021). Injectable silk/hydroxyapatite nanocomposite hydrogels with vascularization capacity for bone regeneration. *J. Mat. Sci. Technol.* 63, 172–181. doi:10.1016/j.jmst.2020.02.030

Wang, L., Fang, M., Xia, Y. J., Hou, J. X., Nan, X. R., Zhao, Z., et al. (2020b). Preparation and biological properties of silk fibroin/nano-hydroxyapatite/graphene oxide scaffolds with an oriented channel-like structure. *RSC Adv.* 10 (17), 10118–10128. doi:10.1039/c9ra09710d

Wang, Q., Zhang, Y. X., Li, B., and Chen, L. (2017). Controlled dual delivery of low doses of BMP-2 and VEGF in a silk fibroin-nanohydroxyapatite scaffold for vascularized bone regeneration. *J. Mat. Chem. B* 5 (33), 6963–6972. doi:10.1039/c7tb00949f

Wang, S. D., Ma, Q., Wang, K., and Chen, H. W. (2018). Improving antibacterial activity and biocompatibility of bioinspired electrospinning silk fibroin nanofibers modified by graphene oxide. *Acs Omega* 3 (1), 406–413. doi:10.1021/acsomega.7b01210

Wang, Y. Q., Yao, D. Y., Li, L. H., Qian, Z. Y., He, W., Ding, R., et al. (2020d). Effect of electrospun silk fibroin-silk sericin films on macrophage polarization and vascularization. *ACS Biomater. Sci. Eng.* 6 (6), 3502–3512. doi:10.1021/acsbiomaterials.0c00175

Watchararot, T., Prasongchean, W., and Thongnuek, P. (2021). Angiogenic property of silk fibroin scaffolds with adipose-derived stem cells on chick chorioallantoic membrane. *R. Soc. open Sci.* 8 (3), 201618. doi:10.1098/rsos.201618

Wenhao, Z., Zhang, T., Yan, J. L., Li, Q. Y., Xiong, P. P., Li, Y. Y., et al. (2020). *In vitro* and *in vivo* evaluation of structurally-controlled silk fibroin coatings for orthopedic infection and *in-situ* osteogenesis. *Acta Biomater.* 116, 223–245. doi:10.1016/j.actbio.2020.08.040

Wenk, E., Merkle, H. P., and Meinel, L. (2011). Silk fibroin as a vehicle for drug delivery applications. *J. Control. Release* 150 (2), 128–141. doi:10.1016/j.jconrel.2010.11.007

Wongpinyochit, T., Johnston, B. F., and Seib, F. P. (2018). Degradation behavior of silk nanoparticles-enzyme responsiveness. *ACS Biomater. Sci. Eng.* 4 (3), 942–951. doi:10.1021/acsbiomaterials.7b01021

Wu, H., Zhao, C. C., Lin, K. L., and Wang, X. D. (2022a). Mussel-inspired polydopamine-based multilayered coatings for enhanced bone formation. *Front. Bioeng. Biotechnol.* 10, 952500. doi:10.3389/fbioe.2022.952500

Wu, R. J., Li, H. T., Yang, Y. L., Zheng, Q. J., Li, S. L., and Chen, Y. F. (2021a). Bioactive silk fibroin-based hybrid biomaterials for musculoskeletal engineering: Recent progress and perspectives. *ACS Appl. Bio Mat.* 4 (9), 6630–6646. doi:10.1021/acsabm.1c00654

Xiong, J. H., Onal, M., Jilka, R. L., Weinstein, R. S., Manolagas, S. C., and O'brien, C. A. (2011). Matrix-embedded cells control osteoclast formation. *Nat. Med.* 17 (10), 1235–1241. doi:10.1038/nm.2448

Yan, L. P., Silva-Correia, J., Oliveira, M. B., Vilela, C., Pereira, H., Sousa, R. A., et al. (2015). Bilayered silk/silk-nanoCaP scaffolds for osteochondral tissue engineering: *In vitro* and *in vivo* assessment of biological performance. *Acta Biomater.* 12, 227–241. doi:10.1016/j.actbio.2014.10.021

Yan, Y. F., Chen, H., Zhang, H. B., Guo, C. J., Yang, K., Chen, K. Z., et al. (2019). Vascularized 3D printed scaffolds for promoting bone regeneration. *Biomaterials* 190, 97–110. doi:10.1016/j.biomaterials.2018.10.033

Zafar, B., Mottaghitalab, F., Shahosseini, Z., Negahdari, B., and Farokhi, M. (2020). Silk fibroin/alumina nanoparticle scaffold using for osteogenic differentiation of rabbit adipose-derived stem cells. *Materialia* 9, 100518. doi:10.1016/j.mtla.2019.100518

Zaharia, C., Tudora, M. R., Stancu, I. C., Galateanu, B., Lungu, A., and Cincu, C. (2012). Characterization and deposition behavior of silk hydrogels soaked in simulated body fluid. *Mater. Sci. Eng. C* 32, 945–952. doi:10.1016/j.msec.2012.02.018

Zarrin, N. K., Mottaghitalab, F., Reis, R. L., Kundu, S. C., and Farokhi, M. (2022). Thermosensitive chitosan/poly(N-isopropyl acrylamide) nanoparticles embedded in aniline pentamer/silk fibroin/polyacrylamide as an electroactive injectable hydrogel for healing critical-sized calvarial bone defect in aging rat model. *Int. J. Biol. Macromol.* 213, 352–368. doi:10.1016/j.ijbiomac.2022.05.176

Zhang, F., and King, M. W. (2020). Biodegradable polymers as the pivotal player in the design of tissue engineering scaffolds. *Adv. Healthc. Mat.* 9 (13), e1901358. doi:10.1002/adhm.201901358

Zhang, H. J., You, R. C., Yan, K., Lu, Z. T., Fan, Q. M., Li, X. F., et al. (2020). Silk as templates for hydroxyapatite biomineralization: A comparative study of *Bombyx mori* and *Antheraea pernyi* silkworm silks. *Int. J. Biol. Macromol.* 164, 2842–2850. doi:10.1016/j.ijbiomac.2020.08.142

Zhang, H. P., Liu, X. T., Yang, M. Y., and Zhu, L. J. (2015). Silk fibroin/sodium alginate composite nano-fibrous scaffold prepared through thermally induced phase-separation (TIPS) method for biomedical applications. *Mater. Sci. Eng. C* 55, 8–13. doi:10.1016/j.msec.2015.05.052

Zhang, L., Zhang, W., Hu, Y. J., Fei, Y., Liu, H. Y., Huang, Z. Z., et al. (2021). Systematic review of silk scaffolds in musculoskeletal tissue engineering applications in the recent decade. *ACS Biomater. Sci. Eng.* 7 (3), 817–840. doi:10.1021/acsbiomaterials.0c01716

Zhang, X. Y., Chen, Y. P., Han, J., Mo, J., Dong, P. F., Zhuo, Y. H., et al. (2019). Biocompatiable silk fibroin/carboxymethyl chitosan/strontium substituted hydroxyapatite/cellulose nanocrystal composite scaffolds for bone tissue engineering. *Int. J. Biol. Macromol.* 136, 1247–1257. doi:10.1016/j.ijbiomac.2019.06.172

Zhou, B. G., He, M., Wang, P., Fu, H. T., Yu, Y. Y., Wang, Q., et al. (2017a). Synthesis of silk fibroin-g-PAA composite using H2O2-HRP and characterization of the *in situ* biomimetic mineralization behavior. *Mater. Sci. Eng. C* 81, 291–302. doi:10.1016/j.msec.2017.08.006

Zhou, B. G., Zhou, Q., Wang, P., Yuan, J. G., Yu, Y. Y., Deng, C., et al. (2018). HRP-mediated graft polymerization of acrylic acid onto silk fibroins and *in situ* biomimetic mineralization. *J. Mat. Sci. Mat. Med.* 29, 72. doi:10.1007/s10856-018-6084-y

Zhou, W. H., Jia, Z. J., Xiong, P., Yan, J. L., Li, Y. Y., Li, M., et al. (2017b). Bioinspired and biomimetic AgNPs/gentamicin-embedded silk fibroin coatings for robust antibacterial and osteogenetic applications. *ACS Appl. Mat. Interfaces* 9 (31), 25830–25846. doi:10.1021/acsami.7b06757

Zuluaga-Velez, A., Quintero-Martinez, A., Orozco, L. M., and Sepulveda-Arias, J. C. (2021). Silk fibroin nanocomposites as tissue engineering scaffolds - a systematic review. *Biomed. Pharmacother.* 141, 111924. doi:10.1016/j.biopha.2021.111924

frontiers | Frontiers in Bioengineering and Biotechnology

TYPE Original Research
PUBLISHED 22 December 2022
DOI 10.3389/fbioe.2022.1032542

OPEN ACCESS

EDITED BY
Vasif Nejat Hasirci,
Acıbadem University, Turkey

REVIEWED BY
Hee-Gyeong Yi,
Chonnam National University, South Korea
Pinar Yilgor Huri,
Ankara University, Turkey

*CORRESPONDENCE
Marta Tunesi,
marta.tunesi@polimi.it

SPECIALTY SECTION
This article was submitted to Tissue Engineering and Regenerative Medicine, a section of the journal Frontiers in Bioengineering and Biotechnology

RECEIVED 31 August 2022
ACCEPTED 06 December 2022
PUBLISHED 22 December 2022

CITATION
Merli M, Sardelli L, Baranzini N, Grimaldi A, Jacchetti E, Raimondi MT, Briatico-Vangosa F, Petrini P and Tunesi M (2022), Pectin-based bioinks for 3D models of neural tissue produced by a pH-controlled kinetics. *Front. Bioeng. Biotechnol.* 10:1032542. doi: 10.3389/fbioe.2022.1032542

Pectin-based bioinks for 3D models of neural tissue produced by a pH-controlled kinetics

Marta Merli[1], Lorenzo Sardelli[1], Nicolò Baranzini[2], Annalisa Grimaldi[2], Emanuela Jacchetti[1], Manuela Teresa Raimondi[1], Francesco Briatico-Vangosa[1], Paola Petrini[1] and Marta Tunesi[1]*

[1]Department of Chemistry, Materials and Chemical Engineering "G. Natta", Politecnico di Milano, Milan, Italy, [2]Department of Biotechnology and Life Sciences, University of Insubria, Varese, Italy

Introduction: In the view of 3D-bioprinting with cell models representative of neural cells, we produced inks to mimic the basic viscoelastic properties of brain tissue. Moving from the concept that rheology provides useful information to predict ink printability, this study improves and expands the potential of the previously published 3D-reactive printing approach by introducing pH as a key parameter to be controlled, together with printing time.

Methods: The viscoelastic properties, printability, and microstructure of pectin gels crosslinked with $CaCO_3$ were investigated and their composition was optimized (i.e., by including cell culture medium, HEPES buffer, and collagen). Different cell models representative of the major brain cell populations (i.e., neurons, astrocytes, microglial cells, and oligodendrocytes) were considered.

Results and Discussion: The outcomes of this study propose a highly controllable method to optimize the printability of internally crosslinked polysaccharides, without the need for additives or post-printing treatments. By introducing pH as a further parameter to be controlled, it is possible to have multiple (pH-dependent) crosslinking kinetics, without varying hydrogel composition. In addition, the results indicate that not only cells survive and proliferate following 3D-bioprinting, but they can also interact and reorganize hydrogel microstructure. Taken together, the results suggest that pectin-based hydrogels could be successfully applied for neural cell culture.

KEYWORDS

3D-printing, reactive printing, 3D-bioprinting, internal gelation, rheology, printability optimization, collagen, cell viability

1 Introduction

Rendering selected aspects of the *in vivo* complexity in a representative laboratory model can greatly enhance our understanding of physiological and pathological phenomena and provide critical and cost-effective tools for diagnostic or high throughput screening, drug discovery and the development of medical devices (Peneda Pacheco et al., 2021). However, this is particularly challenging when modelling nervous tissue. The variety and plurality of topographical and biochemical stimuli driving its development and functions have fascinated the scientific community (Papadimitriou et al., 2020). However, this poses several questions on how it is possible to model nervous tissue.

In the route to the setting up of reliable and accurate *in vitro* engineered models of neural tissue, hydrogel-based 3D models have produced concrete advancements towards this end (Antill-O'Brien et al., 2019). Indeed, although 2D models are inexpensive and highly reproducible, they lack sufficient complexity to gain insight into the biological phenomena driving brain functionality (Hopkins et al., 2015). In contrast, hydrogels provide a rudimentary 3D extra-cellular matrix to reproduce more physiological-*like* conditions. Both natural (e.g. alginate, chitosan, collagen) and synthetic (e.g. polyethylene glycol, polycaprolactone) polymers have been exploited (Oliveira et al., 2019), eventually coupled with glial scar-inhibiting (Lee et al., 2010) or neurotrophic factors (Taylor et al., 2006). More recently, brain decellularized extracellular matrix was also proposed to match the physical (e.g. stiffness) and biochemical properties of native tissue, and modulate biological functions (Bae et al., 2021; Zhang et al., 2021). As an alternative, blending is a common approach to design composite materials with improved properties (Zhao et al., 2020), with one polymer providing suitable mechanical features, while the other(s) promoting cell adhesion and viability.

However, a third dimension is not enough to model highly hierarchical tissues such as the brain. Proper control of the architecture, pore interconnectivity and viscoelastic properties of hydrogels, as well as the distribution of different cell populations in the 3D environment, is still an open challenge to increase the reliability of *in vitro* models of the brain (Samanipour et al., 2022). For the fabrication of highly reproducible layered-based multicellular architectures with positional control over biomaterials and cells (Qiu et al., 2020), 3D-bioprinting technologies have emerged. As the products can be shaped on the architecture of a defect, bioprinting holds a great potential for localized pathological conditions, like stroke or traumatic brain injury. Especially in a delicate environment, such as the central nervous system, direct printing on the patient could improve the integration of engineered tissue with surrounding tissue (Mehrotra et al., 2019), pushing forwards personalized healthcare (Vaz and Kumar, 2021).

Due to the similarity with the sugar-based macromolecules in the extracellular matrix of native tissues, polysaccharide-based inks are extremely common in 3D-bioprinting. Engineering their formulation and properties is fundamental to promote cell viability and easily pattern the constructs (Paxton et al., 2017). To reach the first goal, several polysaccharides require grafting with peptides such as arginine-glycine-aspartic acid (RGD) or tyrosine-isoleucine-glycine-serine-arginine (YIGSR) moieties; for the second goal, the control of crosslinking offers the possibility to tailor and shape the constructs. For example, Schwann cells were loaded in a peptide-conjugated alginate solution then crosslinked by ionotropic external gelation with calcium ions produced by the dissolution of $CaCl_2$, and the system sustained cell viability (Sarker et al., 2019). As previously reported, RGD-functionalization of gellan gum proved to be effective to bioprint cortical neurons in layered structures (Lozano et al., 2015). In this case, the bioink/cell suspension and the crosslinker (e.g. $CaCl_2$ or 5× Dulbecco's modified Eagle's medium, DMEM) were loaded into different syringes and flowed through silicone tubing before automatic mixing and extrusion. According to the hypothesis that weakly crosslinked bioinks before printing can shield from potential damage to cell membranes, Lindsay et al. (2019) also pursued this strategy, but they added a post-printing crosslinking step to stabilize the constructs. They printed neural progenitor cells into RGD-functionalized alginate that had been pre-crosslinked with $CaSO_4$, and then covered the samples with culture medium supplemented with $CaCl_2$ for a further crosslinking step. Overall, these crosslinking approaches rely on the diffusion of highly soluble calcium ions and produce inhomogeneous hydrogels (Skjåk-Bræk et al., 1989; Secchi et al., 2014). Indeed, polymer concentration decreases from the interface with the crosslinking solution to the center of the gels (Secchi et al., 2014), with impact on both cell distribution along the fiber sections and gas/nutrient diffusion.

Alginate is the most widely applied polysaccharide for cell delivery. However, it has limited chemical stability in culture media, where calcium chelators (e.g. phosphate, lactate, citrate) and monovalent cations (e.g. sodium and magnesium) may displace calcium ions. In contrast, Ca-pectinate gels are less sensitive to chemical agents and represent a better choice for cell embedding (Wan-Ping et al., 2011). Pectin, which is a versatile class of anionic and branched polysaccharides found in the cell walls of land-based plants, is regarded as the most structurally and functionally complex polysaccharide in nature (Liang and Luo, 2020). Due to its relatively low cost, stability, and gelation properties, pectin is traditionally used in food industry (Vancauwenberghe et al., 2018). Its bioavailability and biological features have also favored its use in the pharmaceutical industry (e.g. drug administration, Lara-Espinoza et al., 2018; films with antimicrobial properties, Kumar et al., 2020; wound dressing, Andriotis et al., 2020) and in tissue engineering/regenerative medicine (Munarin et al., 2011; Pereira et al., 2018; Campiglio et al., 2021).

Although pectin exhibits several bioactive properties that could be favorably applied in neural tissue engineering, its exploitation in this field is lacking. It displays metal-binding

ability (Lessa et al., 2020), cancer inhibition due to the close interaction with galectin-3 (Gao et al., 2013), and mucoadhesiveness (Sriamornsak et al., 2010). Heavy metals are involved in the control of oxidative stress (Giacoppo et al., 2014; Giampietro et al., 2018), a mechanism that leads to neurodegeneration (Bedini et al., 2021). Galectin-3 is expressed by reactive microglia. It has emerged as a potential biomarker for Alzheimer's and Parkinson's diseases, but it also promotes inflammation in traumatic brain injury (García-Revilla et al., 2022). Finally, mucoadhesiveness could be exploited for the intranasal delivery of cells to the brain (Danielyan et al., 2009). Furthermore, pectin exhibits conductive properties (Dennis et al., 2022) that could represent an effective starting point for enhancing neuronal cell adhesion and neurite formation (Zhong and Bellamkonda, 2008), although its exploitation for neural cell culture is still lacking.

Like gellan gum and alginate, low methoxyl pectin shows cation-binding capacity. It interacts with divalent cations *via* its non-methyl-esterified galacturonic acid units (Celus et al., 2018) to form ionic-bound gels stabilized by non-covalent crosslinks (external gelation). However, another mechanism is possible (i.e. internal gelation). It relies on the slow, progressive dissolution of poorly soluble calcium salts, such as $CaCO_3$ or calcium phosphate particles (Munarin et al., 2014), which are homogeneously mixed with pectin solution. The distinctive features of internal gelation are the time-dependent variation of viscoelastic properties as well as the production of homogeneous networks, which are more advantageous for cell culture. A key factor to drive the crosslinking kinetics is pH (Burey et al., 2008; Moreira et al., 2014), because acidic pH drives the dissolution of calcium salts. Nevertheless, as with external gelation, also in the case of internal crosslinking, polysaccharides are described to be combined with other polymer components or subjected to post-printing treatments such as crosslinking by UV light to achieve suitable viscoelastic properties and stability (Li et al., 2020; Kim et al., 2021).

In this study, we propose a highly controllable method to optimize the printability of internally crosslinked polysaccharides, without the need for additives or post-printing treatments. Starting from the concept that rheology provides useful information to predict ink printability, we expanded the 3D-reactive printing approach (Sardelli et al., 2021) by introducing pH as a key parameter to be controlled, together with printing time. We investigated the suitability of the proposed inks for 3D-printing *a priori*, by analyzing the viscoelastic properties of pectin gels crosslinked with $CaCO_3$. Ink composition was optimized in the view of applications with or without cell models representative of the major brain cell populations, for example by including cell culture medium and collagen. Then, 3D-bioprinted cell-laden constructs were produced according to the optimized printing conditions. Finally, the possibility of exploiting the selected ink for 3D-printed brain models was studied by evaluating cell viability over time.

2 Materials and methods

2.1 Materials

Low methoxyl pectin from citrus fruits (classic CU 701, batch 01907714) was kindly gifted by Herbstreith & Fox (Neuenbűrg, Germany) and stored at −20°C. Sodium bicarbonate was purchased from Zeta Farmaceutici (Sandrigo, Italy), calcium carbonate ($CaCO_3$, code 2117, batch 180,575) from Caesar & Loretz GmbH (Hilden, Germany) and 0.9% w/v sodium chloride (NaCl) from Eurospital (Trieste, Italy). N-2-hydroxyethylpiperazine-N′-2-ethanesulfonic acid (HEPES) solution (pH 7.0–7.6), collagen solution from bovine skin (3 mg/ml, batch SLCH0781), phosphate buffered saline (PBS), resazurin sodium salt, sodium citrate tribasic, sodium hydroxide and reagents for microstructural characterization were obtained from Sigma-Aldrich (Merck KGaA, Darmstadt, Germany). Plasticware was purchased from Corning (Corning, NY, United States), while 3-(4,5-dimethylthiazol-2-yl)-5-(3-carboxymethoxyphenyl)-2-(4-sulfophenyl)-2H-tetrazolium (MTS) was Promega (Madison, WI, United States). Reagents for cell culture and confocal microscopy were obtained from Thermo Fisher Scientific (Waltham, MA, United States).

2.2 Experimental procedures

2.2.1 Material preparation

For the sake of clarity, inks were labelled as *PxCayColl-Z*, where *x* represents pectin concentration (% w/v), *y* is $CaCO_3$ concentration (mmol), Coll highlights the possible presence of collagen, and *Z* is the solvent for pectin solutions and $CaCO_3$ suspensions (Table 1). For $P_{2.4}Ca_{20}$-NaCl and $P_{2.4}Ca_{35}$-NaCl, 2.4% w/v pectin was dissolved overnight in 0.9% w/v NaCl. To partially neutralize the carboxyl groups of pectin backbone, while preventing β-elimination, 20 mM $NaHCO_3$ was progressively added. pH was adjusted to 3.4 ± 0.1 (pHmeter Edge®, Hanna Instruments, Woonsocket, RI, United States) with 0.75 M $NaHCO_3$. To promote hydrogel formation, $CaCO_3$ suspensions (20 or 35 mM) were prepared in 0.9% w/v NaCl and mixed with pectin (1:1.5, volumetric ratio).

For $P_{3.8}Ca_{20}$-DMEM and P_4Ca_{20}-DMEM, pectin (3.8% or 4% w/v, respectively) was dissolved in high glucose DMEM (code 10938-025) supplemented with 10% v/v fetal bovine serum (FBS), 2 mM L-glutamine, 100 U/ml penicillin and 100 μg/ml streptomycin sulfate. pH was adjusted to 3.5 ± 0.1. $CaCO_3$ suspensions (20 mM) were prepared in the same medium and mixed with pectin (1:1.5, volumetric ratio).

TABLE 1 Hydrogel labeling. Hydrogels were labelled as *PxCayColl-Z*, where *x* represents pectin concentration, *y* is $CaCO_3$ concentration, Coll highlights the possible presence of collagen, and *Z* is the solvent for pectin solutions and $CaCO_3$ suspensions.

Hydrogels (*PxCayColl-Z*)	*x*, pectin (% w/v)	*y*, $CaCO_3$ (mmol)	*Coll*, COLLAGEN	*Z*, medium for pectin and $CaCO_3$
$P_{2.4}Ca_{20}$-NaCl	2.4	20	Not present	0.9% w/v NaCl
$P_{2.4}Ca_{35}$-NaCl		35		
P_4Ca_{20}-DMEM	4	20		DMEM
$P_{3.8}Ca_{20}$-DMEM	3.8			
$P_{3.8}Ca_{20}$Coll-DMEM HEPES			Present	DMEM supplemented with HEPES

For $P_{3.8}Ca_{20}$Coll-DMEM HEPES, 3.8% w/v pectin was dissolved in DMEM also supplemented with 10 mM HEPES. pH was adjusted to 3.65 ± 0.1. $CaCO_3$ suspensions (20 mM) were prepared in the same medium, mixed with pectin (1:1.5, volumetric ratio) and 3 min later with collagen 2.16 mg/ml (1: 0.25, volumetric ratio). Collagen solution was obtained by diluting eight parts v/v bovine collagen with one part v/v PBS 10x and one part v/v 0.1 N NaOH, and then by mixing with DMEM HEPES (9:1, volumetric ratio).

For cell experiments, pectin was disinfected by washing it for three times (15 min/each) in ethanol and drying it in a laminar flow cabinet, while $CaCO_3$ was heated overnight in an oven at 121°C.

2.2.2 Rheological characterization and pH measurements

Rheological characterization was performed with a rotational rheometer (Modular Compact Rheometer MCR 502, Anton Paar, Graz, Austria) equipped with parallel-plate geometry (diameter: 25 mm; working gap: 0.5 mm). Experiments were run at 25 ± 0.01°C, controlling the temperature with a Peltier system.

To assess their reproducibility, before mixing with $CaCO_3$, the viscosity of pectin solutions was measured in steady state shear experiments, which were performed at shear rates increasing from 0.1 to 100 s^{-1}. Gelation kinetics was investigated by oscillatory time sweeps at 1.0 Hz and 0.5% shear strain amplitude for 140 min from the instant (t = 0) in which pectin was mixed with $CaCO_3$. To ensure measurements in the linear regime, the linear viscoelastic region (LVR) was defined preliminarily to other tests by applying oscillatory shear amplitude ramps (logarithmic increase from 0.01 to 1000%, frequency 1.0 Hz) to fully gelled samples (i.e. 24 h after mixing pectin with $CaCO_3$). The limit of the LVR was defined as the maximum shear strain amplitude after which the storage (G') and loss (G'') moduli start changing from the previous constant value. During the first hour of crosslinking, pH was assessed every 5 min.

To study the time dependence of flowability and structure recovery within a time window suitable for 3D-bioprinting, samples were extruded in a Petri dish immediately after mixing (0 min), moved to the rheometer with a spatula and tested after 0, 30, 60 min crosslinking. Flowability was deduced from the viscosity curve obtained in a steady state shear test at shear rates increasing from 0.01 to 2,000 s^{-1}. Only data acquired from the lowest shear rate to the maximum shear rate not inducing material removal from the rheometer geometry, was considered.

Hydrogel ability to recover their state after injection was estimated by the following three-step oscillation protocol: first, an oscillatory test was carried out for 100 s at 1.0 Hz and 0.5% strain amplitude to assess the pristine dynamic mechanical properties (G', G''). Second, a 100% amplitude strain was applied at the same frequency for 100 s to cause a possible structural breakdown, and finally a third oscillatory step was carried out for 200 s in the same conditions as the first one to measure the recovery of G', G'' and thus assess the material ability to recover its pristine behavior and relevant microstructure.

The stress required to extrude the material was estimated from the measurements of the yield stress after 60 min crosslinking. Oscillatory tests were run at 1.0 Hz by increasing stress amplitude from 0.1 to 100 Pa. The yield stress was defined as the value of the shear stress at which $G' = G''$ and the hydrogels undergo a transition from a solid- ($G' > G''$, $\tan\delta < 1$) to a liquid-*like* behavior ($G' < G''$, $\tan\delta > 1$).

2.2.3 Printability evaluation

Inks (2.5 ml in 3 ml syringes) were printed with the pneumatic-based extrusion bioprinter Inkredible$^{+™}$ (Cellink, Gothenburg, Sweden) using conical 32 mm-length nozzles. The process applied a predefined code in Repetier-Host (Hot-World GmbH & Co. KG, Willich, Germany) operating in Slic3r (https://slic3r.org). Before cell loading or printing, inks were centrifuged (e.g., 800 rpm for 5 min) to remove air bubbles. Infill pattern, printing speed and layer height were varied to print fibers, two-layer geometries and five-layer grids.

Single fibers were printed after 0, 30, 60 min crosslinking (Figure 1A). Inks in 0.9% w/v NaCl were printed with 410 or 250 μm nozzles (22 or 25 G, respectively) at 10, 15, 25 mm/s; inks in DMEM w/or w/o HEPES were printed with 250 μm nozzles at 10, 15 mm/s. To study the effect of printing

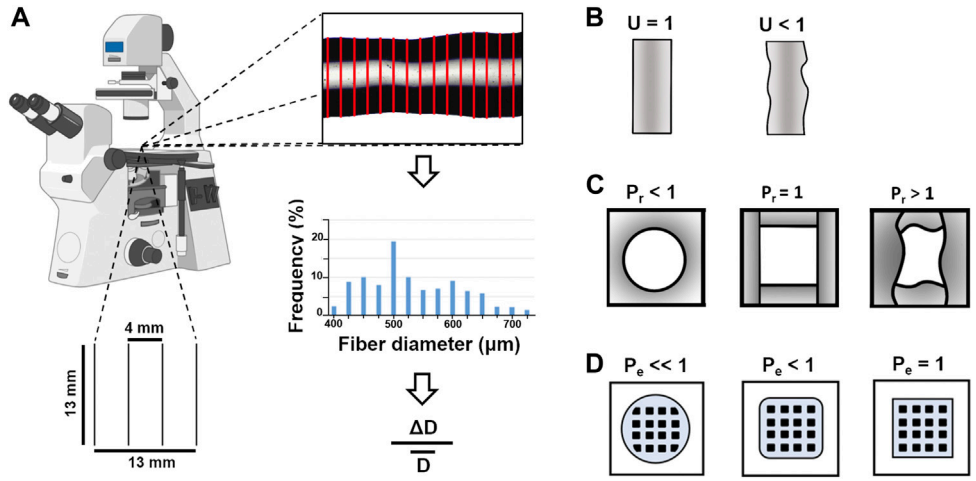

FIGURE 1
Representative sketches of the **(A)** method applied to measure the diameter of the single fibers printed at 0, 30, and 60 min in a 13 × 13 mm grid (10% infill). ΔD is the standard deviation of computed diameters, $\bar{D}$ is the mean diameter **(B)** geometry of fibers with uniformity factor *U* equals to or lower than 1. The lower *U* is, the more inhomogeneous the fiber cross-section is **(C)** geometry of pores with pore factor (P_r, Sardelli et al., 2021) lower, equals or greater than 1. $P_r < 1$ suggests roundish pores, $P_r = 1$ identifies square pores and describes the ideal situation, while $P_r > 1$ refers to irregularly-shaped pores **(D)** geometry of two-layer grids with perimeter coefficient (P_e, Sardelli et al., 2021) lower than or equal to 1. $P_e = 1$ describes the ideal situation.

pressure on fiber diameter, pressure was progressively increased by 4 kPa during the same printing, starting from the minimal pressure for a continuous flow. We defined the maximum pressure as the highest pressure at which we could print without issues, such as extruding a considerable amount of material from the cartridge or blocking the printer. Immediately after printing and before shrinkage due to solvent evaporation, fibers were imaged by an optical microscope (Eclipse Ti2, Nikon, Tokyo, Japan). To account for diameter inhomogeneity during extrusion, the initial, middle and final parts of the fibers were dimensioned. For each image, fiber diameter was measured every 10 pixels by a custom plug-in of ImageJ (http://imagej.nih.gov/ij/) and 290 measurements were obtained to estimate diameter distribution and mean values. Fiber uniformity was evaluated by uniformity factor (*U*, Figure 1B), according to Eq. 1:

$$U = 1 - \frac{\Delta D}{\bar{D}} \tag{1}$$

where ΔD is the standard deviation (SD) of computed diameters and $\bar{D}$ is the mean diameter.

After 0, 30 min crosslinking, two-layer geometries (25 mm × 25 mm × 0.6 mm, 25% infill) were printed at 10, 15 mm/s with 250 μm nozzles. They were made up of two parallel layers superimposed perpendicularly to each other. Each layer was limited by a square border. While printing, pressure was manually adjusted to ensure uniformity and shape integrity. Constructs were imaged following printing. To assess shape fidelity, i.e. the shape retention of the printed construct as a whole compared to the original computer design (Gillispie et al., 2020), pore factor (P_r, Figure 1C) and perimeter coefficient (P_e, Figure 1D) were calculated according to Eqs. 2 and 3 (Sardelli et al., 2021):

$$P_r = \frac{(Pore\ Perimeter)^2}{16 \cdot (Pore\ Area)} \tag{2}$$

$$P_e = \frac{1}{\left\{\left[\frac{1}{2} \cdot \left(\frac{\overline{L_x}}{L_x} \cdot \frac{\overline{L_y}}{L_y}\right) - 1\right] + 1\right\} \cdot \left[1 + \frac{1}{2} \cdot \left(\frac{\Delta L_x}{L_x} + \frac{\Delta L_y}{L_y}\right)\right]} \tag{3}$$

where L_x (L_y) is the theoretical length along the horizontal (vertical) axis, $\overline{L_x}$ ($\overline{L_y}$) is the respective mean value for the printed geometry, and ΔL_x (ΔL_y) is its SD. After selecting the edges of the pores, the perimeter (μm) and the area (μm²) to be used in Eq. 2 were measured by ImageJ.

In the view of cell experiments, after a crosslinking time from 0 to 30 min, five-layer grids (25 mm × 25 mm x 1.50 mm, 25% infill) were printed with $P_{3.8}Ca_{20}$Coll-DMEM HEPES at 10, 15 mm/s with 250 μm nozzles. After printing, grids were imaged and the results were compared to establish the optimal speed and crosslinking time for 3D-bioprinting.

2.2.4 Cell culture

SH-SY5Y human neuroblastoma cells (ATCC® code CRL-2266™), C8-D1A mouse astrocytes (ATCC® code CRL-2541™), and HOG human oligodendroglioma cells (EMD Millipore,

Merck, code SCC163) were grown in high-glucose DMEM (code 10938-025) supplemented with 10% v/v FBS, 2 mM L-glutamine, 100 U/ml penicillin and 100 µg/ml streptomycin sulfate. HMC3 human microglial cells (ATCC® code CRL-3304™) were grown in Advanced minimum essential medium (code 12492-013) supplemented with 10% v/v FBS and 2 mM L-glutamine. All cell lines were cultured at 37°C, 5% CO_2 in a humidified atmosphere. Medium was refreshed every two to 3 days and cells were split twice a week.

2.2.5 Indirect cytocompatibility: MTS assay

After preparation, P_4Ca_{20}-DMEM and $P_{3.8}Ca_{20}$Coll-DMEM were incubated with DMEM (code 10,938–025) supplemented with 10% v/v FBS, 2 mM L-glutamine, 100 U/ml penicillin and 100 µg/ml streptomycin sulfate. After 1, 4, 24, 72 h and 7 days, supernatants were replaced with fresh medium. Cells (62.50×10^3 C8-D1A, HMC3, HOG/cm^2; 93.75×10^3 SH-SY5Y/cm^2) were plated in 96-well plates. The following day, cells were incubated with the supernatants, while controls were cultured in standard medium. After 24 h, cell viability was evaluated by MTS assay. Supernatants were replaced with medium supplemented with 10% v/v MTS. After 3 h incubation, the optical density was measured at 490 nm (reference wavelength 630 nm) by a spectrophotometric plate reader (Infinite 200 PRO, Tecan, Männedorf, Switzerland). The results were normalized to those of the controls.

2.2.6 Microstructural characterization: Transmission electron microscopy

After mixing, samples (0.4 ml) were prepared into cylindrical molds (inner diameter: 11.05 mm) in 12-well plates. The procedure was repeated for cell-loaded constructs, obtained by mixing 2.5×10^6 C8-D1A cells with collagen solution (9:1, volumetric ratio), and then with pectin/$CaCO_3$. The moulds were removed after 1 h.

The 3D organization of $P_{3.8}Ca_{20}$-DMEM and $P_{3.8}Ca_{20}$Coll-DMEM HEPES was evaluated by transmission electron microscopy (TEM, Tunesi et al., 2019). Samples were fixed in 2% glutaraldehyde in 0.1 M cacodylate buffer (pH 7.4) for 2 h, washed for several times in the same buffer, and post fixed in 1% osmium tetroxide for 1 h. After standard ethanol dehydration, specimens were embedded in Epon-Araldite 812 mixture. Ultrathin sections (80 nm thick) were obtained with a Reichert Ultracut S ultratome (Leica, Wien, Austria), placed on copper grids (300 mesh) and stained with uranyl acetate and lead citrate.

For the immunogold assay, cell-loaded samples were fixed in 4% p-formaldehyde and 0.5% glutaraldehyde in PBS for 2 h, and then dehydrated in ethanol series for resin embedding. Ultrathin sections were obtained as above and collected on gold grids (300 mesh). After etching with 3% NaOH in ethanol (Causton, 1984), sections were incubated for 30 min in blocking solution containing 1% bovine serum albumin, 2% PBS and 0.1% Tween. They were incubated with the polyclonal primary antibody rabbit anti-COL1α1 (rabbit polyclonal, EMD Millipore) diluted 1:20 in blocking solution. After several washings in PBS, the primary antibody was visualized after immunostaining for 1 h with the secondary goat anti-rabbit IgG (H + L)-gold conjugate antibody (particle size: 10 nm. GE Healthcare, Amersham, UK) diluted 1:50 in blocking solution. In control experiments, the primary antibody was omitted, sections were treated with bovine serum albumin and incubated only with the secondary antibody. Sections were counterstained with uranyl acetate in water. Samples were observed with a Jeol 1010 EX electron microscope (Jeol, Tokyo, Japan) and data was recorded with a MORADA digital camera system (Olympus, Tokyo, Japan).

2.2.7 Direct cytocompatibility after 3D-bioprinting

Cells (2.5×10^6 C8-D1A, HMC3, HOG; $3{\cdot}10^6$ SH-SY5Y) were mixed to collagen solution (9:1, volumetric ratio), and then with pectin/$CaCO_3$. $P_{3.8}Ca_{20}$Coll-DMEM HEPES was loaded into a cartridge and kept in ice until assembling on the bioprinter. Five-layer grids were printed at 10 mm/s with 250 µm nozzles in 12-well plates after a crosslinking time from 10 to 20 min and covered with 0.75 ml medium.

After about 60 min crosslinking, cell viability following printing was assessed by a trypan blue exclusion assay. To view cells more easily, dissociation of the hydrogel network was promoted by incubation with sodium citrate (20 mM in DMEM (0.2% w/v), ~200 µL). An aliquot of cell suspension was mixed with trypan blue dye and counted with a Neubauer chamber. The percentage of live cells was calculated according to Eq. (4):

$$live\ cells\ (\%) = \frac{\sum_{i=1}^{4} N^{\circ}\ live\ cells}{\sum_{i=1}^{4} N^{\circ}\ cells} \cdot 100 \tag{4}$$

where 4 is the number of squares in which cells were counted and N° *cells* is the total number of cells counted.

To stain cell nuclei of live and dead C8-D1A cells after bioprinting, samples were incubated for 10 min in fresh medium supplemented with 1 µM Hoechst 33342, 0.5 µM Calcein AM and 0.2 µM ethidium homodimer-1 dyes (Thermofisher, Italy). Live fluorescence images were acquired by a confocal microscope (Ar1$^+$, Nikon, Tokyo, Japan), equipped with an incubator chamber and four wavelength diode lasers ($\lambda_{excitation}$ = 405/488/561/640 nm). Stained cells were imaged with a ×10 objective, with 0.45 NA, 4WD. The pinhole was set to one Airy Unit. 1024 × 1024 pixels images were acquired as z-stack images. Samples were imaged with a 10 µm step, resulting in an acquisition depth of approximatively 1.3000 µm.

10.3389/fbioe.2022.1032542

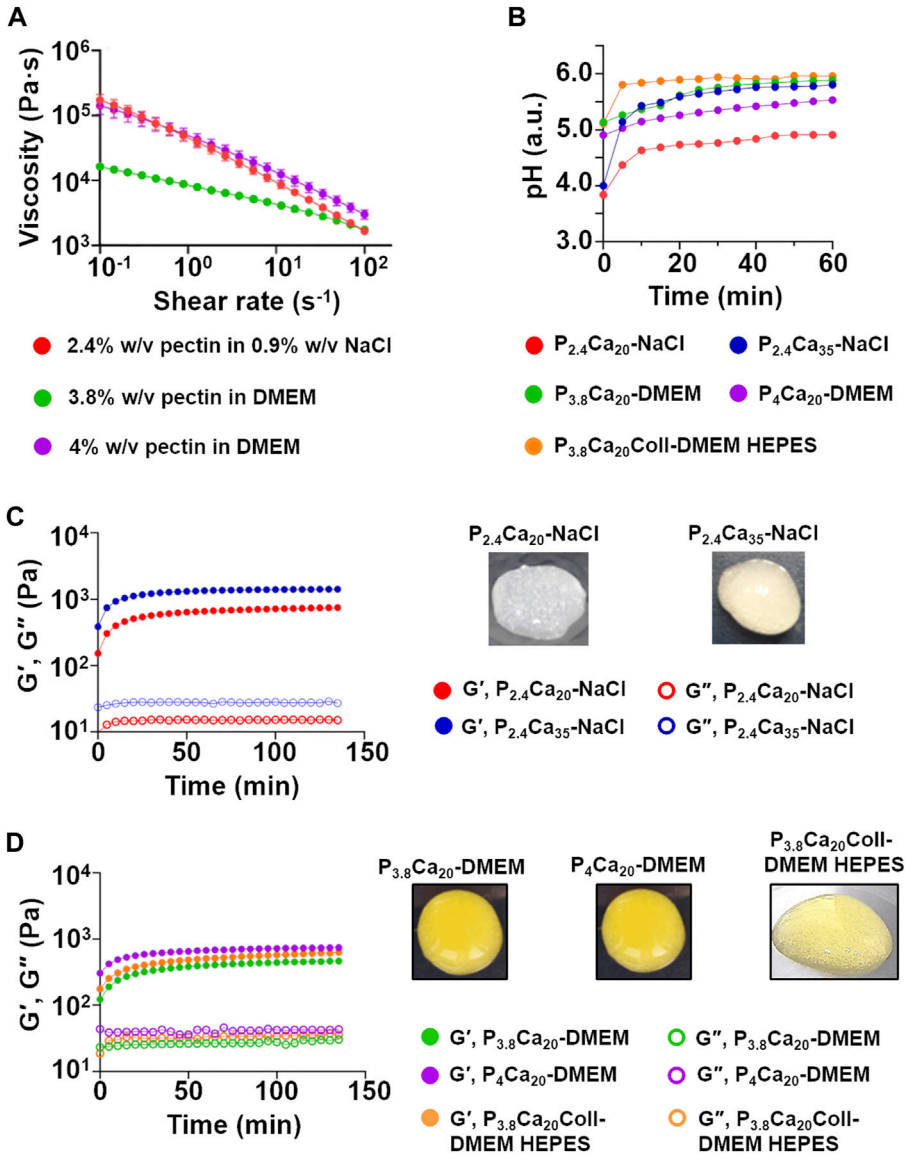

FIGURE 2
(A) Flow curves for 2.4% w/v pectin in 0.9% w/v NaCl, 3.8% w/v and 4% w/v pectin in DMEM. Mean ± SD, 12 replicates/condition **(B)** pH of the tested materials as a function of crosslinking time. Mean values, three replicates/condition **(C)** *G′*, *G″* as a function of crosslinking time for $P_{2.4}Ca_{20}$-NaCl and $P_{2.4}Ca_{35}$-NaCl. Mean values, three replicates/condition. Representative images of both materials at 1 h **(D)** *G′*, *G″* as a function of crosslinking time for $P_{3.8}Ca_{20}$-DMEM, P_4Ca_{20}-DMEM and $P_{3.8}Ca_{20}$Coll-DMEM HEPES. Mean values, three replicates/condition. Representative images of the gels at 1 h.

To investigate the potential of $P_{3.8}Ca_{20}$Coll-DMEM HEPES for 3D-bioprinted models of brain tissue, cell constructs were printed in Transwell® permeable supports in 6-multiwell plates. After 60 min crosslinking, they were covered with 2.5 ml culture medium. On 1, 4, 24 h, 3 and 7 days, cell viability was evaluated by a resazurin assay. Samples were maintained in cell culture medium supplemented with 10% v/v resazurin 0.2 mg/ml in PBS for 3.5 h, then 100 µL supernatants were moved to a 96-well plate and fluorescence was measured at 560 nm (reference wavelength 590 nm, manual gain: 60) by a spectrophotometric plate reader. The analyses were also performed on cell-free samples, whose fluorescence was subtracted from the cell-loaded ones.

2.2.8 Statistical analysis

Results were reported as mean ± SD and analyzed with GraphPad Prism®, release 9 (GraphPad Software, La Jolla, CA, United States). The normality of data distribution was assessed by D'Agostino & Pearson test. For comparisons among groups, one-way analysis of variance (ANOVA) followed by Tukey's multiple comparison test was performed. For comparisons between two groups, a two-tailed Mann-Whitney test was applied. Differences were considered as statistically significant when p-value <0.05 (*).

3 Results

In this study, we exploited the potential of a well-defined set of rheological analyses to study the viscoelastic properties of pectin solutions and gels. Our results predicted ink printability and expanded the 3D-reactive printing approach (Sardelli et al., 2021) by controlling both on printing time and pH. Both parameters were also fundamental to lay the grounds towards the development of pectin-based formulations as novel inks for 3D-bioprinting in neural tissue engineering-related applications.

3.1 Rheological characterization and pH measurements

Pectin solutions exhibited a shear thinning behavior, independently of the solvent adopted (Figure 2A). In agreement with other studies (Kar and Arslan, 1999; Moreira et al., 2014), viscosity depended both on pectin concentration and pH. At all shear rates, viscosity was greater for 4% w/v than 3.8% w/v pectin in DMEM. At low shear rates, the flow curves for 2.4% w/v pectin in 0.9% w/v NaCl and 4% w/v pectin in DMEM were overlapping.

As previously suggested, pH regulation is fundamental to prevent metabolic alterations, maintain cell viability and exert signaling (Chesler, 2003; Flinck et al., 2018). However, the acidic pH of pectin solutions and hydrogels could limit their use for cell delivery (Moreira et al., 2014). For these reasons, pH was monitored over crosslinking time (Figure 2B). At all the time points, the higher amount of $CaCO_3$ (35 mM) led to a faster increase of pH, producing hydrogels with a stiffer consistency (Figure 2C), but with residual deposits of calcium salts (e.g. for $P_{2.4}Ca_{20}$-NaCl, pH = 4.37 at 5 min and pH = 4.91 at 1 h; while 35 mM $CaCO_3$ induced pH = 5.14 at 5 min and pH = 5.80 at 1 h). Dissolving pectin in DMEM (i.e. a buffered solution) was advantageous only in the first time point (at 5 min, for $P_{2.4}Ca_{20}$-NaCl pH = 4.37. In the presence of DMEM, pH = 5.26, Figure 2B). The addition of HEPES and Coll increased the pH both at shorter and longer time points (for $P_{3.8}Ca_{20}$Coll-DMEM HEPES, pH = 5.81 at 5 min and pH = 5.97 at 1 h). Although small, these differences are fundamental. When external pH is lowered from physiological values, cell membranes are deformed, processes stop moving or are retracted, cytoplasmic components start aggregating, and mitosis is paused. How long cells can withstand this condition depends on the acidity of the environment, but for pH values close to 6, slight differences (e.g. ~ 0.3 pH units) can extend this time of some hours (Taylor, 1962).

The different composition and pH values affect the crosslinking kinetics, as was observable by time sweeps (Figures 2C, D). For all the materials, a solid-*like* state ($G' > G''$) was observed from t = 0, indicating that gelation occurred before starting the scans. $P_{2.4}Ca_{35}$-NaCl showed the highest viscoelastic properties (at the end of the scans, $G' = 1.41.10^3$ Pa; $G'' = 0.27.10^3$ Pa). G', but for some materials also G'', increased over time, suggesting that crosslinking continued over time and gels progressively stiffened, in agreement with previous studies (Secchi et al., 2014). After a rapid rise in the first 15 min, the increase in stiffening slowed down and it was noticeable only over longer time frames. After 1 h, G' was equal to 80%–90% of its value at 140 min, when crosslinking could be considered as complete. In contrast, G'' did not vary or only slightly varied over time. At 3.8% w/v pectin concentration, DMEM reduced the crosslinking rate and collagen did not affect it. Based on these results and to identify a relevant time window for extrusion-based bioprinting, we set 60 min crosslinking as the threshold value to study hydrogel properties. Indeed, since 3D-bioprinting experiments were not performed inside a cell culture incubator (i.e. it was not possible to control the temperature, humidity and carbon dioxide concentration to maintain an optimal environment for cell growth), cell viability could not be ensured (the latter can only be ensured if cells are kept out of an incubator for short time frames).

Since extrusion-based printing requires the inks to flow through the nozzle/needle, their extrudability was studied (Figures 3A–C). As previously reported, the commonly accepted rheological indicator of extrudability is the viscosity, with higher viscosity leading to lower extrudability (Copus et al., 2022). Extrudability increased with the shear rate. In agreement with the rapid rise in dynamic moduli in the initial crosslinking phases, for a fixed shear rate extrudability at 0 min was greater than at 30 min, while the differences between 30 min and 60 min were negligible. At low shear rates, after 0 and 30 min crosslinking, $P_{3.8}Ca_{20}$Coll-DMEM HEPES showed the highest extrudability, while hydrogels in 0.9% w/v NaCl exhibited the lowest. At high shear rates, no difference was observed. To account for the influence of crosslinking kinetics, only the flow curves at 60 min were fitted with the power law model of Ostwald and de Waele (Eq. 5):

$$\eta = K(\dot{\gamma})^{n-1} \tag{5}$$

where η is the viscosity, K the consistency index, $\dot{\gamma}$ the shear rate and n the power law index. n ranges from 0 to 1, with one

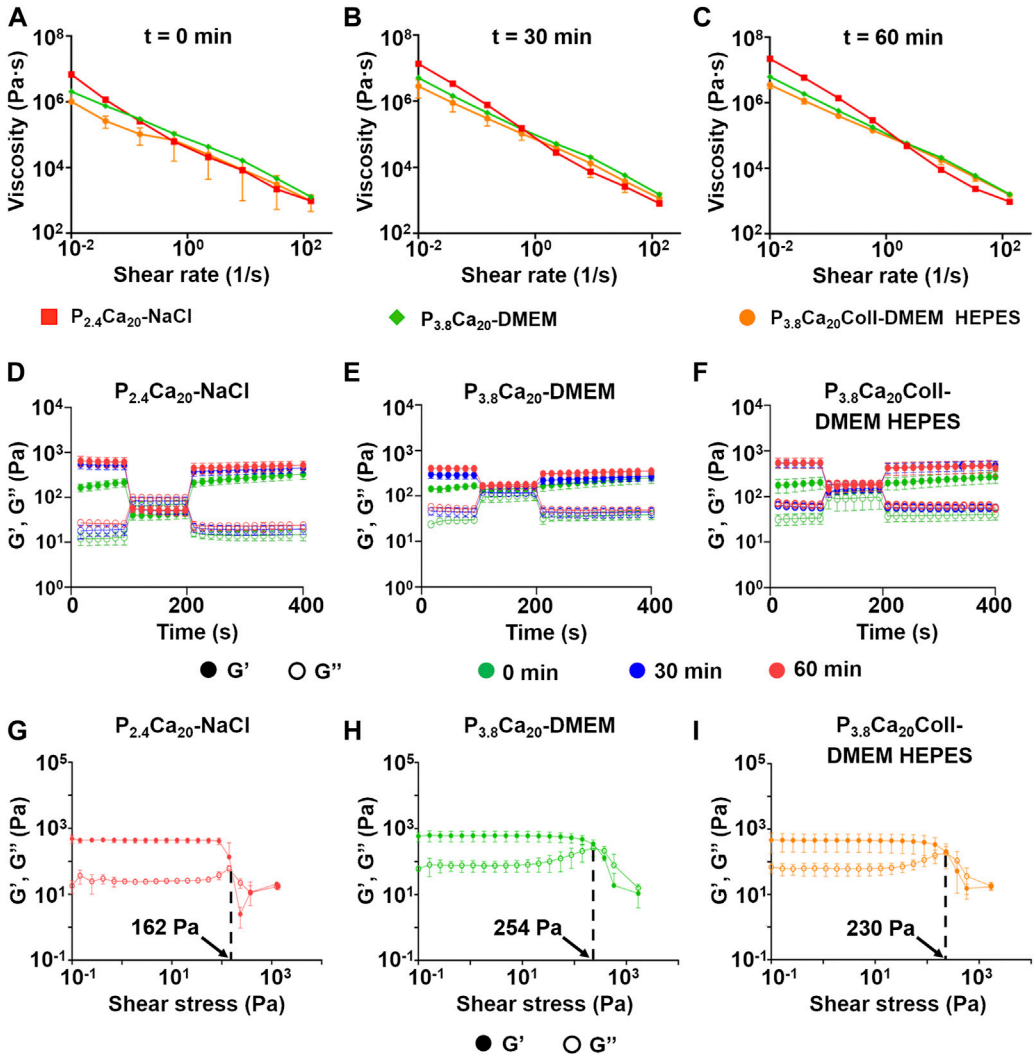

FIGURE 3
Prediction of ink extrudability from the flow curves at 0 **(A)**, 30 **(B)**, and 60 **(C)** min crosslinking for $P_{2.4}Ca_{20}$-NaCl, $P_{3.8}Ca_{20}$-DMEM, and $P_{3.8}Ca_{20}$Coll-DMEM HEPES. Mean ± SD, 4 replicates/condition; Recovery of G', G'' as a function of test time for $P_{2.4}Ca_{20}$-NaCl **(D)**, $P_{3.8}Ca_{20}$-DMEM **(E)**, and $P_{3.8}Ca_{20}$Coll-DMEM HEPES **(F)** after applying a 100% strain at 1 Hz for 100 s. Mean ± SD, 4 replicates/condition. G' and G'' over shear stress after 60 min crosslinking for $P_{2.4}Ca_{20}$-NaCl **(G)**, $P_{3.8}Ca_{20}$-DMEM **(H)**, and $P_{3.8}Ca_{20}$Coll-DMEM HEPES **(I)**. The arrows indicate the yield stress. Mean ± SD, three replicates/condition.

corresponding to a Newtonian (shear rate-independent) viscosity (Supplementary Table S1). As K rises, viscosity increases. Lower K, n values are related to a greater ease of extrusion and potentially to lower printing pressures (Liu et al., 2019). Although in disagreement with the ~~pr~~intability results (see the following section), the lowest K, n values were calculated for $P_{2.4}Ca_{35}$-NaCl (K=6.50 × 10^4, n=7.8 × 10^{-3}). However, in support of the potential of this formulation for extrusion-based printing, the second lowest value of K was computed for $P_{3.8}Ca_{20}$Coll–DMEM HEPES (K=8.39 × 10^4). Moreover, for gels in cell culture medium, n>0.1; while for the ones in 0.9% w/v NaCl, n < 0.01. We hypothesized that in the first situation (e.g. 20 mM $CaCO_3$, DMEM and collagen) the power law was able to accurately models hydrogel behavior and to validate the shear thinning behavior, while in the second one (e.g., 35 mM $CaCO_3$, 0.9% w/v NaCl) the extremely low value of n, if not related to a slippage between the rheometer plates, indicated a plug flow in the nozzle of the printer, rather than the flow of a liquid (Lopez Hernandez et al., 2021).

TABLE 2 *G′_Recovery*, *G″_Recovery*, and Tan(δ)$_{150}$ for the proposed inks. They were calculated according to Eqs 6–8. The measurements were carried out at 0, 30, and 60 min crosslinking. Mean values, 4 replicates/condition.

Time (min)	Ink	G′_Recovery	G″_Recovery	Tan(δ)$_{150}$
0	$P_{2.4}Ca_{20}$-NaCl	+52%	+14%	1.64
30		−14%	+2%	1.63
60		−15%	−6%	1.87
0	$P_{2.4}Ca_{35}$-NaCl	+22%	+19%	4.03
30		−15%	−11%	3.59
60		−12%	−2%	3.94
0	P_4Ca_{20}-DMEM	+44%	+29%	1.00
30		—	+1%	1.20
60		−5%	−2%	1.17
0	$P_{3.8}Ca_{20}$-DMEM	+48%	+29%	0.70
30		−6%	—	0.70
60		−12%	−5%	0.91
0	$P_{3.8}Ca_{20}$Coll-DMEM HEPES	+33%	+22%	0.69
30		−9%	−3%	1.25
60		−24%	−16%	1.09

After 0, 30, and 60 min crosslinking, G' and G'' recovery was calculated (Figures 3D–F and Table 2) according to Eqs. 6 and 7, respectively; after applying a 100% strain for 100 s:

$$G'\_Recovery\ (\%) = \left(\frac{G'_{400}}{G'_{100}}\right).100 - 100 \quad (6)$$

$$G''\_Recovery\ (\%) = \left(\frac{G''_{400}}{G''_{100}}\right).100 - 100 \quad (7)$$

where G'_{400} (G''_{400}) is G' (G'') value at 400 s (i.e. at the end of the test) and G'_{100} (G''_{100}) is G' (G'') value at 100 s (i.e. before applying a 100% strain for 100 s). To assess whether a deformation beyond the LVR affects hydrogel structure, at 150 s after beginning the test, tan(δ) was calculated according to Eq. 8:

$$\mathrm{Tan}\,(\delta)_{150} = G''_{150}/G'_{150} \quad (8)$$

where G'_{150} (G''_{150}) is G' (G'') value at 150 s.

When gels were subjected to an increasing shear immediately after preparation (t = 0), they not only recovered, but they even increased their viscoelastic properties (maximum values were about 50% for G' and about 30% for G''). The situation changed after 30 min crosslinking: except for P_4Ca_{20}-DMEM (no changes), G' values did not recover after the deformation for the considered hydrogels. At this time point G'' values were constant or only slightly modified. After 60 min crosslinking, the inks did not recover their viscoelastic properties. $P_{3.8}Ca_{20}$Coll-DMEM HEPES showed the highest decrease in G' (-24%) and G'' (-16%) values.

At all the crosslinking time points, tan(δ)$_{150}$ was > 1 (liquid-*like* state) for inks in 0.9% w/v NaCl, while tan(δ)$_{150}$ was <1 for DMEM samples w/o collagen, indicating a solid-*like* state. For the other materials, tan(δ)$_{150}$ depended on crosslinking time. At 0 min, for P_4Ca_{20}-DMEM the deformation triggered a solid-to liquid-*like* transition (tan(δ)$_{150}$ = 1), while $P_{3.8}Ca_{20}$Coll-DMEM HEPES maintained its solid-*like* behavior. At 30 min and 60 min, both the materials showed a liquid-*like* behavior. At 60 min, for $P_{3.8}Ca_{20}$Coll-DMEM HEPES, tan(δ)$_{150}$ decreased and approached to 1 (1.09).

For shear stresses larger than the yield stress (Figures 3G–I), G'' was higher than G' and the sample started flowing. Therefore, the presence of a yield stress indicated that the hydrogel was capable to be extruded during printing.

Taken together, these results demonstrate that all the hydrogels efficiently recovered their viscoelastic properties when exposed to a strain beyond the LVR immediately after preparation, because in the early phases of crosslinking the general increase in dynamic moduli was fast. In agreement with the measured values of yield stress, the materials in cell culture medium required a higher deformation for a solid-to liquid-like transition. Between 30 and 60 min crosslinking, the rise in dynamic moduli during the recovery phase was considerably reduced and it could not compensate the effects

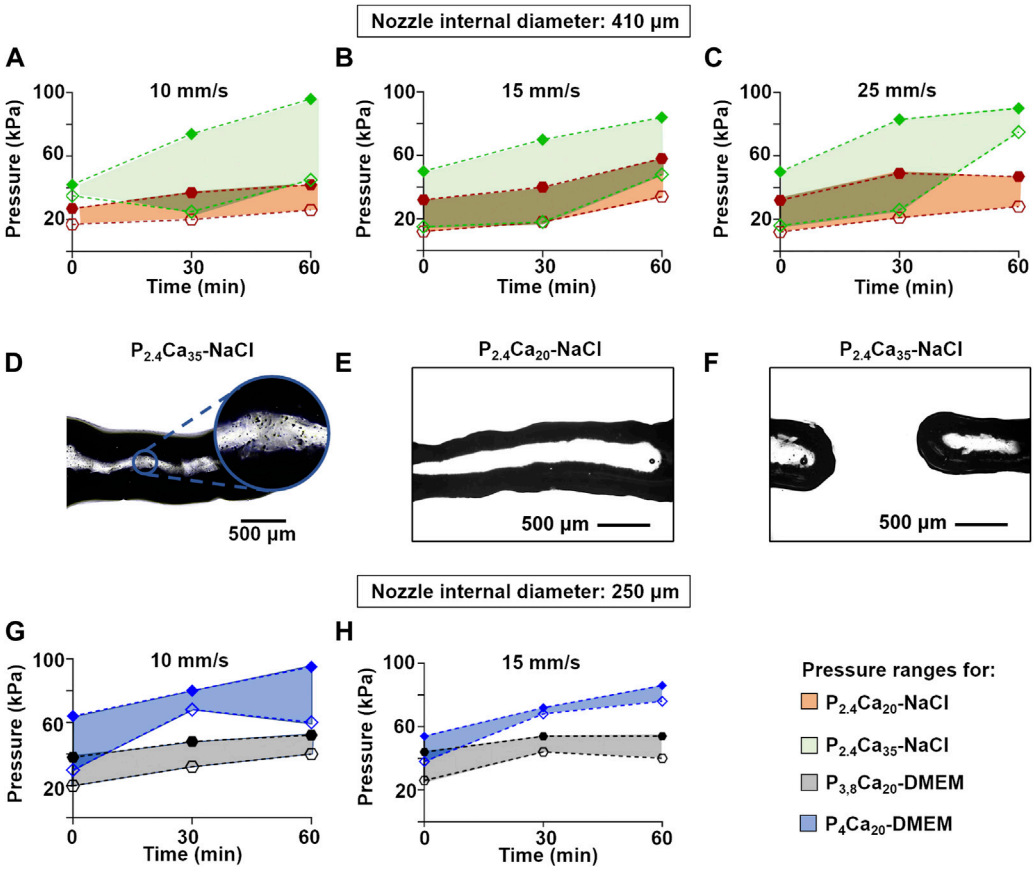

FIGURE 4
Minimum (empty indicators) and maximum (filled indicators) pressures as a function of crosslinking time to extrude single fibers of $P_{2.4}Ca_{20}$-NaCl and $P_{2.4}Ca_{35}$-NaCl with a 410 µm nozzle at 10 **(A)**, 15 **(B)**, and 25 **(C)** mm/s. The results were obtained after comparing 10 replicates/condition. The colored areas represent the printability windows; Representative optical images of **(D)** $P_{2.4}Ca_{35}$-NaCl printed fibers, showing calcium deposits **(E)** $P_{2.4}Ca_{20}$-NaCl printed fibers **(F)** $P_{2.4}Ca_{35}$-NaCl printed fibers, showing the lack of integrity. Scale bar = 500 µm; Minimum (empty indicators) and maximum (filled indicators) pressures as a function of crosslinking time to extrude single fibers of $P_{3.8}Ca_{20}$-DMEM and P_4Ca_{20}-DMEM with a 250 µm nozzle at 10 **(G)**, and 15 **(H)** mm/s. The results were obtained after comparing 10 replicates/condition. The colored areas represent the printability windows.

of an extreme deformation. Except for $P_{3.8}Ca_{20}$-DMEM, all the formulations behaved as liquids, at the end of the recovery period. The exceptional behaviour of $P_{3.8}Ca_{20}$-DMEM could be explained by the fact that this formulation exhibited the greatest yield stress. The addition of collagen to $P_{3.8}Ca_{20}$-DMEM lowered the yield stress and improved the extrudability, with advantages for 3D-bioprinting.

3.2 Printability evaluation

Since cell printing with high viscous inks (i.e. in hydrogels with high polymer content) requires high pressures and printing pressure can impair cell viability (Cidonio et al., 2019; Boularaoui et al., 2020), we studied the influence of speed and crosslinking on printing pressure (Figure 4).

The effect of $CaCO_3$ content was investigated by printing a series of single fibers for $P_{2.4}Ca_{20}$-NaCl and $P_{2.4}Ca_{35}$-NaCl, i.e. for inks with the same pectin concentration (2.4% w/v) dissolved in the same solvent (0.9% w/v NaCl), but with different calcium content (20 or 35 mM)) (Figures 4A–C). At a fixed speed, both minimum and maximum pressures increased over crosslinking time. At a fixed crosslinking time, $CaCO_3$ content affected maximum pressures. The higher amount of $CaCO_3$ led to a greater gap between minimum and maximum pressures and required higher maximum pressures for extrusion. In contrast, comparable minimum pressures could be set at 0 min when printing at 15 or 25 mm/s, and at 30 min independently of speed. For a fixed $CaCO_3$ content, pressures varied with speed. For $P_{2.4}Ca_{35}$-NaCl, fibers could be extruded at lower pressures when printing at 15 mm/s, while for $P_{2.4}Ca_{20}$-NaCl when printing at 10 or 15 mm/s. Since for both inks printing at 25 mm/s required

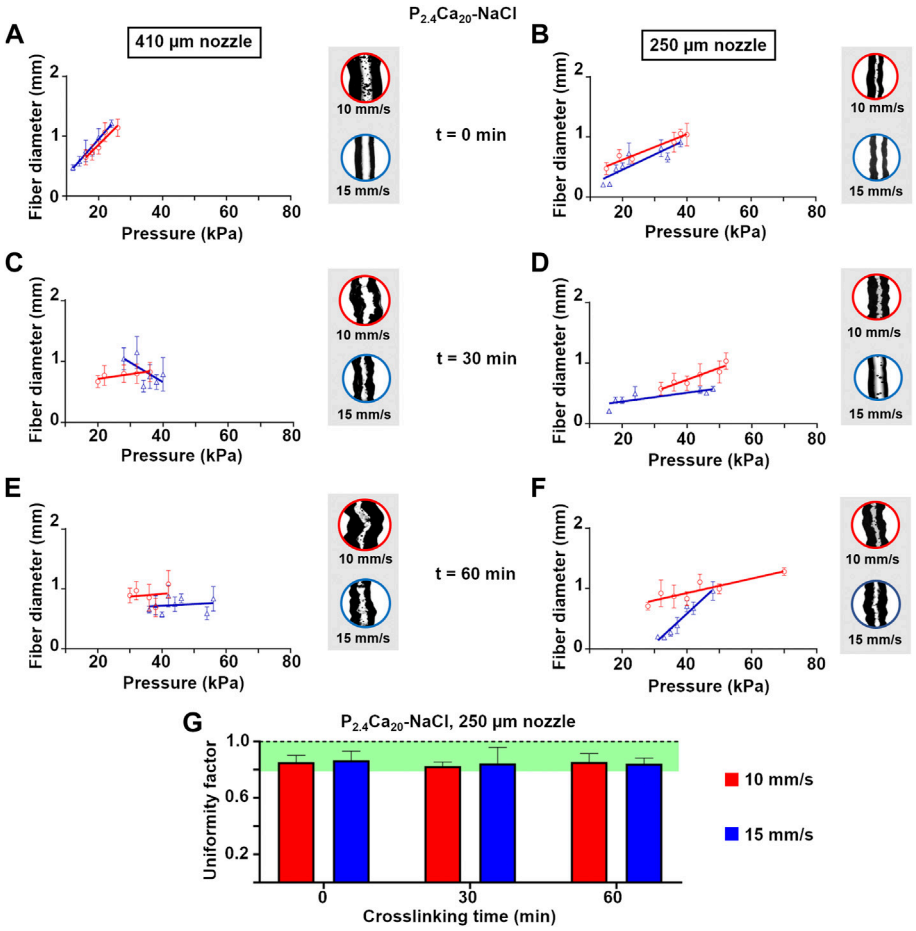

FIGURE 5
Fiber diameter as a function of printing pressure for $P_{2.4}Ca_{20}$-NaCl single fibers extruded with a 410 or 250 μm nozzle at 10 or 15 mm/s after 0 **(A and B)**, 30 **(C and D)**, and 60 **(E and F)** min crosslinking. Mean ± SD, six replicates/condition. For each condition, representative optical images of the central part of the fibers were reported **(G)** Uniformity factor (*U*) for $P_{2.4}Ca_{20}$-NaCl single fibers extruded with a 250 μm nozzle at 10 or 15 mm/s after 0, 30, and 60 min crosslinking. Mean ± SD, six replicates/condition.

pressures comparable or greater than printing at 10 or 15 mm/s, we excluded the fastest speed.

The microscopic observation of fibers with the higher calcium content (35 mM) highlighted dark spots (Figure 4D), indicating deposits of calcium carbonate. For both inks, fiber integrity decreased over crosslinking time and $CaCO_3$ concentration (data not shown). Moreover, $P_{2.4}Ca_{35}$-NaCl frequently clogged the nozzle, requiring the interruption of the process (Figures 4E, F).

The effect of pectin concentration was investigated by printing a series of single fibers for P_4Ca_{20}-DMEM and $P_{3.8}Ca_{20}$-DMEM, i.e. for inks with the same calcium content (20 mM), but with different pectin contents (4% or 3.8% w/v) dissolved in the same solvent (DMEM) (Figures 4G, H). As for inks in 0.9% w/v NaCl, at a fixed speed, both minimum and maximum pressures increased over crosslinking time. Although there were only slight differences compared to inks in 0.9% w/v NaCl, at a fixed crosslinking time, pectin concentration affected both minimum and maximum pressures, with the extrusion of P_4Ca_{20}-DMEM requiring higher pressures than $P_{3.8}Ca_{20}$-DMEM. The printing speed also affected the results: for $P_{3.8}Ca_{20}$-DMEM, pressure values were lower when extruding at 10 mm/s than 15 mm/s; while for P_4Ca_{20}-DMEM lower values were set when printing at 15 mm/s.

The influence of pressure and speed on fiber diameter was related to the print resolution. At the beginning of crosslinking (0 min), the diameter of printed $P_{2.4}Ca_{20}$-NaCl fibers increased with pressure both at 10 or 15 mm/s (Figure 5A). After 30 min crosslinking (Figure 5C), pressure induced a change in diameter only at 10 mm/s. When crosslinking time reached 60 min, the shape was retained regardless of pressure (Figure 5E). Independently of speed, fibers were always larger than the nozzle for the minimum printing pressures (Supplementary Table S2). When the nozzle dimension was reduced from

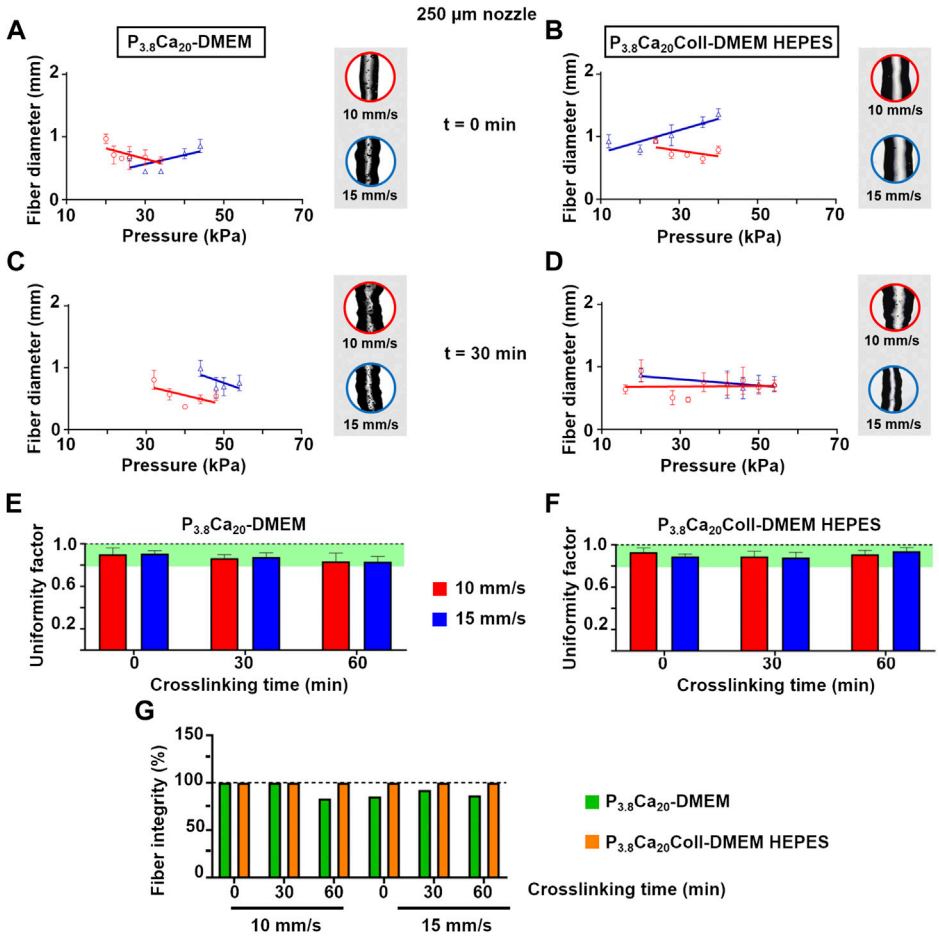

FIGURE 6
Fiber diameter as a function of printing pressure for $P_{3.8}Ca_{20}$-DMEM and $P_{3.8}Ca_{20}$Coll-DMEM HEPES single fibers extruded with a 250 µm nozzle at 10 or 15 mm/s after 0 **(A and B)**, 30 **(C and D)** min crosslinking. Mean ± SD, six replicates/condition. For each condition, representative optical images of the central part of the fibers were reported; Uniformity factor for: $P_{3.8}Ca_{20}$-DMEM **(E)** and $P_{3.8}Ca_{20}$Coll-DMEM HEPES single fibers **(F)** extruded with a 250 µm nozzle at 10 or 15 mm/s after 0, 30, and 60 min crosslinking. Mean ± SD, six replicates/condition **(G)** Fiber integrity for $P_{3.8}Ca_{20}$-DMEM and $P_{3.8}Ca_{20}$Coll-DMEM HEPES single fibers extruded with a 250 µm nozzle at 10 or 15 mm/s after 0, 30, and 60 min crosslinking. Mean ± SD, six replicates/condition.

410 µm to 250 µm (Figures 5B, D, F), fiber diameter (Supplementary Table S2) increased (or slightly increased) with increasing pressure, independently of crosslinking time. More specifically, the speed of 15 mm/s allowed to extrude $P_{2.4}Ca_{20}$-NaCl fibers thinner than the nozzle and with a basically constant diameter (~ about 205 µm, mean value) from 0 to 60 min crosslinking.

Generally, printing through the smaller nozzle (250 µm) produced thinner fibers. Surprisingly, minimum pressures were generally comparable or even lower than the ones for extrusion through the larger nozzle. This result agrees with the shear thinning nature of $P_{2.4}Ca_{20}$-NaCl: a reduction in nozzle dimension, increases the shear strain, and decreases the viscosity, thus reducing printing pressure. For this reason, we selected 250 µm nozzles for further 3D-printing experiments.

The uniformity factor is an important parameter to compare the geometrical features of the set with the experimental results after printing. For $P_{2.4}Ca_{20}$-NaCl fibers extruded through 250 µm nozzles, the uniformity factor was always greater than 0.82 (Figure 5G). For all the crosslinking times, no differences (p-value>0.05) were found between 10 and 15 mm/s. The comparison of mean values showed greater uniformity factors for printing at 15 mm/s at both 0 and 30 min crosslinking. However, at this printing speed a lower number of fibers was available for the analysis. Indeed, when printing at 10 mm/s fiber integrity was greater than 90%; while it dropped to 50% in the tests at 15 mm/s (data not shown).

For DMEM-based hydrogels either with or without collagen (i.e. $P_{3.8}Ca_{20}$-DMEM and $P_{3.8}Ca_{20}$Coll-DMEM HEPES, respectively), pressure and speed influenced fiber diameter

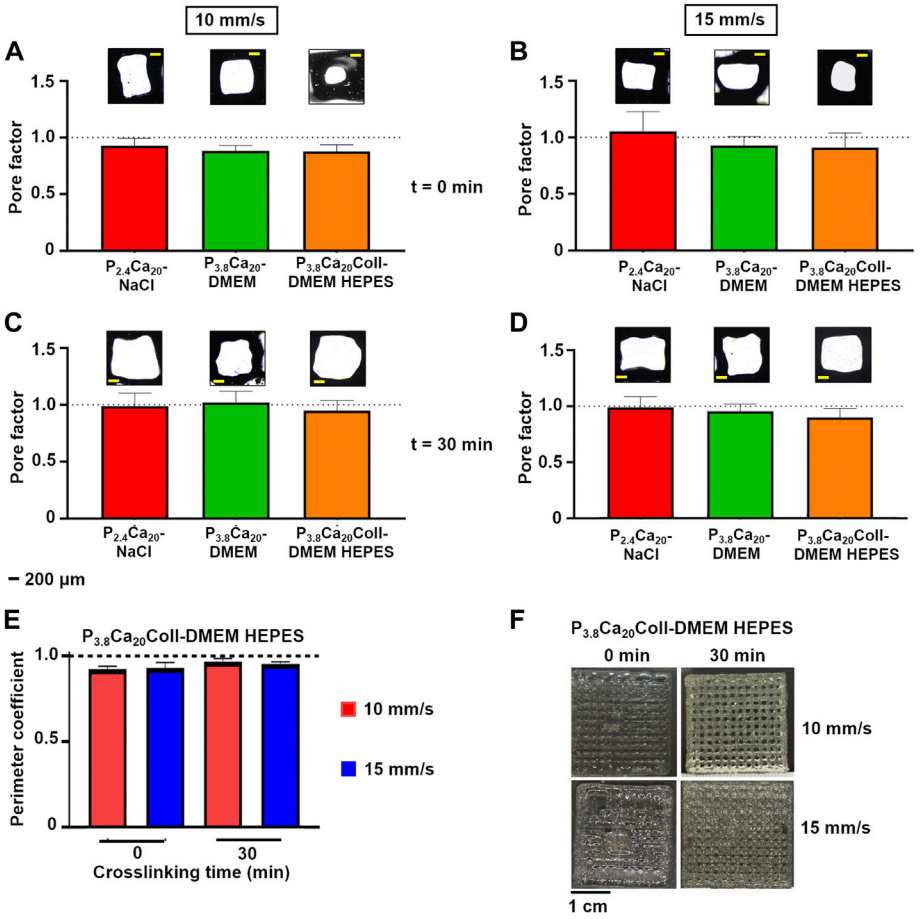

FIGURE 7
Pore factor for $P_{2.4}Ca_{20}$-NaCl, $P_{3.8}Ca_{20}$-DMEM and $P_{3.8}Ca_{20}$Coll-DMEM HEPES two-layer geometries printed after 0 and 30 min crosslinking at 10 **(A and B)** or 15 **(C and D)** mm/s. For each condition, representative optical images of the pores were reported. Scale bar = 200 μm **(E)** Perimeter coefficient for $P_{3.8}Ca_{20}$Coll-DMEM HEPES two-layer geometries printed after 0 and 30 min crosslinking at 10 or 15 mm/s **(F)** Representative images of five-layer grids printed after 0 and 30 min crosslinking at 10 or 15 mm/s. Scale bar = 1 cm.

(Figure 6, Supplementary Table S2). At 0 min (Figures 6A, B), the trends depended on speed, but not on the presence of collagen. For both inks, when printing at 10 mm/s, diameter decreased with increasing pressure, while the opposite was observed when printing at 15 mm/s. At 30 min, the trends were influenced by the presence of collagen. In the absence of collagen (i.e. for $P_{3.8}Ca_{20}$-DMEM), diameter decreased with increasing pressure, while in the presence of collagen (i.e. for $P_{3.8}Ca_{20}$Coll-DMEM HEPES), it was basically independent of pressure and speed (Figures 6C, D). At 60 min crosslinking, the trends varied with both speed and the presence of collagen. In the absence of collagen, when extruding at 10 mm/s, diameter increased with increasing pressure, while when printing at 15 mm/s, the opposite was observed (data not shown). Again, in the presence of collagen, the diameter of printed fibers was basically independent of pressure and speed (data not shown).

For crosslinking times compatible with cell viability outside the incubator during the printing process (i.e. 0 and 30 min), $P_{3.8}Ca_{20}$Coll-DMEM HEPES was extruded at lower pressures than $P_{3.8}Ca_{20}$-DMEM, thus representing an advantage for cell viability. The shift from 0.9% w/v NaCl to DMEM lowered print resolution, although the fibers were smoother and straighter. The addition of collagen to DMEM-based formulations improved fiber uniformity (Figures 6E, F), and integrity (Figure 6G). By extending the analysis up to 60 min, we were able to appreciate that collagen also improved recovery as crosslinking time increased. In fact, for $P_{3.8}Ca_{20}$-DMEM fibers extruded at both 10 mm/s and 15 mm/s, the uniformity factors decreased from 0.91 (0 min) to 0.87 (30 min) and 0.83 (60 min), while for $P_{3.8}Ca_{20}$Coll-DMEM HEPES fibers, they decreased from 0.91 (0 min) to 0.88 (30 min) and then increased to 0.92 (60 min).

TABLE 3 Pressure ranges for printing $P_{2.4}Ca_{20}$-NaCl, $P_{3.8}Ca_{20}$-DMEM, and $P_{3.8}Ca_{20}$Coll-DMEM HEPES two-layered geometries with a 250 μm nozzle. Mean values, six replicates/condition.

Ink	Speed (mm/s)	Time (min)	Minimum pressure (kPa)	Maximum pressure (kPa)
$P_{2.4}Ca_{20}$-NaCl	10	0	15	40
		30	32	68
	15	0	18	30
		30	22	57
$P_{3.8}Ca_{20}$-DMEM	10	0	22	31
		30	32	62
	15	0	20	35
		30	44	74
$P_{3.8}Ca_{20}$Coll-DMEM HEPES	10	0	20	27
		30	27	42
	15	0	9	32
		30	17	41

As a proof of concept that it is possible to fabricate 3D-controlled shapes, we produced multilayered grids. As the uniformity factors did not allow for a unique selection of the printing speed, two-layer geometries were printed at different speeds and crosslinking times (Figures 7A–D). The minimum pressure values were set according to the ones for single fibers, but pressure could be increased during extrusion to allow for a continuous flow (Table 3). At 0 min, $P_{2.4}Ca_{20}$-NaCl grids were more uniform when printed at 10 mm/s than 15 mm/s (p-value<0.01); while at 30 min no differences were found with speed (p-value>0.05). More in general, the most uniform grids were printed at 10 mm/s after 30 min crosslinking (P_r = 0.99 ± 0.09). In these conditions, pores were the largest (i.e. fibers were the thinnest). For $P_{3.8}Ca_{20}$-DMEM, the results were reversed: at 0 min, no differences were found with speed (p-value>0.05); while at 30 min grids were more uniform when printed at 10 mm/s (p-value<0.05). Accordingly, for this ink the most uniform grids (P_r = 1.01 ± 0.14) were printed at 10 mm/s after 30 min crosslinking, and larger pores were obtained at the same crosslinking time when printing at 15 mm/s. However, when printing at 10 mm/s P_r increased with time (p-value<0.0001), whereas no differences were found with time at 15 mm/s (p-value>0.05). Even though for both crosslinking times no differences were found with speed (p-value>0.05), also for $P_{3.8}Ca_{20}$Coll-DMEM HEPES the most uniform grids were printed at 10 mm/s after 30 min crosslinking (P_r = 0.95 ± 0.09, mean ± SD). Again, an increase in the mean values of P_r (from 0.88 to 0.93) was observed over time at 10 mm/s. As regards P_e (Figure 7E), at both crosslinking times, no differences were found with speed (p-value>0.05). After 30 min crosslinking, it increased for both types of grids, independently of speed.

Finally, we printed $P_{3.8}Ca_{20}$Coll-DMEM HEPES five-layer-grids (Figure 7F). Unlike the two-layer geometries, the speeds were not equivalent. For both crosslinking times, more uniform fibers and open porosities were obtained at 10 mm/s, but the shape fidelity increased over time.

Based on the results observed, we selected a crosslinking time between 10 and 20 min as the ideal printing time, and 10 mm/s as the ideal printing speed. They represented a compromise between the values of pore factor (P_r, related to shape fidelity) and printing pressures (influencing cell viability, see the following section). Each five-layer-grid required about 100 s to be completed.

3.3 Indirect cytocompatibility: MTS assay

The effect of both pectin and collagen concentrations on cell viability was investigated by culturing the cells for 24 h in the supernatants from P_4Ca_{20}-DMEM (Figure 8A) or $P_{3.8}Ca_{20}$Coll-DMEM HEPES (Figure 8B). As they were not specifically developed for cell encapsulation, we neglected 0.9% w/v NaCl-based compositions and tested DMEM-based formulations. We considered a pectin concentration of 4% w/v because it is the highest that has been tested in this study, and the pH values in the first crosslinking phases were than the ones for $P_{3.8}Ca_{20}$-DMEM (Figure 2). We hypothesized that P_4Ca_{20}-DMEM is cytocompatible with SH-

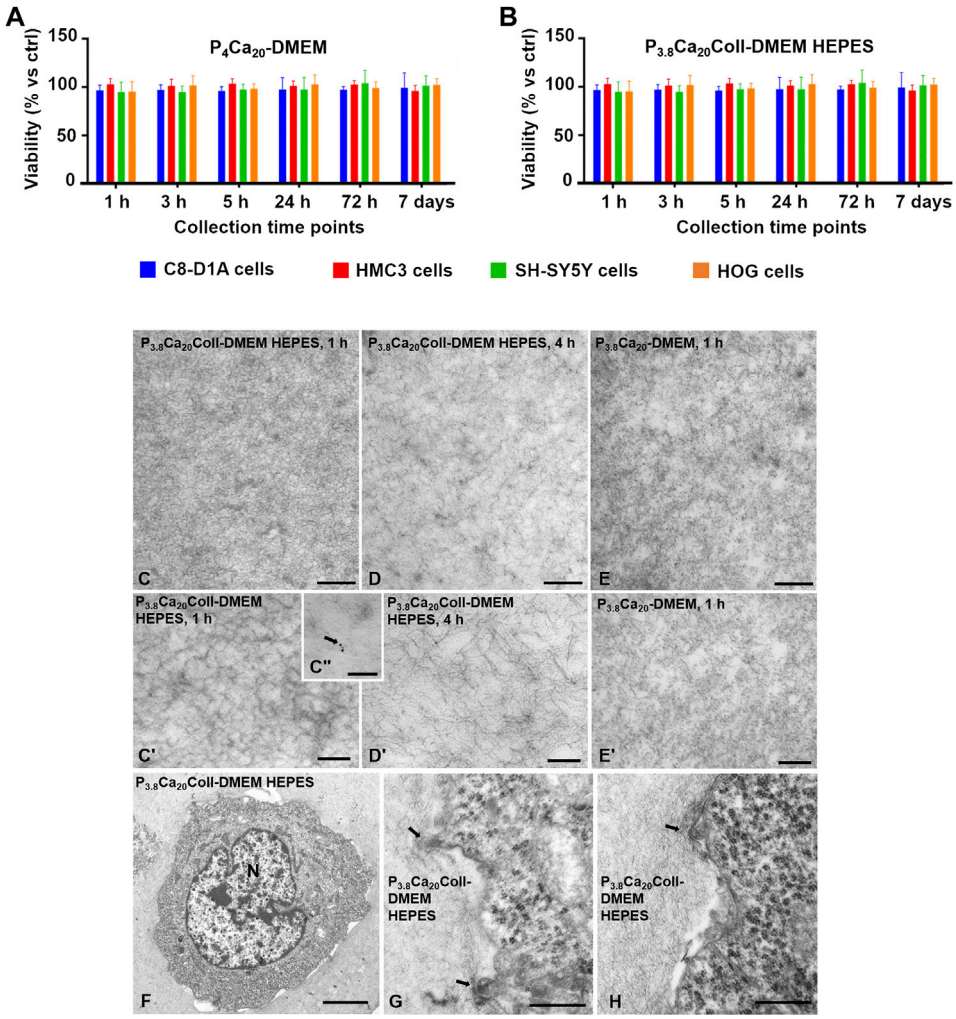

FIGURE 8
Viability of C8-D1A, HMC3, SH-SY5Y and HOG cells after 24 h in the supernatants collected after 1, 3, 5, 24, 72 h, and 7 days from P4Ca_{20}-DMEM **(A)**, and $P_{3.8}Ca_{20}$Coll-DMEM HEPES **(B)** hydrogels. As a control, cells were grown for 24 h in fresh culture medium. Results from the MTS assay. Mean ± SD, 12 replicates/group. Data was analyzed with one-way ANOVA followed by Tukey's multiple comparisons test. All the differences were not statistically significant (p-value >0.05). TEM images of $P_{3.8}Ca_{20}$Coll-DMEM HEPES after 1 h **(C, C')** and 4 h **(D, D')** crosslinking, and $P_{3.8}Ca_{20}$-DMEM after 1 h **(E, E')** crosslinking, showing that in $P_{3.8}Ca_{20}$Coll-DMEM HEPES, collagen fibers were crosslinked together forming a dense network, while in $P_{3.8}Ca_{20}$-DMEM a uniform-looking matrix was present. Immunogold assays highlighted the specific localizations of gold particles associated to collagen fibers (arrow in C″). C8-D1A astrocytic-like cells seeded in $P_{3.8}Ca_{20}$Coll-DMEM HEPES **(F)** showed contact and interacted with collagen fibers (arrows in **(G, H)**). N, nucleus. Bars in C-E, G, and H are 0.5 μm; bars in C′ and D′ are 200 nm; bar in C″ is 100 nm; bar in F is 5 μm.

SY5Y, C8-D1A, HMC3, and HOG cells, any similar pectin gel is expected to be too, but with a lower pectin concentration. For all the collection times and cell populations, viability, which was evaluated by MTS, was comparable with controls in standard medium (p-value>0.05). Although the crosslinking reaction is still not complete, culture medium can be immediately added to cover the samples and its addiction speeds up the reaching of pH values compatible with cell survival. The selected collagen content did not reduce cell viability. Again, for all the cell populations, viability was comparable with controls for all the time points (p-value>0.05).

3.4 Microstructural characterization: Transmission electron microscopy

Ultrastructural analysis by TEM of cell-embedding samples fixed after 60 min (Figures 8C,C') or 4 h culture (Figures 8D,D')

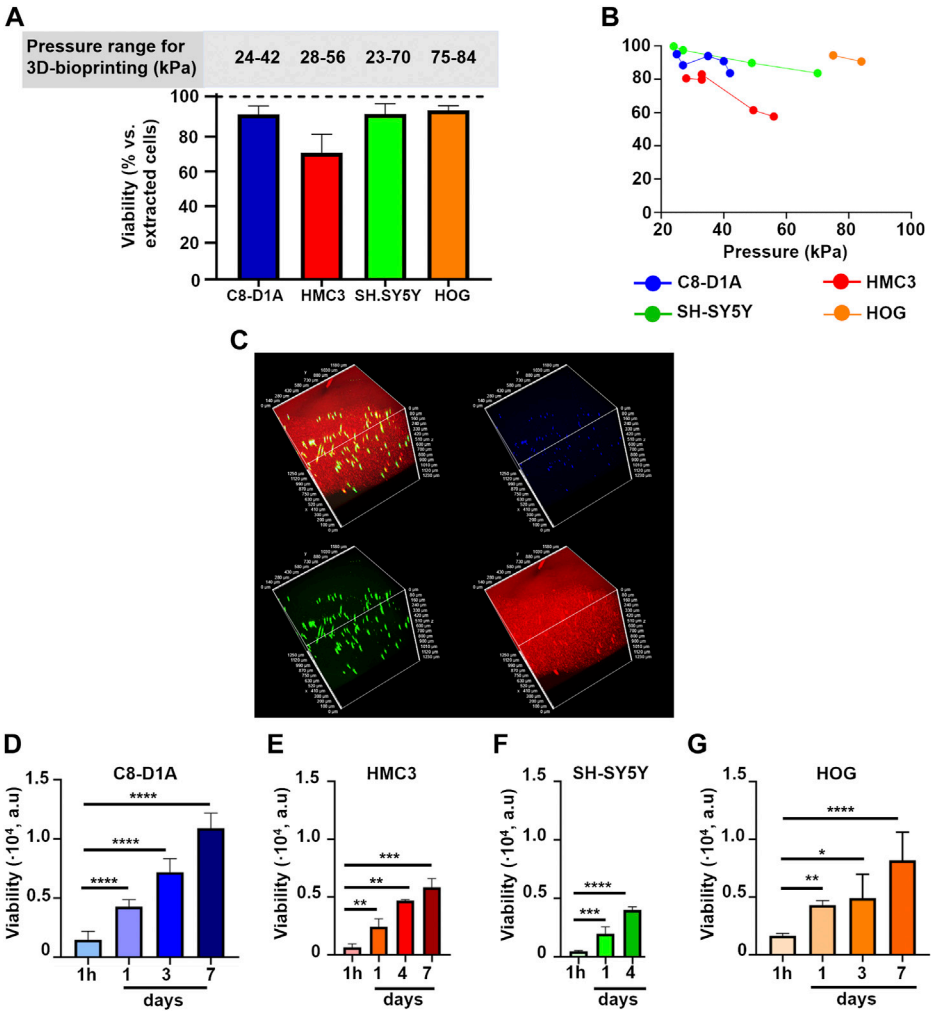

FIGURE 9
(A) Percentage of live cells with respect to the total number of counted cells after dissociating $P_{3.8}Ca_{20}$Coll-DMEM HEPES constructs. Results from the trypan blue exclusion assay for C8-D1A, HMC3, SH-SY5Y, and HOG cells. Mean ± SD, at least six replicates/condition. The upper panel shows the pressure ranges to print the constructs **(B)** Percentage of live cells with respect to the total number of counted cells after dissociating $P_{3.8}Ca_{20}$Coll-DMEM HEPES constructs as a function of printing pressure. Each point on the graph represents the average of three constructs printed consecutively. Results from the trypan blue exclusion assay for C8-D1A, HMC3, SH-SY5Y, and HOG cells **(C)** 3D reconstruction of C8-D1A cells 3D-bioprinted in $P_{3.8}Ca_{20}$Coll-DMEM HEPES. Viable cells were stained green, while cell nuclei were stained blue. $P_{3.8}Ca_{20}$Coll-DMEM HEPES was stained red, because it trapped the ethidium bromide fluorescent probe (Rounds et al., 2011); Viability of C8-D1A **(D)**, HMC3 **(E)**, SH-SY5Y **(F)**, and HOG **(G)** cells printed in $P_{3.8}Ca_{20}$Coll-DMEM HEPES inks and cultured over time. Results from the resazurin-based assay. Mean ± SD, at least 4 replicates/condition. Data was analyzed with one-way ANOVA followed by Tukey's multiple comparisons test. ****: *p*-value <0.0001; ***: *p*-value <0.001; **: *p*-value <0.01; and *: *p*-value <0.05.

showed that collagen fibers enriching pectin matrix in $P_{3.8}Ca_{20}$Coll-DMEM HEPES were crosslinked together forming a dense network. The immunogold assay (Figure 8C'') confirmed the specific localization of the gold-conjugated secondary antibody associated with collagen fibers at both 60 min and 4 h (arrow in C''). In contrast, a loose and uniform-looking matrix was observed in $P_{3.8}Ca_{20}$-DMEM, in which collagen fibers were absent (Figures 8E,E'). In $P_{3.8}Ca_{20}$Coll-DMEM HEPES embedding C8-D1A astrocytic-like cells (Figure 8F), the matrix surrounding the cells appeared more compact and denser (Figures 8F–H).

3.5 Direct cytocompatibility after 3D-bioprinting

A necessary condition to support cell proliferation in $P_{3.8}Ca_{20}$Coll-DMEM HEPES is that cells survive the embedding process and the extrusion-based 3D-bioprinting with different cell types (SH-SY5Y human neuroblastoma cells, C8-D1A mouse astrocytes, HMC3 human microglial cells, and HOG human oligodendroglioma cells). For this reason, we evaluated cell viability immediately ($t \leq 60$ min) after bioprinting. Cell

viability (i.e. the number of live cells with respect to the total number of counted cells, Figure 9A) was similar for HOG cells, SH-SY5Y cells, C8-D1A cells, and slightly lower for HMC3 cells ((73 ± 10) % vs. ~90%). Cell counts were carried out after dissolving the constructs with sodium citrate, a Ca^{2+} chelating agent with improved cytocompatibility with respect to ethylenediaminetetraacetic acid (EDTA, Amaral et al., 2007). To speed up the disaggregation process, we coupled chemical and mechanical actions by pipetting sodium citrate on the constructs for a few minutes. As the process required manipulations after embedding and 3D-bioprinting, our results underestimated cell viability. The fact that cell viability was always comparable with controls supports the potential of $P_{3.8}Ca_{20}$Coll-DMEM HEPES for the 3D-bioprinting of neural cells.

Although derived from pectin solutions in the same pH range, cell constructs were printed at different pressures (Figure 9A), sometimes greater than those for cell-free samples. We observed that the presence of cells could influence the viscoelastic properties (data not shown). For instance, hydrogels with SH-SY5Y and HMC3 cells shared comparable crosslinking kinetics, with minimal changes of viscoelastic properties over time with respect to their cell-free counterparts. After 40 min crosslinking, for samples with SH-SY5Y cells, G' and G'' reduced by 5% and 3%, while for samples with HMC3 cells, G' and G'' decreased by 7% and 2%. On the contrary, C8-D1A cells acted as a reinforcement for $P_{3.8}Ca_{20}$Coll–DMEM HEPES. G' and G'' increased by 51%, and 41% with respect to cell-free samples, respectively (data not shown).

Cell-laden $P_{3.8}Ca_{20}$Coll-DMEM HEPES maintained the shear-thinning behavior, but we observed an increase in viscosity values over crosslinking time. The presence of cells reduced the ability of the material to be extruded through the nozzle, and required an increase in printing pressure. In addition, cells were embedded at high densities. To obtain a homogeneous cell dispersion and avoid aggregation, frequent mixing phases were required, leading to the formation of air bubbles. We speculate that it could explain the high pressures required for HOG-laden constructs. Indeed, visual inspections suggested that HOG cells were the biggest used in this study and thus potentially subjected to a fast sedimentation within the polymer solutions.

Since multiple grids can be printed from the same cartridge, we exploited the results in Figure 9A to investigate whether the increasing pressure could compromise cell survival (Figure 9B). For all the cell populations, the first set of scaffolds showed the highest viability, but a reduction was observed with increasing pressure (i.e. over time). For instance, about 100% of SH-SY5Y cells in the first three constructs (printed at 23 kPa) were viable, but viability dropped to 84% when pressure was increased to 60 kPa. On the contrary, the viability of HMC3 cells showed a drastic decrease after the second set of grids (from 81% at 28 kPa to 58% at 56 kPa).

Sample observation by confocal microscopy (Figure 9C) highlighted that the printing protocol did not affect cell viability, also showing that cells were homogenously distributed within the inks. In fact, they were visible in the green channel, meaning that they internalized the calcein-AM probe. The red background could be explained by ethidium homodimer-1 (sharing structural similarities with propidium iodide), which competed with Ca^{2+} in labelling pectin, as results from the literature (Rounds et al., 2011).

To strengthen the results from the trypan blue exclusion assay, viability after 3D-bioprinting was evaluated for all cell populations by a resazurin-based assay after 1 h, 1, 3 (or 4), and eventually 7 days of culture (Figures 9D–G). For all cell populations, viability increased over time. After embedding and 3D-bioprinting in $P_{3.8}Ca_{20}$Coll-DMEM HEPES, cells survived and kept their proliferative potential, suggesting that the proposed ink could be suitable to print and culture neural cells.

4 Discussion

Pectin and calcium concentrations tested in this study allowed to obtain 3D hydrogels mimicking the basic viscoelastic properties of brain tissue. In fact, at the end of time sweep scans, the elastic moduli of both gels in 0.9% w/v NaCl and DMEM w/and w/o HEPES fell in the range reported for brain tissue (i.e. from few hundreds of Pa to kPa, Leipzig and Shoichet, 2009; Axpe et al., 2020). $P_{2.4}Ca_{35}$-NaCl showed the highest viscoelastic properties ($G' = 1.41 \times 10^3$ Pa; $G'' = 0.27 \times 10^3$ Pa), with tanδ being about 0.2 (i.e. G'' being about 20% G'), as is often found in physiological tissues (Charrier et al., 2018). All the other hydrogels also fulfilled condition $0.1 < \tan\delta < 0.2$ (i.e. 10% $G' < G'' < 20\%$ G'). Also due to its composition, we exploited $P_{3.8}Ca_{20}$Coll-DMEM HEPES for the 3D-bioprinting of neural cells and showed that internally crosslinked pectin-based hydrogels could be suitable for neural cell culture.

This work demonstrates that pectin-based inks produced by pre-crosslinking by internal gelation allow to fabricate self-standing fibers and multi-layer grids with a defined shape after extrusion. Additives or post-printing treatments were shown to be not required. Ink development was guided by the effects of pH and pectin concentration on the viscosity of solutions, together with the impact of the amount of the crosslinker, i.e. the content of calcium salts, on the viscoelastic properties and printability of the gels. Since solvent composition is fundamental to develop a printable ink, we decided to increase complexity to catch up common basic elements and speed up the optimization. Firstly, we tested pectin solutions in 0.9% w/v NaCl, then solutions in DMEM with additives and finally in DMEM also supplemented with HEPES. Our method exploited rheology to give *a priori* information about ink printability and it coupled pH and printing time to gain full control over the kinetics of internal crosslinking. By introducing the pH of pectin solutions as a further parameter to be controlled, we were able to have multiple (pH-dependent) crosslinking kinetics without varying hydrogel composition. Basically, we added a tuning parameter to the time and expanded the

potential of the previously described 3D-reactive printing strategy (Sardelli et al., 2021). This opens to the possibility of applying this approach also to materials whose crosslinking kinetics depended on the pH. Overall, whatever the parameter that controls the crosslinking kinetics, it is possible to exploit it to modulate the printing time, i.e. the stage of the crosslinking in which a hydrogel in formation can be printed. In our case, this was strategic to minimize the persistence time of the cells in the ink before printing, while still allowing for a proper viscosity control.

The content of the crosslinking agent, i.e. $CaCO_3$ as a source of Ca^{2+}, was also a key parameter to determine the presence of insoluble deposits, fiber quality, and printing time. Pectin solutions at a concentration of 2.4% w/v in 0.9% w/v NaCl showed an acidic pH (3.4 ± 0.1), which was able to trigger a fast gelation even when mixed to the lower $CaCO_3$ concentration (20 mM). This concentration also allowed to avoid calcium deposits in printed fibers. In contrast, the higher concentration (35 mM $CaCO_3$) resulted in high pressures for extrusion-based 3D-printing (Figure 4). An increase in $CaCO_3$, that correlates with enhanced hydrogel stiffness and reduced diffusion, may decrease cell viability and proliferation (Banerjee et al., 2009; Ahn et al., 2012). Thus, we produced internal crosslinking with 20 mM $CaCO_3$.

Keeping in mind both 3D-printing and cellular studies, we controlled ink compositions to tune their properties. More specifically, starting from the hypothesis that solutions with comparable viscosity profiles exhibit similar printability in the presence of the same amount of $CaCO_3$, we identified a suitable pectin concentration to reproduce the flow curve for the printable 2.4% w/v pectin in 0.9% w/v NaCl including a cell culture medium (DMEM). Moreover, to mimic common cell culture conditions, we enriched basal DMEM with serum, L-glutamine and antibiotics. The buffering capacity of DMEM was required to increase pectin concentration to 4% w/v to meet similar values of viscosity. The change from 0.9% w/v NaCl to DMEM speeded up the crosslinking kinetics in the early phase (20 min) and increased G'' (Figures 2C, D). In the recovery curves at 0 min (Supplementary Figures S1A, B), G'' values were greater for the ink produced in DMEM than in NaCl, but after 30 and 60 min crosslinking, the recovery trends of G'' were similar. The shift to DMEM also impacted extrudability (Supplementary Figures S1C–E) at time 0, when $P_{2.4}Ca_{20}$-NaCl could be extruded more easily than P_4Ca_{20}-DMEM. At 30 and 60 min, extrudability depended on the shear rate: for shear rates lower than 10 s^{-1}, the extrusion of DMEM ink was easier than the one of the NaCl ink; for higher shear rates, the opposite occurred. The comparison between the printability windows of $P_{2.4}Ca_{20}$-NaCl and P_4Ca_{20}-DMEM highlighted the effect of G'': after 30 and 60 min, the maximum pressures to extrude P_4Ca_{20}-DMEM were like the ones for $P_{2.4}Ca_{35}$-NaCl, but at 0 min they were even greater, and thus excessive for extrusion-based 3D-bioprinting.

To reduce hydrogel G'' without remarkable impact on the crosslinking kinetics, we decreased pectin concentration to 3.8% w/v without varying pH (3.5 ± 0.1) and produced $P_{3.8}Ca_{20}$-DMEM. The shift also reduced the maximum pressures for extrusion to values like the ones for $P_{2.4}Ca_{20}$-NaCl.

But still, we needed to optimize the produced bioink for cell cultures by acting on the pH in the early stages of crosslinking. Towards this aim, the CO_2/bicarbonate system already in basal DMEM (44 mM $NaHCO_3$) was coupled with HEPES. This supplementation did not vary the viscosity of the solution (Supplementary Figure S1F). To improve the cell adhesion properties of pectin (Chen et al., 2018) with a strategy simpler and cheaper than grafting with motif peptides, cells were loaded into collagen solutions at neutral pH and then mixed to pectin/$CaCO_3$ 3 min after the beginning of crosslinking. With this protocol, cells were loaded into pectin gels with pH around 5.81. Cell culture medium was immediately added to speed up the reaching of physiological pHs. For this reason, $P_{3.8}Ca_{20}$Coll-DMEM HEPES was selected for 3D-bioprinting. For its preparation, solutions with 3.55 < pH < 3.70 were used. However, even small pH variations have a remarkable effect on the viscoelastic properties of the final gels (Supplementary Figure S1G). When pH increased from 3.55 to 3.75, G' and G'' decrease. After 60 min crosslinking, for solutions with 3.55 < pH < 3.60, G' and G'' reached 661 Pa and 73 Pa, respectively. For solutions with 3.71 < pH < 3.75, G' and G'' reduced to 213 Pa and 43 Pa, respectively. For pH > 3.79, gelation did not occur in 1 h. The pH of pectin solutions was always measured prior the experiments because it was shown to also influence the crosslinking kinetics and the resting time (i.e. the time before printing constructs with uniform fibers and open porosities): the higher the pH was, the slower was the crosslinking kinetics and the longer the resting time before printing self-standing fibers. This needed to be considered to optimize the viscosity, the printing velocity, and the printing pressure.

Finally, our study proposes an innovative way of exploiting pectin/collagen combinations. Interactions based on surface patch binding were described in collagen/pectin composites loaded with bioactive glass nanoparticles (Wenpo et al., 2015; Goel et al., 2021). As results from previous works, pectin and collagen exhibit the same net charge, but the positively charged patches on collagen bind to the negatively charged segments on pectin, and Ca^{2+} acts as a bridge between—C=O and—COO groups (Goel et al., 2021). When neutral pectin/collagen solutions are combined (Jayakumar et al., 2014), the basic amino acids of collagen primarily interact with pectin, that stabilizes collagen by hydrogen bonding. It creates an effective defense mechanism against collagenase, and promotes collagen stability. Interestingly, an increase in pectin concentration (i.e. in the number of interaction sites) limits the mobility of collagen molecules, leading to the formation of collagen fibrils in the ordered form of precipitates. The mixing in neutral conditions of alkaline de-esterified pectin/CaCl2 with different rations of collagen type I and/or IV (and the subsequent incubation at 37°C) was reported to create an optimal microenvironment for glioblastoma treatment (Belousov et al., 2020).

With these results in mind, together with the possibility of using our inks both for the realization of *in vitro* 3D models of neural tissue, and for cell delivery in clinical practice (e.g. stroke), we deeply focused on ink development and cell encapsulation. The exploitation of pectin as the bulk material provides an extremely varied skeleton on which it is potentially possible to graft molecules and signals to modulate cell behavior. The change from external to internal crosslinking allowed to achieve homogeneous hydrogels, with advantages in terms of providing uniform stimuli for cell culture. By mixing neutral collagen with a high pectin concentration, we speeded up collagen aggregation, and removed the need for incubation at 37°C. The proposed ink was suitable to produce multiple stacks of grids by 3D-printing, and promoted the adhesion of cells to the matrix, favoring their viability over time. Not only cells survived and proliferated after 3D-bioprinting, but they also interacted with the ink, as suggested by the time sweeps of cell-laden constructs. In addition, the structural reorganization of the hydrogels observed by TEM was probably cell-mediated and achieved thanks to the interaction between the matrix and the cell membranes (Figures 8F–H), leading to a change in the orientation of collagen fibers (Webber et al., 2016; Lovrak et al., 2017). Finally, with respect to clinical applications, a strict control over the pH of pectin solution allowed to tune the crosslinking kinetics, i.e. the time available to the ink to conform to the defect to be filled.

Data availability statement

The original contributions presented in the study are included in the article/Supplementary Material, further inquiries can be directed to the corresponding author.

Author contributions

MM, Software, Investigation, Visualization, Data Curation, Writing; LS, Rheological analyses: Methodology, Review and Editing; NB, Transmission electron microscopy: Investigation and Visualization; AG, Transmission electron microscopy: Methodology, Resources and Data Curation, Review and Editing; EJ, Confocal microscopy: Investigation, Visualization and Data Curation; MTR, Resources; FB-V, Rheological analyses: Methodology and Resources, Supervision, Review and Editing; PP, Conceptualization, Resources, Supervision, Writing, Review and Editing; MT, Conceptualization, Supervision, Project administration, Funding acquisition, Writing, Coordination of Review and Editing.

Acknowledgments

We thank Herbstreith and Fox for kindly gifting pectin. We are also very grateful to Sara Mantero (Politecnico di Milano) for the constructive support and useful discussions and to Diego Albani (Istituto di Ricerche Farmacologiche Mario Negri IRCCS) for kindly providing HMC3 cells. A special thanks to Francesca Annis, Maria Carolina Quintero Carmona, and Gloria Romero Vega (Politecnico di Milano) for technical support and to Alice Meroni and the Research Office (Politecnico di Milano) for administrative support. We also thank Luciana Borrelli for her final linguistical revision of the manuscript.

Conflict of interest

The authors declare that the research was conducted in the absence of any commercial or financial relationships that could be construed as a potential conflict of interest.

Publisher's note

All claims expressed in this article are solely those of the authors and do not necessarily represent those of their affiliated organizations, or those of the publisher, the editors and the reviewers. Any product that may be evaluated in this article, or claim that may be made by its manufacturer, is not guaranteed or endorsed by the publisher.

Supplementary material

The Supplementary Material for this article can be found online at: https://www.frontiersin.org/articles/10.3389/fbioe.2022.1032542/full#supplementary-material

References

Ahn, S., Lee, H., Bonassar, L. J., and Kim, G. H. (2012). Cells (MC3T3-E1)-laden alginate scaffolds fabricated by a modified solid-freeform fabrication process supplemented with an aerosol spraying. *Biomacromolecules* 13, 2997–3003. doi:10.1021/bm3011352

Amaral, K. F., Rogero, M. M., Fock, R. A., Borelli, P., and Gavini, G. (2007). Cytotoxicity analysis of EDTA and citric acid applied on murine resident macrophages culture. *Int. Endod. J.* 40, 338–343. doi:10.1111/j.1365-2591.2007.01220.x

Andriotis, E. G., Eleftheriadis, G. K., Karavasili, C., and Fatouros, D. G. (2020). Development of bio-active patches based on Pectin for the treatment of Ulcers and wounds using 3D-bioprinting technology. *Pharmaceutics* 12, 56. doi:10.3390/pharmaceutics12010056

Antill-O'Brien, N., Bourke, J., and O'Connell, C. D. (2019). Layer-by-layer: The case for 3D bioprinting neurons to create patient-specific epilepsy models. *Materials* 12, 3218. doi:10.3390/ma12193218

Axpe, E., Orive, G., Franze, K., and Appel, E. A. (2020). Towards brain-tissue-like biomaterials. *Nat. Commun.* 11, 3423. doi:10.1038/s41467-020-17245-x

Bae, M., Hwang, D. W., Ko, M. K., Jin, Y., Shin, W. J., Park, W., et al. (2021). Neural stem cell delivery using brain-derived tissue-specific bioink for recovering from traumatic brain injury. *Biofabrication* 13, 044110. doi:10.1088/1758-5090/ac293f

Banerjee, A., Arha, M., Choudhary, S., Ashton, R. S., Bhatia, S. R., Schaffer, D. V., et al. (2009). The influence of hydrogel modulus on the proliferation and differentiation of encapsulated neural stem cells. *Biomaterials* 30, 4695–4699. doi:10.1016/j.biomaterials.2009.05.050

Bedini, E., Iadonisi, A., Schiraldi, C., Colombo, L., Albani, D., Petrini, P., et al. (2021). Microbiological-chemical sourced chondroitin sulfates protect neuroblastoma SH-SY5Y cells against oxidative stress and are suitable for hydrogel-based controlled release. *Antioxidants* 10, 1816. doi:10.3390/antiox10111816

Belousov, A., Titov, S., Shved, N., Malykin, G., Kovalev, V., Suprunova, I., et al. (2020). Hydrogels based on modified pectins capable of modulating neural cell behavior as prospective biomaterials in glioblastoma treatment. *Int. Rev. Neurobiol.* 151, 111–138. doi:10.1016/bs.irn.2020.03.025

Boularaoui, S., Al Hussein, G., Khan, K. A., Christoforou, N., and Stefanini, C. (2020). An overview of extrusion-based bioprinting with a focus on induced shear stress and its effect on cell viability. *Bioprinting* 20, e00093. doi:10.1016/j.bprint.2020.e00093

Burey, P., Bhandari, B. R., Howes, T., and Gidley, M. J. (2008). Hydrocolloid gel particles: Formation, characterization, and application. *Crit. Rev. Food Sci. Nutr.* 48, 361–377. doi:10.1080/10408390701347801

Campiglio, C. E., Carcano, A., and Draghi, L. (2021). RGD-pectin microfiber patches for guiding muscle tissue regeneration. *J. Biomed. Mater. Res. A* 110, 515–524. doi:10.1002/jbm.a.37301

Causton, B. E. (1984). Improved bonding of composite restorative to dentine. A study *in vitro* of the use of a commercial halogenated phosphate ester. *Br. Dent. J.* 156, 93–95. doi:10.1038/sj.bdj.4805276

Celus, M., Kyomugasho, C., Van Loey, M., Grauwet, T., and Hendrickx, M. E. (2018). Influence of pectin structural properties on interactions with divalent cations and its associated functionalities. *Compr. Rev. Food Sci. Food Saf.* 17, 1576–1594. doi:10.1111/1541-4337.12394

Charrier, E. E., Pogoda, K., Wells, R. G., and Janmey, P. A. (2018). Control of cell morphology and differentiation by substrates with independently tunable elasticity and viscous dissipation. *Nat. Commun.* 9, 449. doi:10.1038/s41467-018-02906-9

Chen, S., Cui, S., Zhang, H., Pei, X., Hu, J., Zhou, Y., et al. (2018). Cross-linked pectin nanofibers with enhanced cell adhesion. *Biomacromolecules* 19, 490–498. doi:10.1021/acs.biomac.7b01605

Chesler, M. (2003). Regulation and modulation of pH in the brain. *Physiol. Rev.* 83, 1183–1221. doi:10.1152/physrev.00010.2003

Cidonio, G., Glinka, M., Dawson, J. I., and Oreffo, R. O. C. (2019). The cell in the ink: Improving biofabrication by printing stem cells for skeletal regenerative medicine. *Biomaterials* 209, 10–24. doi:10.1016/j.biomaterials.2019.04.009

Copus, P. W., Lee, S. J., and Atala, A. (2022). "Bioink printability and methodologies for cell-based extrusion bioprinting," in *3D bioprinting and nanotechnology in tissue engineering and regenerative medicine*. Editors L. J. Zhang, J. P. Fisher, and K. W. Leong. Second Edition (Elsevier Academic Press), 153–183.

Danielyan, L., Schäfer, R., von Ameln-Mayerhofer, A., Buadze, M., Geisler, J., Klopfer, T., et al. (2009). Intranasal delivery of cells to the brain. *Eur. J. Cell Biol.* 88, 315–324. doi:10.1016/j.ejcb.2009.02.001

Dennis, J. O., Adam, A. A., Ali, M. K. M., Soleimani, H., Bin Abd Shukur, M. F., Ibnaouf, K. H., et al. (2022). Substantial proton ion conduction in methylcellulose/pectin/ammonium chloride based solid nanocomposite polymer electrolytes: Effect of ZnO nanofiller. *Membranes* 12, 706. doi:10.3390/membranes12070706

Flinck, M., Kramer, S. H., and Pedersen, S. F. (2018). Roles of pH in control of cell proliferation. *Acta Physiol. (Oxf).* 223, e13068. doi:10.1111/apha.13068

Gao, X., Zhi, Y., Sun, L., Xue, H., Tai, G., Zhou, Y., et al. (2013). The inhibitory effects of a rhamnogalacturonan I (RG-I) domain from ginseng pectin on galectin-3 and its structure-activity relationship. *J. Biol. Chem.* 288, 33953–33965. doi:10.1074/jbc.M113.482315

García-Revilla, J., Boza-Serrano, A., Espinosa-Oliva, A. M., Sarmiento Soto, M., Deierborg, T., Ruiz Rocío, R., et al. (2022). Galectin-3, a rising star in modulating microglia activation under conditions of neurodegeneration. *Cell Death Dis.* 13, 628. doi:10.1038/s41419-022-05058-3

Giacoppo, S., Galuppo, M., Calabrò, R. S., D'Aleo, G., Marra, A., Sessa, E., et al. (2014). Heavy metals and neurodegenerative diseases: An observational study. *Biol. Trace Elem. Res.* 161, 151–160. doi:10.1007/s12011-014-0094-5

Giampietro, R., Spinelli, F., Contino, M., and Colabufo, N. A. (2018). The pivotal role of copper in neurodegeneration: A new strategy for the therapy of neurodegenerative disorders. *Mol. Pharm.* 15, 808–820. doi:10.1021/acs.molpharmaceut.7b00841

Gillispie, G., Prim, P., Copus, J., Fisher, J., Mikos, A. G., Yoo, J. J., et al. (2020). Assessment methodologies for extrusion-based bioink printability. *Biofabrication* 12, 022003. doi:10.1088/1758-5090/ab6f0d

Goel, H., Gupta, N., Santhiya, D., Dey, N., Bohidar, H. B., and Bhattacharya, A. (2021). Bioactivity reinforced surface patch bound collagen-pectin hydrogel. *Int. J. Biol. Macromol.* 174, 240–253. doi:10.1016/j.ijbiomac.2021.01.166

Hopkins, A. M., DeSimone, E., Chwalek, K., and Kaplan, D. L. (2015). 3D *in vitro* modeling of the central nervous system. *Prog. Neurobiol.* 125, 1–25. doi:10.1016/j.pneurobio.2014.11.003

Jayakumar, G. C., Usharani, N., Kawakami, K., Rao, J. R., and Nair, B. U. (2014). Studies on the physico-chemical characteristics of collagen-pectin composites. *RSC Adv.* 4, 63840–63849. doi:10.1039/C4RA10368H

Kar, F., and Arslan, N. (1999). Effect of temperature and concentration on viscosity of orange peel pectin solutions and intrinsic viscosity-molecular weight relationship. *Carbohydr. Polym.* 40, 277–284. doi:10.1016/S0144-8617(99)00062-4

Kim, E., Seok, J. M., Bin Bae, S., Park, S. A., and Park, W. H. (2021). Silk fibroin enhances cytocompatibilty and dimensional stability of alginate hydrogels for light-based three-dimensional bioprinting. *Biomacromolecules* 22, 1921–1931. doi:10.1021/acs.biomac.1c00034

Kumar, M., Tomar, M., Saurabh, V., Mahajan, S., Punia, S., del Mar Contreras, M., et al. (2020). Emerging trends in pectin extraction and its anti-microbial functionalization using natural bioactives for application in food packaging. *Trends Food Sci. Technol.* 105, 223–237. doi:10.1016/j.tifs.2020.09.009

Lara-Espinoza, C., Carvajal-Millán, E., Balandrán-Quintana, R., López-Franco, Y., and Rascón-Chu, A. (2018). Pectin and pectin-based composite materials: Beyond food texture. *Molecules* 23, 942. doi:10.3390/molecules23040942

Lee, H., McKeon, R. J., and Bellamkonda, R. V. (2010). Sustained delivery of thermostabilized chABC enhances axonal sprouting and functional recovery after spinal cord injury. *Proc. Natl. Acad. Sci. U. S. A.* 107, 3340–3345. doi:10.1073/pnas.0905437106

Leipzig, N. D., and Shoichet, M. S. (2009). The effect of substrate stiffness on adult neural stem cell behavior. *Biomaterials* 30, 6867–6878. doi:10.1016/j.biomaterials.2009.09.002

Lessa, E. F., Medina, A. L., Ribeiro, A. S., and Fajardo, A. R. (2020). Removal of multi-metals from water using reusable pectin/cellulose microfibers composite beads. *Arab. J. Chem.* 13, 709–720. doi:10.1016/j.arabjc.2017.07.011

Li, H., Li, N., Zhang, H., Zhang, Y., Suo, H., Wang, L., et al. (2020). Three-dimensional bioprinting of perfusable hierarchical microchannels with alginate and silk fibroin double cross-linked network. *3D Print. Addit. Manuf.* 7, 78–84. doi:10.1089/3dp.2019.0115

Liang, L., and Luo, Y. (2020). Casein and pectin: Structures, interactions, and applications. *Trends Food Sci. Technol.* 97, 391–403. doi:10.1016/j.tifs.2020.01.027

Lindsay, C. D., Roth, J. G., LeSavage, B. L., and Heilshorn, S. C. (2019). Bioprinting of stem cell expansion lattices. *Acta Biomater.* 95, 225–235. doi:10.1016/j.actbio.2019.05.014

Liu, Z., Bhandari, B., Prakash, S., Mantihal, S., and Zhang, M. (2019). Linking rheology and printability of a multicomponent gel system of carrageenan-xanthan-starch in extrusion based additive manufacturing. *Food Hydrocoll.* 87, 413–424. doi:10.1016/j.foodhyd.2018.08.026

Lopez Hernandez, H., Souza, J. W., and Appel, E. A. (2021). A quantitative description for designing the extrudability of shear-thinning physical hydrogels. *Macromol. Biosci.* 21, e2000295. doi:10.1002/mabi.202000295

Lovrak, M., Hendriksen, W. E. J., Maity, C., Mytnyk, S., van Steijn, V., Eelkema, R., et al. (2017). Free-standing supramolecular hydrogel objects by reaction-diffusion. *Nat. Commun.* 8, 15317. doi:10.1038/ncomms15317

Lozano, R., Stevens, L., Thompson, B. C., Gilmore, K. J., Gorkin, R., Stewart, E. M., et al. (2015). 3D printing of layered brain-like structures using peptide modified gellan gum substrates. *Biomaterials* 67, 264–273. doi:10.1016/j.biomaterials.2015.07.022

Mehrotra, S., Moses, J. C., Bandyopadhyay, A., and Mandal, B. B. (2019). 3D printing/bioprinting based tailoring of *in vitro* tissue models: Recent

advances and challenges. *ACS Appl. Bio Mater.* 2, 1385–1405. doi:10.1021/acsabm.9b00073

Moreira, H. R., Munarin, F., Gentilini, R., Visai, L., Granja, P. L., Tanzi, M. C., et al. (2014). Injectable pectin hydrogels produced by internal gelation: pH dependence of gelling and rheological properties. *Carbohydr. Polym.* 103, 339–347. doi:10.1016/j.carbpol.2013.12.057

Munarin, F., Guerreiro, S. G., Grellier, M. A., Tanzi, M. C., Barbosa, M. A., Petrini, P., et al. (2011). Pectin-based injectable biomaterials for bone tissue engineering. *Biomacromolecules* 14, 568–577. doi:10.1021/bm101110x

Munarin, F., Petrini, P., Barcellona, G., Roversi, T., Piazza, L., Visai, L., et al. (2014). Reactive hydroxyapatite fillers for pectin biocomposites. *Mater. Sci. Eng. C* 45, 154–161. doi:10.1016/j.msec.2014.09.003

Oliveira, E. P., Malysz-Cymborska, I., Golubczyk, D., Kalkowski, L., Kwiatkowska, J., Reis, R. L., et al. (2019). Advances in bioinks and *in vivo* imaging of biomaterials for CNS applications. *Acta Biomater.* 95, 60–72. doi:10.1016/j.actbio.2019.05.006

Papadimitriou, L., Manganas, P., Ranella, A., and Stratakis, E. (2020). Biofabrication for neural tissue engineering applications. *Mater. Today Bio* 6, 100043. doi:10.1016/j.mtbio.2020.100043

Paxton, N., Smolan, W., Böck, T., Melchels, F., Groll, J., and Jungst, T. (2017). Proposal to assess printability of bioinks for extrusion-based bioprinting and evaluation of rheological properties governing bioprintability. *Biofabrication* 9, 044107. doi:10.1088/1758-5090/aa8dd8

Peneda Pacheco, D., Suárez Vargas, N., Visentin, S., and Petrini, P. (2021). From tissue engineering to engineering tissues: The role and application of *in vitro* models. *Biomater. Sci.* 9, 70–83. doi:10.1039/D0BM01097A

Pereira, R. F., Barrias, C. C., Bártolo, P. J., and Granja, P. L. (2018). Cell-instructive pectin hydrogels crosslinked via thiol-norbornene photo-click chemistry for skin tissue engineering. *Acta Biomater.* 66, 282–293. doi:10.1016/j.actbio.2017.11.016

Qiu, B., Bessler, N., Figler, K., Buchholz, M-B., Rios, A. C., Malda, J., et al. (2020). Bioprinting neural systems to model central nervous system diseases. *Adv. Funct. Mater.* 30, 1910250. doi:10.1002/adfm.201910250

Rounds, C. M., Lubeck, E., Hepler, P. K., and Winship, L. J. (2011). Propidium iodide competes with Ca^{2+} to label pectin in pollen tubes and arabidopsis root hairs. *Plant Physiol.* 157, 175–187. doi:10.1104/pp.111.182196

Samanipour, R., Tahmooressi, H., Nejad, H. R., Hirano, M., Shin, S-R., and Hoorfar, M. (2022). A review on 3D printing functional brain model. *Biomicrofluidics* 16, 011501. doi:10.1063/5.0074631

Sardelli, L., Tunesi, M., Briatico-Vangosa, F., and Petrini, P. (2021). 3D-Reactive printing of engineered alginate inks. *Soft Matter* 17, 8105–8117. doi:10.1039/d1sm00604e

Sarker, M. D., Naghieh, S., McInnes, A. D., Ning, L., Schreyer, D. J., and Chen, X. (2019). Bio-fabrication of peptide-modified alginate scaffolds: Printability, mechanical stability and neurite outgrowth assessments. *Bioprinting* 14, e00045. doi:10.1016/j.bprint.2019.e00045

Secchi, E., Munarin, F., Alaimo, M. D., Bosisio, S., Buzzaccaro, S., Ciccarella, G., et al. (2014). External and internal gelation of pectin solutions: Microscopic dynamics versus macroscopic rheology. *J. Phys. Condens. Matter* 26, 464106. doi:10.1088/0953-8984/26/46/464106

Skjåk-Bræk, G., Grasdalen, H., and Smidsrød, O. (1989). Inhomogeneous polysaccharide ionic gels. *Carbohydr. Polym.* 10, 31–54. doi:10.1016/0144-8617(89)90030-1

Sriamornsak, P., Wattanakorn, N., and Takeuchi, H. (2010). Study on the mucoadhesion mechanism of pectin by atomic force microscopy and mucin-particle method. *Carbohydr. Polym.* 79, 54–59. doi:10.1016/j.carbpol.2009.07.018

Taylor, S. J., Rosenzweig, E. S., McDonald, J. W., and Sakiyama-Elbert, S. E. (2006). Delivery of neurotrophin-3 from fibrin enhances neuronal fiber sprouting after spinal cord injury. *J. Control. Release* 113, 226–235. doi:10.1016/j.jconrel.2006.05.005

Taylor, A. C. (1962). Responses of cells to pH changes in the medium. *J. Cell Biol.* 15, 201–209. doi:10.1083/jcb.15.2.201

Tunesi, M., Raimondi, I., Russo, T., Colombo, L., Micotti, E., Brandi, E., et al. (2019). Hydrogel-based delivery of Tat-fused protein Hsp70 protects dopaminergic cells *in vitro* and in a mouse model of Parkinson's disease. *NPG Asia Mater.* 11, 28. doi:10.1038/s41427-019-0128-8

Vancauwenberghe, V., Delele, M. A., Vanbiervliet, J., Aregawi, W., Verboven, P., Lammertyn, J., et al. (2018). Model-based design and validation of food texture of 3D printed pectin-based food simulants. *J. Food Eng.* 231, 72–82. doi:10.1016/j.jfoodeng.2018.03.010

Vaz, V. M., and Kumar, L. (2021). 3D printing as a promising tool in personalized medicine. *AAPS PharmSciTech* 22, 49. doi:10.1208/s12249-020-01905-8

Wan-Ping, V., Ravindra, P., Tey, B-T., and Chan, E-S. (2011). Comparison of alginate and pectin based beads for production of poultry probiotic cells. *J. Biosci. Bioeng.* 111, 294–299. doi:10.1016/j.jbiosc.2010.11.010

Webber, M. J., Appel, E. A., Meijer, E. W., and Langer, R. (2016). Supramolecular biomaterials. *Nat. Mater.* 15, 13–26. doi:10.1038/nmat4474

Wenpo, F., Gaofeng, L., Shuying, F., Yuanming, Q., and Keyong, T. (2015). Preparation and characterization of collagen–hydroxyapatite/pectin composite. *Int. J. Biol. Macromol.* 74, 218–223. doi:10.1016/j.ijbiomac.2014.11.031

Zhang, X., Chen, X., Hong, H., Hu, R., Liu, J., and Liu, C. (2021). Decellularized extracellular matrix scaffolds: Recent trends and emerging strategies in tissue engineering. *Bioact. Mater.* 10, 15–31. doi:10.1016/j.bioactmat.2021.09.014

Zhao, Z., Vizetto-Duarte, C., Moay, Z. K., Setyawati, M. I., Rakshit, M., Kathawala, M. H., et al. (2020). Composite hydrogels in three-dimensional *in vitro* models. *Front. Bioeng. Biotechnol.* 8, 611. doi:10.3389/fbioe.2020.00611

Zhong, Y., and Bellamkonda, R. V. (2008). Biomaterials for the central nervous system. *J. R. Soc. Interface* 6, 957–975. doi:10.1098/rsif.2008.0071

frontiers | Frontiers in Bioengineering and Biotechnology

TYPE Original Research
PUBLISHED 09 January 2023
DOI 10.3389/fbioe.2022.1076345

OPEN ACCESS

EDITED BY
Ranjith Kumar Kankala,
Huaqiao University, China

REVIEWED BY
Gwendolen Clair Reilly,
The University of Sheffield,
United Kingdom
Silvia Joana Bidarra,
Universidade do Porto, Portugal

*CORRESPONDENCE
Yicheng Cheng,
chengyicheng0220@163.com
Wei Li,
wei.li@siat.ac.cn
Huaiyu Wang,
hy.wang1@siat.ac.cn

†These authors have contributed equally to this work

SPECIALTY SECTION
This article was submitted to Biomaterials, a section of the journal Frontiers in Bioengineering and Biotechnology

RECEIVED 21 October 2022
ACCEPTED 23 December 2022
PUBLISHED 09 January 2023

CITATION
Ren X, Gao X, Cheng Y, Xie L, Tong L, Li W, Chu PK and Wang H (2023), Maintenance of multipotency of bone marrow mesenchymal stem cells on poly(ε-caprolactone) nanoneedle arrays through the enhancement of cell-cell interaction. *Front. Bioeng. Biotechnol.* 10:1076345. doi: 10.3389/fbioe.2022.1076345

Maintenance of multipotency of bone marrow mesenchymal stem cells on poly(ε-caprolactone) nanoneedle arrays through the enhancement of cell-cell interaction

Xiaoxue Ren[1†], Xiaoting Gao[1,2†], Yicheng Cheng[3*], Lingxia Xie[1], Liping Tong[1], Wei Li[1*], Paul K. Chu[4] and Huaiyu Wang[1*]

[1]Institute of Biomedicine and Biotechnology, Shenzhen Institute of Advanced Technology, Chinese Academy of Sciences, Shenzhen, China, [2]University of Chinese Academy of Sciences, Beijing, China, [3]Department of Stomatology, Jinling Hospital, School of Medicine, Nanjing University, Nanjing, China, [4]Department of Physics, Department of Materials Science and Engineering, Department of Biomedical Engineering, City University of Hong Kong, Kowloon, Hong Kong SAR, China

Mesenchymal stem cells (MSCs), with high self-renewal ability and multipotency, are commonly used as the seed cells for tissue engineering. However, the reduction and loss of multipotential ability after necessary expansion *in vitro* set up a heavy obstacle to the clinical application of MSCs. Here in this study, we exploit the autologous crystallization ability of biocompatible poly (ε-caprolactone) (PCL) to obtain uniformly distributed nanoneedle arrays. By controlling the molecular weight of PCL, nanoneedle with a width of 2 μm and height of 50 nm, 80 nm, and 100 nm can be successfully fabricated. After surface chemical modification with polydopamine (PDA), the water contact angle of the fabricated PCL nanoneedle arrays are reduced from 84° to almost 60° with no significant change of the nanostructure. All the fabricated substrates are cultured with bone marrow MSCs (BMMSCs), and the adhesion, spreading, proliferation ability and multipotency of cells on different substrates are investigated. Compared with the BMMSCs cultured on pure PCL nanoneedle arrays, the decoration of PDA can improve the adhesion and spreading of cells and further change them from aggregated distribution to laminar distribution. Nevertheless, the laminar distribution of cultured cells leads to a weak cell-cell interaction, and hence the multipotency of BMMSCs cultured on the PCL-PDA substrates is decimated. On the contrary, the pure PCL nanoneedle arrays can be used to maintain the multipotency of BMMSCs *via* clustered growth, and the PCL1 nanoneedle array with a height of 50 nm is more promising than the other 2 with regard to the highest proliferation rate and best multipotential differentiation ability of cultured cells. Interestingly, there is a positive correlation between the strength of cell-cell interaction and the multipotency of stem cells *in vitro*. In conclusion, we have successfully maintained the multipotency of BMMSCs by using the PCL nanoneedle arrays, especially the PCL1 nanoneedle array with a height of 50 nm, as the substrates for *in vitro* extension, and further revealed the importance of cell-cell interaction on the multipotency of MSCs. The study provides a theoretical basis for the behavioral regulation of MSCs, and is instructive to the design of tissue engineering scaffolds.

KEYWORDS

autologous crystallization, bone marrow mesenchymal stem cells, multipotency, cell-cell interaction, poly (ε-caprolactone)

1 Introduction

Mesenchymal Stem Cells (MSCs) are commonly used as the seed cells for tissue engineering, which is due to their multidirectional differentiation potential, self-renewal ability and immunomodulatory function (Tavakoli et al., 2020; Chen et al., 2022). However, the scarcity of MSCs in human bodies is a great obstacle severely impeding the clinical application of MSCs. Take bone marrow mesenchymal stem cells (BMMSCs) as an example, BMMSCs only accounts for .1‰ of bone marrow cells, of which the activity would reduce rapidly with the increase of age (McKee and Chaudhry, 2017; Najar et al., 2021). Hence, the *in vitro* expansion of MSCs are necessary to complement this shortage. Conventional tissue culture polystyrene (TCP) is the most commonly-used substrate for *in vitro* MSCs expansion. Nevertheless, the *in vitro* expansion of MSCs using TCP will inevitably reduce the multipotency and self-renewal ability of MSCs, and ultimately causing MSCs useless for the clinical applications. Although a short-term maintenance of MSCs multipotency can be achieved by adding active molecules (e.g., endothelial growth factors, interleukin-6, immobilized leukemia inhibitory factor) to the culture medium, and maintaining an appropriate hypoxic environment for *in vitro* expansion (Grayson et al., 2007; Pricola et al., 2009; Khalil et al., 2020; Rawat et al., 2021; Samal et al., 2021). However, the related regulation processes are too complex and very hard to control. The recent studies on the *in vitro* regulation of MSCs behaviors have shown that the surface topography and biochemical properties of culture substrates can significantly influence the adhesion, proliferation, spread, distribution as well as the multipotency of MSCs (Li et al., 2017). Therefore, development of culture substrates that can help maintain the multipotential differentiation and self-renewal ability of MSCs during their *in vitro* expansion is urgently needed.

As one of the major properties of culture substrates, the surface topography of substrates is a crucial factor for determining the behaviors and fate of cultured cells (Chen et al., 2014; Cun and Hosta-Rigau, 2020). The methodologies for constructing micro/nanostructures on substrates are diversified, and studies have shown that the multipotency of MSCs can possibly be maintained by tuning the micro/nano-topography of substrates. For instance, (McMurray et al. (2011) combined electron beam lithography with hot embossing to fabricate PCL nanopillar arrays with 120 nm in diameter and 300 nm in space. By adjusting the arrangement of nanopillars, the improvement of osteogenic differentiation and the maintenance of MSCs multipotency were separately achieved. This study demonstrated the feasibility of maintaining MSCs multipotency *in vitro* by regulating the surface topography of culture substrates. In addition, Rico et al. (2016) fabricated a fibronectin nanonetwork by controlling the assembly of fibronectin and used it to maintain the multi-differentiation potency of MSCs. These studies demonstrated the importance of surface physical and chemical properties of substrates for maintaining the multipotency of cultured MSCs (Hofmeister et al., 2015). However, the aforementioned methods are still criticized for the operational complexity, which is unsuitable for further promotion. Therefore, it is of great research significance and clinical value to explore a substrate that is highly controllable, reproducible, simple to operate, easy to achieve large-scale preparation, and can effectively maintain the multipotency of MSCs during *in vitro* expansion.

It is worth noting that crystallization is a simple and controllable method for fabricating micro/nano-topographies, and more than two-thirds of the synthetic and natural polymers have crystallization ability (Crist and Schultz, 2016). Spherical crystals, string crystals, dendritic crystals, etc. with a wide range of dimensions can be obtained by regulating the mode and parameters of crystallization. What is more important, the methodology of crystallization also provides the advantages such as wide selection of materials, high reproducibility, simple operation as well as large-scale preparation, hence is drawing more and more attention in the field of materials regulating cellular behaviors and functions (Wang et al., 2012; Li et al., 2016; Ren et al., 2019).

Here in this study, we employed the biocompatible poly (ε-caprolactone) as the base material and utilized its semi-crystalline ability to fabricate nanoneedle arrays. By changing the average molecular weight of PCL, nanoneedles with average height of 50 nm, 80 nm and 100 nm were successfully obtained. In addition, the surface chemical state of PCL nanoneedles could be modified by polydopamine (PDA) without obvious changes in surface topography. Furthermore, the adhesion, spreading, distribution, proliferation, and multipotency of BMMSCs on different substrates were systematically studied and compared. Our study demonstrates that the nanoneedle of 50 nm high can be used to maintain the multipotency of MSCs during *in vitro* expansion and a positive correction between cell-cell interaction and multipotency of MSCs has been revealed. Overall, we have developed a simple, controllable, reproducible, and easy-to-achieve batch preparation method to maintain the multipotency of MSCs during *in vitro* expansion, which is also instructive for the understanding and *in vitro* regulation of stem cell behaviors and functions.

2 Materials and methods

2.1 Materials

Poly (ε-caprolactone) (PCL, M_n~10,000, 40,000, 80,000), dexamethasone, dimethyl sulfoxide (DMSO), Alizarin Red S, and Red Oil O were purchased from Sigma-Aldrich (United States). Dopamine hydrochloride, Triton X-100, isobutylmethylxanthine (IBMX), indomethacin, insulin, Tris and bovine serum albumin (BSA) were purchased from Aladdin (China). All chemical reagents were used as received. Sprague Dawley (SD) rats of 4 weeks were obtained from Guangdong Charles River Laboratory Animal Technology Co., Ltd (China). Fetal bovine serum (FBS, Gibco, United States), α-MEM culture medium (Hyclone, United States), .25% trypsin (Gibco, United States), penicillin/streptomycin (P/S, Gibco, United States), PBS (pH 7.4, Gibco, United States), 4% paraformaldehyde (Beyotime Biotechnology, China), cell counting kit-8 (CCK-8, Beyotime Biotechnology, China), Alexa Fluor™ 488 Phalloidin (Life Technologies, United States), Hoechst 33,258 (Life Technologies, United States), Trizol (life technologies,

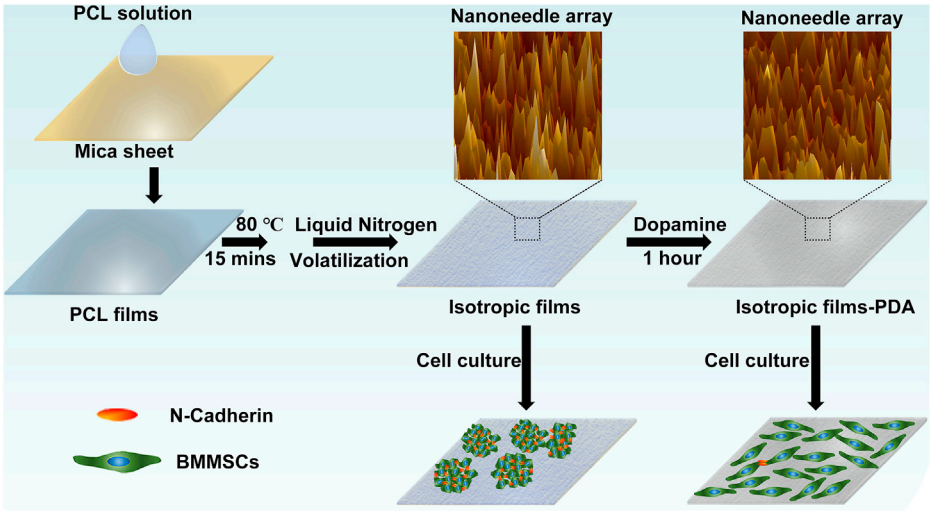

SCHEME 1
The process of sample preparation and cell culture.

United States), anti-Nanog antibody (Proteintech, United States), anti-N-cadherin antibody (Proteintech, United States), Alexa Fluor 488-conjugated AffiniPure Goat Anti-Rabbit IgG (H + L) (Proteintech, United States), Alexa Fluor 561-conjugated AffiniPure Goat Anti-Rabbit IgG (H + L) (Proteintech, United States), PrimeScript™ RT Master Mix Kit (TaKaRa, Japan) and TransStart Top Green qPCR SuperMix (TransGen Biotech, China) were applied according to the instructions.

2.2 Preparation of PCL nanoneedle arrays

The isotropic films were prepared by controlling the self-crystallizing process of poly (ε-caprolactone) (PCL). In particular, 30 μl of .02 g/ml PCL solution in trichloromethane was dropped on a clean mica sheet (1 cm^2 × 1 cm^2) and dried at room temperature for 1 h. Afterwards, the formed PCL films were treated at 80°C for 15 min to eliminate the heat history. Finally, the PCL films were quickly transferred into liquid nitrogen in an open system and maintained overnight for full self-crystallization.

2.3 Decoration of PDA (PCL-PDA)

PCL samples were placed vertically in a 24-well plate. Dopamine was dissolved in 10 mM Tris-HCl (pH 8.5) by magnetic stirring to .02 g/ml (Lee et al., 2007). In the next step, the solution was quickly added to the 24-well plate with an amount of 4 ml per well and then reacted for 1 h in the dark. The samples were finally washed with sufficient deionized water and dried at room temperature.

2.4 Surface characterization

An X-ray photoelectron spectrometer (EscaLab 250Xi, Thermal Fisher, United States) was applied to analyze the surface chemical states of PCL and PCL-PDA. Compared to PCL, the appearance of N-signal peak at ~400 eV of PCL-PDA is the hallmark of successful modification. Atomic force microscope (AFM, MultiMode 8, Bruker, United States) was applied to characterize the micro/nanostructures of PCL and PCL-PDA films in the tapping mode in the air. The obtained data were analyzed using the Nanoscope software. Furthermore, the hydrophilicity of the films in the air were measured using a contact angle meter (Data-Physics OCA-20 Appa-raus, Germany). 4 μl of the deionized water were dropped onto different sample surfaces, and the water contact angles were measured after stabilization for 5 s.

2.5 Isolation and culture of BMMSCs

BMMSCs were obtained from 4-weeks SD rats using the whole bone marrow adherence method as previously reported (Friedenstein et al., 1970; Li et al., 2015). Briefly, rats were firstly sacrificed with cervical dislocation, and the femurs and tibias were flushed with basal α-MEM medium containing 10% fetal bovine serum and 1% penicillin/streptomycin to obtain the bone marrow. Afterwards, the bone marrow was cultured in a cell culture incubator (37°C, 5% CO_2) for 36 h and then rinsed with phosphate buffer solution (PBS). The fresh culture medium was added and refreshed every 2 days. Finally, when being fused to 90%, the cells were digested with .25% trypsin and passaged 1:3. BMMSCs at passages 1–3 were utilized in our study.

2.6 Cell adhesion, proliferation, spreading, and distribution

Taking TCPS as control, the adhesion and proliferation of BMMSCs on PCL and PCL-PDA were determined by CCK-8 assay. Briefly, the various samples were placed in a 24-well plate and sterilized by UV irradiation. BMMSCs seeded onto different samples at a density of 2 × $10^4/cm^2$ and the culture medium was changed every 2 days. After incubation for 1 day, 3 days, 7 days, and 10 days, CCK-8 reagent was added to the basal α-MEM medium at a ratio of 1:10 (v/v), and then added to the culture wells for another 1 h

TABLE 1 Primers used for quantitative RT-PCR.

Gene	Forward primer (5′–3′)	Reverse primer (5′–3′)
GAPDH	GTTACCAGGGCTGCCTTCTC	GATGGTGATGGGTTT CCCGT
OCN	TGGCACCACCGTTTAGGGCA	TTTGGAGCAGCTGTG CCGTC
OPN	AACCGCACCCACAACCGAGT	ACCGTGTTTCGCTCT GGGGT
LPL	ATGGCACAGTGGCTGAAAGT	CCGGCTTTCACTCGGATCTT
C/EBPα	GACCATCCGCCTTGTGTGTA	CTGACATTGCACAAG GCACC
Nanog	CCGTGTTGGCTGCATTTGTC	ACCTGGGGGAGGATA GAGTG
Sox-2	AGAACTAGACTCCGGGCGAT	ACCCAGCAAGAACCC TTTCC
N-Cadherin	GTATGGATGAAACGCCGGGA	TTGTGGCTCAGCGTG GATAG

of incubation. Finally, the absorption of each group at 450 nm was measured by a microplate reader (BL340, Biotech, United States).

Fluorescent staining was utilized to characterize the morphology and distribution of cells on different samples. In detail, BMMSCs were cultured on the PCL and PCL-PDA for 1 day and 7 days, fixed with 4% paraformaldehyde and then successively stained with Alexa Fluor™ 488 Phalloidin and Hoechst 33,258. Subsequently, the stained cells were observed under a confocal laser scan microscope (A1, Nikon, Japan) at 408 nm and 488 nm.

2.7 Immunofluorescent staining for multipotency and cell-cell interaction

After 14 days of incubation, BMMSCs on different samples were fixed with 4% polyparaformaldehyde for 15 min. After permeation with .1% Triton X-100 for 5 min, the cells were blocked with 10% normal goat serum, separately incubated with the primary anti-Nanog antibody (1:200) and primary anti-N-cadherin antibody (1:400) for 2 h at 37°C, and then the second antibody Alexa Fluor 561-conjugated AffiniPure Goat Anti-Rabbit IgG (H + L) (1:500) and Alexa Fluor 488-conjugated AffiniPure Goat Anti-Rabbit IgG (H + L) (1:500) were correspondingly added into each well for another 1 h of incubation at 37°C. Finally, the nuclei of BMMSCs were stained with Hoechst 33,258, and cells were observed under a confocal laser scan microscope (A1, Nikon, Japan) at 408 nm, 488 nm, and 561 nm.

2.8 Induced differentiation and staining

BMMSCs were cultured on different samples for 14 days. Afterwards, the cells were resuspended and seeded onto the 24-well plates at a density of $2 \times 10^4/cm^2$. When being fused to 80%, the cells were further subjected to osteogenic induction by using the basic culture medium added with 10 mM β-glycerophosphate, 50 μM ascorbic acid, and .1 μM dexamethasone (Wu et al., 2021; Xie et al., 2021). After 14 days of osteogenic induction, the cells were fixed with 4% paraformaldehyde and then stained with Alizarin Red S solution (.1% w/v) for 30 min. Adipogenic induction of BMMSCs was implemented by adding 1 μM dexamethasone, 10 mg/L insulin, .5 mM isobutyl-1-methylxanthine and .2 mM indomethacin to the basic medium for cell culture (Sekiya et al., 2004). After 7 days of adipogenic induction, the cells were fixed and stained with Red Oil O solution (6 mg/ml in the mixture of isopropoyl alcohol and H_2O (3: 2, v/v)) for 30 min. Finally, all the stained samples were observed by light microscopy (IX71, Olympus, Japan).

2.9 Quantitative real time-polymerase chain reaction (RT-PCR)

To investigate the multipotency and induced differentiation, BMMSCs were cultured on different samples for 14 days, and then total RNA was extracted using the Trizol reagent according to the manufacturer's protocol. Reverse transcription was performed using Life ECO TC-96 (BIOER, China) and quantitative RT-PCR was performed on the CFX 96 RT-PCR system (Bio-Rad, United States) using a mixture of SYBR Green Realtime PCR Master Mix, cDNA in each group, as well as forward and reverse primers listed in Table 1. The expression of various genes was normalized to the housekeeping gene glyceraldehyde-3-phosphate dehydrogenase (GAPDH).

2.10 Statistical analysis

All the biological experiments were performed at least in triplicate ($n \geq 3$) and each biological experiment was repeated at least three times ($N \geq 3$). The results were presented as mean ± standard deviation. The normality test was performed with SPSS software and the Student's *t*-test was performed to determine the levels of statistical significance between different groups. * Denotes $p < .05$, ** denotes $p < .01$ and *** denotes $p < .001$. A difference of $p < .05$ was considered to be significant and that of $p < .01$ was considered to be highly significant.

3 Results and discussion

3.1 Preparation of PCL nanoneedle arrays and PDA decoration

Straight-chain PCL, which is a synthetic polymer with excellent biocompatibility, is utilized in this study. PCL has been approved by Food and Drug Administration and widely used in tissue engineering (Woodruff and Hutmacher, 2010). As a typical semi-crystalline polymer, PCL can form regular spherical crystalline structures with radii up to 500 microns by autologous crystallization and can be used to obtain a variety of specific microstructure by epitaxial crystallization (Wittmann and Paul, 1991; Toda et al., 2012). Therefore, PCL nanoneedle microcrystal arrays with uniform distribution can be fabricated by controlling the process of autologous crystallization.

To our knowledge, the molecular weight of polymer, crystallization mode and crystallization temperature are decisive to the crystallization process and hence can influence the fabricated structures (Zhang et al., 2016). Generally speaking, the higher the molecular weight is, the longer the polymer chains are, and the longer duration it will take to achieve regular alignment (Wurm et al., 2012).

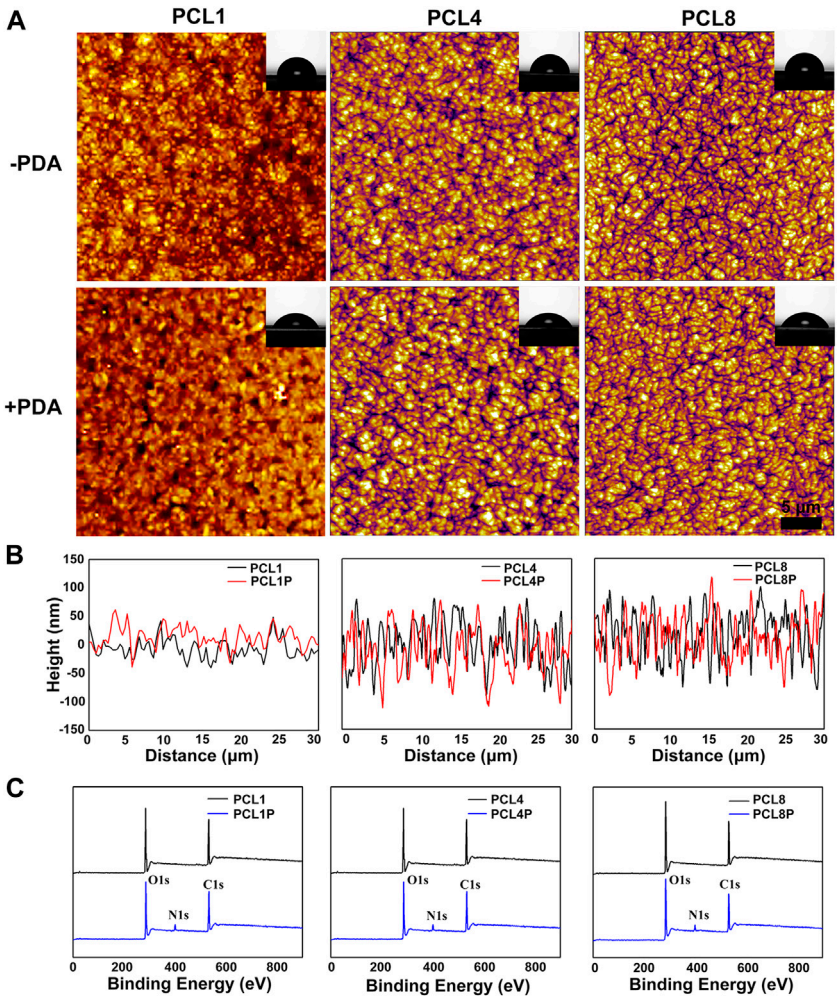

FIGURE 1
Characterization of nanoneedle arrays. **(A)** AFM images of nanoneedle arrays, the inset images show the corresponding water contact angles. **(B)** The height of nanoneedle arrays. **(C)** Survey XPS spectra determined on different samples.

In this regard, three different kinds of PCL samples with number average molecular weight of 10,000 (PCL1), 40,000 (PCL4) and 80,000 (CPL8) respectively are chosen for the following study.

In addition, the higher the crystallization temperature is, the faster the polymer chains move and the shorter time it needs to form crystals (Phillipson et al., 2015). Since the glass transition temperature of PCL is −60°C, the crystallization rate of PCL at room temperature is too fast to form spherical crystals or ring-banded spherical crystals of large size eventually. Hence, crystallization temperature of PCL should be decreased to slow down its crystallization rate. As shown in schematic diagram 1, the PCL films were firstly obtained by the drop addition method, then the thermal history was eliminated by heat treatment at 80°C (20°C above the melting point of PCL) for 15 min. To slow down the crystallization rate of PCL as much as possible, the PCL films were rapidly transferred to liquid nitrogen (−186°C) atmosphere, in which the ambient temperature would gradually increase with the volatilization of liquid nitrogen.

As shown in Figure 1A, nanoneedle arrays of PCL could be successfully fabricated according to our protocol, and the width of nanoneedles did not change significantly with the increase of molecular weight. On the other hand, the average height of nanoneedles could be increased from 50 nm to 80 nm or even 100 nm by changing the number average molecular weight of PCL from 10,000 to 80,000 (Figure 1B). This is probably because the increase of molecular weight and the growth of molecular chains may lead to the increase in molecular chain folding space, so the height of crystalline nanoneedles increases. In the meantime, there is no significant difference in the width of crystalline nanoneedles because the nucleation rate of PCL with different molecular weight is similar.

In addition to the construction of micro/nanostructures, surface chemical modification was further performed in this study using a classical strategy of dopamine polymerization. In particular, a large number of catechol groups could be introduced onto the nanoneedle arrays of PCL by the rapid and spontaneous polymerization of dopamine under alkaline and aerobic conditions (Liu et al., 2014). Consequently, the introduced catechol groups could significantly improve the surface hydrophilicity of PCL substrates (Lee et al., 2007). As shown in Figure 1C, the appearance of the characteristic peak of N element at ~400 eV indicated the successful chemical modification of PCL *via* dopamine polymerization. Furthermore,

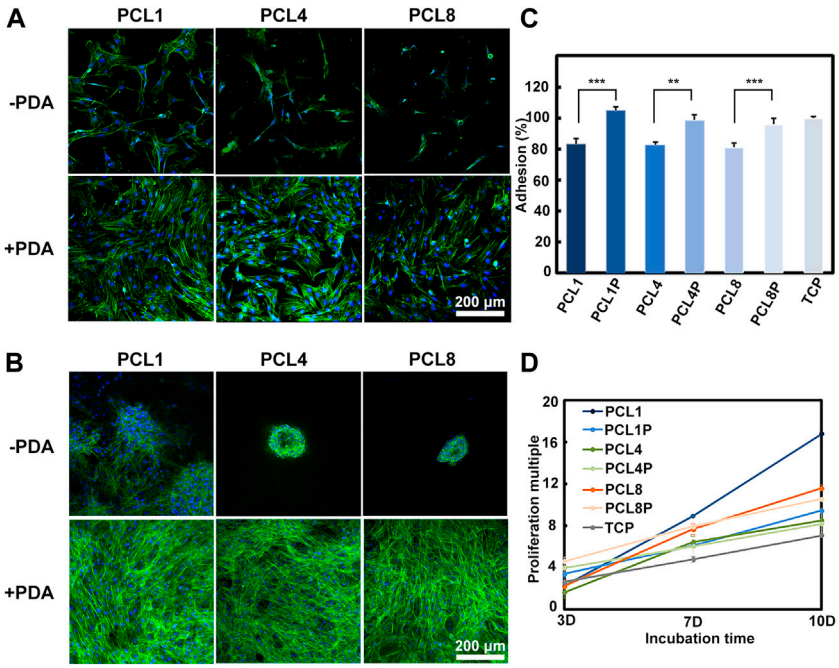

FIGURE 2
Behaviors of BMMSCs cultured on different substrates. **(A)** The fluorescent images of BMMSCs cultured on different substrates for 1 day and **(B)** 7 days (green: Actin; blue: Nuclear) (n = 3). **(C)** CCK-8 assay of BMMSCs cultured on samples for 1 day (n = 4). **(D)** The proliferation of MSCs on different substrates for up to 10 days (n = 4).

the water contact angle of PCL1, PCL4, and PCL8 are 83.48° ± 1.37°, 84.17° ± .77°, and 87.49° ± 1.52°, which could be respectively reduced to 59.49° ± .55° (PCL1-PDA), 62.81° ± .33° (PCL4-PDA) and 65.29° ± 1.20° (PCL8-PDA) after PDA decoration. At the same time, the thin coatings of polydopamine did not significantly change the topography of nanoneedle arrays (Figure 1A). Therefore, we could successfully fabricate nanoneedle crystalline arrays by regulating the crystallization process of PCL, with the height of crystalline nanoneedles ranging from 50 nm to 100 nm. The surface chemical states of nanoneedle arrays were also tunable by subsequent modification with PDA, which could avoid the obvious changes in surface topography.

3.2 Adhesion, spreading, distribution, and proliferation ability of BMMSCs on different substrates

With the rapid development of material biology, numerous studies have revealed that the behaviors and functions of stem cells can be readily regulated by the chemical and topographic features of culture substrates through contact guidance effect (Nguyen et al., 2016). Therefore, the adhesion, spreading, distribution and proliferation of BMMSCs on different substrates were systematically investigated.

It is well recognized that the primary adhesion and subsequent spreading are the initial two steps of cells in contact with substrates, which depends on the physicochemical-biological properties of the substrates (Martino et al., 2018). As shown in Figures 2A, C, BMMSCs could adhere on different substrates after 24 h of cell culture, but the cell number and spreading area were different. The adhesion number of BMMSCs in the pure PCL groups (PCL1, PCL4, PCL8) was about 80% of that on TCP, and the spreading area decreased with an increase of the height of nanoneedle arrays. In contrast, the adhesion number and spreading area of BMMSCs in the PCL + PDA groups (PCL1P, PCL4P, PCL8P) were comparable to that of TCP. This is because PDA is abundant with the catechol groups, which can increase the surface hydrophilicity of PCL substrates (Liu et al., 2014). Moreover, the introduction of polar groups such as hydroxyl groups after PDA modification can increase the adsorption of proteins from culture medium onto the substrates, which is beneficial to cell adhesion spreading (Liu et al., 2016).

With the increase of culture time to 7 days, as shown in Figure 2B, agglomerative growth of BMMSCs could be observed in the pure PCL groups, which was accompanied by reduced actin expression and a decrease in BMMSCs size. Additionally, the agglomerative size decreased with the increase of nanoneedle height. In contrast, the cells cultured on the PDA-modified substrates showed similar laminar growth as those cultured on TCP, and there were no significant changes with the increase of nanoneedle height. Our results demonstrated that the hydrophilicity of substrates is crucial for the different growth modes of stem cells in long-term culture.

The proliferation ability is the basic function requirement of MSCs when they are used for tissue engineering. However, the telomeres length of MSCs would reduce during the traditional culture and passage *in vitro*, causing the decrease and even loss of proliferation ability (Trivanovic et al., 2015). So it is important to investigate whether our substrates could maintain the proliferation activity of MSCs *in vitro* or not. As shown in Figure 2D, with the increase of cell

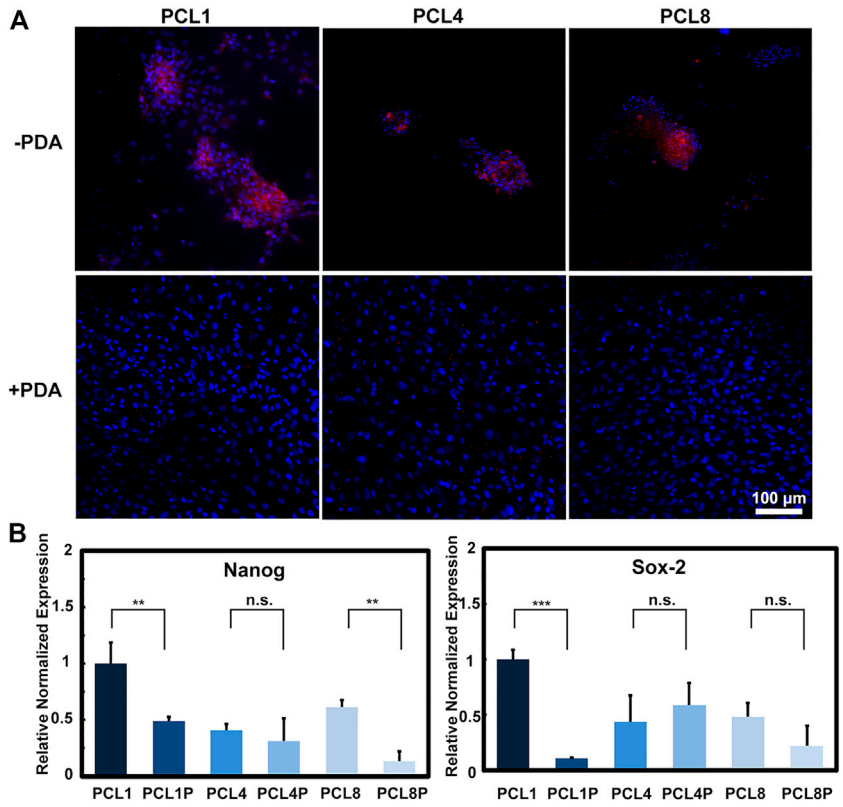

FIGURE 3
The multipotency of BMMSCs after being cultured on different substrates for 14 days. **(A)** Immunofluorescence staining of Nanog protein (red: Nanog, blue: Nuclear) (n = 3) and **(B)** gene expressions of Nanog and Sox-2 of the cultured cells (n = 4).

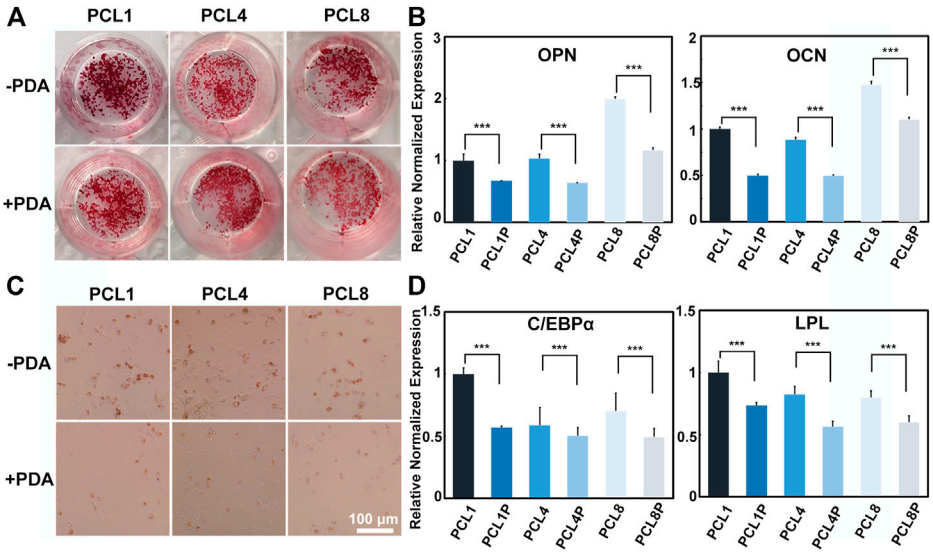

FIGURE 4
Induced differentiation of BMMSCs after being cultured on different substrates. **(A)** Alizarin Red S staining and **(B)** osteogenesis-related gene expressions of the cells after osteogenic induction for 14 days; **(C)** Red Oil O staining and **(D)** adipogenesis-related gene expressions of the cells after adipogenic induction for 7 days (n = 4).

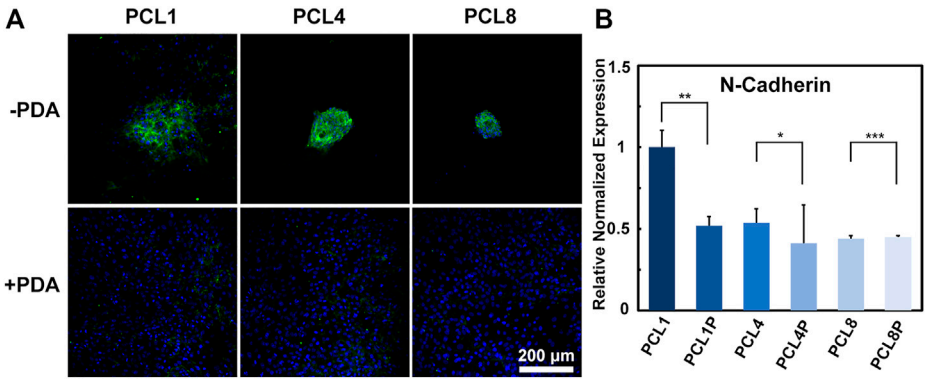

FIGURE 5
Cell-cell interaction of BMMSCs cultured on different substrates for 14 days. **(A)** Immunofluorescence staining for N-Cadherin protein (green: N-Cadherin; blue: Nuclear) (n = 3) and **(B)** gene expressions of N-Cadherin of the cultured cells (n = 4).

culture time, BMMSCs could proliferate on all substrates. Noteworthily, the proliferation rate of BMMSCs on PCL1 was significantly higher than on the other substrates, indicating that this substrate was the most favorable for the proliferation of BMMSCs *in vitro*.

Taken together, we could regulate the adhesion, spreading, distribution and proliferation behaviors of BMMSCs by changing the topographical and chemical properties of culture substrates. A three-dimensional clustered growth of BMMSCs could be achieve on the pure PCL substrates, which was similar to the three-dimensional culture of cells in matrigel. Most importantly, our results demonstrated that the nanoneedle arrays with a height of 50 nm obtained from PCL1 were more preferable than the others for facilitating the proliferation of BMMSCs *in vitro*.

3.3 Multipotency of BMMSCs on different substrates

In our research, BMMSCs cultured on the pure PCL nanoneedle arrays also grew in clustered aggregates, which was similar to the three-dimensional culture of cells in three-dimensional scaffolds and commercial Matrigel (Tavassoli et al., 2018). Hence, we further investigated the multipotency of BMMSCs cultured on PCL nanoneedle arrays and compared them with the PCL-PDA groups.

As is well known, Nanog and Sox-2 are pluripotent transcription factors, which can be used to evaluate the differentiation potentials of stem cells including BMMSCs (Hoch and Leach, 2014; Yoon et al., 2014). Therefore, BMMSCs were cultured on PCL and PCL-PDA for 14 days, and then examined for the expression of Nanog protein using immunofluorescence staining and quantitatively analyzed for the gene expression of Nanog and Sox-2 using quantitative RT-PCR. As shown in Figure 3A, clustered cells could be observed on the pure PCL nanoneedle arrays, which showed relatively higher expression of Nanog protein than the laminar distributed cells cultured on PCL-PDA. Figure 3B revealed that the gene expressions of Nanog and Sox-2 showed a similar trend as the Nanog protein levels detected in different groups, of which the BMMSCs cultured on the pure PCL nanoneedle array of 50 nm high (PCL1) showed the highest expressions of multipotential markers.

Multipotency also refers to the capacity of stem cells differentiating into particular cell types. As for BMMSCs, the capability of osteogenic and adipogenic differentiation are representative of the multipotency (Jiang et al., 2002). Hence, we further analyzed the induced differentiation ability of BMMSCs cultured on different substrates. After being cultured on PCL and PCL-PDA for 14 days with a basal culture medium, the cells were resuspended into a 24-well plate and induced with the osteogenic culture medium and adipogenic culture medium respectively.

After osteogenic induction for 14 days, the osteogenic differentiation of BMMSCs was determined by Alizarin Red S staining and quantitative RT-PCR. During the process of osteogenic differentiation, BMMSCs would secrete calcium and deposit it around the cells to form calcified nodules, and the amount and size of calcified nodules increase with the maturation of osteoblasts. As shown in Figure 4A, the number and size of calcified nodules formed by cells harvested from the pure PCL nanoneedle arrays were larger than those detected in the PCL-PDA groups, indicating that the clustered cells grown on PCL provided better capacity of osteogenic differentiation. By comparing PCL nanoneedle arrays with different heights, we found that the cells harvested from the nanoneedle array with a height of 50 nm showed the best capacity of *in vitro* mineralization. At the same time point, quantitative RT-PCR was also performed to analyze the gene expressions of osteopontin (OPN) and osteocalcin (OCN) as they are typical biomarkers of osteogenic differentiation (Tong et al., 2019; Mo et al., 2021; Chen et al., 2022). As shown in Figure 4B, the cells cultured on the pure PCL nanoneedle arrays exhibited the higher expression of osteogenesis-related gene than the PCL-PDA groups. Both the Alizarin Red S staining and quantitative RT-PCR results showed that the BMMSCs cultured on all groups, especially the pure PCL nanoneedle array with a height of 50 nm (PCL1) and 100 nm (PCL8), provided relatively high capacity of osteogenic differentiation.

As for adipogenic differentiation, the resuspended cells were incubated with the adipogenic culture medium for 7 days, and then determined by Oil Red O staining and quantitative RT-PCR. By inducing the differentiation of stem cells to adipocytes, lipid droplets would form, increase and then fuse to larger-sized droplets with the development of adipocyte maturity (Ntambi and Kim, 2000). As shown in Figure 4C, the lipid droplets formed by cells harvested

from the pure PCL nanoneedle arrays were more mature than those detected in the PCL-PDA groups. Further analysis by quantitative RT-PCR in Figure 4D showed that the adipogenesis-related gene expressions of cells harvested from the pure PCL nanoneedle arrays were higher than their PDA-modified counterparts, indicating that the cells expanded on PCL substrates provided the better capability of adipogenic differentiation than those in PCL-PDA groups. Noteworthily, the cells harvested from the pure PCL nanoneedle array with a height of 50 nm (PCL1) exhibited the highest expression of CCAAT/enhancer binding proteins α (C/EBPα) and LipoProtein Lipase (LPL). It means that this kind of PCL nanoneedle array is likely better than others for maintaining the adipogenic differentiation ability of cultured cells.

The above results showed that the pure PCL nanoneedle arrays were more favorable than their PDA-modified counterparts for maintaining the multipotency of BMMSCs during *in vitro* expansion. Especially, BMMSCs harvested from the pure PCL nanoneedle array with a height of 50 nm (PCL1) could provide the best performances of multidirectional differentiation.

3.4 Cell-cell interaction of BMMSCs on different substrates

On one hand, cells can sense the extracellular matrix through integrin etc. and achieve a response to the extracellular matrix through cell-substrate interactions. On the other hand, cells can also interact with each other by direct communication with neighboring cells through desmosomes, gap junctions and tight junctions (Belardi et al., 2020). In the present study, the fabricated pure PCL nanoneedle arrays could achieve aggregated growth of the cultured BMMSCs, but the further modification of PCL nanoneedle arrays with PDA resulted in a typical laminar distribution of cultured cells, eventually compromising the multipotency of stem cells during *in vitro* expansion. Probably, the changes in cell functions might be related to cell-cell interaction. Hence, after culturing BMMSCs on different samples for 14 days, we further investigated the expression of N-cadherin (a specific marker of cell-cell adhesion) by immunofluorescence staining and quantitative RT-PCR (Cosgrove et al., 2016). As shown in Figure 5A, the expression of N-Cadherin was significantly higher in agglomerated-grown BMMSCs of the pure PCL groups than that in laminar-grown cells of the PCL-PDA groups. Further combined with the quantitative RT-PCR results shown in Figure 5B, we found that the pure PCL nanoneedle array with a height of 50 nm (PCL1), could not only support the highest proliferation ability while maintaining the multipotency of cultured cells, but also provide the strongest cell-cell interactions among the different substrates Scheme 1.

4 Conclusion

In summary, our study demonstrates a feasible strategy for the *in vitro* expansion of MSCs without compromising their multipotency. In particular, PCL nanoneedle arrays can be fabricated by regulating temperature of autologous crystallization process, and utilized as the substrates for the *in vitro* expansion of MSCs. Furthermore, the height of PCL nanoneedle arrays is tunable, and the PCL1 nanoneedle array of 50 nm high is more promising than the others with regard to the highest proliferation rate and best multipotential differentiation ability of cultured cells. Although the further decoration of PDA can improve the adhesion and spreading of cultured cells, it also changes the cells from aggregated distribution to laminar distribution, which will weaken the strength of cell-cell interaction and compromises the multipotency of cells eventually. Our study not only broadens the application of polymer crystals, but also provides a theoretical basis and experimental guidance for the *in vitro* regulation of MSCs, and makes the tissue engineering using multipotential MSCs more feasible.

Data availability statement

The original contributions presented in the study are included in the article/supplementary material, further inquiries can be directed to the corresponding authors.

Author contributions

Conceptualization: XR and HW; Methodology: XR, XG, and HW; Investigation: XR, YC, LX, and WL; Funding acquisition: YC, WL, LT, and HW; Supervision: HW; Writing—original draft: XR and XG; Writing—review and editing: PC and HW.

Funding

The authors acknowledge financial support from the National Key R&D Program of China (No. 2021YFB3800800), National Natural Science Foundation of China (Nos. 31922040, 81901046, 81903057, and 32000962), Shenzhen Science and Technology Research Funding (Nos. JCYJ20180507182637685, JCYJ20190806165616542, and JSGG20200225152648408), Youth Innovation Promotion Association of Chinese Academy of Sciences (No. 2020353) as well as Guangdong Basic and Applied Basic Research Foundation (No. 2020B1515120078).

Conflict of interest

The authors declare that the research was conducted in the absence of any commercial or financial relationships that could be construed as a potential conflict of interest.

Publisher's note

References

Belardi, B., Son, S., Felce, J. H., Dustin, M. L., and Fletcher, D. A. (2020). Cell-cell interfaces as specialized compartments directing cell function. *Nat. Rev. Mol. Cell. Biol.* 21 (12), 750–764. doi:10.1038/s41580-020-00298-7

Chen, J. F., Xie, L. X., Ruan, Q. D., Gao, A., Liao, Q., Mo, S., et al. (2022a). Diamond-like carbon coating and surface grafting of osteoprotegerin and alendronate on polyetheretherketone to ameliorate the mechanical performance and osseointegration simultaneously. *Compos Part B* 236, 109815. doi:10.1016/j.compositesb.2022.109815

Chen, W. Q., Shao, Y., Li, X., Zhao, G., and Fu, J. P. (2014). Nanotopographical surfaces for stem cell fate control: Engineering mechanobiology from the bottom. *Nano Today* 9 (6), 759–784. doi:10.1016/j.nantod.2014.12.002

Chen, X., Huang, J., Wu, J., Hao, J., Fu, B., Wang, Y., et al. (2022b). Human mesenchymal stem cells. *Cell. Prolif.* 55 (4), e13141. doi:10.1111/cpr.13141

Cosgrove, B. D., Mui, K. L., Driscoll, T. P., Caliari, S. R., Mehta, K. D., Assoian, R. K., et al. (2016). N-Cadherin adhesive interactions modulate matrix mechanosensing and fate commitment of mesenchymal stem cells. *Nat. Mater* 15 (12), 1297–1306. doi:10.1038/nmat4725

Crist, B., and Schultz, J. M. (2016). Polymer spherulites: A critical review. *Prog. Polym. Sci.* 56, 1–63. doi:10.1016/j.progpolymsci.2015.11.006

Cun, X., and Hosta-Rigau, L. (2020). Topography: A biophysical approach to direct the fate of mesenchymal stem cells in tissue engineering applications. *Nanomaterials* 10 (10), 2070. doi:10.3390/nano10102070

Friedenstein, A. J., Chailakhjan, R. K., and Lalykina, K. S. (1970). The development of fibroblast colonies in monolayer cultures of guine-pig bone marrow and spleen cells. *Cell. Tissue Kinet.* 3, 393–403. doi:10.1111/j.1365-2184.1970.tb00347.x

Grayson, W. L., Zhao, F., Bunnell, B., and Ma, T. (2007). Hypoxia enhances proliferation and tissue formation of human mesenchymal stem cells. *Biochem. Biophys. Res. Commun.* 358 (3), 948–953. doi:10.1016/j.bbrc.2007.05.054

Hoch, A. I., and Leach, J. K. (2014). Concise review: Optimizing expansion of bone marrow mesenchymal stem/stromal cells for clinical applications. *Stem Cells Transl. Med.* 3 (5), 643–652. doi:10.5966/sctm.2013-0196

Hofmeister, L. H., Costa, L., Balikov, D. A., Crowder, S. W., Terekhov, A., Sung, H. J., et al. (2015). Patterned polymer matrix promotes stemness and cell-cell interaction of adult stem cells. *J. Biol. Eng.* 9, 18. doi:10.1186/s13036-015-0016-x

Jiang, Y., Jahagirda, B., R, R., Schwartz, R. E., Keenek, C. D., Ortiz-Gonzalezk, X. R., et al. (2002). Pluripotency of mesenchymal stem cells derived from adult marrow. *Nature* 484, 41–49. doi:10.1038/nature00870

Khalil, A. S., Xie, A. W., Johnson, H. J., and Murphy, W. L. (2020). Sustained release and protein stabilization reduce the growth factor dosage required for human pluripotent stem cell expansion. *Biomaterials* 248, 120007. doi:10.1016/j.biomaterials.2020.120007

Lee, H., Dellatore, S. M., Miller, W. M., and Messersmith, P. B. (2007). Mussel-inspired surface chemistry for multifunctional coatings. *Science* 318 (5849), 426–430. doi:10.1126/science.1147241

Li, R., Liang, L., Dou, Y., Huang, Z., Mo, H., Wang, Y., et al. (2015). Mechanical stretch inhibits mesenchymal stem cell adipogenic differentiation through tgfβ1/smad2 signaling. *J. Biomech.* 48 (13), 3656–3662. doi:10.1016/j.jbiomech.2015.08.013

Li, W., Lu, L., Jiao, Y., Zhang, C., and Zhou, C. (2016). Poly(L-lactide) crystallization topography directs mc3t3-E1 cells response. *J. Biomater. Sci. Polym. Ed.* 27 (13), 1317–1330. doi:10.1080/09205063.2016.1196530

Li, Y., Xiao, Y., and Liu, C. S. (2017). The horizon of materiobiology: A perspective on material-guided cell behaviors and tissue engineering. *Chem. Rev.* 117 (5), 4376–4421. doi:10.1021/acs.chemrev.6b00654

Liu, M., Zeng, G., Wang, K., Wan, Q., Tao, L., Zhang, X., et al. (2016). Recent developments in polydopamine: An emerging soft matter for surface modification and biomedical applications. *Nanoscale* 8 (38), 16819–16840. doi:10.1039/c5nr09078d

Liu, Y., Ai, K., and Lu, L. (2014). Polydopamine and its derivative materials: Synthesis and promising applications in energy, environmental, and biomedical fields. *Chem. Rev.* 114 (9), 5057–5115. doi:10.1021/cr400407a

Martino, F., Perestrelo, A. R., Vinarsky, V., Pagliari, S., and Forte, G. (2018). Cellular mechanotransduction: From tension to function. *Front. Physiol.* 9, 824. doi:10.3389/fphys.2018.00824

McKee, C., and Chaudhry, G. R. (2017). Advances and challenges in stem cell culture. *Colloids Surf. B Biointerfaces* 159, 62–77. doi:10.1016/j.colsurfb.2017.07.051

McMurray, R. J., Gadegaard, N., Tsimbouri, P. M., Burgess, K. V., McNamara, L. E., Tare, R., et al. (2011). Nanoscale surfaces for the long-term maintenance of mesenchymal stem cell phenotype and multipotency. *Nat. Mater* 10 (8), 637–644. doi:10.1038/nmat3058

Mo, S., Zhao, F. L., Gao, A., Wu, Y. Z., Liao, Q., Xie, L. X., et al. (2021). Simultaneous application of diamond-like carbon coating and surface amination on polyether ether ketone: Towards superior mechanical performance and osseointegration. *Smart Mater Med.* 2, 219–228. doi:10.1016/j.smaim.2021.07.004

Najar, M., Melki, R., Khalife, F., Lagneaux, L., Bouhtit, F., Moussa Agha, D., et al. (2021). Therapeutic mesenchymal stem/stromal cells: Value, challenges and optimization. *Front. Cell. Dev. Biol.* 9, 716853. doi:10.3389/fcell.2021.716853

Nguyen, A. T., Sathe, S. R., and Yim, E. K. (2016). From nano to micro: Topographical scale and its impact on cell adhesion, morphology and contact guidance. *J. Phys. Condens Matter* 28 (18), 183001. doi:10.1088/0953-8984/28/18/183001

Ntambi, J. M., and Kim, Y. C. (2000). Adipocyte differentiation and gene expression. *J. Nutr.* 130 (12), 3122S–3126S. doi:10.1093/jn/130.12.3122S

Phillipson, K., Jenkins, M. J., and Hay, J. N. (2015). The kinetics of crystallization of poly(ε-caprolactone) measured by FTIR spectroscopy. *J. Therm. Anal. Calorim.* 123 (2), 1491–1500. doi:10.1007/s10973-015-5047-5

Pricola, K. L., Kuhn, N. Z., Haleem-Smith, H., Song, Y., and Tuan, R. S. (2009). Interleukin-6 maintains bone marrow-derived mesenchymal stem cell stemness by an ERK1/2-dependent mechanism. *J. Cell. Biochem.* 108 (3), 577–588. doi:10.1002/jcb.22289

Rawat, S., Dadhwal, V., and Mohanty, S. (2021). Dexamethasone priming enhances stemness and immunomodulatory property of tissue-specific human mesenchymal stem cells. *BMC Dev. Biol.* 21 (1), 16. doi:10.1186/s12861-021-00246-4

Ren, X. X., Jiang, S. D., Wu, M., Shi, H. G., Tian, Y., and Niu, Z. W. (2019). Phenotype regulation of smooth muscle cells through facial crystallization of poly(ε-caprolactone). *J. Nanosci. Nanotechnol.* 19 (4), 2269–2275. doi:10.1166/jnn.2019.15763

Rico, P., Mnatsakanyan, H., Dalby, M. J., and Salmerón-Sánchez, M. (2016). Material-driven fibronectin assembly promotes maintenance of mesenchymal stem cell phenotypes. *Adv. Funct. Mater* 26 (36), 6563–6573. doi:10.1002/adfm.201602333

Samal, J. R. K., Rangasami, V. K., Samanta, S., Varghese, O. P., and Oommen, O. P. (2021). Discrepancies on the role of oxygen gradient and culture condition on mesenchymal stem cell fate. *Adv. Healthc. Mater* 10 (6), e2002058. doi:10.1002/adhm.202002058

Sekiya, I., Larson, B. L., Vuoristo, J. T., Cui, J. G., and Prockop, D. J. (2004). Adipogenic differentiation of human adult stem cells from bone marrow stroma (MSCs). *J. Bone Min. Res.* 19 (2), 256–264. doi:10.1359/JBMR.0301220

Tavakoli, S., Ghaderi Jafarbeigloo, H. R., Shariati, A., Jahangiryan, A., Jadidi, F., Jadidi Kouhbanani, M. A., et al. (2020). Mesenchymal stromal cells; A new horizon in regenerative medicine. *J. Cell. Physiol.* 235 (12), 9185–9210. doi:10.1002/jcp.29803

Tavassoli, H., Alhosseini, S. N., Tay, A., Chan, P. P. Y., Weng Oh, S. K., and Warkiani, M. E. (2018). Large-scale production of stem cells utilizing microcarriers: A biomaterials engineering perspective from academic research to commercialized products. *Biomaterials* 181, 333–346. doi:10.1016/j.biomaterials.2018.07.016

Toda, A., Taguchi, K., and Kajioka, H. (2012). Growth of banded spherulites of poly(ϵ-caprolactone) from the blends: An examination of the modeling of spherulitic growth. *Polymer* 53 (8), 1765–1771. doi:10.1016/j.polymer.2012.02.030

Tong, L. P., Liao, Q., Zhao, Y. T., Huang, H., Gao, A., Zhang, W., et al. (2019). Near-infrared light control of bone regeneration with biodegradable photothermal osteoimplant. *Biomaterials* 193, 1–11. doi:10.1016/j.biomaterials.2018.12.008

Trivanovic, D., Jaukovic, A., Popovic, B., Krstic, J., Mojsilovic, S., Okic-Djordjevic, I., et al. (2015). Mesenchymal stem cells of different origin: Comparative evaluation of proliferative capacity, telomere length and pluripotency marker expression. *Life Sci.* 141, 61–73. doi:10.1016/j.lfs.2015.09.019

Wang, K., Cai, L., Jesse, S., and Wang, S. (2012). Poly(ε-caprolactone)-Banded spherulites and interaction with mc3t3-E1 cells. *Langmuir* 28 (9), 4382–4395. doi:10.1021/la205162d

Wittmann, J. C., and Paul, S. (1991). Highly oriented thin films of poly(tetrafluoroethylene) as a substrate for oriented growth of materials. *Nature* 352, 414–417. doi:10.1038/352414a0

Woodruff, M. A., and Hutmacher, D. W. (2010). The return of A forgotten polymer—polycaprolactone in the 21st century. *Prog. Polym. Sci.* 35 (10), 1217–1256. doi:10.1016/j.progpolymsci.2010.04.002

Wu, Y. Z., Liao, Q., Wu, L., Luo, Y. X., Zhang, W., Guan, M., et al. (2021). ZnL2-BPs integrated bone scaffold under sequential photothermal mediation: A win-win strategy delivering antibacterial therapy and fostering osteogenesis thereafter. *ACS Nano* 15 (11), 17854–17869. doi:10.1021/acsnano.1c06062

Wurm, A., Zhuravlev, E., Eckstein, K., Jehnichen, D., Pospiech, D., Androsch, R., et al. (2012). Crystallization and homogeneous nucleation kinetics of poly(ε-caprolactone) (PCL) with different molar masses. *Macromolecules* 45 (9), 3816–3828. doi:10.1021/ma300363b

Xie, L. X., Wang, G. M., Wu, Y. Z., Liao, Q., Mo, S., Ren, X. X., et al. (2021). Programmed surface on poly(aryl-ether-ether-ketone) initiating immune mediation and fulfilling bone regeneration sequentially. *Innov. (Camb)* 2 (3), 100148. doi:10.1016/j.xinn.2021.100148

Yoon, D. S., Choi, Y., Jang, Y., Lee, M., Choi, W. J., Kim, S. H., et al. (2014). SIRT1 directly regulates SOX2 to maintain self-renewal and multipotency in bone marrow-derived mesenchymal stem cells. *Stem cells* 32, 3219–3231. doi:10.1002/stem.1811

Zhang, M., Guo, B. H., and Xu, J. (2016). A review on polymer crystallization theories. *Crystals* 7 (1), 4. doi:10.3390/cryst7010004

frontiers | Frontiers in Bioengineering and Biotechnology

TYPE Original Research
PUBLISHED 10 January 2023
DOI 10.3389/fbioe.2022.1075715

OPEN ACCESS

EDITED BY
Lifeng Kang,
The University of Sydney, Australia

REVIEWED BY
Giovanni Vozzi,
University of Pisa, Italy
Gina Lisignoli,
Rizzoli Orthopedic Institute (IRCCS), Italy
Pu Chen,
Wuhan University, China

*CORRESPONDENCE
Giovanna Della Porta,
gdellaporta@unisa.it

SPECIALTY SECTION
This article was submitted to Biomaterials, a section of the journal Frontiers in Bioengineering and Biotechnology

RECEIVED 20 October 2022
ACCEPTED 28 December 2022
PUBLISHED 10 January 2023

CITATION
Scala P, Manzo P, Lamparelli EP, Lovecchio J, Ciardulli MC, Giudice V, Selleri C, Giordano E, Rehak L, Maffulli N and Della Porta G (2023), Peripheral blood mononuclear cells contribute to myogenesis in a 3D bioengineered system of bone marrow mesenchymal stem cells and myoblasts.
Front. Bioeng. Biotechnol. 10:1075715.
doi: 10.3389/fbioe.2022.1075715

Peripheral blood mononuclear cells contribute to myogenesis in a 3D bioengineered system of bone marrow mesenchymal stem cells and myoblasts

Pasqualina Scala[1], Paola Manzo[1,2], Erwin Pavel Lamparelli[1], Joseph Lovecchio[3], Maria Camilla Ciardulli[1], Valentina Giudice[1,2], Carmine Selleri[1,2], Emanuele Giordano[3], Laura Rehak[4], Nicola Maffulli[1,5] and Giovanna Della Porta[1,6]*

[1]Department of Medicine, Surgery and Dentistry, University of Salerno, Baronissi, Italy, [2]Hematology and Transplant Center, University Hospital "San Giovanni di Dio e Ruggi D'Aragona", Salerno, Italy, [3]Department of Electrical, Electronic and Information Engineering "Guglielmo Marconi" (DEI), University of Bologna, Bologna, Italy, [4]Athena Biomedical innovations, Florence, Italy, [5]Centre for Sports and Exercise Medicine, Barts and The London School of Medicine and Dentistry, Queen Mary University of London, London, England, [6]Interdepartment Centre BIONAM, University of Salerno, Fisciano, Italy

In this work, a 3D environment obtained using fibrin scaffold and two cell populations, such as bone marrow-derived mesenchymal stem cells (BM-MSCs), and primary skeletal muscle cells (SkMs), was assembled. Peripheral blood mononuclear cells (PBMCs) fraction obtained after blood filtration with HemaTrate® filter was then added to the 3D culture system to explore their influence on myogenesis. The best cell ratio into a 3D fibrin hydrogel was 1:1 (BM-MSCs plus SkMs:PBMCs) when cultured in a perfusion bioreactor; indeed, excellent viability and myogenic event induction were observed. Myogenic genes were significantly overexpressed when cultured with PBMCs, such as *MyoD1* of 118-fold at day 14 and *Desmin* 6-fold at day 21. Desmin and Myosin Heavy Chain were also detected at protein level by immunostaining along the culture. Moreover, the presence of PBMCs in 3D culture induced a significant downregulation of pro-inflammatory cytokine gene expression, such as *IL6*. This smart biomimetic environment can be an excellent tool for investigation of cellular crosstalk and PBMC influence on myogenic processes.

KEYWORDS

myogenesis, tissue engineering, mesenchymal stem cells, peripheral blood mononuclear cells, 3D Co-culture model

1 Introduction

In vitro skeletal muscle regeneration (SkMR) models are extremely challenging to reproduce because resident satellite cells (SCs) - that mediate the entire process *in vivo*-are very difficult to harvest from muscle tissue, and lose their engraftment potential in *ex vivo* conditions with progressive growth rate reduction (Montarras et al., 2005; Kuang et al., 2007; Charville et al., 2015; Garcia et al., 2017). Bone marrow-derived mesenchymal stem cells (BM-MSCs) represent the gold standard for musculoskeletal regeneration study and research (Ciardulli et al., 2020; Ciardulli et al., 2021; Lamparelli et al., 2021). They were also proposed as a promising alternative in SkMR because of their ability to differentiate

towards various lineages, low immunogenicity, and high immunomodulatory activity (Vater et al., 2011; Shi et al., 2018). However, BM-MSCs are still poorly investigated for *in vitro* myogenesis purpose because of the lack of standardized medium composition and appropriate culture system approaches, although BM-MSCs co-cultured with myoblasts show significant upregulation of muscle markers, such as *Myogenic Regulatory Factors* (*MRFs*), *Desmin*, and *Myosin heavy chain II* (*MYH2*) (Beier et al., 2011; Scala et al., 2022).

Myogenesis is also strongly influenced by cytokines secreted by peripheral blood mononuclear cells (PBMCs) involved in tissue regenerative processes, like clearance of necrotic debris, inflammation, and remodeling processes (Scala et al., 2021). Moreover, pro-inflammatory cytokines, including interferon-γ (IFN-γ), tumor necrosis factor (TNF), interleukin (IL)-6 and IL-1, released by PBMCs influence SkMR fate by driving the first phase of repair process and by modulating immune responses and SC activation (Chen et al., 2007; Cheng et al., 2008; Londhe and Davie, 2011; Belizário et al., 2016; Chaweewannakorn et al., 2018). Conversely, anti-inflammatory cytokines, especially IL-10, are associated with the transition from proliferative to differentiation phase of myogenesis (Villalta et al., 2011; Deng et al., 2012). Indirect evidence of the essential role of PBMCs in SkMR is the efficacy of autologous transplantation of peripheral blood cells isolated by commercial blood filtration systems for treatment of critic limb ischemia by increasing regenerated myofibers and by improving clinical outcomes (Spaltro et al., 2015; Rigato et al., 2017).

On the other hand, biomimetic 3D cultures of stem cell represent a versatile tool for the study of myogenic commitment events (Witt et al., 2017; Ergene et al., 2020). Indeed, BM-MSCs are frequently cultured in 3D hydrogel scaffolds, like fibrin hydrogels (Govoni et al., 2017; Ciardulli et al., 2020; 2021; Manzo et al., 2022) that efficiently mimic SC niche (Pollot et al., 2018) and may reproduce *in vitro* the hierarchical structure of skeletal muscle tissue. Moreover, fibrin-based scaffolds constitute a regenerative myogenic environment without fibrosis, as cells produce their own extracellular matrix (ECM) proteins and degraded fibrin excess allowing long-term skeletal muscle cell culture (Huang et al., 2005; Gilbert-Honick et al., 2018; Matthias et al., 2018). When a perfusion bioreactor system is adopted for these 3D *in vitro* cultures, the medium easily diffuses through the 3D structure enhancing metabolite mass transfer, nutrient transport, and oxygenation rate. In addition, 3D perfused cultures show excellent viability, high proliferation rates, and more efficient commitment processes (Grayson et al., 2011; Birru et al., 2018; Pasini et al., 2019; Engel et al., 2021; Lamparelli et al., 2021).

In this study, we aimed to develop an *in vitro* model of myogenic commitment using human BM-MSCs (*h*BM-MSCs) and human primary skeletal myoblasts (*h*SkMs) cultured in 3D dynamic conditions assembled within a fibrin scaffold. Moreover, PBMCs were added within the same 3D co-culture to investigate their activity on *h*BM-MSC myogenic commitment. To our knowledge, 3D *in-vitro* models studying the effects of PBMCs on stem cell commitment has been proposed only in osteogenic events (Gamblin et al., 2014; Tang et al., 2019); whereas, 3D dynamic co-cultures of BM-MSCs and PBMCs applied to SkMR are not reported yet. *h*BM-MSC myogenic events evolution was performed by qRT-PCR and immunohistochemistry, whereas, PMBCs characterization was performed by flow cytometry.

2 Materials and methods

2.1 PBMC concentration and harvesting

PBMCs were collected by HemaTrate® Blood Filtration System, following same protocol of clinical practice in limb rescue (De Angelis et al., 2015; Persiani et al., 2018), Whole peripheral blood (PB) obtained from three healthy volunteers (M/F, 2/1; age ranged from 38 to 45 years old) was concentrated using a HemaTrate® Blood Filtration System (CH-WB110C, Patent n. EP 2602315A1; Pall Medistad B.V. (Medemblik; Netherlands) from Cook Regentec (Indianapolis, Indiana, United States). After filtration, PBMCs were isolated by Ficoll-Paque density gradient centrifugation (Cytiva, Marlborough, Massachusetts, United States), according to manufacturer's instructions, for flow cytometer immunophenotyping. Conversely, filtrated PBMCs were directly used for 3D culture experiments, or were stored in 70% RPMI (Gibco™), 20% Fetal Bovine Serum (FBS, Gibco™), and 10% DMSO (Sigma-Aldrich, Milan, Italy) at -80°C until use.

2.2 *h*BM-MSC isolation, harvesting, and characterization

BM specimens for *h*BM-MSC isolation were obtained from three healthy male donors (aged 26, 24, and 28 years old) after informed written consent in accordance with the Declaration of Helsinki and protocols approved by our Institutional Review Board (Ethic Committee "Campania Sud", Brusciano, Naples, Italy; prot./SCCE n. 24,988). BM aspirate culture was described elsewhere (Giordano et al., 2014). BM-MSCs were subsequently seeded at 4,000 cells/cm^2 and expanded up to the third passage. Mesenchymal phenotype was confirmed according to the International Society of Cellular Therapy guidelines: i) ability to adhere to tissue culture plastics; ii) fibroblast-like spindle shape; and iii) characteristic immunophenotype by flow cytometry with positivity for CD90, CD105, and CD73, and negativity for CD34, CD14, CD45, and HLA-DR (Supplementary Figure S1) (Dominici et al., 2006). *h*BM-MSCs were co-cultured in a 3D system with *h*SkMs, with and without PBMCs. All experiments were performed in biological triplicates (N = 3).

2.3 *h*SkM characterization

*h*SkMs were purchased from (Gibco™). *h*SkMs were embedded in fibrin scaffolds to investigate their behavior in a 3D environment through qRT-PCR, as reported in the following section. Then, *h*SkMs were co-cultured with *h*BM-MSCs with and without PBMCs. Seeding ratio between *h*BM-MSCs:*h*SkMs was 2:1, as previously optimized in (Scala et al., 2022). All experiments were performed in biological triplicates (N = 3).

2.4 Flow cytometry

MSC and PBMC immunophenotype was investigated by flow cytometry. Briefly, for BM-MSCs, a minimum of 1 × 10^5 cells at the third passage was stained with the following antibodies: 2.5 µl of fluorescein isothiocyanate (FITC) - conjugated anti-CD90 or 5 µl of

10.3389/fbioe.2022.1075715

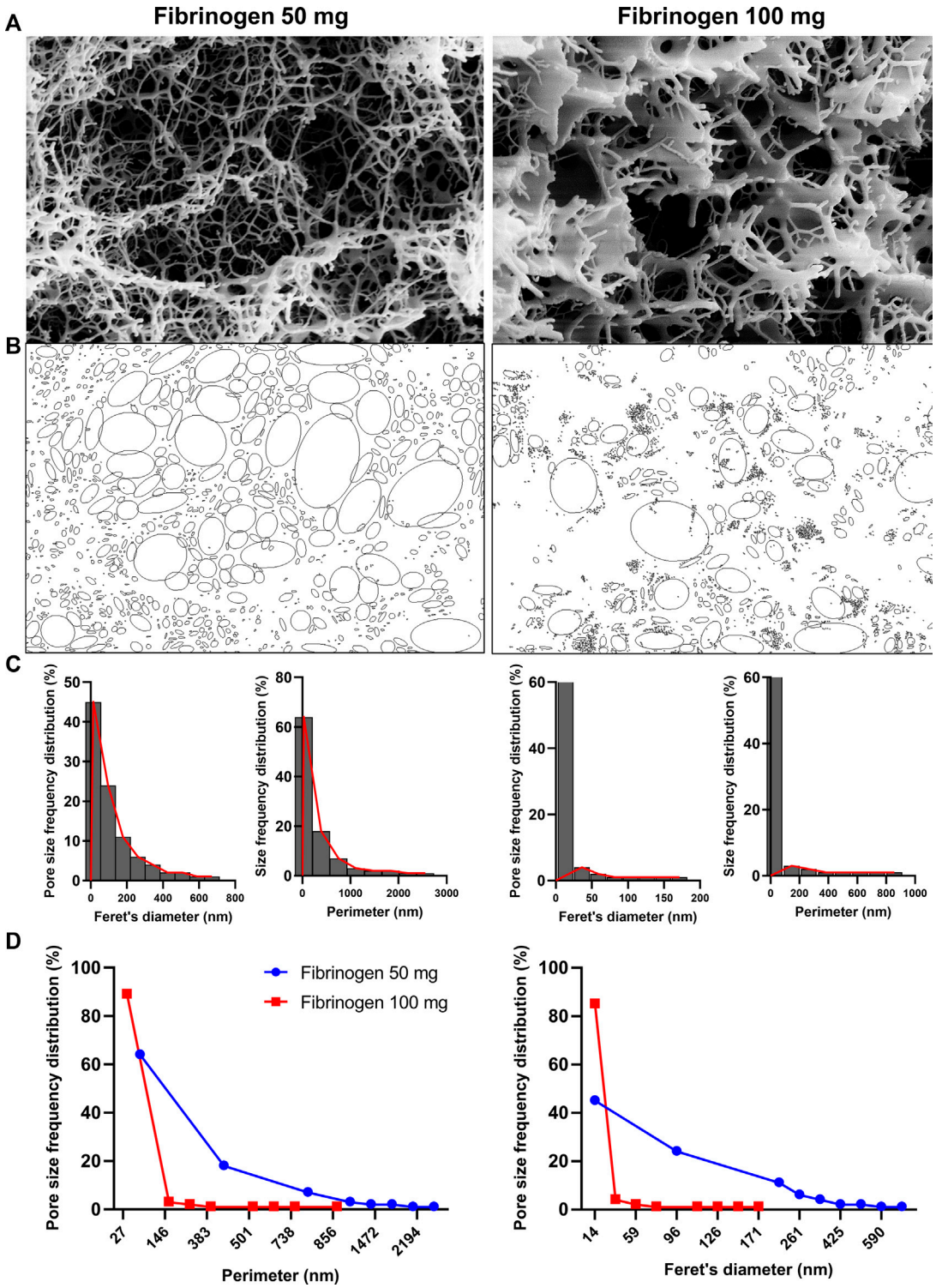

FIGURE 1
Field Emission-Scanning electron microscopy (FE-SEM) images of aerogels and of their internal structure morphology at two tested fibrinogen concentrations, 100 mg/ml and 50 mg/ml scaffolds were dried by dense gas in order to avoid 3D structure shrinkage of aerogel that was clearly observed after scaffold freeze-fracturing in liquid nitrogen **(A);** Perimeter and Feret's diameter values were calculated with ImageJ software, and pores were automatically determined after threshold adjustment in 100 mg/ml and 50 mg/ml fibrinogen scaffolds **(B)**. Size frequency distributions are shown for perimeter and Feret's diameter values in 100 mg/ml and 50 mg/ml fibrinogen scaffolds **(C),** and **(D)** compared between the two concentrations.

FITC - conjugated anti-HLA-DR; 5 µl of allophycocyanin (APC) - conjugated anti-CD73; 10 µl of phycoerythrin (PE) - conjugated anti-CD105 or 10 µl of PE - conjugated anti-CD34; and 10 µl of phycoerythrin cyanin 7 (PC7) - conjugated anti-CD45 or 10 µl of PC7 - conjugated anti-CD14 (all antibodies from Beckman Coulter, Fullerton, CA, United States). Cells were incubated at room

temperature (RT) for 20 min in the dark, washed with phosphate buffered saline (PBS, Gibco™), and resuspended in 300 µl of the same buffer for acquisition. For PBMC immunophenotyping, before and after filter and separation procedures, a minimum of 2×10^5 cells were stained with the following antibodies: 5 µl of APC–conjugated anti-CD3; 5 µl PC7 - conjugated anti-CD14; 5 µl of FITC–conjugated CD34; 5 µl of phycoerythrin cyanin 5 (PC5)—conjugated CD8; and 5 µl of PE - conjugated anti-CD4. Cells were then incubated at RT for 20 min in the dark, washed with PBS and resuspended in 300 µl of the same buffer for acquisition. Sample acquisition was performed on a BD FACSVerse flow cytometer (Becton Dickinson, BD, NJ, United States) equipped with blue (488 nm) and red lasers (628 nm) and BD FACSuite software (BD Biosciences). PMT voltage setting, and compensation were carried out using single-color controls for each fluorochrome and an unstained sample as negative control. All samples were run with the same PMT voltages, and a minimum of 30,000 events were recorded. FlowJo software (v.10.7.1, LLC, BD Biosciences) was employed for post-acquisition compensation and analysis.

BM-MSCs were first identified using linear parameters (forward scatter area (FSC-A) vs. side scatter area (SSC-A), and double cells were excluded (area vs. height, FSC-A vs. FSC-H) (Supplementary Figure S1).

2.5 Scaffold drying and FE-SEM analysis

Cylindrical 3D scaffolds were prepared by mixing fibrinogen at 50 or 100 mg/ml (Sigma-Aldrich), α-aprotinin 15,600 U/ml (Sigma-Aldrich), α-MEM (Corning, NY, United States), and thrombin at 100 U/ml (Sigma-Aldrich), and then were incubated at 37°C for 30 min to allow fibrinogen polymerization (Supplementary Figure S2A). Samples were fixed in 4% paraformaldehyde (PFA; 4°C, overnight) and then dehydrated by multiple passages across ethanol: water solutions (10 min each) with increasing percentages of ethanol and dried using a dense carbon dioxide drying operating at 200 bar and 38°C for 4 h; other details on the dense gas drying protocol were reported elsewhere (Della Porta et al., 2013). System technology scheme is illustrated in Supplementary Figure S2B. Samples were immersed in liquid nitrogen and fractured with a needle, then placed on a double-sided adhesive carbon tape previously glued to an aluminium stub and coated with a gold film (250 A thickness) using a sputter coater (mod.108 A; Agar Scientific, Stansted, United Kingdom), before observation. Internal scaffold morphology was observed by field emission-scanning electron microscopy (FE-SEM, mod. LEO 1525; Carl Zeiss, Oberkochen, DE). Pore size frequency distribution was studied with ImageJ software (rel.1.52p National Institutes of Health, United States), and average perimeter and average Feret's diameter values were reported (Figure 1).

2.6 3D bioengineered scaffold assembly

Cylindrical 3D scaffolds were prepared by mixing fibrinogen at 50 mg/ml (Sigma-Aldrich), α-aprotinin 15,600 U/ml (Sigma-Aldrich), and α-MEM (Corning, NY, United States) containing 1×10^6 cells. Two cell suspension solutions were prepared, composed by *h*BM-MSCs and *h*SkMs with PBMCs ([*h*BM-MSCs + *h*SkMs]: PBMCs, 1:1) and without PBMCs. This ratio was chosen based on previously published literature showing that lower PBMCs:co-cultured cells ratios are preferable (Sturlan et al., 2009; Zhang et al., 2015).

Suspensions were pipetted in different wells of a 96-well plate, thrombin at 100 U/ml (Sigma-Aldrich) was added, and samples incubated at 37°C for 30 min to allow fibrinogen polymerization. 3D scaffolds were then transferred to a culture plate (Supplementary Figure S2C).

2.7 Dynamic culture system by perfusion bioreactor

3D scaffolds were placed in a perfusion bioreactor, formed by a custom multi-well plate, milled in poly (methyl methacrylate) (PMMA, Altuglas® CN 100 10000, Altuglas International, La Garenne-Colombes Cedex, FR), a biocompatible material for biomedical application (Samavedi et al., 2014). This plate has two holes allowing the insertion of silicon tubes (Tygon®, FR) for medium flowing at a constant flow rate of 1.0 ml/min maintained by peristaltic pumps (Pasini et al., 2019). This bioreactor system operates within a standard cell culture incubator (Supplementary Figure S2D).

2.8 Live and dead assay

Cell viability was detected by fluorescence live and dead assay after preparation (day 0) and at each time point (day 7, 14, and 21). Calcein AM solution (Cat. No C1359, Sigma-Aldrich) was used to stain live cells, while cell membrane-impermeable Ethidium homodimer I solution (Cat. No E1903, Sigma-Aldrich) for nuclei of dead cells. Cells were incubated for 1 h at 37°C, then washed in 1X PBS, and imaged using a fluorescence microscope (Eclipse Ti Nikon Corporation, Tokyo, Japan). Signal intensity was quantified using ImageJ software. Original RGB images were converted to 8-bit (grey scale) format, and tagged area intensities were expressed as mean value of pixel intensity within a range from 0 (dark) to 255 (white), as previously reported (Spaepen et al., 2011).

2.9 RNA isolation and gene expression profiling

Expression of myogenic genes, including *Pax3*, *Myo D1*, *Myf5*, *Myf6*, *Desmin*, and *MYH2* (Bio-Rad, Foster City, CA, United States), and cytokines, such as *IL6*, *TNF*, *IL12A*, *IL1B*, *IFNG*, *IL10*, *IL4*, *TGFB1*, and *TGFB2* (sequences are reported in Table 1) were investigated by reverse transcription quantitative polymerase chain reaction (RT-qPCR).

Total RNA from 3D dynamic cultures at each time point was extracted using QIAzol Lysis Reagent (Qiagen), chloroform (Sigma-Aldrich), and RNeasy Micro Kit (Qiagen). For each sample, 1 µg of total RNA was reverse transcribed using iScript™ cDNA synthesis kit (Bio-Rad), and relative gene expression analysis was performed on a LightCycler® 480 Instrument (Roche, Basel, Switzerland) using SsoAdvanced™ universal SYBR® Green Supermix (Bio-Rad). Specificity of formed products was assessed by melting curve analysis. Experiments were run in triplicate.

Data were normalized to glyceraldehyde-3-phosphate dehydrogenase (*GAPDH*) expression (reference gene) applying the geNorm method (Hellemans et al., 2007) and using CFX Manager software ($M < 0.5$). Fold changes were determined by $2^{-\Delta\Delta Ct}$ method

TABLE 1 Cytokine RNA sequences.

Gene symbol	Gene bank accession number	Sequences	Product size	Primer efficiency (%)
IL6	NM-000600.5	Forward: ACTTGCCTGGTGAAAATCAT	135	106
		Reverse: CAGGAACTGGATCAGGACTT		
TNF	NM-000594.4	Forward: GCCCATGTTGTAGCAAACCC	97	105
		Reverse: TATCTCTCAGCTCCACGCCA		
IL12A	NM-000882.4	Forward: TCAGAATTCGGGCAGTGACT	163	110
		Reverse: AGTCCCAQTCCTTCTTTCCCC		
IL1B	NM-000576.3	Forward: GGAGAATGACCTGAGCACCT	185	110
		Reverse: GGAGGTGGAGAGCTTTCAGT		
IFNG	NM-000619.3	Forward: TGCAGAGCCAAATTGTCTCC	194	110
		Reverse: TGCTTTGCGTTGGACATTCA		
IL10	NM-000572.3	Forward: AAGACCCAGACATCAAGGCG	85	110
		Reverse: AATCGATGACAGCGCCGTAG		
IL4	NM-000589.4	Forward:CTGCTTCCCCCTCTGTTCTTC	117	110
		Reverse:TTCGCTCTGTGAGGCTGTT		
TGFB1	NM-000660.7	Forward: GCACTCGCCAGAGTGGTTAT	81	95
		Reverse: AAGCCCTCAATTTCCCCTCC		
TGFB2	NM-0001135599.4	Forward: CCCTAAGCGCAATTCCAC	213	106
		Reverse: CTGCTCCTCCTTCTCTTGCT		

and presented as relative levels *versus* *h*SkMs and *h*BM-MSCs at day 0. All experiments were performed in biological triplicates (N = 3), and each experiment in technical triplicate.

2.10 Immunofluorescence assay

Fibrin scaffolds were fixed in 4% PFA for 2 h at RT, cryo-protected in 30% sucrose (4 °C, overnight), included in optimal cutting temperature (OCT) compound, and cut in slices of 10 µm thickness using a cryostat (CM 1950, Leica, Wetzlar, Germany). Slices were permeabilized with 0.1% Triton X-100 for 10 min and blocked with horse serum solution for 1 h. Samples were then stained for Desmin (1:100; Abcam) and MYH2 (1:50, Thermo Fisher Sci.), incubated overnight at 4°C, and subsequently incubated for 1 h at RT with Alexa Fluor ™ 488 goat anti-rabbit IgG (1:400; Thermo Fisher Sci.), VectaFluor™ anti-mouse IgG Dylight 594® kit (Vector laboratories), and DAPI. Slices were also stained for FITC-conjugated CD90 and PE-conjugated CD105 (Beckman Coulter), incubated overnight at 4°C, and the cell nuclei were counterstained using DAPI. Separate images were acquired using identical settings of light intensity, exposure time, and gain using a fluorescence microscope (Eclipse Ti Nikon Corporation, Tokyo, Japan).

2.11 Cytokine detection

For quantification of secreted cytokines in culture medium, an immunobead-based multiplex assay (Merck, Millipore) was employed for measurement of EGF, Eotaxin, GM-CSF, IFN-γ, IL-10, IL-12p70, IL-1RA, IL-1a, IL-1b, IL-2, IL-3, IL-4, IL-5, IL-7, MIP-1a, MIP-1b, TNF-α, bFGF, G-CSF, GRO, IL-6, IL-8, MCP-1, and VEGF, following manufacturer's instructions.

2.12 Hematoxylin&Eosin staining

Scaffold slices (15 µm thickness) were hydrated using a decreasing ethanol gradient, washed for 5 min in water and incubated with hematoxylin and eosin for 60 min, then dehydrated using an increasing ethanol gradient and cleared in xylene for 5 min. Sections were mounted using Eukitt (Sigma-Aldrich) mounting medium. Images were acquired using an Olympus microscope BX53 equipped with ProgRes SpeedXT ^{core} five camera.

2.13 Statistical analysis

Data were analyzed using Prism software (v.9.0, GraphPad software, LLC, San Diego, California, United States). Results are presented as mean ± standard deviation (SD). Statistical analysis was performed using two-tailed independent Student's t-test for two group comparisons, or two-way analysis of variance (ANOVA) test for three or more group comparison with Tukey's test for multiple comparisons between group. For flow cytometry data, results are presented as percentage of positive cells, and expression of each marker on single cells is also reported as histograms and using unstained samples as negative controls. For characterization of

mesenchymal cells in the co-culture system, percentage of positive cells and median fluorescence intensity (MFI) values were calculated for each marker. Surface marker expression variations were calculated as fold change normalizing MFI values for each marker and from each time point to MFI obtained from *h*BM-MSC cultured alone (Tsai et al., 2020). A p-value < 0.05 was considered statistically significant (de Winter 2013).

3 Results

3.1 3D scaffold optimization

Different concentrations of fibrinogen (50 and 100 mg/ml) were tested to check the best concentration to simultaneously assure good scaffold integrity and void spaces with totally interconnected cells within 3D fibrin system. Fibrinogen concentrations of 5 mg/ml was too low to induce polymerization, whereas, scaffold obtained at 20 mg/ml were difficult to be managed and were discharged (unpublished data). To better observe internal scaffold morphology obtained at 50 and 100 mg/ml, hydrogels were converted to aerogels by dense gas drying process, a procedure already documented as capable to avoid the natural shrinkage and collapsing of the 3D hydrated system, normally observed in lyophilization, as previously optimized (Della Porta et al., 2013). Indeed, derived alcohol gels were processed with dense carbon dioxide for 4 h at 38°C and 200 bar with a flow rate of 1.2 kg/h (system technology scheme in Supplementary Figure S2B). Collected aerogels maintained the same volume with a shrinkage <2%. Thanks to this extremely low shrinkage scaffold morphology was investigated after their freeze-fracture and the internal void structure was observed by FE-SEM (Figure 1). Scaffolds obtained using 50 mg/ml of fibrinogen showed thinner and wider meshes than those obtained with 100 mg/ml of fibrinogen. Pores of the 50 mg/ml of fibrinogen scaffold showed a mean perimeter of 548 nm and a mean Feret's diameter of 180 nm, while at 100 mg/ml of fibrinogen, pores had smaller perimeter (mean, 128 nm) and Feret's diameter (mean, 40 nm). Therefore, scaffolds made with 50 mg/ml of fibrinogen were chosen for further experiments, because they displayed a more spacious microenvironment suitable for a better cell distribution and viability.

3.2 Dynamic culture by perfused systems assures long-term viability

Next, a myogenic commitment model of *h*BM-MSCs-*h*SkMs co-cultured (ratio 2:1) with or without PBMCs was established using scaffolds composed by fibrinogen at 50 mg/ml as support for cell culture and placed in dynamic conditions using a custom-made perfusion bioreactor for maintaining a constant medium flow rate of 1 ml/min (Della Porta et al., 2015) (Supplementary Figures S2C,D). To confirm suitability of this *in vitro* system before performing further experiments, cell viability within fibrin scaffolds was assessed by live and dead assay over a culture period of 21 days. As expected, total cells were almost represented by live cells (>80%) throughout the culture (Figure 2). Furthermore, fibrin scaffolds also maintained structure and integrity, as cells were homogenously distributed and were in close contact throughout the culture period. This regular distribution was also documented by histological evaluation of 3D scaffold culture slices using hematoxylin and eosin staining (Figure 3). Furthermore, fibrin matrix behaves as inert matrix not really influencing myogenic marker expression of *h*BM-MSCs-*h*SkMs co-culture; indeed, when, those cells were co-seeded in 2D culture, almost similar gene expression profile has been observed (Scala et al., 2022).

3.3 *h*BM-MSC and filtrated PBMC characterization

First, mesenchymal phenotype of our primary *h*BM-MSCs was confirmed following International Society of Cellular Therapy criteria (Dominici et al., 2006): adherence to tissue culture plastics; fibroblast-like shape; positivity for CD90, CD105, and CD73 mesenchymal markers; and negativity for CD34, CD14, CD45, and HLA-DR by flow cytometry (Supplementary Figure S1). Then, PBMCs were collected by filtration of 120 ml of whole blood adopting a system conventionally used in clinical practice (HemaTrate® system), and nucleated cell fraction was concentrated in 10 ml of physiological solution. PBMC immunophenotyping and whole blood composition were investigated by flow cytometry on cells separated by Ficoll-Paque density gradient; filter waste bag was considered as a negative control for each donor employed (Figure 4). No significant variations were described in blood frequency and composition before and after filtration or separation, while no PBMCs were observed in specimens obtained from filter waste bags (Figure 4). Moreover, no differences were described for total $CD3^+$ T Cells and $CD4^+/CD8^+$ subpopulations (all $p > 0.05$), and for circulating $CD34^+$ hematopoietic stem cells ($p = 0.2875$), confirming that HemaTrate® filter was highly efficient in selective PBMC collection and concentration in a 10 ml final volume of filtrate.

3.4 *h*BM-MSCs co-cultured with *h*SkMs and PBMCs in 3D dynamic conditions show a stable myogenic phenotype

Myogenic commitment potential of our 3D system was investigated by gene expression profiling (Figure 5). First, *h*SkMs behavior in 3D culture was explored, as shown in Figure 5A *h*SkMs showed a significant upregulation of *Pax3* and *MYH2* at day 21 (258-fold and 261-fold, respectively, $p < 0.0001$), as well as *MyoD1*, *Myf5*, *Myf6*, and *Desmin* genes with an increasing trend from day 0–21. This behavior was reported for comparison purpose.

Then, in Figure 5B gene expression profiling of *h*BM-MSCs-*h*SkMs in 3D co-culture with and without PBMCs is showed. *Pax3* expression levels significantly differed between the two culture conditions over time. In details, *Pax3* expression was upregulated at day 7 in the presence of PBMCs (20-fold), while decreased at day 14 (7-fold), and significantly upregulated at day 21 (27-fold, $p < 0.05$). A similar trend was described in the absence of PBMCs (from 8.6-fold at day 7 to 6.4-fold at day 14 and 11.3-fold at day 21).

For MRF genes, *MyoD1* expression showed lower fold-change values than those without PBMCs at day 7 (28.35-fold vs. 70-fold); however, at day 14 in the presence of PBMCs a significant upregulation occurred (118-fold, $p < 0.05$) as well as at day 21 (81-fold vs. 51-fold). In cultures with PBMCs, *Myf5* expression was increased about 220-fold and without PBMCs about 329-fold ($p < 0.05$) at day 7, while at day 14 slightly decreased with PBMCs (152-fold with vs. 186-fold without PBMCs), remaining stable at

10.3389/fbioe.2022.1075715

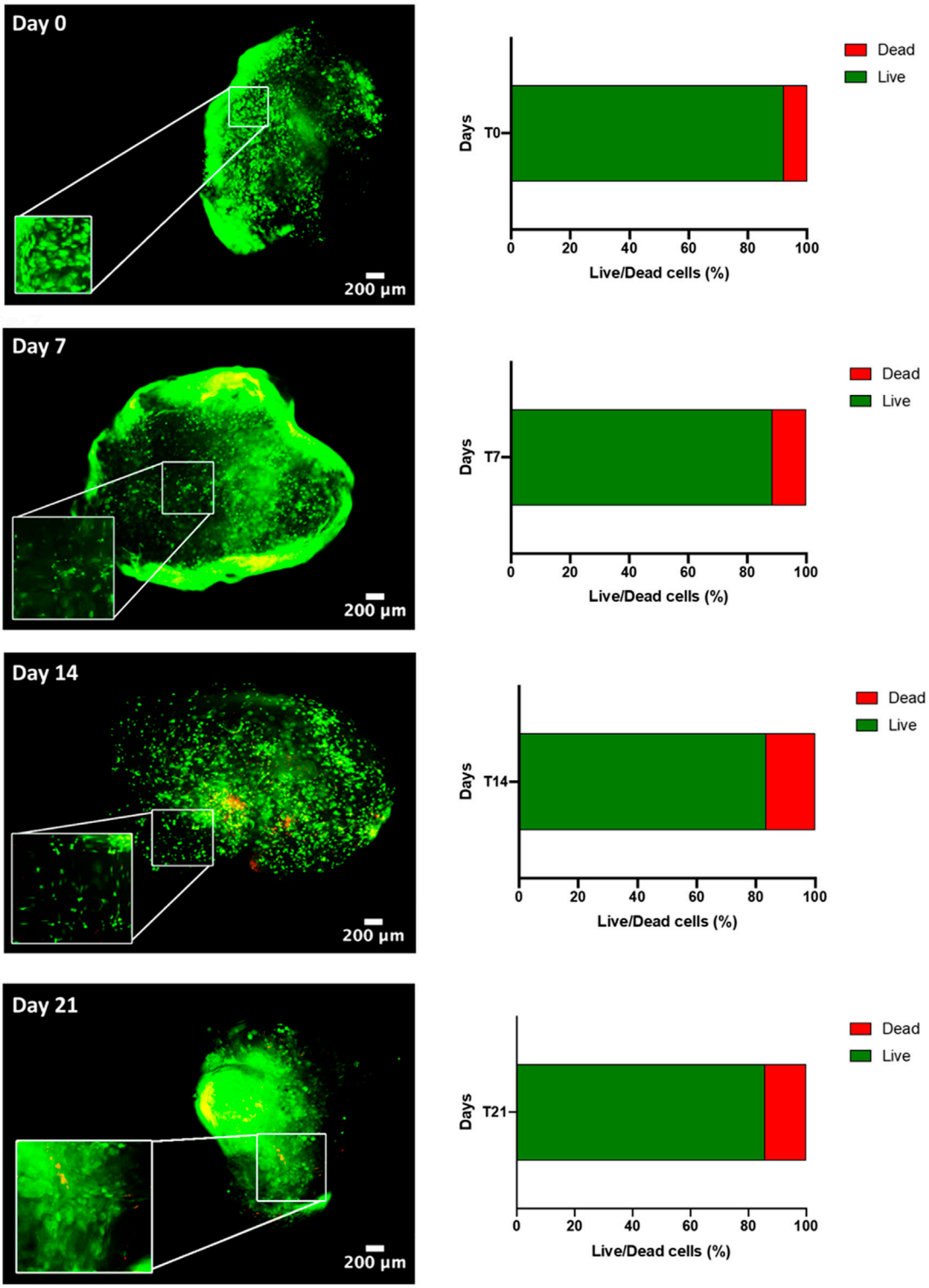

FIGURE 2
Live & Dead of *h*BM-MSC-*h*SkM-PBMC viability in a 3D fibrin scaffold cultured in perfusion system. Live cells are in green while dead cells in red. Images were captured at day 0, 7, 14 and 21 of culture, at ×4 magnification, scale bar: 200µm, while zoomed areas are at 200%. Histograms report viability quantification.

day 21 (136-fold with vs. 99-fold without PBMCs). Generally, *Myf6* expression decreased along the culture with PBMCs, from 215-fold ($p < 0.5$) at day 7, to 75.2-fold at day 14, and 31-fold at day 21. Without PBMCs, the expression was of 165-fold at day 7, about 105-fold at day 14, and decreased at 64-fold at day 21. *Desmin* expression displayed an increasing trend with PBMCs about 3-fold at day 7, 5-fold at day 14, and 6-fold at day 21. When cultured without PBMCs, *Desmin* expression was slightly upregulated at

10.3389/fbioe.2022.1075715

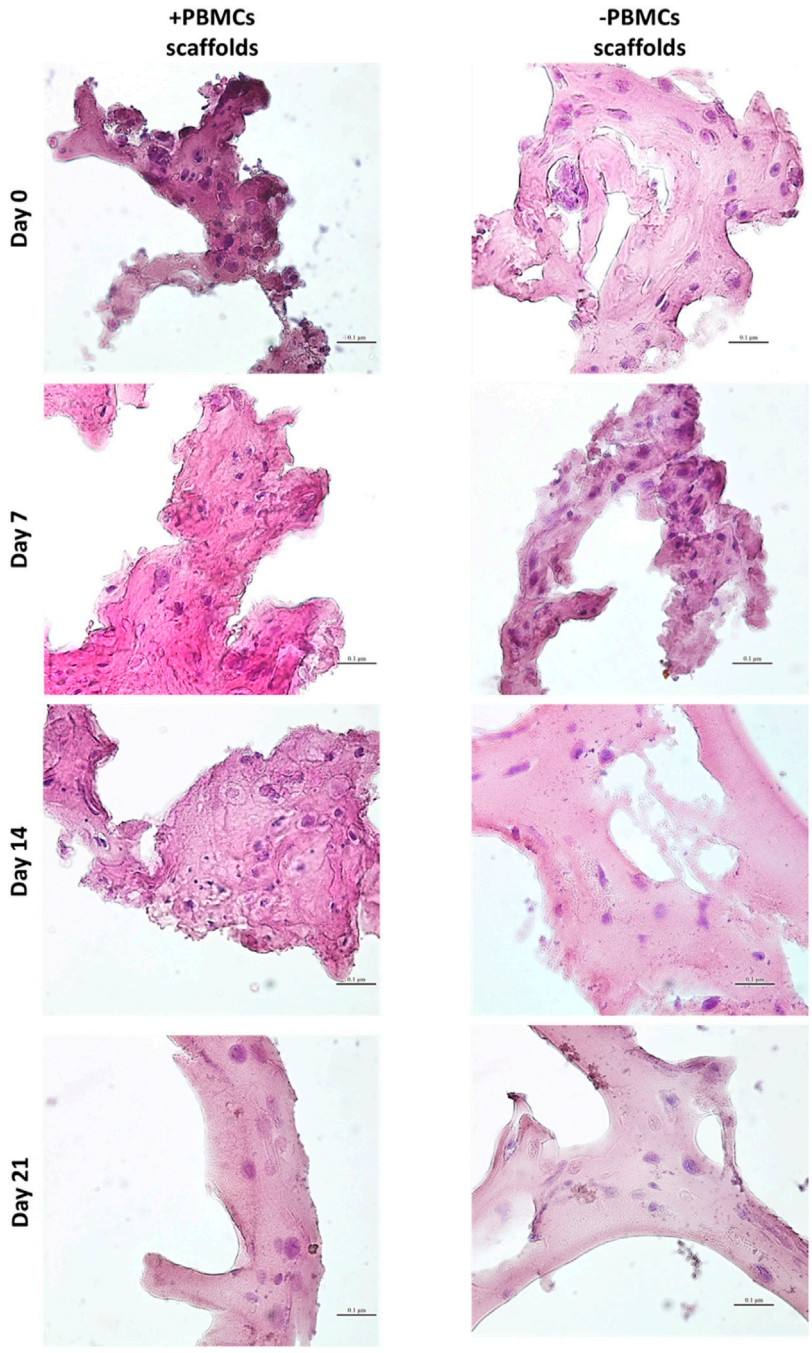

FIGURE 3
Hematoxylin & Eosin staining on 3D fibrin scaffolds embedded with *h*BM-MSCs-*h*SkMs with and without PBMCs. Images were acquired at day 7, 14 and 21 at ×40 magnification, scale bar: 20 μm.

day 7 and 14 (10-fold and 9.5-fold, respectively; $p < 0.01$), and at day 21 of 8-fold ($p < 0.05$). *MYH2* was also investigated but not detected at any time point along the culture. All these profiling were also different from those observed for the *h*SkMs alone in 3D culture, suggesting a fundamental role of the different cell population cross-talk within the 3D system.

To further confirm myogenic commitment of *h*BM-MSCs with or without PBMCs in a 3D culture system, myogenic-related proteins, such as Desmin and MYH2, were assayed by IF (Figures 6, 7). In the presence of PBMCs, Desmin was detectable from day 7 with a signal that became brighter throughout the culture. Despite not well detected by qRT-PCR, MYH2 protein was highlighted by IF assay at day 21 days but only in the culture with PBMCs. Furthermore, almost all 3D cultures of *h*BM-MSCs-*h*SkMs without PBMCs displayed IF signals less intense at each time point compared to cultures with PBMCs (Figure 6). CD90 and CD105 protein expression was also investigated to confirm mesenchymal phenotype at baseline. Signals were clearly detected at day 0, confirming the mesenchymal phenotype of cultured *h*BM-MSCs, while very low or undetectable expression was observed at day 21 (Figure 7).

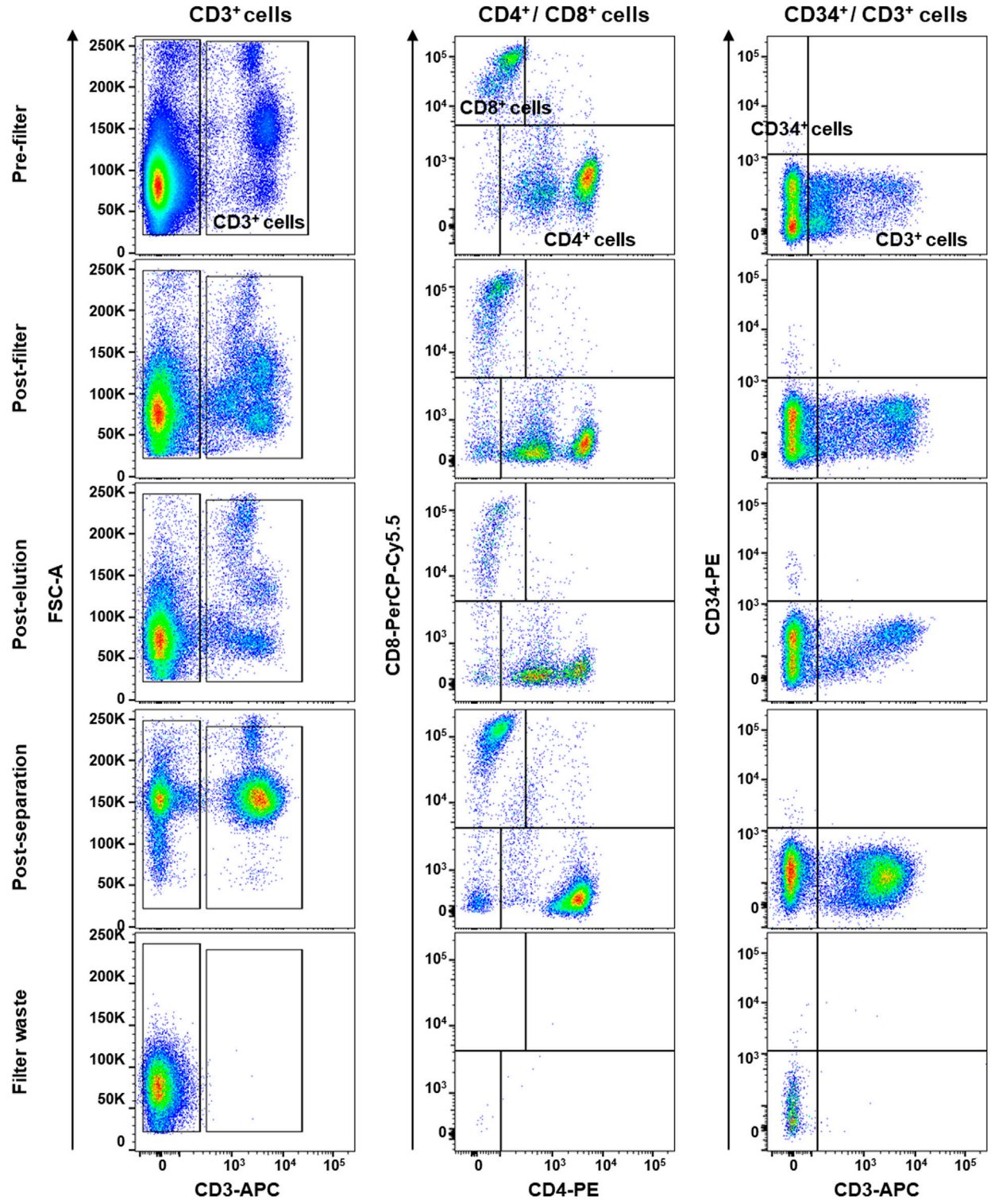

FIGURE 4
Flow cytometry immunophenotyping of peripheral blood mononuclear cells (PBMCs) obtained by whole blood was collected and filtered by a HemaTrate® Blood Filtration system. PBMC different population fraction was subsequently separated by Ficoll-Paque density gradient separation to perform flow cytometry immunophenotyping on pre- and post-filtration, post-elution, post-separation, and on the filter bag waste, as negative control. Frequencies of $CD3^+$ T lymphocytes and $CD8^+$ and $CD4^+$ subsets and circulating $CD34^+$ hematopoietic stem cells were studied.

3.5 PBMCs influence cytokine expression

We next explored paracrine and cell-to-cell contact effects of PBMCs on cytokine expression in *h*BM-MSCs-*h*SkMs cultured in a 3D *in vitro* perfused model (Figure 8). *h*SkMs showed a significant upregulation of pro-inflammatory cytokine as *TNF*, 478-fold ($p < 0.0001$) and *IL12A*, 14-fold ($p < 0.5$) (Figure 8A). In co-culture system, pro-inflammatory cytokines were downregulated with

10.3389/fbioe.2022.1075715

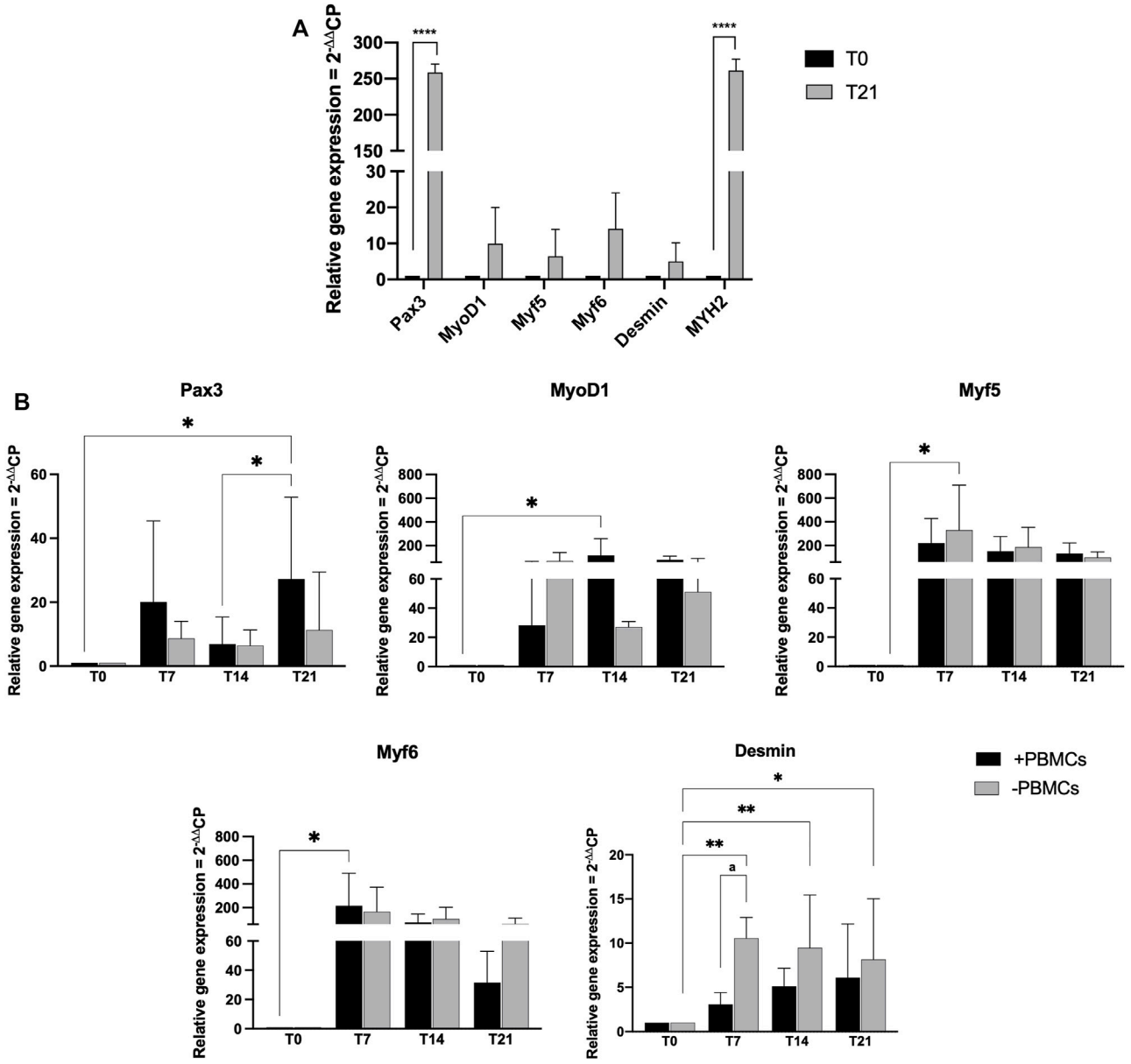

FIGURE 5
Gene expression profiling for myogenic markers by quantitative RT-PCR of *h*SkMs **(A)** and of *h*BM-MSCs-*h*SkMs-PBMCs **(B)**, both within 3D fibrin scaffold. mRNA levels of myogenic markers (*Pax3*, *MyoD1*, *Myf5*, *Myf6* and *Desmin*) were assayed by qRT-PCR at day 7, 14 and 21 of culture. Relative quantification of each mRNA gene expression normalized to endogenous *GAPDH* (internal control) was calculated using the $2^{-\Delta\Delta Ct}$ method and presented as fold change over *h*SkMs at day 0 **(A)** and over *h*BM-MSCs at day 0 **(B)**, selected as a control. All experiments were performed in biological triplicates (N = 3) and each experiment in technical triplicates. *, significant compared to day 0 (T0); a, significant comparison between ± PBMCs at day 7. *$p < 0.05$; **$p < 0.01$; ****$p < 0.0001$.

PBMCs, especially *IL6* (0.04-fold at day 7, 0.1-fold at day 14, and 0.05-fold at day 21; $p < 0.01$). At day 14 and 21, *IL12A* increased of 6-fold and 17-fold with PBMCs, and of 75-fold and 13-fold without PBMCs; similarly, *IL1B* increased at 6-fold and 15-fold with PBMCs, while 20.5-fold and 8-fold without PBMCs. Conversely, among investigated anti-inflammatory cytokines, *IL10* was the most expressed and was higher in the presence of PBMCs (23.3-fold vs. 11.5-fold at day 7, or 9-fold vs. 5-fold at day 14, with vs. without PBMCs, respectively). *TGFB1* showed an increasing trend in the presence of PBMCs from 1.8-fold at day 7 to 9.5-fold at day 14 and 12-fold at day 21. *TGFB2* displayed the maximum expression at day 14, about 7-fold without PBMCs. *TNF*, *IL4*, and *IFNG* were not detected (Figure 8B).

Cytokine secretion was also investigated by analyzing culture medium supernatants at 7, 14 and 21 days by multiplex bead-based immunoassay (Figure 8C). Among 24 cytokines studied, growth-regulated alpha protein (GRO; 2.5 ng/ml), IL-6, granulocyte-colony stimulating factor (G-CSF), IL-8, monocyte chemoattractant protein-1 (MCP-1), and vascular epidermal growth factor (VEGF; 0.1 ng/ml) were detected in culture medium at day 7. Remaining cytokines were not present in culture medium supernatants at day 7, and no cytokines were detected at day 14 and 21.

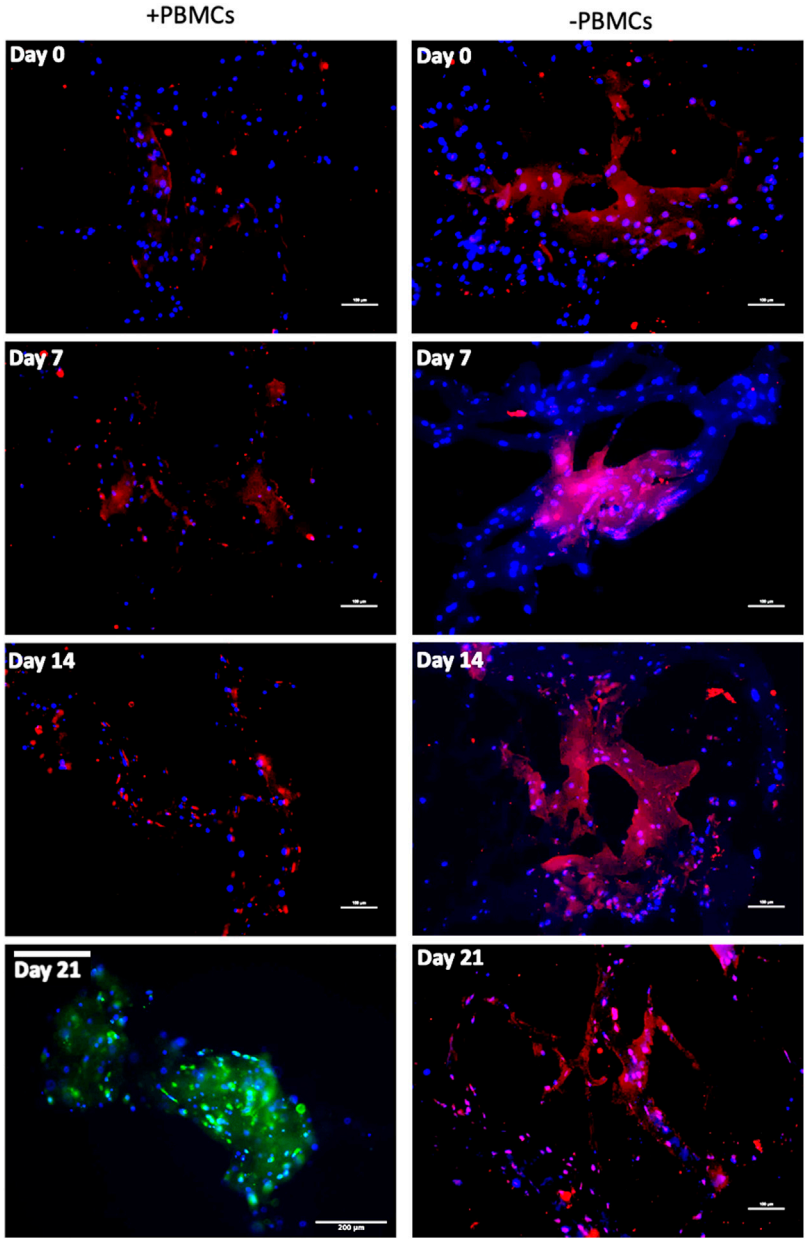

FIGURE 6
Immunofluorescence images of 3D fibrin scaffold for Desmin and MYH2 obtained by IF assay performed at day 7, 14 and 21 of culture. Desmin was stained in red and MYH2 in green; scaffolds embedded with *h*BM-MSCs-*h*SkMs-PBMCs (left column) and scaffolds embedded with *h*BM-MSCs-*h*SkMs (right column) are shown. MYH2 was not detected. All images were captured using ×20 magnification, scale bar: 200 µm.

4 Discussion

The development of accurate *in vitro* myogenic commitment models from *h*BM-MSCs is still challenging, and the exact role of PBMCs in influencing myogenic events is under debate, despite clinical reports indicated that the pharmacological targeting of inflammation and immune functions results in faster healing processes. Spontaneous healing skeletal muscle capacity in case of severe injuries appears insufficient, and conventional injury management, including RICE protocol (rest, ice, compression and elevation), drug therapies with non-steroidal anti-inflammatory drugs and intramuscular corticosteroids do not provide optimal restoration to preinjury status (Longo et al., 2012). Therefore, biological treatments, like cell therapy are of high clinical interest. In this sense, the development of biomimetic *in vitro* SkMR models are precious tools to better understand the complex mechanism of muscle healing process, as recently reported using an *in vitro* model of myogenic commitment by co-culture *h*BM-MSCs with *h*SkMs (Scala et al., 2022).

In this work, we implemented our previous *h*BM-MSC-*h*SkM co-culture system with PBMCs in a 3D fibrin scaffold to investigate their potential roles in muscle injury resolution through paracrine and cell-to-cell contact effects. Indeed, indirect evidence of PBMCs contribution in muscle tissue regeneration is in the clinical efficacy

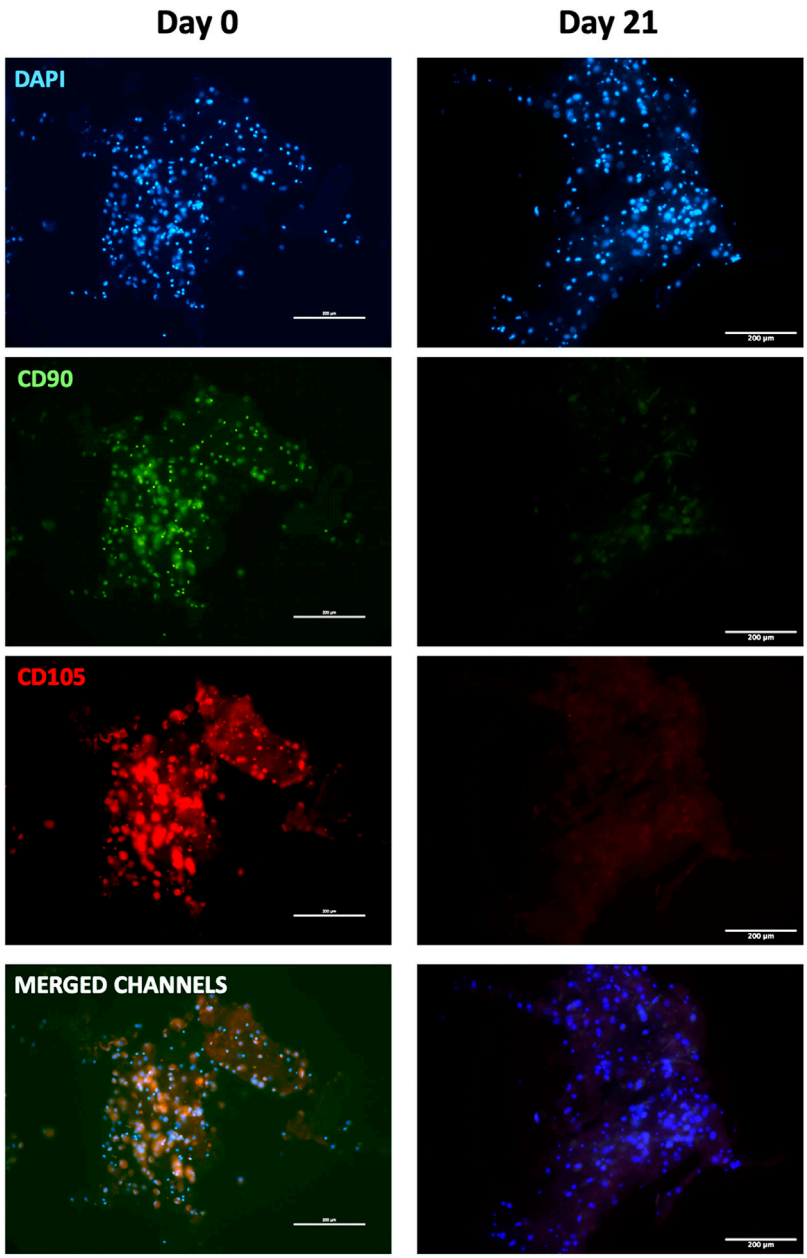

FIGURE 7
Immunofluorescence images of 3D fibrin scaffold for stemness markers by IF assay performed staining FITC-conjugated CD90 and PE-conjugated CD105 fibrin scaffolds embedded with *h*BM-MSCs-*h*SkMs-PBMCs at day 0 and 21. All images were captured using ×20 magnification, scale bar: 200 µm.

of autologous peripheral cell transplantation in critic limb ischemia treatments (De Angelis et al., 2015). In this case, PBMCs are collected from the patient by blood filtration using a commercial filter device (HemaTrate®), are concentrated in a smaller volume, and are then reinfused without any external cell manipulation. However, the exact mechanisms underlying clinical efficacy of autologous filtered peripheral blood cell transplantation are still under debate. Here, we sought to investigate the role of PBMCs in myogenesis using a 3D biomimetic *in vitro* model where PBMCs were added to a myogenic model composed by a co-culture of *h*BM-MSCs and *h*SkMs.

Scaffold porosity is another important parameter when setting up a 3D scaffold-based *in vitro* system, as cells require an appropriate void volume to locate and to permit oxygen and mass exchange (Lovecchio et al., 2014; Lamparelli et al., 2021; Lovecchio et al., 2020). Fibrinogen concentration can affect internal porosity with formation of irregular geometric areas. At the lowest fibrinogen concentrations tested (e.g., 5 mg/ml), polymerization reaction did not occur, while scaffold obtained at 20 mg/ml were difficult to be managed (unpublished data). Therefore, 50 mg/ml concentration was chosen to build fibrin scaffold because scaffold structure showed larger porosity with higher interconnectivity, whereas, higher fibrinogen concentrations decreased the scaffold pore size diameters, even if an increase in tensile strength is documented by the literature (Chiu et al., 2012). However, because tensile strength was not the focus of our study, fibrinogen concentration at 50 mg/ml was selected for our 3D system, allowing a better nutrient and gas exchange, confirmed by

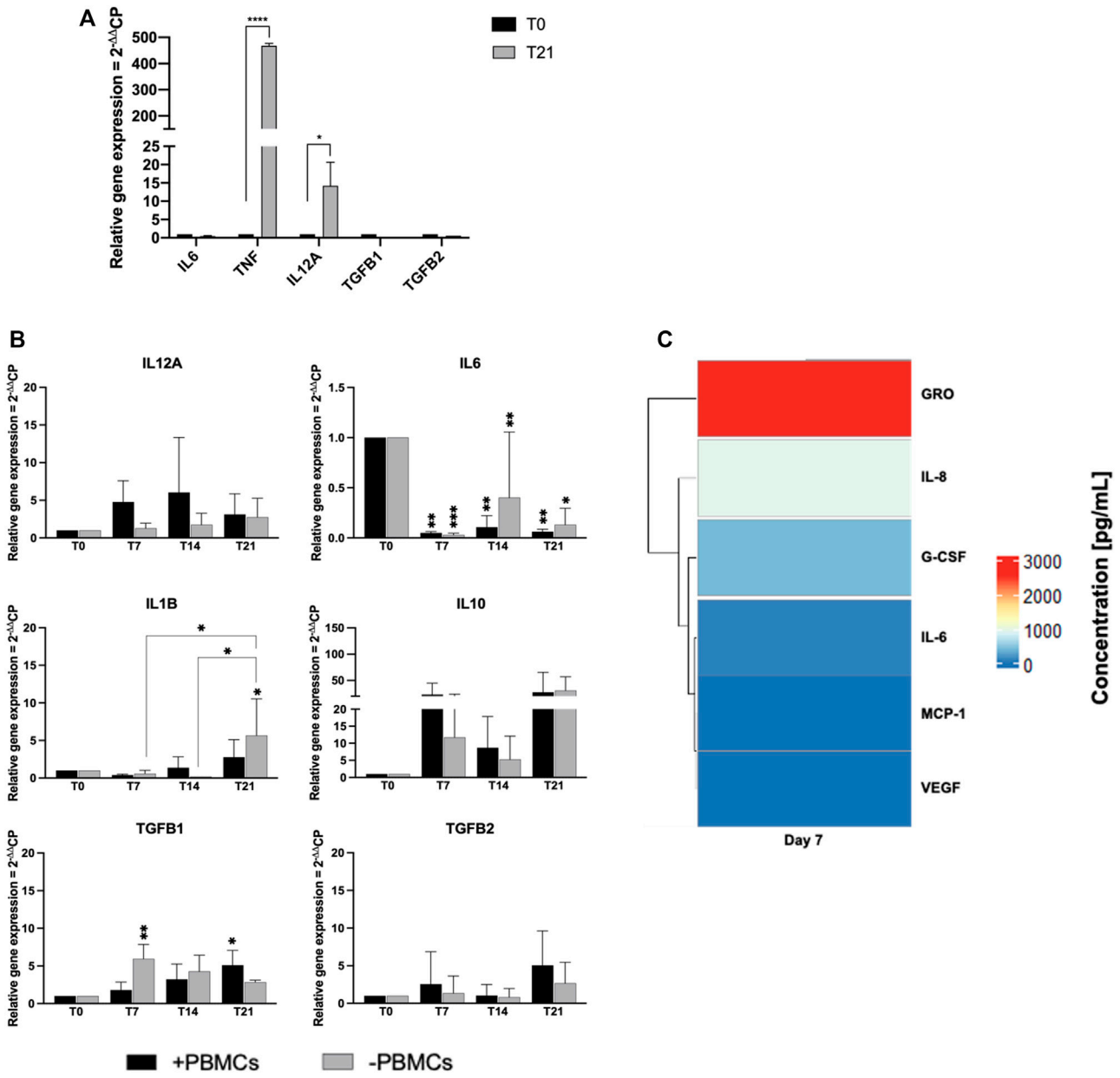

FIGURE 8
Gene expression profiling for pro- and anti-inflammatory cytokines by quantitative RT-PCR of *h*SkMs **(A)** and of *h*BM-MSCs-*h*SkMs-PBMCs **(B)**, both within 3D fibrin scaffold. The mRNA levels of pro-inflammatory cytokines (*IL12A*, *IL6* and *IL1B*) and anti-inflammatory cytokines (*IL10*, *TGFB1* and *TGFB2*) were assayed by qRT-PCR at day 7, 14 and 21 of culture. The relative quantification of each mRNA gene expression normalized to endogenous *GAPDH* (internal control) was calculated using the $2^{-\Delta\Delta Ct}$ method and presented as fold change over *h*SkMs at day 0 **(A)** and over *h*BM-MSCs at day 0 **(B)**, selected as a control. Cytokine levels measured in culture medium supernatants at day 7, 14, and 21 by magnetic bead-based multiplex immunoassay **(C)**. Data are reported as heatmap from blue (lowest value, 0 pg/ml of concentration) to red (highest value). Cytokines were hierarchical clustered based on expression pattern. Heatmap was made using *Pheatmap* and *ComplexHeatmap* packages in R Studio software (v. 2022.07.1 + 554; R Studio, Boston, MA, US). All experiments were performed in biological triplicates (N = 3) and each experiment in technical triplicates. *$p < 0.05$; **$p < 0.01$; ****$p < 0.0001$.

excellent cell viability up to 21 days of culture. Furthermore, to assure proper oxygen and metabolite mass transfer into the 3D high-density culture, scaffolds were placed within a close system in which culture medium re-circulated at a constant flow rate of 1 ml/min, maintained by a perfusion bioreactor. Indeed, even in standard 2D conditions, dynamic cultures assured a better myogenic commitment, as previously shown in our optimized co-culture system. Fibrin is widely used in tissue engineering and derives from thrombin-mediated fibrinogen monomer polymerization. Fibrin is naturally degraded by serine protease, and α-aprotinin, a serine protease inhibitor, is usually added to fibrinogen mix to prevent fibrin scaffold degradation in *vitro* and *in vivo* conditions, as previously demonstrated (Thomson et al., 2013; Mühleder et al., 2018).

*h*BM-MSCs cultured in 3D fibrin scaffold displayed upregulation of myogenic genes with conserved kinetics, as *MRFs*, such as *Myf5* and *Myf6*, were expressed earlier than *Desmin*, upregulated at later time points (Asfour et al., 2018). When PBMCs were embedded in the 3D fibrin scaffold together with *h*BM-MSCs and *h*SkMs, *h*BM-MSCs

differentiated toward myogenic phenotype, although less efficiently when in the absence of PBMCs. However, in both conditions, *h*BM-MSCs lost their mesenchymal for a mature myocyte phenotype with $CD90^{-}CD73^{+}CD105^{+/-}$ (Gago-Lopez et al., 2014) and showed Desmin and Myosin Heavy Chain II protein production. In our immunofluorescence analysis, cells appeared in a spherical shape and immunofluorescence signals were detected as single dots, because cells in a 3D system were in close contact with fibrin and embedded in the pores, as already reported (Sun et al., 2012; Ahmed et al., 2015).

The use of complex co-cultures could create a bias in gene expression normalization, as different cell populations were embedded together in the same scaffold and could not be separately recovered for gene expression analysis. For this reason, cultures with single populations, including *h*BM-MSCs and *h*SkMs alone, were used as controls and for gene expression normalization. Moreover, *h*SkMs were seeded at a lower density compared to *h*BM-MSCs (seeding ratio, 2:1, *h*BM-MSCs:*h*SkMs) in our 3D fibrin system, as previously optimized (Scala et al., 2022) thus, gene expression from co-culture experiments can be reconducted to *h*BM-MSC behavior. PBMCs were added to this well-established myogenic model at the lowest possible ratio (1:1), as lower PBMC ratios are the optimal solution in co-culture systems (Sturlan et al., 2009; Zhang et al., 2015).

Based on our results, PBMCs played an effective role in myogenic commitment, while their main activity was the influence on cytokine expression by *h*BM-MSCs. Fibrin can also induce synthesis of pro-inflammatory cytokines, especially from PBMCs (Jensen et al., 2007); however, pro-inflammatory cytokines were detected at very low levels in our 3D system throughout the culture period at both gene and protein levels, suggesting that fibrin scaffold did not influence gene and protein expression of BM-MSCs. Moreover, in our system, *TGFB2* was increased, contributing to a transient matrix deposit (Osses and Brandan, 2002; Ge et al., 2011), while *IL-10* upregulation, especially in the first 14 days of culture at gene and protein levels, could suggest a possible anti-inflammatory paracrine effect of PBMCs on microenvironment composition, promoting *h*BM-MSC commitment (Khodayari S., 2019). Secretion of chemoattracts and growth factors in culture medium could co-adiuvate physiological myogenic differentiation by triggering cell recruitment and neovascularization.

To our knowledge, this is the first study using a complex co-culture system composed by mesenchymal stem cells, muscle cells, and immune cells in a 3D microenvironment, representing a novelty in the tissue engineering field. In this *in vitro* myogenic model, immune cells exerted their effects only in a paracrine manner, while not influencing myogenic gene expression. Indeed, immune cells could reduce pro-inflammatory cytokines early in the healing process, while later induce anti-inflammatory molecules favoring muscle cell differentiation and regeneration (Tidball, 2017).

5 Conclusion and perspectives

The present work described the study of myogenic commitment of *h*BM-MSCs using a 3D scaffold of fibrin hydrogel bioengineered with different cell populations such as *h*SkMs and PBMCs in a perfused bioreactor system. The proposed system could be successfully employed for further studies on more complex crosstalk mechanisms involving multiple cell types. Furthermore, our *in vitro* biomimetic 3D model could allow to better understand the role of PBMCs in myogenic events in both physiological and pathological simulated conditions. Indeed, despite several clinical reports indicated that filtrated PBMCs fraction can be potentially useful in case of muscle severe injuries, biological mechanisms underlying stem cell differentiation and muscle regenerative events are still poorly understood. In this sense, the described 3D *in vitro* model might open perspectives for further exploration of the role of PBMCs behavior in myogenic healing events.

Data availability statement

The original contributions presented in the study are included in the article/Supplementary Material, further inquiries can be directed to the corresponding author.

Ethics statement

The studies involving human participants were reviewed and approved by the Hospital Institutional Review Board (Ethic Committee "Campania Sud", Brusciano, Naples, Italy; prot./SCCE n. 24988). . The patients/participants provided their written informed consent to participate in this study.

Author contributions

PS developed the experimental activity and methodology; she was responsible of the paper draft preparation and revision; PM isolated the stem cells and characterized them with formal analysis; EPL contributed to experimental activity and qRT-PCR data acquisition; JL designed the bioreactor and related operative protocols; MCC provided methodology for 3D cell culture and scaffold assembly; VG characterized stem cell with validated methodology; CS provided the methodology for stem cell culture; EG supervised the bioreactor protocols; LR provided contribution in supervision and paper writing; NM helped in the interpretation of the data, reviewed the manuscript and was responsible of funding acquisition; GDP was responsible of experimental data design, production, curation and supervision, paper writing and editing, funding acquisition and research project administration.

Funding

The present study was only partially funded by the Athena Srl and mainly funded by the University of Salerno. Collection, analysis, interpretation of data or the decision to submit it for publication. LR provided the methodology for PBMC fraction collection; she also provided a literature survey useful for the organization of the introduction section.

PS is the recipient of a PhD grant Cycle XXXV in Translational Medicine at Dept. Of Medicine, Surgery and Dentistry, University of Salerno entitled: "Skeletal muscle regeneration modulated by inflammation: an *in vitro* study on a 3D bioengineered system" funded by Athena Srl 139, Viale Europa—50,126 Firenze (IT).

Conflict of interest

The authors declare that the research was conducted in the absence of any commercial or financial relationships that could be construed as a potential conflict of interest.

Publisher's note

All claims expressed in this article are solely those of the authors and do not necessarily represent those of their affiliated organizations, or those of the publisher, the editors and the reviewers. Any product that may be evaluated in this article, or claim that may be made by its manufacturer, is not guaranteed or endorsed by the publisher.

Supplementary material

The Supplementary Material for this article can be found online at: https://www.frontiersin.org/articles/10.3389/fbioe.2022.1075715/full#supplementary-material

References

Ahmed, T. A. E., Ringuette, R., Wallace, V. A., and Griffith, M. (2015). Autologous fibrin glue as an encapsulating scaffold for delivery of retinal progenitor cells. *Front. Bioeng. Biotechnol.* 2, 85. doi:10.3389/fbioe.2014.00085

Asfour, H. A., Allouh, M. Z., and Said, R. S. (2018). Myogenic regulatory factors: The orchestrators of myogenesis after 30 years of discovery. *Exp. Biol. Med. (Maywood)* 243, 118–128. doi:10.1177/1535370217749494

Beier, J. P., Bitto, F. F., Lange, C., Klumpp, D., Arkudas, A., Bleiziffer, O., et al. (2011). Myogenic differentiation of mesenchymal stem cells co-cultured with primary myoblasts. *Cell. Biol. Int.* 35, 397–406. doi:10.1042/CBI20100417

Belizário, J. E., Fontes-Oliveira, C. C., Borges, J. P., Kashiabara, J. A., and Vannier, E. (2016). Skeletal muscle wasting and renewal: A pivotal role of myokine IL-6. *SpringerPlus* 5, 619. doi:10.1186/s40064-016-2197-2

Birru, B., Mekala, N. K., and Parcha, S. R. (2018). Improved osteogenic differentiation of umbilical cord blood MSCs using custom made perfusion bioreactor. *Biomed. J.* 41, 290–297. doi:10.1016/j.bj.2018.07.002

Charville, G. W., Cheung, T. H., Yoo, B., Santos, P. J., Lee, G. K., Shrager, J. B., et al. (2015). *Ex vivo* expansion and *in vivo* self-renewal of human muscle stem cells. *Stem Cell Rep.* 5, 621–632. doi:10.1016/j.stemcr.2015.08.004

Chaweewannakorn, C., Tsuchiya, M., Koide, M., Hatakeyama, H., Tanaka, Y., Yoshida, S., et al. (2018). Roles of IL-1α/β in regeneration of cardiotoxin-injured muscle and satellite cell function. *Am. J. Physiology-Regulatory, Integr. Comp. Physiology* 315, R90–R103. doi:10.1152/ajpregu.00310.2017

Chen, S.-E., Jin, B., and Li, Y.-P. (2007). TNF-α regulates myogenesis and muscle regeneration by activating p38 MAPK. *Am. J. Physiology-Cell Physiology* 292, C1660–C1671. doi:10.1152/ajpcell.00486.2006

Cheng, M., Nguyen, M.-H., Fantuzzi, G., and Koh, T. J. (2008). Endogenous interferon-γ is required for efficient skeletal muscle regeneration. *Am. J. Physiology-Cell Physiology* 294, C1183–C1191. doi:10.1152/ajpcell.00568.2007

Chiu, C. L., Hecht, V., Duong, H., Wu, B., and Tawil, B. (2012). Permeability of three-dimensional fibrin constructs corresponds to fibrinogen and thrombin concentrations. *BioResearch Open Access* 1, 34–40. doi:10.1089/biores.2012.0211

Ciardulli, M. C., Lovecchio, J., Scala, P., Lamparelli, E. P., Dale, T. P., Giudice, V., et al. (2021). 3D biomimetic scaffold for growth factor controlled delivery: An *in-vitro* study of tenogenic events on wharton's jelly mesenchymal stem cells. *Pharmaceutics* 13, 1448. doi:10.3390/pharmaceutics13091448

Ciardulli, M. C., Marino, L., Lovecchio, J., Giordano, E., Forsyth, N. R., Selleri, C., et al. (2020). Tendon and cytokine marker expression by human bone marrow mesenchymal stem cells in a hyaluronate/poly-lactic-Co-glycolic acid (PLGA)/Fibrin three-dimensional (3D) scaffold. *Cells* 9, 1268. doi:10.3390/cells9051268

De Angelis, B., Gentile, P., Orlandi, F., Bocchini, I., Di Pasquali, C., Agovino, A., et al. (2015). Limb rescue: A new autologous-peripheral blood mononuclear cells technology in critical limb ischemia and chronic ulcers. *Tissue Eng. Part C. Methods* 21, 423–435. doi:10.1089/ten.tec.2014.0245

de Winter, J. C. F. (2013). Using the Student's t-test with extremely small sample sizes. *Pract. Assess. Res. Eval.* 18. doi:10.7275/E4R6-DJ05

Della Porta, G., Del Gaudio, P., De Cicco, F., Aquino, R. P., and Reverchon, E. (2013). Supercritical drying of alginate beads for the development of aerogel biomaterials: Optimization of process parameters and exchange solvents. *Ind. Eng. Chem. Res.* 52, 12003–12009. doi:10.1021/ie401335c

Della Porta, G., Nguyen, B.-N. B., Campardelli, R., Reverchon, E., and Fisher, J. P. (2015). Synergistic effect of sustained release of growth factors and dynamic culture on osteoblastic differentiation of mesenchymal stem cells: Sustained Growth Factor Release for Osteoblastic Differentiation. *J. Biomed. Mat. Res.* 103, 2161–2171. doi:10.1002/jbm.a.35354

Deng, B., Wehling-Henricks, M., Villalta, S. A., Wang, Y., and Tidball, J. G. (2012). IL-10 triggers changes in macrophage phenotype that promote muscle growth and regeneration. *J. I.* 189, 3669–3680. doi:10.4049/jimmunol.1103180

Dominici, M., Le Blanc, K., Mueller, I., Slaper-Cortenbach, I., Marini, F. C., Krause, D. S., et al. (2006). Minimal criteria for defining multipotent mesenchymal stromal cells. The International Society for Cellular Therapy position statement. *Cytotherapy* 8, 315–317. doi:10.1080/14653240600855905

Engel, N., Fechner, C., Voges, A., Ott, R., Stenzel, J., Siewert, S., et al. (2021). An optimized 3D-printed perfusion bioreactor for homogeneous cell seeding in bone substitute scaffolds for future chairside applications. *Sci. Rep.* 11, 22228. doi:10.1038/s41598-021-01516-8

Ergene, E., Sezlev Bilecen, D., Kaya, B., Yilgor Huri, P., and Hasirci, V. (2020). 3D cellular alignment and biomimetic mechanical stimulation enhance human adipose-derived stem cell myogenesis. *Biomed. Mat.* 15, 055017. doi:10.1088/1748-605X/ab95e2

Gago-Lopez, N., Awaji, O., Zhang, Y., Ko, C., Nsair, A., Liem, D., et al. (2014). THY-1 receptor expression differentiates cardiosphere-derived cells with divergent cardiogenic differentiation potential. *Stem Cell Rep.* 2, 576–591. doi:10.1016/j.stemcr.2014.03.003

Gamblin, A. L., Renaud, A., Charrier, C., Hulin, P., Louarn, G., Heymann, D., et al. (2014). Osteoblastic and osteoclastic differentiation of human mesenchymal stem cells and monocytes in a miniaturized three-dimensional culture with mineral granules. *Acta Biomater.* 10, 5139–5147. doi:10.1016/j.actbio.2014.08.033

Garcia, S. M., Tamaki, S., Xu, X., and Pomerantz, J. H. (2017). "Human satellite cell isolation and xenotransplantation," in Skeletal muscle development *methods in molecular biology*. Editor J. G. Ryall (New York, NY: Springer New York), 105–123. doi:10.1007/978-1-4939-7283-8_8

Ge, X., McFarlane, C., Vajjala, A., Lokireddy, S., Ng, Z. H., Tan, C. K., et al. (2011). Smad3 signaling is required for satellite cell function and myogenic differentiation of myoblasts. *Cell Res.* 21, 1591–1604. doi:10.1038/cr.2011.72

Gilbert-Honick, J., Iyer, S. R., Somers, S. M., Lovering, R. M., Wagner, K., Mao, H.-Q., et al. (2018). Engineering functional and histological regeneration of vascularized skeletal muscle. *Biomaterials* 164, 70–79. doi:10.1016/j.biomaterials.2018.02.006

Giordano, R., Canesi, M., Isalberti, M., Isaias, I., Montemurro, T., Viganò, M., et al. (2014). Autologous mesenchymal stem cell therapy for progressive supranuclear palsy: Translation into a phase I controlled, randomized clinical study. *J. Transl. Med.* 12, 14. doi:10.1186/1479-5876-12-14

Govoni, M., Berardi, A. C., Muscari, C., Campardelli, R., Bonafè, F., Guarnieri, C., et al. (2017). An engineered multiphase three-dimensional microenvironment to ensure the controlled delivery of cyclic strain and human growth differentiation factor 5 for the tenogenic commitment of human bone marrow mesenchymal stem cells. *Tissue Eng. Part A* 23, 811–822. doi:10.1089/ten.tea.2016.0407

Grayson, W. L., Marolt, D., Bhumiratana, S., Fröhlich, M., Guo, X. E., and Vunjak-Novakovic, G. (2011). Optimizing the medium perfusion rate in bone tissue engineering bioreactors. *Biotechnol. Bioeng.* 108, 1159–1170. doi:10.1002/bit.23024

Hellemans, J., Mortier, G., De Paepe, A., Speleman, F., and Vandesompele, J. (2007). qBase relative quantification framework and software for management and automated analysis of real-time quantitative PCR data. *Genome Biol.* 8, R19. doi:10.1186/gb-2007-8-2-r19

Huang, Y.-C., Dennis, R. G., Larkin, L., and Baar, K. (2005). Rapid formation of functional muscle *in vitro* using fibrin gels. *J. Appl. Physiology* 98, 706–713. doi:10.1152/japplphysiol.00273.2004

Jensen, T., Kierulf, P., Sandset, P., Klingenberg, O., Joø, G., Godal, H., et al. (2007). Fibrinogen and fibrin induce synthesis of proinflammatory cytokines from isolated peripheral blood mononuclear cells. *Thromb. Haemost.* 97, 822–829. doi:10.1160/TH07-01-0039

khodayari, S., Khodayari, H., Amiri, A. Z., Eslami, M., Farhud, D., Hescheler, J., et al. (2019). Inflammatory microenvironment of acute myocardial infarction prevents regeneration of heart with stem cells therapy. *Cell Physiol. Biochem.* 53, 887–909. doi:10.33594/000000180

Kuang, S., Kuroda, K., Le Grand, F., and Rudnicki, M. A. (2007). Asymmetric self-renewal and commitment of satellite stem cells in muscle. *Cell* 129, 999–1010. doi:10.1016/j.cell.2007.03.044

Lamparelli, E. P., Lovecchio, J., Ciardulli, M. C., Giudice, V., Dale, T. P., Selleri, C., et al. (2021). Chondrogenic commitment of human bone marrow mesenchymal stem cells in a perfused collagen hydrogel functionalized with hTGF-β1-Releasing PLGA microcarrier. *Pharmaceutics* 13, 399. doi:10.3390/pharmaceutics13030399

Londhe, P., and Davie, J. K. (2011). Gamma interferon modulates myogenesis through the major histocompatibility complex class II transactivator, CIITA. *Mol. Cell. Biol.* 31, 2854–2866. doi:10.1128/MCB.05397-11

Longo, U. G., Loppini, M., Berton, A., Spiezia, F., Maffulli, N., and Denaro, V. (2012). Tissue engineered strategies for skeletal muscle injury. *Stem Cells Int.* 2012, 1–9. doi:10.1155/2012/175038

Lovecchio, J., Jonsdottir-Buch, S. M., Einarsdottir, G. K., Kjartan Gislason, M., Örlygsson, G., Sigurjonsson, O. E., et al. (2014). Assessment of perfusion bioreactors system using μCT technology and 3D modeling methods. *Biomed. Technik/Biomedical Eng.* 59, 302–305. doi:10.1515/bmt-2014-4130

Lovecchio, J., Pannella, M., Giardino, L., Calzà, L., and Giordano, E. (2020). A dynamic culture platform enhances the efficiency of the 3D HUVEC-based tube formation assay. *Biotechnol. Bioeng.* 117, 789–797. doi:10.1002/bit.27227

Manzo, P., Scala, P., Giudice, V., Gorrese, M., Bertolini, A., Morini, D., et al. (2022). c-Kit M541L variant is related to ineffective hemopoiesis predisposing to clonal evolution in 3D in vitro biomimetic co-culture model of bone marrow niche. *Heliyon* 8, e11998. doi:10.1016/j.heliyon.2022.e11998

Matthias, N., Hunt, S. D., Wu, J., Lo, J., Smith Callahan, L. A., Li, Y., et al. (2018). Volumetric muscle loss injury repair using *in situ* fibrin gel cast seeded with muscle-derived stem cells (MDSCs). *Stem Cell Res.* 27, 65–73. doi:10.1016/j.scr.2018.01.008

Montarras, D., Morgan, J., Collins, C., Relaix, F., Zaffran, S., Cumano, A., et al. (2005). Direct isolation of satellite cells for skeletal muscle regeneration. *Science* 309, 2064–2067. doi:10.1126/science.1114758

Mühleder, S., Pill, K., Schaupper, M., Labuda, K., Priglinger, E., Hofbauer, P., et al. (2018). The role of fibrinolysis inhibition in engineered vascular networks derived from endothelial cells and adipose-derived stem cells. *Stem Cell Res. Ther.* 9, 35. doi:10.1186/s13287-017-0764-2

Osses, N., and Brandan, E. (2002). ECM is required for skeletal muscle differentiation independently of muscle regulatory factor expression. *Am. J. Physiology-Cell Physiology* 282, C383–C394. doi:10.1152/ajpcell.00322.2001

Pasini, A., Lovecchio, J., Ferretti, G., and Giordano, E. (2019). Medium perfusion flow improves osteogenic commitment of human stromal cells. *Stem Cells Int.* 2019, 1–10. doi:10.1155/2019/1304194

Persiani, F., Paolini, A., Camilli, D., Mascellari, L., Platone, A., Magenta, A., et al. (2018). Peripheral blood mononuclear cells therapy for treatment of lower limb ischemia in diabetic patients: A single-center experience. *Ann. Vasc. Surg.* 53, 190–196. doi:10.1016/j.avsg.2018.05.036

Pollot, B. E., Rathbone, C. R., Wenke, J. C., and Guda, T. (2018). Natural polymeric hydrogel evaluation for skeletal muscle tissue engineering. *J. Biomed. Mat. Res.* 106, 672–679. doi:10.1002/jbm.b.33859

Rigato, M., Monami, M., and Fadini, G. P. (2017). Autologous cell therapy for peripheral arterial disease: Systematic Review and meta-analysis of randomized, nonrandomized, and noncontrolled studies. *Circ. Res.* 120, 1326–1340. doi:10.1161/CIRCRESAHA.116.309045

Samavedi, S., Poindexter, L. K., Van Dyke, M., and Goldstein, A. S. (2014). "Synthetic biomaterials for regenerative medicine applications," in *Regenerative medicine applications in organ transplantation* (Elsevier), 81–99. doi:10.1016/B978-0-12-398523-1.00007-0

Scala, P., Lovecchio, J., Lamparelli, E. P., Vitolo, R., Giudice, V., Giordano, E., et al. (2022). Myogenic commitment of human stem cells by myoblasts Co-culture: A static vs. a dynamic approach. *Artif. Cells, Nanomedicine, Biotechnol.* 50, 49–58. doi:10.1080/21691401.2022.2039684

Scala, P., Rehak, L., Giudice, V., Ciaglia, E., Puca, A. A., Selleri, C., et al. (2021). Stem cell and macrophage roles in skeletal muscle regenerative medicine. *IJMS* 22, 10867. doi:10.3390/ijms221910867

Shi, Y., Wang, Y., Li, Q., Liu, K., Hou, J., Shao, C., et al. (2018). Immunoregulatory mechanisms of mesenchymal stem and stromal cells in inflammatory diseases. *Nat. Rev. Nephrol.* 14, 493–507. doi:10.1038/s41581-018-0023-5

Spaepen, P., De Boodt, S., Aerts, J.-M., and Sloten, J. V. (2011). "Digital image processing of live/dead staining," in Mammalian cell viability *methods in molecular biology*. Editor M. J. Stoddart (Totowa, NJ: Humana Press), 209–230. doi:10.1007/978-1-61779-108-6_21

Spaltro, G., Straino, S., Gambini, E., Bassetti, B., Persico, L., Zoli, S., et al. (2015). Characterization of the Pall Celeris system as a point-of-care device for therapeutic angiogenesis. *Cytotherapy* 17, 1302–1313. doi:10.1016/j.jcyt.2015.04.006

Sturlan, S., Sachet, M., Baumann, S., Kuznetsova, I., Spittler, A., and Bergmann, M. (2009). Influenza A virus induces an immediate cytotoxic activity in all major subsets of peripheral blood mononuclear cells. *PLoS ONE* 4, e4122. doi:10.1371/journal.pone.0004122

Sun, W., Tiemessen, D. M., Sloff, M., Lammers, R. J., de Mulder, E. L. W., Hilborn, J., et al. (2012). Improving the cell distribution in collagen-coated poly-caprolactone knittings. *Tissue Eng. Part C. Methods* 18, 731–739. doi:10.1089/ten.tec.2011.0593

Tang, H., Husch, J. F. A., Zhang, Y., Jansen, J. A., Yang, F., and Beucken, J. J. J. P. (2019). Coculture with monocytes/macrophages modulates osteogenic differentiation of adipose-derived mesenchymal stromal cells on poly(lactic-co-glycolic) acid/polycaprolactone scaffolds. *J. Tissue Eng. Regen. Med.* 13, 785–798. doi:10.1002/term.2826

Thomson, K. S., Korte, F. S., Giachelli, C. M., Ratner, B. D., Regnier, M., and Scatena, M. (2013). Prevascularized microtemplated fibrin scaffolds for cardiac tissue engineering applications. *Tissue Eng. Part A* 19, 967–977. doi:10.1089/ten.tea.2012.0286

Tidball, J. G. (2017). Regulation of muscle growth and regeneration by the immune system. *Nat. Rev. Immunol.* 17, 165–178. doi:10.1038/nri.2016.150

Tsai, W. L., Vian, L., Giudice, V., Kieltyka, J., Liu, C., Fonseca, V., et al. (2020). High throughput pSTAT signaling profiling by fluorescent cell barcoding and computational analysis. *J. Immunol. Methods* 477, 112667. doi:10.1016/j.jim.2019.112667

Vater, C., Kasten, P., and Stiehler, M. (2011). Culture media for the differentiation of mesenchymal stromal cells. *Acta Biomater.* 7, 463–477. doi:10.1016/j.actbio.2010.07.037

Villalta, S. A., Rinaldi, C., Deng, B., Liu, G., Fedor, B., and Tidball, J. G. (2011). Interleukin-10 reduces the pathology of mdx muscular dystrophy by deactivating M1 macrophages and modulating macrophage phenotype. *Hum. Mol. Genet.* 20, 790–805. doi:10.1093/hmg/ddq523

Witt, R., Weigand, A., Boos, A. M., Cai, A., Dippold, D., Boccaccini, A. R., et al. (2017). Mesenchymal stem cells and myoblast differentiation under HGF and IGF-1 stimulation for 3D skeletal muscle tissue engineering. *BMC Cell Biol.* 18, 15. doi:10.1186/s12860-017-0131-2

Zhang, H., Shao, B., Zhuge, Q., Wang, P., Zheng, C., Huang, W., et al. (2015). Cross-talk between human neural stem/progenitor cells and peripheral blood mononuclear cells in an allogeneic Co-culture model. *PLoS ONE* 10, e0117432. doi:10.1371/journal.pone.0117432

frontiers | Frontiers in Bioengineering and Biotechnology

TYPE Review
PUBLISHED 26 January 2023
DOI 10.3389/fbioe.2023.1076179

OPEN ACCESS

EDITED BY
Chaenyung Cha,
Ulsan National Institute of Science and Technology, South Korea

REVIEWED BY
Sinan Guven,
Dokuz Eylul University, Türkiye
Jenny Robinson,
University of Kansas, United States

*CORRESPONDENCE
Ranjith Kumar Kankala,
ranjithkankala@hqu.edu.cn
Chunyan Duan,
dcyan@fspt.edu.cn

SPECIALTY SECTION
This article was submitted to Biomaterials, a section of the journal Frontiers in Bioengineering and Biotechnology

RECEIVED 21 October 2022
ACCEPTED 06 January 2023
PUBLISHED 26 January 2023

CITATION
Duan C, Yu M, Hu C, Xia H and Kankala RK (2023), Polymeric microcarriers for minimally-invasive cell delivery. *Front. Bioeng. Biotechnol.* 11:1076179. doi: 10.3389/fbioe.2023.1076179

Polymeric microcarriers for minimally-invasive cell delivery

Chunyan Duan[1]*, Mingjia Yu[1], Changji Hu[1], Hongying Xia[2] and Ranjith Kumar Kankala[2]*

[1]School of New Energy and Environmental Protection Engineering, Foshan Polytechnic, Foshan, China, [2]Fujian Provincial Key Laboratory of Biochemical Technology, Institute of Biomaterials and Tissue Engineering, College of Chemical Engineering, Huaqiao University, Xiamen, China

Tissue engineering (TE) aims at restoring tissue defects by applying the three-dimensional (3D) biomimetic pre-formed scaffolds to restore, maintain, and enhance tissue growth. Broadly speaking, this approach has created a potential impact in anticipating organ-building, which could reduce the need for organ replacement therapy. However, the implantation of such cell-laden biomimetic constructs based on substantial open surgeries often results in severe inflammatory reactions at the incision site, leading to the generation of a harsh adverse environment where cell survival is low. To overcome such limitations, micro-sized injectable modularized units based on various biofabrication approaches as ideal delivery vehicles for cells and various growth factors have garnered compelling interest owing to their minimally-invasive nature, ease of packing cells, and improved cell retention efficacy. Several advancements have been made in fabricating various 3D biomimetic microscale carriers for cell delivery applications. In this review, we explicitly discuss the progress of the microscale cell carriers that potentially pushed the borders of TE, highlighting their design, ability to deliver cells and substantial tissue growth *in situ* and *in vivo* from different viewpoints of materials chemistry and biology. Finally, we summarize the perspectives highlighting current challenges and expanding opportunities of these innovative carriers.

KEYWORDS

tissue engineering, minimally-invasive, microfluidic technology, polymeric carriers, injectable architectures

1 Introduction

Despite the sophisticated surgical reconstruction procedures costing billions of dollars, end-stage organ failure or tissue loss is bothering each year, resulting in millions of deaths. In addition, the shortage of donors for organ replacement healing worsens the problem (Langer and Vacanti, 1993). Although the life span is prolonged to some extent, the currently available solutions remain imperfect in treating these tissue defects. Moreover, these surgical reconstruction procedures using various techniques, such as mechanical devices, often lead to long-term problems and, eventually, deterioration (Santana et al., 2020). Over the decades, several efforts in developing diverse, innovative technologies for next-generation medical treatments have continued to rise.

Recently, tissue engineering (TE) and regenerative medicine (RM) fields have garnered captivating interest owing to their promising potential for repairing tissue defects ensuing from chronic infections and aging (Langer and Vacanti, 1993). Conceptually, this innovative biomedical field assimilates several disciplines, including chemistry, engineering, biology, and material science, to fabricate arbitrary-sized three-dimensional (3D) biomimetic tissue constructs with enriched performance. These fabricated systems can reinstate the structure and function of the malfunctioned tissues, considering the homeostasis regulation, physiochemical

factors, and biochemical cues required for tissue growth (Kankala et al., 2017; Kankala et al., 2018a). Moreover, the fabrication of such complex physiological systems requires accumulated knowledge on the deepened understanding of tissue-specific microenvironments as well as various dynamic structural organizations, involving cell-matrix-based biophysical and biochemical interactions, as well as cell-cell crosstalk using the intercellular components (integrin, selectin, and other cell adhesion molecules and extracellular matrix, ECM, proteins), among others (Li et al., 2015; Jiang et al., 2016). Intriguingly, this area of research has already shown promising outcomes acting against diabetes, cancer, skin burns, osteoarthritis, cardiovascular conditions, congenital disabilities, injured tissue sections, and tumor resections (Leijten et al., 2016).

In past decade, efforts have been dedicated to develop engineered implantable scaffolds mimicking the anatomical and physiological aspects of the tissue microenvironment, ranging from the organ stage to the tissue and cellular levels (Liu et al., 2019). Along this line, several scaffolding systems that could emulate the native counterparts have been fabricated, such as photo-cross-linkable hydrogels, biodegradable porous scaffolds, and nano/microfibrous biocompatible materials (Martin et al., 2004; Asakawa et al., 2010). Considering the highly organized complexity in both areas of cell surfaces and intracellularly, further advancements on the nanoscale have also been made by researchers in search of innovative nano-sized components to augment the intrinsic performance of large-sized scaffolds (Kankala et al., 2018a). Compared to the implantable bulk scaffolds, these 3D scaffolding systems combining the micro- and nano-sized components play pivotal roles in repairing the malfunctioned tissues and offering efficient control over the microenvironment for cell and tissue growth (Ferrari et al., 1998; Kankala et al., 2018a). These injectable biomaterials present a new era of minimally-invasive therapeutics, representing the delivery of biologics, drugs, and other bioactives. To solve tissue defects or fill the irregularities in the tissues, the micro-sized carriers can encapsulate cells in their interiors and deliver them appropriately in the region of interest towards improved cell proliferation and subsequent tissue growth. Various kinds of microcarriers for cell delivery have been fabricated, depending on porosity (porous and non-porous/solid microcarriers) and texture (rigid and soft), among others. Compared to bulk scaffolds, these microcarriers offer several advantages, such as enhanced cell encapsulation and retention efficiencies, improved cell proliferation in the interiors, and minimally invasiveness, among others (Van Wezel, 1967; Khademhosseini et al., 2006; Jiang et al., 2016). Although the design of microcarriers for cell delivery is successful, it should be noted that several factors, such as porosity, cell retention efficacy, and administration route, play predominant roles in the success of these minimally-invasive cell carriers for TE (Khademhosseini et al., 2006). These modular units for minimally-invasive delivery of cells have been developed for various organs in the body, such as hepatic (Liu et al., 2014), bone (Ligorio et al., 2019), chondral (Malda et al., 2003), muscle (Kankala et al., 2019) skin (Gualeni et al., 2018), and neural (Jeon et al., 2021) among others (Langer and Vacanti, 1993; Hollister, 2005; Khademhosseini et al., 2006; Bhatia and Ingber, 2014; Wang et al., 2018). In addition to the regeneration of various tissues, these modular units for TE can be applied to repair various tissues, including congenital disabilities, deep-cut injuries, and areas of tumor resections, among others.

Although reviews have been published on exploring the potential of TE, (Khademhosseini et al., 2006; Bhatia and Ingber, 2014; Li et al., 2015; Kankala et al., 2018b; Li et al., 2018) only a few are focused on the utilization of functional micro- as well as nano-sized constructs as minimally-invasive cell delivery vehicles towards repairing the malfunctioned tissues either through facilitating the natural ECM-like environment and drug delivery characteristics. Motivated by these considerations, in this compilation, herein we give a comprehensive overview of the microarchitectures for minimally-invasive cell delivery towards the growth of various tissues and substantial enrichment of molecular cues in guiding vascularization and nerve innervation processes. Initially, we emphasize the significance and classification of microarchitectures towards cell delivery, highlighting their importance compared to the bulk scaffolds and non-scaffolds-based designs for TE (Figure 1). Then, we highlight various engineering strategies utilized to fabricate various carriers for cell delivery applications. Further, we emphasize various micro-sized carriers for cell delivery and factors affecting their performance efficiency. Finally, a note on the applicability of these carriers to different engineering tissues is emphasized.

2 Significance of microarchitectures

Over the past few decades, tremendous efforts have resulted in fabricating various artificial tissue constructs using biomaterials based on organic and inorganic-based materials for tissue regeneration (Braccini et al., 2020). In addition to tissue growth, these biomaterials can be applied for vascularization and nerve innervation, improving the tissue repair efficiency of these implanted scaffolds (Langer and Vacanti, 1993). To mimic the natural tissues, further advancements in various tremendous technologies have been evidenced in the generation of highly organized artificial 3D constructs composed of different cell types, ECM, and numerous signaling cues (Liu et al., 2019). Along this line, various scaffold-free and scaffold-based designs have been utilized for replicating the natural constituents of human tissues (Song et al., 2017). On the one hand, scaffold-free cell-rich architectures have been developed by generating 3D cell aggregates for TE (Lee et al., 2007). Notably, these 3D cell aggregates replicate the native tissue environment, in terms of hypoxia, pH, protein expressions, cell-cell interactions, and growth factor profiling, among others (Lu and Stenzel, 2018; Zanoni et al., 2019). These cellular blocks are also estimated to be programmed hierarchical assemblies with a precise design toward organ-like structures. It should be noted that the assembly of cell aggregates reduces the possible risk factors of cell-based therapies and guide cellular differentiation (Kankala et al., 2018b). Despite the advantages of replicating the natural intricacies, these cell-based aggregates are often loosely bound, lacking the critical components of cell-ECM interactions (integrins, cadherins, and selectins-ECM proteins), heterogeneity in sizes, and growth trends (Kankala et al., 2019). Moreover, the cells in the interior of the spheroids may suffer from a deprived survival rate due to hypoxia conditions and lack the vascularization, limiting their applicability in TE. In addition, the hierarchical assembly of the cells as tissue organization and biomimetic designs may certainly limit somatic mutations (Khademhosseini and Langer, 2016). On the other hand, scaffold-based architectures have been developed to address the limitations mentioned above of scaffold-free architectures (Hollister, 2005). These scaffolding materials from

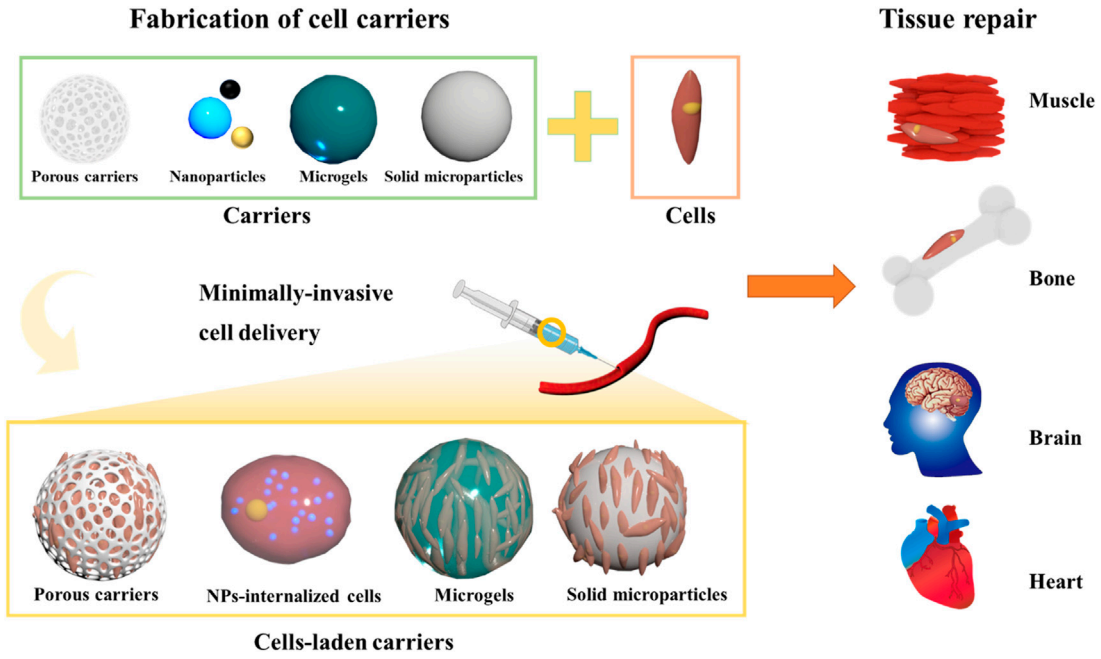

FIGURE 1
Schematic illustrating several kinds of 3D microcarriers for cell delivery applications.

biodegradable polymeric materials support bulk materials for improving adhesion and substantial tissue growth (Choi et al., 2012). Various solid architectures, including photo-cross-linkable hydrogels, biodegradable scaffolding systems, and nano/microfibrous biocompatible constructs, have been developed (Martin et al., 2004; Asakawa et al., 2010; Choi et al., 2012). The regulated interplay and the intricately controlled crosstalk between the materials and the biological components played substantial roles in TE and RM toward tissue growth (Khademhosseini and Langer, 2016). However, various key attributes, such as growth factors and their precise actions, would play the predominant role in cell proliferation, requiring them in the engineered constructs in *ex-vivo* and *in vivo* (Kankala et al., 2018a; Braccini et al., 2020). Despite the success, the large-sized scaffolds require sophisticated, highly invasive surgical procedures, leaving a scar (Wei et al., 2018). These surgical incisions result in a substantial generation of inflammatory reactions resulting in a harsh environment, where the survival of cells in the implanted scaffolds remains low (Kankala et al., 2019).

Various biofabrication approaches have been developed to generate micron-sized templates, which could be convenient for minimally-invasive delivery with improved cell adhesion and tissue growth trends to address the limitations (Wei et al., 2018). Indeed, these micron-sized carriers, with an average size ranging from 1 to 1,000 μm, offer various advantages of widespread encapsulation and carrying abilities, biodegradability, and biocompatibility for various biomedical applications (Li et al., 2015; Jiang et al., 2016; Khademhosseini and Langer, 2016; Kankala et al., 2018b; Imai et al., 2018; Li et al., 2018; Liu et al., 2019; Santana et al., 2020). Since, ever the first report on encapsulation of mammal cells in diethyl aminoethyl (DEAE)-Sephadex A50 from Van Wezel (1967), several efforts resulted in diverse varieties of microengineered 3D architectures for encapsulating cells and their subsequent *ex-vivo* expansion (Khademhosseini et al., 2006; Li et al., 2015; Jiang et al., 2016; Santana et al., 2020). These 3D structures offer several benefits, such as high surface area, efficient monitoring, and a convenient supply of nutrients (Li et al., 2018). Despite the advantages, several other notable factors depend on the successful adhesion and growth of cells, such as chemical nature and compatibility, physical characteristics, surface properties, and porosity (Hollister, 2005). Indeed, material compatibility is often influenced by the applied substrates' chemical composition. In most instances, biocompatible polymers from natural (chitosan, dextran, gelatin, and alginic acid) (Bae et al., 2006; Huang et al., 2018; Chen et al., 2015) and synthetic [poly(lactic-*co*-glycolic acid, PLGA, polyurethane, polylactic acid, PLA, polycaprolactone, PCL, polyhydroxyalkanoate (PHA), polystyrene, polyhydroxylethyl methacrylate, PHEMA, and polyacrylamide] (Liu et al., 2011; Kim et al., 2016; Kankala et al., 2019) origins are often applied to generate 3D microarchitectures. The critical morphological characteristics (size and shape) play significant roles in designing these architectures, facilitating improved encapsulation, convenient administration, and delivery efficiencies (Li et al., 2018). In general, microcarriers with a spherical shape and an average size of 100–500 μm would facilitate the encapsulation of numerous cells, avoiding cell necrosis in their interiors (Hong et al., 2005; Wei et al., 2018). In addition to chemical nature and physical characteristics, surface texture and porosity are other significant features that play crucial roles in the encapsulation efficiency of diverse cell types (Wei et al., 2018). Initially, the fabricated biocompatible solid microspheres with a rough surface and tiny pores have shown improved adhesion efficiency on the surface compared to

TABLE 1 Summary of various cell-laden carriers for minimally-invasive delivery of cells for tissue repair and regeneration purposes.

Design	Material	Micro-engineering strategy	Delivered cell type	Size	Targeted site	Outcome	References
Solidified PMs	PLGA	Microfluidics	Skeletal myoblasts	280–370 μm	Skeletal muscle	These microcarriers improved cell retention and vascularization and partial myoblast differentiation in mice	Kankala et al. (2019)
	Alginate-gelatin microspheres	Electrospray	Adipose-derived stem cells (ADSCs)	360 μm	Knee cartilage	Microspheres increased the viability of ADSCs and supported their proliferation and deposition of cartilage matrix	Liao et al. (2022)
	Collagen-Poly-lactide (PLA)	Emulsion-solvent evaporation	Chondrocyte	180–280 μm	Cartilage	The larger amount of collagen on these PLA microspheres could attach, proliferate and spread chondrocytes	Hong et al. (2005)
	Polycaprolactone (PCL)	Molding	Neural progenitor cells	244–601 μm	Brain	PC-12 cells attached to microspheres were populated within their macropores, applicable for neuron TE.	Kim et al. (2016)
	Polyhydroxyalkanoate (PHA)	Double emulsification	human bone marrow mesenchymal stem cells (BMMSCs)	300–360 μm	Defect tissues	PHA OPMs protected cells against stresses during injection, allowing more living cells to proliferate and migrate to damaged tissues	Wei et al. (2018)
	Calcium-alginate	Freeze-drying	Osteoblasts	5 mm * 5 mm (2D)	Bone	This system preserved the cell proliferation and upregulated bone-related gene expression towards skeletal defects	Chen et al. (2015)
	Star-shaped PLA	Self-assembly	Chondrocytes	60 μm	Knee repair	The nanofibrous hollow microspheres achieved better cartilage repair than chondrocytes-alone	Liu et al. (2011)
	Gelatin methacryloyl (GelMA)-alginate core-shell microcapsules	Co-axial electrostatic microdroplet	HDPSCs and HUVECs	~359 μm	Tooth	Microvessel formation and pulp-like tissue regeneration occurred in the co-culture group toward endodontic regeneration	Liang et al. (2022)
	PCL–gelatin	Electrospinning and electrospraying	Rat BMMSCs	125–200 μm	Bone marrow	The microspheres improved the viability and maintenance of stem cells for cell therapy	Boda et al. (2018)
	Methacrylated hyaluronic acid (HA) and N-vinylpyrrolidone	Photopolymerization	Bovine articular chondrocytes	2.5–2.9 mm	Repairing tissue defects	HA hydrogel beads could be used as injectable cell delivery vehicles	Bae et al. (2006)
	PCL	Isolated particle-melting method and melt-molding particulate-leaching	Chondrocytes	400–550 μm	Cell delivery	The PCL microscaffolds showed biocompatibility and infiltration of cells for cell delivery applications	Lim et al. (2009)

(Continued on following page)

TABLE 1 (*Continued*) Summary of various cell-laden carriers for minimally-invasive delivery of cells for tissue repair and regeneration purposes.

Design	Material	Micro-engineering strategy	Delivered cell type	Size	Targeted site	Outcome	References
	Sodium alginate (SA)/ TOCNF and β-Tricalcium phosphate	Droplet extrusion-crosslinking technique	MC3T3-E1	1.25 mm	Bone	The prepared microspheres showed significantly better bone formation in a rabbit model than in the control group	Ho et al. (2020)
	Silk fibroin/gelatin (SF/G)	Self-assembly	Rat MSCs	300–400 μm	Bone	SF/G microcarriers supported the adhesion of rat MSCs with high efficiency under dynamic culture	Luetchford et al. (2020)
	Acrylic acid onto plasma-treated poly(ethylene terephthalate)	Graft polymerization	Smooth muscle cells	—	Smooth muscle cells	Collagen-immobilized surfaces increased the surface area and subsequent substrate for cell seeding	Gupta et al. (2002)
	Flexible wood membrane	Chemical treatment	HEK293 cells	—	Surgical practices	The extracted material based on flexible wood could be used as a 3D bioscaffold	Song et al. (2017)
	Alginate	Chemical cross-linking	HepG2	90–900 μm	Cell delivery	These scaffolds supported the expansion of HepG2 and maintained the albumin secretion function	Li et al. (2014)
	Chitosan	Emulsion-based thermal-induced phase separation	Hepatocyte	150 μm	3D cell culture	The biocompatibility and porous structure attributes resulted in the high performance of hepatocyte culture.	Huang et al. (2018)
Microgels	Magnetic microcryogels based on gelatin and Poly(ethylene glycol) diacrylate (PEGDA)	Cryogelation and micro-molding	HepaRG	400 μm	Hepatic	The robust, controllable, and magnetic resonance imaging (MRI) traceable magnetic microtissues are provided to solve multiple critical issues in TE and RM.	Liu et al. (2014)
	Graphene oxide (GO)-β-sheet forming self-assembling peptide hydrogels	Hybrid injectable 3D scaffolds	Nucleus pulposus cells	—	Intervertebral disc (IVD)	These hybrid hydrogels promoted high cell viability and retained cell metabolic activity for IVD degeneration	Ligorio et al. (2019)
	Microscale alginate beads-thermosensitive hydrogel	Electrospray	MSCs	>200 μm	Skin	The arrangement of collagen fibrils and high angiogenesis confirmed the wound-healing process of the hydrogel	Nilforoushzadeh et al. (2020)
	Modified gelatin matrix with PLA-co-trimethyl carbonate [P(DLLA-co-TMC)]	UV Crosslinking	Embryonic stem cells (ESCs)	Gels	Spinal cord injury	The ESCs-loaded composite hydrogels are identified to enhance tissue regeneration and motor function significantly	Wang et al. (2018)

(Continued on following page)

TABLE 1 (*Continued*) Summary of various cell-laden carriers for minimally-invasive delivery of cells for tissue repair and regeneration purposes.

Design	Material	Micro-engineering strategy	Delivered cell type	Size	Targeted site	Outcome	References
	Quaternized β-Chitin (QC) and oxidized dextran (OD)	Schiff base reaction	NIH-3T3 and mouse BMMSCs	Gels	3D culture	These gels act as antibacterial vehicles for delivering cells toward RM, drug/gene/cell delivery, and cell therapy	Xu et al. (2019)
	Poly(lactide-co-glycolide)-b-poly(ethylene glycol)-b-poly(lactide-co-glycolide) and clay nanosheets	Self-assembly	L929 cells	Gels	—	These gels with appropriate compatibility features and textural attributes could be used as injectable cell delivery carriers	Oyama et al. (2014)
	Keratin allyl thioether biopolymer	Photo-crosslinking	hMSCs	Gels	Bone and cartilage	The keratin allyl thioether hydrogel with controllable degradation could act as a viable matrix for encapsulation and delivery of stem cells for tissue repair	Barati et al. (2017)
	PLGA-chitosan/PLGA-alginate	Self-assembly homogenization	Human umbilical cord mesenchymal stem cells (hUCMSCs)	Gels	TE and drug release	These biodegradable colloidal gels could act as injectable scaffolds for tissue repair	Wang et al. (2011)
Cells internalized with micro/nanocarriers	Superparamagnetic iron oxide nanoparticles	Poly-L-lysine- surface modified	Human nasal turbinate stem cells	Iron oxide: 15–30 nm	Brain	The intranasal administration of cells internalized with nanocarriers could effectively treat CNS disorders	Jeon et al. (2021)

the microspheres with smooth surfaces due to the improved and non-slippery interactions between the cells and microcarriers (Matsushita, 2020). Although the rough surfaces provide improved adhesion of cells, these solid microcarriers suffer from a significant limitation of low encapsulation yields due to less surface area (Choi et al., 2012). To overcome this limitation, several biofabrication approaches have been explored in the generation of porous microspheres (PMs) and their highly open prototype with controlled structure and porosity. These microarchitectures with high surface area, heterogeneous porosity in the range of 10–100 μm, and interconnected windows subsequently facilitate a series of events, such as the adhesion of cells initially on the surface and improved migration to the interiors through the pores (Wei et al., 2018). In addition, the abundant porosity of the biocompatible carriers enables the interchange of gases and nutrients, facilitating improved viability and proliferation efficiencies of the harbored cells in the interiors (Choi et al., 2012). The material characteristics and the cellularized secretions can generate and mimic the ECM-like environment (Hollister, 2005). Nonetheless, several biochemical cues and the desired architectures are required as a significant prerequisite for TE to substantially control the microenvironment. Considerably, the combination of polymers from both natural and synthetic origins can be applied to improving the compatibility, increasing the biochemical cues, and varying the mechanical properties of the 3D microcarriers (Pradhan et al., 2017).

3 Classification of cell carriers

Broadly speaking, the cell delivery microcarriers can be categorized into two major classes based on the arrangement of cells and the size constraints, such as cells-encapsulated microcarriers and cells internalized with micro/nanocarriers (Hafeman et al., 2008; Xu et al., 2019). The cells-laden microcarriers are often based on polymeric microarchitectures, referred to as the large-sized carriers in which the cells can be accommodated. On the one hand, considering the structural attributes, these micro-sized carriers can be further classified into solid (non-porous/porous) microparticles and liquid-rich micro-sized gels (Oyama et al., 2014; Wei et al., 2018). On the other hand, the sub-micro-sized particles can be utilized to improve the delivery of cells to the target tissue for tissue repair. In this section, we present an overview of these cell carriers (Table 1), highlighting the emphasis on encapsulation and delivery efficacies of cells from their interiors to the target organs for tissue repair.

3.1 Solid (non-porous/porous) microcarriers

By employing different microfabrication approaches, diverse varieties of microcarriers have been generated towards engineering various tissue defects, such as bone (Chen et al., 2015), muscle (Kankala et al., 2019), dental (Liang et al., 2022), cartilage (Hong et al., 2005), brain (Kim et al., 2016), and hepatocytes (Huang et al.,

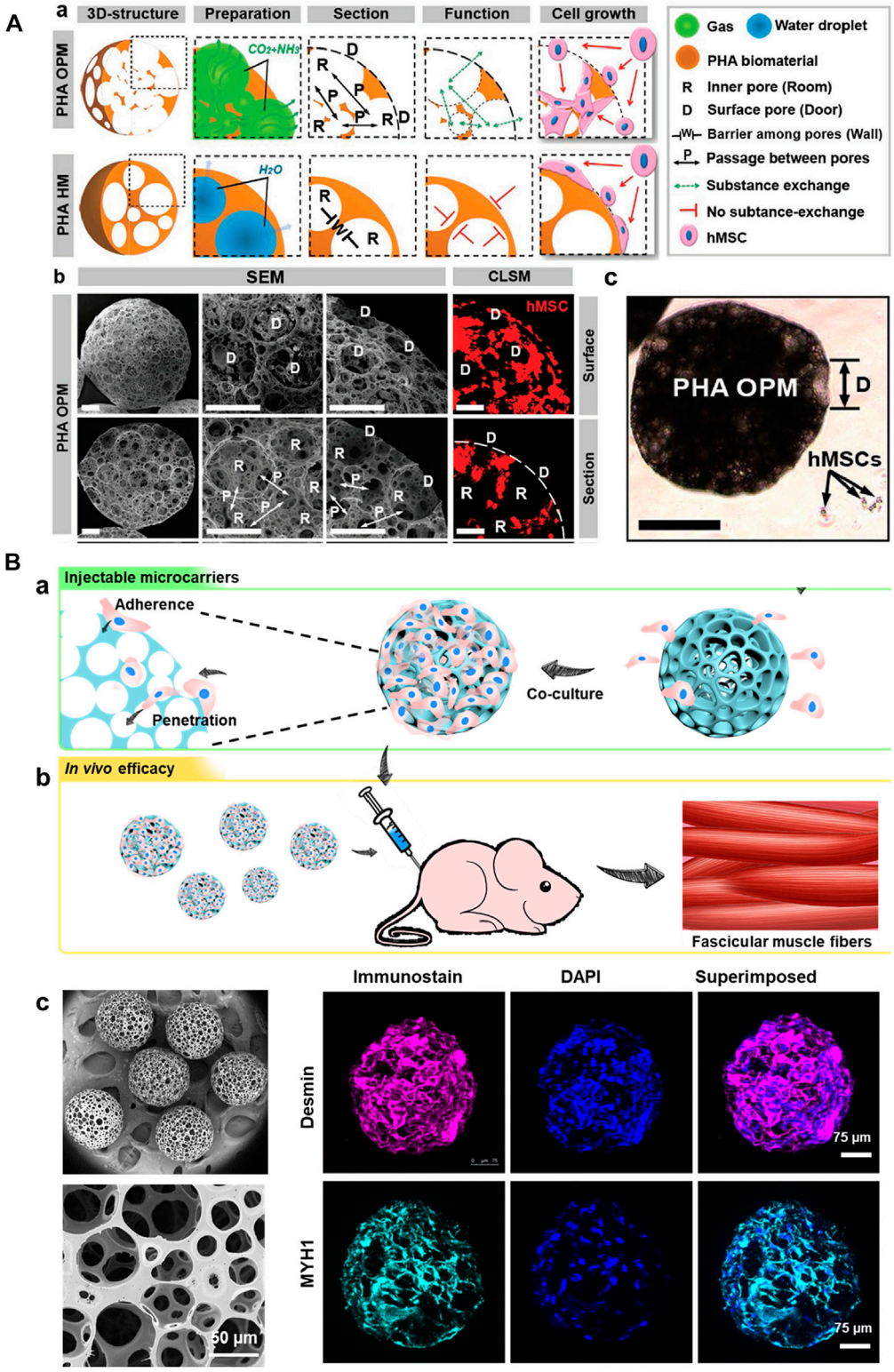

FIGURE 2
(A) Structures of PHA highly open PMs (PHA OPMs) and traditional PHA hollow microspheres (PHA HMs), respectively. a) Illustrations of PHA OPM and HM, including 3D structures, preparation, section, functions, and cell growth. b) SEM images of surfaces and sections of PHA OPM and confocal laser scanning microscopy (CLSM) images of hMSCs adhered to PHA HOPM. The bars are 50 μm. The actin of hMSC is stained in red. D: surface pore (door); R: inner pore (room); P: passage; and W: barrier among pores (wall). c) Sizes of hMSCs digested with trypsin versus a PHA HOPM. The bar is 150 μm. D: surface pore (door). Reproduced with permission from Ref. (Wei et al., 2018). Copyright 2018, John Wiley & Sons. **(B)** a) Schematic illustration showing the fabrication of modular cell-laden HOPMs by populating the C2C12 cells on the microcarriers *in vitro*, and b) evaluating their performance *in vivo* after administering these cell-laden HOPMs in nude mice. c) SEM images showing the size distribution of PLGA HOPMs, and surface morphology of a microcarrier as well as immunohistological analysis of myoblasts in the PLGA HOPMs by staining them against desmin and MYH1 (counterstained by DAPI for nuclei) for 7 days. Reproduced with permission from Ref. (Kankala et al., 2019), Copyright 2019, John Wiley & Sons.

2018) among others (Bae et al., 2006). Considering the porosity, these solid microcarriers can be classified into non-porous and porous carriers. The former type possesses no substantial pores on their surfaces but with micro-sized pores. In contrast, the latter carrier contains highly-open pores with interconnecting windows. These microcarriers present improved adhesion and subsequent carrying ability of diverse cell types, as well as cell proliferation and growth abilities on their surfaces and interiors (Almería et al., 2010). Comparatively, the open porous microcarriers facilitate more viability of cells in terms of encapsulation and delivery efficacies compared to the non-porous type. Nevertheless, the non-porous microcarriers with tiny pores intuitively allow the cells to adhere to their surfaces, facilitating improved delivery efficacy (Li et al., 2014; Akamatsu et al., 2018). These microcarriers also offer advantages, such as ease of fabrication and validation, biodegradability, biocompatibility, and cost-effectiveness (Choi et al., 2012).

In this context, various hydrophilic polymers, including PLGA, PHA, and PCL, among others, have been employed to generate these solidified microarchitectures (Hafeman et al., 2008; Wei et al., 2018; Liao et al., 2022). These solidified microparticles offer advantages of compatibility, excellent textural properties, and stability (thermal, colloidal, and suspension), which are of particular interest for minimally-invasive cell delivery towards TE applications (Hafeman et al., 2008; Jiang et al., 2016). The highly porous structures would substantially offer predominant encapsulation and proliferation abilities, leading to the subsequent convenience for their delivery in the injectable location (Wei et al., 2018). In a case, PHA-based open PMs (OPMs) with an average diameter of 300–360 μm were generated to avoid open surgery (Figure 2A) (Wei et al., 2018). These minimally-invasive scaffolding systems harbored with the proliferating stem cells (human mesenchymal stem cells, hMSCs) showed cell adhesion (93.4%) and proliferation efficiencies to repair the tissue defects. Compared with the PLA-based and hollow microcarriers, these PHA-based OPMs presented improved tissue restoration ability towards osteogenic regeneration. These PHA-based OPMs substantially presented the adhesion and encapsulation of skeletal myoblasts, indicating exceptional proliferation efficacy *in vitro* and regeneration capacity *in vivo*. In another instance, we generated PLGA-based microcarriers using the microfluidic approach in a two-step process for skeletal muscle cell delivery (Figure 2B) (Kankala et al., 2019). The resultant gelatin-assisted highly porous microcarriers based on PLGA enabled subsequent adhesion and infiltration of myoblasts in a more significant number. Then, immunohistochemical staining was performed using the myogenesis-specific biomarkers (myosin heavy chain (MYH) 1 and desmin). Finally, the subsequent delivery of myoblasts from the PLGA carriers resulted in tissue regeneration ability *in vivo*.

Although these solid microcarriers with porous connectivity in their interiors facilitate enough room for cell adhesion, infiltration, and proliferation, cells require certain additional supplements of biophysical and biochemical cues, such as growth factors and specific adhesion molecules (integrins, cadherins, and selectins)-ECM proteins (for example, fibronectin), to mimic the natural ECM-like microenvironment (Kim et al., 2015). In addition, strict utilization of hydrophilic polymers would substantially enable improved biocompatibility for cell adhesion and proliferation abilities for tissue repair and drug screening applications. For example, Li et al. (2014) reported the generation of alginate microspheres using the microemulsion and freeze-drying approaches. These microcarriers with anarchic microporous cavities on their surfaces resulted in the encapsulation of human hepatocellular carcinoma cells.

3.2 Micro-sized hydrogels

Due to advantageous hydrophilicity and ECM-mimicking features, micro-sized hydrogels have garnered interest from researchers in the delivery and recruitment of cells to promote TE (Bidarra et al., 2014; Oyama et al., 2014). Although similar to microparticles in terms of morphology, these water-rich gels with a 3D hydrophilic network, biocompatibility, and reactive chemistries make them appropriate for TE applications. These micro-sized hydrogels with polymeric building blocks are preferred over the solidified microparticles due to their tailorable physicochemical properties and similar ECM-like architecture (Bae et al., 2006). These building blocks are often engineered by crosslinking using various chemical reactions or physical interactions, forming the hydrogel in the presence of cells and proteins either during the fabrication or *in situ*. In addition to incorporating biological functionalities for modulating hydrogel properties, the ease of tailoring ability enables their applicability in the delivery of cells (Lavanya et al., 2020). Notably, the dimensions of hydrogels play a crucial role in the encapsulation of cells in their liquid environment, which, however, is often dependent on the engineering strategy and application requirements. Typically, the ideal size of the micro-sized gels should be around 200 μm in diameter with a volume of 1.0 nL to rapidly deliver gases and nutrients and excreting metabolic waste (Sheikhi et al., 2019).

Many polymers have been applied as building blocks to fabricate these polymeric injectable hydrogels. The compatibility and reaction chemistry attributes are crucial in selecting an appropriate polymer source as a building block. In addition, other specific criteria include crosslinking and subsequent degradability in the physiological fluids, as well as biochemical properties to facilitate cell growth. In this context, hydrophilic polymers are often preferred from natural and synthetic sources. The former type is derived from tissues or other natural origins, and the latter type is referred to as synthetic components attained through organic reactions (Velasco et al., 2012). The natural polymers for synthetic hydrogels include chitosan, hyaluronic acid (HA), keratin, heparin, fibrin, collagen, chondroitin sulfate, and alginate (Bidarra et al., 2014; Lavanya et al., 2020). These natural building blocks offer to replicate the native environment, including the mechanical and biochemical cues. Considering these aspects, the natural microgels offer advantages under mild conditions for minimally-invasive cell delivery towards RM (Wang et al., 2018). In a case, Kim and coworkers generated an alginate hydrogel system with a degradability attribute to encapsulate human adipose stem cells (hASCs) for engineering adipose tissues. Notably, the alginate was oxidized to improve the degradability and modified with the integrin-binding peptide (G4RGDASSKY) sequence to promote cell adhesion towards attaining cell-ECM interactions. These injectable hydrogels provided a suitable environment for cell growth and delivery for preconditioned cryopreserved hASCs to engineer adipose tissue. In another case, young and colleagues fabricated HA-based hydrogels for controlled survival, delivery, and differentiation of mouse retinal

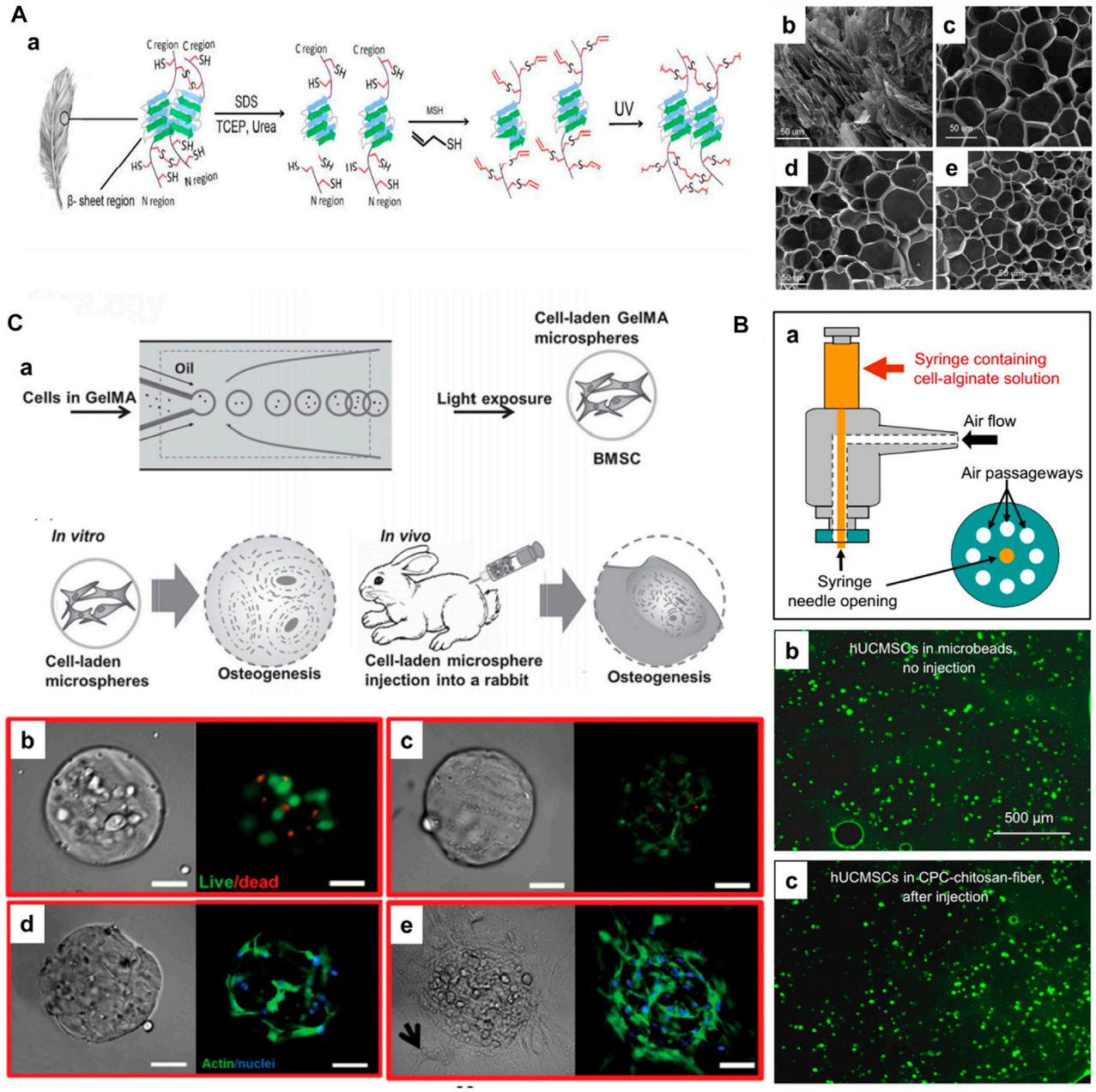

FIGURE 3
(A) a) Schematic illustrating the extraction of keratin and subsequent processing steps for preparing photocrosslinkable keratin hydrogels for stem cell encapsulation. SEM images of freeze-dried KeratATE precursor solution before ultraviolet (UV) crosslinking (b, 25 wt%) and after crosslinking with KeratATE concentrations of 15 (c), 20 (d), and 25 (e) wt% (scale bar in b–e is 50 μm). Reproduced with permission from Ref. (Barati et al., 2017), Copyright 2017, American chemical Society. **(B)** Schematic of the human umbilical cord MSCs (hUCMSCs)-encapsulating microbead synthesizer. hUCMSCs viability without injection or after injection. (b) hUCMSCs in microbeads (without CPC, without injection). (c) hUCMSCs in microbeads after mixing with CPC-chitosan-fiber paste and after injection. Reproduced with permission from Ref. (Zhao et al., 2010), Copyright 2010, Elsevier. **(C)** a) Schematic diagram of fabrication of BMSCs-laden gelatin methacryloyl (GelMA) microspheres and its application for osteogenesis and regeneration of injured bones. Photocrosslinking-microfluidic fabrication of GelMA microspheres and their encapsulated BMSCs differentiation and regeneration of bone *in vitro* and *in vivo*. Viability, spreading, and proliferation of BMSCs encapsulated in GelMA microspheres. b, c) Viability of BMSCs encapsulated in GelMA after b) 1 and c) 7 d of culture. Live (green) cells are labeled with calcein AM, and dead (red) cells are labeled with ethidium homodimer. d, e) Phalloidin/DAPI images of BMSCs cultured in GelMA after d) 2 and e) 4 weeks. Phalloidin stains cell filament green, and DAPI stains cell nuclei blue. Scale bar = 100 μm. Reproduced with permission from Ref. (Zhao et al., 2016), Copyright 2016, John Wiley & Sons.

progenitor cells (Liu et al., 2013). The designed hydrogels were viscous, resulting in the ideal properties for transplanting and promoting the self-renewal and differentiation of retinal progenitor cells for retinal repair.

Some natural hydrogels are functionalized to improve their cell-attachment motif (for example, keratin) and regulate the degradation (Du et al., 2015). In a case, Jabbari and colleagues demonstrated the generation of photocrosslinkable feather barbs keratin-based

biopolymer for stem cell delivery towards tissue regeneration (Figure 3A-a) (Barati et al., 2017). Initially, the disulfide bonds were reduced in the extracted keratin from feather barbs. Then, the free thiols were converted to dehydrooalanine by oxidation and s-allyl cysteine in the presence of allyl mercaptan, resulting in the keratin allyl thioether (KeratATE) biopolymer. These biopolymeric honeycomb-like porous microgels with improved mechanical properties in the range of 1–8 kPa depending on the KeratATE concentration, resulted in the encapsulation and delivery of hMSCs, which turned out to be elongated spindle-shaped morphology after seeding into scaffolds (Figure 3A-b–e). These hydrogels showed improved proliferation of hMSCs, further supporting their differentiation to osteogenic and chondrogenic lineages. In another instance, Burdick and coworkers modified HA with aldehyde and hydrazine functional groups, enabling the modulation of myofibroblasts (Purcell et al., 2014).

To this end, the synthetic polymers for fabricating injectable hydrogels include poly(ethylene glycol), poly(vinyl alcohol) (PVA), poly(N-isopropyl acrylamide) (PNIPAAm), PEG, and PCL, among others, due to their low batch-to-batch variation, commercial availability, and ease of chemical modification, leading to controllable mechanical properties. Several synthetic polymers suffer from a major disadvantage of lack of inert biochemical cues. Among various synthetic polymers, PEG is one of the widely applied synthetic building blocks. PEG offers the major advantage of being relatively inert for introducing specific bioactive groups, for instance, modulating interactions with the cells through conjugating with acrylates or maleimides. In an instance, Phelps and coworkers generated PEG-maleimide matrices through maleimide cross-linking chemistry and peptides functionalized with thiols (Phelps et al., 2012). These hydrogels improved the viability of progenitor cells and promoted their spreading. Nevertheless, synthetic and natural polymers have been combined to improve the inherent biochemical cues toward improved cell interactions (Headen et al., 2014; Wieduwild et al., 2015; Wang et al., 2020).

In addition to chemical crosslinking, as evidenced in the aforementioned studies, physical crosslinking-based injectable hydrogels have been generated using various ionic, hydrogen bonding, and hydrophobic interactions, among others (Wang and Heilshorn, 2015). The most commonly used physical crosslinking-based injectable hydrogels are generated using ion- and/or temperature-induced gelation (Agarwal et al., 2013). Notably, synthetic polymers containing carboxylic acids, alcohols, and other side chains are often preferred (Du et al., 2015). In a case, Xu and colleagues generated alginate-based injectable hydrogels for encapsulating the human umbilical cord MSCs (hUCMSCs) for bone TE (Figure 3B) (Zhao et al., 2010). In another case, Sa-Lima and coworkers generated thermoresponsive PNIPAAm-g-methylcellulose (PNIPAAm-g-MC) as a 3D support for articular cartilage regeneration. Wang et al. (2017) demonstrated the covalently adjustable hybrid hydrogels based on the elastin-like protein–HA (ELP–HA) derivatives with secondary thermoresponsive crosslinking for minimally invasive delivery of stem cells. The combination of aldehyde-modified HA and hydrazine-modified ELP promoted improved mechanical properties (tuning the stiffness of the network in the range of 50–5,000 Pa) and substantially encapsulated MSCs for their delivery. Similarly, photo-crosslinking has garnered interest in TE and RM applications. The classic example of photocrosslinking of hydrogels includes the modification of gelatin with methacryloyl substituents, referred to as gelatin methacryloyl (GelMA), in the presence of light and photoinitiator. Gelatin, with abundant hydration properties and compatibility due to arginine–glycine–aspartic acid (RGD) residues, facilitate natural interactions with the cells and tissues. To improve the mechanical strength and gelation at physiological temperatures, the derivatization of gelatin to GelMA due to the photo-crosslinking property forms covalent links in the presence of a photoinitiator (Irgacure-2959). Notably, the degree of methacrylation can be regulated by controlling the amount of methacrylic anhydride. Owing to its considerable compatibility and controllable physicochemical properties, GelMA can be applied in TE applications, including cell delivery. Weitz and colleagues fabricated injectable photocrosslinkable microspheres based on GelMA for encapsulating bone marrow-derived MSCs (BMMSCs) towards osteogenic tissue constructs (Figure 3C) (Zhao et al., 2016). Notably, the GelMA could sustain stem cell viability, migration to the interiors, and substantial proliferation *in vitro* and *in vivo*. These minimally-invasive photocrosslinkable GelMA microspheres increased mineralization and facilitated bone regeneration. In another case, Hölzl et al. (2022) demonstrated the photo-crosslinked GelMA as a candidate for the delivery of chondrocytes. Similarly, Bae et al. (2006) generated HA-based hydrogel beads using the facile photo-polymerization of its methacrylated derivatives and N-vinylpyrrolidone using the alginate as a temporal mold. After optimization of conditions, such as methacrylated conditions and irradiation time, these beads were encapsulated with cells, resulting in a highly suitable environment for the viability and proliferation of bovine articular chondrocytes, suitable for minimally-invasive cell delivery applications.

In addition to polymeric hydrogels, several composite hydrogels with inorganic constructs have been reported to potentiate their minimally-invasive cell delivery applications toward tissue repair. In a case, magnetic microgels based on gelatin and PEG diacrylate (PEGDA) were prepared by cryogelation and micromolding approach for culturing HepaRG cells (Liu et al., 2014). These controllable MRI-traceable magnetic microtissues could be helpful in exploring tissue repair abilities and other critical issues in TE applications. In another instance, graphene oxide (GO)-encapsulated self-assembling peptide-based hydrogels for intervertebral disc repair (Ligorio et al., 2019). The use of GO fulfilled the applicability of nanofillers for reinforcing FEFKFEFK peptide hydrogel. Moreover, the strong interactions between the GO and hydrogel facilitated the mechanical properties, i.e., the storage modulus of >1,500 Pa compared to free hydrogel (<500 Pa), towards improving the cell viability as potential cell delivery scaffolds. Despite the success, these hydrogels suffer from several disadvantages, such as being fragile and lacking dynamic, as well as colloidal stabilities. While injecting cells, these attributes may lead to an inappropriate dosage of injectable cells at the administration site. Notably, these water-rich hydrogels enable convenience for fabricating biological substitutes (organoids and spheroids) and investigating cell-cell interactions. Further, the performance of delivery and subsequent tissue repair and regeneration abilities are dependent on various cellular and environmental factors.

3.3 Cells encapsulated with nanocomposites

In addition to encapsulating cells in micron-sized particles and gels, guided delivery can be achieved by internalizing various nanocomposites into the cells. These small-sized sub-micron bots can be employed for guiding toward minimally-invasive cell delivery. Although these materials are in the sub-micron size range, it is worth noting that the internalized constructs would substantially facilitate

10.3389/fbioe.2023.1076179

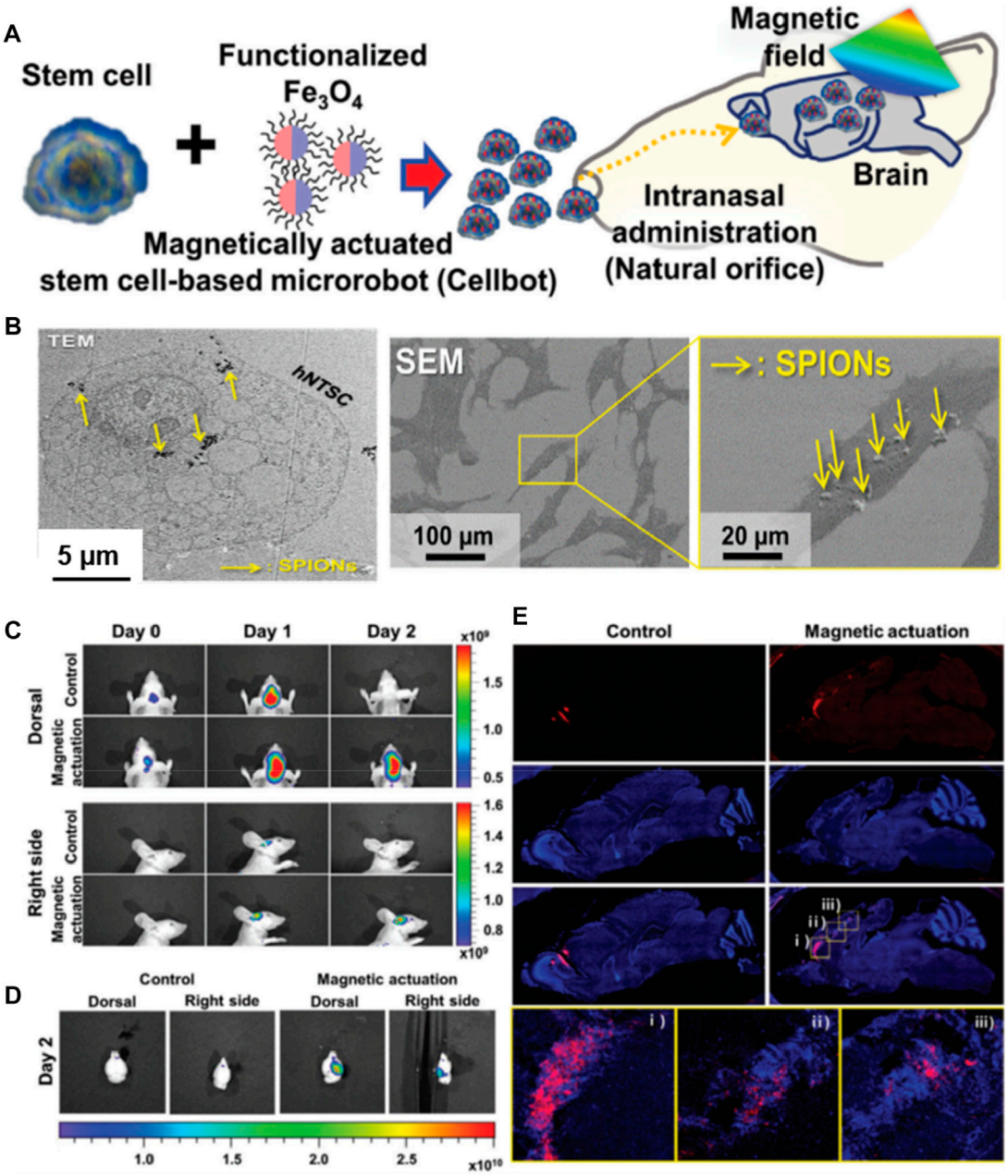

FIGURE 4
(A) Schematic of the intranasal administration and magnetic actuation of Cellbots. **(B)** TEM image visualizing cellular uptake of PLL-SPIONs in the cytoplasm and SEM images of the SPION-labeled hNTSCs (arrows indicate PLL-SPIONs). *In vivo* delivery of Cellbots into the target brain region *via* intranasal administration and magnetic guidance. **(C)** *In vivo* imaging of the control group (without magnetic field) and magnetic actuation group (with magnetic field) for 3 days. **(D)** Fluorescence images of the extracted mouse brain after 2 days. **(E)** Sequential migration and engraftment of the cell bots from the injection site (olfactory bulb) to the cerebral cortex. Reproduced with permission from Ref. (Jeon et al., 2021). Copyright 2021, John Wiley & Sons.

the transportation of cells toward the target site, similar to the polymeric microcarriers. In a case, cell bots were generated by Jeon and colleagues by internalizing the superparamagnetic iron oxide nanoparticles (SPIONs) into human nasal turbinate stem cells (hNTSCs) (Figure 4) (Jeon et al., 2021). These cell bots were constructed by culturing the hNTSCs with the poly-$_L$-lysine (PLL)-coated SPIONs with highly positive-charged amino acid chains for minimally-invasive targeted delivery of stem cells to the brain tissues. The intranasal administration of cell bots was targeted by magnetic actuation using the external magnetic field, which could be efficient for treating central nervous system (CNS)-based diseases in terms of therapeutic delivery.

4 Microfabrication strategies

Broadly speaking, several conventional biofabrication approaches for recreating such building blocks predominantly include top-down and bottom-up approaches (Santana et al., 2020). These approaches aim to recapitulate the complex 3D architectures that mimic the

tissue-specific environment and their bio-functionalities. In the top-down processing-based approaches, cells are expected to be populated in support of the fabricated porous scaffolds towards recapitulating the native ECM, including the biochemical and physicochemical cues (Langer and Vacanti, 1993). To accomplish these tasks, several scaffolding systems have been fabricated to mimic the tissue microarchitecture, anatomical, and physiological features along with the spatiotemporal rearrangements of ECM. Numerous technologies, including lithography (photo-/soft-), two-photon polymerization, and 3D printing, among others, are often practiced for fabricating such 3D architectures (Choi et al., 2012). Furthermore, mechanical stimulants or enhancers, such as growth factors, regulate tissue biology involving mechanical and biomolecular signaling attributes. Despite the progress, these approaches often suffer from various limitations, such as challenges in cell immobilization in the scaffolds, resulting in low yield and irregularities in their spatial distribution, and failing to mimic unit-repetitive modular designs in derived ECM similar to native tissues. To this end, diverse types of bottom-up approaches have emerged as promising alternatives to top-down approaches for developmental biology toward fabricating bioinspired components (Kankala et al., 2018a). This bottom-up biofabrication offers a unique design of building blocks of highly flexible arbitrary-sized constructs in the range of atomic scale to supramolecular large-sized assemblies (Choi et al., 2012). The cellular-rich building blocks of polymeric carriers can be built through self- or guided cell assembly feasibly using the controlled distribution of different types of cells. Despite the availability of various approaches, several challenges exist to fabricating microcarriers with uniform size distribution and controllable, as well as reproducible morphologies. This section presents different microfabrication strategies for generating microcarriers, highlighting the pros and cons of harboring cells and their subsequent delivery.

4.1 Microfluidic technology

Droplet microfluidics refers to an approach of perceiving behavior and precise manipulation of fluids (10^{-9}–10^{-18} L) on the microscale at which surface forces take control of the volumetric forces towards generating the microminiaturized devices (Bhatia and Ingber, 2014). This multidisciplinary field is practically utilized in systems that process low volumes of fluids to achieve automation, multiplexing, and high-throughput screening, by integrating various areas of physics, engineering, chemistry, and nanotechnological concepts. Although various traditional microfabrication technologies are available, droplet microfluidics has garnered captivating interest for generating microparticles due to the tunability of the composition, controllable geometrical topographies, and high-throughput generation (Bhatia and Ingber, 2014; Jiang et al., 2016). Typically, the first-applied microfluidic devices in the 1980s were designed using silicon and glass. Typically, the emulsion droplets in the microfluidics process, one at a time, are initially generated using the device set-up through the careful balance between various forces, including inertial forces, interfacial tension, and viscous (Ofner et al., 2017). Besides, other external forces (centrifugal, magnetic, and electric) are applied to generate droplets. The droplet generation plays a vital role in the eventual quality of the microcarriers, as the precise manipulation of fluid miscibility would influence the outcome. In addition, other factors play substantial roles in the processing and quality of microcarriers, such as channel geometries and flow conditions. In this context, various channel geometries (co-flow, T-junction, and flow-focusing), along with the parallelization of multiple channels, would result in the generation of uniform-sized droplets with high-throughput efficiency (Garstecki et al., 2006; Ofner et al., 2017). The well-defined geometry of the device set-up and compatibility are crucial in generating emulsion droplets. The glass capillary-based microfluidic setup is predominantly used due to high chemical resistance and ideal co-axial fabrication of droplets. Despite the success, reproducibility and scale-up issues yet remain to be addressed (Benson et al., 2013). To a considerable extent, soft lithography-based polydimethylsiloxane (PDMS) and polytetrafluoroethylene (PTFE)-based microfluidic devices have emerged due to elasticity, compatibility, optical transparency, and non-inflammability (Xia and Whitesides, 1998; Bhattacharjee et al., 2016). Several reviews explored detailed mechanistic insights based on droplet generation involving dynamic forces and their effects on the outcome (Zhu and Wang, 2017).

Using the microfluidics technology, the cells-encapsulated microcarriers for cell delivery applications can be fabricated in two ways, direct and indirect approaches. In the direct encapsulation strategy, the cells are incorporated in the emulsion droplets and further subjected to the solidification of polymers-encapsulated cells by cross-linking (Yanagawa et al., 2016; Siltanen et al., 2017). Numerous advantages include the formation of uniform-sized particles, convenience in regulating the physicochemical properties, and control over the cell encapsulation efficiency (Siltanen et al., 2017). Despite the success in generating cells-encapsulated microcarriers, maintaining the extensive surface area and porosity is often required, facilitating the convenience of exchanging nutrients and gases for substantial growth and delivery of cells (Yanagawa et al., 2016; Li et al., 2018). In addition to the one-step approach, a two-step indirect approach has been employed to fabricate cell-encapsulated microcarriers. The biocompatible polymeric carriers (both porous and non-porous) can be initially generated using the microfluidic technology, which are then cultured with the desired cells of interest for a specified time period, for instance, 14–28 days (Leong et al., 2003). Despite the multi-step processing and time-consuming, this approach presents the additional advantage of the ease of mounting the cells in the carriers. These carriers offer a conducive microenvironment for the growth and proliferation of cells, depending on the porosity, biocompatibility, and hydrophilicity of the carriers (Loh and Choong, 2013; Chen et al., 2015). For instance, our group has generated PLGA-based microcarriers using the microfluidic approach in a two-step process for skeletal muscle cell delivery (Figure 5A-a) (Kankala et al., 2019). Firstly, the microfluidics resulted in highly porous architectures (average diameter of >300 μm and porosity range of 10–80 μm) with the support of gelatin as a porogen (Figure 5A-b–d). In addition to polymeric solid microcarriers, the microfluidic approach can generate liquid-rich micro-sized injectable hydrogels. Although various materials are available, including natural (alginate) and synthetic (PEGDA) polymers, these materials lack cell-responsive motifs, such as anchorage proteins. Considering these issues, in a case, Zhao and colleagues generated hydrogel microspheres using the microfluidic approach to encapsulate BMSCs and their subsequent delivery to

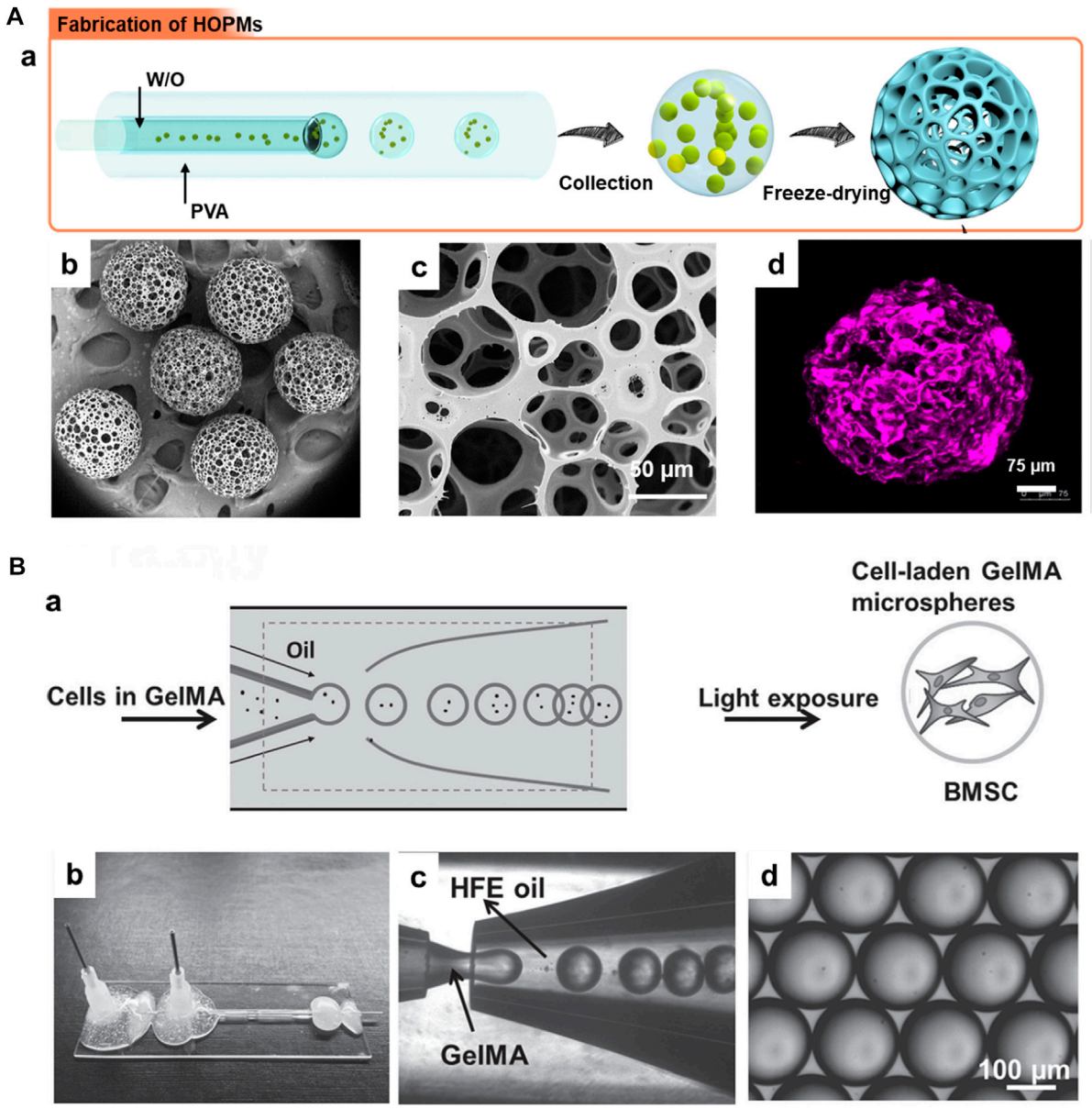

FIGURE 5
(A) a) Schematic illustration showing the generation of PLGA HOPMs by microfluidic technology towards the fabrication of modular cell-laden HOPMs by populating the C2C12 cells on the microcarriers. b) SEM images showing the size distribution of PLGA HOPMs, and c) surface morphology of a microcarrier. d) immunohistological analysis of myoblasts in the PLGA HOPMs by staining them against desmin for 7 days. Reproduced with permission from Ref. (Kankala et al., 2019), Copyright 2019, John Wiley & Sons. **(B)** a) Schematic diagram illustrating the photocrosslinking-microfluidic fabrication of GelMA microspheres encapsulated with BMSCs. Aqueous droplets containing GelMA gel precursors are produced from a microfluidic flow-focusing device and photopolymerized to form GelMA microspheres. b) A Photograph of the microfluidic device, c) a microscope image of the device generating GelMA droplets, and d) monodisperse GelMA droplets in HFE oil. Reproduced with permission from Ref. (Zhao et al., 2016), Copyright 2016, John Wiley & Sons.

promote osteogenesis *in vitro* and *in vivo* (Figure 5B). Initially, the droplets of GelMA, photocrosslinkable gelatin, and photoinitiator for photopolymerization were introduced into the microfluidic device. Further, the polymerization of the droplets resulted in the fabrication of monodisperse GelMA microspheres with an average size of over 165 μm. As specified in the advantages of injectable microgels in Section 3, the gentle gelling condition could substantially minimize the damage to the encapsulated proteins and cells in the microgels. These microgels substantially promoted the viability of BMSCs and spread inside the microgels.

4.2 Emulsification

Although the microfluidics technique is predominantly based on the emulsification of droplets towards the fabrication of microcarriers (ofner et al., 2017), the polymeric microcarriers can be generated using the facile emulsification process without microfluidics. In general, the fabrication process is based on the initial emulsification (W/O or O/W) of the droplets containing polymers and porogens followed by the mineralization, using crosslinking with ions, freeze-drying, and thermal-induced phase separation (Li et al., 2015; Zhang et al., 2017).

Similar to microfluidics, several polymers can be used to fabricate cell-laden microcarriers, including cellulose, collagen, alginate, chitosan, and PLGA (Zhang et al., 2017; Huang et al., 2018). In an instance, Zhang et al. (2017) generated cellulose-based aerogel microspheres using the single emulsification approach followed by freeze-drying. These cellulose microspheres provided abundant cell surface area for the adhesion and proliferation abilities of the mouse fibroblasts (NIH/3T3). Similarly, the emulsion (O/W)-based porogen leaching-phase separation processes were implemented to fabricate the PLGA-based microcarriers, which showed tremendous cell encapsulation efficiency (Chung and Park, 2009). Fernandes Patrício et al. (2019) generated collagen-based superparamagnetic microspheres, which were further mineralized using (Fe^{2+}/Fe^{3+})-doped hydroxyapatite (HAp) and emulsified using citrate species. The resultant carriers displayed a suitable microenvironment for the growth of mouse pre-osteoblast cell line (MC3T3-E1), showing cytocompatibility and subsequent osteogenesis. In another instance, chitosan microspheres with high porosity were fabricated for 3D culturing of cells using the micro-emulsification approach followed by the thermally-induced phase separation (Huang et al., 2018). In addition to the single-emulsion-based method, several attempts based on the double-emulsification approach have been made to fabricate cell-laden microcarriers. For instance, Nilsson et al. (1986) applied the double emulsification method followed by freeze-drying to encapsulate various animal cells (Baby Hamster Kidney cells, BHK, and African green monkey cells, VERO). Similar to generating various cell-laden microcarriers for cell delivery and tissue repair applications, several efforts have been dedicated to generating cells-encapsulated tumor models (pancreatic ductal adenocarcinoma (PDAC) using the emulsification-assisted photo-crosslinking methods to reiterate the TME for drug screening applications (Brancato et al., 2017; Pradhan et al., 2017).

4.3 Self-assembly approach

The self-assembly process, a bottom-up approach, is often referred to as the organization of various disordered species to supramolecular highly organized architectures (Miller et al., 2021). This approach often depends on diverse interactions between the precursors, such as hydrogen bonding, capillary, and van der Waals, resulting in fabricating architectures with varied dimensions (Salem et al., 2003; Oyama et al., 2014). Although these notified interactions are independent of the charge of the precursors, the overall surface charge of the components may facilitate their convenient assembly. For instance, contrarily charged species enable the ionic interactions substantially augment the assembly process (Ligorio et al., 2019). As cells are negatively-charged, the positively-charged material surfaces, for instance, chitosan and PLL, conveniently facilitate their assembly as composite scaffolds (Salem et al., 2003; Huang et al., 2018). In a case, Jeon et al. (2021) generated targeted cell bots in which hNTSCs were internalized with SPIONs for minimally-invasive delivery of stem cells to brain tissues. These cell bots were fabricated by culturing the cells with the PLL-coated SPIONs with highly positive charged amino acid chains. These composites with insignificant toxicity were substantially internalized into the hNTSCs, and employed for minimally-invasive targeting of stem cells to brain tissues. The intranasal administration of cell bots was targeted by magnetic actuation using the external magnetic field, which could be efficient for treating CNS-based diseases in terms of therapeutic delivery. In another instance, a simple solvent-exchange-assisted lyophilization was applied to generate nanofibrous hollow microspheres through the self-assembly of star-shaped polymeric constructs as minimally-invasive carriers of cells for knee repair (Liu et al., 2011). These self-assembled nanofibrous microcarriers showed improved adhesion and proliferation of chondrocytes *in vitro* and *in vivo*, presenting osteochondral repair. Although this process is often used to fabricate microarchitectures, obtaining uniform-sized architectures is challenging, requiring control over all the parameters, and the need for high temperatures to dissolve polymers is inevitable.

4.4 Isothermal spherulitic crystallization

Recently, a unique microfabrication strategy, named isothermal spherulitic crystallization, has been proposed to generate microcarriers. These generated microcarriers exhibit several advantages, such as convenience for operation, simple set-up, scale-up, and adaptability (Kuterbekov et al., 2018). In addition, the major advantage of this approach is the non-utilization of organic solvents, which would be convenient for the adhesion and growth of cells due to the biocompatibility of resultant microcarriers. In a case, PLA-based porous architectures were synthesized using the organic solvent-free spherulitic crystallization approach, resulting in the regulated morphological attribute in terms of particle size and pore diameter (Kuterbekov et al., 2018). The resultant microcarriers were highly biocompatible to culture hASCs, exhibiting potential in adhesion and growth, and differentiation abilities of hASCs.

4.5 Graft polymerization

Graft polymerization refers to synthesizing polymerized constructs by imbedding monomers with covalent linkages as side chains onto the main polymer, resulting in the altered polymer composite. This approach has been applied to impart various chemical functionalities to the polymeric chains, for instance, hydrophilicity to hydrophobic polymers and vice versa (Le et al., 2019). Often, this method can be applied to alter the surface chemistry and morphological attributes of the polymeric constructs. Plasma-induced grafting, one of the grafting-based approaches, has attracted captivating attention to alter surface morphology (Liu et al., 2022). This approach acts by polymerizing the surface of a plasma-activated polymer, resulting in brush-like polymeric layered surfaces. The highly active grafted surfaces can extend several nanometers of depth, facilitating the immobilization of cells and biomolecules, for instance, proteins. These active surfaces can enable the interactions between the protein chains on the cellular surfaces and polymeric functional groups on the layers. In an instance, acrylic acid was graft-polymerized onto plasma-treated poly(ethylene terephthalate) (PET) films to facilitate the surfaces feasible for collagen immobilization and further seeding smooth muscle cells (Gupta et al., 2002). The collagen immobilization efficiency increased with the grafting density of the films. Finally, the collagen-immobilized grafts were tested for seeding the smooth muscle cells, resulting in the improved growth of smooth muscle cells.

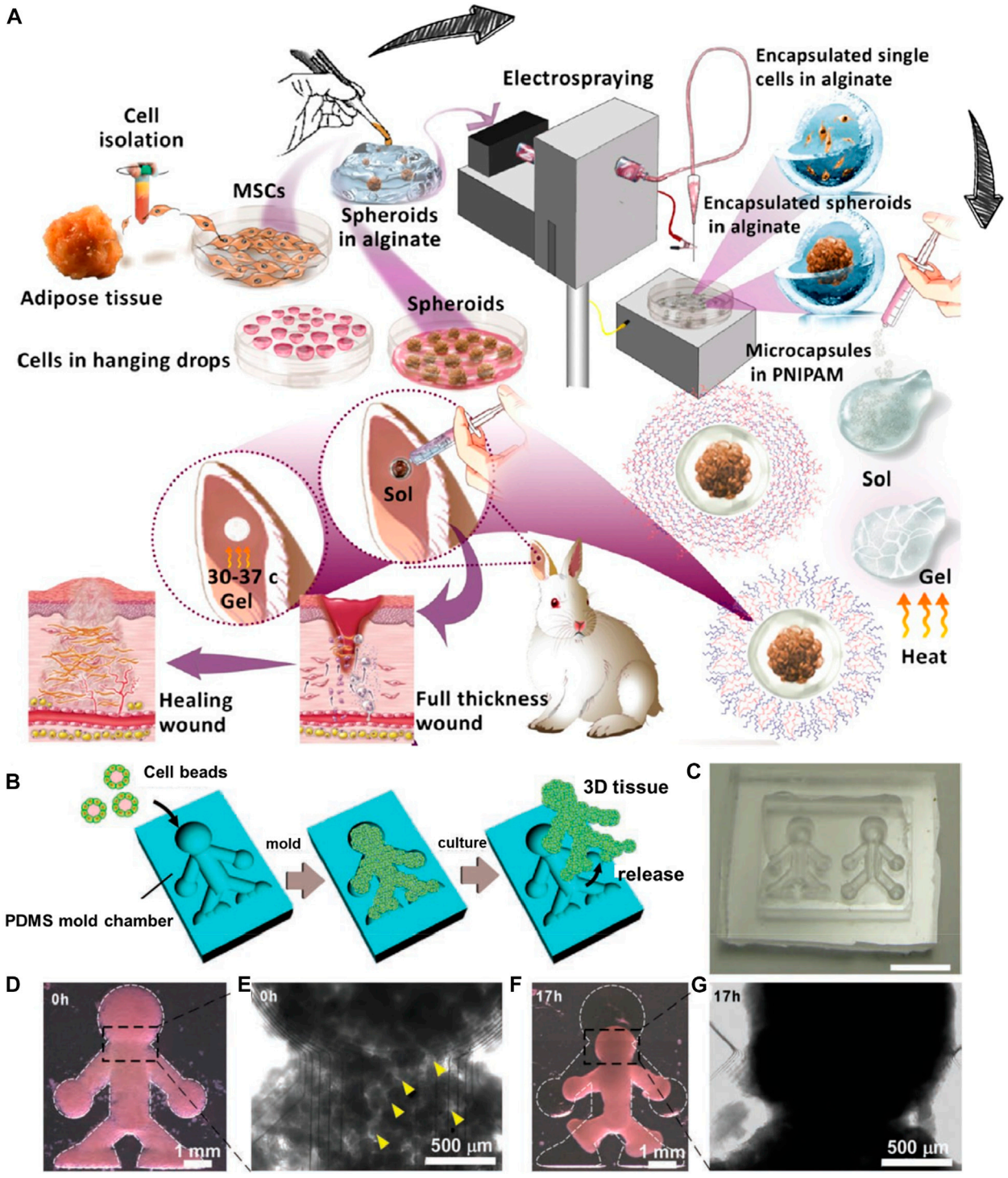

FIGURE 6
(A) Schematic illustration of the electrospray setup used for microencapsulation. Reproduced with permission from Ref. (Nilforoushzadeh et al., 2020). Copyright 2020, American Chemical Society. **(B)** The method used to produce the 3D tissue architectures using monodisperse cell beads. **(C)** A microscopy image of the doll-shaped PDMS mold chamber reveals 3D tissue formation. **(D,E)** Microscopy images of NIH/3T3 cell beads immediately after stacking. Cavities (indicated with yellow arrows) among the cell beads are observed at this time point (0 h). **(F,G)** Microscopy images of NIH/3T3 cell beads, 17 h after stacking. Reproduced with permission from Ref. (Matsunaga et al., 2011). Copyright 2011, John Wiley & sons.

4.6 Miscellaneous

Various other techniques have recently garnered interest in fabricating various carriers for cell delivery and subsequent TE applications. Although some of the techniques are not directly related to cell delivery, the discussions related to such techniques are worth discussing their potential towards injectable constructs for TE applications, for instance, electrospraying (Nilforoushzadeh et al.,

2020). In this section, we present discussions relevant to some of these techniques, such as electrospray, molding, and acid-dissolved/alkali-solidified self-sphering shaping methods.

Electrospraying, referred to as electrohydrodynamic atomization, is a voltage-driven approach capable of producing micro- and nano-sized particles. The liquid/polymeric solution is sprayed through the nozzle in the presence of high electrical forces. This cost-effective approach offers several significant advantages of altering the processing parameters to regulate the resultant particles, such as the distance between the collector and nozzle and the applied voltage (Wang et al., 2018; Clohessy et al., 2020; Miller et al., 2021). In a case, Mozari et al. initially generated 3D spheroids of MSCs, which were then encapsulated using the electrospray technique in the micro-scale alginate beads and subsequently into the injectable thermosensitive PNIPAAm-based hydrogel matrices (Figure 6A) (Nilforoushzadeh et al., 2020). These gels could dissociate at the skin temperature, delivering cells, sealing the wound cavities, and protecting the alginate beads from the harsh wound environment. Several investigations *in vitro* and *in vivo* were performed to determine the secretion of various biological mediators, such as α-smooth muscle actin (α-SMA) and transforming growth factor β1 (TGF-β1), toward effective cell-based wound therapies. In another instance, Tian and coworkers demonstrated the generation of injectable gelatin methacryloyl-alginate core-shell microcapsules using the coaxial electrostatic microdroplet approach. These carriers efficiently delivered co-encapsulated human dental pulp stem cells (hDPSCs) and human umbilical vein endothelial cells (HUVECs) for endodontic regeneration (Liang et al., 2022). These constructs showed promotion of osteo/odontogenic differentiation along with vascularization in the microcapsules, resulting in the deposited ECM. Similarly, Peng and colleagues utilized the electrospray technique to prepare alginate-gelatin microspheres embedded with adipose-derived stem cells for cartilage tissue regeneration (Liao et al., 2022).

Indeed, the electrospray approach has garnered interest from researchers due to the ease of control over the mass production of micro-sized particles. Moreover, the generation of solid microspheres may suffer from poor cell encapsulation efficiency. However, nanofibrous and highly porous polymeric constructs are challenging to obtain using the electrospray approach alone. To address this limitation, Xie and colleagues used a combination of electrospinning and electrospraying approaches to generate injectable nanofibrous microspheres (Boda et al., 2018; John et al., 2020). In a case, electrospun aligned PCL-gelatin and PLGA-gelatin fibrous segments were electrosprayed (voltage = 8–10 kV, flow rate = 2.0 mL/h, and distance of 10 cm) into injectable nanofibrous microspheres for minimally-invasive cell therapy (Boda et al., 2018). These microspheres exhibited improved stem cell proliferation and differentiation efficiencies compared to solidified microparticles.

In addition to the aforementioned significant approaches, several other approaches have been employed to explore the generation of injectable modular units with the potential of cell delivery, such as molding (Bae et al., 2006; Hafeman et al., 2008; Lim et al., 2009). Molding can generate 3D architectures at arbitrary sizes based on mold dimensions. In a case, PCL microspheres with large pores as minimally-invasive cell delivery carriers were generated using the liquid mold room temperature ionic liquid (RTIL) and porogen camphene for microsphere development (Kim et al., 2016). The microspheres were modified with nerve growth factors on their surface along with gelatin to improve the attachment and delivery of neural progenitor cells (PC-12). In another instance, moldable bone substitutes based on sodium alginate (SA)/*β*-Tricalcium phosphate (β-TCP) microspheres cross-linked with an aqueous calcium chloride solution were generated for improved osteoconductivity toward curing bone defects (Ho et al., 2020). In addition, a micromolding approach based on the on-chip technology was applied to generate magnetic microcryogels-assisting microtissue formation with improved robustness and controllability, which could be applied for TE and drug screening applications (Liu et al., 2014). These carriers after delivering cells would facilitate their bottom-up assembly into well-organized structures (Luetchford et al., 2020).

Despite the generation of carriers based on size and shape interest, it often results in large-sized constructs. However, it is worth discussing that the resultant structures often provide enough space for fabricating complex architecture for designing the ECM-mimicking environment for cell growth. In these circumstances, the pre-designed microcarriers using other approaches have been adapted to molding approaches to generate complex structures (Wu et al., 2018). In an instance, Matsunaga et al. (2011) initially generated cells-coated collagen microbeads using microfluidics, which were further deposited in the silicone chamber as a mold (Figures 6B–G). Although the mold suggested the boundary for the growth of cells, the collagen beads supported the cell adherence, growth, and proliferation, resulting in the 3D microtissues.

Recently, an acid-dissolved/alkali-solidified self-shaping approach was proposed to generate 3D microcarriers (Zhang et al., 2018). This self-shaping strategy presents advantages, such as ease of operation, mono-disperse end products, and cost-effectiveness. In an instance, chitosan-based microcarriers were fabricated and reinforced with GO (Zhang et al., 2018). The resultant microcarriers displayed biocompatibility, and adhesion, as well as proliferation abilities to hUCMSCs for their long-term survival and differentiation capabilities. In another instance, PCL-based microscaffolds were prepared using the combinatorial approach. The isolated particle-melting method resulted in the non-porous beads and melt-molding particulate-leaching approach for obtaining the porous beads in the size range of 400–550 μm (Bidarra et al., 2014). These biocompatible beads displayed encapsulation efficacy of chondrocytes and their infiltration for cell delivery applications. Although most of these techniques have been utilized to generate 3D microcarriers with cell encapsulation ability, these techniques remained on the lab scale, require further parameter optimization and subsequent exploration on various cell types yet remain to be explored comprehensively.

5 Factors influencing cell delivery

According to a formulator anticipation, the designed carriers must offer ideal delivery attributes, specifically in terms of precise and controlled delivery of drugs and biomolecules (growth factors). Regarding cell delivery, the ideal carriers must possess specific abilities, such as high encapsulation of viable cells and their subsequent delivery abilities at the target site, promoting tissue regeneration. In this context, several factors predominantly influence the offered abilities by the carriers for cell delivery, such as type of polymer (source and functionalities), morphology (size, porosity, and shape), and injectability. This section presents a brief

overview of these factors, highlighting their influence on the fabrication, encapsulation, and delivery of cells toward tissue repair.

5.1 Type of polymer

Owing to the successful encapsulation of cells in a viable form, the biocompatibility of the polymer substantially attributes to its selection process, depending on the nature and chemical composition of the raw materials, i.e., polymers. To a considerable extent, the selection of polymer mainly plays a vital role in fabricating microcarriers for cell delivery. Based on the source of origination, different kinds of polymers have been employed to fabricate these 3D microcarriers (non-porous and porous) for cell delivery applications, such as natural (gelatin, dextran, cellulose, chitin and its derivatives, and alginic acid) (Bidarra et al., 2014; Ho et al., 2020; Lavanya et al., 2020; Rahman et al., 2021; Liang et al., 2022; Liao et al., 2022), and synthetic (PLGA, PLA, silk fibroin, SF, polyurethane, polyacrylamide, and PHEMA) (Hong et al., 2005; Hafeman et al., 2008; Braccini et al., 2020). Considering the pros and cons, polymers from natural sources possess high biocompatibility due to biomolecules, recyclability, and mechanical properties (Rahman et al., 2021). These natural polymers significantly facilitate the conduciveness for forming an ECM-like microenvironment concerning the composition of polysaccharides and other biomolecules (Wang et al., 2021). Synthetic polymers offer mechanical attributes, reproducibility, tunable physicochemical features, and alterable morphological attributes of the eventual 3D microcarriers (John et al., 2020). Despite the advantageous features, some polymers would hinder the encapsulation and growth of cells in the interiors of cells due to depriving compatibility and non-favorable chemical composition, failing to form an ECM-like environment and severely affecting the adhesion and growth of the encapsulated cells. In comparison between natural and synthetic polymers, natural polymers offer improved biocompatibility, while synthetic polymers present improved mechanical properties. Considerably, the combination of synthetic and natural polymers at an appropriate proportion would substantially lead to the developing of excellent microcarriers with improved biocompatibility and appropriate mechanical properties. These features facilitate conducive encapsulation and proliferation abilities of cells in the interiors and on the surface of the designed microcarriers (Wang et al., 2011).

5.2 Morphology

In addition to the selection of raw materials, the predominant morphological attributes (for instance, size and shape) of resultant polymeric architectures play substantial roles in developing injectable microarchitectures and their subsequent TE applications (Li et al., 2018). The eventual particle/microgel size is one of the predominant factors of morphological features of microarchitectures, as the size quality plays a critical role in their injectability. In general, the acceptable size range of microarchitectures suitable for the delivery of cells is in the range of 100–500 μm. This optimal size and spherical-shaped containers range substantially facilitate the ample amount of cells in the interiors of the microarchitectures (Hong et al., 2005; Wei et al., 2018). In the case of hydrogels, the ideal size of the microgels is around 200 μm and a volume of 1 nL to achieve the rapid delivery of nutrients and water, as well as gases exchange in the interiors for the survival of the encapsulated cells (Vasile et al., 2020; Wang et al., 2021). In addition to improved encapsulation, these morphological attributes would avoid avoiding cell necrosis in their interiors.

5.3 Porosity

In addition to morphological attributes, textural properties, such as surface texture and porosity, play critical roles in encapsulating diverse cell types and their delivery. Initially, the rough surface texture provides feasibility in improving the adhesion efficiency of cells. In this context, the fabricated biocompatible solid microspheres with rough surfaces and tiny pores provided improved adhesion efficiency on their surfaces compared to the smooth surfaces (Matsushita, 2020). The plausible reason for improved adhesion by rough surfaces could be the non-slippery interactions between the cells and microcarriers. Although the rough surface enables improved adhesion, these solid microcarriers suffer from a significant limitation of low encapsulation yields due to less surface area (Choi et al., 2012). It is often required to provide extensive porosity with highly open and interconnected windows to enable improved encapsulation efficacy of different cell types. Considerably, the rough surfaces and highly open porosity facilitates improved adhesion and encapsulation efficacy, determining their delivery efficacy. Several biofabrication approaches have been employed to develop microarchitectures with high and controlled porosity with open and interconnecting windows to address these issues. Generally, the ideal porosity of the microparticles of an average diameter of 300 μm must be in the range of 10–100 μm (Choi et al., 2012). The plausible reason for these PMs with heterogeneous porosity is due to the high surface area. The abundant porosity of the carriers enables the exchange of gases and nutrients for the improved proliferation of cells in interiors (Kankala et al., 2019). In addition, the porous architectures substantially facilitate the cells encapsulating in the interiors and delivering to the tissue region of interest.

5.4 Surface charge

Indeed, several physicochemical characteristics of the raw materials determine various attributes of microcarriers; for instance, the chemical composition of the precursor defines the compatibility of the particles (Wang et al., 2021). Among various such characteristics, hydrophilicity and surface charge determine the adhesion and growth of cells in the carriers. In this vein, the selection of polymer, along with various surface-altering approaches (surface grafting, chemical modification, and plasma functionalization), have been applied to improve the affinity of the surface (Gupta et al., 2002). Despite the success in improving the surfaces for better adhesion of cells compared to unaltered surfaces, these approaches require multi-functionalization steps, which may alter the robustness and durability of the carriers (Wang et al., 2021). To this end, tissue-derived ECM has been developed to avoid these issues, for instance, decellularized adipose tissue, and micronized acellular dermal matrix. In addition, these support by offering biocompatibility and proliferation efficiency due to the natural ECM.

In addition to the factors mentioned above, several other factors play significant roles in influencing encapsulation and delivery efficiencies, for instance, injectability. In general, the delivery of the

cells often depends on the target site, which is often designed based on the route of administration and injectability attributes. Preferably, intramuscular and intravenous injection routes are often used to deliver cells. Notably, the material characteristics and the cellularized secretions can generate and mimic the ECM-like environment (Hollister, 2005; Choi et al., 2010; Choi et al., 2012). However, various biochemical cues are required along with the desired microarchitectures as prerequisites for TE to control the microenvironment substantially.

6 Scope for preclinical/clinical applicability

Owing to their morphological attributes and textural properties, these polymer-based micron-sized carriers (solidified porous and non-porous carriers, as well as liquid-rich hydrogels) offer numerous advantages such as widespread cell encapsulation and carrying abilities, biodegradability, and biocompatibility, which are of unique interest for various biomedical applications. Compared to large-sized scaffolds (photo-cross-linkable hydrogels and biodegradable scaffolding systems) that require sophisticated fabrication steps, and highly invasive surgical procedures for implantation, these microcarriers facilitate room for the encapsulation of different cell types for tissue growth. Nevertheless, it should be noted that different carriers offer some unique attributes. For instance, solidified carriers with interconnecting windows facilitate enough room for the infiltration of cells and their subsequent metabolic activities, requiring additional elements or altered surfaces to provide an ECM-like environment. Contrarily, the liquid-rich hydrogels provide an abundant hydrophilic environment similar to a natural tissue-like microenvironment.

Before discussing the preclinical outcomes and scope for clinical translation, it is necessary to understand various attributes, such as biocompatibility and biodegradability. In most of the instances, several polymers with compatibility have been demonstrated, for instance, natural [chitosan (Huang et al., 2018), HA (Bae et al., 2006), and alginate (Chen et al., 2015)], and synthetic [PLGA (Kankala et al., 2019), PLA (Liu et al., 2011), and PCL (Kim et al., 2016)], as well as their mixture (Hong et al., 2005). In this framework, several cell lines from humans and mice have been encapsulated to demonstrate the potential of the microcarriers, such as osteoblasts (Chen et al., 2015), skeletal myoblasts (Kankala et al., 2019), chondrocytes (Hong et al., 2005; Liu et al., 2011), and MSCs (Liu et al., 2011; Barati et al., 2017; Luetchford et al., 2020; Liao et al., 2022), indicating their biocompatibility due to viability and proliferation abilities (Ho et al., 2020). Although these carriers showed compatibility with different cell lines, comprehensive toxicity evaluations must be systematically evaluated, including the genotoxicity and other toxicity evaluations. In some instances, the degradability attribute of the designed microcarriers, specifically solidified microcarriers, was demonstrated *in vitro*, requiring further investigations to explore the time of degradation and validations for degraded products. Further, the biocompatibility along with performance attributes have been evaluated *in vivo* in mice (Wei et al., 2018). In addition, these carriers with hydrophilicity and surface charge often result in the degradability *in vivo*, indicating no damage to the major organs (Kankala et al., 2019).

Although various cell lines have been used to explore the potential of such microcarriers as cell delivery vehicles, specific polymers for some specific cell lines have been used predominantly. In this framework, polymers from natural and synthetic origins have been applied. However, some polymers have been often applied, such as alginate, keratin, and PCL, in the solidified carriers and gelatin-based hydrogels as liquid-rich microgels (Wang et al., 2018). In some instances, the combination of natural and synthetic polymers has also been employed to generate hydrogels and solidified carriers, such as collagen-PLL (Hong et al., 2005), chitosan-PLGA (Wang et al., 2011), and gelatin-PCL (Boda et al., 2018). The predominant reasons behind the selection of polymers might be the hydrophilicity and compatibility attributes. To this end, several cell lines have been used to generate microcarriers for tissue repair. To a considerable extent, only a few kinds of cell lines have been abundantly studied, such as MSCs (Liu et al., 2011; Barati et al., 2017; Luetchford et al., 2020; Liao et al., 2022), osteoblasts (Chen et al., 2015), skeletal myoblasts (Kankala et al., 2019), and chondrocytes (Hong et al., 2005; Liu et al., 2011). In most instances, the MSCs (human/rat BMMSCs) have been intended to deliver them into the appropriate region of interest and explore their proliferation and differentiation efficiencies. Moreover, the specific reason for selecting such cell lines could be due to ease of growth and infiltration and the route of administration, i.e., minimally invasive. Eventually, the preference in selecting polymer and cell line remains arbitrary, depending on the specific attributes of applicability, cell morphology, and growth conditions. Considering the optimization of syntheses and formulation parameters, biocompatibility, biodegradability, and outcomes of the therapeutic applications, several preclinical investigations have been performed in various animals, such as mice (Lim et al., 2009; Liu et al., 2014; Wang et al., 2018; Liang et al., 2022) and rabbit (Liu et al., 2011; Ho et al., 2020; Nilforoushzadeh et al., 2020), to explore their safety and performance efficacy. In most instances, the performance efficacy of these designed carriers have resulted in improved tissue repair and regeneration abilities. However, the performance of microcarriers in a species with long term safety and treatment time considerations yet remain to be elucidated comprehensively. Despite the success, it is still a long way to go to explore the comprehensive evaluations in terms of PK-PD parameters and toxicity attributes. Further, these parameters must be explored and validate their proficiency in humans, requiring extensive investigations and validations.

7 Conclusion and perspectives

In conclusion, this article has summarized the discussions on diverse polymeric microarchitectures for minimally-invasive cell delivery towards TE and RM. The significance and classification of diverse injectable microcarriers are initially presented, emphasizing their importance, pros, and cons regarding cell encapsulation and subsequent delivery processes. Further, various microfabrication approaches are explored, stressing their importance in designing cellularized microarchitectures and the feasibility of encapsulating cells and substantial tissue growth *in situ* and *in vivo*.

Recently, several efforts have been dedicated to produce highly biocompatible microcarriers using various biomaterials for cell delivery applications. In this regard, these 3D micro-sized scaffolding systems offered attributes of improved cell encapsulation and delivery efficiencies. Despite the success, several attributes in terms of material fabrication and

the performance of delivered cells remain to be addressed. Regarding fabrication, strict optimization of morphological properties (surface and textural attributes) and cell encapsulation are required. Predominantly, the optimal size convenient for injection and the precise evaluation of pore sizes must be explicitly investigated. Regarding cell encapsulation, several steps must be taken to address the fabrication of tissue-like and organ-like multicellular spheroids for TE. Moreover, the encapsulation efficiencies and physiological phenomena, such as apoptosis of encapsulated cells, must be explored to make these 3D microarchitectures more robust. The strict validation of assessments and the establishment of various cell seeding and encapsulation tools is required.

In terms of performance efficacy, these 3D microcarriers carrying cells, after injection, would facilitate the delivery of cells from the exterior to the surrounding ECM. In this view, it is required to explore the pathway of delivered cells in the case of a free-flowing medium. However, it is highly challenging to deliver cells from the interiors due to the excessive growth and proliferation of cells. On the one hand, it is required to explore the controlled proliferation efficiency of cells. On the other hand, the degradation profiling of microcarriers must be explored in case of uncontrolled growth, achieving appropriate physicochemical and mechanical attributes. In addition, control over the cellular microenvironment on the microscale must be achieved as the factors of cell-cell interactions and cell-ECM (integrin and fibronectin) interactions, along with the biochemical cues, play crucial roles. Finally, it is required to explore the functionalities related to integrating with the existing vascularization and neovascularization should be explored along with the validations *in vivo*. Although the fabrication and delivery are achieved to a considerable extent, the reproducibility of these 3D carriers by various microfabrication approaches on a large scale remains to be explored. Along this line, strict optimization of the processing parameters should be done prior to large-scale development.

Despite the success in generating various 3D microarchitectures, the suitability and generation of immune responses would limit the growth of the delivered cells. Interestingly, precision medicine will be the trend soon, in which patient-derived cells can be cultivated and generated for the treatment of individual patients. The success of these models can be achieved by substantially loading the appropriate patient-derived cell lines, providing gradient oxygen and nutrient supply, and considering growth factors. Finally, the optimization on a large scale and their applicability will undoubtedly offer great potential in the future.

Author contributions

CD, MY, and RK conceived the idea and conceptualization. CD, MY, CH, HX, and RK wrote the initial draft and supported it in figure illustrations. CD and RK supervised the work and fund acquisition. CD and RK revised the article with some meticulous discussions.

Funding

We sincerely acknowledge financial support from the National Natural Science Foundation of China (NSFC, 31800794), Funds for Foreign Experts from Ministry of Science and Technology, China (G20190013023), Funds for Guangdong Intelligent Photovoltaic Product Engineering Technology Development Center (2019GGCZX003), Program for Guangdong smart photovoltaic technology production-education integration innovation platform (2020CJPT033), and Funds for Guangdong University Innovation Team Project (2021KCXTD081).

Conflict of interest

The authors declare that the research was conducted in the absence of any commercial or financial relationships that could be construed as a potential conflict of interest.

Publisher's note

References

Agarwal, P., Zhao, S., Bielecki, P., Rao, W., Choi, J. K., Zhao, Y., et al. (2013). One-step microfluidic generation of pre-hatching embryo-like core-shell microcapsules for miniaturized 3D culture of pluripotent stem cells. *Lab A Chip* 13, 4525. doi:10.1039/c3lc50678a

Akamatsu, K., Ide, Y., Inabe, T., and Nakao, S. (2018). Preparation of monodisperse calcium alginate micro-/nanospheres via shirasu porous glass membrane emulsification followed by classification using microfiltration membranes. *Industrial Eng. Chem. Res.* 57, 9465–9470. doi:10.1021/acs.iecr.8b02473

Almería, B., Deng, W., Fahmy, T. M., and Gomez, A. (2010). Controlling the morphology of electrospray-generated PLGA microparticles for drug delivery. *J. Colloid Interface Sci.* 343, 125–133. doi:10.1016/j.jcis.2009.10.002

Asakawa, N., Shimizu, T., Tsuda, Y., Sekiya, S., Sasagawa, T., Yamato, M., et al. (2010). Pre-vascularization of *in vitro* three-dimensional tissues created by cell sheet engineering. *Biomaterials* 31, 3903–3909. doi:10.1016/j.biomaterials.2010.01.105

Bae, K. H., Yoon, J. J., and Park, T. G. (2006). Fabrication of hyaluronic acid hydrogel beads for cell encapsulation. *Biotechnol. Prog.* 22, 297–302. doi:10.1021/bp050312b

Barati, D., Kader, S., Pajoum Shariati, S. R., Moeinzadeh, S., Sawyer, R. H., and Jabbari, E. (2017). Synthesis and characterization of photo-cross-linkable keratin hydrogels for stem cell encapsulation. *Biomacromolecules* 18, 398–412. doi:10.1021/acs.biomac.6b01493

Benson, B. R., Stone, H. A., and Prud'homme, R. K. (2013). An "off-the-shelf" capillary microfluidic device that enables tuning of the droplet breakup regime at constant flow rates. *Lab A Chip* 13, 4507–4511. doi:10.1039/c3lc50804h

Bhatia, S. N., and Ingber, D. E. (2014). Microfluidic organs-on-chips. *Nat. Biotechnol.* 32, 760–772. doi:10.1038/nbt.2989

Bhattacharjee, N., Urrios, A., Kang, S., and Folch, A. (2016). The upcoming 3D-printing revolution in microfluidics. *Lab. Chip* 16, 1720–1742. doi:10.1039/c6lc00163g

Bidarra, S. J., Barrias, C. C., and Granja, P. L. (2014). Injectable alginate hydrogels for cell delivery in tissue engineering. *Acta Biomater.* 10, 1646–1662. doi:10.1016/j.actbio.2013.12.006

Boda, S. K., Chen, S., Chu, K., Kim, H. J., and Xie, J. (2018). Electrospraying electrospun nanofiber segments into injectable microspheres for potential cell delivery. *ACS Appl. Mater. Interfaces* 10, 25069–25079. doi:10.1021/acsami.8b06386

Braccini, S., Pecorini, G., Chiellini, F., Bakos, D., Miertus, S., and Frecer, V. (2020). Adhesion of fibroblast cells on thin films representing surfaces of polymeric scaffolds of human urethra rationalized by molecular models of integrin binding: Cell adhesion on polymeric scaffolds for regenerative medicine. *J. Biotechnol.* 324, 233–238. doi:10.1016/j.jbiotec.2020.11.001

Brancato, V., Comunanza, V., Imparato, G., Corà, D., Urciuolo, F., Noghero, A., et al. (2017). Bioengineered tumoral microtissues recapitulate desmoplastic reaction of pancreatic cancer. *Acta Biomater.* 49, 152–166. doi:10.1016/j.actbio.2016.11.072

Chen, C.-Y., Ke, C.-J., Yen, K.-C., Hsieh, H.-C., Sun, J.-S., and Lin, F.-H. (2015). 3D porous calcium-alginate scaffolds cell culture system improved human osteoblast cell clusters for cell therapy. *Theranostics* 5, 643–655. doi:10.7150/thno.11372

Choi, S.-W., Yeh, Y.-C., Zhang, Y., Sung, H.-W., and Xia, Y. (2010). Uniform beads with controllable pore sizes for biomedical applications. *Small* 6, 1492–1498. doi:10.1002/smll.201000544

Choi, S.-W., Zhang, Y., Yeh, Y.-C., Lake Wooten, A., and Xia, Y. (2012). Biodegradable porous beads and their potential applications in regenerative medicine. *J. Mater. Chem.* 22, 11442–11451. doi:10.1039/c2jm16019f

Chung, H. J., and Park, T. G. (2009). Injectable cellular aggregates prepared from biodegradable porous microspheres for adipose tissue engineering. *Tissue Eng. A* 15, 1391–1400. doi:10.1089/ten.tea.2008.0344

Clohessy, R. M., Cohen, D. J., Stumbraite, K., Boyan, B. D., and Schwartz, Z. (2020). *In vivo* evaluation of an electrospun and 3D printed cellular delivery device for dermal wound healing. *J. Biomed. Mater. Res. Part B Appl. Biomaterials* 108, 2560–2570. doi:10.1002/jbm.b.34587

Du, X. W., Zhou, J., Shi, J. F., and Xu, B. (2015). Supramolecular hydrogelators and hydrogels: From soft matter to molecular biomaterials. *Chem. Rev.* 115, 13165–13307. doi:10.1021/acs.chemrev.5b00299

Fernandes Patrício, T. M., Panseri, S., Montesi, M., Iafisco, M., Sandri, M., Tampieri, A., et al. (2019). Superparamagnetic hybrid microspheres affecting osteoblasts behaviour. *Mat. Sci. Eng. C* 96, 234–247. doi:10.1016/j.msec.2018.11.014

Ferrari, G., Cusella-De, A. G., Coletta, M., Paolucci, E., Stornaiuolo, A., Cossu, G., et al. (1998). Muscle regeneration by bone marrow-derived myogenic progenitors. *Science* 279, 1528–1530. doi:10.1126/science.279.5356.1528

Garstecki, P., Fuerstman, M. J., Stone, H. A., and Whitesides, G. M. (2006). Formation of droplets and bubbles in a microfluidic T-junction-scaling and mechanism of break-up. *Lab A Chip* 6, 437–446. doi:10.1039/b510841a

Gualeni, B., Coulman, S. A., Shah, D., Eng, P. F., Ashraf, H., Vescovo, P., et al. (2018). Minimally invasive and targeted therapeutic cell delivery to the skin using microneedle devices. *Br. J. dermatology* 178, 731–739. doi:10.1111/bjd.15923

Gupta, B., Plummer, C., Bisson, I., Frey, P., and Hilborn, J. (2002). Plasma-induced graft polymerization of acrylic acid onto poly(ethylene terephthalate) films: Characterization and human smooth muscle cell growth on grafted films. *Biomaterials* 23, 863–871. doi:10.1016/s0142-9612(01)00195-8

Hafeman, A. E., Li, B., Yoshii, T., Zienkiewicz, K., Davidson, J. M., and Guelcher, S. A. (2008). Injectable biodegradable polyurethane scaffolds with release of platelet-derived growth factor for tissue repair and regeneration. *Pharm. Res.* 25, 2387–2399. doi:10.1007/s11095-008-9618-z

Headen, D. M., Aubry, G., Lu, H., and García, A. J. (2014). Microfluidic-based generation of size-controlled, biofunctionalized synthetic polymer microgels for cell encapsulation. *Adv. Mat.* 26, 3003–3008. doi:10.1002/adma.201304880

Ho, H. V., Tripathi, G., Gwon, J., Lee, S.-Y., and Lee, B.-T. (2020). Novel TOCNF reinforced injectable alginate/β-tricalcium phosphate microspheres for bone regeneration. *Mater. Des.* 194, 108892. doi:10.1016/j.matdes.2020.108892

Hollister, S. J. (2005). Porous scaffold design for tissue engineering. *Nat. Mater.* 4, 518–524. doi:10.1038/nmat1421

Hölzl, K., Fürsatz, M., Göcerler, H., Schädl, B., Žigon-Branc, S., Markovic, M., et al. (2022). Gelatin methacryloyl as environment for chondrocytes and cell delivery to superficial cartilage defects. *J. tissue Eng. Regen. Med.* 16, 207–222. doi:10.1002/term.3273

Hong, Y., Gao, C., Xie, Y., Gong, Y., and Shen, J. (2005). Collagen-coated polylactide microspheres as chondrocyte microcarriers. *Biomaterials* 26, 6305–6313. doi:10.1016/j.biomaterials.2005.03.038

Huang, L. X., Xiao, L., Jung Poudel, A., Li, J. X., Zhou, P., Gauthier, M., et al. (2018). Porous chitosan microspheres as microcarriers for 3D cell culture. *Carbohyd. Polym.* 202, 611–620. doi:10.1016/j.carbpol.2018.09.021

Imai, K., Shimizu, K., Kamimura, M., and Honda, H. (2018). Interaction between porous silica gel microcarriers and peptides for oral administration of functional peptides. *Sci. Rep.* 8, 10971. doi:10.1038/s41598-018-29345-2

Jeon, S., Park, S. H., Kim, E., Kim, J.-y., Kim, S. W., and Choi, H. (2021). A magnetically powered stem cell-based microrobot for minimally invasive stem cell delivery via the intranasal pathway in a mouse brain. *Adv. Healthc. Mater* 10, 2100801. doi:10.1002/adhm.202100801

Jiang, W., Li, M., Chen, Z., and Leong, K. W. (2016). Cell-laden microfluidic microgels for tissue regeneration. *Lab a Chip* 16, 4482–4506. doi:10.1039/c6lc01193d

John, J. V., McCarthy, A., Wang, H., Chen, S., Su, Y., Davis, E., et al. (2020). Nanofiber microspheres: Engineering biomimetic nanofiber microspheres with tailored size, predesigned structure, and desired composition via gas bubble–mediated coaxial electrospray (small 19/2020). *Small* 16, 2070104. doi:10.1002/smll.202070104

Kankala, R. K., Wang, S. B., and Chen, A. Z. (2018). Microengineered organ-on-a-chip platforms towards personalized medicine. *Curr. Pharm. Des.* 24, 5354–5366. doi:10.2174/1381612825666190222143542

Kankala, R. K., Zhang, Y. S., Wang, S. B., Lee, C. H., and Chen, A. Z. (2017). Supercritical fluid technology: An emphasis on drug delivery and related biomedical applications. *Adv. Healthc. Mater* 6, 1700433. doi:10.1002/adhm.201700433

Kankala, R. K., Zhao, J., Liu, C.-G., Song, X.-J., Yang, D.-Y., Zhu, K., et al. (2019). Cell delivery: Highly porous microcarriers for minimally invasive *in situ* skeletal muscle cell delivery (small 25/2019). *Small* 15, 1970132. doi:10.1002/smll.201970132

Kankala, R. K., Zhu, K., Sun, X.-N., Liu, C.-G., Wang, S.-B., and Chen, A.-Z. (2018). Cardiac tissue engineering on the nanoscale. *ACS Biomaterials Sci. Eng.* 4, 800–818. doi:10.1021/acsbiomaterials.7b00913

Khademhosseini, A., and Langer, R. (2016). A decade of progress in tissue engineering. *Nat. Protoc.* 11, 1775–1781. doi:10.1038/nprot.2016.123

Khademhosseini, A., Langer, R., Borenstein, J., and Vacanti, J. P. (2006). Microscale technologies for tissue engineering and biology. *Proc. Natl. Acad. Sci. U. S. A.* 103, 2480–2487. doi:10.1073/pnas.0507681102

Kim, S. E., Yun, Y. P., Shim, K. S., Park, K., Choi, S. W., Dong, H. S., et al. (2015). Fabrication of a BMP-2-immobilized porous microsphere modified by heparin for bone tissue engineering. *Colloids Surfaces B Biointerfaces* 134, 453–460. doi:10.1016/j.colsurfb.2015.05.003

Kim, S. Y., Hwang, J.-Y., and Shin, U. S. (2016). Preparation of nano/macroporous polycaprolactone microspheres for an injectable cell delivery system using room temperature ionic liquid and camphene. *J. colloid interface Sci.* 465, 18–25. doi:10.1016/j.jcis.2015.11.055

Kuterbekov, M., Machillot, P., Lhuissier, P., Picart, C., Jonas, A. M., and Glinel, K. (2018). Solvent-free preparation of porous poly(l-lactide) microcarriers for cell culture. *Acta Biomater.* 75, 300–311. doi:10.1016/j.actbio.2018.06.009

Langer, R., and Vacanti, J. P. (1993). Tissue engineering. *Science* 260, 920–926. doi:10.1126/science.8493529

Lavanya, K., Chandran, S. V., Balagangadharan, K., and Selvamurugan, N. (2020). Temperature- and pH-responsive chitosan-based injectable hydrogels for bone tissue engineering. *Mater. Sci. Eng. C* 111, 110862. doi:10.1016/j.msec.2020.110862

Le, D., Keller, D., and Delaittre, G. (2019). Reactive and functional nanoobjects by polymerization-induced self-assembly. *Macromol. rapid Commun.* 40, e1800551. doi:10.1002/marc.201800551

Lee, G. Y., Kenny, P. A., Lee, E. H., and Bissell, M. J. (2007). Three-dimensional culture models of normal and malignant breast epithelial cells. *Nat. Methods* 4, 359–365. doi:10.1038/nmeth1015

Leijten, J., Rouwkema, J., Zhang, Y. S., Nasajpour, A., Dokmeci, M. R., and Khademhosseini, A. (2016). Advancing tissue engineering: A tale of nano-micro-and macroscale integration. *Small* 12, 2130–2145. doi:10.1002/smll.201501798

Leong, K. F., Cheah, C. M., and Chua, C. K. (2003). Solid freeform fabrication of three-dimensional scaffolds for engineering replacement tissues and organs. *Biomaterials* 24, 2363–2378. doi:10.1016/s0142-9612(03)00030-9

Li, B., Wang, X., Wang, Y., Gou, W., Yuan, X., Peng, J., et al. (2015). Past, present, and future of microcarrier-based tissue engineering. *J. Orthop. Transl.* 3, 51–57. doi:10.1016/j.jot.2015.02.003

Li, C. G., Zhao, S., Zhao, Y. Y., Qian, Y. F., Li, J. J., and Yin, Y. J. (2014). Chemically crosslinked alginate porous microcarriers modified with bioactive molecule for expansion of human hepatocellular carcinoma cells. *J. Biomed. Mater. Res. B* 102, 1648–1658. doi:10.1002/jbm.b.33150

Li, W., Zhang, L., Ge, X., Xu, B., Zhang, W., Qu, L., et al. (2018). Microfluidic fabrication of microparticles for biomedical applications. *Chem. Soc. Rev.* 47, 5646–5683. doi:10.1039/c7cs00263g

Liang, X., Xie, L., Zhang, Q., Wang, G., Zhang, S., Jiang, M., et al. (2022). Gelatin methacryloyl-alginate core-shell microcapsules as efficient delivery platforms for prevascularized microtissues in endodontic regeneration. *Acta Biomater.* 144, 242–257. doi:10.1016/j.actbio.2022.03.045

Liao, S., Meng, H., Zhao, J., Lin, W., Liu, X., Tian, Z., et al. (2022). Injectable adipose-derived stem cells-embedded alginate-gelatin microspheres prepared by electrospray for cartilage tissue regeneration. *J. Orthop. Transl.* 33, 174–185. doi:10.1016/j.jot.2022.03.007

Ligorio, C., Zhou, M., Wychowaniec, J. K., Zhu, X., Bartlam, C., Miller, A. F., et al. (2019). Graphene oxide containing self-assembling peptide hybrid hydrogels as a potential 3D injectable cell delivery platform for intervertebral disc repair applications. *Acta Biomater.* 92, 92–103. doi:10.1016/j.actbio.2019.05.004

Lim, S. M., Lee, H. J., Oh, S. H., Kim, J. M., and Lee, J. H. (2009). Novel fabrication of PCL porous beads for use as an injectable cell carrier system. *J. Biomed. Mater. Res. Part B Appl. Biomaterials* 90B, 521–530. doi:10.1002/jbm.b.31313

Liu, T., Stradford, C., Ambi, A., Centeno, D., Roca, J., Cattabiani, T., et al. (2022). Plasma-initiated graft polymerization of carbon nanoparticles as nano-based drug delivery systems. *Biofouling* 38, 13–28. doi:10.1080/08927014.2021.2008376

Liu, W., Li, Y., Feng, S., Ning, J., Wang, J., Gou, M., et al. (2014). Magnetically controllable 3D microtissues based on magnetic microcryogels. *Lab a Chip* 14, 2614–2625. doi:10.1039/c4lc00081a

Liu, X., Jin, X., and Ma, P. X. (2011). Nanofibrous hollow microspheres self-assembled from star-shaped polymers as injectable cell carriers for knee repair. *Nat. Mater.* 10, 398–406. doi:10.1038/nmat2999

Liu, Y. Q., Yu, Q. Q., Chang, J., and Wu, C. T. (2019). Nanobiomaterials: From 0D to 3D for tumor therapy and tissue regeneration. *Nanoscale* 11, 13678–13708. doi:10.1039/c9nr02955a

Liu, Y., Wang, R., Zarembinski, T. I., Doty, N., Jiang, C., Regatieri, C., et al. (2013). The application of hyaluronic acid hydrogels to retinal progenitor cell transplantation. *Tissue Eng. Part A* 19, 135–142. doi:10.1089/ten.tea.2012.0209

Loh, Q. L., and Choong, C. (2013). Three-dimensional scaffolds for tissue engineering applications: Role of porosity and pore size. *Tissue Eng. Part B Rev.* 19, 485–502. doi:10.1089/ten.teb.2012.0437

Lu, H., and Stenzel, M. H. (2018). Multicellular tumor spheroids (MCTS) as a 3D *in vitro* evaluation tool of nanoparticles. *Small* 14, 1702858. doi:10.1002/smll.201702858

Luetchford, K. A., Chaudhuri, J. B., and De Bank, P. A. (2020). Silk fibroin/gelatin microcarriers as scaffolds for bone tissue engineering. *Mater. Sci. Eng. C* 106, 110116. doi:10.1016/j.msec.2019.110116

Malda, J., van Blitterswijk, C. A., Grojec, M., Martens, D. E., Tramper, J., and Riesle, J. (2003). Expansion of bovine chondrocytes on microcarriers enhances redifferentiation. *Tissue Eng.* 9, 939–948. doi:10.1089/107632703322495583

Martin, I., Wendt, D., and Heberer, M. (2004). The role of bioreactors in tissue engineering. *Trends Biotechnol.* 22, 80–86. doi:10.1016/j.tibtech.2003.12.001

Matsunaga, Y. T., Morimoto, Y., and Takeuchi, S. (2011). Molding cell beads for rapid construction of macroscopic 3D tissue architecture. *Adv. Mat.* 23, H90–H94. doi:10.1002/adma.201004375

Matsushita, K. (2020). Adhesion-stabilizing long-distance transport of cells on tissue surface. *Phys. Rev. E* 101, 052410. doi:10.1103/physreve.101.052410

Miller, B., Hansrisuk, A., Highley, C. B., and Caliari, S. R. (2021). Guest–host supramolecular assembly of injectable hydrogel nanofibers for cell encapsulation. *ACS Biomaterials Sci. Eng.* 7, 4164–4174. doi:10.1021/acsbiomaterials.1c00275

Nilforoushzadeh, M. A., Khodadadi Yazdi, M., Baradaran Ghavami, S., Farokhimanesh, S., Mohammadi Amirabad, L., Zarrintaj, P., et al. (2020). Mesenchymal stem cell spheroids embedded in an injectable thermosensitive hydrogel: An *in situ* drug formation platform for accelerated wound healing. *ACS Biomaterials Sci. Eng.* 6, 5096–5109. doi:10.1021/acsbiomaterials.0c00988

Nilsson, K., Buzsaky, F., and Mosbach, K. (1986). Growth of anchorage-dependent cells on macroporous microcarriers. *Nat. Biotechnol.* 4, 989–990. doi:10.1038/nbt1186-989

Ofner, A., Moore, D. G., Rühs, P. A., Schwendimann, P., Eggersdorfer, M., Amstad, E., et al. (2017). High-throughput step emulsification for the production of functional materials Using a glass microfluidic device. *Macromol. Chem. Phys.* 218, 1600472. doi:10.1002/macp.201600472

Oyama, N., Minami, H., Kawano, D., Miyazaki, M., Maeda, T., Toma, K., et al. (2014). A nanocomposite approach to develop biodegradable thermogels exhibiting excellent cell-compatibility for injectable cell delivery. *Biomaterials Sci.* 2, 1057–1062. doi:10.1039/c4bm00074a

Phelps, E. A., Enemchukwu, N. O., Fiore, V. F., Sy, J. C., Murthy, N., Sulchek, T. A., et al. (2012). Maleimide cross-linked bioactive PEG hydrogel exhibits improved reaction kinetics and cross-linking for cell encapsulation and *in situ* delivery. *Adv. Mater.* 24, 64–70. doi:10.1002/adma.201103574

Pradhan, S., Clary, J. M., Seliktar, D., and Lipke, E. A. (2017). A three-dimensional spheroidal cancer model based on PEG-fibrinogen hydrogel microspheres. *Biomaterials* 115, 141–154. doi:10.1016/j.biomaterials.2016.10.052

Purcell, B. P., Lobb, D., Charati, M. B., Dorsey, S. M., Wade, R. J., Zellars, K. N., et al. (2014). Injectable and bioresponsive hydrogels for on-demand matrix metalloproteinase inhibition. *Nat. Mater.* 13, 653–661. doi:10.1038/nmat3922

Rahman, M. S., Hasan, M. S., Nitai, A. S., Nam, S., Karmakar, A. K., Ahsan, M. S., et al. (2021). Recent developments of carboxymethyl cellulose. *Polymers* 13, 1345. doi:10.3390/polym13081345

Salem, A. K., Rose, F. R. A. J., Oreffo, R. O. C., Yang, X., Davies, M. C., Mitchell, J. R., et al. (2003). Porous polymer and cell composites that self-assemble *in situ*. *Adv. Mater.* 15, 210–213. doi:10.1002/adma.200390047

Santana, H. S., Palma, M. S. A., Lopes, M. G. M., Souza, J., Lima, G. A. S., Taranto, O. P., et al. (2020). Microfluidic devices and 3D printing for synthesis and screening of drugs and tissue engineering. *Industrial Eng. Chem. Res.* 59, 3794–3810. doi:10.1021/acs.iecr.9b03787

Sheikhi, A., de Rutte, J., Haghniaz, R., Akouissi, O., Sohrabi, A., Di Carlo, D., et al. (2019). Microfluidic-enabled bottom-up hydrogels from annealable naturally-derived protein microbeads. *Biomaterials* 192, 560–568. doi:10.1016/j.biomaterials.2018.10.040

Siltanen, C., Diakatou, M., Lowen, J., Haque, A., Rahimian, A., Stybayeva, G., et al. (2017). One step fabrication of hydrogel microcapsules with hollow core for assembly and cultivation of hepatocyte spheroids. *Acta Biomater.* 50, 428–436. doi:10.1016/j.actbio.2017.01.010

Song, J., Chen, C., Wang, C., Kuang, Y., Li, Y., Jiang, F., et al. (2017). Superflexible wood. *ACS Appl. Mater. Interfaces* 9, 23520–23527. doi:10.1021/acsami.7b06529

Van Wezel, A. L. (1967). Growth of cell-strains and primary cells on micro-carriers in homogeneous culture. *Nature* 216, 64–65. doi:10.1038/216064a0

Vasile, C., Pamfil, D., Stoleru, E., and Baican, M. (2020). New developments in medical applications of hybrid hydrogels containing natural polymers. *Molecules* 25 (7), 1539. doi:10.3390/molecules25071539

Velasco, D., Tumarkin, E., and Kumacheva, E. (2012). Microfluidic encapsulation of cells in polymer microgels. *Small* 8, 1633–1642. doi:10.1002/smll.201102464

Wang, C., Yue, H., Feng, Q., Xu, B., Bian, L., and Shi, P. (2018). Injectable nanoreinforced shape-memory hydrogel system for regenerating spinal cord tissue from traumatic injury. *ACS Appl. Mater. Interfaces* 10, 29299–29307. doi:10.1021/acsami.8b08929

Wang, H., and Heilshorn, S. C. (2015). Adaptable hydrogel networks with reversible linkages for tissue engineering. *Adv. Mater.* 27, 3717–3736. doi:10.1002/adma.201501558

Wang, H., Zhu, D., Paul, A., Cai, L., Enejder, A., Yang, F., et al. (2017). Covalently adaptable elastin-like protein - hyaluronic acid (ELP - HA) hybrid hydrogels with secondary thermoresponsive crosslinking for injectable stem cell delivery. *Adv. Funct. Mater.* 27, 1605609. doi:10.1002/adfm.201605609

Wang, Q., Jamal, S., Detamore, M. S., and Berkland, C. (2011). PLGA-chitosan/PLGA-alginate nanoparticle blends as biodegradable colloidal gels for seeding human umbilical cord mesenchymal stem cells. *J. Biomed. Mater. Res. Part A* 96A, 520–527. doi:10.1002/jbm.a.33000

Wang, Y., Kankala, R. K., Wang, S.-B., Zhang, Y. S., and Chen, A.-Z. (2021). Cellularized polymeric microarchitectures for drug screening. *Smart Mater. Med.* 2, 96–113. doi:10.1016/j.smaim.2021.03.002

Wang, Y., Zhang, W. S., Gong, C. C., Liu, B., Li, Y. D., Wang, L. C., et al. (2020). Recent advances in the fabrication, functionalization, and bioapplications of peptide hydrogels. *Soft Matter* 16, 10029–10045. doi:10.1039/d0sm00966k

Wei, D.-X., Dao, J.-W., and Chen, G.-Q. (2018). A micro-ark for cells: Highly open porous polyhydroxyalkanoate microspheres as injectable scaffolds for tissue regeneration. *Adv. Mater.* 30, 1802273. doi:10.1002/adma.201802273

Wieduwild, R., Krishnan, S., Chwalek, K., Boden, A., Nowak, M., Drechsel, D., et al. (2015). Noncovalent hydrogel beads as microcarriers for cell culture. *Angew. Chem. Int. Edi.* 54, 4034–4038. doi:10.1002/ange.201411400

Wu, C. Y., Stoecklein, D., Kommajosula, A., Lin, J., Owsley, K., Ganapathysubramanian, B., et al. (2018). Shaped 3D microcarriers for adherent cell culture and analysis. *Microsystems Nanoeng.* 4, 21. doi:10.1038/s41378-018-0020-7

Xia, Y., and Whitesides, G. M. (1998). Soft lithography. *Angew. Chem. Int. Ed.* 37, 550–575. doi:10.1002/(sici)1521-3773(19980316)37:5<550::aid-anie550>3.0.co;2-g

Xu, H., Zhang, L., and Cai, J. (2019). Injectable, self-healing, β-chitin-based hydrogels with excellent cytocompatibility, antibacterial activity, and potential as drug/cell carriers. *ACS Appl. Bio Mater.* 2, 196–204. doi:10.1021/acsabm.8b00548

Yanagawa, F., Sugiura, S., and Kanamori, T. (2016). Hydrogel microfabrication technology toward three dimensional tissue engineering. *Regen. Ther.* 3, 45–57. doi:10.1016/j.reth.2016.02.007

Zanoni, M., Pignatta, S., Arienti, C., Bonafè, M., and Tesei, A. (2019). Anticancer drug discovery using multicellular tumor spheroid models. *Expert Opin. Drug Discov.* 14, 289–301. doi:10.1080/17460441.2019.1570129

Zhang, C., Zhai, T., and Turng, L.-S. (2017). Aerogel microspheres based on cellulose nanofibrils as potential cell culture scaffolds. *Cellulose* 24, 2791–2799. doi:10.1007/s10570-017-1295-9

Zhang, S., Ma, B., Wang, S., Duan, J., Qiu, J., Li, D., et al. (2018). Mass-production of fluorescent chitosan/graphene oxide hybrid microspheres for *in vitro* 3D expansion of human umbilical cord mesenchymal stem cells. *Chem. Eng. J.* 331, 675–684. doi:10.1016/j.cej.2017.09.014

Zhao, L., Weir, M. D., and Xu, H. H. K. (2010). An injectable calcium phosphate-alginate hydrogel-umbilical cord mesenchymal stem cell paste for bone tissue engineering. *Biomaterials* 31, 6502–6510. doi:10.1016/j.biomaterials.2010.05.017

Zhao, X., Liu, S., Yildirimer, L., Zhao, H., Ding, R., Wang, H., et al. (2016). Injectable stem cell-laden photocrosslinkable microspheres fabricated using microfluidics for rapid generation of osteogenic tissue constructs. *Adv. Funct. Mater.* 26, 2809–2819. doi:10.1002/adfm.201504943

Zhu, P. G., and Wang, L. Q. (2017). Passive and active droplet generation with microfluidics: A review. *Lab A Chip* 17, 34–75. doi:10.1039/c6lc01018k

Frontiers in
Bioengineering and Biotechnology

Accelerates the development of therapies, devices, and technologies to improve our lives

A multidisciplinary journal that accelerates the development of biological therapies, devices, processes and technologies to improve our lives by bridging the gap between discoveries and their application.

Discover the latest Research Topics

See more →

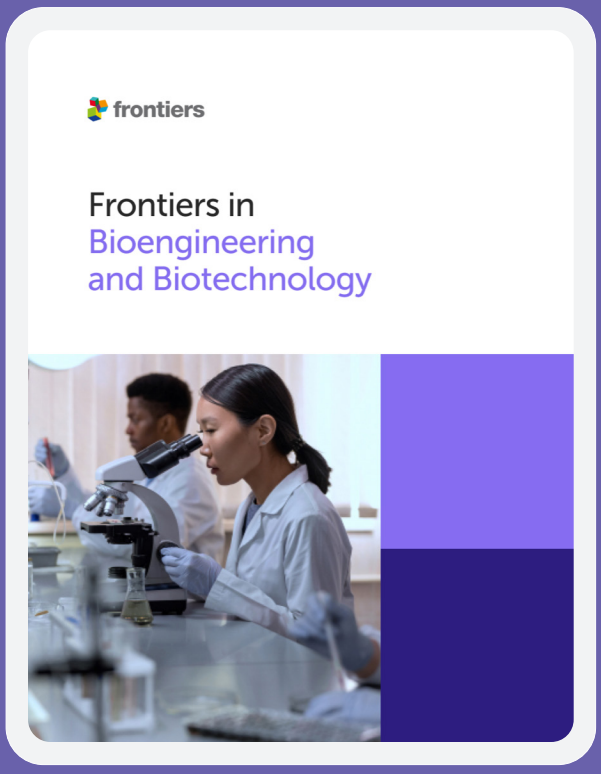

Frontiers

Avenue du Tribunal-Fédéral 34
1005 Lausanne, Switzerland
frontiersin.org

Contact us

+41 (0)21 510 17 00
frontiersin.org/about/contact